

# SENSORS & TRANSDUCERS

ISSN 1726-5479

vol. 156

9/13



**Sensors and Sensor Systems:  
Design, Data Fusion and Signal Processing**

# Sensors & Transducers

**International Official Journal of the International  
Frequency Sensor Association (IFSA) Devoted to  
Research and Development of Sensors and Transducers**

Volume 156, Issue 9, September 2013

---

**Editor-in-Chief**  
Sergey Y. YURISH



IFSA Publishing: Barcelona • Toronto

Copyright © 2013 IFSA Publishing. All rights reserved.

This journal and the individual contributions in it are protected under copyright by IFSA Publishing, and the following terms and conditions apply to their use:

*Photocopying:* Single photocopies of single articles may be made for personal use as allowed by national copyright laws. Permission of the Publisher and payment of a fee is required for all other photocopying, including multiple or systematic copyright, copyright for advertising or promotional purposes, resale, and all forms of document delivery.

*Derivative Works:* Subscribers may reproduce tables of contents or prepare list of articles including abstract for internal circulation within their institutions. Permission of the Publisher is required for resale or distribution outside the institution.

Permission of the Publisher is required for all other derivative works, including compilations and translations.

Authors' copies of Sensors & Transducers journal and articles published in it are for personal use only.

Address permissions requests to: IFSA Publisher by e-mail: [editor@sensorsportal.com](mailto:editor@sensorsportal.com)

Notice: No responsibility is assumed by the Publisher for any injury and/or damage to persons or property as a matter of products liability, negligence or otherwise, or from any use or operation of any methods, products, instructions or ideas contained in the material herein.

Printed in the USA.



# Sensors & Transducers

Volume 156, Issue 9,  
September 2013

www.sensorsportal.com

e-ISSN 1726-5479  
ISSN 2306-8515

**Editors-in-Chief:** professor Sergey Y. Yurish,  
Tel.: +34 696067716, e-mail: editor@sensorsportal.com

## Editors for Western Europe

Meijer, Gerard C.M., Delft Univ. of Technology, The Netherlands  
Ferrari, Vittorio, Università di Brescia, Italy  
Mescheder, Ulrich, Univ. of Applied Sciences, Furtwangen, Germany

## Editor for Eastern Europe

Sachenko, Anatoly, Ternopil National Economic University, Ukraine

## Editors for North America

Katz, Evgeny, Clarkson University, USA  
Datskos, Panos G., Oak Ridge National Laboratory, USA  
Fabien, J. Josse, Marquette University, USA

## Editor South America

Costa-Felix, Rodrigo, Inmetro, Brazil

## Editors for Asia

Ohyama, Shinji, Tokyo Institute of Technology, Japan  
Zhengbing, Hu, Huazhong Univ. of Science and Technol., China  
Li, Gongfa, Wuhan Univ. of Science and Technology, China

## Editor for Asia-Pacific

Mukhopadhyay, Subhas, Massey University, New Zealand

## Editor for Africa

Maki K., Habib, American University in Cairo, Egypt

## Editorial Board

Abdul Rahim, Ruzairi, Universiti Teknologi, Malaysia  
Abramchuk, George, Measur. Tech. & Advanced Applications, Canada  
Aluri, Geetha S., Globalfoundries, USA  
Ascoli, Giorgio, George Mason University, USA  
Atalay, Selcuk, Inonu University, Turkey  
Atghiaee, Ahmad, University of Tehran, Iran  
Augutis, Vyantas, Kaunas University of Technology, Lithuania  
Ayesh, Aladdin, De Montfort University, UK  
Baliga, Shankar, B., General Monitors, USA  
Barlingay, Ravindra, Larsen & Toubro - Technology Services, India  
Basu, Sukumar, Jadavpur University, India  
Bousbia-Salah, Mounir, University of Annaba, Algeria  
Bouvet, Marcel, University of Burgundy, France  
Campanella, Luigi, University La Sapienza, Italy  
Carvalho, Vitor, Minho University, Portugal  
Changhai, Ru, Harbin Engineering University, China  
Chen, Wei, Hefei University of Technology, China  
Cheng-Ta, Chiang, National Chia-Yi University, Taiwan  
Chung, Wen-Yaw, Chung Yuan Christian University, Taiwan  
Cortes, Camilo A., Universidad Nacional de Colombia, Colombia  
D'Amico, Arnaldo, Università di Tor Vergata, Italy  
De Stefano, Luca, Institute for Microelectronics and Microsystem, Italy  
Ding, Jianning, Changzhou University, China  
Djordjević, Alexandar, City University of Hong Kong, Hong Kong  
Donato, Nicola, University of Messina, Italy  
Dong, Feng, Tianjin University, China  
Erkmen, Aydan M., Middle East Technical University, Turkey  
Gaura, Elena, Coventry University, UK  
Gole, James, Georgia Institute of Technology, USA  
Gong, Hao, National University of Singapore, Singapore  
Gonzalez de la Rosa, Juan Jose, University of Cadiz, Spain  
Goswami, Amarjyoti, Kaziranga University, India  
Guillet, Bruno, University of Caen, France  
Hadjiloucas, Sillas, The University of Reading, UK  
Hao, Shiyong, Michigan State University, USA  
Hui, David, University of New Orleans, USA  
Jaffrezic-Renault, Nicole, Claude Bernard University Lyon 1, France  
Jamil, Mohammad, Qatar University, Qatar  
Kaniusas, Eugenijus, Vienna University of Technology, Austria  
Kim, Min Young, Kyungpook National University, Korea  
Kumar, Arun, University of Delaware, USA  
Lay-Ekuakille, Aime, University of Lecce, Italy  
Li, Si, GE Global Research Center, USA  
Lin, Paul, Cleveland State University, USA  
Liu, Aihua, Chinese Academy of Sciences, China  
Liu, Chenglian, Long Yan University, China

Mahadi, Muhammad, University Tun Hussein Onn Malaysia, Malaysia  
Mansor, Muhammad Naufal, University Malaysia Perlis, Malaysia  
Marquez, Alfredo, Centro de Investigacion en Materiales Avanzados, Mexico  
Mishra, Vivekanand, National Institute of Technology, India  
Moghavvemi, Mahmoud, University of Malaya, Malaysia  
Morello, Rosario, University "Mediterranea" of Reggio Calabria, Italy  
Mulla, Imtiaz Sirajuddin, National Chemical Laboratory, Pune, India  
Nabok, Aleksey, Sheffield Hallam University, UK  
Neshkova, Milka, Bulgarian Academy of Sciences, Bulgaria  
Passaro, Vittorio M. N., Politecnico di Bari, Italy  
Patil, Devidas Ramrao, R. L. College, Parola, India  
Penza, Michele, ENEA, Italy  
Pereira, Jose Miguel, Instituto Politecnico de Seteбал, Portugal  
Pogacnik, Lea, University of Ljubljana, Slovenia  
Pullini, Daniele, Centro Ricerche FIAT, Italy  
Reig, Candid, University of Valencia, Spain  
Restivo, Maria Teresa, University of Porto, Portugal  
Rodríguez Martínez, Angel, Universidad Politécnica de Cataluña, Spain  
Singhal, Aji, University of Mississippi, USA  
Sadeghian Marnani, Hamed, TU Delft, The Netherlands  
Sapozhnikova, Ksenia, D. I. Mendeleev Institute for Metrology, Russia  
Singhal, Subodh Kumar, National Physical Laboratory, India  
Shah, Kriyang, La Trobe University, Australia  
Shi, Wendian, California Institute of Technology, USA  
Shmaliy, Yuriy, Guanajuato University, Mexico  
Song, Xu, An Yang Normal University, China  
Srivastava, Arvind K., LightField, Corp, USA  
Stefanescu, Dan Mihai, Romanian Measurement Society, Romania  
Sumriddetchajorn, Sarun, Nat. Electr. & Comp. Tech. Center, Thailand  
Sun, Zhiqiang, Central South University, China  
Sysoev, Victor, Saratov State Technical University, Russia  
Thirunavukkarasu, I., Manipal University Karnataka, India  
Thomas, Sadiq, Heriot Watt University, Edinburgh, UK  
Tianxing, Chu, Research Center for Surveying & Mapping, Beijing, China  
Vazquez, Carmen, Universidad Carlos III Madrid, Spain  
Wang, Jiangping, Xian Shiyong University, China  
Xu, Han, Measurement Specialties, Inc., USA  
Xu, Weihe, Brookhaven National Lab, USA  
Xue, Ning, Agiltron, Inc., USA  
Yang, Dongfang, National Research Council, Canada  
Yang, Shuang-Hua, Loughborough University, UK  
Yaping Dan, Harvard University, USA  
Zakaria, Zulkarnay, University Malaysia Perlis, Malaysia  
Zhang, Weiping, Shanghai Jiao Tong University, China  
Zhang, Wenming, Shanghai Jiao Tong University, China

# Contents

Volume 156  
Issue 9  
September 2013

www.sensorsportal.com

ISSN: 2306-8515  
e-ISSN 1726-5479

## Research Articles

<b>The Novel Image Signal Analysis of Monitoring Video Based on CMOS Image Sensor</b> <i>Junhui Fu, Jingqiao Lv</i> .....	1
<b>Development CMOS Sensor Image Acquisition Algorithm Based on Wireless Sensor Networks</b> <i>Chongke Wang, Zhengben Zhang</i> .....	10
<b>Application of RFID Technology and Ontology Model in Designing Smart Home System</b> <i>Hongsheng Xu, Ruiling Zhang</i> .....	18
<b>Design and Development of Multimedia Video Monitoring System Based on Wireless Sensor Network</b> <i>Liang Song, Ming Xu, Hong Qiao</i> .....	26
<b>Error Analysis of Rotary SINS Sensor</b> <i>Zhenguo Yuan, Lin Zhao</i> .....	35
<b>Design of Reflective Optical Fiber Current Sensor Based on Improved Phase Modulation</b> <i>Yajun Wang, Xuemei Guo</i> .....	40
<b>Modeling of Microdiaphragm Based Pressure Sensor with Application for Gas Turbine Engine Condition Monitoring</b> <i>Ahmad Ghanbari, Ehsan Qaredaghi</i> .....	48
<b>Development of a Model Depicting Optimum Performance of Liquid Catheter Sensor for Pressure Measurement</b> <i>Suman Halder</i> .....	55
<b>Manufacture of Piezoelectric Sensor Dedicated to Airflow Velocity Detection</b> <i>Xiaoping Wang, Dengpan Wang, Jing Yang</i> .....	62
<b>Magnetic Flux Leakage (MFL) Capsule Material Selection and Its Robustness Analysis in Oil and Gas Pipeline</b> <i>Maliki Ibrahim, Zulkarnay Zakaria, Ali Aiman Mustapha, Dennis Desmond Surin, Mohdhasir Ayob, Ibrahim Balkhis, Ruzairi Abdul Rahim</i> .....	67
<b>Design and Analysis of Magnetic Flux Leakage Capsule</b> <i>Maliki Ibrahim, Zulkarnay Zakaria, Ali Aiman Mustapha, Marisah Norhasan, Mohd Nasir Ayob, Ibrahim Balkhis, Ruzairi Abdul Rahim</i> .....	75
<b>Using BP Neural Network and Kalman Filter to Signal Processing of MEMS Inertial Sensors</b> <i>Wenxian Xiao, Hao Zhang, Xiaoqin Ma</i> .....	81

<b>An Embedded-technology-based Security Monitoring System Design of Intelligent Building</b> <i>Yuanyi Zhang, Ying Zhang</i> .....	89
<b>Design of Novel Intelligent Transportation System based on Wireless Sensor Network and ZigBee Technology</b> <i>Zhou Yu, Weizeng Gao, Xiangang Zuo</i> .....	95
<b>Method for Identifying Mechanical Vibration Source Based on Detected Signals by Optical Fiber</b> <i>Hongquan Qu, Guoxiang Li, Liping Pang</i> .....	103
<b>Increasing Geometric Resolution of Data Supplied by Quickbird Multispectral Sensors</b> <i>Claudio Parente and Raffaele Santamaria</i> .....	111
<b>Research on Infrared Small Target Detection and Tracking Algorithms Based on Wavelet Transformation</b> <i>Liping Lu</i> .....	116
<b>The Design of Check Control System of Strip Steel Deviation Correction and the Heat Structure Coupling Analysis on Relative Sensor</b> <i>Hong-Yu Liu, Ze-Ning Xu</i> .....	123
<b>Multi-sensor Target Recognition Based on VIKOR</b> <i>Haiping Ren, Lianwu Yang</i> .....	130
<b>Design of Wireless Sensor Network Security and Solution by MAC Protocol and Topology Control Technology</b> <i>Zhen Liu, Yanhao Chen, Xiaoqin Ma</i> .....	136
<b>Real-Time Surveillance Performance under Different Sensing Models in Duty-Cycled Sensor Networks</b> <i>Yanjun Li</i> .....	144
<b>A General Robust Key Management Scheme for Wireless Multihop Communication Network</b> <i>Danyang Qin, Renheng Xu, Lin Ma and Qun Ding</i> .....	150
<b>System Dynamics Modeling and Intelligent Tracking Control Based on Wireless Sensor Networks for Robot</b> <i>Qu Xiao-Yuan, Zhang Feng, Zhang Yong-Heng, Dong Jian-Gang</i> .....	156
<b>WSN Message Authentication Code Based on Chaos and XOR-Encryption</b> <i>Bai En-Jian, Zhu Jun-Jie, Wu Liang-Cheng</i> .....	161
<b>Three Dimensional Acoustical Imaging Based on Isosurface Technique for Bulk Material</b> <i>He Guochao, Ding Jinwen, V. M. Levin, Dong Lanfang, A. N. Bogachenkov, Li Kang, Yao Chuanming, K. V. Zakutailov, Yu. S. Petronyuk, Li Feng, E. S. Morokov</i> .....	168
<b>Design and Simulation of Two Stage Pressure-controlling Anti-overflow Breathing Valve in Tanker</b> <i>Yonggang Zuo, Zhuxin Li, Jun Chen, Jing Yang, Zhen Zhang</i> .....	176
<b>Research on Key Technology of Cloud Design for Mechanical Equipment</b> <i>Jun Chen, Gang Guo, Yonggang Zuo</i> .....	181
<b>The Experimental Study of the Plateau Performance of the F6L913 Diesel Engine</b> <i>Weiming Zhang, Jiang Li</i> .....	187

<b>The Diagnosis of Tool Wear Based on EMD and GA-B-Spline Network</b> <i>Weiqing Cao, Pan Fu, Xiaohui Li</i> .....	195
<b>Risk Assessment on Railway Signal System Based on Fuzzy-FMECA Method</b> <i>You-Peng Zhang, Zheng-Jie Xu, Hong-Sheng Su</i> .....	203
<b>Study on Monte Carlo Simulation of Intelligent Traffic Lights Based on Fuzzy Control Theory</b> <i>Zeng Shengda, Wu Lurong, Jing Lin, Wu Bizhi</i> .....	211
<b>Computational-geometry-based Plant Organs Classification and Foliage 3D Reconstruction from Point Cloud Data</b> <i>Ting Yun, Mingxing Gao, Yanming Wang, Xiaofeng Liu</i> .....	217
<b>Intelligent Model of Home Furnishing and Transportation Based on Improved RFID Web Fuzzy Clustering</b> <i>Xiaohong Luo, Yali Wang</i> .....	263
<b>MEMS Multi-Fields Uniform Model Simulation and Optimization Method Research and Application</b> <i>Gong Youping, Chen Huipeng, Liu Haiqiang, Li Zhihua, Chen Guojin</i> .....	237
<b>Classification of Fatty Fat Acid in Palm Oil Using Near Infrared Spectroscopy</b> <i>Herlina Abdul Rahim, Siti Nurhidayah Naqiah Abdull Rani</i> .....	247
<b>Near Infrared Spectroscopy Measurement: The Assessment of Amylose Content in Rice Grain</b> <i>Herlina Abdul Rahim, Syahira Ibrahim</i> .....	251
<b>Portable Synthetic Testing System Based on Information Fusion</b> <i>Zhao Li Ming, Liu He Ping, Zhang Bing</i> .....	259
<b>Investigating the Fire Behavior of a Boiler Explosion in a Semiconductor Factory Using Computer Simulation and Verification</b> <i>C. S. Lin, C. C. Yu, T. C. Chen, C. C. Lai, S. C. Wang, and H. C. Lu</i> .....	268
<b>The Design of an Embedded Video Data Acquisition System</b> <i>Chongyu Wei, Weichen Wei, Zuping Gu</i> .....	276
<b>Application of Serial Min-max Decoding Algorithm Based on Variable Weighting for Nonbinary LDPC Codes in Optical Communication</b> <i>Zhongxun Wang, Xinglong Gao</i> .....	286
<b>The AUV Location and Location Error Analysis Based on Binocular Stereo Vision</b> <i>Jun-Chai Gao, Ming-Yong Liu, Fei Xu</i> .....	291
<b>Semi-Supervised Based Hyperspectral Imagery Classification</b> <i>Zhijun Zheng, Yanbin Peng</i> .....	298
<b>Humidity Sensing Properties and Temperature Conductivity Studies of Sol-Gel Derived Novel Nanomaterials of Lanthanum Strontium Chromites</b> <i>B. Avila Josephine, V. Jeseentharani, V. Mary Teresita, Mary George, S. Arul Antony</i> .....	304
<b>Synthesis, Characteristics and Enhanced Sulfur Dioxide Sensing Properties of Cu-doped SnO<sub>2</sub> Microspheres</b> <i>Shudi Peng, Gaolin Wu, Wei Song</i> .....	310
<b>Preparation and Test of Fe/Cr/Al -Ni/Cr Composite Film Micro-heater</b> <i>Qiaohua Feng, Yunbo Shi, Mengmeng Wang, Fang Du, Lining Sun</i> .....	317
<b>Digital Double-loop PID Controller for Inverted Pendulum</b> <i>Ming Li</i> .....	324

<b>Computational Method of Aging Index for Catalytic Converter Based on Wavelet Transform</b> <i>Guosheng Feng, Bo Feng, Sumei Jia, Xiaoyan Niu</i> .....	330
<b>The Short-term Predicting Method of Algal Blooms Based on Libsvm and Elman Neural Network Modeling</b> <i>Mengxun Li, Zaiwen Liu Wei, Hua, Xue Zhang, Chengrui Wu</i> .....	337
<b>A NLOS Localization Algorithm Based on BPNN</b> <i>Bi Zeng, XiaoHu Chen, JianQi Liu, XiaoHua Ha</i> .....	345
<b>A Frequent Pattern Mining Algorithm Based on Concept Lattice</b> <i>Changsheng Zhang, Jing Ruan, Haijiang Xia, Hailong Huang, Bingru Yang</i> .....	351
<b>The Algorithms of Image Wavelet Optimize Splicing and Fusion based on Improved Region Energy</b> <i>Xiangqian Chen, Dong Dai</i> .....	360
<b>Aptamer Biosensor for Antibiotic Residues Detection in Food Analysis</b> <i>Yemin Guo, Xiangyou Wang, Xia Sun</i> .....	368
<b>Electrochemical Immunosensor for Pesticide Residues Detection in Food Analysis</b> <i>Yemin Guo, Zhili Gong, Yaoyao Cao, Xiangyou Wang, Xia Sun</i> .....	374
<b>Forecast Surface Quality of Abrasive Water Jet Cutting Based on Neural Network and Verified by Experiments</b> <i>Gui-Lin Yang</i> .....	379
<b>Computational Simulation and Analysis of Energy-saving Glazing Units in Residential Buildings</b> <i>Zhuolun Chen</i> .....	384

Authors are encouraged to submit article in MS Word (doc) and Acrobat (pdf) formats  
by e-mail: [editor@sensorsportal.com](mailto:editor@sensorsportal.com). Please visit journal's webpage with preparation instructions:  
<http://www.sensorsportal.com/HTML/DIGEST/Submission.htm>

## The Novel Image Signal Analysis of Monitoring Video Based on CMOS Image Sensor

<sup>1</sup> Junhui FU, <sup>2</sup> Jingqiao LV

<sup>1</sup> Henan Institute of Science and Technology, Henan Xinxiang, 453003, China

<sup>2</sup> Xinxiang Medical University, Henan Xinxiang, 453003, China

<sup>1</sup> Tel.: 13782582500

<sup>1</sup> E-mail: wangguoedu@163.com

Received: 1 September 2013 / Accepted: 25 August 2013 / Published: 30 September 2013

---

**Abstract:** The image sensor is the most important part of video and still image processing line in digital video or still camera. Data of CMOS process will produce noise in long transmission distance; therefore it must first be amplified and integrated each pixel data. The choice of medium and apparatus for transmitting image and the other the control signal will be directly related to the quality and reliability of the monitoring system. CMOS image sensor has the characteristics of low power, high integration and flexible function. The paper proposes the novel image signal analysis of monitoring video based on CMOS image sensor. In this paper, simulation results shows by using analog signal hardware simulation that the system can achieve the intended function and achieve the ideal effect. *Copyright © 2013 IFSA.*

**Keywords:** CMOS, Image sensor, Image signal analysis.

---

### 1. Introduction

Image sensor is the principle of photoelectric conversion converts the image data into a device for a series of electronic signals. Contact image sensor CIS is a new type of image sensor appeared in the late 80's, is a kind of photoelectric scanning device based on CMOS technology. CIS compared to CCD has the advantages of small volume, high speed, low cost, simple installation and debugging etc. But whether CIS or CCD should consider the interference signal, and it is sensor bias and other factors on the image signal, only to exclude these effects, to a true representation of image information.

CMOS image sensor is produced in the nineteen eighties, the manufacturing technology of CMOS technology was not high, and so the noise sensor in the application of large, commercial process has been very slow. Now, with the continuous improvement process, the application range of CMOS image sensor

is also expanding, relates to the digital products, communications, industrial, medical and other fields. Compared with CCD, CMOS image sensor has the advantages of small volume, low power consumption, low cost [1]. CMOS image sensor, IBIS5-B-1300 image sensor is a high performance, high dynamic range. Image sensor work needs to have driven timing signal is correct.

The system is mainly composed of a plane mirror tracking device, control and drive circuit, position limiting circuit, CMOS image sensor etc. Tracking device object, image sensor is fixed on the plane mirror center. The image sensor products are mainly divided into CCD, CMOS and CIS sensor three. At present, CMOS is not only inexpensive, and has realized the digital output, software programmable control, greatly reduce the difficulty of system design; improve the flexibility of the system, design of anti-interference and stability.

The image sensor is according to the manufacturing process and design. Therefore, the final device, light enters from the front line of control between the metal, and then focused on the photoelectric detector. Since, for the larger pixels, FSI is very effective, because the pixel stack (pixel stack) and the height of the pixel area ratio is large, the pixel aperture is large. Pixel shrinking to a series of pixel technology innovation is to solve the limitations of front illumination technology in material and manufacture. For example, FSI has to take a number of technical innovation and process improvement, such as the shape optimization of micro lens, color filter, optimization of concave type pixel array, light guides and antireflection coating technology, optical path optimization FSI pixels.

Recently the CMOS image sensor attached importance to the primary reason is that the past is much lower than the sensitivity of the CCD gradually resolved. As compared with CCD, CMOS sensor has a better production, and it is easy to implement other logic circuits, SoC (System on Chip) products, and it is difficult to achieve in the CCD. Especially the CMOS sensor, unlike the CCD requires special manufacturing processes; it can be directly used for DRAM and other large batch production equipment. In this way, CMOS image sensor is likely to cost structure formation is different from that of CCD image sensor. The paper proposes the novel image signal analysis of monitoring video based on CMOS image sensor.

## 2. Analysis Monitoring Video of Image Sensor

In the monitoring system, monitoring and image transmission is a vital part of the system, the choice of medium and apparatus for transmitting image and the other the control signal will be directly related to the quality and reliability of the monitoring system. At present, in the monitoring system for image signal transmission medium main coaxial cable, twisted pair and optical fiber, transmission equipment are corresponding to the coaxial video amplifier, twisted pair video transmission equipment and optical.

This change in the field of image sensor is a microcosm of the sensor technology changes. New technology development of new features, the biggest characteristic of sensor technology is introduced into the multidisciplinary now, along with the electronics, MEMS (Micro-Electro-Mechanical System), the rapid development of biotechnology, physics, chemistry, optics and so on technology, as well as human cognition of natural change, sensor technology has entered a critical stage from traditional to new breakthrough sensor technology development, is expected in the future will show the miniaturization, digitization, multifunction, intelligent and networked trend.

Because the camera optical axis and the ground form a certain angle, so the imaging are trapezoidal distortion; in order to expand the field of vision, the wide-angle lens is increasingly used by many teams, so there is a barrel distortion. These two kinds of distortion, each using wide-angle lens camera team have problems [2]. Many teams have avoided this problem, directly using the pixel image after preprocessing control. But if the pixel is converted into the actual physical coordinates, is undoubtedly more intuitive, convenient for programming or modeling, and the method proposed in this paper, which can solve these two kinds of distortion effectively, the actual operation is not complicated.

Image acquisition is the key part of security and surveillance video chain, it is because it is closely related with the image quality acquired for image signal processing ability to extract effective information from the video stream, may seem esoteric, but in fact, is the sensor quality and processing quality of the combination sensor output. The development trend of safety monitoring system is the image processing function of migration – to the network edge is moved to a camera inside, close to the sensor, as is shown by equation 1.

$$L(x(k),u(k))=(R(k)-x(k))^T(R(k)-x(k)) \quad (1)$$

Remove the signal on CMOS imaging device in the acquisition of photoelectric image signals at the same time, the image information it and at the same time of each unit, so the speed is much faster than the CCD imaging device. Because the CMOS imaging device, the column electrode can be high-speed driving, plus on the same chip as the A/D conversion, image signal can quickly take out, so it can move at a very high frame rates. If some designed for machine vision CMOS, claims can be up to 1000 frames per second frame.

Control for position, through the I2C bus with the external microprocessor to display controller route in FPGA. A total of 256 control and parameter register. In order to avoid the emergence of television interference, through the parameter I2C write must deal with in the blanking period. Data input and can be activated, the processor release control register. Through further register, processor controller rows currently displayed. These functions can be solved directly in FPGA design. According to the monitoring of the IC2 register set, designers need from IC2 device (slave), I/O port, state machine replication, and these parameters, the access from IC2 device (slave) internal memory interface, providing for arbitration. For VHDL or Verilog HDL to develop the FPGA spend relatively more time, code reusability is limited to HDL coding controller.

Because the experimental plane and true sight plane is a pure geometric relation, so this part of the conversion function can use geometric derivation. The formula is more complex, not the one listed here. The disadvantage is that a lot of formula of the

maximum of  $\sin()$ ,  $\cos()$ , the operation of trigonometric function, but the single-chip to do this operation will spend a lot of time, so we should try to avoid trigonometric, square root operation. Moreover, if the wide-angle lens or camera frame lower, B will be from the A point far away and cannot find B. So this method is not universal. The experiment itself is more complex, as is shown by equation 2.

$$\hat{v}_x^2(\tau_j) = \frac{1}{M_j} \sum_{k=L_j-1}^{N-1} \tilde{W}_{j,k}^2 \quad (2)$$

Using these sensors manufacturers interface, so that the electronic image signal from the sensor, and into the processing logic downstream. FPGA provides a cost effective, very small size of the programmable logic platform, can easily converts the signal from the image sensor of the interface to a digital signal, the logic for downstream processing.

FPGA provides programmable mechanism of cost-effective, to adapt to a variety of signal coding scheme, register management schemes and sensor interfaces, and different types of sensors to provide programming support.

The pixel array is the most important part of CMOS image sensor, now most pixel unit using active pixel structure, as shown in Fig. 1. PD is usually N+ / P-well diodes, the reverse bias of PD, as a photosensitive element in the sensor [3]. In the charging period, a reset pulse  $V_{reset\_p}$  is high level, M1 conduction, PD power supply for charging; the integration period,  $V_{reset\_p}$  is low, M1 is off, due to the incident light irradiation, PD generates a reverse photocurrent, the discharge of PD; VN node voltage N decreases, and the VN of the incident light intensity slope drop is proportional to the. When the integral cycle is over, the row selection signals  $V_{row\_s}$  generates a pulse on the M3, VN the source follower output to the post-processing circuit.

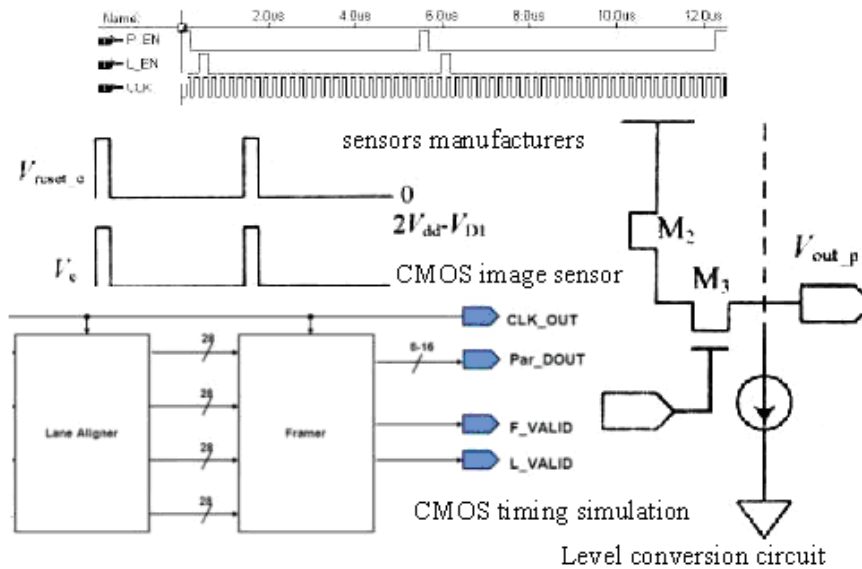


Fig. 1. The design of CMOS timing simulation and level conversion circuit

The camera has three core components: camera, image sensor and compression processing chip. Among them, the image sensor is the core part of the image acquisition and processing. At present, the CCD and CMOS sensors are two kinds of image sensors are widely used, both by the photosensitive diode (photodiode) is a photoelectric conversion, the image is converted into digital data, but the main difference is the digital data transfer in different ways. CCD no distortion in the transmission of data, so each pixel data can be collected to the edge and then amplifying processing; and CMOS process will produce noise in the data transmission distance is long, therefore, must first be amplified, integrated each pixel data. Also because of its different data transmission mode, CCD and CMOS sensor has many differences in effectiveness and application.

The sensor manufacturers to configure a series interface, used for image signal will leave the chip to the downstream logic processing. It is very common, the data quantity of the same sensor manufacturers from the chip extracted according to the need to use different interface [4]. For example, modern sensor with mega pixel resolution required in the given cycle time was more than sensor has only a VGA resolution data. Like the high dynamic range (HDR) this requirement also increases the amount of data, need to read data from the image sensor in each image frame, and to support the smooth, low latency and high quality video, need to extract frames from the sensor chip in a given period of time, it also affects the sensor interface selection, as is shown by Fig. 1.

In addition to mobile phone market, OV7675 has attracted a notebook computer, Net book and Webcam customers pay more attention to. The OV7675's small size allowed ultra-thin camera module, when combined with the low light performance is remarkable, which of these terminal market becomes an attractive solution. 1/9 inch OV7675 using 2.5 micron OmniPixel3 – a unique HS<sup>TM</sup> pixel design, which makes it possible to provide first-class low light sensitivity best (1800 MV/Lux seconds), relative to the solution of most competitive VGA, greatly reduce the noise and provides excellent color reproduction. The OV7675 SOC sensor provides full functional integrity of the VGA (640x480) camera, is able to run at full resolution at a rate of 30 frames per second, and the user can fully control the image quality, format and output data transmission.

Most of the ISP (image processing) parallel sensor interface device supports the traditional CMOS, but usually lack of high-speed serial interface support. Many ISP parallel running speed interface is far more than the parallel interface sensor. However, because the sensor is moved to different serial interface, ISP logic device needs to switch to the parallel interface. Therefore FPGA bridging devices require high speed serial data into parallel format. For manufacturers of ASSP signal processing (they have the support of parallel CMOS sensor interface faster ready-made products), FPGA solves is connected to a high speed serial sensor problem.

Because the CMOS sensor using CMOS technology semiconductor circuit is the most commonly used, can easily be peripheral circuit (such as AGC, CDS, Timing, generator, or DSP) is integrated into the sensor chip, so it can save the periphery chip cost; in addition, because CCD uses charge transfer way of transmitting data, as long as there is a pixel cannot run, will lead to a whole row of data cannot be transmitted, so CCD control sensors yield many more than the CMOS sensor is difficult, even experienced manufacturer also is very difficult in the products of the half a year to break through the 50 % level, therefore, the cost will be higher than the CCD sensor, CMOS sensor, as is shown by equation 3.

$$PV(x) = \frac{1}{y_2 - y_1} \sum_{y=y_1}^{y_2} I(x, y), \quad x \in (x_1, x_2) \quad (3)$$

The FPGA chip is parallel operation, each oscillation cycle can perform tasks, while the microcontroller (such as the 8051 series) of each instruction requires 12 oscillation cycles. For example, changes in I/O port of the fastest also need 24 oscillation cycle, while FPGA only need 2 oscillation cycle, so the oscillation period under the same, FPGA faster [5].

From the current trend, CMOS wins a significantly greater chance. On the one hand, with the development of technology, the sensitivity of

CMOS is improved rapidly, it is reported on the market at present is committed to research CMOS makers have developed CMOS specific 720 p and 1080 p device sensitivity performance with CCD approach. On the other hand, although the same size CCD sensor resolution is better than CMOS sensor, but if we do not consider the size limit, the advantage of CMOS in the volume rate can effectively overcome the difficulties of large size of photosensitive component manufacture, so CMOS will have more advantage in higher resolution. In addition, the response speeds of the CMOS faster than CCD, a large amount of data, so it is more suitable to the characteristics of high-definition monitor.

Programmable logic as a bridge between the image sensor and ASSP is facing three challenges. First of all, the FPGA must provide support for the interface signal. Second, FPGA I/O must have the gearing logical enough to support a fast serial sensor interface. Third, the FPGA must provide cost-effective very small size, to adapt to the modern camera for compact appearance requirements.

Color sensor used in this design is CLS9032. The sensor has 2 vertical connecting the PN junction, the thickness can be to an optical filter to the role of color sensors play. The shorter wavelengths of light on the silicon surface are absorbed, and the longer wavelength light to reach the deeper position will be absorbed. This sensitivity based on spectrum, to select the signal according to the wavelength of light (color). The use of logarithmic current between the 2 photodiode ratio methods is as signal processing. Irradiation with light of different colors, the 3 pin of the color red, green, blue sensor area will output current signal, but the current signal corresponding color pin output than the other pin output current signal strength. Using this principle can effectively avoid the output current external environment caused by the ups and downs, so this device has high reliability.

The sensor core (Sensor Core) part comprises a photosensitive array, exposure control and readout circuit, variable gain amplifier (PGA) and an analog-to-digital converter (ADC), mainly to complete the image acquisition function. Data of the original image sensor nuclear export to image processor (ISP), ISP completed a series of image processing and image conversion function, which comprises the following process: compensation, digital gain and white balance, lens shading correction, bad pixel detection and correction, color interpolation, smoothing and edge enhancement, GAMMA correction, color correction, brightness, saturation and contrast adjustment, image size conversion, color space conversion, image data packing output. The control module to complete the automatic exposure control, automatic white balance, 50 Hz/60 Hz scintillation detection and other functions, to control the sensor core and ISP, communication and multimedia processor.

$$F(\phi, \theta) = \sum_{n=0}^{N-1} A_n e^{j[\alpha_n - \kappa R \cos(\phi - \phi_n) \sin \theta]} \quad (4)$$

In the monitoring system, monitoring and image transmission is a vital part of the system, the choice of medium and apparatus for transmitting image and the other the control signal will be directly related to the quality and reliability of the monitoring system. At present, in the monitoring system for image signal transmission medium main coaxial cable, twisted pair and optical fiber, transmission equipment are corresponding to the coaxial video amplifier, twisted pair video transmission equipment and optical.

In the process of use, there are moments in non detection work. But this system also is in working state, SOPC will control the A/D converter to sample and the SOPC itself will be processed after the conversion to digital signals, and produces the color alert. In order to eliminate the false alarm and it is required magnification control amplifier. The incident differs a few nm light is amplified; the electric signals of the great difference, the numerical A/D conversion will overflow or close to overflowing. Using this characteristic, set a limit value, if the value than the upper limit, then system to make non detection work of judgment, the program execution is restarted.

### 3. Image Signal Analysis Based on CMOS Image Sensor

CMOS was an important chip in the computer system; it can save large amounts of data required for the system boot. In the early nineteen seventies, it was found, introducing CMOS photo diode can be used as a sensor, but in terms of resolution, noise, power consumption and image quality than CCD at the time difference, could not obtain development. With the development of CMOS technology, CMOS technology uses standard CMOS imaging device for producing high quality, low cost. This device is convenient for mass production, the characteristics of low power consumption and low cost are businessmen dream of. Now, CCD and CMOS both exist, CCD temporary or "mainstream", but the CMOS will replace CCD and become the mainstream of the image sensor.

According to the control timing characteristics of CIS sensor, CPLD sensor provides the clock signal for CIS CIS\_CLK, a strobe signal CIS\_SI and a light source control signal CIS\_LED. When the microprocessor P\_EN is set to a high level, and it is CPLD at the initial state. When P\_EN is low, CPLD is in the preparation stage. At this time, once the microprocessor to L\_EN tube generates a pulse signal on the foot, CPLD will then automatically generates the CIS\_SI signal to start the CIS, while the internal counter CPLD to the external CLK to count. In the control signal is generated by AD converter based on

CPLD value. The timing circuit hardware description is as follows, where CNT is a 0 to 685 of the counter, as is shown by equation 5.

$$J = \sum_{i=0}^{\infty} x^T(i+1)Qx(i+1) + u^T(i)Qu(i) \quad (5)$$

In an infrared image transmission system, multi-channel communication situation exists, the infrared image and other information through the air channels to the accused platform, send to the battlefield state \* estimation, target selection and control instructions. In the wireless channel wartime always exist in the noise, interference, multipart fading and other effects, which requires the design of transmission system should adopt effective data to reduce the transmission bit rate compression method, try to save the transmission channel bandwidth, but also introduce error control mode to resist interference channel noise.

Standard IC fabrication technology and imaging technology in continuous progress, and it is promoted by the front illumination (FSI) development of image sensor technology [6]. In this technique, such as the human eye eagle, light falls in front of IC, and then through the reading circuit and interconnection, was finally converged to the photoelectric detector. FSI is the mainstream technology currently used by the image sensor, has confirmed the mass production capacity, high reliability and high yield and attractive price and other advantages, greatly promoting its application in many fields of mobile phone, notebook computer, digital camera and digital camera etc. These advantages, coupled with the high performance characteristics, making this technology has a unique cost, performance and value orientation, the future application can be further expanded.

Contact image sensor (CIS) is composed of a row of the same width and scans the original photoelectric sensor array, LED light source array and cylindrical lens array of components such as a new image sensor. These components are integrated in a strip in the square box, without the need of additional optical accessories, not to adjust the optical path and depth of field, has the advantages of simple structure, small volume, convenient application and etc. In some applications of CIS sensors than CCD or COMS sensor has incomparable advantages. In a very wide range of fax machines, scanners, currency sorter against the application of zero field, as is shown by equation 6.

$$Y(\tau_j) = \log(\hat{v}_x^2(\tau_j)) - \psi\left(\frac{\eta_j}{2}\right) + \log\left(\frac{\eta_j}{2}\right) \quad (6)$$

In recent years, tube designers removed from the MCP ion barrier film to get no film light tube, while adding 1 automatic door switch power supply, the switch speed control photoelectric cathode voltage, and improved the low corona imaging technology,

helps to enhance the visual performance in bright sunlight. It is developed the first successful MCP imaging without membrane tube, in the target detection range and improved resolution, especially in very low light conditions. Automatic pulse gated power supply and its key techniques related to the new high performance without membrane MCP, photoelectric cathode and MCP with and without halo imaging technology [7]. This film without the BCG-MCPIV generation LLL tube technology although just started but good performance so that it will become the new hot spot image intensifier technology field, as is shown by Fig. 2.

The photodiode is arranged in the chip, can minimize the no uniformity of the incident light radiation, thereby increasing the color recognition accuracy; on the other hand, 16 photodiodes of the same color are connected in parallel, uniform distribution in the diode array, can eliminate the position error of color. When working, through two programmable pin to dynamically select the desired filter. The sensors are typically the output frequency range from 2 Hz~500 kHz, the user can also through two programmable pin to select the output scaling factor 100 %, 20 % or 2 %, or a power off mode [8].

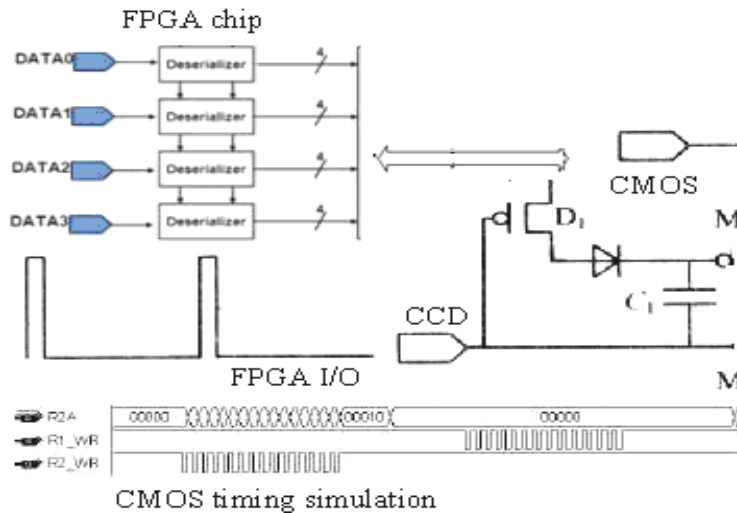


Fig. 2. CMOS sensor and FPGA I/O with image analysis.

Only with the intelligent video surveillance products as an example, although has made great progress, the optimal methods in the field of intelligent video analysis there is no generally recognized [9]. The complexity of its research content, which makes the algorithm complexity is high, the limited scope of application, the methods and tools of diversity, not the robustness, accuracy, speed meets the common needs. At the same time, the network of video surveillance system and distributed processing requirements, and large-scale installation cost, size and power constraints, the computing power and bandwidth have become the mainstream of video surveillance system in the embedded processor to continuously improve. Instead of intelligent analysis of video coding standard, is DSP's play, as is shown by equation 7.

$$\|\nabla f(x, y)\| = 0, \lambda_1 > 0, \lambda_2 > 0 \quad (7)$$

Because the CIS integration superiority, makes the CIS compared to CCD with the interface more varied. The current monitoring using CIS not only can output RGB, YUV, CCIR656 and other digital signal, and can simulate the PAL/NTSC television signal system, not only meet the traditional CCTV

application, also can satisfy the applications such as IP Camera and other digital. In addition, CIS also provides the I2C control interface, convenient external MCU control of CIS. CCD image sensor can only output analog signals, if you want to increase the variety of interface; you need "sleeve" with the use of it.

The past, performance and quality requirements, the digital SLR Camera application has been the most standard CMOS image sensor barriers to entry. Relying on its unique pixel technology innovation and it is the new Aptina MT9H004 into this growing market in various application attractive choices. In fact, CMOS image sensor shipments analysis firm TSR predicts a digital SLR camera market will from 2007 4000000 to 2013 12500000, a large part of this growth comes from compact emerging in the market without a mirror products division.

At the same time, video monitoring has its special requirements for confidentiality and other security technology, whether it is business or home appliance, equipment have been illegal intrusion and hacker attacks, to fully guarantee the safety equipment is a great challenge for product design. At this time, a single chip CMOS sensor products built-in ISP showed be congenitally deficient disadvantage, because it still could not complete such a complex

function, and must be equipped with image processor can separate meet the requirements. Although ASIC has a cost advantage, but it has inherent defects in the improvement and upgrading of the media formats, algorithm, video surveillance market continuous improvement in audio and video standard unceasing evolution and the algorithm, ASIC is inferior to many.

#### 4. Novel Image Signal Analysis of Monitoring Video based on CMOS Image Sensor

Dynamic range is a measure of the scene image sensor for a larger difference between the performance of light and shade of light. In practical application, reflected in the image sensor can be in one image can clearly show the dark scene, and can clearly display the well-lit scene [10]. Especially when the Camera alignment window, you can see the window scene, but also can see out of the window of the scene, but not "overexposed" phenomenon. The dynamic range is higher, and that in different situations, image sensor performance. At present, the high-end CIS can achieve up to the dynamic range of more than 100 dB, and the dynamic range of common basic CCD at about 60 dB. From the dynamic scope, CIS be a stroke above.

ME1010 is a comprehensive image sensors use convenient, use the patent structure development, designed to make it easier to form a whole and computer products. CCD image sensor is different from the traditional or some new CMOS image sensor, ME1010 image sensor can provide very low X-Y address image output, so as to connect computer or DSP. It provides  $352 \times 290$  pixels ( $352 \times 288$  effective pixels), an on-chip amplifier and supporting the ADC circuit, as is shown by equation 8.

$$(R^n)^k u^{(0)} = \sum_{i=1}^N \alpha_i \lambda_i^{nk} e_i + \sum_{i=N+1}^M \alpha_i \lambda_i^{nk} e_i \quad (8)$$

Image signal processing traditional is accomplished through image processor. With the continuous development of CMOS technology, also appeared the image signal processing (ISP) is built into the CMOS image sensor in the single chip products, this kind of sensor products with integrated function modules inside some image processing algorithms, including auto exposure, auto white balance, and color transformation of these basic algorithms. These kind of ASIC products appear once controversial, because although the ISP built-in sensor has lower power consumption and saving the occupied area advantage, but the mobile phone applications, from a cost perspective, ISP will be integrated in the sensor cost in mobile multimedia

processor or base band is much higher than the ISP integration.

The main difference between CMOS Image Sensor is made of a photosensitive unit and readout circuit structure is different in different manufacturing process. The photoelectric conversion realize CCD photosensitive unit, output in order to charge storage and charge transfer mode, need special process implementation; CIS image photographic unit for the photodiode, may be in general CMOS integrated circuit process to achieve, in addition to the image processing circuit, power consumption of the integrated and the lower the higher.

The image sensor can be said to be in the digital video or still camera video or still image processing line is the most important part of. If there is no sensor, there is no image signal processed [11]. As everyone knows the sensor is not standardized. In the scheme, they are different from the following: conversion of visible or infrared light into electrical signals in the way; especially before the signal from the chip, the signal by encoding and compression (sometimes) way. The sensor internal registers are programmed by the way, in order to adjust the gain, exposure time, sensor models (such as linear, HDR), the sensor image coordinates.

$$\frac{\partial \Phi_C}{\partial u} = 2(B^T Q B + S)u + 2B^T Q A x(0) = 0 \quad (9)$$

The CIS sensor is high speed, if directly by a microprocessor (MPU) control timing generation CIS sensor, is the consumption of processor time and resources. Therefore, the drive circuit used CPLD as the control core; the microprocessor does not directly control the CIS sensor. The microprocessor only need is to control the CPLD page to enable signal (P\_EN) and line enable signal (L\_EN) the two signals line. CPLD can automatically generate A/D converter, control the timing generation, data storage and the ping-pong memory bus switching function of the CIS sequence control. The CPLD independently accomplish the image acquisition and data storage, reduced the control microprocessor on the bottom of the device, and improves the efficiency of the microprocessor in the image processing.

The main part of the software for the PC machine, and it is PC machine environment for Windows XP, using the software Microsoft Visual C++6.0 and Matlab 7. Startup VC++ is responsible for calling a sun function, altitude angle and the azimuth angle to return the current monitoring, and transformed into FYP and FWP operation steps. By calling the Windows API function, to realize the transfer of data between PC and MCU. By programming with MCC VC++ and Matlab, control of image acquisition camera in video surveillance, according to deviation monitoring the centurion coordinates and image coordinates of the center into FYP and FWP correction step number.

In order to improve the efficiency of the system, and it is when the CPLD in the acquisition of data, the microprocessor finished the processing of image data, so using double buffer in the system. When CPLD is to RAM1 write data, and buffer of RAM2 bus control is to the microprocessor. When the microprocessor finished in RAM2 data processing and CPLD to complete the current image acquisition, switching bus, the CPLD will be the next image data is written to the RAM2, the RAM1 bus control switch to the microprocessor. The bus switch triggered by the rising edge of P\_EN EXCH signal inversion. The following program is EXCH signal in different situations, the bus working state of hardware description, as is shown by Fig. 3.

System working process: start, PC VC++ calls the sun function video motion control of height, angle and the azimuth angle of access to surveillance video,

and transformed into the operation step pitch and level of the stepper motor, through the RS 485 bus communication with MCU, drive tracking device operation, ensure that the video monitoring spots from the perspective of CMOS image sensor. Through the realization of MCC VC++ and Matlab joint programming, real-time control of image sensor collect the monitoring video image. VC++ program for every 4 min automatically calls take a photo sensor, processing the Matlab images, to calculate the deviation of surveillance video center coordinates and image coordinates of the center, into a horizontal and pitching motor need to adjust the number of steps, return to VC++ again, sent to MCU, stepper motor driver, and a fine adjustment of plane mirror tracking device, the monitoring video always in the image center position.

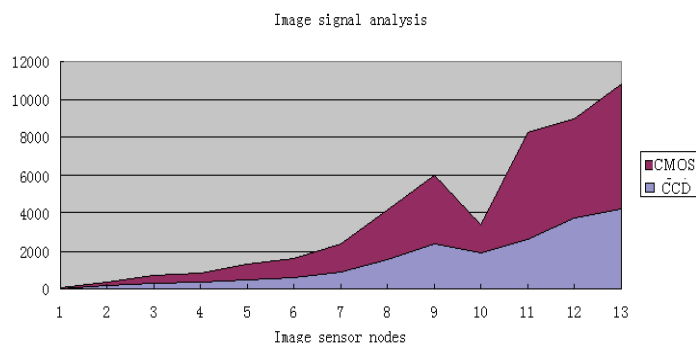


Fig. 3. Comparison results of image signal analysis of monitoring video based on CMOS image sensor with CCD.

The author of this article innovation: bus switching and microprocessor interface function with CPLD as the core to realize CIS sensor timing driver, A/D converter control, double buffer; the microprocessor does not directly control the device, improves the efficiency of microprocessor; the use of video surveillance work mode of double buffer, image acquisition and image processing to realize the parallel work, improve the performance of image processing system.

## 5. Conclusions

Because the CIS fabricated in a standard CMOS process, the readout circuit (including CDS correlated double sampling, automatic gain amplifier AGC), analog-digital conversion circuit (ADC), image signal processing (ISP), television signal encoding circuit (TV-Encoder) are all integrated on a single chip. While the CCD manufacturing process because of special and complex, the need for a separate existence, processing circuit supporting the use of, it is "CCD chip set in the application". "CCD" contains a CCD image sensor, V-Driver (timing control /CCD multi-channel power, gradually be integrated with CDS/AGC circuits), CDS/AGC (readout circuit

corresponding to the CIS), DSP (corresponding to CIS ISP) four. The paper proposes the novel image signal analysis of monitoring video based on CMOS image sensor. As one of the most important technical index of image sensor, the image sensor sensitivity is a measure of sensitivity to light.

## References

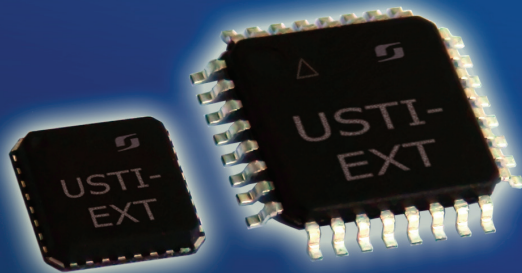
- [1]. Yan Liping, Song Kai, Wang Chao, Design and realization of forest fire monitoring system based on image analysis, *International Journal of Digital Content Technology & its Application*, Vol. 5, No. 12, 2011, pp. 452-458.
- [2]. Jing Zhang, The application of CMOS image sensor and ZigBee in building smart home solutions, *Journal of Convergence Information Technology*, Vol. 8, No. 5, 2013, pp. 444-453.
- [3]. Hui Fan, Yongliang Wang, Jinjiang Li, Exposing image fuzzy forgeries based on dyadic contrast contourlet, *Journal of Convergence Information Technology*, Vol. 6, No. 7, 2011, pp. 38-46.
- [4]. Chen Xuefeng, Niu Lei, Study on the multi-focus image fusion based on combined opportunity curvelet and wavelet transform, *Journal of Convergence Information Technology*, Vol. 7, No. 18, 2012, pp. 266-273.

- [5]. Hong Ye, Zhan-ping Yang, Jun Li, Shi-ling Li, A survey of temporal registration algorithm in multi-sensor systems, *International Journal of Digital Content Technology & its Application*, Vol. 6, No. 8, 2012, pp. 72-79.
- [6]. Fuzhong Wang, Fukai Zhang, Linear motor positioning system based on acceleration sensor, *International Journal of Digital Content Technology & its Application*, Vol. 7, No. 7, 2013, pp. 868-878.
- [7]. Likun Tian, Xiaohong Liu, Jie Li, Xiaoguang Guo, Image preprocessing of CMOS image acquisition system based on FPGA, *International Journal of Digital Content Technology & its Application*, Vol. 6, No. 20, 2012, pp. 130-139.
- [8]. Wei Wei, Bin Zhou, Features detection based on a variational model in sensornets, *International Journal of Digital Content Technology & its Application*, Vol. 4, No. 7, 2010, pp. 115-127.
- [9]. Junchai Gao, Zhiyong Lei, Zemin Wang, Hanshan Li, Sequence image match based on salient point invariants moments, *International Journal of Digital Content Technology & its Application*, Vol. 6, No. 11, 2012, pp. 124-130.
- [10]. Chunyao Fu, Wei Wei and Ang Wei, Application of quadratic-standard form based on LEACH protocol analysis, *International Journal of Digital Content Technology & its Application*, Vol. 6, No. 6, 2012, pp. 16-26.
- [11]. Peiyi Zhu, Weili Xiong, Baoguo Xu, A sensor management method based on an improved PSO algorithm, *International Journal of Advancements in Computing Technology*, Vol. 4, No. 9, 2012, pp. 259-265.

2013 Copyright ©, International Frequency Sensor Association (IFSA). All rights reserved.  
(<http://www.sensorsportal.com>)

## Universal Sensors and Transducers Interface (USTI-EXT) for extended temperature range

**-55 °C ... +150 °C**



26 measuring modes for all frequency-time parameters,  
rotational speed, capacitance Cx, resistance Rx, resistive bridges  
Frequency range, 0.05 Hz ... 7.5 MHz (120 MHz);  
Programmable relative error, % 1 ... 0.0005 %  
Conversion speeds 6.25 us ... 12.5 ms  
SPI, I2C, RS232 (master and slave, up to 76 800 baud rate)  
Packages: 32-lead, 7x7 mm TQFP and 32-pad, 5x5 mm (QFN/MLF)

**Applications: automotive industry, avionics, military, etc.**

<http://www.techassist2010.com/> [info@techassist2010.com](mailto:info@techassist2010.com)

## Development CMOS Sensor Image Acquisition Algorithm Based on Wireless Sensor Networks

**Chongke WANG, Zhengben ZHANG**

Henan Mechanical and Electrical Engineering College,

Henan Xinxiang, 453003, China

Tel.: 13782509858, fax: 0373-3691057

E-mail: wangchongkeedu@163.com

*Received: 5 July 2013 /Accepted: 25 August 2013 /Published: 30 September 2013*

---

**Abstract:** Image acquisition system consists of four major components: CMOS circuit cameras, camera cache control logic, SRAM memory and embedded system bus interface. Wireless sensor network is composed of numerous tiny sensor nodes which are randomly laid in a specific detection area consisting of self-organizing networks. The paper presents development CMOS sensor image acquisition system based on Wireless sensor networks and develops image acquisition system works by sending the correct timing signal for CPLD to CMOS image sensor, drive their normal work to take the appropriate shutter mode, and the collected image data manipulation packages, output to the USB chip, then the incoming image data transmission chip host. Experimental results show that the designs of the image sensor drive timing to meet the image requirements. Copyright © 2013 IFSA.

**Keywords:** Wireless sensor network, CMOS, Image Acquisition, Image Sensor.

---

### 1. Introduction

The user can control two digital methods to alter the default parameters of CMOS image sensors, CMOS image sensors that better meet the requirements of the specific application environment. One way is through the number of pins on the external pull-up or pull-down resistors to change the default parameters, and the other way is through the I2C bus programming CMOS image sensor internal registers to change the default parameters. CMOS image sensors as a limited number of pins, the former method can only change the default parameters for the most commonly used. The latter method, you can change all of the default parameters.

Wireless sensor node structure, the data collection includes various sensors and analog, and to obtain necessary sensors for sensing a variety of external information and through analog-digital conversion to

convert the information into a digital signal processor can handle, is detected form of signals needed to determine the type of sensor. Data processing section including embedded processor and a memory, the main parts of the sensor nodes to coordinate the collaborative work, such as the sensor for processing the information obtained the power supply mode of operation selection automatically.

CMOS imaging unit consists of a CMOS image sensor, a control circuit, the power supply and the external circuit. Cypress's image sensor with high-speed image sensor chip CMOS LUPA-300, it is in full resolution (640 × 480) to provide the highest operating speed of 250 fps [1]. Control circuit is mainly constituted by a microprocessor and FPGA, microprocessor ATMEL Corporation AT89S51 microcontroller, which has ISP (In System Programmable) function, the program easy to modify; FPGA using XILINX XC2S200's Spartan II

series chip, according to different the need for field-programmable, general good.

A large number of tiny wireless sensor nodes are randomly laid down in a particular fixed network infrastructure is not easy detection area. These nodes are self-organized manner to dynamically build networks, collaboration and awareness, collection and processing of the network coverage area at any time and at any place within a specific information, embedded systems within the network of these data to certain rules of calculation and data fusion, and through random self-organizing wireless communication networks to multi-relay system with temporary or long-term monitoring of the entire wireless link within the region to send data to a remote terminal for centralized treatment. WSN network generally include: sensor nodes, Sink nodes, interconnected networks and user terminals.

CMOS sensor image acquisition mode is active, the photosensitive diode charge generated by the transistor amplifier output directly, but the CCD sensor is a passive collection, the applied voltage required to allow movement of charge in each pixel, so external power supply is usually required to achieve 12-18 V; therefore, CCD sensor in addition to the power management circuit design more difficult than (need external power IC), high drive voltage power far more so than CMOS sensor level. In the image acquisition, the image sensor output sync timing signal identification need to use the ARM interrupt, and interrupt handling, the microprocessor needs to complete the program jumps to save the context of the work, reducing the speed of image acquisition, suitable for acquisition speed less demanding, low power consumption occasions. With CPLD to identify the image sensor synchronization timing signals, without going through the microprocessor interrupt, and system acquisition speed increase, but the involvement of CPLD system power consumption will increase. The paper presents development CMOS sensor image acquisition system based on Wireless sensor networks.

## 2. Design of CMOS Sensor Image Acquisition System

In each pixel CMOS sensor is needed to achieve a certain number of transistors electronic shutter function, increased electronic shutter function will increase the number of transistors in the pixel. Compression sensitive area should reduce the duty cycle of the device, particularly in the pixel size further reduced when this contradiction is more prominent. CMOS sensor, the designer uses at different times for different lines rolling shutter exposure resolve this problem, this approach is to reduce the pixel transistors, improved duty cycle, but moving targets in high-performance applications will be significant image distortion, so only suitable for

certain commercial applications. Besides the larger size of the pixel can be used to both high performance and image at the same time are having a similar exposure CCD electronic shutter function.

This article is using this solution to solve a single processor can not complete image capture issue. Specific program was developed by a programmable logic device comes with MT9V011 interface, control the image data to an SRAM cache, and then notify the processor to read data. So while addressing the processor I/O, and memory is not big enough slow two questions, can set up the system to complete the image acquisition. Image acquisition system frame system consists of four major components: CMOS circuit cameras, camera cache control logic, SRAM memory and 32-bit embedded system bus interface. System Camera cache control logic circuit consists of CPLD (programmable logic device) EPM7128S implementation.

CMOS image sensor dynamic range is defined as the maximum non-saturated signal light conditions with no noise ratio of the standard deviation [2]. The dynamic range of the image sensor is very important indicator of the quality of the image has a great influence and improve the dynamic range can be improved image contrast and resolution. Have a variety of programs have been proposed to improve the dynamic range: Chen Xu et PMOS pixel units used as a replacement (Reset) switch, and using a complementary source follower to adjust the signal to the rail to rail, but this structure occupies a plurality of pixels in the area, reducing the percentage of the photosensitive area (Fill Factor), while the PMOS low mobility of carriers rate, extending the charging time, reducing the frame rate of the sensor.

$$S_x(\omega) = \lim_{T \rightarrow \infty} \left\{ E \left[ \frac{X_r(\omega)^2}{2T} \right] \right\} \quad (1)$$

Currently the CMOS image sensor is divided into a passive pixel sensor (PPS) and an active pixel sensor (APS). PPS simple structure, high quantum efficiency, but the drawback is noise, and is not conducive to the development of large arrays; APS pixel is added in at least one transistor to achieve signal amplification and buffering, improved PPS noise problem, but worsen the threshold value and gain consistency, but also reduces the fill factor.

High frame CMOS imaging system working at full resolution frame rate of up 250 fps, image size is  $640 \times 480$  pixels, so its data rate of about 768 Mbit/s, we use a static memory device of SRAM for data output CMOS Camera storage time, so do not affect the operating speed CMOS camera, suitable for image data post-processing and analysis. This design uses IDT's CMOS SRAM devices 71V416VL complete imaging unit output data for high-speed storage. 71V416VL storage capacity of 4 Mbit, clock cycle is 15 ns, the working voltage of 3.3 V. System uses two chips of the storage array.

CMOS image sensor with a digital / analog hybrid image processor, greatly reducing the image processing part of the power consumption. Chip as well as low-power mode and standby mode, you can further reduce power consumption, ideal for use in portable devices. OV5006 CMOS camera module series consists of two sub-series: OV5016 OV5026 sub-series and sub-series. Which OV5016 sub-series are compatible with the PAL system, OV5026 sub-series is compatible with the NTSC system.

FPGA to CMOS high-speed data acquisition method, the CMOS device through the FPGA to become active in a controlled manner, PC can be indirectly addressed memory bank operation. In this system using the PC's parallel port to achieve a high-speed CMOS signal acquisition and processing, according to the aforementioned method of production of hardware and software systems, the actual sampling rate reached steady 15 frames / s, the system has been applied in the pipeline NDT prototype, the effect good [3]. This signal acquisition method can also be needed in many other high-speed image data acquisition occasions.

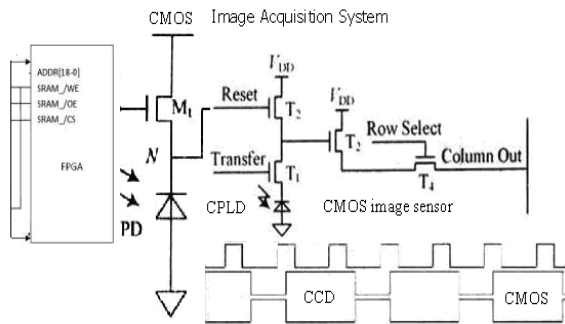


Fig. 1. Design of CMOS Sensor Image Acquisition System.

CMOS sensor in the improved resolution and sensitivity deficiencies, to apply more sophisticated imaging products, CCD and CMOS image sensors, the current is almost equal in terms of price. This is mainly CCD with a mature technology and market, CMOS devices have a high technology market development costs. CMOS and CCD image sensor photoelectric conversion on the same principle, are fabricated on a silicon integrated circuit technology curved process line equipment also similar, but different production processes and make the two different device structures and performance capabilities of the device has a large difference. Visible CMOS and CCD image sensors complement destroy anyone who does not appear the outcome, in the foreseeable future will coexist development and common prosperity of the image sensor market.

Because the system is not a real-time image acquisition and processing, the digital CMOS image sensor can reduce the rate of the output image. This can change the input clock to achieve. CPLD system clock using 40 MHz, after 10 minutes after the clock

frequency is as a CMOS image sensor of the clock. This reduces the image output rate, reducing the processor load for image data processing, the processor idle time for other control operations. As CPLD CMOS image sensor to read the image data outputted and the SRAM cache, so the CPLD logic chip image sensor is mainly based on the timing of the output image data and to write the SRAM read and write timing. CPLD chip control logic circuit mainly consists of an electronic hardware description language write state machine implementation. There are also some additional gates, multiplexers and adders, which together form a state machine and camera system cache control logic circuit, as is shown by equation 2.

$$\bar{w}(m) := [\bar{w}^T(m,1), \bar{w}^T(m,2), \dots, \bar{w}^T(m,M)]^T \quad (2)$$

A typical CMOS image sensor typically includes: an image sensor core, the corresponding timing logic and control circuit, AD converter, memory, a timing pulse generator and a decoder, etc., the timing control circuit is used to set the operating mode of the sensor, resulting in timing data, control data, such as the output. Pixel signal collected on the chip is exaggerated, AD conversion, storage, etc., at last, the digital signal can be output needs, you can also output analog signals, which are designed to provide users greater flexibility.

Image Acquisition System uses an image acquisition unit to complete the system of data collection tasks. Since a large amount of data collected, so the acquisition unit acquisition rate and data transmission systems have high demands. Acquisition interface circuit and hardware data bus and control bus, and provides a standard data acquisition card interfaces; acquisition card through acquisition interface circuits and systems control bus and data bus based on PCI bus frame grabber.

The video capture system as a whole can be divided into three parts according to the function: CMOS imaging section, CPLD timing control section, USB transmission parts. The entire image acquisition system works as follows: through the CPLD to send the correct timing signal to CMOS image sensors, drive their normal work, to take the appropriate shutter mode, and the collected image data manipulation packages, output to the USB chip, USB transfer chip and then the image data into the host, and through the upper application to get the collected images [4].

$$W_{\psi} f(m, n) = a_0^{-\frac{m}{2}} \int_{-\infty}^{+\infty} f(t) \psi(a_0^{-m} t - nb_0) dt \quad (3)$$

CMOS technology can be used for radiation production; this product compared with the CMOS image sensor usually has a strong resistance to ionizing radiation (ionizing radiation). Thick epitomical layer or the use of CMOS technology

backlighting little improvement, the sensor can be a near infrared (NIR) sensitivity is improved, leading to a new medical image processing applications. The cost-effective splicing technology to take advantage of 8-inch wafers, the future can also use the 12-inch wafer production of large (up to wafer level) CMOS image sensors.

$$G(x, y, \sigma) = (2\pi\sigma^2)^{-\frac{1}{2}} \exp\left(-\frac{x^2 + y^2}{2\sigma^2}\right) \quad (4)$$

CMOS sensor can capture the light signal is significantly smaller than the CCD elements, low sensitivity; reflected in the output, that is the CMOS sensor to capture the image content is more abundant than CCD sensors, image detail is lost in serious condition and the noise significantly, which early CMOS sensor is used only for low-end occasions a big reason. Another opening rate CMOS trouble is caused, it can not be comparable to the pixel density point of the CCD, because with increasing density of the photosensitive member will thus reduce the proportion of area, the CMOS low aperture ratio, the effective sensitive area pitifully small, image detail is lost as the situation will be more severe. Therefore, under the premise of the same sensor size, CCD pixel size is always higher than the same period of the CMOS sensor.

The design of the final selection NiosII processor system is to complete the color signal processing and identification, NiosII processor system-on-chip systems include NiosII CPU, on-chip RAM, timers, ADC interfaces, Avalon bus, Avalon tristate bridge, PIO, JTAGUART other parts. In addition, the chip extends the Flash (used to store programs and corresponding data) and SSRAM, as is shown by equation 5.

$$\bar{R}_i(k) = \frac{1}{k} \sum_{j=1}^k R_i(j) = \frac{1}{k} \left[ \sum_{j=1}^{k-1} R_i(j) + R_i(k) \right] \quad (5)$$

CYPRESS USB transfer part of the selection of the company's EZ-USB FX2 chip, which is a USB2.0 integrated peripheral controller, the chip supports 12 M/S full-speed transmission and 480 M/S high-speed transmission, you can use (with) four kinds of USB transmission: control transfer, interrupt transfer, block transfer and isochronous transfer; this device integrates an enhanced 8051, 8.5 kB of RAM, 4 kB FIFO memory, serial interface engine (SIE), General Programmable Interface (GPIF), I/O ports, data bus, address bus.

Based on high-speed CMOS image sensor with an image acquisition system is easy to control, safe, reliable, stable performance. The system can not change the system in accordance with requirements under the premise of hardware extensions, the image less demanding situations can increase the image compression unit to increase the flexibility of the system, making it wider range of applications.

However, the present system can only output the CMOS camera image data stored in real time, and then the stored computer data acquisition and processing, that while not affecting the operating speed CMOS camera, but can not be real-time monitoring, is only suitable for image data post-processing and analysis.

$$H = [u_1 \ u_2] \cdot \text{diag}(\lambda_1, \lambda_2) \cdot [u_1 \ u_2]^T \quad (6)$$

In the data sampling period, will READY pulled, said it is collected, then the FPGA based on the OV7620 VSYNC, HREF, PCLK produce an image MEM\_WR (write signal) and ADDRESS (address), OV7620 read data into the cache, to the next VSYNC signal, which means that a data has been mined out, and then sent to the PC for the READY signal, the image acquisition is complete, if the PC does not give acknowledge signal ACK, FPGA start sampling the next frame data into the cache, and overwrite the original some data; if PC response, FPGA stop sampling data.

ME1010 sensor type CMOS image sensor, and its peripheral circuits and the driving circuit has an address decoder, a data bus, the sampling clock and a control circuit, A / D control circuit components [5]. Key circuit is relatively simple, mainly meter flower, length, Pause, etc., to achieve total spend, length, suspension overhaul and other functions. The reference voltage circuit for the image sensor is to provide A / D converter reference voltage level.

$$F(a, b) = \sum_{i=0}^n \varepsilon_i^2 = \sum_{i=0}^n (y_i - ax_i - b)^2 \quad (7)$$

CMOS integrated circuit using MOSFETs, and are complementary structure, working two series FET conduction is always in a tube, and the other MOSFET is off, the circuit static power is theoretically zero. In fact, because of the leakage current, CMOS circuits there are trace static power. Typical power consumption of a single gate value is only 20 mW; dynamic power dissipation (at 1 MHz operating frequency) is only a few mW. Wide range: CMOS IC power supply is simple, small power supply, basically do not need regulation. Domestic CC4000 series of integrated circuits, and it is available in 3 ~ 18 V voltage to work.

By function and composition of the system is divided into two parts, prepared as two 4-layer PCB board. The first part is the front imaging portion, CMOS image sensor and LDO power composed of a CMOS image sensor as the core, and the external resistor and capacitor, and two PC104 interface, constituting the front board; the second part is the rear end of the timing control and USB data acquisition part, including CPLD, JTAG interface and power supply and USB transmission chip LDO, constitute the back-end circuit boards. This part of the front end through the PC104 interface and connected to control the output timing of the CMOS

image sensor and USB data acquisition synchronization chip timing for data transmission; two circuit boards using Protel platform to build the circuit.

$$X_{i,r,D}(m) = \overline{G}_{r,i} X_{i+1,V}(m) \quad (8)$$

TLC5540 reference voltage by a precision voltage reference TL431, resistors R6 and R7 form a circuit. TLC5540 the CLK pin and OE pin directly controlled by the CPLD, respectively AD\_EN and AD\_CLK. When the CPLD AD\_EN generated when the falling edge, CPLD enable the OE pin TLC5540 data AD [0 ... 7] read to the CPLD's internal registers and the signal from analog to digital conversion process.

CPLD of the CMOS image sensor using the data collection methods, the CMOS active components can be changed through the CPLD in a controlled manner, the realization of high-speed CMOS image sensors read the data, produced by the method according to this system, after experimental verification results good [6]. The signal reading method can also be many other high-speed image data acquisition to occasions.

Image sensor drive timing is correct or not it can work play a decisive role. This paper analyzes the CMOS image sensor IBIS5-B-1300 timing of work, based on the design of two configuration registers, and two shutter modes, and FPGA embedded digital clock management unit (DCM) to complete the system clock and ACD clock design. Experimental results show that the design of the image sensor drives timing to meet the driving requirements.

### 3. Research of Wireless Sensor Networks and Image Sensor

For the self-organizing wireless sensor networks, the network topology control has a special significance. Topology control through automatic generation network topology to improve the routing protocol and MAC protocol efficiency for data fusion, time synchronization and other lay a good foundation, help save node energy and prolong the network lifetime. Network topology control current research problem is to meet the network coverage and connectivity of the premise, by the power control and backbone node selection, eliminate unnecessary wireless communication between nodes generate a link energy-efficient data forwarding network topology.

Sensor network energy constraint exists. Reducing the amount of data can be effectively save energy, each sensor node in the data collection process, can use the node's local computing and storage capacity data fusion process, removing redundant information, to achieve the purpose of energy saving. For nature prone to failure, the sensor nodes need multiple copies of data fusion technology to data integration, improve data accuracy, data

fusion technology to save energy, improve the accuracy of the information at the same time, at the expense of other aspects of performance for the price. The first is the cost of the delay in the process of data transfer is easy to find a route for data fusion, data fusion operations, data fusion while waiting for the arrival of other data.

The design of the traditional design methods and methods based on the combination of chip design, the use of integrated circuits and complex programmable logic device (CPLD) together to achieve system function, the system has high integration, reliability, flexibility, designed to facilitate debugging and so on. The system with the two boards to complete the overall system construction, one for driving and controlling the CMOS image sensors to capture continuous video images; another one representing a USB data acquisition card, the former image data acquisition, transfer the PC input [7].

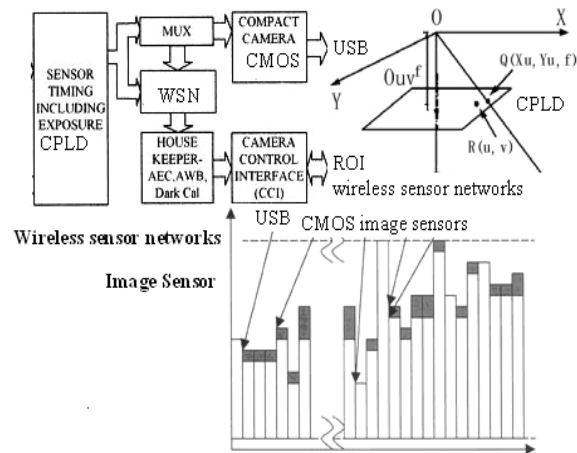


Fig. 2. Design of Wireless sensor networks and Image Sensor figure.

Wireless sensor networks as a task-based network, the need for data collection, transmission and integration, as well as the task of coordination control. How to ensure the confidentiality of task execution, the reliability of the data generated, the efficiency of data fusion and data transmission security, has become wireless sensor network security issues requires a comprehensive consideration of the content, in order to ensure the confidentiality arrangement of tasks and task execution results of safety transfer and integration, wireless sensor networks need to implement some basic security: confidentiality, point to point message authentication, integrity, identification, freshness, authentication broadcast and security management.

Wireless sensor network is composed of numerous tiny sensor nodes are randomly laid in a specific detection area consisting of self-organizing networks. These tiny sensor nodes powered by battery, and is in inaccessible areas is not easy to replace the battery, in order to try to extend the

lifetime of wireless sensor networks, all the phenomenon of inefficient energy use must be eliminated [8]. Therefore, the design of effective strategies to prolong the network lifetime for wireless sensor network design core problem, as is shown by equation 9.

$$f(t) = C_V^{-1} \iint_{R^2} W_{\psi} f(a, b) \psi_{a, b}(t) \frac{dad b}{a^2} \quad (9)$$

The sensitivity of the image sensor largely depends on the pixel size, pixel size and large specific applications that require large area image sensor customized. Internal multiplexer technology can support higher frame rate random windows. If the window size is reduced to a smaller ROI (circle the target area), and it is then the fastest speed of the device frame rate of up to 170,000 frames per second. Most sensors are used 0.25 processes.

For the large amount of image data, if the use of the serial RS-232 protocol for data acquisition, image data acquisition speed can not meet the requirements needed; rather use USB data acquisition, although able to meet the required speed, but requires peripherals must support the USB protocol, while the USB protocol commonly used engineering software interface is not widespread, difficult to use. Some users to take advantage of the standard parallel port (SPP) for data acquisition, but SPP agreement 150 kb/s transfer rate for image data acquisition, also seems too low.

Wireless sensor network energy consumption mainly in communication and computing aspects. Communication energy related portion includes a transmitter, transponder and receiver. Transmission is mainly used to send control signals to route the request and response, and the node generates and transfer of data packets, the receiver for receiving data and control packets, the control packet may put the node as an end point may also be via the node is forwarded to other nodes. A clear understanding of these wireless mobile devices energy characteristics for the design of efficient wireless communication protocol has a very important significance. A typical mobile wireless communications device may be in one of three modes: transmit mode, the receive mode and monitor mode. When the node is in transmit mode energy up.

In different applications, the sensor network nodes composition varies, but generally by the data acquisition, data processing, data transmission and power supply that 4 parts (see equation 10). Depending on the application requirements, the system may be positioned to determine the position of the sensor nodes, a mobile unit so that the sensor can move in the area to be monitored or with power supply unit from the environment to obtain the necessary energy. In addition, there must be some relevant parts of the application, for example, there may be some sensor nodes or in the deep sea, there may be chemical contamination or biological

contamination in place, which requires the design of sensor nodes using some special precautions.

$$C_i = \frac{\sum_{k=1}^n \mu_{ik} x_{i,k}}{\sum_{k=1}^n \mu_{ik}}, \quad (1 \leq i \leq c) \quad (10)$$

CMOS image sensor based on surveillance camera is basically a two-chip solution that contains a standard CMOS imaging sensor and an integrated CMOS image sensor interface, including digital image processing unit, a microcontroller, TV Encoder and Peripheral Interface variety of digital image processing functions such as control chip. This has powerful capabilities of digital system architecture, to meet the fundamental right from a surveillance camera digital functions growing demand [9]. At present, this two-chip solution economically more reasonable – and the yield difference between CMOS process, put a lot of digital processing functions and the associated storage unit integrated with CMOS imaging sensors lack economic feasibility.

As wireless sensor networks exist large number (thousands) of sensor nodes, nodes in the network cost is not too high, the node can not be installed in addition to small size of the local oscillator and a wireless communication module for synchronization outside the more device, therefore, the price and volume of the wireless sensor network time synchronization is important constraints. Most wireless sensor network nodes are deployed in unattended remote or dangerous areas, and so can only carry a small number of limited energy, even listening communication will consume energy, and time synchronization mechanism must be designed to take into account energy problem.

#### 4. Development CMOS Sensor Image Acquisition System based on Wireless Sensor Networks

CMOS image sensor of simple structure, internal integration, so only a few external control signal to complete the output video image capture, the system timing using VHDL hardware description language design, the core part of a finite state machine, the specific state relationship is as follows [10]. The system works as follows: When the system is powered on, CPLD generates a reset signal resets the entire chip to its initial state, and then injected into parallel data on the chip, CMOS image sensors to the special register to write a predetermined value, such as pixel integration time is set, the pixel read row number, the output amplifier gain and other parameters.

FPGA to CMOS high-speed data acquisition method, the CMOS device through the FPGA to

become active in a controlled manner, PC can be indirectly addressed memory bank operation. In this system using the PC's parallel port to achieve a high-speed CMOS signal acquisition and processing, according to the aforementioned method of production of hardware and software systems, the actual sampling rate reached steady 17 frames / s, the system has been applied in the pipeline NDT prototype, the effect good.

Wireless sensor network transmission medium can be wireless, infrared or optical media. For example, and it is in the dust projects and the use of optical is media for communication [11]. There sensor networks using infrared technology, they all require line of sight between the two sides of the transceiver transmission path. And a large number of sensor network node based on RF circuit, wireless sensor networks recommend using license-free frequency bands (ISM). The physical layer technology selection, signal propagation characteristics of the environment, the physical layer technology is the energy consumption of key design issue. A typical channel sensor networks belonging to near terrestrial channel, its propagation loss factor greater.

$$\begin{cases} X_i(k+1) = \Phi(k+1, k)X_i(k) + \Gamma(k+1)w(k) \\ Z_i(k) = H(k)X_i(k) + v_i(k) \end{cases} \quad i = 1, 2, 3 \quad (11)$$

Sensor architecture by two fractions and it is a quarter or a pixel array formula composition. Parallel output for analog output, or a 10-bit digital output or digital serial LVDS outputs. Each output can be up to 50 million times per second sampling rate, so that we can achieve 5.5 billion pixels per second throughput. So far, it is the image sensor having a maximum throughput of consecutive pixels. Image quality at least 10-bit precision, and it is so the digital camera,

the data throughput for the second 55 Gbit. Such high-speed applications typically require six transistors snapshots pixels, and require high sensitivity and dynamic range [12]. The sensitivity of the image sensor largely depends on the pixel size, pixel size and large specific applications that require large area image sensor customized.

In this paper, high-speed CMOS image sensor LUPA-300 is briefly introduced, and based on this sensor, the design of high frame rate CMOS imaging unit, an image storage unit, an image data acquisition unit and system software, to establish a high-speed CMOS image acquisition system.

Host application developed using VC ++, VC ++ using the MFC framework, the preparation of a multi-threaded image acquisition and processing procedures. User by calling the correlation function, you can complete the configuration of the data acquisition card. Applications received through the PCI bus SRAM memory of the original image data after the data to be received, the application can perform simple image data processing and analysis, and the image is displayed, while the image data is stored on the hard drive, complete the image data acquisition, display and storage. Applications can also capture images for further processing.

In order to verify the system to achieve the image acquisition function, the need for CPLD cached is data processing and display the image. Since the PC has a wealth of software and hardware resources, so we use a PC to display images, validate the correctness of image capture function. The specific method is: the system host processor LPC2104 SRAM read the image data sent through the serial port to the PC, the PC receives the data and writing software to do simple processing on the PC can be displayed on the screen image, which can verify system.

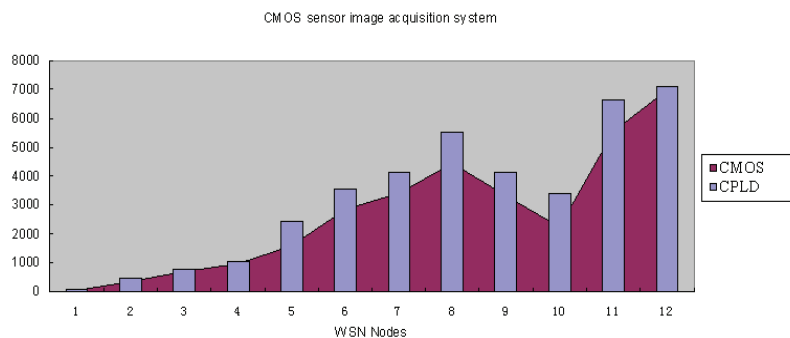


Fig. 3. Comparison development of CMOS sensor image acquisition system based on Wireless sensor networks.

The system's data acquisition module EZUSB FX2, USB transmission chip, and it are by writing firmware, so that the chip operates at high speed bulk transfer mode. The system uses a chip SLAVE FIFO transfer mode is not via a USB chip enhanced 8051 core control and intervention, the data directly

through the USB bus, the high-speed transmission to the pc machine. Finally, write the upper Visual C 6.0 client program, using multi-threading technology to create two threads: USB transfer threads and real-time image display thread, realized in the PC machine in real-time image display. Taken from the

test identification rate target image can be seen, CMOS image sensor imaging clear, stable and high resolution. Entire CMOS video capture system structure is simple, easy timing design, short development cycle; the finished size is small, peripheral devices, low cost, using USB bus-powered, plug and play, with high practical value.

Wireless sensor network is a random dispersal through the monitoring area to deploy a large number of sensor network nodes, each node through self-coordination, self-configuring a network, you can not rely on other ancillary facilities or that means to configure the network. As energy constraints, environmental interference and vandalism and other factors, the sensor nodes will damage, leading to some node does not work, there are some nodes to compensate for the failed node to increase the monitoring accuracy and added to the network, so that the sensor network nodes number to dynamically increase or decrease, so that the resulting network topology changes dynamically. This requires that the sensor nodes self-organizing capacity to adapt to this dynamic network topology.

## 5. Conclusions

CMOS image sensor based video acquisition system. USB2.0 data bus transmission system using data and power to the system, and it is greatly reducing the system size and power consumption. As the structural characteristics of the CMOS image sensor, this is suitable for large area array image acquisition. The paper presents development CMOS sensor image acquisition system based on Wireless sensor networks. Wireless sensor network domain existing Ad Hoc network is quite different, resulting in many of the existing network technologies and can not be directly applied to wireless sensor networks. MAC protocol for wireless sensor networks is the main objective of saving and self-organization, and each node fairness and latency is secondary.

## References

[1]. Ji-Woong Kim, Kyoung-Su Park, and Kae-Dal Kwack, A 12-b low voltage CMOS pipelined analog-

- to-digital converter without sample and hold circuit, *RNIS*, Vol. 5, 2010, pp. 28-30.
- [2]. Hong Jiang, Xiaohui Su, The embedded image acquisition system based on the ARM, *Journal of Convergence Information Technology*, Vol. 8, No. 9, 2013, pp. 845-852.
- [3]. Muktar Hussaini, Farhat Anwar, Aisha Hassan A. H., A survey of power-efficient gathering of sensor information system based routing protocols of wireless sensor networks, *Sensors & Transducers*, Vol. 142, No. 7, July 2012, pp. 10-22.
- [4]. Likun Tian, Xiaohong Liu, Jie Li, Xiaoguang Guo, Image preprocessing of CMOS image acquisition system based on FPGA, *International Journal of Digital Content Technology & its Application*, Vol. 6, No. 20, 2012, pp. 130-139.
- [5]. Xiaoke Wei, Zuqiang Wang, Hui Xu, A low-noise, wideband CMOS charge sensitive preamplifier for the high precision pixel detector, *Advances in Information Sciences & Service Sciences*, Vol. 4, No. 22, 2012, pp. 99-105.
- [6]. Yu-Cherng Hung, Kuei-Ching Tsai, A new delay-line sharing based CMOS digital PWM circuit, *International Journal of Advancements in Computing Technology*, Vol. 4, No. 18, 2012, pp. 177-186.
- [7]. Naveen Kumar V., Santhi Prabha I, Comparative analysis of energy-efficient cluster-based routing protocols for wireless sensor networks, *Sensors & Transducers*, Vol. 142, No. 7, July 2012, pp. 23-32.
- [8]. Jianping Hu, Lv Yu, P-type adiabatic computing based on dual-threshold CMOS and gate-length biasing techniques, *Journal of Convergence Information Technology*, Vol. 7, No. 6, 2012, pp. 154-162.
- [9]. Tao Ji, Wencheng Wang, Fengnian Guan, Qianqian Yuan, Research and design of multi-focus image acquisition system, *Advances in Information Sciences & Service Sciences*, Vol. 5, No. 2, 2013, pp. 591-597.
- [10]. Zeng Cheng, Tonghe Li, Xiaoqing Zheng, Implementation of low power strategies in a base-band chip in 40nm CMOS technologies, *Advances in Information Sciences & Service Sciences*, Vol. 4, No. 5, 2012, pp. 114-121.
- [11]. Xiao Liu, Agent-based load balancing DV-hop positioning algorithm for wireless sensor networks, *International Journal of Digital Content Technology & its Application*, Vol. 7, No. 3, 2013, pp. 787-794.
- [12]. Fan Xiangning, Li Bin, Wang Zhigong, A 0.18 $\mu\text{m}$  CMOS based programmable integer-fractional combined frequency divider for frequency synthesizer of multi-standard wireless systems, *Advances in Information Sciences & Service Sciences*, Vol. 4, No. 23, 2012, pp. 104-111.

## Application of RFID Technology and Ontology Model in Designing Smart Home System

Hongsheng XU, Ruiling ZHANG

College of Information Technology, Luoyang Normal University,  
Henan LuoYang, 471022, China  
Tel.: 0086+13403793403  
E-mail: xhs\_ls@sina.com

*Received: 29 June 2013 /Accepted: 25 August 2013 /Published: 30 September 2013*

---

**Abstract:** The purpose of building smart home system is some home devices (audio and video equipment, lighting systems, air conditioning control, security systems, digital cinema systems, network appliances, etc.) through smart home network automation, broadband and wireless networks, and we can achieve remote control home devices. The paper proposes application of RFID technology and ontology model in designing smart home system. RFID system is composed of two parts: the read / write unit and electronic transceiver. RFID technology can identify the moving objects and can also identify multiple tags; the operation is fast and convenient. Ontology is the concept of shared explicit and formal specification; it can be used to describe the concepts and relationships between concepts. This paper uses RFID embedded platforms and other types of home sensor ontology model to design a smart home control system. *Copyright © 2013 IFSA.*

**Keywords:** Smart home, RFID, Ontology.

---

### 1. Introduction

Smart Home is a comprehensive interdisciplinary. Intelligent home furnishing can be defined as a process or a system, the use of advanced computer technology, network communication technology, integrated wiring technology, will work with family life various subsystems related, organically unifies in together. Intelligent home furnishing goal is to use various methods or equipment to make home furnishing life automation, intelligent home furnishing, to become more comfortable, safe and effective, so as to improve people's quality of life.

Smart Home is the use of micro electronic technology, electronic electric appliance product or system integration or control in the home. Home network is in the home range (can be expanded to a neighbor, PC, home appliances, small) security system, lighting system and wide area network connecting a new technology. Network appliance is a

common household appliance using digital technology, network technology and intelligent control model of household electrical appliances technology design improvement. Network appliance is a kind of low price, convenient operation, strong practicability, with the main function of PC home appliance products [1]. Smart home furnishing now in the initial stage, the intelligent home furnishing limited by product manufacturers, in a short period of time has not unified standard protocol, it is generally a manufacturer to make system development alone.

RFID radio frequency identification is a kind of automatic recognition technology of non-contact, RF signal through its automatic target recognition and access to relevant data, identify the work without human intervention, it can work in various environments. RFID technology can identify the moving objects and can also identify multiple tags; the operation is fast and convenient.

Ontology is a description of the shared concepts clear, formal specification, can be used to describe the relationship between concepts and, describes the modeling means of semantic knowledge in the semantic Web, semantic Web system as the core, it is the formal definition in common in the domain knowledge. Therefore, study on the theories of ontology for semantic annotation is very important.

Smart Home is a residential platform, buildings, network communications, information appliances, equipment, automation, assembly systems, structures, services and management as one of the efficient, comfortable, safe, convenient, environmentally friendly living environment. Smart home can be defined as a process or a system. The use of advanced computer technology, network communication technology, integrated wiring technology, will work with home life about the various subsystems together organically, through integrated management, make home life more comfortable, safe and effective. The paper proposes application of RFID technology and ontology model in designing smart home system.

## 2. Development of Smart Home System based on RFID Technology

Smart home control system is based on HFC, Ethernet, field bus, public telephone network, wireless network transmission network for the physical platform, computer network technology as the technology platform for the application of field bus operating platform, a complete set of home communications, home automatic control equipment, home security and other functions of the control system. Intelligent home control system's overall goal is through the use of computer technology, network technology, control technology and integration technology to build a community and the whole family to the city's comprehensive information services and management systems, in order to improve residential high-tech content and residents live environmental levels.

The basic principle of RFID Technology: label into the field, RF signals received reader, by sending the induction current of energy out of the product information stored in the chips (Passive, Tag, passive tags or passive tags), signal or take the initiative to send a frequency (Active Tag, active tags or active tags); reader to read and decode, sent to the central information system on the data processing.

According to the smart home furnishing system needs to carry out development and design, mainly to achieve the following goals: design when the air conditioning switch users need remote control, as long as the use of mobile phone short message sends the specified command, by receiving GPRS module, and the short message is translated into commands can be identified to the family controller, the controller through processing, will the command sent to the controller is connected with the air conditioner

through wireless transmission module ZigBee, control of the air conditioner is realized by the controller.

Smart home not only has the traditional residential function, providing comfortable and safe, high-quality and pleasant family living space. The original will be transformed into a passive static structure with active intelligence tool that provides a full range of information exchange capabilities to help families keep the information exchange with external flow, optimize people's lifestyles and help people to arrange a time effective to enhance the security of home life even for a variety of energy cost savings [2]. System's network capabilities to provide remote control, home appliances (air conditioning, water heaters, etc.) control, lighting control, indoor and outdoor remote control, curtain automation, burglar alarm, telephone remote control, programmable timing control, and computer control and other functions and means, as is shown by equation 1.

$$p_0 = \left[ \left( 1 + \rho + \frac{\rho^2}{2!} + \dots + \frac{\rho^n}{n!} \right) + \frac{\rho^{n+1}}{n!(n-\rho)} \right]^{-1}, \quad (1)$$

Electronic label is a carrier of information, usually by the coupling element (coil, microwave antenna) and memory for storing and microelectronic chip application identification information. Information stored in the data obtained by the reader, a typical reader comprises a high frequency module (transmitter and receiver), the control unit and a coupling element (antenna). According to the electronic tag has no power can be divided into active and passive RFID electronic tag, according to different types of memory can be divided into internal use only label and read-write tag.

RFID tag antenna has two forms: (1) the antenna wire wound inductor antenna; (2) the imprint in the dielectric substrate or printed spiral antenna rot. Antenna is determined by the carrier frequency, tag package form, performance and assembly cost factors. For example, need mH inductance frequency is less than 400 kHz, this type of antenna can only use wire wound inductor fabricated; frequency in 4~30 MHz, only a few Yu, a few turn wire wound inductors can, or use the moment rot antenna dielectric substrate.

$$q_{ii} = \lim_{h \rightarrow 0^+} \frac{p_{ij}(h)}{h} = \begin{cases} \lambda_i, & j=i+1, \\ u_i, & j=i-1, \\ 0, & |i-j| \geq 0. \end{cases} \quad (2)$$

Embedded smart home to make the system greatly enhanced processing power that can bring more lifelike images and more realistic voice. According to the real-time operating system customization system can not only maximize the use of hardware resources but also to avoid too large a

system caused by system redundancy. Generally only one main processing chip and it is the system architecture more clear and simple. Software using hierarchical design, easy maintenance and upgrades, greatly improving the code efficiency and shorten the development cycle.

RFID technology is a new automatic identification technology of non-contact, automatic recognition of multiple targets through its radio frequency signal to stationary or moving, acquisition data and efficiently, with Internet technology further combine can also realize the target tracking and the worldwide information sharing [3]. Identify work without human intervention, fast and convenient operation, can work in harsh environment. As a wireless version of the RFID bar code, bar code technology has not possessed by the non-contact, reading speed, no wear, without environmental impact, waterproof, antimagnetic, high temperature resistant, long service life, reading distance, the label data can be encrypted data storage capacity, larger, storage information easily change, has the advantages of preventing conflict function, can simultaneously process multiple cards etc...

RFID technology is widely used and promoted in the low frequency. The frequency is mainly carried out by inductively coupled way, also is the write coil and inductor coil in transformer coupling at the reading. Voltage through the role of reader alternating field in the sensor antenna induction is rectified, can be used as a power supply voltage. The magnetic field region can be well defined, but the field falling so fast, as is shown by equation 3.

$$\frac{f'(x_1)}{2x_1} = (b^2 + a^2) \frac{f'(x_2)}{4x_2^3} = \frac{\ln \frac{b}{a}}{b^2 - a^2} x^3 f'(x_3) \quad (3)$$

Intelligent residential lighting control system can control part of incandescent, fluorescent, and a variety of new lamps on and off, or dimming functions. Can be distributed multi-point control, centralized control, remote telephone and automatic process control. Lighting can be a single point of control, there may be a combination of the lighting group control. Meanwhile, the system has high reliability; it can completely replace the traditional mechanical switches.

Smart home modular design can be adapted to the needs of a variety of occasions to protect the interests of users and allows the system to gradually put in place. Between modules follow certain protocol, you can communicate and coordinate with each other. Practicality: people buy home automation products are more convenient to enjoy a comfortable life, not chase the trend concept. Popularity: home automation system should be cost-oriented, high-performance target design, households are more price-sensitive, and so the technology used in smart homes can be more economical. Meanwhile, home automation systems compatible with the user should be able to

maximize the existing electrical equipment, protecting user investment.

RFID (radio frequency identification) system is composed of two parts: the read / write unit and electronic transceiver. The reader through the antenna emits electromagnetic pulse; the pulse transceiver receives and sends the stored information to the reader as a response. In fact, this is the memory data read, write or delete non-contact processing. Technically speaking, "smart tags" contains RFID circuit including the RFID chip with RFID RF part and a thin antenna loop, the antenna with a plastic sheet is embedded into the tag, as is shown by Fig. 1.

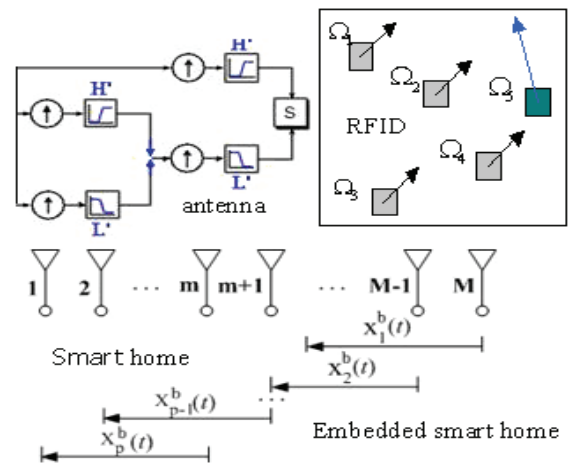


Fig. 1. Development of Smart Home System based on RFID Technology

Signal receiver, commonly called the reader. According to the label type supports different with the different function, the complexity is significantly different [4]. The basic function is to provide the reader with the label of the path for data transmission. In addition, the reader also provides signal state quite complex control, parity error checking and correction functions. In addition to store label need to transfer information, but also must contain certain additional information, such as the error checking information etc. The identification data and additional information is in accordance with the structure of the certain together, and in a particular order to send.

Household equipment, including electrical equipment, automatic monitoring centralized, and it is remote control, remote offsite (via telephone or the Internet) to monitor, control and data acquisition. (A) monitoring and control of household appliances, according to a preset program requirements for water heaters, microwave ovens, video audio and other home appliances to monitor and control. (2) heat meters, gas meters, water meters, meter data acquisition, measurement and transmission according to the requirements of residential property management data collection procedures set by the sensor on the heat meter, gas

meter, water meter, power meter amount for automated data collection, measurement, and will gather the results transmitted to a remote residential property management system.

The RFID subsystem by RFID label, RFID reader and RFID software application support system. Each user is holding RFID tags from main label and tag. Main label is pasted on the mobile phone shell, from the label shape from ordinary card; mobile phone is not suitable for the environment. Because the online without mobile phone support, and it is so from the label on the type of business to be less main label, mainly some small offline payment business. According to the characteristics of mobile payment business, storage space in the RFID tags can be divided into: application identifier directory, issue area, the personal information of the user, mobile payment business district and other business application reservation data area, as is shown by equation 4.

$$\begin{cases} x_0^1(t) = (1 - c^1(t))f^1(t) \\ x_i^1(t+1) = \beta^1(t) \sum_{i=i_1}^{i_2} b_i^1(t) * x_i^1(t) \\ x_{i+1}^1(t+1) = (1 - d_i^1(t))x_i^1(t) \end{cases} \quad (4)$$

RFID IC has a 154 bit memory, for storing tag data. IC also has a turn-on resistance modulation gating low tube (CMOS), working with a certain frequency. When the reader transmits electromagnetic wave, the tag antenna inductive voltage reaches VPP, the device, sending data back to Manchester. Data transmission is through tuning and tuning external resonant circuit to complete the. Specific process is as follows: when the data to a logic high level, gated pipe cut-off, cut wave frequency tuning circuit is tuned to the reader, is this state of tuning, induction voltage maximum [5]. Thus, tuning and tuned in the tag coil generates an amplitude modulation signal, the reader detects voltage waveform envelope signal can be reconstructed, data from the tags.

RFID reader can read the data stored in the tags. Auto-ID plans to EPC system development has become a global standard, the standard mainly includes: the specific code to target recognition (EPC); definition of the data owner (EPC manager); the rest of the information code is defined and marked goods; definition parameters, such as inventory unit number; convert the EPC code into the Internet address (ONS object naming service); used to describe the target (physical markup language PML); gathering and processing RFID data (Expert System); assigned to a specific number of each kind of target (serial number).

$$u = \int_0^x x dx + \int_1^y \left(\frac{x^2}{2} + \frac{1}{y}\right) dy = \frac{x^2}{2} y + \ln y \quad (5)$$

Smart home control system can be defined as a process or a system. The use of advanced computer technology, network communication technology, integrated wiring technology, will work with home life about the various subsystems together organically, through integrated management, make home life more comfortable, safe and effective. Compared with ordinary home, smart home features not only traditional residential function, providing comfortable and safe, high-quality and pleasant family living space. The original will be transformed into a passive static structure with active intelligence tool that provides a full range of information exchange capabilities to help families keep the information exchange with external flow, optimize people's lifestyles and help people to arrange a time effective to enhance the security of home life even for a variety of energy cost savings [6]. System's network capabilities to provide remote control, home appliances (air conditioning, water heaters, etc.) control, lighting control, indoor and outdoor remote control, curtain automation, burglar alarm, telephone remote control, computer control and other functions and means.

Things smart home automation control system integration products, computer network systems and network communication technology, and the various home devices (such as audio and video equipment, lighting systems, curtain control, air conditioning control, security systems, digital cinema systems, network appliances, etc.) through the intelligent home network networking automation, through broadband and wireless network, you can achieve remote control home devices. Compared with ordinary home, smart home not only offers comfortable and high-quality family living space, to achieve a more intelligent home security systems; also the home environment from the original passive static structure into the wisdom of having a dynamic tool that provides a full range of information exchange capabilities, as is shown by equation 6.

$$\frac{dy}{dx} = \frac{a_1x + b_1y}{a_2x + b_2y} = g\left(\frac{y}{x}\right) \quad (6)$$

RFID reader mainly includes the issue of reader and RFID POS. Issue of reader is the main issue before the initial configuration of RFID tag, RFID tag to the main, from the write data and the activation of RFID label; in addition, it read and writes access to the highest. RFID POS is required to read RFID tag information, while the other transaction information such as transaction serial number, merchant code, business code, payment amount is sent to the mobile payment platform, and after receiving the complete payment confirmation message according to the payment business requirements to specific data is written to the RFID tab.

RFID is a RF analog front-end (RF AFE) and base band signal processing monolithic integrated circuit two parts. Baseband system includes a control logic (or microprocessor) and the necessary memory,

AFE energy and RFID signal interface, to provide the necessary base band system work on power and clock and other auxiliary signal, complete the receiving and sending data. Because RF AFE shielded power, smart cards on the clock, reset (POR) signal of contact with the outside world, reducing the attack points in a certain extent, and the contact type intelligent card compared to a certain improvement in security.

Smart home system integration of computer technology, communications technology, and control technology will work with home life about the various subsystems together organically, through integrated management, make home life more comfortable, safe and effective. Generally smart home system to achieve the functions required lighting control, electrical control, security alarm and other functions [7]. The Smart home system designed to meet the basic functions required to achieve the functions are: mobile phone users to send text messages to receive control commands to the GSM terminal module, turn on the lights, turn off the corresponding control and lighting system with automatic dimming function, when indoor light intensity changes, intelligently control the number of lamps to light off.

Smart home products for the home environment, appliances provide a shared access centers to realize the Smart home environment and its equipment management, remote management, centralized management and resource sharing. With the network technology rapid development in the foreseeable future, in the intelligent residential to broadband networks will be home computers, televisions, home appliances, security systems and other fused autonomous control, extensions, enjoy work, study, entertainment, family integrated information service platform.

system, complete alarm signal processing and transmission; compared to various parts of the power supply supplies power. Sensor temperature sensors, smoke sensors, pressure sensors, light sensors.

Definition of ontology from the form of point of view there are many, but from the connotation, different researchers is unified with the body, take it as the field (field range can be a specific application, can also be a wider range of different subject (people), the machine, the software system. For communication between (dialogue), interoperability, sharing and so on) a semantic basis, namely ontology provides a consensus [9]. But the consensus ontology provides objective is more important is the machine service, the computer can not like people fully understand the semantics expressed in natural language, it can only take the text as a string processing. Therefore, to discuss the ontology in the field of computer, and it is to discuss how to express recognition of common knowledge, formal and conceptual, as is shown by Fig. 2.

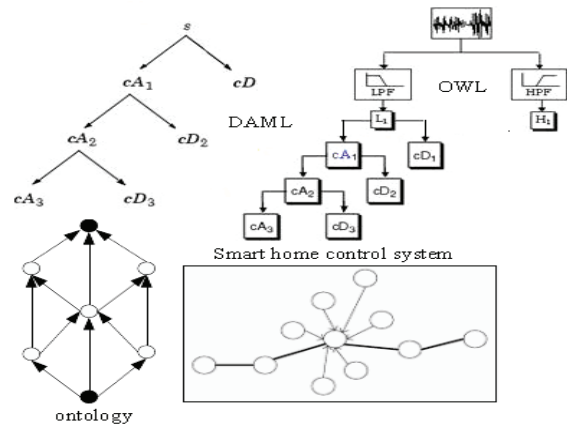


Fig. 2. Using Ontology Model to Building Smart home Systems.

### 3. Using Ontology Model to Building Smart Home System

Smart home control system usually consists of system server, Family Controller (various modules), a variety of routers, cable modem head-end equipment CMTS, switches, communications, controller, wireless transceiver, a variety of probes, sensors, various implementing agencies, printers and other major components. Smart home control system can be defined as a process or a system [8]. The use of advanced computer technology, network communication technology, integrated wiring technology, will work with home life about the various subsystems together organically, through integrated management, make home life more comfortable, safe and effective.

Smart home control system whose hardware consists of the following major parts, namely the control unit, sensor data acquisition systems, interfaces, and power supply. Integral part of the control unit controls function; sensor data acquisition

The formal is definition of ontology. As can be seen from the definition of core ontology defines the connotation and extension of knowledge, knowledge is composed of concept and relation instances of the knowledge base. The definition and instantiation knowledge process is called ontology instantiation. It is defined as follows: the body (or core ontology) said is available as follows [10].

$$\lambda p_2 = 3up_3, p_3 = \left(\frac{\lambda}{u}\right)^3 \frac{p_0}{3!} = \frac{\rho^3}{3!} p_0 \quad (7)$$

To describe and store Ontology, people study a lot description language, mainly divided into two categories: one is based on the AI ontology language, mainly in the following language or environment represented: KIF and Ontolingua, OKBC (open knowledge base connectivity), Loom, OCML (operational conceptual modeling connectivity),

FLogic like. In recent years, with the development of Web technology will be combined with the Web Ontology Web development is the inevitable trend in this context, they have appeared in a series of Web-based ontology languages such as RDF and RDFS, OIL, DAML, OWL (Ontology Web language), SHOE (simple HTML Ontology extension), XOL (XML one based Ontology an exchange language), OML (ontology markup language) and so on. Which, in addition SHOE is HTML-based, the rest are based on XML.

Mobile phone users is to send text messages using the GSM network control commands to the GSM transceiver control terminal, the realization of household appliances, curtains remote control. The design of the smart home, the curtain is controlled by stepper motors and DC 5 V analog appliances and curtains, small motor controller.

Environmental monitoring and alarm system, through the gas sensing sensors to monitor the room environment, when the index exceeds the set value, the alarm signal will immediately feedback via SMS to a smart phone, and can be based on the content of the feedback, make on-site processing, such as remotely open the windows, start ventilation equipment [11]. Intelligent security, security system with fingerprint recognition system, when the current entry is correct fingerprint access control system lifted, when the current entry is incorrect fingerprint access control system via the GSM network to send a message prompts the user into a stranger, as is shown by equation 8.

$$\xi_{ij}(k) = \left[ 1 + \left| \frac{\Delta x_i(k)}{\sigma_i} - \frac{\Delta x_j(k)}{\sigma_j} \right| \right]^{-1} \quad (8)$$

When users need to switch the remote control window, as long as the specified command using a mobile phone to send text messages via GPRS module receives and short message translated into commands can be identified to the family transmission controller, the controller has been treated by the ZigBee module wireless transmission to send commands to the controller connected with the windows, through the realization of the controller to control the windows.

Smart home control system hardware consists of five of its major parts, namely switched telephone network portion of program-controlled exchange signaling, control unit, sensor data acquisition system, GSM module TC35 modem with the interface and power supply section [12]. Program-controlled telephone switching network exchange signaling some of the major components MT8870 and a voltage detector, the system control section which is a key element which is integral with the control unit controls some features; sensor data acquisition system, GSM module TC35 modem and the control unit performs an alarm such as signal processing and transmission; compared to various parts of the power supply supplies power.

Ontology is domain experts and professional staff, with the continuous development of ontology, the ontology application gradually to the popularization, now more and more ordinary users began to establish their own body. Therefore, a lot of ontology construction tools were developed to build their own body to assist the user. At present, many domestic and foreign research institutions and scholars have a lot of Ontology development tools, the common feature of these tools is: by providing a good GUI interface, so that the construction of ontology instances and the information resource ontology annotation becomes simpler, easy to operate.

#### 4. Application of RFID Technology and Ontology Model in Designing Smart Home System

Smart home system consists of six modules circuits: GSM module and a GSM transceiver STC89C52 communications constitute control terminal circuit, dual MCU communication circuit, smoke sensor circuit, windows and curtain control circuits, lighting adjustment circuit, analog appliance circuits. The design STC89C52 as the core for smart home control block diagram of the hardware circuit, and it is in order to ensure reliable implementation of functions, circuit design with dual CPU architecture. In software programming work by the master and slave means to achieve the overall control system.

Things to smart home into the system, subsystem coordinate unconnected, there must be a strong compatibility central home processing platform, to accept and process control facilities give a message, and then send a signal to the appliance you wish to control or any other home subsystems. Functions of the central processing platform is Smart LAN at home, planning household subsystem guide and a variety of signals, with it, you can hand-held wireless remote control devices and home for rapid communication subsystem. Home central processing platform must also have good scalability to meet the user in the course of the growing demand points.

RFID application architecture: such as all kinds of RFID application system software and hardware and data interface technology and service technology. RFID system integration and data management: integrated technology such as RFID and wireless communication, sensor network, information security, industrial control, RFID, middleware technology application system, a mass of RFID information resources organization, storage, management, exchange, distribution, data processing and cross-platform computing technology [13]. RFID public service system: to provide the basic service system to support RFID social application certification, registration, code management, coding system mapping, code analysis, searching and tracking technology and services, as is shown by equation 9.

$$\frac{f'(x_1)}{2x_1} = (b^2 + a^2) \frac{f'(x_2)}{4x_2^3} = \frac{\ln \frac{b}{a}}{b^2 - a^2} x^3 f'(x_3) \quad (9)$$

RFID tags embedded products, card reader, RFID middleware and object name server ONS (Object Name Server), IS information server (Information Server), IS query. Context awareness is a kind of environmental information label sensor network and based on RFID, context-aware systems based on RFID and wireless sensor network is in this environment information label as the main object of the build for the future of various environmental. In the future, the RFID tag components and sensors will be integrated into the perception of label (Sensing Tag, SG), family or building automation system will automatically control the indoor environmental equipment.

Semantic Web ontology is located seven fourth layer architecture, will introduce the Semantic Web ontology architecture is to capture the relevant knowledge in the field, provide a common understanding of the domain knowledge to identify common recognition in the field of vocabulary, and gives them the relationship between words and vocabulary clear definition of the concept through to describe the relationship between the concept of semantics.

In the model building phase, an abstract representation of domain knowledge ontology modeling occupy most of the time, knowledge representation that is found in related field concept, conceptual integration between the level of potential relationships between concepts and axioms [14]. Because the body can not determine the domain ontology modeling phase involved all instances of the field, so the ontology modeling stage is generally no need to consider the field of instances. Typically researchers hope to establish a body which has got to versatility, able to represent all the knowledge of a particular field.

The entire system as a smart home information center console control center, which is responsible for the coordination of the various modules can be sent to the host mobile terminal query and command information, air conditioning control module and curtain control module for the intelligent control module has a separate module control programs, they sent to the host temperature and humidity information, but were conditioned to receive control signals sent by the host, the host queries the way through the process to obtain this information. Human body sensing module with gas leak detection module can only send signals to the host, the host gets its information through the interrupt mode.

1) The ontology L (K2) in the grid nodes are small to large content stored in the order in the queue V;

2) The working principle of the RFID system point of view, the system generally consists of signal

transmitters, signal receiver, transmitting and receiving antennas of several parts;

3) GPRS communication module is installed in the smart home controller, the main function of the network connected to the Internet via GPRS networks, and establish a communication link with the monitoring center, two-way data communication;

4) if  $f^*(\{x^*\}) \not\subseteq \text{Intent}(\text{inf}(L))$  then

if  $\text{Extent}(\text{inf}(L)) = \Phi$  then

$\text{Intent}(\text{inf}(L)) := \text{Intent}(\text{inf}(L)) \cup f^*(\{x^*\});$

5) Software design mainly consists of the following major sections: the data acquisition and data analysis part and Analysis control part.

The use of smart home system design XSBBase270 embedded platform, C8051F series microcontroller, MAX232, and various types of home sensor design a smart home control system. System design include: system design and debug hardware and control software to program and debug. The system uses a variety of sensors to detect and feel the outside of the signal, and through a program has been set to complete the intended action, and ultimately intelligent.

This smart home system adopts XSBBase270 configured 32M FLASH ROM, 64M SDRAM, and equipped with a touch screen, Ethernet, USB, serial port, CF / MMC, PCMCIA and other interfaces. Smart home system meets the hardware requirements for the control center. In a smaller volume of the overwhelming majority of the integration of embedded systems commonly used functions. XSBBase270 development platform built-in GPS module, you can directly XSBBase270 platform validation and development of GPS navigation applications or engage in research, as is shown by Fig. 3.

Smart home system is to test first unit test, mainly in the completion of each module of the entire system after a comprehensive test to determine compatibility between modules to ensure the overall system performance and stability. In this section will be windows, curtain remote control, gas detection module testing, lighting control system testing. Test environment for the indoor room temperature, electromagnetic environment as dense urban neighborhood. The paper proposes application of RFID technology and ontology model in designing smart home system.

Reader according to different structures and techniques may be read or read / write device, the RFID system information control and processing center. Usually coupled to the reader module and it is the transceiver module, and the control module and interface unit. Between reader and transponder generally use half-duplex communication for information exchange, while the reader through a passive transponder coupled to provide energy and timing. RFID system is aimed at the identification information environment can identify and use of resources.

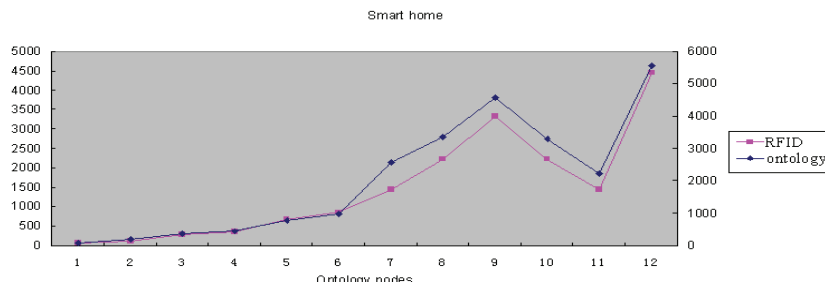


Fig. 3. Comparison results of designing smart home system based on RFID with ontology.

## 5. Conclusions

Smart home control system's main functions include communications, automatic control equipment, and security three aspects. With the development of new technologies and automation, increasing the number of sensors used, the function is getting stronger; various sensors have been standardized, modular, which gives smart home control system design. Ontology is used to describe a certain area or even a wider range of concepts and relationships between concepts, making these concepts and relationships within the shared recognition with common, clear, single definition, in order to achieve between human and machine interaction. RFID software application support system includes a run on the tag and reader software and between the reader and the mobile payment platform between the middleware.

## Acknowledgements

This paper is supported by the National Natural Science Funds of China (61272015), and also is supported by the science and technology research major project of Henan province Education Department (13B520155) and Key scientific and technological project of Henan province (102102310058).

## References

- [1]. Kee-Hyun Choi, Kyung-Soo Jang, Ho-Jin Shin, RFID-ACP: RFID-based digital content identification and authentication mechanism in smart home environments, *International Journal of Digital Content Technology & its Application*, Vol. 5, No. 6, 2011, pp. 129-141.
- [2]. Shakeb A. Khan, Alka Nigam, A. K. Agarwala, Mini S. Thomas, T. Islam, Advanced oscilloscope triggering based on signal frequency, *Sensors & Transducers*, Vol. 136, Issue 1, January 2012, pp. 105-117.
- [3]. Bhuptani Manish, Moradpour Shahram, RFID field guide: deploying radio frequency identification systems, *Prentice Hall PTR*, 2005.
- [4]. Huang Haiping, Wang Ruchuan, Qin Xiaolin, Sun Lijuan, Jin Yichao, A novel Internet of things' paradigm for smart home using agent-based solution with hybrid intelligence, *International Journal of Digital Content Technology & its Application*, Vol. 5, No. 10, 2011, pp. 136-151.
- [5]. Weiyi Qi, Hai Shen, Hanning Chen, A discrete artificial bee colony algorithm for RFID network scheduling, *International Journal of Advancements in Computing Technology*, Vol. 4, No. 14, 2012, pp. 324-332.
- [6]. He Jialiang, Ouyang Dantong, Ye Yuxin, An efficient lightweight RFID authentication protocol for low-cost tags, *Advances in Information Sciences & Service Sciences*, Vol. 3, No. 9, 2011, pp. 331-338.
- [7]. A. Venkateswaran, A. Amalin Prince, A novel MEMS based current sensor design for smart grid applications, *Sensors & Transducers*, Vol. 138, No. 3, March 2012, pp. 2-13.
- [8]. Houjie Li, Tianshuang Qiu, Haiyu Song, Cheng Zou, Liping Guo, Optimization and implementation of lighting system for smart home based on RF technology and GSM network, *International Journal of Digital Content Technology & its Application*, Vol. 7, No. 5, 2013, pp. 653-661.
- [9]. M. Daoud, and L. Tamine, et al., Learning implicit user interests using ontology and search history for personalization, in *Proceedings of the Workshops on Web Information Systems Engineering (WISE' 2007)*, pp. 325-336.
- [10]. Sunong Wu, Design and development of real-time production monitoring system base on RFID and multi-agent technology, *Advances in Information Sciences & Service Sciences*, Vol. 4, No. 22, 2012, pp. 690-697.
- [11]. Xiaotie Qin, Yuesheng Gu, Xiaorong Wang, Fang Wang, A comprehensive smart home networking system, *Advances in Information Sciences & Service Sciences*, Vol. 5, No. 3, 2013, pp. 708-716.
- [12]. M. Missikoff, R. Navigli, P. Velardi, Integrated approach for web ontology learning and engineering, *IEEE Computer*, Vol. 35, Issue 11, 2002, pp. 60-63.
- [13]. Klaus Finkenzeller, RFID handbook: fundamentals and applications in contactless smart cards and identification, Second Edition, *John Wiley & Sons*, 2003.
- [14]. A. Maedche, S. Staab, Ontology learning for the semantic web, *Special Issue on the Semantic Web, IEEE Intelligent System*, Vol. 16, Issue 2, 2001, pp. 72-79.

## Design and Development of Multimedia Video Monitoring System Based on Wireless Sensor Network

Liang SONG, Ming XU, Hong QIAO

Modern Education Technology Center of Beijing University of Technology,  
Beijing, 100124, China  
Tel.: 13681591432  
E-mail: [songliangedu@163.com](mailto:songliangedu@163.com)

*Received: 17 June 2013 / Accepted: 25 August 2013 / Published: 30 September 2013*

---

**Abstract:** The nodes of wireless sensor network are mainly responsible for the collection and processing of the information and send to neighboring nodes. The paper presents design and development of multimedia video monitoring system based on wireless sensor network. Video monitoring system is designed to analysis and judgment of target behavior in the scene, so that let the computer correctly understanding of the target behavior analysis and the classification of the target. The wireless sensor network self-organization protocol is analyzed and studied. This paper designs a real-time transmission system of adaptive network video monitoring. FISCO can not only guarantee the arrival of a new node quickly joins, but caused only local changes in network communication structure. The results show that different structures may have different maintenance methods and energy consumption, global and local structure is better than pure global structure type.

*Copyright © 2013 IFSA.*

**Keywords:** Wireless sensor network, Video monitoring system, Self-organization protocol, Multimedia.

---

### 1. Introduction

Wireless sensor network is deployed in the region to monitor many micro-sensor nodes, through wireless communication to form a multi-hop self-organized network system, its purpose is to cooperative sensing, collecting and processing the network coverage area perceived objects, and then send to the observer. Sensor, sensing object and the observer constitute the three elements of wireless sensor network. These small sensors generally referred to as the sensor node (senor node) or dust (mote). There are one or several base stations generally such networks (called gathering base station) to focus on the small.

Sensor nodes by airplane seeding artificial arrangement, etc., are deployed in the perception of objects inside or near. These nodes through the self-

organizing way constitute wireless sensor network, in a collaborative manner perception, acquisition and processing network coverage information specific to the region, can realize the acquisition, processing and analysis of any place at any time, and the data is transferred back to the Sink nodes in a multi-hop relay nodes, Sink emission ability! With high power, the whole area of the data to the remote control center for centralized processing. Satellite link can be used as a sink link; with the help of unmanned aircraft recovery of sink nodes in the monitoring area above the data is also a kind of way.

The video monitoring system is one of important modern safety precautions. The infrared perimeter alarm system, peripheral electronic fence, access control intercom system and indoor infrared alarm system constitute the safety barrier of modern intelligent buildings [1]. Video monitoring system

structure includes two parts, one for the front-end monitoring, and the management of the background. Fang Anzhuang was in need of surveillance camera, commonly known as the front-end monitoring. Front-end monitoring functions include the collection and coding of video processing. Then through video cables or network is to send data to the distal end of the end, commonly known as video surveillance management background. Management background will be responsible for decoding video data received and displayed, so as to achieve the effects of real-time monitoring. At present, the market demand of monitoring is not limited to large factories, banks and other places, the ordinary family is also an urgent demand for monitoring and real-time monitoring, monitoring of the interaction of the people there are increasingly high requirements.

All of the wireless sensor network nodes have the same function, but at one time, each node may be performing different functions. According to the function, can put the nodes into the sensor nodes, cluster head node and sink node 3 types. When a node as a sensor node, is mainly collected data about the surrounding environment (temperature, humidity, brightness and) and A/D conversion, by the processor, and finally by the communication module to send to neighboring nodes, and the nodes to executive function data forwarding, or send the data sent over to the sink node the node or nodes closer to the sink node; when a node as cluster head node, main is to collect all the nodes in the cluster to collect information, data fusion, sent to the sink node; when a node as the sink node, its main function is to connect sensor network and external network (such as the Internet) the data, collected by sensors to the user through the Internet or satellite transmission. The paper presents design and development of multimedia video monitoring system based on Wireless Sensor Network.

## 2. Self-Organization Protocol for Wireless Sensor Network

Wireless sensor network is composed of a number of low power consumption, small size of sensor nodes, and the wireless communication mode since the formation of a network. These distributed nodes can cooperate to implement monitoring, sensing and collecting all kinds of environment information, has a very broad application prospects. In recent years, research in wireless sensor network is very rapid, gained abundant research achievements. The self-organizing algorithm is one of the core technology of wireless sensor network, through the good network topology automatically generate self-organizing algorithm, can improve the routing protocol and the media access control (Medium Access Control, MAC) the efficiency of the protocol, can lay the foundation with the step and the goal of many aspects of data fusion, time, but also conducive to save energy of the node to prolong the network lifetime.

This paper analyzed the wireless sensor network MAC protocol the problem: S-MAC protocol according to the data flow in the network is not adaptive to change the duty ratio, further saving energy; at the same time, also discusses the problems of a MAC layer protocol for this problem based on the development of it [2]. On this basis, put forward according to the node data packet retransmission times to determine when the former network data flow rate, which is based on a weighted 5 period the average retransmission times judge network data flow current, when the average value exceeds a threshold, it should increase the sense of time duty ratio, conversely, decreased sense time of the duty ratio, and emergencies should be on the network data flow suddenly increased, the node listens time duty ratio were amplified, so as to cope with large data traffic in the network.

Wireless sensor network using the traditional "flat" structure, micro sensor nodes deployed for isomorphic data acquisition in the monitoring area, each node's computing ability, communication distance and energy supply is quite. The node of the data collected through multi-hop communication manner, by means of forwarding to other nodes in the network, the data back to the sink node, the sink node to connect with other networks, remote access and network query, management. Flat structure of the network can work, but with the increasing of the number of nodes, expanding network coverage, the communication path length will lead to increase the probability of packet loss, network performance degradation, can also cause the intermediate nodes for forwarding data more energy consumption, reduce the network life cycle.

$$w(n+1) = w(n) + \frac{1}{2} \mu [-\nabla (E\{\varepsilon^2(n)\})] \quad (1)$$

Energy-saving MAC protocols in wireless sensor network research work shows when sending a RTS packet, the remaining time domain has been sent to the entire message reserved channel occupancy time, and then the data and ACK packets in time with the packet to send descending. And repeat work shows, when a fragment of the sender's packet is not received ACK, it immediately retransmission and the expansion of the residual time. Because each packet and ACK have the remainder of the domain, so even if a node to wake up (due to retransmission delay time), can also be the time remaining until the new, and again into sleep, waiting for the end of transmission. The use of ACK in each data segment after the purpose is to prevent the hidden terminal problem.

Wireless sensor network architecture design an adaptive is difficult, partly because of the wireless sensor is dynamic and mobility is very high, on the other hand is because wireless sensor by computing ability, communication ability and energy constraints. So, for the development of wireless mobile sensor

network protocols and architecture must have ability of self configuration and self adaptation, and it increases with the expansion of network scale and the sensor network members, but also has scalability and high reliability. Usually use network coverage and network core node way now to find the members in a communication network, but due to the core node coverage and maintenance cost is very high, these methods are not suitable for wireless sensor networks.

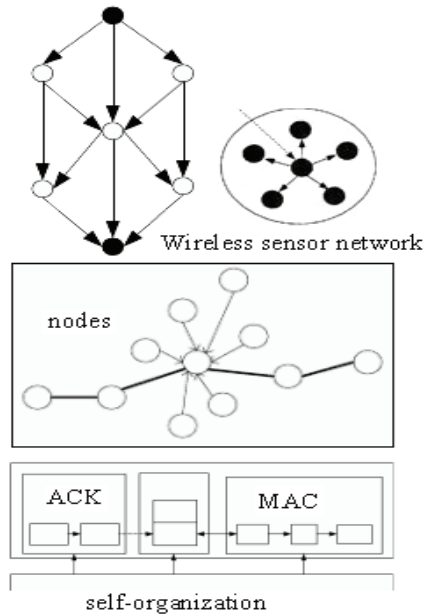


Fig. 1. Self-organization Protocol for Wireless Sensor Network.

In the process of transmission, it is possible to a neighbor node wakes up or a new node joins. If the node is the receiver neighbors rather than the sender, it would not hear the sender of the data being transmitted. If the receiver does not send ACK frequently, the new node may be false from the carrier sense it concluded in the media is free, and began to send data, resulting in the transmission will be available was damaged in the recipient.

The nodes of wireless sensor network is a wireless sensor network deployed to the study area for collecting and forwarding information, object collaboration to complete the assigned task. The sensor node is the basic unit of wireless sensor networks; node design directly affects the quality of whole network. The nodes of wireless sensor network is mainly responsible for the collection and processing of the information around, and send the collected data to the neighboring nodes or node adjacent nodes send data is forwarded to the base station or closer to the base station [3]. It is generally composed of data acquisition module (sensor, A/D converter), processing module (microprocessor, memory), data forwarding module (wireless transceiver module) and power supply (battery).

$$STD = \sqrt{\sum_{i=0}^{M-1} \sum_{j=0}^{N-1} (f(i, j) - MEAN)^2 / (M \times N)} \quad (2)$$

This paper first describes the definition of wireless sensor networks and its architecture, node structure and network protocol stack, and the widely application of wireless sensor network. Then analyzes the difference between wireless sensor network and other networks, as well as the characteristics of wireless sensor network self-organization protocol, and according to the organizational structure of wireless sensor network of self-organizing protocols are classified, according to the classification of self-organization protocol in each category, and proposed a self-organizing protocol FISCO. At the end of each class of self-organizing protocols are simulated, and the Imote2 platform realized these self-organizing protocols.

Wireless sensor network consists of sensor nodes in spontaneous networks, sensor nodes have limited capacity and energy resources information processing is one of the major characteristics of the wireless sensor network [4]. In wireless sensor networks, there is no communication model and the center of predefined control unit, connect the network effectively without human intervention. In the sensor network, sensor nodes are usually placed in no infrastructure. Position sensor nodes could not precisely determined, each neighbor relationship between nodes in advance do not know, as by airplane seeding a large number of sensor nodes to a vast area of virgin forest, or randomly placed into human inaccessible or dangerous area. This requires the sensor node has the ability of self-organization, automatic configuration and management, to form a multi-hop wireless network system monitoring data through the topology control mechanism and network protocol.

$$PV(x) = \frac{1}{y_2 - y_1} \sum_{y=y_1}^{y_2} I(x, y), \quad x \in (x_1, x_2) \quad (3)$$

This algorithm uses the LEACH algorithm in the “wheel” thought; each round consists of 2 stages: one is the cluster establishment stage; two stages is the data transmission. In a cluster, mainly to complete the generation of cluster head selection marry cluster, and time allocation; in data transmission phase, mainly to complete the various sensor nodes send the collected data to upload to the base layer, which includes the necessary data fusion, data encryption and so on.

Wireless ad hoc network is composed of tens to hundreds of nodes, using wireless communications network, dynamic multi-hop mobile peer-to-peer network. Its purpose is to through dynamic routing and mobility management technology of multimedia information transmission with quality of service requirements flow. Usually the node with energy supply continued. Wireless sensor networks with

wireless ad hoc networks have similarities, but there is great difference. Wireless sensor network has no communication structure defined in advance, no center control unit, in this sense, wireless sensor networks and wireless ad hoc network is very similar, but the wireless sensor network more vulnerable to low processing ability, limited energy and a large number of nodes deployment of chaos.

Wireless sensor network is used for low power wireless communication technology (such as IEEE802.15.4) to communicate in a wireless ad-hoc manner [5]. To construct a no human intervention effectively connected network, there are two key mechanisms: self configuration and self organization. Since the configuration is to solve the problem of dynamic distributed network address assignment and network configuration parameters, and the self-organizing network is constructed to provide effective communication. In order to confirm the nodes in the network and the establishment of a connected network, each node in the target network must have a unique identifier, as is shown by equation 4.

$$p(s(\hat{k}) | a(\hat{k})) = \frac{p(a(\hat{k}) | s(\hat{k}))p(s(\hat{k}))}{p(a(\hat{k}))} \quad (4)$$

Methods using cluster heads multi-hop data transmission, how to elect the next hop cluster head node is highlighted in this part of the problem. Firstly, a threshold value TD\_MAX, if the cluster head to the rendezvous point distance is less than TD\_MAX, directly with the converging point of communication; otherwise, it should be possible to use multi-hop routing mode transmits the data to the sink node. Suppose that  $D(A, DS) > TD\_MAX$ , each cluster head near the cluster computing in cluster head A the first episode,  $E_{relay} = d^2$  link quality cost brought about by  $(A, X) + d^2(X, DS)$ . Among them,  $D(A, X)$  is the first A cluster to cluster head X distance.

In some protocols, nodes with flooding queries are organized into the global tree (global tree). This kind of network structure is a plane without a local structure. Another type of protocol, and the existence of global structure and local structure (global tree and local cluster), most of the protocols are such. The protocol consists of two stages. First of all, node based on heuristics or probability of different algorithms are organized in clusters; then the cluster head will be further organized into a global tree, cover the entire network, to ensure connectivity. Between two adjacent cluster heads can be connected directly, can also be called gateway (gate) intermediate nodes connected. The network structure of cluster head direct connections between will produce a stratified, cluster head has a variety of power requirements can be adjusted.

$$C(t) = \frac{E[B(t), B(-t)]}{E[B(t)^2]} = 2^{2H-1} \quad (5)$$

Wireless sensor network in a highly dynamic environment, mobile and communication failure will always occur, thus not only to adapt to dynamic characteristics of network and network information transmission function correctly, but also to maintain a certain degree of rationality, that is to say reliability is a very important factor. Therefore, in the network architecture in the hierarchy with the absolute mobility model and relative stability model, and use distributed cyber source to find ways to avoid causing the whole network fault conditions due to a problem of single point.

The communication model in wireless network is a graph  $G = (V, E)$  said,  $V$  is the vertex set,  $E \subseteq V^2$  is the set of edges. Only the vertex  $v$  can correctly receive vertex  $u$  messages between  $V$  and  $u$ , and then the edge  $(U, V)$  exists [6]. We assume that all nodes in wireless range are the largest  $R$ , and all of the links  $(U, V)$  is symmetric:  $(U, V) = (V, u)$ . This map is a non directed graph (non-orientation). We assume that there are some obstacles in the communication area, only between points  $u$  and  $V$  when the distance is less than the transmission range  $R$ , link exists only between  $u$  and  $V$ , while  $(U, V)$  is  $E$ .  $E = \{(U, V) \in V^2 | d(U, V) \leq R\}$ .

Because the nodes of wireless sensor networks and traditional ad hoc network node in the performance, energy, network and the number of deployed in different ways, we first describe the model of sensor nodes and the network. In order to provide fast, scalable and efficient network organization, in order to behind the introduction of new structure, defines some specific requirements to support self organization and self configuration. Wireless sensor nodes deployed in a certain size of chaos in the region, we believe that sensor nodes have the following characteristics: (1) all nodes have the processing power and communication capabilities of the same, but they can be equipped with sensing module different (temperature, light, wind speed and so on.). That is not a node can have an important role in the communication structure and information processing. (2) All nodes have the same storage node energy, once started; the battery will not be replaced. Therefore, energy efficiency is the primary requirements of protocol design, as is shown by equation 6.

$$\|Y_m\| = \left( \sum_{n=1}^N |Y_m(n)|^2 \right)^{1/2} \quad (6)$$

The plane structure of the network scalability is not very good, so it is not suitable for highly dynamic, highly mobile characteristics and the need for highly scalable wireless mobile sensor networks. Therefore a hierarchical network architecture design, and which is a hierarchical structure of landmarks (LMH) of a kind of improvement. The design of the network information into data information and control information, the core routing node is not used to transfer help within its

area of node data and forwarding, but to coordinate information transmission path between ordinary nodes and network structure based on traditional string comparison, ability has the dynamic self-configuration, and not depending on the area of the management and the size of the routing table. Because of all the information flow string without signposts core node, this increases the reliability of the network.

In a geographical area, a plurality of grouping nodes constitutes a cluster. There is a cluster head of each cluster, some specific functions for the entire cluster. Using the cluster to form a wireless network is with distributed cluster head election algorithm. There is one based on the minimum identification number (ID) cluster head election algorithm: in all the neighbors mark the minimum node is elected as cluster head [7]. The cluster algorithm based on applies only to reach all the nodes in the network is assigned a unique identification number. Initially, all nodes are candidates.

$$q(n) = \frac{\gamma^{-1} R^{-1}(n-1)x(n)}{1 + \gamma^{-1} x^H(n) R^{-1}(n-1)x(n)} \quad (7)$$

In this section of the self-organizing protocol is a connected dominating set on the network based on CDS (Connected Dominating Set). CDS connected dominating set of a small base (Connected Dominating Set) is very useful for some protocols, such as broadcast protocols in wireless sensor networks, because it can reduce the redundant messages. CDS connected dominating set minimum cardinality (Connected Dominating Set) is called MCDS, is a NP problem. Therefore, CDS connected dominating set many distributed (Connected Dominating Set) algorithm is designed to compute an approximate MCDS. Each node having algorithms assume that the network has a unique label.

Although the characteristics of the wireless sensor network is the backbone infrastructure is not physical, but can through the node connected dominating set to form a virtual backbone network, nodes and the rest to communicate through the backbone network. The virtual backbone is composed of a few selected by constructing algorithm of nodes, can not only bear the routing function, but also can flow control, the connectivity of network management functions. Only a small number of nodes participate in routing function, and this will greatly reduce the network cost, improve the utilization of system resources.

### 3. Development of Multimedia Video Monitoring System

Front-end equipment in video surveillance system is a camera. Image sensor is the first element of video

signal acquisition. The image sensor is a group of photosensitive chip; they used the number of pixels to record visual information. On the light response and the intensity of reaction is converted into the corresponding numerical. When light passes through from the red, green, blue filter mirror, can get every color reaction values. Then, it is in the processing by software, to determine each pixel color. Now commonly it is used with CCD and CMOS two kinds of image sensor.

In the application of multimedia, video image information takes up a lot of space. Not after the image video compression for storage and transmission has brought great inconvenience. This chapter first introduces the mainstream video compression standard at present, and then through the analysis and comparison of the selection of the most suitable for compression method is designed in this thesis. Video compression standard MPEG-4 MPEG-4 is a set of audio, video information coding standard, by the international organization for standardization of IEC moving picture expert group set. MPEG-4 multimedia system pays attention to the interactivity and flexibility, mainly used in video phone, video conference [8]. Coding based on MPEG-4 standard object, convenient operation and control. In the bit rate control, even in low bandwidth condition, MPEG-4 can also use rate allocation method, the object of interest to the user multiple distribution of bit rate, on the other, less distribution, ensure the subjective quality.

$$\delta I_i = \begin{cases} I(P) - I(P_i), & i = 0, 1, 2, 3 \\ I(P_i) - I(P), & i = 4, 5, 6, 7 \end{cases} \quad (8)$$

Video compression is the image compression coding, which is convenient for transmission and storage capacity decrease. According to analysis of statistical characteristics of images, between the adjacent pixels, adjacent line or between adjacent frames, there are strong correlation. These correlations reflect to a large number of redundant information in the image, such as due to the presence of correlation between adjacent pixels spatial redundancy, the spectral redundancy due to the presence of correlation between color elements, caused by the human visual system the psycho visual redundancy etc. The compressed video data is to use the statistical characteristics of image signal inherent, to reduce the digital transmission rate by removing the correlation, to achieve the purpose of compression.

The first problem encountered in video surveillance is often extracted from image sequences in the interesting part, namely the prospects, such as moving people, vehicles and so on, can also be called motion detection. Since the end of last century, the research technique is widely. In the fixed scene conditions, mainly divided into two categories: one is based on background difference method, the starting point is the

background model maintenance monitoring scene, the current difference between image and background larger parts as foreground; another method is a method based on optical flow field, the starting point is the large area has obvious motion in image sequence as the foreground. Recently some scholars morphological filtering is applied to the image sequence, space time structure.

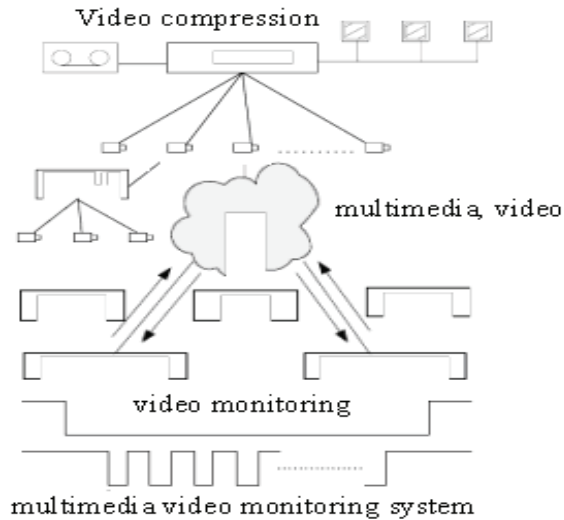


Fig. 2. The design of multimedia video monitoring system.

The hardware monitoring application system architecture of the system is based on a multimedia processor ARM9. But currently on the market has a lot of monitoring products based on embedded, so in order to make the system is competitive in price and performance, we must first do the hardware research selection, secondly in terms of software, requires a combination of hardware platform, in-depth analysis and detailed design [9]. Streaming media system consists of two parts: the server system and the operation monitoring at the front end of the PC client management system, as is shown by equation 9.

$$\begin{aligned} C(a(k) | \mathcal{R}_k) &:= \text{cov}(a(k) | \mathcal{R}_k) \\ &= \sigma_{s,s_0}^2 \beta \beta^T + \Sigma_\varepsilon \end{aligned} \quad (9)$$

The ultimate goal of video surveillance system is to the scene in the target behavior analysis and judgment, in order to let the computer correctly understanding of the target behavior analysis, the classification of the target. Current research in this area is very extensive, classification methods have many characteristics in different scenarios, goals are not the same, the classification methods are not the same, such as the traffic system, by whether the periodic motion resolution people and vehicles, can also according to the target appearance, shape and motion of the statistical characteristics of the truck,

car to distinguish; on human and animal can be differentiated according to their shape characteristics of different size and shape; similar objects by the shape is very difficult to distinguish, for example, on the road bicycle and motorcycle, in this case we can use the target movement speed to distinguish, because their speed is not the same; according to area and compact we can distinguish between the individual and the crowd.

Each local monitoring system adopts centralized control of distributed monitoring, fashion design. Baoshan court this department as an example: system acquisition signal front entrance, walls, floors, parking, staircase aisle, registration hall, court, detention room and other parts of the hospital, do the monitoring without blind angle; video signal transmission system using coaxial cable or twisted-pair as transmission media, these two ways have their own characteristics, the system for indoor network information port room using twisted pair transmission signal; video signal is sent to the monitoring center through the video distributor will signal.

Video transmission system is using coaxial cable and unshielded twisted pair category five super mixed transmission mode [10]. The wiring simple and close to the point of using coaxial cable, wiring pipes have difficulty or a distance of more than 500 meters of the point, the use of the original horizontal subsystem or discharge of unshielded twisted pair five. Realization of video distribution, and when the video signal is transmitted to the control room, the first to enter the video signal distributor. Video Splitter is a video signal is divided into signal multiple identical in the case of no loss of signal, and the output to a plurality of display device, a device. Its role is to drive the input current, because the input current to drive a few road the same display equipment, will shunt caused driving ability is not enough, so you will need to input current can be enlarged, so that the output of each road and input are capable of driving the same phase.

#### 4. Design of Multimedia Video Monitoring System based on Wireless Sensor Network

Due to the adoption of digital recording technology, the recorded image anti-damping anti-interference ability greatly enhanced. Digital image record does not exist copy deterioration, so no matter how many times the retrieval or video playback will not affect the play of image clarity. While recording the conventional way of simulation video tape in several retrieval and playback, image quality will have certain attenuation and thus decrease the signal-to-noise ratio, image after each copy will be deteriorated again. Therefore, in the video surveillance system, hard disk video recorder

instead of analog video recorder will become the mainstream trend of technology development. Hard disk recorders in video monitoring system should have the following basic functions: compression, video, image, backup, network, PTZ control etc.

In the cluster head election stage, the cluster head node election in the network. Different connected dominating design goal set CDS for the purpose of use and different. Design goals may be as follows: the performance range, the degree of localization, time and message complexity and topological stability. In any case, connected dominating set CDS algorithm must be distributed to local, in order to achieve a set of goals. Said from some kind of degree, the cluster head chosen is a collection of a relationship exists between the points. The simplest method is based on the mark ID. Nodes with minimum mark were selected as the cluster head. Find the cluster head node, will start construction of the maximum independent set, as is shown by equation 10 [11].

$$\binom{\delta}{k} \equiv \frac{\delta!}{k!(\delta-k)!} = \frac{\Gamma(\delta+1)}{\Gamma(k+1)\Gamma(\delta-k-1)} \quad (10)$$

Data acquisition includes audio and video data, audio data through the MIC collection, video data collected through the camera (CCD camera or CMOS camera) and the A/D converts the analog signal into digital signal.

The local real-time monitoring through the chip is to achieve four segment displays. The chip can display 16 channel video at the same time, display and output can be TV or VGA Monitor. Audio and video coding, coding DSP processor through the I interface for audio and video data after A/D conversion, audio and video data coding compressed into MPEG4 video and MP3 audio stream by software. Data storage, DSP processors will be compressed MPEG4 video and MP3 audio stream through DPRAM transmitted to the main processor, the main processor audio and video data stream is stored to the local SATA hard disk.

$$\begin{cases} \Psi^1(x, y) = \varphi(x)\psi(y) \\ \Psi^2(x, y) = \psi(x)\varphi(y) \\ \Psi^3(x, y) = \psi(x)\psi(y) \end{cases} \quad (11)$$

Because of the special constraints of wireless sensor networks, self-organization and self-configuration independent design will lead to an inefficient network. In particular, the configuration time and control message cost, node self-organization has efficiency of a valid address this assumption limits the network formation mechanism. Since the main task is to ensure that the allocation is unique in the whole network to address. Since the organization aims are to node through the local information network. The network

structure can be used to produce each logical link to the neighbor nodes and each node roles (such as leader) to the relationship between the representatives.

Network real-time monitoring, when a remote real-time monitoring network client, the encoded audio and video stream will be transmitted through the network to the client. Local video playback, the main processor user selected video read out from the local hard disk and through DPRAM transmitted to the decoding of DPS processor, the DPS processor decodes the audio and video stream. The video data is sent to the four segment display chip, the audio data is sent to the audio D/A digital-analog conversion and output. Network playback, the main processor user selected video read out from the local hard disk and sent to the client through the network controller. Audio and video data client will receive the package composed of frame, and decoding and playing.

FISCO (Fully Integrated Scheme of self-Configuration and self-Organization) point of view is self configuration and self organization is connected together, it can improve efficiency of network formation, reduce the information consumption, prolong the network life cycle. FISCO can not only guarantee the arrival of a new node quickly joins, but caused only local changes in network communication structure. In this mechanism, to avoid periodic reorganization, it can reduce message cost and save energy of sensor nodes.

FISCO is an event driven mechanism, including the node join, leave and partition management process. Local recombination of cluster head and gateway conversion for members is to save energy. FISCO is carried out in a fixed in the 2D space; nodes are randomly distributed, and random in time of need. Nodes broadcast transmission radius and the same nicest transmission radius. According to the geographic locations of the nodes, there will be a separate partition.

In the DVR software system, application of multi-process structure, interposes communication via parameters. Application can be divided into two categories: storage and management system; network communication. Network communication software mainly includes system management, network communication module, communication module and real-time network and playback module. Other applications are stored in the system and management software, including video storage and UBS burner and UBS hard disk backup, alarm logic management process, image parameter management process, PI management process, PTZ control management process. In addition, the system management and set all are set by the local user interface process.

The simulation on the Transim simulation framework, Transim simulation framework is developed with OMNet++, OMNet++ is a discrete event simulation environment based on C++. The

simulation framework of the same means, eliminating power model same, transmission model of the same, medium access control protocol (MAC protocol) messages of the same size.

The paper presents design and development of multimedia video monitoring system based on Wireless Sensor Network. Wireless sensor network is composed of some finite nodes, the communication path between nodes can use the unit disk graph to represent, in the unit disk graphs, if two nodes in the transmission range, and that between the two nodes is a connection. In the unit disk graphs, all nodes have the same transmission range. The sink node: node does not participate in the organization, which in the network; communication model: through a multi-hop network, node and sink node communication, node and sink node does not make a multi-hop communication; media access: we use the network model of random access. Because the control data overhead, we think the complex medium access control is not appropriate, but in a dense network.

In this paper, the design and implementation of multimedia video monitoring system based on wireless sensor network, key technology of video capture, video transmission, video distribution,

video signal switching, video storage, remote video surveillance and other major aspects of research and analysis, realizes the real-time remote monitoring, also can be local or remote call of video data.

## 5. Conclusions

The platform test, it is difficult to obtain the information of nodes during operation. So we need some special method to estimate the energy consumption of self-organized protocol. We use byte information to estimate the energy consumption, obtained by byte of information results, although the data is not very accurate, but reflects a general trend. In the experiment of FISCO, gateway and the cluster head failure need not through global restructuring. It can be seen from Fig. 3, after the 3 round of restructuring, connected dominating set maximum independent set (MIS-CDS) based on the energy consumption will be lower than the flooding tree (Flooding tree) energy consumption. After about the 8 round after the reorganization, FISCO energy consumption will be lower than the connected dominating set based on maximal independent set (MIS-CDS).

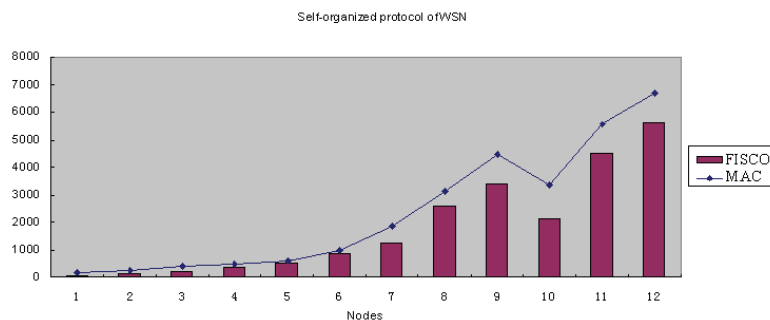


Fig. 3. Comparison results of multimedia video monitoring system based on Wireless Sensor Network.

This paper presents a video monitoring system network real-time transmission design scheme optimization, and modular design, analysis and implementation strategies to the working principle of the system. To some extent, solve the network transmission of real-time monitoring of the client.

## References

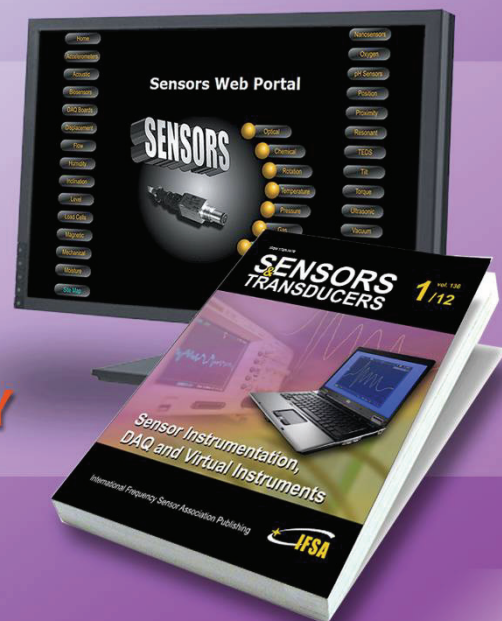
- [1]. Longzhuang Li, Yan Zhang, Yuzhe Wei, Shanxian Mao, Multi-hop qualitative direction estimation in ad-hoc wireless sensor networks, *International Journal of Information Processing & Management*, Vol. 3, No. 1, 2012, pp. 1-16.
- [2]. Natalija Nelson, Self-healing wireless sensor networks: results that may surprise, *Globecom Workshops*, 2007, pp. 1-6.
- [3]. Muktar Hussaini, Farhat Anwar, Aisha Hassan A. H., A survey of power-efficient gathering of sensor information system based routing protocols of wireless sensor networks, *Sensors & Transducers*, Vol. 142, No. 7, July 2012, pp. 10-22.
- [4]. Song Yu, Liu Hong-Wei, Yang Xiao-Zong, SPTCE: a maximal matching and effective energy multi-channel MAC protocol for wireless sensor networks, *International Journal of Advancements in Computing Technology*, Vol. 4, No. 15, 2012, pp. 1-11.
- [5]. W. Heinzelman, A. Chandrakasan, H. Balakrishnan, An application-specific protocol architecture for wireless microsensor networks, *IEEE Trans. Wireless Commun.*, Vol. 1, No. 4, October 2002.
- [6]. Feng Guoliang, Application of improved moving target detection and shadow elimination algorithm in video monitoring, *Journal of Convergence Information Technology*, Vol. 7, No. 18, 2012, pp. 283-289.
- [7]. Yuxia Sun, Yong Tang, Dynamic analysis of wireless sensor network programs based on binary tool and simulator, *Sensors & Transducers*, Vol. 142, No. 7, July 2012, pp. 54-60.

- [8]. Zhang Qigui, Zhang Rui, A design of intelligent video surveillance system based on 3G network, *International Journal of Digital Content Technology & its Application*, Vol. 7, No. 1, 2013, pp. 257-263.
- [9]. Mrutyunjaya Panda, Application of swarm intelligence based routing protocols for wireless ad hoc sensor network, *Sensors & Transducers*, Vol. 130, No. 7, July 2011, pp. 48-60.
- [10]. Weipeng Jing, Xiangfei Pan, Zhenyang Li, Yuelin Tang, The application of embedded teaching and experiment platform, *Journal of Convergence Information Technology*, Vol. 6, No. 8, 2011, pp. 327-333.
- [11]. S. Jacobs, A. Eleftheriad, Streaming video using dynamic rate shaping and TCP congestion control, *Journal of Visual Communication and Image Representation*, Vol. 9, Issue 3, 1998, pp. 211-222.

2013 Copyright ©, International Frequency Sensor Association (IFSA). All rights reserved.  
(<http://www.sensorsportal.com>)

## Sensors Web Portal - world's source for sensors information

**TURN  
OUR VISITORS  
INTO  
YOUR CUSTOMERS  
BY THE SHORTEST WAY**



Advertise in  
Sensors Web Portal and its media:  
**[sales@sensorsportal.com](mailto:sales@sensorsportal.com)**  
[http://www.sensorsportal.com/DOWNLOADS/Media\\_Kit\\_2013.pdf](http://www.sensorsportal.com/DOWNLOADS/Media_Kit_2013.pdf)

## Error Analysis of Rotray SINS Sensor

Zhenguo YUAN, Lin ZHAO

College of Automation, Harbin Engineering University,

Harbin 150001, China

Tel.: 15946718088

E-mail: yuanzhenguodaohang@163.com

Received: 7 July 2013 /Accepted: 25 August 2013 /Published: 30 September 2013

**Abstract:** Using rotating modulation techniques for strap-down inertial navigation system (SINS) sensor is a self-compensation way to improve the accuracy. Inertial component errors can be effectively inhibited the inertial navigation system. The rotation principle and the error analysis of rotary SINS are presented in this paper, a two-axis rotary scheme is proposed. Simulation of rotary SINS calculation is made and rotation modulation is effective to the output of SINS sensor. *Copyright © 2013 IFSA.*

**Keywords:** Error analysis, Rotation, SINS, Rotary scheme.

### 1. Introduction

Last century, variety of strapdown inertial navigation sensors appeared. Laser, fiber optic gyroscope as the representative of the emergence of solid state gyro enlarges new energy to the SINS. Advanced manufacturing Technology and new material could improve the accuracy of SINS to some extent, which has its limitation [1]. Compared with the general series of SINS sensor, using a rotary SINS sensor with rotational modulation compensation technology, can effectively inhibit the inertia constant drift, which greatly improves the inertial navigation accuracy for a long time running. It is of great significance especially to ships, submarines requiring long-term support of autonomous navigation. Research on the rotary SINS sensor has a broad and important application value [2].

Automatic compensation by rotating gyro drift is one effective way to achieve high-precision inertial navigation. Rotary SINS technology is one of correction methods, it has a similar system with the

platform rotating mechanism. SINS sensor is mounted on a rotating mechanism. In accordance with certain rules rotation, the inertial component errors on SINS can be eliminated [3].

Rotating SINS still uses SINS algorithm and the basic principle of rotation modulation is shown in Fig. 1.

### 2. Error Model

The error equation of SINS reflects the relationship between inertial components error and positioning error. On the basis of literature, SINS error model is:

$$\delta \dot{\mathbf{v}} = [\mathbf{I} - (\mathbf{C}_t^i)^T] \mathbf{C}_b^i \dot{\mathbf{f}}^b + \mathbf{C}_b^i \delta \mathbf{f}^b - (2\hat{\boldsymbol{\omega}}_{ie}^t + \hat{\boldsymbol{\omega}}_{et}^t) \times \delta \mathbf{v}, \quad (1)$$

$$-(2\delta \boldsymbol{\omega}_{ie}^t + \delta \boldsymbol{\omega}_{et}^t) \times \mathbf{v} + \delta \mathbf{g} \\ \dot{\boldsymbol{\phi}} = (\mathbf{I} - \mathbf{C}_t^i) \hat{\boldsymbol{\omega}}_{it}^t + \delta \boldsymbol{\omega}_{it}^t - \mathbf{C}_b^i \delta \boldsymbol{\omega}_{ib}^b, \quad (2)$$

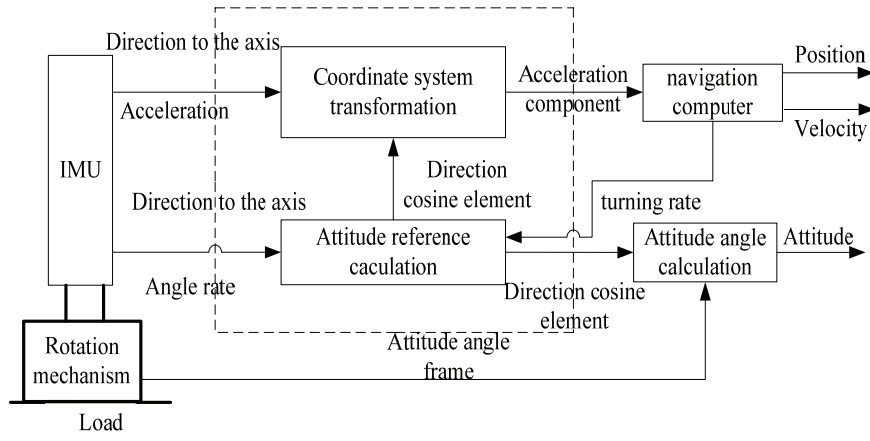


Fig. 1. Principle of rotation modulation.

where  $\delta \mathbf{v}$  is velocity error vector,  $\phi$  is misalignment angle vector,  $C_b^i$  is direction cosine matrix from carrier coordinate to geography coordinate,  $C_b^t$  is direction cosine matrix from carrier coordinate to calculated geography coordinate.  $\hat{\mathbf{f}}^b$  is real proportional output,  $\delta \mathbf{f}^b$  and  $\delta \omega_{ib}^b$  are measurement errors,  $\hat{\omega}_{ie}^t$  is earth rotation angle rate in calculated geography coordinate,  $\hat{\omega}_{et}^t$  is rotation angle rate relative to geography coordinate,  $\hat{\omega}_{it}^t$  is rotation angle rate relative to inertial coordinate,  $\delta \mathbf{g}$  is error of gravity acceleration.

Where  $C_t^i = [a_{ij}]_{3 \times 3}$ ,  $i, j = 1, 2, 3$ , each element is below:

$$\begin{cases} a_{11} = \cos \phi_y \cos \phi_z - \sin \phi_y \sin \phi_x \sin \phi_z, \\ a_{13} = -\sin \phi_y \cos \phi_x, \\ a_{23} = \sin \phi_x \\ a_{22} = \cos \phi_z \cos \phi_x, \\ a_{21} = -\sin \phi_z \cos \phi_x \\ a_{31} = \cos \phi_z \sin \phi_x + \cos \phi_y \sin \phi_x \sin \phi_z, \\ a_{32} = \sin \phi_y \sin \phi_z - \cos \phi_y \sin \phi_x \cos \phi_z, \\ a_{33} = \cos \phi_y \cos \phi_x \end{cases}, \quad (3)$$

And other parameters are as follows:

$$\begin{cases} \hat{\omega}_{it}^t = \omega_{it}^t + \delta \omega_{it}^t \\ \omega_{it}^t = \omega_{ie}^t + \omega_{et}^t \\ \delta \omega_{it}^t = \delta \omega_{ie}^t + \delta \omega_{et}^t \\ \omega_{ie}^t = [0 \quad \omega_{ie} \cos \varphi \quad \omega_{ie} \sin \varphi]^T \end{cases}, \quad (4)$$

$$\begin{cases} \delta \omega_{ie}^t = [0 - \delta \varphi \omega_{ie} \sin \varphi \\ \delta \varphi \omega_{ie} \cos \varphi]^T \\ \omega_{et}^t = \begin{bmatrix} -\frac{v_y}{R_m + h} & \frac{v_x}{R_n + h} \\ \frac{v_x \tan \varphi}{R_n + h} \end{bmatrix}^T \end{cases}, \quad (5)$$

$$\begin{cases} \hat{\omega}_{it}^t = \omega_{it}^t + \delta \omega_{it}^t \\ \omega_{it}^t = \omega_{ie}^t + \omega_{et}^t \\ \delta \omega_{it}^t = \delta \omega_{ie}^t + \delta \omega_{et}^t \\ \omega_{ie}^t = [0 \quad \omega_{ie} \cos \varphi \quad \omega_{ie} \sin \varphi]^T \end{cases}, \quad (6)$$

$$\begin{cases} \delta \omega_{ie}^t = [0 - \delta \varphi \omega_{ie} \sin \varphi \\ \delta \varphi \omega_{ie} \cos \varphi]^T \\ \omega_{et}^t = \begin{bmatrix} -\frac{v_y}{R_m + h} & \frac{v_x}{R_n + h} \\ \frac{v_x \tan \varphi}{R_n + h} \end{bmatrix}^T \end{cases}, \quad (7)$$

$$\begin{cases} \delta \omega_{et}^t = [\omega_1 \quad \omega_2 \quad \omega_3]^T \\ \omega_1 = -\frac{\delta v_y}{R_m + h} + \delta h \frac{v_y}{(R_m + h)^2} \\ \omega_2 = \frac{\delta v_x}{R_n + h} - \delta h \frac{v_x}{(R_n + h)^2} \\ \omega_3 = \frac{\delta v_x \tan \varphi}{R_n + h} + \frac{\delta \varphi v_x \sec^2 \varphi}{R_n + h} - \frac{\delta h v_x \tan \varphi}{(R_n + h)^2} \end{cases}, \quad (8)$$

IMU (Inertial measurement unit) belongs to SINS sensor. Gyro and accelerometer are major component

of IMU, which directly affect the accuracy of the inertial system accuracy. In practice, due to the inevitable interference factors which led to the gyro and accelerometer produce errors, beginning from the initial alignment, the navigational error will grow with time, especially in the position error, which is the principal inertial navigation system shortcoming. IMU has three accelerometers and three angular rate sensor (gyroscope) composed of accelerometers to sense the vertical plane relative to ground acceleration component, the speed sensor to sense the angle of the aircraft information [4, 5].

### 3. Error Analysis

IMU is mounted on the rotating frame. Suppose  $r$  coordinate is a new coordinate rotating with IMU [6]. Analyze the effect of rotation. IMU revolves round z-axis:  $x_b y_b z_b \xrightarrow{\beta} x_r y_r z_r$ .

$$C_b^r = \begin{bmatrix} \cos \beta & \sin \beta & 0 \\ -\sin \beta & \cos \beta & 0 \\ 0 & 0 & 1 \end{bmatrix} = (C_r^b)^T, \quad (9)$$

The output of angular velocity and proportion is:

$$\left. \begin{aligned} \omega_{ib}^b &= C_r^b \omega_{ir}^r + \omega_{rb}^b \\ f_{ib}^b &= C_r^b f_{ir}^r \end{aligned} \right\}, \quad (10)$$

where  $\omega_{br}^r = [0 \ 0 \ \omega]^T$ ,  $f_{br}^r = 0$ . The output of gyroscope and accelerometer is:

$$\left. \begin{aligned} \omega_{ir}^r &= C_b^r \omega_{ibd}^b + [\varepsilon_x \ \varepsilon_y \ \varepsilon_z]^T + \omega_{br}^r \\ f_{ir}^r &= C_b^r f_{ibd}^b + [\nabla_x \ \nabla_y \ \nabla_z]^T \end{aligned} \right\}, \quad (11)$$

That changes into:

$$\begin{bmatrix} \omega_{ibx}^b \\ \omega_{iby}^b \\ \omega_{ibz}^b \end{bmatrix} = \begin{bmatrix} \omega_{ibd}^b \\ \varepsilon_x \cos \omega t - \varepsilon_y \sin \omega t \\ \varepsilon_x \sin \omega t + \varepsilon_y \cos \omega t \\ \varepsilon_z \end{bmatrix}, \quad (12)$$

$$\begin{bmatrix} f_{ibx}^b \\ f_{iby}^b \\ f_{ibz}^b \end{bmatrix} = \begin{bmatrix} f_{ibd}^b \\ \nabla_x \cos \omega t - \nabla_y \sin \omega t \\ \nabla_x \sin \omega t + \nabla_y \cos \omega t \\ \nabla_z \end{bmatrix}, \quad (13)$$

The error changes into:

$$\left. \begin{aligned} \varepsilon_x \\ \varepsilon_y \\ \varepsilon_z \end{aligned} \right\} \rightarrow \left. \begin{aligned} \varepsilon_x \cos \omega t - \varepsilon_y \sin \omega t \\ \varepsilon_x \sin \omega t + \varepsilon_y \cos \omega t \\ \varepsilon_z \end{aligned} \right\}$$

and

$$\left. \begin{aligned} \nabla_x \\ \nabla_y \\ \nabla_z \end{aligned} \right\} \rightarrow \left. \begin{aligned} \nabla_x \cos \omega t - \nabla_y \sin \omega t \\ \nabla_x \sin \omega t + \nabla_y \cos \omega t \\ \nabla_z \end{aligned} \right\}$$

In a complete rotary alternation, the error except z-axis could be inhibited.

### 4. Rotation Method and Simulation

Here proposed a two-axis rotary scheme. IMU revolves round the z-axis negative 180 degree, y-axis negative 180 degree, z-axis 180 degree, y-axis 180 degree, z-axis 180 degree, y-axis 180 degree, z-axis 180 degree, y-axis 180 degree. The error of three axes can be inhibited.

The rotation scheme is shown in Fig. 2.

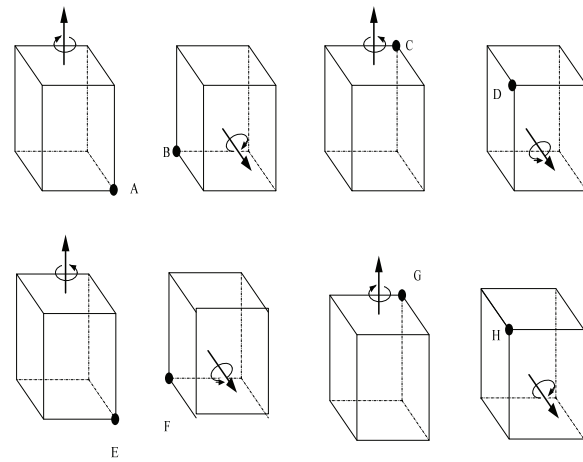


Fig. 2. Rotation scheme.

The attitude angle and the velocity error are shown in Fig. 3 and Fig. 4.

IMU revolves round the y/z axes to make an arbitrary axis rotation axis. The sensitive axis perpendicular to the shaft axis of inertia element can be modulated in a complete cycle, the accumulated error tends to be zero.

And position error for SINS sensor without rotation is shown in Fig. 5 and Fig. 6.

The position error of Rotary SINS sensor is shown in Fig. 7 and Fig. 8.

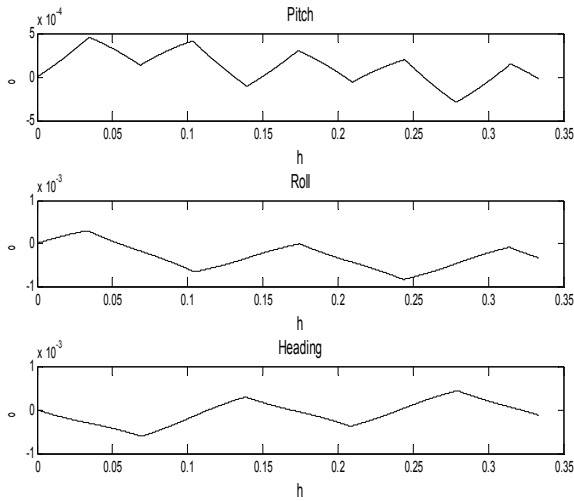


Fig. 3. Attitude angle.

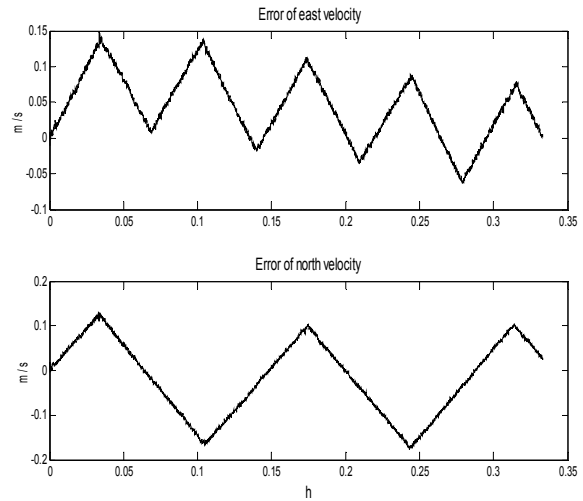


Fig. 4. Error of velocity.

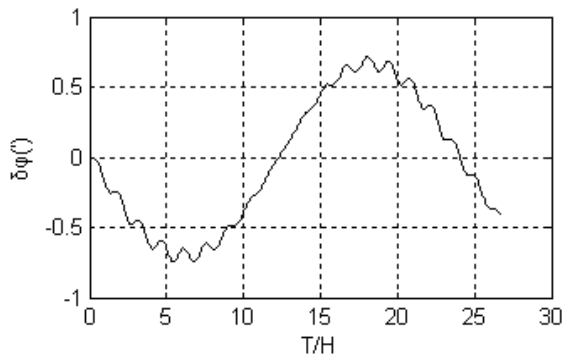


Fig. 5. Longitude error without rotation.

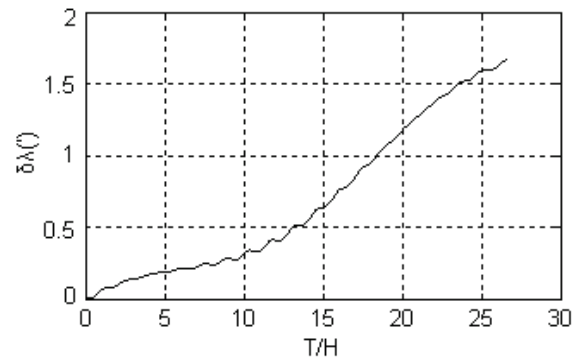


Fig. 6. Latitude error without rotation.

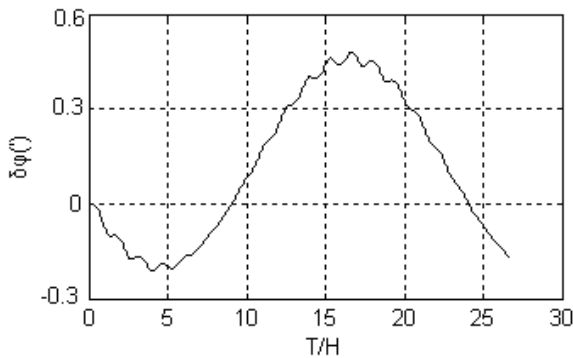


Fig. 7. Longitude error of rotary SINS sensor.

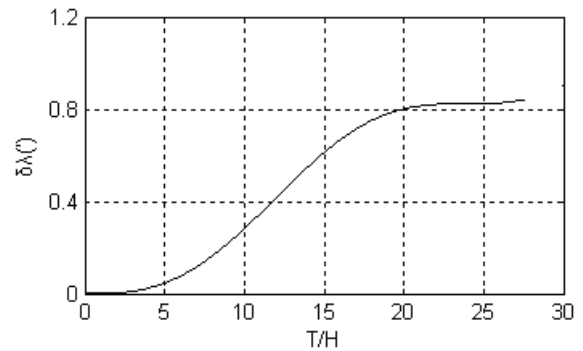


Fig. 8. Latitude error of rotary SINS sensor.

The positioning accuracy is superior to the traditional SINS.

### 5. Conclusion

Rotary technology improves the accuracy of SINS sensor. The system cost is relatively small, the Rotary SINS sensor can fully tap the potential to obtain higher precision navigation.

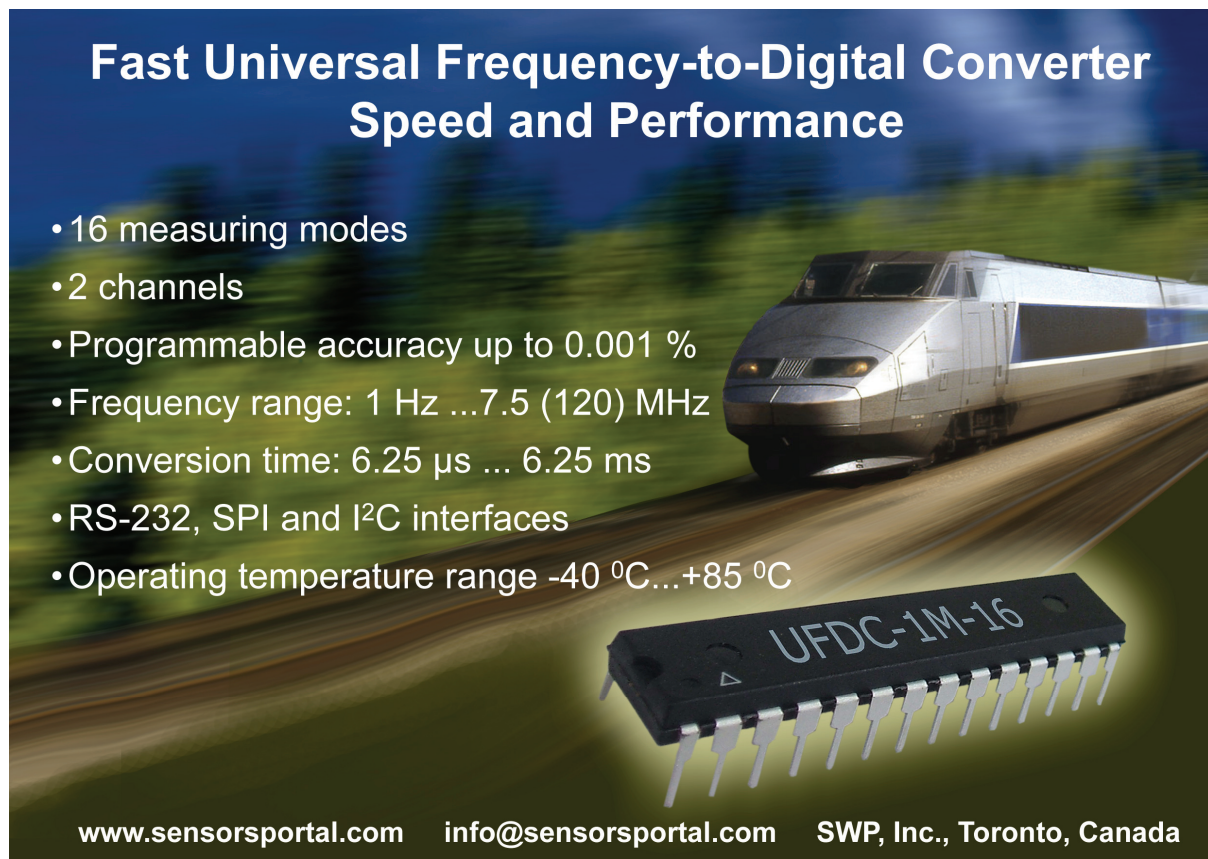
### References

- [1]. N. Barbour, Inertial components – past, present and future, Invited paper, AIAA Guidance, in *Proceedings of Navigation and Control Conference*, Montreal, Canada, 2001, pp.1-11.
- [2]. S. Ishibashi, S. Tsukioka, H. Yoshida, T. Hyakudome, T. Sawa, J. Tahara, T. Aoki, A. Ishikawa, Accuracy improvement of an inertial navigation system brought about the rotational motion, *Japan Agency for Marine-Earth Science & Technology (JAMSTEC)*, Yokosuka, 2007, pp. 1-5.

- [3]. Huang Wei-Quan, Cheng Jian-Hua, Yu Qiang, Wu Lei, Research of gyro case rotation monitor technique based on random drift characteristics of gyro, in *Proceedings of IEEE International Conference on Mechatronics and Automation, 2005*, pp. 862-967.
- [4]. H. David, L. John, Strapdown inertial navigation technology, 2<sup>nd</sup> Edition [M], *The Institution of Electrical Engineerings*, 2004, pp. 377-420.
- [5]. David J. Allerton and Huamin Jia, Redundant multi-mode filter for a navigation system, *IEEE Transactions on Aerospace and Electronic Systems*, Vol. 43, No. 1, 2007, pp. 371-391.
- [6]. S. Ishibashi, S. Tsukioka, H. Yoshida, T. Hyakudome, T. Sawa, J. Tahara, T. Aoki, A. Ishikawa, The rotation control system to improve the accuracy of an inertial navigation system installed in an autonomous underwater, *Underwater Technology and Workshop on Scientific Use of Submarine Cables and Related Technologies*, Tokyo, 2007, pp. 495-498.

---

2013 Copyright ©, International Frequency Sensor Association (IFSA). All rights reserved.  
(<http://www.sensorsportal.com>)



## Fast Universal Frequency-to-Digital Converter Speed and Performance

- 16 measuring modes
- 2 channels
- Programmable accuracy up to 0.001 %
- Frequency range: 1 Hz ...7.5 (120) MHz
- Conversion time: 6.25  $\mu$ s ... 6.25 ms
- RS-232, SPI and I<sup>2</sup>C interfaces
- Operating temperature range -40 °C...+85 °C

**UFDC-1M-16**

[www.sensorsportal.com](http://www.sensorsportal.com)   [info@sensorsportal.com](mailto:info@sensorsportal.com)   SWP, Inc., Toronto, Canada

## Design of Reflective Optical Fiber Current Sensor Based on Improved Phase Modulation

Yajun WANG, Xuemei GUO

Xinxiang University,  
Henan Xinxiang, 453003, China  
Tel.: 13663900097  
E-mail: wangyajunedu@163.com

*Received: 2 July 2013 /Accepted: 25 August 2013 /Published: 30 September 2013*

---

**Abstract:** Full optical fiber current sensor phase modulation is the use of magnetic field made the refraction different of left-handed and right-handed circularly polarized light, and the linearly polarized light can be decomposed into a left-handed and right-handed circularly polarized light. The paper proposes research and design of reflective optical fiber current sensor based on improved phase modulation. This paper analyzes the current sensor reflective polarization of light changes, and using the Jones matrix analysis method to establish a reflective fiber optic current sensor model. Design of reflection type optical fiber current sensor model can improve the sensitivity of optical fiber current sensor. *Copyright © 2013 IFSA.*

**Keywords:** Optical fiber current sensor, Phase modulation, Reflective optical sensors.

---

### 1. Introduction

Optical fiber current sensor since, has been attention. The existing optical fiber current sensor in the sensor head which is different can be divided into optical fiber current sensor, bulk glass optical fiber current sensor and a hybrid fiber current sensor. The basic principle of bulk glass optical fiber current sensor is: using total reflection, the linear polarized light through a glass material internal multiple reflections, formed around the closed optical path through an electrical conductor.

Optical fiber sensor has the advantages of small volume, light weight, can do the non-contact, non-destructive in harsh environment and remote measurement. Also have the advantages of high sensitivity, good reliability, raw material silicon resources Wei Fu, anti-electromagnetic interference, corrosion resistance, high pressure resistance, good electrical insulation properties, bendable, explosion-proof, wide frequency band, and low loss. At the

same time, it also makes it easy to connect with the computer, the realization of intelligent and remote monitoring. To improve the effect on the traditional sensors, able to complete the difficult to accomplish even cannot finish task in many cases.

This paper describes the current measurement applications in high-strength fiber-optic current sensor has the following advantages: fiber-optic current sensor is not magnetic saturation, unlike the usual electromagnetic transformer dynamic range limited by the magnetic saturation effect; fiber-optic current sensors resistant to electromagnetic interference, low demands on the environment; fiber optic current sensors over a wide frequency band, resulting in high linearity response; fiber optic current sensor size is relatively small, relatively easy installation [1]. In short, the fiber-optic current sensor has many advantages, especially its insulation performance, small size, low cost, and frequency bandwidth, short response time, which can be used to measure DC, AC and pulse current, so under high

pressure is expected to become ideal sensor for the measurement of large currents.

The main disadvantage of phase modulation type optical fiber current sensor is: polarization optical fiber birefringence induced changes tend to drown Faraday rotation angle, so the measurement accuracy is reduced. In view of this situation, mainly to solve two: one is to improve the intrinsic birefringence of optical fiber, but managed to increase the Faraday rotation angle. To improve the inherent birefringence fiber rate methods have been proposed in the previous section, in this chapter, mainly to improve the Faraday rotation angle. When light by the Faraday rotator is placed in a magnetic field when facing the external observation, magnetic induction intensity, polarization direction of light always along with the magnetic field (H) constitute a right-handed helix direction to the direction of rotation, which has nothing to do with the direction of propagation of light.

When light waves along the forward and reverse direction two times through the Faraday rotator, whose polarization direction rotating angle is the superposition and not offset, this is the Faraday effect of rotation to irreversibility, called the nonreciprocal optical rotation. Using the nonreciprocal Faraday Effect, improvements are made on the structure, namely the reflection type optical fiber current sensor model. The paper put forward research and design of reflective optical fiber current sensor based on improved phase modulation.

## 2. Study on Phase Modulation Type Optical Fiber Current Sensor

Full optical fiber current sensor phase modulation is the use of magnetic field made the refraction of left-handed and right-handed circularly polarized light is different, and the linearly polarized light can be decomposed into a left-handed and right-handed circularly polarized light, and transmit a distance, showed linear polarized light vibration surface rotates, the rotation angle depends on the propagation along the magnetic field direction of circularly polarized light and left-handed right-handed circularly polarized light refractive index difference. Phase generated so by measuring the polarization and right-handed circularly polarized light propagating a distance difference measurement, can also make the current.

Phase modulation sensor and its basic principle is to use the object to be measured to the sensitive element, make the sensitive components of the refractive index and propagation constant changes, resulting in optical phase changes, the interference fringes produced by two beams of monochromatic light changes, to determine the phase change in the amount of light by detecting the interference fringe variation, thus get the information of the measured object. Usually the photo elastic effect, the sound

pressure or vibration sensor using current, magnetic field sensor; magnetostrictive effect; using electrostrictive electric field, and the use of optical fiber voltage sensor Saigenake rotating angular velocity sensor effect (FOG). This kind of sensor is with high sensitivity. But because must use special fiber and high precision detection system, so the cost is high.

Optical fiber current sensor based on the Faraday Effect of magneto-optical materials, in a transparent medium optically isotropic, external magnetic field H can make the plane of polarization of polarized light propagating along the direction of the magnetic field in the medium surface is rotated, and the deflection angle can be determined by the analyzer. Its principle as shown in Fig. 1, B is two polarizer angle, theta into planar light through the angle of magneto-optic crystal after the occurrence.

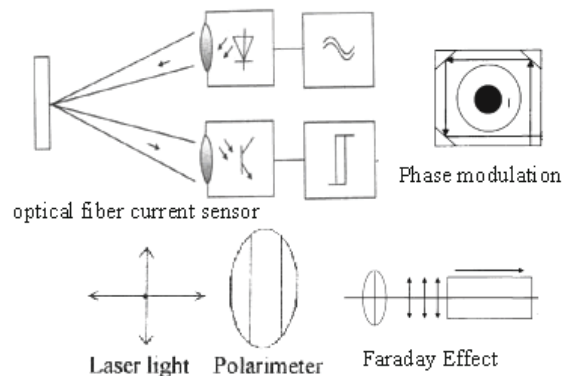


Fig. 1. Design of phase modulation type optical fiber current sensor.

Optical fiber current sensor has the following advantages: (1) the insulation performance is very good, from materials: the use of optical fiber current sensor materials are mainly quartz fiber, an insulator itself is very good; (2) the core contains no fiber current sensor structure, because of the absence of magnetic saturation, ferromagnetic resonance and other issues, the measurement accuracy is improved. (3) the strong electromagnetic interference resistance, signal optical fiber current sensor to transmit by the light, with resistance to electromagnetic interference, measurement accuracy so that it can increase it.

The dimming control circuit for photoelectric coupler MOC3041 as the SCR drives; isolation and can realize the strong, weak [2]. MOC3041 has zero crossing detection circuit, when P0.0 is low, the voltage output end 6 pin, 4 pin between the slightly zero, MOC304.1 internal bidirectional thyristor, trigger external thyristor T1 conduction. When PO.0 is high, and it is MOC304l internal bidirectional turn-off, and it is external thyristor T1 shutdown.

The low-pressure side not fiber current sensor has caused high risk for open circuit, thus eliminating the flammable and explosive traditional electromagnetic current transformer problem. Optical fiber current

sensor is small in size, light in weight. Sensing head of optical fiber sensor, the weight is less than 1 kg, adapted to the power protection and measurement of digital, intelligent and the development trend of optical communication. The dynamic range of the measurement, can maintain a good linearity in a wide range of current.

$$Z_{RC} = RC * C + (1 - RC) * R \quad (1)$$

Thru-beam sensor if the light emitting device and receiving from light, and it can make the detection distance. A light emitting device and a receiving device of photoelectric switch is called bisection separated photoelectric switch, referred to as the photoelectric switch. Its detection distances of up to a few meters or even tens of meters. When using the light emitting device and a light receiving device are respectively arranged in the detection of the two sides, detection by optical path is blocked, the light receiving device on the action of a switch control signal output.

Laser light emitted from the light source through the polarizer for linearly polarized light, through the coupler is divided into two parts, respectively after 1/4 delay is transformed into rotation circularly polarized light are same, clockwise and counterclockwise direction through the sensing fiber ring, due to the Faraday effect, the plane of polarization of the two circular polarization light is rotated, and then after another 1/4 delay to transform into linearly polarized light returns polarizer interference.

Because the rotation of polarization of light beams interference surface point of equal size, in the opposite direction, so the phase difference of two times for the Faraday shift, so the sensitivity in the same number of turns at two times the polarization modulated fiber optic current sensor. Phase only needs to detect the output light difference can get the current to be measured, so the effect of power fluctuation on the system than the polarization rotation scheme, system stability is better than the polarization modulation scheme of main disadvantage is the structure contains the Sagnac ring structure, so it is easily influenced by the Sagnac effect, as is shown by equation 2.

$$q(n) = \frac{\gamma^{-1} R^{-1} (n-1) x(n)}{1 + \gamma^{-1} x^H(n) R^{-1} (n-1) x(n)} \quad (2)$$

Fiber optic fiber sensors only as transmission medium, only has the transmission light effect, to the outside information "feel" is to rely on other material sensitive element to complete, therefore, must add other sensitive components to form the sensor on the surface of optical fibers or intermediate. Thus, fiber sensor is interrupted, discontinuous, interrupted part to connect the sensitive elements of other media.

The maximum current can be measured value is greater, so in the experiment of increasing angle B

way to increase the measuring range. But in practice, increasing the angle of B to will make the focusing optical path becomes more difficult to a certain value, and the small signal more difficult to measure, in the previous experiments generally B=45 degrees or less value. In this experiment the laser of 2 MW adjusted light source, the magneto-optical crystal light into 1 m away in order to eliminate the birefringence may appear in the first focus, and sealed the jointing surface using optical glue, so that the optical path adjustment is more easy to operate, so the angle B chose 80°. In the formula, B in the sensor after the completion of angle is constant, so as long as measured by P, the P0 value will be the current value, as is shown by equation 3.

$$e_1 \text{ S.T. } \text{Max}(R(W_j^\sigma, F_e), j=1, 2, \dots, M) \quad (3)$$

Transmittance of T is one of the temperature T and the transmission wavelength lambda function. Based on the theory of solid physics and electromagnetic can get its concrete expression. But the transmittance of T thus obtained (a, t) is a very complicated formula, the practical application is not easy. According to the shape of the curve can be approximated to the combination of the 3 lines as shown in it [3]. The first section is  $\lambda < \lambda_T$ , T=0; the second paragraph is  $\lambda_T < \lambda < \lambda_T + \Delta T$ , then sharply; third section is  $\lambda > \lambda_T + \Delta T$ , then a gradual linear approximation. The intersection point of the 3 straight A, B, C coordinates are a ( $\lambda_T$ , 0), B ( $\lambda_T + \Delta T$ , Tb), C (100).

In the TFFI interferometer, in order to reflect the formation of optical surface, surface of the plating a layer of film on the optical wedge, and the coating has certain thickness, so the coating on the surface of the reflection light will form the interference, will affect the measurement results. Therefore, coating thickness should be controlled in the center wavelength of the 1/4 light source, such as a light source wavelength is 600 nm~1000 nm, the coating thickness is 800 nm (refractive hypothesis of the coating material rate was 1), this kind of coating on the surface of most of the reflective phase difference of 180 DEG, intensity attenuation.

Photoelectric sensor is an optical transmitter and a receiver face-to-face mounted on both sides of a slot is the slot photoelectric. Light emitting device can emit infrared or visible light; in the open case optical receiver can receive the light. But when the channel object is detected, the light is blocked, photoelectric switch action. The output of a switch control signal, cut off or connected to the load current, thus completing a control action. Trough switch detection distance because of the overall structure of the limit is generally only a few centimeters.

Photoelectric sensor through the Faraday rotation angle measurement of polarized light, and it is thereby measuring the current indirect. The current sensor with a wide linear range, good stability, high precision, less affected by linear birefringence in

optical fiber advantages; but there are large processing difficulty, the sensor head is fragile, high cost, and the inevitable reflection of light in the process of introducing reflective phase shift, so that the two orthogonal linear polarized into elliptical polarized light, thus affecting the performance of the system.

$$\binom{\delta}{k} \equiv \frac{\delta!}{k!(\delta-k)!} = \frac{\Gamma(\delta+1)}{\Gamma(k+1)\Gamma(\delta-k-1)} \quad (4)$$

In the optical path design and it is using the new structure. The dark grey arrow line transmission path of the light in the sensor: the light emitted by the light source with optical fiber sensor by entering the self lens, reflected by the evaporation of reflecting film right-angle prism change for linearly polarized light into the magneto-optical crystal, polarization by a magnetic field modulation polarized light passes through a rectangular prism analyzer and the corresponding the other area through the selfoc lens fiber into the photoelectric detector.

Photoelectric detector choice to make the spectral responsively of  $R(\lambda)$  corresponding to the light peak wavelength, the best makes the peak response wavelength corresponding to the peak wavelength and light source, to achieve the maximum output. Therefore, selection of silicon PIN photodiode as photo detector, stable performance, its price is cheap, easy to use, especially in the 800~900 nm band photoelectric conversion efficiency is the highest, consistent with the working wavelength selected light source LED.

In this paper, dimming control according to the luminance calculated value; the P87LPC768 PWM output duty ratio is based on counting image CNSW register value and comparative mapping register CPSW<sub>n</sub> value determination, the PWM output remains high during the period of MCU clock pulse number (CNSW - CPSW<sub>n</sub>+1). Thus, the greater is the high level of CPSW<sub>n</sub>, the time is short, the dimming control circuit of T1 turn-on time is longer, the brightness of lighting equipment is higher; the brightness and lighting equipment is low, as is shown by equation 5.

$$\bar{w}(m) := [\bar{w}^T(m,1), \bar{w}^T(m,2), \dots, \bar{w}^T(m,M)]^T \quad (5)$$

The actual use of the sensor and the reader (Demodulator) connection, emit white light diode light source reader of light from one end of the optical fiber connecting readouts incident, transmission connection to the Fabry-Perot sensor, and then ejected from the multimode fiber, irradiation in TFFI interferometer (wedge) surface. When the level of TFFI mobile and it is light point position will be different. Wedge two upper and lower surfaces are coated with a reflective film, which consists of the Fabry-Perot cavity [4]. When the reader launch white light was part of the first half of mirrors, the rest of

the white light passes through a Fabry-Perot cavity, and once again by second and a half mirror reflected back, two reflected light interference, the spectra of the original incident light is modulated.

Structural element photoelectric is switch and transmitter and optical fiber. Triangular reflector is launching device firm structure. It consists of a triangular pyramidal reflective material is very small, can make the beam accurately returned from the reflecting plate, has the practical significance. It can be in the optical axis of the 0 to 25 range change the emission angle, so that the beam is almost rays from a root, after reflection, or from the reflected ray returns.

Sagnac effect and Faraday effect are generating nonreciprocal phase shift, could not detected, resulting in the measurement error, reducing the stability of the system; the intrinsic birefringence of the sensing fiber is difficult to handle, because the fiber preparation process is not perfect, medium of impurities, defects, destruction of the axial symmetry of the fiber, and bending reasons to use when the inevitable, so that the inherent birefringence in the sensing fiber [5]. While the ordinary silica fiber Verdet constant is small, light polarization fiber birefringence induced changes tend to drown Faraday rotation angle, in order to improve the sensitivity, it is necessary to increase the number of sensing fiber ring, it will increase the intrinsic birefringence and bending caused by linear birefringence, so that the sensor sensitivity is much lower than the theoretical prediction value.

$$F(x, y) = \frac{\sum_i w(d(x, y)) I_i(x, y)}{\sum_i w(d(x, y))} \quad (6)$$

Light is an electromagnetic wave of high frequency, the electric vector and magnetic vector and its direction are perpendicular to the direction of propagation of Yu Bo. Light disturbance is actually changed the intensity of electric field and magnetic field intensity of light. When light interacts with matter, theoretical and experimental results show that, the optical detector was an electrical vector instead of magnetic vector, so only need to consider the effect of electric field, so the electric vector to represent the light vector. Light waves are transverse wave, so the wave with polarization. Polarization of light can generally be divided into polarized light, natural light and polarized light. The size and direction of light vector rule changes called polarized light.

$$(X_m, Z_i) = \sum_{n=1}^N X_m(n) Z_i^*(n) \quad (7)$$

A linear polarizer coordinate system will be the combination of these two components in the X, Y axis projection again, get the outgoing light of the two components A2 and B2, i.e. to make and B1cos

to make (1) Jones matrix line polarizer polarizer transmission shaft and the X shaft arranged forming angle. As shown in Fig. 2 builds XY coordinate system, the incident light of two components in the X, Y axis were A1 and B1, their online polarizer transmission direction projection. The incident light through a linear polarizer and it is components A1 and B1 along the light axis direction.

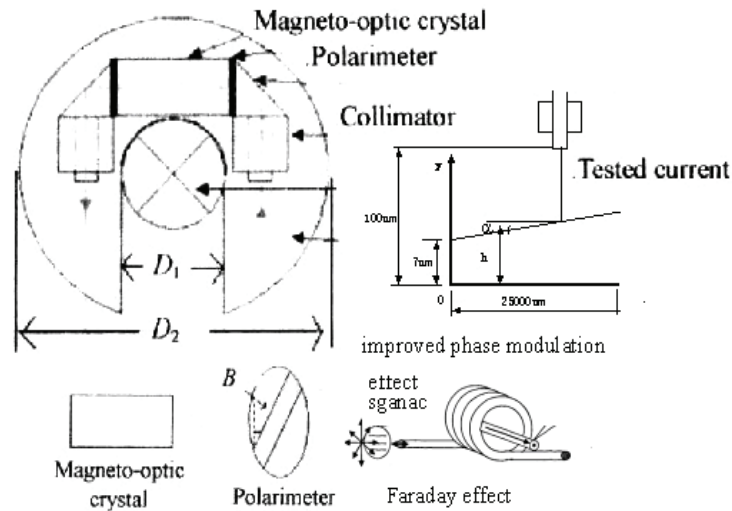


Fig. 2. The structure of Improved Reflective Fiber Optic Current Sensor.

### 3. Development of Improved Reflective Fiber Optic Current Sensor

The basic structure of reflection type optical fiber current sensor, the light emitted by the light source with single-mode optical fiber transmission after being sent to the polarizer, a linearly polarized light, the two light beams through 45 degrees of melting point into the polarization direction perpendicular to each other, and then through the 1/4 wave incident light into two opposite rotation direction (left and right) circle polarized light, into the sensing area, after a Faraday effect, reach the mirror reflection, polarization, they exchanged in the reflection, namely original left-handed light into the right rotation, the original right-handed rotation into the left rotation.

But the reflection structure in practical application, because of two orthogonal polarization optical transmission in the same optical fiber and also by the modulation, therefore must use the biaxial modulator, usually the polarization-maintaining fiber wound on a piezoelectric ceramic tube (PZT) made of phase modulator, when PZT and modulating signal, linearly polarized along the polarization fiber two orthogonal axes transmission will introduce phase and modulation signal changes of the same difference, as is shown by equation 8 [6].

$$PI(x) = \frac{1}{y_2 - y_1} \sum_{y=y_1}^{y_2} I(x, y), \quad x \in (x_1, x_2) \quad (8)$$

Optical fiber current sensor is based on the Faraday Effect to detect the current size of the optical sensor. The Faraday Effect refers to the linear polarized along the magnetic field direction through the medium of the polarization plane rotation phenomenon. The Jones matrix is an effective method of polarization and polarization of light.

At present, the light intensity signal is processed directly is very difficult, usually converts the optical signal into electrical signal processing. The photoelectric conversion directly affects behind the signal quality, so choose a good photoelectric detector is very important. The light detector is mainly divided into two kinds: one kind is to absorb photons to device temperature thermoelectric devices to detect incident light; the other is the incident light into a photoelectric device current or voltage.

The return light reflection structure in the mirror back to the coil, deflection optical rotation of the 90, the positive and negative through the fiber coil polarized orthogonal to each other, so that the additional line in optical fiber birefringence offset each other, and the Faraday effect is a nonreciprocal, so light and two times through the optical fiber ring, Faraday rotation effect not offset each other, but doubled, so the structure can reduce the effect of linear birefringence in optical fiber, also can make the Faraday effect doubling; two reflected structural interference optical transmission in the same optical fiber, it can reduce the external factors (such as temperature, pressure and so on) interference, and is not affected by the Sagnac effect [7]. Another reflection structure using relatively small, easy to build, and polarization rotation and phase modulation structure compared to the reflection structure has the advantages of high sensitivity, stronger anti-interference ability, good stability and so.

When linearly polarized along the magnetic field direction through the magnetic optical medium is arranged in the magnetic field, the polarization plane rotation, this phenomenon is called the Faraday effect, often called the Faraday effect. The essence of Faraday Effect for magnetic circular birefringence, namely the circularly polarized light through the Faraday Effect phase change. Because the linear polarized light can be expressed as the superposition of orthogonal circularly polarized beams of left and right of the, is cubic and isotropic materials Faraday effect, the rotation angle depends on the propagation along the magnetic field direction of the left-handed circularly polarized light and right-hand circularly polarized refractive index difference.

A white light source with the reader, from multimode fiber return light passes through the cylindrical lens into parallel light, be reflected in the TFFI interferometer on an inclined plane, and the lower surface of the TFFI to a CCD sensor is sensitive to light intensity. Hypothesis of monochromatic light irradiation on the surface of the wedge, is in the X direction of each point, wedge reflection light the surface and form the interference, and the lower surface of the transmission light is detected by the CCD.

The light emitting device and the light receiving device into the same device internal reflection type photoelectric switch, a reflecting plate in front of it, using the reflection principle complete the photoelectric control function is called reflection plate type (or mirror reflection type photoelectric switch). Under normal circumstances, a light emitting light is reflected back by the light reflecting plate is received; once the light path detecting object block, light receiving device does not receive the light, a photoelectric switch on the action, the output of a switch control signal.

After a circularly polarized light reflected by the original way back, again by the Faraday effect, and then by 1/4 wave conversion loop through polarized light, reflected light carrying phase difference information through the coupling device is transmitted to the photoelectric detector [8]. In the whole process, the two beams have undergone a polarization-maintaining optical fiber sensing fiber two axis and the left-handed and right-handed modes, so the light path is fully reciprocal. Phase difference depends on the size of magnetic field sensing region. Because the two beams of light have experienced two times of Faraday Effect, so the phase difference is 4 times the Faraday phase shift. Optical fiber current sensor, this structure, in other conditions are the same, the sensitivity is 4 times the deflection type optical fiber current sensor described earlier, 2 times the phase modulation type optical fiber current sensor.

$$W_{j,k} = \sum_{l=0}^{L_j-1} h_{j,l} X_{2^{j(k+1)-l \bmod N}} \quad (9)$$

In order to further analysis the principle of reflection type optical fiber current sensor, analysis of y to change through the polarization state of the light signal (t). Output 1, 2 optical phase difference is: X (T) and for optical transmission time. Upon reflection, 1, 3 and 2, 4 exchange of fast and slow axis, so by the modulation of the phase modulation respectively, which makes y and X1 light source light polarizer P into a linearly polarized light, after 45 degree melting point after decomposing into two beams of light polarized vertically, the two beams of light by Faraday effect and produce a certain phase difference, return again when it is 45 degrees of melting point light, get up to the polarizer P four beam of light.

This paper designs the reflection type optical fiber current sensor model, improves the sensitivity of optical fiber current sensor, and from the angle of polarization of detailed analysis of each physical process, then the Jones matrix, theoretical calculation and Analysis on the conducted for reflection type optical fiber current sensor, the mathematical model of reflection type current sensor.

#### 4. Design of Reflective Optical Fiber Current Sensor based on Improved Phase Modulation

The theoretical foundation of optical fiber current sensor technology, and from the angle of polarization of detailed analysis of each physical process, analyzes the changes of light polarization; then the Jones matrix, theoretical calculation and Analysis on the conducted for reflection type optical fiber current sensor [9]. Considering the characteristics and application of reflection type optical fiber current sensor of the environment and other factors, according to the source, the reflection type optical fiber current sensor system of photoelectric detector, phase shifter, phase modulator in various parts of the detailed design, device of reflection type optical fiber current sensor has been selected.

The diffuse reflection type photoelectric switch, detection and it is also provided with a light emitting device and a light receiving device, but there's no reflector. Under normal circumstances, the light emitted by the light emitting device receiving device is not found. When the detection by blocking the light, and the back reflected light, light receiving device receives the light signal, the output of a switch signal.

Linearly polarized light is in the process of communication, the same light vector direction, the size of phase changes with light, then in the plane perpendicular to the propagation direction of the light vector, the endpoint trajectory is a straight line. Circularly polarized light is in the process of communication, the light vector of constant size, direction of rule changes, the endpoint of the path is a circle. All rules in the process of spreading light

vector magnitude and direction of elliptically polarized light, the light vector endpoints along the elliptical orbit rotates.

$$X_{i+1,V}(m) = \bar{H}_i^* X_{i,V}(m) + \sum_{r=1}^{q-1} \bar{G}_{r,i}^* X_{i,r,D}(m) \quad (10)$$

Jones matrix provides a method to express the most succinct for polarization and polarization device. Using matrix arithmetic is to calculate the polarization components of the complex system of radio waves of state changes. But not to pursue specific physical meaning of each process, matrix representation method is to use a known as columns of a matrix to represent the Jones vector polarized light, through the matrix operation simple, convenient the plurality of polarized light after the superposition of new polarization, such as left and right circularly polarized light wave superposition, the results show that the synthesized light vector along the X axis of the linearly polarized light, the amplitude is 2 times of group polarization amplitude.

Polarization of polarized light can keep the influence of external conditions are not affected by the magnetic field outside, maintain the linear polarization and not into elliptical polarized light, polarized light the way for closed loop [10]. Only these two conditions are met, this paper firstly based on the theory of optical fiber current sensor, introduces the theory of Faraday effect; introduced Jones matrix method for the analysis of polarization system; Jones matrix is derived. Several main

polarization devices and it are as the foundation for establishing the system model.

Wavelengths of light emitted by the light source should be suitable for the requirements, in order to reduce the energy loss in optical fiber. The light source is to have enough brightness. In the optical fiber sensor is much also coherence on the light source is required. In addition, require light stability is good, can be at room temperature for the long-term and stable work, also asked the source of noise, convenient use etc. At the same time for the full optical fiber current sensor, the signal is usually through the communication is transmitted to the control room remote sensing or monitoring of optical fiber transmission, so the signal to be modulated in low loss window wavelength optical communications.

This paper describes the optical fiber current sensing technology theory, the optical fiber current sensor, current and analysis and summary; a kind of phase modulation type optical fiber current sensor is improved, the reflection type current sensor, the sensitivity of the sensor is two times more than the phase modulation type optical fiber current sensor is common, more than four times polarization type optical fiber current sensor. This paper analyzes in detail the polarization variation of reflection type current sensor in the light, and analyzes the theoretical model of reflection type optical fiber current sensor was established by using Jones matrix. The reflection type optical fiber current sensor system source, phase shifter, phase modulator and other parts are analyzed in detail, select or design a device suitable for reflection type optical fiber current sensor.

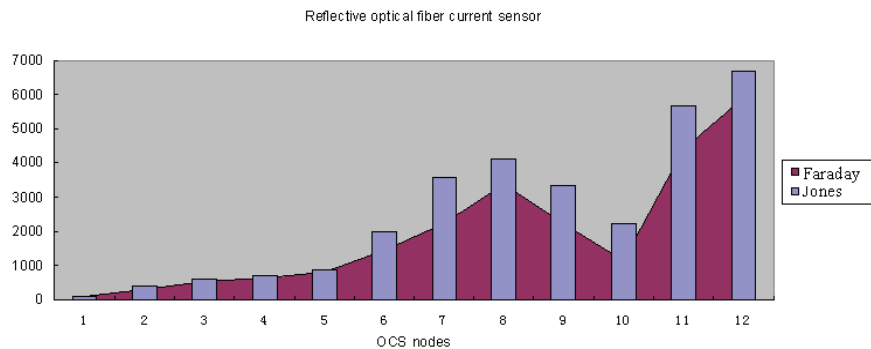


Fig. 3. Comparison reflective optical fiber current sensor based on improved phase modulation Faraday with Jones.

Reflection type current sensor has the advantages of high sensitivity, interference effects of small, good stability and so on, the reflection type optical fiber current sensor is modeled, there will be for each reflection type current sensor in the model design and choice. The light source is one of the indispensable parts of the optical fiber current sensor. Its performance directly affects the technical indexes of the system. The light source is the role of the electric signal into optical signal power, converting light, so that in optical fiber transmission. Because of the special working environment of optical fiber sensor,

request light source has the advantages of small volume, convenient and fiber fitting etc. The paper put forward research and design of reflective optical fiber current sensor based on improved phase modulation.

In this system, because of the principle of phase modulation of the coherent light source, a request to, therefore cannot choose the incoherent light source; the choice is the main gas lasers and semiconductor lasers. Semiconductor laser, especially the type of semiconductor laser distribution can control for single longitudinal mode laser output feedback (DFB)

performance is good, has the certain coherence and high stability, is an ideal light source for optical fiber current sensor system.

## 5. Conclusions

In the optical system, the phase delay can be used to realize optical fiber polarization controller. The polarization controller refers to the arbitrary input polarization state into any desired output polarization state. Fiber polarization controller usually used is photo elastic effect to change in the birefringence fiber, the fiber optical polarization control.

In the design of reflective fiber optic current sensor in the delay of the scheme is: in polarization-maintaining optical fiber exit end, will be a certain length of polarization-maintaining fiber torsion angle, realize the linearly polarized light conversion to a circularly polarized light. The advantages of this method are: between optical fiber and optical fiber sensor can be used welding method to directly link, make the whole system structure is simple, easy to debug.

## References

- [1]. Peng He, Zhen Zhou, Yong Qin, Fiber optic sensor technology for measuring soybean milk concentration in tofu making, *Journal of Convergence Information Technology*, Vol. 8, No. 2, 2013, pp. 580-586.
- [2]. Yu A-Long, Study on non-linearity mode building method based on Lagurre orthogonal polynomial basis functions neural network for Eddy current sensor, *International Journal of Advancements in Computing Technology*, Vol. 4, No. 21, 2012, pp. 574-581.
- [3]. Xiaoyan Kuai, Haixin Sun, Weijie Shen, En Cheng, Qi Jie, Peak-to-average power ratio reduction in underwater acoustic CE-OFDM system by phase modulation, *Journal of Convergence Information Technology*, Vol. 7, No. 9, 2012, pp. 380-386.
- [4]. Dai Zhiyong, Lin Hui, Sun Xinxin, Modified vector control of five-phase PMSM drives for aircraft all-electric braking system, *International Journal of Digital Content Technology & its Application*, Vol. 7, No. 4, 2013, pp. 717-725.
- [5]. Qinghui Zhang, Zenggang Xiong, Gang Liu, Noise elimination of vibration signal of distributed optical fiber-sensing system based on wavelet analysis, *International Journal of Digital Content Technology & its Application*, Vol. 5, No. 10, 2011, pp. 315-321.
- [6]. Xiaolan Bao, Lingling Zhao, Jiangang Jin, Intelligent transport control system based on PIC single chip, *International Journal of Advancements in Computing Technology*, Vol. 4, No. 10, 2012, pp. 99-108.
- [7]. Peng Gao, The application of distributed optical fiber sensing in seepage flow monitoring system, *International Journal of Digital Content Technology & its Application*, Vol. 6, No. 12, 2012, pp. 175-181.
- [8]. WANG-Yong Jiao, LIANG-Lei, Realizing optical refractive index sensor by using the nano-fiber, *International Journal of Digital Content Technology & its Application*, Vol. 7, No. 6, 2013, pp. 300-308.
- [9]. Jingwen Tian, Meijuan Gao, Guangshuang Ge, In-line measurement system of bore well mud viscosity based on multisensor data fusion with wavelet neural network, *International Journal of Advancements in Computing Technology*, Vol. 5, No. 5, 2013, pp. 1011-1018.
- [10]. De En, Changsheng Zhou, Xiaolong Shi, Research of optic-fiber pressure sensor based on MOEMS, *International Journal of Digital Content Technology & its Application*, Vol. 7, No. 7, 2013, pp. 627-634.

2013 Copyright ©, International Frequency Sensor Association (IFSA). All rights reserved.  
(<http://www.sensorsportal.com>)



**Universal Frequency-to-Digital Converter  
(UFDC-1 and UFDC-1M-16)  
in MLF (5 x 5 x 1 mm) package**

**SMALL WORLD -  
BIG FEATURES**

SWP, Inc., Toronto, Ontario, Canada,  
Tel. +34 696067716, fax: +34 93 4011989, e-mail: [sales@sensorsportal.com](mailto:sales@sensorsportal.com)  
[http://www.sensorsportal.com/HTML/E-SHOP/PRODUCTS\\_4/UFDC\\_1.htm](http://www.sensorsportal.com/HTML/E-SHOP/PRODUCTS_4/UFDC_1.htm)

## Modeling of Microdiaphragm Based Pressure Sensor with Application for Gas Turbine Engine Condition Monitoring

<sup>1</sup> Ahmad GHANBARI, <sup>2</sup> Ehsan QAREDAGHI

<sup>1</sup> Department of Mechanical Engineering,

School of Engineering-Emerging Technologies, University of Tabriz, Tabriz, Iran

<sup>2</sup> School of Engineering-Emerging Technologies, University of Tabriz, Tabriz, Iran

E-mail: a-ghanbari@tabrizu.ac.ir, e.qaredaghi@gmail.com

*Received: 23 April 2013 /Accepted: 25 August 2013 /Published: 30 September 2013*

---

**Abstract:** The miniaturization of sensors represents a promising approach for various systems health management. Dynamic pressure measurements have a very good potential to provide GTE diagnostics, maintenance management, and optimized performance, based on pressure variation measurements. In this paper, we will investigate vibrational behavior of piezoelectric microdiaphragm based pressure sensor with application for GTEs condition monitoring. The general formulation based on transverse vibration of circular plates will be introduced and the response of diaphragm under forced excitation will be discussed. The obtained results show that the application of pressure sensor for condition monitoring of GTEs could have major benefits and improve their performance. *Copyright © 2013 IFSA.*

**Keywords:** MEMS, Pressure sensor, Piezoelectric, GTEs, Condition monitoring, Transverse vibration, Circular microdiaphragm.

---

### 1. Introduction

The miniaturization of sensors represents a promising approach for various systems health management. The main advantages of miniaturized systems include low mass and low power consumption. MEMS based sensor systems will play a significant role in the development of miniature, on-line, in-situ, low cost, health monitoring platforms.

In literature, many condition monitoring applications have been proposed for pressure sensors [1-7]. One application area with major impact is condition monitoring of Gas Turbine Engines (GTEs) [1]. The application of MEMS pressure sensors makes it possible obtaining engine

performance characteristics with high sensitivity and fast response time. Moreover, these devices replace macro-sensors which provide offline condition monitoring.

For these purposes, dynamic behavior characterization of microdiaphragm based pressure sensors could help to optimize the health management system and provide better performance for GTEs. Many researches have been done to characterize dynamic behavior of circular microdiaphragms. Yu et al. have been introduced a mathematical modeling of microdiaphragms under initial tension [13]. Olfatnia et al. theoretically modeled the dynamic behavior of circular microdiaphragms and the influences of pressure loading on the behavior of the diaphragm in different vibration modes [8-10].

In this paper, first we acquire the mathematical formulation of dynamic behavior of circular microdiaphragm including damped condition. Then, a model will be introduced to be applicable to GTEs condition monitoring.

## 2. Theory

### 2.1. General Formulation

The sensor is modeled as a clamped circular diaphragm with initial tension and rigidity, as shown in Fig. 1, with radius  $a$ , thickness  $h$ , Young's modulus  $E$ , and Poisson's ratio  $\nu$ . The non-linear partial differential equation of that diaphragm with a transverse loading per unit area, is governed as equation [14]

$$\rho h \frac{\partial^2 w}{\partial t^2} + D \nabla^4 w - T \nabla^2 w = -2\mu \frac{\partial w}{\partial t} + f(r, \theta, t), \quad (1)$$

where  $\rho$  is the density,  $w$  is the transverse displacement and

$$D = Eh^3/12(1-\nu^2), \quad (2)$$

is the flexural rigidity,  $\nabla^2$  is the laplacian, and  $T$  is the initial tension of the diaphragm per unit length. The boundary conditions are as follow:

$$w(a, \theta, t) = 0, \quad \left. \frac{\partial w(r, \theta, t)}{\partial r} \right|_{r=a} = 0. \quad (3)$$

In the absence of forcing in equation (1), we will search for a modal solution of form

$$w(r, \theta, t) = W(r, \theta) e^{(\alpha+i\omega)t}, \quad (4)$$

where  $W$  is the unknown function,  $\alpha$  is the term characterizing damped condition, and  $\omega$  is natural frequency. Substituting (4) into equation (1), we obtain

$$\left[ (\alpha^2 - \omega^2 + 2i\alpha\omega) \rho h + 2\mu(\alpha + i\omega) \right] W + D \nabla^4 W - T \nabla^2 W = 0 \quad (5)$$

Equation (5) can be expressed as

$$(\nabla^2 + \gamma_1^2)(\nabla^2 - \gamma_2^2)W = 0. \quad (6)$$

It is found that

$$\gamma_1^2 = \frac{-T + \sqrt{T^2 - 4D\Gamma}}{2D}, \quad (7)$$

$$\gamma_2^2 = \frac{+T + \sqrt{T^2 - 4D\Gamma}}{2D}$$

where  $\Gamma$  is as follow:

$$\Gamma = \rho h (\alpha^2 - \omega^2) + 2\mu\alpha + 2i\omega(\mu + \rho h\alpha). \quad (8)$$

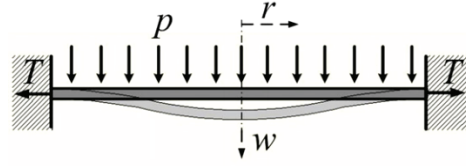


Fig. 1. Illustration of the clamped diaphragm [8].

It can be shown that

$$\alpha = -\frac{\mu}{\rho h}. \quad (9)$$

Expanding the transverse displacement amplitude as

$$W(r, \theta) = R(r)\Theta(\theta), \quad (10)$$

results in equation (11),

$$\Theta(\theta) = A_{1m} \sin m\theta + A_{2m} \cos m\theta$$

$$R(r) = B_{1m} J_m(\gamma_{1m} r) + B_{2m} Y_m(\gamma_{1m} r) + B_{3m} I_m(\gamma_{2m} r) + B_{4m} K_m(\gamma_{2m} r) \quad (11)$$

The solution of equation (11) must be continuous, and therefore  $m$  must be an integer. The functions  $J_m$ ,  $Y_m$ ,  $I_m$ , and  $K_m$  are the Bessel functions of the first and second kind, and the modified Bessel functions of the first and second kind, respectively. The coefficients  $A$  and  $B$  in equation (11) are constants which are determined by the boundary conditions. Both  $Y_m$  and  $K_m$  are singular at  $r = 0$ . Therefore, for a plate with a finite displacement at the plate center, the coefficients  $B_{2m}$  and  $B_{4m}$  are equal to zero. Applying function  $R(r)$  into the boundary condition, equation (3) results in the following equation

$$\begin{bmatrix} J_m(\gamma_{1m} a) & I_m(\gamma_{2m} a) \\ J'_m(\gamma_{1m} a) & I'_m(\gamma_{2m} a) \end{bmatrix} \begin{bmatrix} B_{1m} \\ B_{3m} \end{bmatrix} = 0. \quad (12)$$

The prime indicates a derivative with respect to  $r$ . For non-trivial solutions of  $B_{1m}$  and  $B_{3m}$ , the characteristic equation should be equal to zero:

$$J_m(\gamma_{1m} a) J_m(\gamma_{2m} a) - I_m(\gamma_{2m} a) J'_m(\gamma_{1m} a) = 0 \quad (13)$$

By determining the roots of equation (13), and replacing them into the rearranged form of equation (7), the natural frequencies are obtained as follows:

$$\omega_{mn}^d = \sqrt{\frac{1}{\rho h} (D\gamma_{1mn}^4 + T\gamma_{1mn}^2) - \left(\frac{\mu}{\rho h}\right)^2}, \quad (14)$$

where the superscript  $d$  shows the damped natural frequency. Under un-damped condition the natural frequency is as follows [9]:

$$\omega_{mn}^n = \sqrt{\frac{1}{\rho h} (D\gamma_{1mn}^4 + T\gamma_{1mn}^2)}. \quad (15)$$

If we assume that,

$$\frac{\mu}{\rho h} = \zeta_{mn} \omega_{mn}^n, \quad (16)$$

we can rewrite equation (14) as follows

$$\omega_{mn}^d = \omega_{mn}^n \sqrt{1 - \zeta_{mn}^2}, \quad (17)$$

Finally, the mode shape is obtained as follows:

$$\begin{aligned} W(r, \theta) &= R(r)\Theta(\theta) \\ R(r) &= J_m(\gamma_{1mn}r) - \frac{J_m(\gamma_{1mn}a)}{I_m(\gamma_{2mn}a)} I_m(\gamma_{2mn}r), \quad (18) \\ \Theta(\theta) &= A_{1m} \sin m\theta + A_{2m} \cos m\theta \end{aligned}$$

A non-dimensional tension parameter  $k$  is defined as [11]

$$k = a\sqrt{\frac{T}{D}}, \quad (19)$$

This non-dimensional parameter determines the behavior of the diaphragm. If the internal tension is so high that it dominates the flexural rigidity, the diaphragm behaves as tension dominated membrane. On the other hand, if internal tensions are so low that flexural rigidity is dominated, the diaphragm behaves as flexural rigidity dominated plate.

Fig. 2 shows the natural frequency versus  $k$ . As it is obvious from the figure, if  $k$  is less than 1 the flexural rigidity is dominated, if  $k$  is greater than 20 tension is dominated, and the range between this two values is called transition region, and in this region diaphragm behaves between plate and membrane.

The effect of parameter  $k$  is not limited to determination of natural frequency. We can conclude from equation (7):

$$\gamma_{2mn}^2 = \gamma_{1mn}^2 + k. \quad (20)$$

This means that  $k$  effects mode shapes through characteristic equation. Fig. 3 shows first vibrational mode of diaphragm respect to different values of  $k$ .

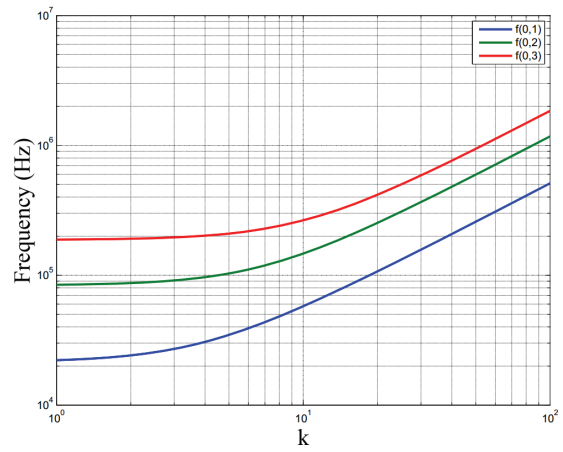


Fig 2. Variations of the first three resonant frequencies with respect to the tension parameter  $k$ .

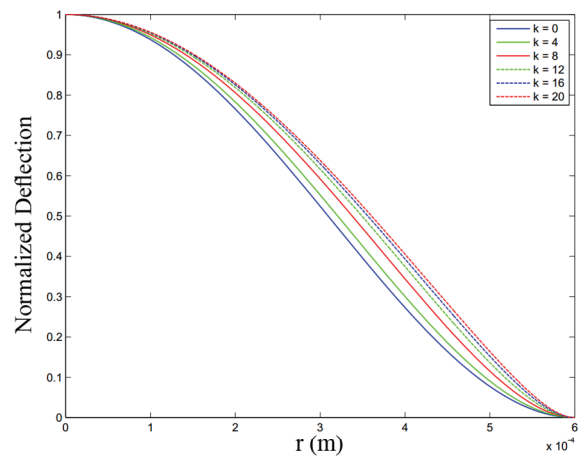


Fig 3. Variation of first mode shape with respect to parameter  $k$ .

## 2.2. Forced Response

To consider the forced response of a damped diaphragm to harmonic excitations loading is assumed to be the form

$$f(r, \theta, t) = p(r, \theta)e^{i\omega t}, \quad (21)$$

where the pressure amplitude  $p(r, \theta)$  is assumed to be uniform and denoted by  $p$ , and  $\omega$  is the excitation frequency. The aim is to find the steady state response of the diaphragm when it is excited close to the diaphragms first natural frequency. To that end, to that end, a single-mode approximation is assumed as

$$w(r, \theta, t) \approx W_{01}(r, \theta)\eta_1(t), \quad (22)$$

where  $\eta_1$  is the modal amplitude and  $W_{01}$  is the first mode shape of the linear system. The approximation

for the steady state forced response of the diaphragm can be obtained as

$$w(r, \theta, t) \approx U(r, \theta) e^{i(\omega t - \phi_0)} = \Lambda_{01} W_{01}(r, \theta) e^{i(\omega t - \phi_0)}. \quad (23)$$

It can be shown that vibration amplitude,  $U(r, \theta)$ , at the center of the diaphragm is as follow [13]:

$$U(0, \theta) = \frac{2\pi pa}{\rho h T} \left[ 1 - \frac{J_0(\gamma_{101} a)}{I_0(\gamma_{201} a)} \right] \times \left[ \frac{1}{\gamma_{101}} J_1(\gamma_{101} a) - \frac{J_0(\gamma_{101} a)}{\gamma_{201} I_0(\gamma_{201} a)} I_1(\gamma_{201} a) \right] \times \omega_1 \sqrt{\left[ 1 - \left( \frac{\omega}{\omega_{01}} \right)^2 \right]^2 + 4\zeta_{01}^2 \left( \frac{\omega}{\omega_{01}} \right)^2}. \quad (24)$$

### 3. Validation

For validation of our general formulation of damped vibration of diaphragm, we used the experimental results obtained by Olfatnia et al. [9]. Fig. 4 shows the configuration of diaphragm used by Olfatnia et al. for experimental purposes. This figure shows that multi-morph diaphragm consist of 5 layers.

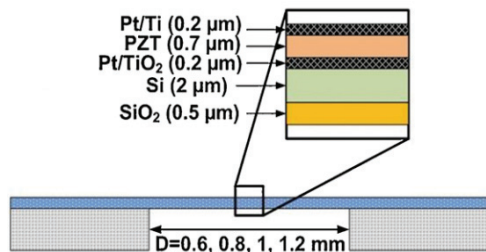


Fig. 4. Cross-section schematic of diaphragm [9].

In micro/nano scale there are many phenomena effect damping of structure that are negligible in macro scale. Some of these phenomena have some other effects that have major impact on vibrational behavior of the structure. For example, squeeze film has effects on both damping and mechanical stiffness of the structure. However, the total effect of damping in structure is estimated by a quantity called quality-factor, the effect of quality-factor is obvious from vibration basic equation below [12],

$$\ddot{x}(t) + \frac{\omega_n}{Q} \dot{x}(t) + \omega_n^2 x(t) = \frac{f(t)}{m_{eff}}. \quad (25)$$

The quality-factor in air is measured to be 137. So the value of  $\zeta$  in this configuration will be 0.004.

Fig. 5 shows the comparison between experimental and theoretical values of first for natural frequencies. We can readily see that formulation of vibrational behavior in damped condition is more accurate than un-damped condition.

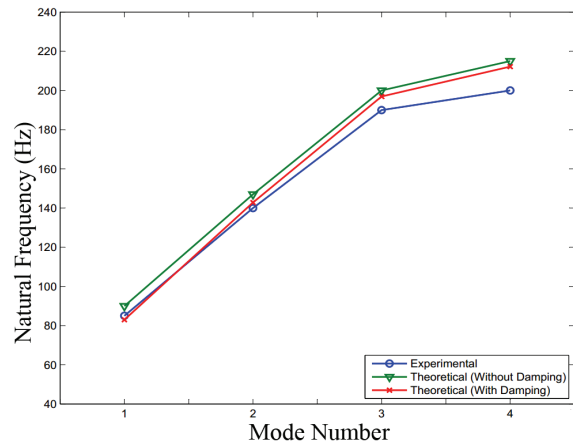


Fig 5. First four Natural Frequencies: Comparison between experimental and theoretical results.

## 4. Application

### 4.1. Gas Turbine Engines (GTEs)

Gas turbine engine (GTE) propulsion systems are used in many areas of human activity, and they have an excellent record in both reliability and safety. In this regard, a reliable condition monitoring system is especially important for aircraft GTEs, because a fault in the GTE can lead to disastrous results. However, real-time condition monitoring of such complex nonlinear dynamic systems is a very complicated problem. During normal operation, the GTEs experience significant changes in pressure, temperature, Mach number, and power output. These intrinsic variations will alter the GTE dynamics in a nonlinear manner. Hence, careful attention must be paid during GTE operation to ensure that the mechanical, aerodynamic, thermal, and flow limitations of the GTEs are maintained [1].

### 4.2. Dynamic Pressure Measurement

In-situ dynamic pressure measurements have a very good potential to provide GTE diagnostics, maintenance management, and optimized performance, based on pressure variation measurements. The versatility of pressure-based measurements will provide a foundation for active-control methodologies through the evaluation and interpretation of changes to the dynamic pressure flow within the GTE environment.

Application of traditional bulky and off-line pressure sensors does not provide very useful

condition monitoring of GTEs. So a new approach introduced by Rinaldi et al. is to use MEMS based dynamic pressure sensor for condition monitoring of GTEs. In the work done by Rinaldi et al., application of MEMS based dynamic pressure sensor on J-85 engine have been studied (shown in Fig. 6 and 7) [1].



Fig. 6. J-85 engine [1].



Fig 7. J-85 engine cutaway [1].

Dynamic pressure, by definition, consists of a variation in pressure over a given time interval. This is especially true for rotating machinery such as fans, where the dynamic pressure flow is generated by the rotation of the fan blades. In this regard, for the work presented here in, the time dependence of the pressure flow is taken from the point of view of the individual GTE fan blades passing beneath a reference point (sensor location) as shown in Fig. 8. With this implementation some parameters could be monitored: (1) the speed of the rotary fans, (2) the health of single blades, and (3) radial and axial alignment of fans.

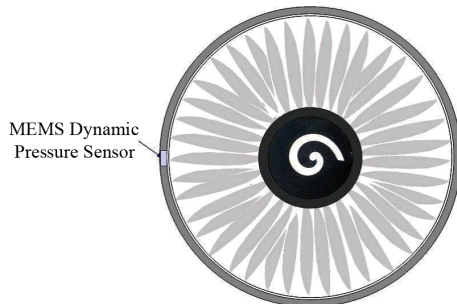


Fig. 8. Schematic front-view of the location of the MEMS dynamic pressure sensor with respect to the fan blades of a GTE [1].

### 4.3. MEMS Pressure Sensor Specifications

Due to their low-pressure sensitivity, MEMS silicon microphones are proposed as the main components of the sensor for monitoring the dynamic pressure variations generated by the GTE fan and compressor stages. The sensor consists of two Knowles Acoustics SiSonic microphones. Two microphones were used for redundancy in the measurements. This is an added advantage in using small scale components as they allow for redundancy even within a small surface area and provide added system reliability. Presented in Fig. 9 is an image of the main component of the MEMS microphone. The active area of the silicon diaphragm has a diameter of 500  $\mu\text{m}$  and a thickness of 1  $\mu\text{m}$  [1].

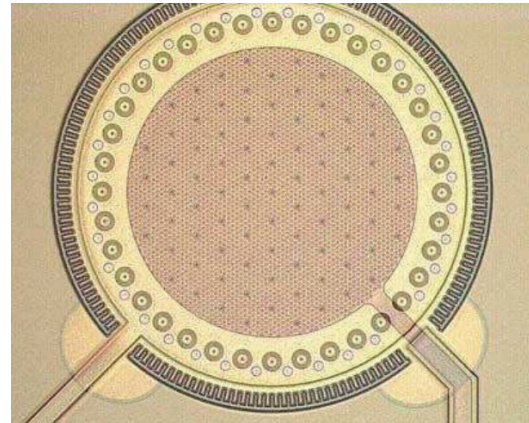


Fig 9. MEMS SiSonic microphone diaphragm [1].

With the specifications above we can use equation (14) to determine natural frequencies of pressure sensor. With the assumption of no internal tension and discarding damping effects, the first and second natural frequency will be 15.6 and 32.5 kHz, respectively.

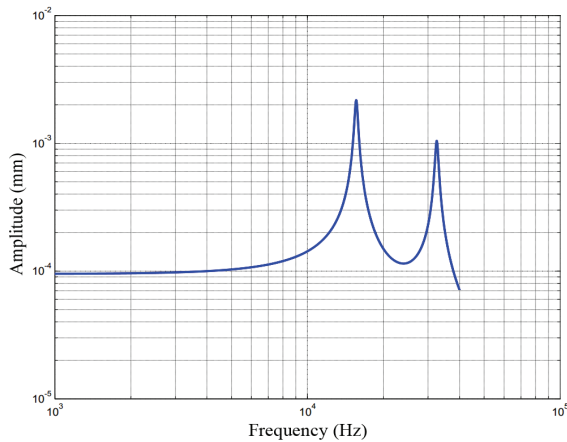
### 4.4. Gas Turbine Engine Tests

As we said, J-85 engine have been used for this illustration. The J-85 engine has 8 compressor stages on a single shaft. Given in Table 1 is the number of blades for the stages, and the theoretical nominal RPM and stage-frequency at engine idle and 80 % of maximum power. In this regard, the stage-frequency is defined as the frequency detected by the sensor for that particular stage at a given engine operating condition.

As it is obvious from Table 1, the working frequency is up to about 32 kHz. So this range of operation includes only two of first natural frequencies. These operating conditions help the sensor to reach its maximum signal output. Fig. 10 shows frequency response of pressure sensor for two, first natural frequencies [1].

**Table 1.** An overview of the compressor stages [1].

Compressor Stage	Number of Blades	Nominal RPM @ 80%	Nominal Frequency (Hz) @ 80%
1 <sup>st</sup>	30	13400	6923
2 <sup>nd</sup>	60	13400	13400
3 <sup>rd</sup>	87	13400	19430
4 <sup>th</sup>	106	13400	23673
5 <sup>th</sup>	131	13400	29257
6 <sup>th</sup>	132	13400	29480
7 <sup>th</sup>	140	13400	31267
8 <sup>th</sup>	120	13400	26800

**Fig. 10.** Estimated frequency response of pressure sensor in J-85 engine operation range.

## 5. Discussion

As we saw in section 2, the theoretical model to predict Vibrational behavior of circular microdiaphragms is investigated. This formulation includes damped conditions. The damping effects are mainly different in micro- and macro-scale. Energy dissipation mechanisms do not equally contribute to the total energy loss of the system. Size and ambient pressure are the two main parameters, which clarify the contribution of these terms. Size reduction from macro to micro scale increases surface-to-volume ratio, and hence signifies the effect of surface forces, and dominates them over the body forces. Therefore, bulk losses are negligible in micro-scale regions compared to medium damping terms. The main energy dissipation mechanisms are identified as (a) medium loss, which is the loss into the surrounding (fluid) medium due to acoustic radiation or viscous drag, (b) clamping or support loss, which is the dissipation of energy through the support, and (c) bulk loss, which is composed of a variety of physical mechanisms, such as internal friction, thermoelastic dissipation (TED), phonon-phonon scattering, motion of lattice defects, and piezoelectric damping in piezoelectric materials. Effect of these phenomena in damping is different so to determine the damping coefficient all conditions should be checked and their effects should be considered.

The effect of internal tension should not be neglected. The value of internal tension determines the actual behavior of microdiaphragm. Microfabrication methods often involve high temperature thin film deposition processes, and the mismatch between thermal expansion coefficients of different layers could cause internal tension.

The validation of formulation shows that introduction of damping in modeling decreased difference between theoretical and experimental results. The remained error could be for difference in properties of materials, instrument errors and skipping some phenomena that have effect on damping like squeeze film effect.

As we saw in section 4, the application of microdiaphragm based pressure sensor in dynamic pressure condition monitoring of GTEs has major impact on health management and performance improvement of these systems. As discussed before, with this implementation some parameters could be monitored: (1) the speed of the rotary fans, (2) the health of single blades, and (3) radial and axial alignment of fans. Two of first natural frequencies of proposed sensor are in the operational range of testing GTE. This could help for better performance of condition monitoring, because of high amplitude signal output and noise cancelation. The high sensitivity associated with acoustic dynamic pressure measurements allowed for the extraction of pressure signals J-85 engine.

## 6. Conclusions

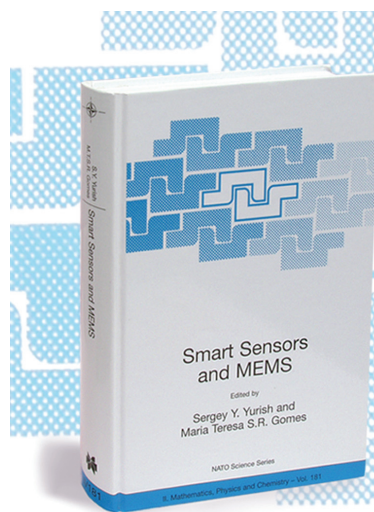
In this paper, we investigated vibrational behavior of piezoelectric microdiaphragm based pressure sensor with application for GTEs condition monitoring. The general formulation based on transverse vibration of circular plates introduced and the response of diaphragm under forced excitation has discussed. The validation of theoretical models with experimental results shows that introduction of damping effect in theoretical modeling improves the vibrational behavior prediction. Application of MEMS pressure sensors for condition monitoring of GTEs offers special features. In-situ dynamic pressure measurements have a very good potential to provide GTE diagnostics, maintenance management, and optimized performance, based on pressure variation measurements.

## References

- [1]. G. Rinaldi, I. Stiharu, M. Packirisamy, V. Nerguizian, R. J. Landry, J. P. Raskin, Dynamic pressure as a measure of gas turbine engine (GTE) performance, *Measurement Science and Technology*, Vol. 21, No. 4, 2010, 045201.
- [2]. K. T. Kim, J. G. Lee, B. D. Quay, D. A. Santavicca, Spatially distributed flame transfer functions for predicting combustion dynamics in lean premixed gas turbine combustors, *Combustion and Flame*, Vol. 157, No. 9, 2010, pp. 1718-1730.

- [3]. V. Muralidharan, V. Sugumaran, Feature extraction using wavelets and classification through decision tree algorithm for fault diagnosis of mono-block centrifugal pump, *Measurement*, Vol. 46, 2013, pp. 353-359.
- [4]. L. Barelli, G. Bidini, F. Bonucci, Diagnosis methodology for the turbocharger groups installed on a 1MW internal combustion engine, *Applied Energy*, Vol. 86, No. 12, 2009, pp. 2721-2730.
- [5]. J. M. Luján, V. Bermúdez, C. Guardiola, A. Abbad, A methodology for combustion detection in diesel engines through in-cylinder pressure derivative signal, *Mechanical Systems and Signal Processing*, Vol. 24, No. 7, 2010, pp. 2261-2275.
- [6]. S. Fricke, A. Friedberger, H. Seidel, U. Schmid, A robust pressure sensor for harsh environmental applications, *Sensors and Actuators A: Physical*, Vol. 184, 2012, pp. 16-21.
- [7]. L. Barelli, G. Bidini, C. Buratti, R. Mariani, Diagnosis of internal combustion engine through vibration and acoustic pressure non-intrusive measurements, *Applied Thermal Engineering*, Vol. 29, No. 8, 2009, pp. 1707-1713.
- [8]. M. Olfatnia, T. Xu, J. M. Miao, L. S. Ong, X. M. Jing, L. Norford, Piezoelectric circular microdiaphragm based pressure sensors, *Sensors and Actuators A: Physical*, Vol. 163, No. 1, 2010, pp. 32-36.
- [9]. M. Olfatnia, T. Xu, L. S. Ong, J. M. Miao, Z. H. Wang, Investigation of residual stress and its effects on the vibrational characteristics of piezoelectric-based multilayered microdiaphragms, *Journal of Micromechanics and Microengineering*, Vol. 20, No. 1, 2010, 015007.
- [10]. M. Olfatnia, V. R. Singh, T. Xu, J. M. Miao, L. S. Ong, Analysis of the vibration modes of piezoelectric circular microdiaphragms, *Journal of Micromechanics and Microengineering*, Vol. 20, No. 8, 2010, 085013.
- [11]. M. Sheplak, J. Dugundji, Large deflections of clamped circular plates under initial tension and transitions to membrane behavior, *Journal of Applied Mechanics*, Vol. 65, No. 1, 1998, pp. 107-115.
- [12]. M. Olfatnia, Z. Shen, J. M. Miao, L. S. Ong, T. Xu, M. Ebrahimi, Medium damping influences on the resonant frequency and quality factor of piezoelectric circular microdiaphragm sensors, *Journal of Micromechanics and Microengineering*, Vol. 21, No. 4, 2011, 045002.
- [13]. M. Yu, B. Balachandran, Sensor diaphragm under initial tension: linear analysis, *Experimental Mechanics*, Vol. 45, No. 2, 2005, pp. 123-129.
- [14]. S. P. Timoshenko, S. Woinowsky-Krieger, Theory of plates and shells, New York: *McGraw-Hill*, 1959.
- [15]. M. Yu, X. Long, B. Balachandran, Sensor diaphragm under initial tension: nonlinear responses and design implications, *Journal of Sound and Vibration*, Vol. 312, No. 1, 2008, pp. 39-54.

2013 Copyright ©, International Frequency Sensor Association (IFSA). All rights reserved.  
(<http://www.sensorsportal.com>)



## Smart Sensors and MEMS

Edited by  
Sergey Y. Yurish and  
Maria Teresa S.R. Gomes

The book provides an unique collection of contributions on latest achievements in sensors area and technologies that have made by eleven internationally recognized leading experts ...and gives an excellent opportunity to provide a systematic, in-depth treatment of the new and rapidly developing field of smart sensors and MEMS.

The volume is an excellent guide for practicing engineers, researchers and students interested in this crucial aspect of actual smart sensor design.

**Kluwer Academic Publishers**

Order online: [www.sensorsportal.com/HTML/BOOKSTORE/Smart\\_Sensors\\_and\\_MEMS.htm](http://www.sensorsportal.com/HTML/BOOKSTORE/Smart_Sensors_and_MEMS.htm)

## Development of a Model Depicting Optimum Performance of Liquid Catheter Sensor for Pressure Measurement

**Suman HALDER**

St. Thomas' College of Engineering and Technology,  
Kolkata-700023, India  
Tel.: +919432128293  
E-mail: sum\_hal@yahoo.co.in

*Received: 1 July 2013 /Accepted: 25 August 2013 /Published: 30 September 2013*

---

**Abstract:** In this paper the author proposed a model that depicts not only the basic features of liquid catheter sensor but also improvement of those features. The optimum performance of the 2nd order liquid catheter sensor system depends on parameters namely natural frequency of oscillation and damping ratio and two basic features namely high frequency response and flat frequency response. As the system dynamics of the liquid catheter sensor is evolved as closed loop transfer function therefore it is very difficult to design this system with help of root locus method where the open loop gain is varied to estimate the behavior of the closed loop poles of the system. In this paper the author has used a novel approach of basic vector field method for two dimensional linearized systems. The model clearly indicates the optimum performance criterion of the liquid catheter sensor based on the model proposed by the author. The proposed model not only gives the various dynamic features of liquid catheter sensor but also highlights both inertia controlled and thermally controlled vapor bubble dynamics. *Copyright © 2013 IFSA.*

**Keywords:** Liquid catheter, Flat frequency response, Two dimensional vector field, Stable spiral, Inertia controlled bubble dynamics.

---

### 1. Introduction

With linearized two dimensional approaches one can realize the hidden dynamics of the sensor system that governs the total operation. An understanding of the dynamic properties of arterial pressure measurement is important if we wish to preserve the dynamic accuracy of the measured pressure. The liquid filled catheter sensor serves this purpose. The liquid filled catheter sensor is hydraulic system that can be represented either distributed or lumped parameter models. Distributed parameters are described in the literature (Fry, 1960) which gives an accurate description of the dynamic behaviour of the

catheter sensor system. However, distributed parameter models are not normally employed because single degree of freedom (lumped parameter) model is much easier to work with, and the accuracy of the results obtained by using these models is acceptable for the clinical situation [1]

With the approximations the lumped parameter model of liquid filled catheter sensor is reduced to second order system. The liquid catheter has inertial, frictional and elastic properties represented by inertance, resistance and compliance respectively. Similarly the sensor has these same properties in addition to the compliance of diaphragm. Fig.1 shows the electric analog of pressure measuring system.

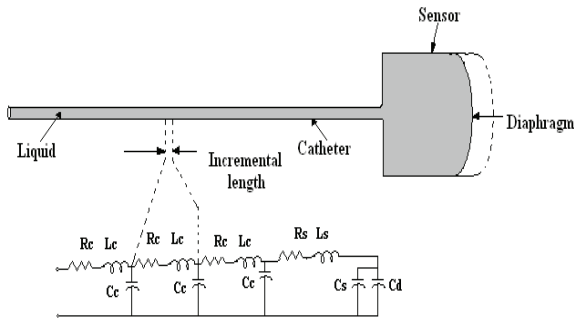


Fig. 1. Electric analog of pressure measuring system.

The above diagram represents measurement of pressure in terms of electrical voltage. Therefore pressure-voltage analogy has been used. Thus hydraulic circuit is converted to analog electrical circuit. As the compliance of the sensor diaphragm is much larger than that of liquid catheter or sensor cavity provided that saline solution is bubble free and catheter material is relatively non compliant. The resistance and inductance of the liquid in the sensor can be neglected compared to those of liquid in catheter. Thus the catheter sensor system can be modified in Fig. 2.

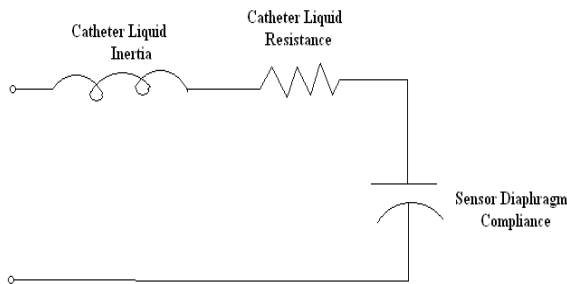


Fig. 2. Modified diagram of electrical analog of pressure measuring system.

The liquid resistance in catheter is given by  $R_c = \frac{\Delta P}{F}$  (Pa.s/m<sup>3</sup>) where P = pressure difference across the segment in Pascal; F = flow rate, m<sup>3</sup>/sec

or  $R_c = \frac{\Delta P}{uA}$  where u = average velocity m/sec;

A = cross sectional area, m<sup>2</sup> Poiseuille's flow equation enables us to calculate Rc when we are given the values of catheter length L, in meters; radius r, in meters; and liquid viscosity η, in Pascal-seconds. The equation applies for laminar flow

$$R_c = \frac{8\eta L}{\pi r^4} \quad (1a)$$

The liquid inductance Lc of the catheter is due to primarily to the mass of liquid. It can be represented by the equation

$$L_c = \frac{\Delta P}{\frac{dF}{dt}} \text{ (Pa.s}^2\text{/m}^3\text{)}$$

OR

$$L_c = \frac{\Delta P}{aA},$$

where a = acceleration, m/s<sup>2</sup>. This equation reduces further to

$$L_c = \frac{m}{A^2} \text{ where } m = \text{mass of the liquid in Kg or}$$

$$L_c = \frac{\rho L}{\pi r^2}, \quad (1b)$$

where ρ = density of the liquid (kg/m<sup>3</sup>).

Now the compliance of the sensor diaphragm is given by equation

$$C_d = \frac{\Delta V}{\Delta P} = \frac{1}{E_d}, \quad (1c)$$

where E<sub>d</sub> = volume modulus of elasticity of the sensor diaphragm.

One can find the input output equation of the above system

$$V_i(t) = \frac{L_c C_d d^2 V_o(t)}{dt^2} + \frac{R_c C_d dV_o(t)}{dt} + V_o(t),$$

where Vi(t) is the input and Vo(t) is the output

$$\frac{V_o(S)}{V_i(S)} = \frac{\omega_n^2}{S^2 + 2\zeta\omega_n S + \omega_n^2}, \quad (1d)$$

where  $\omega_n = 2\pi f_n$ .

This system corresponding to 2<sup>nd</sup> order system (in frequency domain) having natural frequency of vibration

$$f_n = \frac{1}{2\pi} \sqrt{\frac{1}{L_c C_d}} = \frac{r}{2} \left( \frac{1}{\pi \rho L \Delta V} \right)^{\frac{1}{2}} \quad (1e)$$

and damping ratio

$$\zeta = \left( \frac{R_c}{2} \right) \sqrt{\frac{C_d}{L_c}} = \frac{4\eta}{r^3} \left( \frac{L(\Delta V / \Delta P)}{\pi \rho} \right)^{\frac{1}{2}} \quad (1f)$$

As the cavitations phenomena is evident in liquid catheter system thus liquid bubbles generated will acts as an additional compliance C<sub>b</sub> due bubble

(considering lumping effect) may be assumed in parallel with the compliance of diaphragm. Then the circuit is modified to Fig. 3.

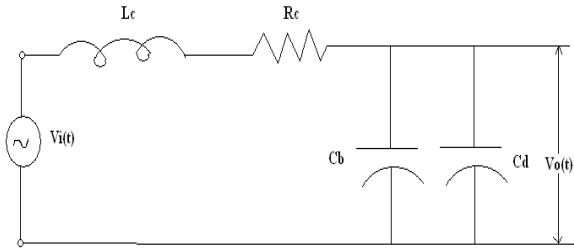


Fig. 3. Modified diagram considering the effect of bubble compliance.

As the bubbles are present in the liquid catheter sensor thus capacitance will be changed from Cd to (Cd + Cb) from idealized bubble free model to actual model considering the effect of bubble. As a result the natural frequency of oscillation decreases and damping ratio increases. Decrement in natural frequency oscillations mean the band width of the system is reduced. Thus high frequency behavior of the liquid catheter sensor deteriorates. But increment in damping ratio means the frequency response becomes flat. Thus the bubbles have one improving effect and another deteriorating effect [1, 3, 5].

Let us elucidate more on bubble growth in the liquid catheter sensor. Neglecting surface tension and viscosity, Rayleigh (1917) showed from momentum equation that the bubble boundary R(t) obeyed the relation

$$R \ddot{R} + \frac{3}{2} (\dot{R})^2 = \frac{P(R) - P_\infty}{\rho}, \quad (2a)$$

where  $\rho$  is the liquid density;  $P_\infty$  is the pressure of the liquid at a large distance from the bubble; P(R) is the pressure in the liquid at bubble boundary.

For a spherical bubble viscosity affects only the boundary condition so that it becomes

$$P(R) = P_i - \frac{2\sigma}{R} - \frac{4\mu}{R} \dot{R}, \quad (2b)$$

where  $P_i$  is the pressure in the bubble and P(R) is the pressure in the liquid at bubble boundary.  $\sigma$  and  $\mu$  are surface tension constant and coefficient of liquid viscosity respectively. Thus generalized Rayleigh's bubble dynamics equation becomes

$$R \ddot{R} + \frac{3}{2} (\dot{R})^2 = \frac{1}{\rho} \left[ P_i - P_\infty - \frac{2\sigma}{R} - \frac{4\mu}{R} \dot{R} \right] \quad (2c)$$

Thus equilibrium radius of the gas nucleus for given values of  $P_i$  and  $P_\infty$  is given by

$$R_0 = \frac{2\sigma}{P_i - P_\infty} \quad (2d)$$

For inertia controlled bubble growth velocity  $\dot{R}$  is given by

$$\dot{R}^2 = \left( \frac{R_0}{R} \right)^3 \dot{R}_0^2 + \frac{2P_v - P_\infty}{3\rho} \left\{ 1 - \left( \frac{R_0}{R} \right)^3 \right\} - \frac{2\sigma}{\rho R} \left\{ 1 - \frac{R_0}{R} \right\}^2 \quad (2e)$$

If the vapor pressure  $P_v > P_\infty$ , then for  $R \gg R_0$  the above can be simplified to

$$\dot{R}^2 = \left( \frac{2}{3} \frac{P_v - P_\infty}{\rho} \right) \quad (2f)$$

thus

$$\dot{R} = \left( \frac{2}{3} \frac{P_v - P_\infty}{\rho} \right)^{\frac{1}{2}} \quad (2g)$$

Thus we see that the bubble growth due to liquid inertia is inversely related to the density of liquid to be used [2].

Again for thermally controlled bubble growth requires large vapor density so that the heat flow at the liquid interface is governed by latent heat only.

The equation for thermally controlled bubble growth is given by

$$\dot{R} = \left( \frac{3}{\pi} \right) \frac{k_l}{L_h \rho_v^e(T_b)} \frac{T_\infty - T_b}{(D_l t)^{1/2}} \quad (2h)$$

$\dot{R}$  is the growth velocity;  $k_l$  and  $D_l$  are liquid thermal diffusivity and conductivity and  $\rho_v^e(T_b)$  is the equilibrium vapor density corresponding to boiling temperature.  $L_h$  is the latent heat.  $T_\infty$  is the uniform temperature inside spherical bubble and  $T_b$  is the boiling temperature. In this equation the bubble growth is inversely related to equilibrium vapor density and latent heat of vaporization. The above equation expresses only an asymptotic relationship that is valid only for times large enough so that the growth velocity predicted by it is smaller than the inertia-controlled value of bubble radius.

Therefore we can conclude that generation of bubble mainly due inertia controlled bubble growth [2].

Thus our prime objective is to find a solution such that natural frequency of oscillation remains same but

damping ratio is increased. The author has incorporated all these features in this model.

As the liquid catheter sensor model has been developed in frequency domain one can not find what are solutions of the differential equation governing the dynamics of the sensor. Thus the author is interested about the nature of the solution of the system and dynamicity governing mechanism [1, 3].

An one dimensional vector field can be expressed by the equation

$$\dot{X} = f(X) \tag{3a}$$

In the above differential equation, fixed points represent equilibrium solutions i.e., the values of X for which  $\dot{X} = 0$

Thus a fixed point can be represented by  $X = X^*$  so that

$$\dot{X} = 0 \text{ for } f(X)/_{X=X^*} = f(X^*) = 0$$

An equilibrium is defined to be stable if all sufficiently small disturbances from it damp out in time. Thus stable equilibria are represented geometrically by stable fixed points. Conversely, unstable equilibria in which disturbances grow in time are represented by unstable fixed points (stogatz).

But two dimensional vector field governed by the equation

$$\dot{X} = f(X, Y) \tag{3b}$$

$$\dot{Y} = g(X, Y) \tag{3c}$$

It is not to easy the predict the nature of the fixed points  $X = X^*$  and  $Y = Y^*$  and their interrelationships by the expression  $f(X^*, Y^*) = 0 = g(X^*, Y^*)$ . Thus a new method for two dimensional vector field has been proposed. It is given as below.

A two dimensional linearized system is of the form

$$\dot{x} = ax + by \tag{3d}$$

$$\dot{y} = cx + dy \tag{3e}$$

where a, b, c, d are the parameters. This system can be written in matrix form

$$\dot{X} = AX \tag{3f}$$

where  $\dot{X} = \begin{bmatrix} \dot{x} \\ \dot{y} \end{bmatrix}$ ;  $A = \begin{bmatrix} a & b \\ c & d \end{bmatrix}$  and  $X = \begin{bmatrix} x \\ y \end{bmatrix}$

If V is an eigen vector of matrix A and  $\lambda$  is the corresponding eigen value then characteristic equation becomes

$$\det \begin{bmatrix} a - \lambda & b \\ c & d - \lambda \end{bmatrix} = 0 \tag{3g}$$

Expanding the determinant yields

$$\lambda^2 - \tau\lambda + \Delta = 0, \tag{3h}$$

where

$$\tau = \text{trace}(A) = a + d \tag{3i}$$

$$\Delta = \det(A) = ad - bc \tag{3j}$$

then  $\lambda_1 = \frac{\tau + \sqrt{\tau^2 - 4\Delta}}{2}$  and  $\lambda_2 = \frac{\tau - \sqrt{\tau^2 - 4\Delta}}{2}$

are the solutions of equation (3h)

This can be written as

$$\lambda_{1,2} = \frac{\tau \pm \sqrt{\tau^2 - 4\Delta}}{2} \tag{3k}$$

The nature of the solutions is given by Fig. 4.

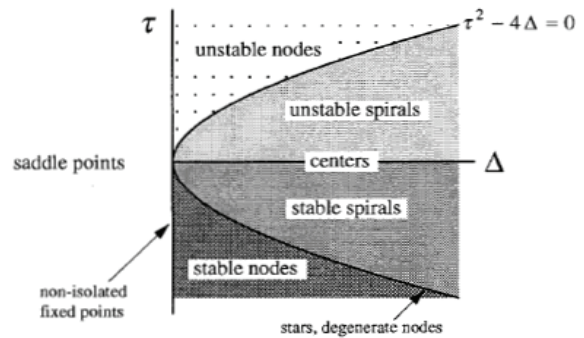


Fig. 4. Nature of the solutions in two dimensional linearized system.

Now from the concept of quadratic equation  $\Delta = \lambda_1 \lambda_2$ ;  $\tau = \lambda_1 + \lambda_2$

If  $\Delta < 0$ , the eigen values are real and have opposite signs; hence the fixed point is a saddle point.

If  $\Delta > 0$ , the eigen values are either real with the same sign (nodes) or complex conjugate (spirals and centers).

Nodes satisfy  $\tau^2 - 4\Delta > 0$  and spirals satisfy  $\tau^2 - 4\Delta < 0$

Or it can be proved in other ways that

$$\dot{X}^2 + \dot{Y}^2 = Ce^{2\alpha t}, \quad (31)$$

where  $\alpha$  indicates the real part of eigen value i.e., coefficient of damping.

for  $\alpha < 0$  i.e., eigen value has negative real part then the above equation will form stable spiral

for  $\alpha > 0$  the i.e., eigen value has positive real part then the above equation will form unstable spiral and

for  $\alpha = 0$  i.e., eigen value has only imaginary part then the equation will form vortex [4].

## 2. Modelling Methods

Our system is 2<sup>nd</sup> order system. Our main aim is to convert it first to two dimensional linearized system. This can be done by the method proposed below.

Taking time domain expression of equation (1) we have

$$\ddot{V}_o + 2\zeta\omega_n \dot{V}_o + \omega_n^2 V_o = \omega_n^2 \ddot{V}_i \quad (4a)$$

Taking state variable approach

Let  $X_1(t) = V_o(t)$

$$X_2(t) = \dot{X}_1 = \frac{dV_o(t)}{dt}$$

$$\dot{X}_2 = \frac{d^2 X_1(t)}{dt^2} = \frac{d^2 V_o(t)}{dt^2} = -\omega_n^2 X_1(t) - 2\zeta\omega_n X_2(t) + \omega_n^2 V_i(t)$$

In matrix form we can write

$$\begin{bmatrix} \dot{X}_1 \\ \dot{X}_2 \end{bmatrix} = \begin{bmatrix} 0 & 1 \\ -\omega_n^2 & -2\zeta\omega_n \end{bmatrix} \begin{bmatrix} X_1(t) \\ X_2(t) \end{bmatrix} + \begin{bmatrix} 0 & 0 \\ 0 & \omega_n^2 \end{bmatrix} \begin{bmatrix} 0 \\ V_i(t) \end{bmatrix}$$

Thus the coefficient matrix A is given by

$$A = \begin{bmatrix} 0 & 1 \\ -\omega_n^2 & -2\zeta\omega_n \end{bmatrix} \quad (4b)$$

Now the trace of A is given by

$$\tau = -2\zeta\omega_n \quad (4c)$$

thus trace is negative indicating stable operation.

And the determinant of the matrix A is given by

$$\Delta = \omega_n^2 \quad (4d)$$

thus determinant of matrix A is positive.

Our main topic of discussion is about the term  $(\tau^2 - 4\Delta)$

$$\tau^2 - 4\Delta = (-2\zeta\omega_n)^2 - 4\omega_n^2 = 4\omega_n^2(\zeta^2 - 1) \quad (4e)$$

Now equation (31) states that more the damping more will be rate of convergence as evidenced by the Fig. 5.

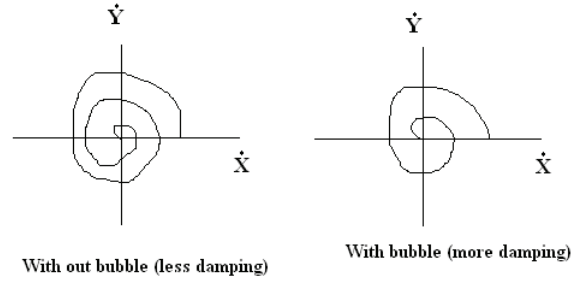


Fig. 5. Phase trajectory of the above mentioned liquid catheter sensor with and with out bubble.

Due to presence of bubble when the damping ratio increases then the magnitude of coefficient of damping will be more. Thus the state trajectories seen in Fig. 5 reaches the stable equilibrium point at less time indicated less number of spirals. Thus we can say that the eigen value of the coefficient matrix has more negative part as a result the rate of convergence of the spiral is more [1, 4]. This increment in damping causes frequency response to flat [1, 3].

Thus the Fig. 5 indicates how the performance of the catheter sensor depends on the value of damping. It is usual that higher damping will cause frequency response to be flat, which is essential for any sensor. But the generation of bubble will cause natural frequency of oscillation to decrease. Therefore Fig. 5 will not alone highlight the frequency response characteristics because it fails to indicate whether there is any change of natural frequency of oscillation or not. Then using the equations (4c) and (4d) we can find the find the operating points of the above in  $\tau - \Delta$  plane for  $\zeta=0.033$ ,  $f_n = 91$  Hz (with out bubble) and  $\zeta=0.137$ ,  $f_n=22$  Hz (with bubble) which is shown in Fig. 6.

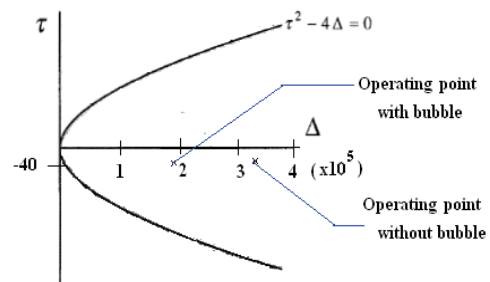


Fig. 6. Operating point of liquid catheter sensor in  $\tau - \Delta$  plane with and without bubble.

Fig. 6 alone indicates the deterioration high frequency response of the liquid catheter sensor when the operating point is shifted from right to left in the  $\tau-\Delta$  plane as natural frequency of oscillation decreases from 91 Hz (no bubble) to 22 Hz (with bubble). Thus we can say that Fig. 5 and Fig. 6 completely describe the optimal performance of the liquid catheter sensor.

In order to obtain high frequency response from the liquid catheter sensor we have to keep eye on the magnitude of natural frequency of oscillation. The presence of the bubble can not be avoided, in such cases we have to ensure that natural frequency of oscillation reduces by very little margin so that high frequency behavior can not be deteriorated. Also we have keep in eye in Fig. 5 all time so that how the rate of convergence can be increased i.e., how the damping can be increased so that the frequency response will be more flat for successful operation of the sensor.

### 3. Design of Liquid Catheter Sensor Based on Fig. 5 and Fig. 6

Fig. 5 indicates effect of damping where as Fig. 6 indicate pronounce effect of natural frequency of oscillation.

The length of catheter (L) in directly related with  $\zeta$  and inversely related with  $f_n$ . Thus increment of L will cause  $\zeta$  to increase ratio means high rate of convergence in Fig. 5 causing improve of flat frequency behavior of the sensor. Also decrement of  $f_n$  means the operating point will be shifted left in Fig. 6 causing deterioration of high frequency behavior. Thus a comprise between flat frequency behavior and high frequency behavior have to be remembered while choosing the length of the catheter.

The radius of the catheter (r) is directly related with  $f_n$  but inversely related with  $\zeta$ . So the increment in radius will cause  $f_n$  to be increased causing improvement of high frequency behavior but decreased damping ratio means less rate of convergence of the phase trajectory indicating deterioration of flat frequency response. Thus radius of the catheter must be chosen carefully maintaining compromise between flat frequency and high frequency behavior.

Modulus of elasticity  $E_d$  of sensor diaphragm is directly related with  $f_n$  and inversely related with  $\zeta$ . Thus choosing a material which has very high  $E_d$  as diaphragm will cause  $f_n$  to increase causing improvement of high frequency response and  $\zeta$  will decrease causing deterioration of flat frequency behavior. Thus very high valued  $E_d$  can not be chosen optimum operation of liquid catheter sensor.

Now the coefficient of viscosity ( $\eta$ ) of the liquid is directly related with the  $\zeta$  only. Thus if in someway  $\eta$  can be increased then the flat frequency behavior can be improved without the deterioration of high

frequency behavior. We know that for liquid viscosity is due to intermolecular cohesive forces because the effect of transfer of momentum is negligible due small spacing between the molecules. Thus if the temperature of the catheter liquid is decreased there will be increment of cohesive force which will result increment of viscosity.

The most important part is the choice of density of the liquid. As we see that density of the liquid is inversely related with both  $f_n$  and  $\zeta$  but the bubble wall velocity  $\dot{R}$  for inertia controlled bubble dynamics is inversely related with density as seen from equations (1e), (1f) and (2g). Thus if liquid of low density is chosen for catheter then inertia controlled bubble generation will be high which will degrade the high frequency behavior of the sensor. Moreover the compressibility effect of the catheter liquid must be incorporated. In our basic assumption of the liquid catheter sensor we have assumed that the liquid used for the catheter is incompressible. We know that bulk modulus of elasticity of a liquid is given by

$$E_v = -\frac{dp}{\frac{dV}{V}}, \quad (5a)$$

where V is the original liquid volume. Again density  $\rho$  is equal to mass divided by volume

$$\rho = \frac{m}{V} \quad (5b)$$

$$d\rho = d\left(\frac{m}{V}\right) = -\frac{m dV}{V^2} = -\rho \frac{dV}{V} \quad (5c)$$

Thus

$$E_v = \rho \frac{dp}{d\rho} \quad (5d)$$

Therefore low density liquid will indicate small value bulk modulus of elasticity of the liquid. Then the coefficient of compressibility

$$\beta = \frac{1}{E_v} \quad (5e)$$

can not be ignored. Thus we can not use the very small density liquid otherwise our basic model of liquid catheter sensor developed in Fig. 1 will be inappropriate.

Again the liquid having high latent ( $L_h$ ) must be chosen so for thermally controlled bubble growth can reduced to minimum as evidenced from equation (2h) even if high generation of vapor occurs so there will be minimum shift of operating point towards left of

Fig. 6. Thus the high frequency behavior can be restored.

To reduce the effect of both inertia controlled and thermal controlled bubble growth care must be taken so that the local pressure can not reduced to the vapor pressure of the fluid. Thus by any means the pressure differential in liquid catheter system must be reduced minimum so the deterioration of the high frequency behavior of the sensor is least.

Lastly when the catheter is used many times then there will be large numbers of bubbles due to both inertia controlled and thermally controlled growth. Thus the high frequency behavior of the sensor is completely deteriorated. Before reusing the catheter, it must be flushed with bubble free saline solution so that the number of bubbles inside the catheter can be reduced to minimum [1, 5].

#### 4. Discussion & Conclusions

For proper measurement of pressure, we always want that frequency response to be flat and high frequency behavior must be restored. Our best possible achievement will be the increment of both  $\omega_n$  and  $\zeta$ . This is possible only choosing low density liquid for catheter keeping all other factor fixed. It demands finite value of compressibility thus bulk modulus will be much smaller in low density liquid than incompressible liquid. Then compliance offered by the liquid can not be ignored and it will act in parallel with the bubble compliance as well as diaphragm compliance there by increasing the total compliance of the sensor. Also low density liquid will cause more inertia controlled bubble generation.

For abnormality in blood pressure i.e., if there is any hemorrhage thus there will be sudden fall in

arterial pressure. This operation can tracked by the liquid catheter sensor operating in stable spiral mode and care must be given so that the operating point in  $\tau - \Delta$  plane does not shift to the left.

Thus the model proposed by the author gives the information by which the features of the liquid catheter sensor can be improved. The model also highlights the facts how the inertia controlled and thermally controlled bubble growth can be minimized.

#### Acknowledgements

The author is grateful to the authorities of St. Thomas' College of Engg & Technology, Kolkata. Dr. Suman Halder is particularly indebted for inspiration received from Late Prof. N. C. Ray of IIT Kharagpur, India and Prof. P. K. Sen of NIT Durgapur, India.

#### References

- [1]. John G. Webster, Medical instrumentation, application and design, *John Wiley & Sons*, 2002.
- [2]. Milton S. Plesset and Andrea Prosperetti, Bubble dynamics and cavitation, *Annual Review of Fluid Mechanics*, Vol. 9, 1977, pp. 145-185.
- [3]. Steven H. Strogatz, Nonlinear dynamics and chaos, *Perseus Books, Reading Massachusetts*, 1994.
- [4]. John E. Gibson, Nonlinear automatic control, *McGraw Hill Book Company*, 1963.
- [5]. Herman L. Falsetti, Robert E. Mates, Robyn J. Carroll, Ramji L. Gupta, Adam C. Bell, Analysis and correction of pressure wave distortion in fluid-filled catheter systems circulation, *Circulations*, Vol. 48, 1974, pp. 165-172.

2013 Copyright ©, International Frequency Sensor Association (IFSA). All rights reserved.  
(<http://www.sensorsportal.com>)

## Sensors & Transducers Journal (ISSN 1726-5479)

Open access, peer review  
international journal devoted to research,  
development and applications of sensors,  
transducers and sensor systems.  
The 2008 e-Impact Factor is 205.767

Published monthly by  
**International Frequency Sensor Association (IFSA)**



Submit your article online:  
<http://www.sensorsportal.com/HTML/DIGEST/Submission.htm>

## Manufacture of Piezoelectric Sensor Dedicated to Airflow Velocity Detection

<sup>1</sup> Xiaoping WANG, <sup>2</sup> Dengpan WANG, <sup>2</sup> Jing YANG

<sup>1</sup>Chongqing City Management College,  
ChongQing, 401331, China

<sup>2</sup>Sichuan Institute of Piezoelectric and sound and light technology,  
ChongQing, 400060, China

<sup>1</sup>Tel.: +8615909369470

E-mail: workmail73@126.com, mangoms@hotmail.com

Received: 14 August 2013 /Accepted: 25 August 2013 /Published: 30 September 2013

**Abstract:** This paper researches the dedicated piezoelectric sensor for airflow information sensitivity which uses PZT-5A piezoelectric material and rigid polyurethane foam to act as its matching materials. It adopts multiplex mode to realize the broadband design of sensor and does finite element simulation to establish admittance grid, sound field distribution diagram and model in which cylinder is added with matching layer. Finally dedicated piezoelectric sensor is manufactured through technical study. It keeps the features of center frequency 230 kHz, resonance point sound pressure level 90 dB, resonance point -3 dB and beam width 7.6° in which doublet coupling helps form wider working band. Copyright © 2013 IFSA.

**Keywords:** Piezoelectric sensor, Ultrasonic wave, Finite element, Multiplex mode.

### 1. Introduction

Nowadays making use of superimposed effect of airflow and ultrasonic wave to detect airflow information of flow velocity, flow rate and flow direction becomes hot for the technical research of airflow information sensitivity. However, most researches put emphasis on multi-sensor topology and detecting algorithm. On the contrary researches on sensor are less. Aiming at airflow detection features of ultrasonic wave and by doing theoretical study, researching matching materials, studying piezoelectric materials, designing and simulating finite element and doing technical study, this paper finally designs the transmitting and receiving air sound pressure sensor catering for the requirements of miniaturization, broadband, high directivity [1, 2].

### 1. Theoretical Design

#### 1.1. Theoretical Design of Piezoelectric Wafer

Piezoelectric ceramic thin wafer acts as the frequently used sensitive element form in the traditional piezoelectric transducer. When doing free vibration, its vibration equation, circuit state equation, equivalent circuit, frequency equation and electrical admittance equation have given relevant analytical formula through which early theoretical design will be done.

Vibration equation of piezoelectric ceramic wafer is [3]:

$$F = j\rho vS \left[ -\frac{J_0(ka)}{J_1(ka)} + \frac{1-\sigma}{ka} \right] \dot{\xi}_a + nV$$

In the formula, vibration velocity of circumference is  $\dot{\xi}_a$  and  $a$  is the radius of wafer.

Circuit state equation is:

$$I = j\omega C_0 V - n \dot{\xi}_a$$

In the formula,  $C_0 = \pi a^2 \bar{\epsilon}_{33} / t$  is two-dimensional dielectric capacitor and  $t$  is thickness of piezoelectric wafer.

Mechanical equivalent circuit diagram of piezoelectric wafer is (Fig. 1):

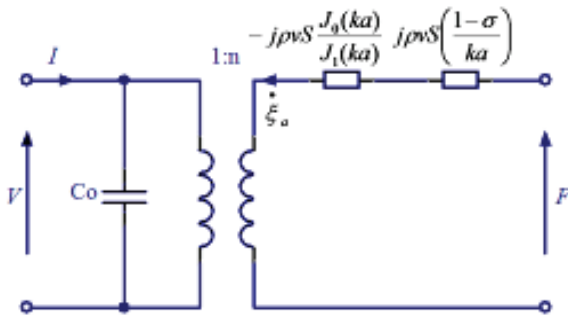


Fig. 1. Equivalent Circuit Diagram of Free Vibration of Piezoelectric Ceramic Thin Wafer.

Frequency Equation

$$kaJ_0(ka) = (1 - \sigma)J_1(ka)$$

Admittance Equation

$$Y = \frac{j\omega\pi a^2 \bar{\epsilon}_{33}^T}{t} \left[ 1 - k_p^2 + k_p^2 \frac{(1 + \sigma)J_1(ka)}{kaJ_0(ka) - (1 - \sigma)J_1(ka)} \right]$$

Radiating surface of piezoelectric sensor can be approximately viewed as circle-surface piston radiation whose beam width can be preliminarily designed according to the following formula.

Directivity function of circular piston in an infinite rigid plane is [4]:

$$D(\theta, \alpha, \omega) = \left| \frac{2\pi \int_0^a (k\rho \sin \theta) J_0(k\rho \sin \theta) d\rho}{\pi a^2 k \sin \theta} \right|$$

Its beam width can be calculated through the formula above:

$$\Theta_h = 2 \arcsin(0.26\lambda / a)$$

In the formula,  $\lambda$  is the sound wavelength in air dielectric and  $a$  is the radius of radiating surface.

Through the above-mentioned equations and equivalent circuits, influences of each parameter on

mechanical and electrical property parameters of thin wafer's free vibration can be intuitively seen. However, when thickness and diameter of piezoelectric wafer compare with each other, coupling phenomenon will happen between its radial direction and thickness vibration thus a series of new vibration modes come into being. At the moment wafer cannot be equivalent into thin wafer which needs new ways to do design. Aiming at the above-mentioned problems, this paper adopts the method of combination between theoretical analysis and finite element simulation design to do design on piezoelectric wafer sensor which is multi-mode coupled.

## 1.2. Theoretical Design of Matching Layer

The choice of matching materials is one of the key problems needing solving during the design aiming at piezoelectric ultrasonic sensor. Acoustic impedance of air is just  $4 \times 10^2 \text{ kg} \cdot \text{m}^{-2} \cdot \text{s}^{-1}$  while that of piezoelectric ceramics is  $1 \sim 35 \times 10^6 \text{ kg} \cdot \text{m}^{-2} \cdot \text{s}^{-1}$ . There exists serious impedance mismatch between them. Therefore matching materials need introducing to increase transmittance of sound wave and improve radiation efficiency of sensor [5].

Calculation of acoustic impedance of matching materials has several theoretical references. As specialized sound absorption materials have been introduced into the current studied sensor to act as backing, here adopts traditional theory to calculate acoustic impedance of matching materials. It is that acoustic impedance of matching layer material is  $Z_2 = \sqrt{Z_1 Z_3}$  and that of double matching layer is  $Z_1 = \sqrt[4]{Z_0^3 Z_L}$ . Through calculation, it is seen that acoustic impedance of matching materials is  $0.2 \sim 1.18 \times 10^6 \text{ kg} \cdot \text{m}^{-2} \cdot \text{s}^{-1}$ .

Nowadays some frequently-used pouring sealants in acoustical devices are polyurethane soft rubber, epoxy resin, butyl rubber and natural rubber whose acoustic impedances are respectively  $1.64 \times 10^6 \text{ kg} \cdot \text{m}^{-2} \cdot \text{s}^{-1}$ ,  $3.03 \times 10^6 \text{ kg} \cdot \text{m}^{-2} \cdot \text{s}^{-1}$ ,  $1.53 \times 10^6 \text{ kg} \cdot \text{m}^{-2} \cdot \text{s}^{-1}$  and  $1.51 \times 10^6 \text{ kg} \cdot \text{m}^{-2} \cdot \text{s}^{-1}$ . These materials cannot meet the requirement of piezoelectric ceramic matching with air. In order to realize their nice matching, acoustic impedance has to be about  $0.4 \times 10^6 \text{ kg} \cdot \text{m}^{-2} \cdot \text{s}^{-1}$  to cater for the requirement.

## 2. Finite Element Analysis

In order to provide powerful guidance for the design of miniaturization sensor with high sensitivity, finite element analysis software ANSYS is applied during research process to do simulation on the formation, vibration mode and sound field distribution of sensor. Finite element method can avoid restricted by element's structure, size and

material. Through coupled field analysis, vibration mode, electrical property and acoustic performance of piezoelectric sensor can be accurately simulated so that design efficiency would be improved [6, 7].

During the simulation process, piezoelectric materials adopt two-dimensional coupling field unit plane13 and three-dimensional coupling field unit solid5 and structure applies two-dimensional structural units plane42 and solid45. When doing piezoelectric analysis, matrix equation of the used coupling unit is as follows:

$$\begin{bmatrix} [M] & [0] \\ [0] & [0] \end{bmatrix} \begin{Bmatrix} \{\ddot{u}\} \\ \{\ddot{v}\} \end{Bmatrix} + \begin{bmatrix} [C] & [0] \\ [0] & [0] \end{bmatrix} \begin{Bmatrix} \{\dot{u}\} \\ \{\dot{v}\} \end{Bmatrix} + \begin{bmatrix} [K] & [K^c] \\ [K^c]^T & [K^d] \end{bmatrix} \begin{Bmatrix} \{u\} \\ \{v\} \end{Bmatrix} = \begin{Bmatrix} \{F\} \\ \{L\} \end{Bmatrix}$$

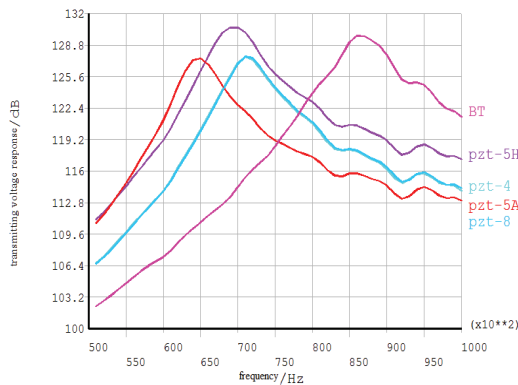


Fig. 2. Transmitting and Receiving Frequency Response Curves of Each Piezoelectric Material.

It is seen from the figure that receiving sensitivity of PZT-5A is the highest whose resonant frequency is the lowest under the same volume. It keeps both transmitting and receiving characteristics which accords with the design direction of miniaturization and high sensitivity sensor.

Piezoelectric sensor keeps advantages under high frequency and narrow beam transmission. While its frequency bandwidth is a little bit low under single-mode transmission which is difficult to transmit broadband envelope signal and which influences velocity precision. Therefore one of the design purposes is to do broadband transmission through cylinder multi-mode coupling.

In order to realize the above-mentioned purpose, pzt-5A Piezoelectric Material and solid5 Coupling Field Unit are adopted to establish the cylinder model and analyze modal which is shown in Fig. 3.

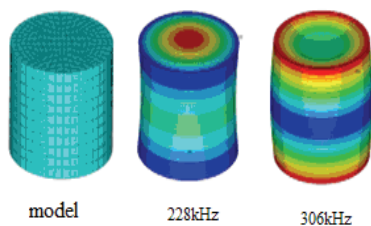


Fig. 3. Nephogram of Cylinder Model and Vibration Displacement Distribution.

Finite element equation between fluid and structure is below:

$$\begin{bmatrix} [M_e] & [0] \\ [M^s] & [M_e^p] \end{bmatrix} \begin{Bmatrix} \{\ddot{U}_e\} \\ \{\ddot{P}_e\} \end{Bmatrix} + \begin{bmatrix} [C_e] & [0] \\ [0] & [C_e^p] \end{bmatrix} \begin{Bmatrix} \{\dot{U}_e\} \\ \{\dot{P}_e\} \end{Bmatrix} + \begin{bmatrix} [K_e] & [K^s] \\ [0] & [K_e^p] \end{bmatrix} \begin{Bmatrix} \{U_e\} \\ \{P_e\} \end{Bmatrix} = \begin{Bmatrix} \{F_e\} \\ \{0\} \end{Bmatrix}$$

where  $[M^s] = \rho_0[R_e]^T$ ,  $[K^s] = -[R_e]$ .

Before doing sensor design, transmitting and receiving performance comparisons among each frequently-used piezoelectric ceramic material PZT-4, PZT-5A, PZT-5H, PZT-8 and BT are done whose simulation curves are shown in Fig. 2.

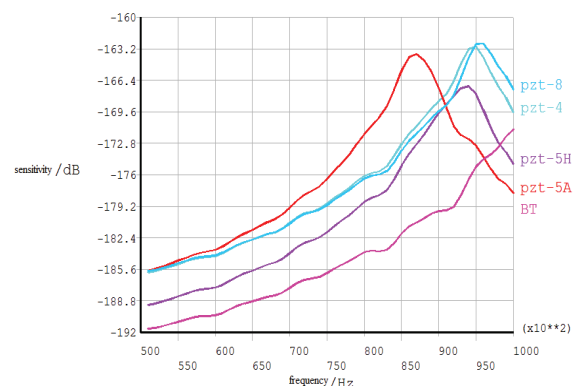


Fig. 3 shows that two modals are inspired out on the frequency points 228 kHz and 306 kHz which provides essential condition for mode coupling to form broadband.

Through structure size optimizing, piezoelectric sensor model in air dielectric is finally established and frequency response curves of its electrical admittance and sound pressure level are calculated. Also sound pressure distribution diagram is drawn at the highest point of sound pressure level (shown in Fig. 5) and -3 dB beam width is got. Fig. 4 shows the analysis model which has been added with matching layer. Fig. 5 shows its admittance curve and sound field distribution.

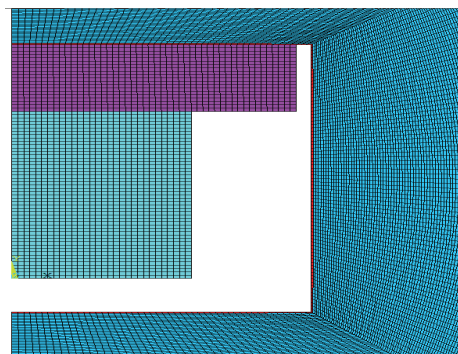


Fig. 4. Cylinder Model Added with Matching Layer.

The final optimization result of piezoelectric ultrasonic sensor is that its operating frequency is 233 kHz, sound pressure level of resonant point is 90 dB, resonant point is -3 dB and beam width is 7.43°.

### 3. Technical Study

On the basis of the above-mentioned design, technological process and key technology of sensor are studied and explored in which technological process of piezoelectric sensor is drew up to be as follows:

Clean-Splice Matching Layer-Solidify-Splice Protective Film-Solidify-Assemble-Embedment-Test.

During the process of making dedicated piezoelectric sensor, the following two points should be noticed:

#### 1) Backing Material

In terms of backing materials, the method that tungsten powder is mixed into polyurethane soft

rubber is used in order to lead it to present sound absorption effect under the circumstance of not influencing piezoelectric cylinder vibration. By changing the matching ratio of polyurethane and tungsten powder, acoustic impedance of backing material is changed. Finally through measuring acoustic performance of sensor, the best backing material matching ratio would be determined.

#### 2) Protective Film

In order to increase the ability of sensor to adapt to the environment, a layer of metal protective film needs covering on its radiating surface. The introduction of protective film need two conditions: one is that it has to keep low influence on ultrasonic transmission in which film thickness should be far less than acoustic wave length. The second one is that it must be high-strength and keep corrosion resistance. Upper limit of the studied sensor in this paper is 325 kHz. At this moment wave length in the metal is about 10 mm. Therefore here uses 0.1 mm-thick titanium alloy film to serve as protective layer.

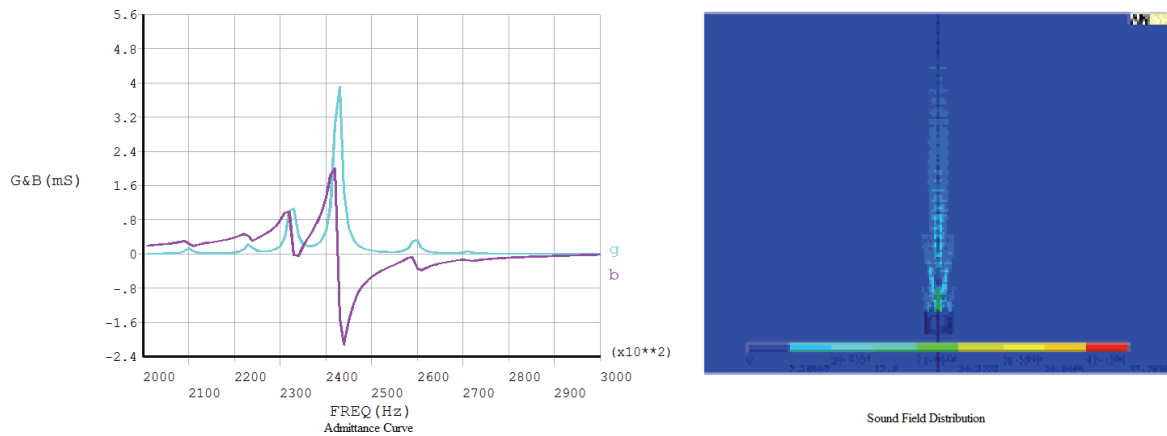


Fig. 5. Admittance Curve and Sound Field Distribution Diagram of Cylinder Added with Matching Layer.

### 4. Result and Discussion

By technical research, experimental sample of piezoelectric sensor is finally produced as is seen in Fig. 6.



Fig. 6. Physical Map of Piezoelectric Sensor.

Utilizing impedance analyzer Agilent4294 to measure the electrical admittance curve of sensor shown in Fig. 7.

It is seen from comparison that measured result of sensor operating frequency is a little lower than that of simulation result. It is obviously seen from the measured admittance curve that couplings between two modals form wide frequency band. During the process of producing sensor, backing material and metal protective film both increase load quality and radiation resistance of piezoelectric ceramic. Therefore its resonant frequency slightly declines. The increasing of radiation resistance reduces the mechanical quality factor of unimodal and increases conductance bandwidth of unimodal thus improving coupling among modals and finally forming the wide frequency band seen in Fig. 7.

Electrical property, transmitting and receiving signal and directivity of the piezoelectric sensor sample manufactured are measured in which center

frequency is 230 kHz, sound pressure level of resonant point is 90 dB, resonant point is -3 dB and beamwidth is 7.6°.

## 5. Conclusions

This paper adopts finite element design method to do design on the multi-mode coupled broadband piezoelectric sensor and to do research on the workmanship of sensor. Finally experimental sample of broadband sensor is produced. Agilent4294 is used to measure its electrical admittance curve whose result shows that this sensor has two obvious resonant peaks.

It is seen from the research of this paper that miniaturization broadband sensor could be designed through using the two coupled peaks between thickness vibration and radial direction vibration of

piezoelectric ceramic cylinder; PZT-5A keeps certain advantages in the design of air acoustic sensor; Finite element design method provides powerful references for the design of piezoelectric sensor; Workmanship of sensor greatly and directly influences its property; The influence of the choice of assisted structure in the sensor structural simulation on simulation precision still needs further study.

On the basis of common operation, performances of piezoelectric sensor for air acoustic also need improving in which sound pressure level may be enhanced and bandwidth may be increased. In order to realize this purpose, matching layer materials and splicing technology would be further improved as well as structure is optimized. This helps increase ultrasonic transmission rate. The improving of backing materials also reduces influences of back-end echo on sensitive element.

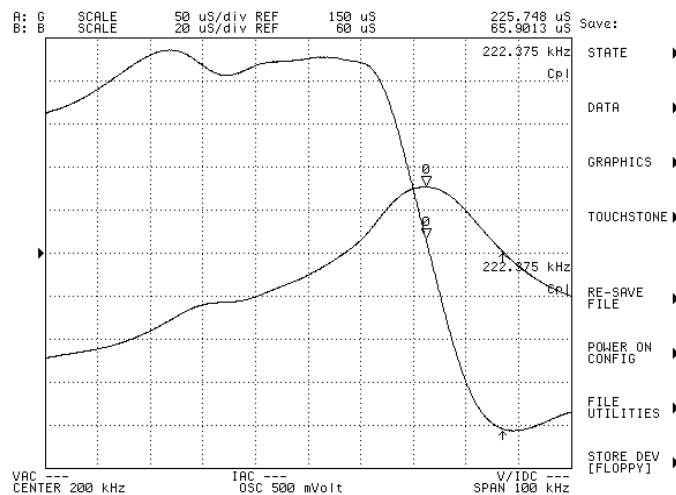


Fig. 7. Admittance Measured Curve of Piezoelectric Sensor.

## References

- [1]. Ying Chong Fu, Ultrasonics, Beijing: Science and Technology Press, 1993, pp. 249-252.
- [2]. Guidong Luan, A piezoelectric transducer and transducer array, Peking University Press, 2005, pp. 121-126.
- [3]. Guidong Luan, A piezoelectric transducer and transducer array, Peking University Press, 2005, pp. 371-373.
- [4]. P. Brasser, B. Hosten, F. Vulovic, High frequency transducers and correlation method to Enhance ultrasonic gas flow metering, Flow Measurement and Instrumentation, Vol. 12, No. 3, 2001, pp. 201-211.
- [5]. I. Ladabaum, X. Jin, H. T. Soh, A. Atalar, B. T. Khuri-Yakub, Surface micromachined capacitive ultrasonic transducers, IEEE Transactions on Ultrasonics, Ferroelectrics and Frequency Control, Vol. 45, No. 3, 1998, pp. 678-690.
- [6]. S. Olcum M. N. Senlik, A. Atalar, Optimization of the gain-bandwidth product of capacitive micromachined ultrasonic transducers, IEEE Transactions on Ultrasonics, Ferroelectrics and Frequency Control, Vol. 52, Issue 12, 2005, pp. 2211-2219.

## Magnetic Flux Leakage (MFL) Capsule Material Selection and Its Robustness Analysis in Oil and Gas Pipeline

<sup>1</sup> Maliki IBRAHIM, <sup>2</sup> Zulkarnay ZAKARIA, <sup>2</sup> Ali Aiman MUSTAPHA,  
<sup>1</sup> Dennis Desmond SURIN, <sup>2</sup> Mohd Nasir AYOB, <sup>2</sup> Ibrahim BALKHIS,  
<sup>3</sup> Ruzairi ABDUL RAHIM

<sup>1</sup> School of Manufacturing Engineering, Universiti Malaysia Perlis,  
02600 Arau, Perlis, Malaysia

<sup>2</sup> School of Mechatronic Engineering, Universiti Malaysia Perlis,  
02600 Arau, Perlis, Malaysia

<sup>3</sup> Process Tomography and Instrumentation Research Group (PROTOM-i),  
INFOCOMM Research Alliance,  
Faculty of Electrical Engineering, Universiti Teknologi Malaysia,  
81310 Skudai, Johor Bahru, Malaysia

E-mail: maliki@unimap.edu.my, zulkarnay@unimap.edu.my, Ali\_Aiman\_Mustapha@yahoo.com,  
marissa.norhasan@gmail.com, nasirayob@unimap.edu.my, Ibrahim\_balkhis@gmail.com,  
ruzairi@fke.utm.my

*Received: 25 January 2013 / Accepted: 25 August 2013 / Published: 30 September 2013*

---

**Abstract:** This paper discussed on the material selection and its robustness analysis towards the design of magnetic flux leakage capsule that most applied in oil and gas pipeline. Magnetic Flux Leakage is among the most famous and expensive technique in large scale oil and gas pipe diagnosis system. This technique applies strong magnetic fields to detect any strange in the inner surface of the pipes such as corrosion, crack or other symptoms which is bad to the pipe condition. The aim of this research is to study and develop a small scale, low cost and portable Magnetic Flux Leakage diagnosis system which suitable in detecting the defect in the inner side of steel pipe or steel tank structures. This system uses strong permanent magnet to generate strong magnetic field while Hall Effect sensor act as a receiver. It is found that the best suitable material for the Magnetic Flux Leakage Capsule is carbon steel. *Copyright © 2013 IFSA.*

**Keywords:** Magnetic Flux Leakage, Material selection, Robustness analysis.

---

### 1. Introduction

Material selection is crucial for a Magnetic Flux Leakage (MFL) system which operates in a harsh environment such as in oil and gas pipelines. The material selected dictates the performance, reliability and robustness of the system.

For an MFL system to be efficiently and effectively diagnose defects on the pipeline, it must be protected from the harsh condition of its operating environment. This requires a casing (the capsule) that is made from a properly selected material. An alloy of a metal is preferable because they are generally rigid and tough while their alloying constituent

enable them to have an added properties which can help it performs well according to its requirement.

An analysis of the material robustness ensures the material meet up with the demand of the application while at the same time it gives out a sense of magnitude of the properties and performance of the material.

## 2. Review

MFL is among one of a number of Non Destructive Evaluation (NDE) method which can be used to inspect oil and gas pipelines. MFL system ranges from simple, visual line inspection such as those on Magnetic Particle Inspection, to complex arrangement of hardware and software such as those on MFL Pipeline Inspection Gauges (PIG) for example Intelligent Pipeline Monitoring Capsule as shown in Fig. 1. The operating requirement determines which method is effective both in term of cost and efficiency. The aim of this paper is to review the properties and interaction of the constituent element of a MFL capsule's alloy when certain method of processing is done, to analyze carbon steel material analysis in terms of MFL application, and discusses about the basic principle concerning MFL and also material selection method.

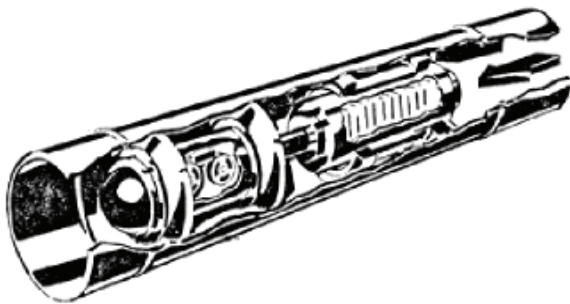


Fig. 1. Intelligent pipeline monitoring capsule uses in oil and gas industries.

## 3. Capsule Based Detection

PIG is frequently used for pipeline commissioning, cleaning, filling, de-waxing, batching, and more recently pipeline monitoring. The pig should be designed with consideration of the operation condition of the system. The system is made up of electronic circuitry, sensor, and software. The hardware part of the system is encased in a capsule which functions as a casing for the system and also it enable the system to be close enough to the inspection surface without any harm such as collision, dragging, and crashing. This can damage the hardware because the flow rate and pressure of the oil and gas is high and thus can cause damage if the hardware were to crash

onto the inner pipe surface. Other than that the capsule should be designed to utilize the flow of the oil and gas as its mean of movement. This method of detection offer an effective method of diagnosing the pipeline since the diagnosis is being carried while the capsule drifts passively inside pipeline.

## 4. Hall Effect Sensor

A Hall Effect sensor is a transducer that varies its output voltage in response to a magnetic field. Hall Effect sensors are used for proximity switching, positioning, speed detection, and current sensing applications. In its simplest form, the sensor operates as an analogue transducer, directly returning a voltage. With a known magnetic field, its distance from the Hall plate can be determined. Using groups of sensors, the relative position of the magnet can be deduced. Electricity carried through a conductor will produce a magnetic field that varies with current, and a Hall sensor can be used to measure the current without interrupting the circuit. Typically, the sensor is integrated with a wound core or permanent magnet that surrounds the conductor to be measured. Frequently, a Hall sensor is combined with circuitry that allows the device to act in a digital (on/off) mode, and may be called a switch in this configuration [1].

Hall Effect sensor is commonly seen in industrial applications such as the pictured pneumatic cylinder, they also used in consumer equipment; for example some printers use them to detect missing paper and open covers. When high reliability is required, they are used in the keyboards. Hall sensors are commonly used to time the speed of wheels and shafts, such as for internal combustion engine ignition timing, tachometers and anti-lock braking systems. They are used to detect the position of the permanent magnet. A wheel with two equally spaced magnets, the voltage from the sensor will peak twice for each revolution. This arrangement is commonly used to regulate the speed of disk drives.

## 5. Magnetic Flux Shield

Everywhere are surrounded by magnetic fields (both AC and DC) from the earth's magnetic field to man-made sources such as magnets, motors and transformers. To avoid effect of this field on sensitive equipments, magnetic shielding is required example cathode ray tubes, photomultiplier tubes, audio transformers, scanning electron microscopes, position sensors. The shield is made of soft ferromagnetic material with a high Permeability ( $\mu$ ). 36 %, 48 % & 80 % Nickel Ferum are most commonly used soft magnetic alloys. In order to have a low Hysteresis, the shield is annealed after shaping. Any

stress after annealing will deteriorate the performance [3].

There is no known material that can block magnetic fields without itself being attracted to the magnetic force. A magnetic shield acts as a kind of sponge redirecting the magnetic field around the shield instead of passing through the sensitive instruments. A good magnetic shielding material must have high permeability which means that the magnetic field lines are strongly attracted to the shielding material. If the magnetic field is too high for the material chosen, the material will be saturate and become ineffective. In this case, a multilayer shield with a combination of the above alloys can be used.

## 6. Magnetic Flux Leakage

In theory, magnetic particle inspection (MPI) is a relatively simple concept as shown in Fig. 2. It can be considered as a combination of two non-destructive testing methods: magnetic flux leakage testing and visual testing. Consider the case of a bar magnet. It has a magnetic field in and around the magnet. Any place that a magnetic line of force exits or enters the magnet is called a pole. A pole where a magnetic line of force exits the magnet is a north pole and a pole where a line of force enters the magnet is a south pole. When a bar magnet is broken in the centre of its length, two complete bar magnets with magnetic poles on each end of each piece will result. If the magnet is just cracked but not broken completely in two, a north and south pole will form at each edge of the crack. The magnetic field exits the North Pole and re-enters at the South Pole. The magnetic field spreads out when it encounters the small air gap created by the crack because the air cannot support as much magnetic field per unit volume as the magnet can. When the field spreads out, it appears to leak out of the material and, thus is called a flux leakage field [4].

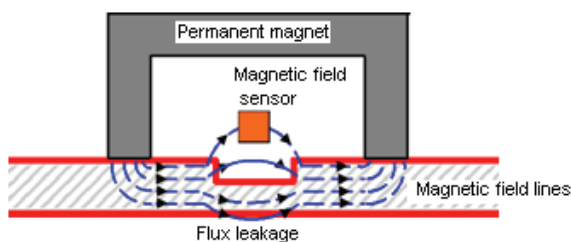


Fig. 2. Principle of magnetic flux leakage used in crack detection of a material.

If iron particles are sprinkled on a cracked magnet, the particles will be attracted to and cluster not only at the poles at the ends of the magnet, but also at the poles at the edges of the crack. This cluster of particles is much easier to see than the actual crack and this is the basis for magnetic particle inspection.

The first step in a magnetic particle inspection is to magnetize the component that is to be inspected. If any defects on or near the surface are present, the defects will create a leakage field. After the component has been magnetized, iron particles, either in a dry or wet suspended form, are applied to the surface of the magnetized part. The particles will be attracted and cluster at the flux leakage fields, thus forming a visible indication that the inspector can detect [4].

## 7. Robustness Analysis

Robustness testing is any quality assurance methodology focused on testing the robustness of software. Robustness testing has also been used to describe the process of verifying the robustness (i.e. correctness) of test cases in a test process. ANSI and IEEE have defined robustness as the degree to which a system or component can function correctly in the presence of invalid inputs or stressful environmental conditions. The term “robustness testing” was first used by the Ballista project at Carnegie Mellon University. They performed testing of operating systems for dependability based on the data types of POSIX API, producing complete system crashes in some systems. The term was also used by OUSPG and VTT researchers taking part in the PROTOS project in the context of software security testing. Eventually the term fuzzing (which security people use for mostly non-intelligent and random robustness testing) extended to also cover model-based robustness testing. An overview of robustness testing methods and tools can be found in the state of the art report of the AMBER research project [7].

## 8. Alloying in Steel

Steel is one of the world’s cheapest and useful metals. Indeed, steel finds application in numerous fields, from building construction purposes to kitchen utensils. Hence, so as to be able to respond to such a great demand and to suit the requirements to different applications, steel needs to offer several desired properties and these properties is achieved by alloying it. Like stated above, several other elements need to be added to iron and carbon to form adequate alloys with enhanced properties. Alloyed steel in brief is made by adding a small percentage of alloying metals to liquid steel to subsequently alter the hardness, toughness, elasticity or durability. Naturally each of the alloying elements will have a specific property on the steel and are added to it in certain proportions on the different properties required [5].

### **8.1. Aluminum**

Aluminum is mainly used as an alloying element of steel because of its ability to deoxidize the steel and also because of its capacity of extracting gasses from the steel. Aluminum also does resistance to ageing to the steel. Moreover, aluminum helps in the formation of fine grain structure, and since it combines well with nitrogen to form very hard nitride, it is considered to be favorable alloying constituent of nitriding steel.

### **8.2. Boron**

Boron is an alloying element that can be placed in the category of those whose main function is to enhance the hardenability of the material and this is, without having any effect neither on the ductility nor on the ferrite strength of the steel. As a result, formability and machinability of the steel are boosted due to the presence of Boron. Indeed thus alloying element finds most of its applications in low carbon steels.

### **8.3. Calcium**

Calcium, for its part, is mainly used in a silicocalcium combination. In truth calcium (as well as silicon) has for main function to deoxidize the steel. In doing so, the calcium does also contribute towards imparting the steel with a non-scaling property. In addition to this, calcium is also recommended for alloying purposes, as it is quite good in enhancing the toughness, the formability and the machinability of the alloyed material.

### **8.4. Carbon**

Carbon is an element whose purpose is imperative in all steel. Indeed, carbon is the principle hardening element of steel. That is, this alloying element determines the level of hardness or strength that can be attained by quenching. Furthermore, carbon is essential for the formation of cementite (as well as other carbides) and of pearlite, spheridite, bainite, and iron-carbon martensite, with martensite being the hardest of the microstructures. Carbon is also responsible for increase in tensile strength, hardness, resistance to wear and abrasion. However, when present in high quantities it affects the ductility, the toughness and the machinability of steel.

### **8.5. Chromium**

Among the alloying elements of steel, chromium forms part of those which best promote hardenability. In fact, its effect on steel is quite similar to that of manganese in the way that it enhances much hardness

penetration. When being present in reasonable quantities, chromium contributes much in reducing the quenching speed. In fact, such a slow quenching is achieved thereby enabling steel to be oil or air hardened. Chromium is also recommended when there is good wear resistant steel of appreciable toughness required. Chromium is also very popular as alloying element as it is quite efficient in rendering steel resistant to staining and corrosion. Moreover, chromium forms carbides that improve edge-holding capacity. Steel, rich in chromium have also high temperature strength and they are quite resistant to high-pressure hydrogenation.

### **8.6. Copper**

Although being favorable when it comes to rendering steel more resistant to corrosion, copper is not considered as such as being a good alloying element since it does have some bad repercussions on the steel. Indeed, copper is harmful to the surface quality of steel and it renders the steel less machinable at high temperature.

### **8.7. Manganese**

Manganese also contributes greatly towards increasing strength and hardness, but to a less extent than carbon. To be more precise, the degree to which manganese increases hardness and strength is dependent upon the carbon content of the steel. In fact, manganese contributes to increasing the strength of the ferrite, and also toward increasing the hardness of penetration of steel in the quench by decreasing the critical quenching speed. Moreover, still consisting of a considerable amount of manganese can be quenched in oil rather than in the water, and are therefore less susceptible to cracking because of reduction in the shock of the quenching. This alloying is also considered as a degasified reacting favorably with sulphur to improve forging ability and surface quality. This is achieved by interacting with the sulphur to give manganese sulphide. Naturally, in doing so, the risk of hot shortening is considerably decreased. In addition, manganese enhance the tensile strength, the hardness, the hardenability, the resistance to wear, and it also increase the rate of carbon penetration in the coefficient of thermal expansion of steel whereas it is detrimental to both thermal and electrical conductivity.

### **8.8. Molybdenum**

Molybdenum is an alloying element which is seldom used on its own. In fact, molybdenum is used in combination with other alloying elements. This alloying element increases the hardness penetration of steel and also contributes in slowing down the

critical quenching speed. Molybdenum proves to be useful also for increasing tensile strength of steel. Furthermore, it prevents temper brittleness and it favors the formation of a fine grain structure. It is good also to mention that molybdenum forms carbides readily and it thus improves the cutting properties in high-speed steels. Hence, it can be said that molybdenum helps much in increasing machinability.

### **8.9. Nickel**

Nickel is beneficial to steel in the way that it boosts up the strength of ferrite. It is a fact that nickel causes considerable increase in the impact strength of steel. Nickel found its common use generally in low alloy steels.

### **8.10. Nitrogen**

Being a residual element, nitrogen is present, in small quantities, in all steels. In fact, the nitrogen will normally combine with other elements in the steel (like aluminum, for example) to form hard nitrides. Thus nitrogen increases hardness, tensile and yield strength, but still, there are certain drawbacks related to nitrogen as it causes a considerable decrease in toughness and ductilability of steel.

### **8.11. Titanium**

Titanium can be associated to boron as it plays also a great role in increasing the hardenability of steel. In fact, titanium helps much towards increasing the effectiveness of boron as an alloying element of steel.

### **8.12. Tungsten**

Being very powerful carbide former, and the fact that its carbides are very hard, tungsten does provide to steel good toughness and it inhibits grain growth. Tungsten is also quite good towards increasing the strength and hardness retention as well as wear resistance at high temperatures and cutting power.

### **8.13. Vanadium**

Vanadium has for main effect on steel that it helps controlling the grain growth during heat treatment. It is used rather in medium carbon steel where when added in relatively large quantities it causes a reduction in the hardenability of the steel. Indeed, vanadium is known as a strong carbide former and this carbide dissolves difficultly in

austenite thereby explaining why vanadium is good.

## **9. Material Selection Method**

The materials selection process should reflect the overall philosophy regarding design life, cost profile, inspection and maintenance philosophy, safety and environmental profile, failure risk evaluations and other specific project requirements. Materials selection should be optimized and provide acceptable safety and reliability. At a minimum, the following should be considered:

1. Corrosively, taking into account specified operating conditions including start up and shut-down conditions;
2. Design life and system availability requirements;
3. Failure probabilities, failure modes and failure consequences for human health, environment, safety and material assets;
4. Resistance to brittle fracture;
5. Inspection and corrosion monitoring; and
6. Access for maintenance and repair.

For the final materials selection, the following additional factors should be included in the evaluation: priority should be to select materials with good market availability and documented fabrication and service performance; and the number of different materials should be minimized considering stock, costs, interchange ability and availability of relevant spare parts [4].

## **10. Carbon Steel Material Analysis**

There are several types of carbon steel materials. Among them are:

### **10.1. Mild and Low Carbon Steel**

1. Most common form of steel due to its price is relatively low.
2. Provides material properties that are acceptable for many applications.
3. Malleable and ductile, unable to be hardened by heat treatment.
4. Low tensile strength, but it is cheap and malleable.
5. Surface hardness can be increased through carburizing.
6. Mild steel contains approximately 0.16-0.29 % of carbon content.
7. Low carbon steel contains approximately 0.05-0.15 % of carbon content.

## 10.2. Higher Carbon Steel

1. Can successfully undergo heat-treatment.
2. Higher carbon steel contains approximately 0.30-1.70 % of carbon content.

## 10.3. Medium Carbon Steel

1. Balances ductility and strength and has good wear resistance.
2. Used for large parts, forging and automotive components.
3. Medium carbon steel contains approximately 0.30-0.59 % of carbon content.
4. High Carbon Steel.
5. Very strong, used for springs and high-strength wires.
6. High carbon steel contains approximately 0.60-0.99 % of carbon content.

## 10.4. Ultra-High Carbon Steel

1. Steels that can be tempered to great hardness.
2. Used for special purposes like (non-industrial-purpose) knives, axles or punches. Ultra-high carbon steel contains approximately 1.00-2.00 % of carbon content.
3. Most steels with more than 1.2 % carbon content are made using powder metallurgy.  
\*Note that steel with carbon content above 2.0 % is considered cast iron.

## 11. Result

### 11.1. Plain Carbon Steel Analysis

Carbon steel is by far the most widely used kind of steel in oil and gas industries. The properties of carbon steel depend primarily on the amount of carbon it contains. Most carbon steel has a carbon content of less than 1 %. In fact, there are 3 types of plain carbon steel and they are low carbon steel, medium carbon steel, high carbon steel, and as their names suggests all these types of plain carbon steel differs in the amount of carbon they contain. Indeed, it is good to precise that plain carbon steel is a type of steel having a maximum carbon content of 1.5 % along with small percentages of silica, sulphur, phosphorus and manganese.

### 11.2. Properties Analyzing

Table 1 is the physical properties result by analyzing three types of steels with different level of carbon content (% percentage), whereas Fig. 3 shows the graph of carbon versus density, Fig. 4 represents carbon material vs. thermal conductivity, Fig. 5 for carbon material vs. thermal expansion, Fig. 6 shows carbon material vs. Young Modulus while Fig. 7 and Fig. 8 show the results of carbon material vs. tensile strength and percent elongation respectively. It is found that, carbon content of 0.2% gives the best performance compared to others. Table 2 shows the different effect of alloying on different element while Table 3 lists the alloying elements involved in carbon steel. It is found that Molybdenum has relatively provided the best effect compared to other tested materials.

**Table 1.** Physical properties of plain carbon used in the experiments.

Material	Density (kgm <sup>-3</sup> )	Thermal Conductivity (Jm <sup>-1</sup> K <sup>-1</sup> s <sup>-1</sup> )	Thermal Expansion (10 <sup>-6</sup> K <sup>-1</sup> )	Young's Modulus (GNm <sup>-2</sup> )	Tensile Strength (MNm <sup>-2</sup> )	Percentage of Elongation (%)
0.2% C	7.88	51	11.7	210	350	30
0.4% C	7.86	49	11.3	210	600	20
0.8% C	7.84	47	10.9	210	800	8

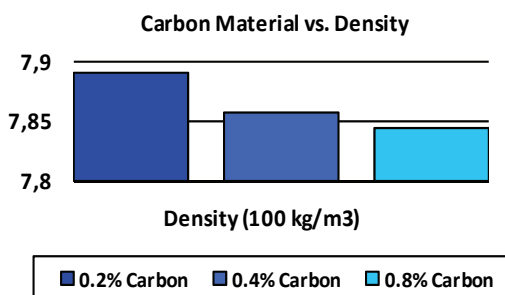


**Fig. 3.** Graph of Carbon material vs. Density.

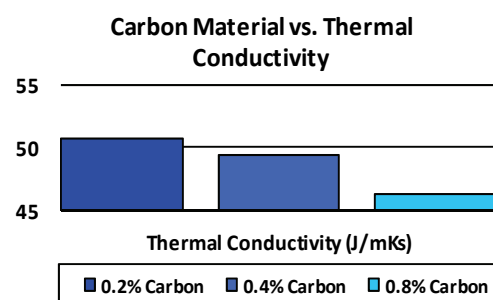


**Fig. 4.** Graph of Carbon material vs. Thermal conductivity.

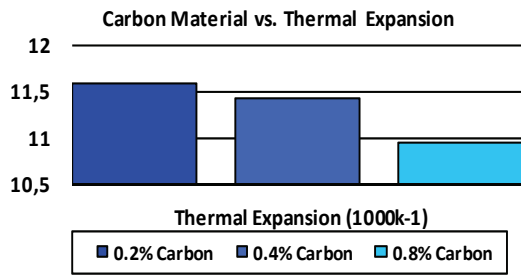


Fig. 5. Graph of Carbon material vs. Thermal expansion.

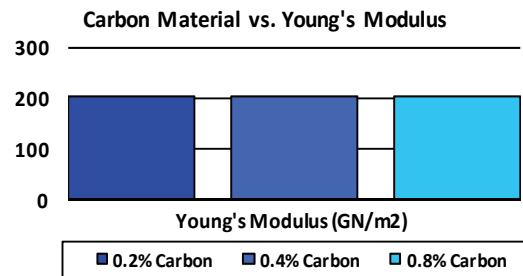


Fig. 6. Graph of Carbon material vs. Young's modulus.

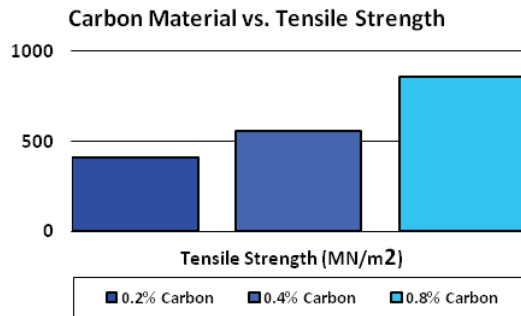


Fig. 7. Graph of Carbon material vs. Tensile strength.

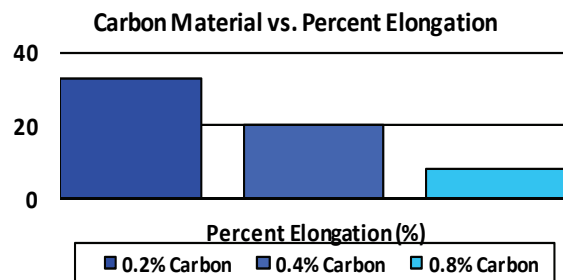


Fig. 8. Graph of Carbon material vs. Percent elongation.

Table 2. Different effects of alloying elements on carbon steel tested for the module development.

Alloying Element	Cr	Co	Mn	Mo	Ni	Ti	W	V
Hardenability	++	-	++	++	+	++	++	+++
High Temp. Strength	+	+	-	++	-	+	++	++
Ductility and Toughness	-	-	+	-	++	-	-	-
Abrasion Resistance	+	-	-	+	-	+	++	+
Fine Austenite Grain size	-	-	-	+	-	++	+	+++
Corrosion Resistance	++	-	-	+	+	-	-	-

Table 3. Several alloying elements tested for module material.

Code	Element
Cr	Chromium
Co	Copper
Mn	Manganese
Mo	Molybdenum
Ni	Nickel
Ti	Titanium
W	Tungsten
V	Vanadium

### 13. Introduction of Carbon Steel

Generally, with an increase in the carbon content from 0.01 to 1.5 % in the alloy, its strength and

hardness increases but still such an increase beyond 1.5 % causes appreciable reduction in the ductility and malleability of the steel. Low carbon steel or mild steel containing carbon up to 0.25 % responds to heat treatment as improvement in the ductility is concerned but has no effect in respect of its strength properties. Medium carbon steels having carbon content ranging from 0.25 to 0.70 % improves in the machinability by heat treatment. It must also be noted that this steel is especially adaptable for machining or forging and where surface hardness is desirable. High carbon steels is steel-containing carbon in the range of 0.70 to 1.05 %.

### 14. Limitations of Plain Carbon Steel

Like everything, the plain carbon steels do have some appreciable properties but also consists of some limitations which is there cannot be strengthening beyond about 100000 psi without significant loss in toughness (impact resistance) and ductility. Besides, for large sections cannot be made with a marten site structure throughout, and thus are not deep hard enable. Furthermore certain rapid quench rates are necessary for full hardening in medium-carbon leads to shape distortion and cracking of heat-treated steels. Hence Plain carbon steels have poor impact resistance at low temperatures, have poor corrosion resistance for engineering problems and oxidizes readily at elevated temperatures.

## 15. Residual Element Affecting Properties of Carbon Steel

Steel, is an alloy, which is mainly produced from pig iron. In fact, the manufacture of steel is quite a long process as it comprises of numerous stages and one of these stages is refining. Indeed, once produced in furnace, the steel does contain quite significant amount of impurity and thus, it requires being refined to a certain degree. However, even after the refining process, the steel still contain small amounts of residual elements (also termed as trace elements) which has some negative influence on the properties of steel.

## 16. Conclusion

A study and research that had carried to determine the correlation and synchronizing the best material to coat the MFL Capsule in order to submerge and flow with the oil and gas fluid in the pipelines and tanks with good robustness. There are few main factors that need to be pay attention; they are the flux penetration, flux behavior in pipeline, the tough robustness of material and the life stand of the material in order to suite with oil and gas fluid. From the data analysis gained by using the method of flux analyzing in few types of carbon steel (low carbon steel, medium carbon steel and high carbon steel), determined that high carbon steel is the best material

to apply on the MFL Capsule due to several chemical and mechanical properties as explained and examined.

## Acknowledgment

This work was supported in part by the Malaysian Government under FRGS Grant 9003-00285.

## References

- [1]. M. T. Covington, Pipe line rupture detection and control, *ASME Paper 78-PET-54, British Petroleum*, 1978.
- [2]. G. G. Bernard, Energy balance derivation, *CRC Bethany Internal Report*, Germany, 1982.
- [3]. Anon, Pin-pointing capsule in pipelines, 14-15, R&D Digest, *British Gas Corporation*, 1986.
- [4]. T. L. Stewart, Operating experience using a computer model for pipeline leak detection, Book of pipelines 3, *Halliburton*, 1983.
- [5]. J. H. Perry, Chemical engineers handbook, 3<sup>rd</sup> Edition, New York, *McGraw-Hill Book Co., Inc.*, 1950.
- [6]. R. A. Furness, *Modern pipe line monitoring techniques*, in *Proceedings of Pipes and Pipelines International*, Schlumberger, May-June 7-11 and September-October 14-18, 1985.
- [7]. R. L. Mailloux, J. D. Van Reet, Real time transient flow modelling applications, in *Proceedings of PSIG Annual Meeting*, U.S.A., 1983.

## Design and Analysis of Magnetic Flux Leakage Capsule

<sup>1</sup>Maliki IBRAHIM, <sup>2</sup>Zulkarnay ZAKARIA, <sup>2</sup>Ali Aiman MUSTAPHA,  
<sup>1</sup>Marisah NORHASAN, <sup>2</sup>Mohd Nasir AYOB, <sup>2</sup>Ibrahim BALKHIS,  
<sup>3</sup>Ruzairi ABDUL RAHIM

<sup>1</sup>School of Manufacturing Engineering, Universiti Malaysia Perlis,  
02600 Arau, Perlis, Malaysia

<sup>2</sup>School of Mechatronic Engineering, Universiti Malaysia Perlis,  
02600 Arau, Perlis, Malaysia

<sup>3</sup>Process Tomography and Instrumentation Research Group (PROTOM-i),  
INFOCOMM Research Alliance,  
Faculty of Electrical Engineering, Universiti Teknologi Malaysia,  
81310 Skudai, Johor Bahru, Malaysia

E-mail: maliki@unimap.edu.my, zulkarnay@unimap.edu.my, Ali\_Aiman\_Mustapha@yahoo.com,  
marissa.norhasan@gmail.com, nasirayob@unimap.edu.my, Ibrahim\_balkhis@gmail.com,  
ruzairi@fke.utm.my

*Received: 25 January 2013 /Accepted: 25 August 2013 /Published: 30 September 2013*

---

**Abstract:** Magnetic flux leakage (MFL) is among the current in-line non-invasive popular technique applied in pipeline condition control and monitoring. This paper discussed on the design and development of magnetic flux leakage capsule prototype which involve design, fabrication and analysis. This paper discussed three proposed design concept and had gone through scoring and screening process in selecting the best development concept. Copyright © 2013 IFSA.

**Keywords:** Magnetic flux leakage capsule, Design, Development, Analysis.

---

### 1. Introduction

Magnetic Flux Leakage (MFL) is the oldest and most commonly used magnetic method of non-destructive testing used in In-Line Inspection (ILI) method for detecting any strange in the inner surface of the pipes such as corrosion, crack or other symptoms which is bad to the pipe condition in transmission pipelines [1]. MFL can reliably detect metal loss due to corrosion and sometime gouging. The basic principle is that a powerful magnet is used to magnetize the steel. At areas where there is corrosion or missing metal, the magnetic field

“leaks” from the steel [2]. Therefore, the “leaks” helps user by giving the information on the location, sizes and also the level of potential damage area in the pipeline.

The term pipeline refers to a long line connected segments of pipe, with pumps, valves, control devices, and other equipment/facilities needed for operating the system. It is intended for transporting a fluid (liquid or gas), mixture of fluids, solids, fluid-solid mixture, or capsules (freight-laden vessels or vehicles moved by fluids through a pipe). The term also implies a relatively large pipe spanning a long distance [3].

The area of this research is to study, design and develop magnetic flux leakage capsule which suitable in detecting defect of the inner side of steel pipe or steel tank structures. Therefore this project considers the shape of the capsule, the moving mechanism of the capsule, and also the characteristic of the pipeline that can affect the performance of the capsule.

### 1.1. History of Magnetic Flux Leakage Capsule

Magnetic flux leakage technique was used as early as 1868 by the Institute of Naval Architect in England, where defects in magnetized cannon tubes were found with a compass [4]. In 1918, Magnetic Particles Inspection was accidentally discovered [5]; magnetic particles (iron shavings) were held in place by a local change in magnetic flux at the surface near the defect. The development and commercialization of magnetic particles inspection followed soon after [6, 7].

MFL inspection system is based on the same principle as magnetic particles inspection. The main differences between MFL and MPI is the used of sensors. MFL sensors, which were developed in the 1920's and 30's measure the magnetic field around a defect. MFL sensors allow a quantitative measurement, rather than the more qualitative information provided by MPI [8].

The first MFL in-line inspection tool for pipelines was introduced in 1965 by Tuboscope [9]. Since 1965, MFL tools have gain acceptance by the gas-transmission industry. As a result, MFL tools are some of the most widely used and effective tools available for in-line inspection of gas-transmission pipelines [8].

## 2. Working Principle

The MFL had developed time to time since principle of MPI. MFL was first used commercially to inspect pipeline in 1964. Today it is the most commonly used in in-line inspection method for pipelines [10, 11]. MFL technology can successfully overcome the physical and practical inspection challenges presented by transmission pipelines. The system can be designed to remain functional in an abusive pipeline environment for long distance and at product flow speeds. The permanent magnets used in this inspection technology need no energy source during an inspection, and the sensors and data recorders require reasonably low power to operate. The magnetic flux naturally enters the pipe and distributes evenly to produce a full volumetric inspection. Often various deficiencies of MFL system are highlighted, but the attributes described above keep MFL at the forefront of pipeline inspection technologies. There are two widely used implementations of MFL that can be differentiated by

the orientation of the magnetization terms of axial or circumferential direction [12].

The MFL inspection Pipeline Investigation Gauge (PIG) uses a circumferential array of MFL detectors embodying strong permanent magnets to magnetize the pipe wall to near saturation flux density. Abnormalities in the pipe wall, such as corrosion pits, result in magnetic flux leakage near the pipe's surface. These leakage fluxes are detected by Hall probes or induction coils moving with the MFL detector.

## 3. Moving Mechanism

Pipeline Investigation Gauge (PIG) is designed so that sealing element for example as shown in Fig. 1 provides a positive interference with the pipe wall. Once inserted into the line, PIGs are driven through the line by applying pressure in the direction of required movement as shown in Fig. 2. A pressure differential is created across the PIGs, resulting in movement in the direction of the pressure drop. In operational lines, this pressure is applied by the line product, whereas, in un-commissioned lines the propelling medium can be chosen to suit the task being carried out [13].

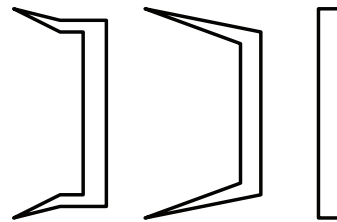


Fig. 1. Types of seal element used in PIGs.

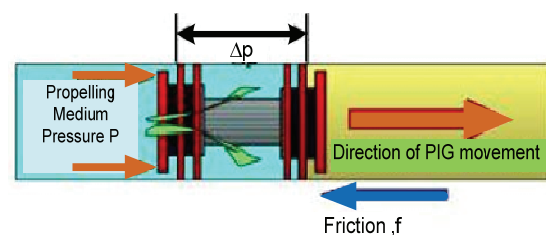


Fig. 2. Movement mechanisms inside a pipeline of a PIG

Sufficient flow required to ensure PIG movement at suitable velocity. Once the force behind the PIG becomes greater than the opposing frictional force, the PIG will move in the direction of the applied force (pressure).

The pressure at which the PIG begins to move is known as the "break-out" or "stiction" pressure. This tends to be greater than the pressure required maintaining movement and is characterized by a

pressure rise followed by a pressure drop to a plateau for the PIG launching operation.

The movement of the PIGs are depends on the sealing element design. Pigs can be run in single direction, either backwards or forwards through a line. Pigs that can only run in one direction are known as unidirectional PIGs, and have polyurethane sealing elements of the cone or cup design. Sealing elements in bidirectional PIGs are flat, providing an identical seal in either direction and therefore, giving more adaptability in previously unpigged lines. Additional sealing element might be added to PIGs, leading to better sealing properties along with higher pressure differential required to drive the PIG.

#### **4. Pigging Medium**

Pigging medium are used to move the capsule from one end to another. There are three pigging mediums that commonly used:

a) Liquid

Liquid are the most preferred medium for propelling PIGs in an incompressible liquid. Incompressible liquids provide maximum control over PIG speed as well as lubrication for the PIG seals, minimizing wear and maximizing seal effectiveness and life. Liquids such as water, crude oil or process product and chemicals can be used as propelling mediums. Care should be taken to ensure sealing element materials are compatible with fluid medium and prevailing pressure and flow condition.

b) Gas

As gasses are compatible, the amount of stored energy behind a PIG propelled with gas is far greater than that of a similar PIG propelled with liquid. Appropriate consideration should be given to safety implications resulting from this stored energy. Pig movement can also be affected by improper use of a compressible gas as a propulsion fluid. Failure to deliver adequate quantities of gas required to maintain sufficient pressure behind the PIG can result in a stop-start motion of the PIG. This effect can be minimized to some extent by sizing equipment properly and maintaining a constant back pressure on the PIG to minimize velocity changes.

c) Multiphase fluid

Multiphase is the commingled flow of different phase fluids, such as water, oil and gas. Multiphase fluid flow is a complex factor, important in understanding and optimizing production hydraulics in both oil and gas wells. Four multiphase fluids flow regimes are recognized when describing flow in oil and gas wells, bubble flow, slug flow, transition flow and mist flow [15].

Multiphase fluid safety consideration should give as high as pigging operation using gas propelling medium. Extra care should be taken to consider effect if slugging and the associated forces at the receiving end. Any temporary pipe work should be secured and permanent facilities and equipment should be rated for multiphase flow [13].

#### **5. Pipeline**

Pipelines are used to transport all manner of powders and fluids from one point to another. From the food industry to oil and gas transportation, millions of lives are affected by the ability to maintain flow through pipelines that cross over land and undersea to deliver a product [13]. Pipelines can be categorized depending on the commodity transported. According to fluid mechanics or type of flow encountered, pipelines can be classified as single-phase incompressible flow (such as water pipelines, oil pipelines and sewers), single-phase compressible flow (natural gas pipelines, air pipelines, etc.), two-phase flow of solid-liquid mixture (hydrotransport), two-phase flow of solid – gas mixture (pneumotransport), two-phase flow of liquid-gas mixture (oil gas pipelines), non-Newtonian fluid, and finally the flow of capsules [3].

#### **6. Concept Generation and Development**

After analyzing existing MFL Capsule, a new design of MFL Capsule developed using an Orthographic analysis as shown in Fig. 3. Orthographic analysis present two or three attribute of a problem in a graphical two or three dimensional array. The possible solutions to be explore by means of combination, permutation, interpolation or extrapolation (technique for problem reduction and expansion). There are three concepts of the design have been developed and will go through concept screening and concept scoring. Several selection criteria listed which used as the references to choose the best concept.

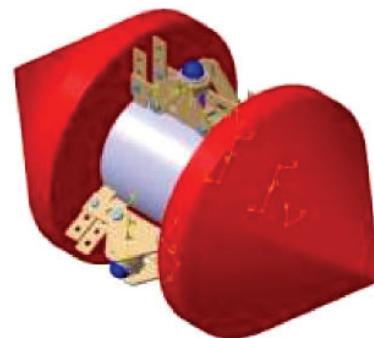


**Fig. 3.** MFL capsule model developed using ANSYS.

## 7. Analysis

Engineering analysis of this project divided into two parts. There is capsule analysis using calculation as shown in Fig. 4 to find the minimum pressure require to push the capsule forward and also contact body interaction analysis using explicit dynamic workbench in Computational Fluid Dynamics (CFD) software.

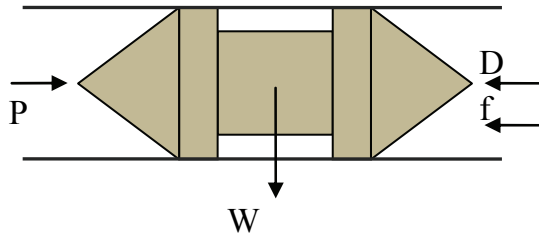


Fig. 4. Free body diagram of the MFL capsule.

$$F - F_D + F_{clearance} > (w.f = F_{friction}) \quad (1)$$

To find the drag force of the capsule, pressure drop is required

$$F_D = A\Delta p_C = AC_D \frac{\rho(v-v_C)^2}{2} \quad (2)$$

$$\Delta p_C = C_D \frac{\rho(v-v_C)^2}{2} \quad (3)$$

$$C_D = \frac{2k_D}{(1-k_D^Z)^Z} \quad (4)$$

$$k_d = \frac{D_d}{D}, \quad (5)$$

where  $C_D$ ,  $\rho$ ,  $v$ ,  $v_C$ ,  $D_d$  and  $D$  are drag coefficient of the capsule drag, air density in the pipe, bulk velocity of fluid (air), capsule velocity, sealing element diameter and pipe inner diameter respectively.

## 8. Result

### 8.1. Capsule with 400 mm Diameter

The minimum forces required to allow the capsule with diameter of 400 mm to moves forward in the pipe;

$$\begin{aligned} F - F_D + F_{clearance} &> (w.f = F_{friction}) \\ F - 0.5434N - 0.0056F &> (321.688 \text{ kg} \times 9.81 \text{ ms}^{-1}) \times 0.18 \\ 0.9944F &> 1.11177 \text{ kN} \\ F &> 1.1177 \text{ kN} \end{aligned}$$

$$p > \frac{F}{A} = \frac{1.1177 \text{ kN}}{0.12576 \text{ m}^2} > 8.8919 \text{ kPa}$$

### 8.2. Capsule with 500 mm Diameter

The minimum forces required to allow the capsule with diameter of 500 mm to moves forward in the pipe;

$$\begin{aligned} F - F_D + F_{clearance} &> (w.f = F_{friction}) \\ F - 0.8293N - 0.1124F &> (469.6968 \text{ kg} \times 9.81 \text{ ms}^{-1}) \times 0.18 \\ 0.8876 F &> 1.6578 \text{ kN} \\ F &> 1.8687 \text{ kN} \end{aligned}$$

Therefore the minimum pressure of the capsule in the pipe;

$$p > \frac{F}{A} = \frac{1.8687 \text{ kN}}{0.1963 \text{ m}^2} > 9.5172 \text{ kPa}$$

From the analysis of the capsule with 400 mm and 500 mm diameter, results show that the minimum force to allow the capsule with sealing element diameter of 400 mm is bigger than and minimum force to allow the capsule with sealing element diameter of 500 m. The differences of force value in allowing the starting motion of the capsule because of the difference of its diameter of sealing element other than difference in normal force of both capsules. For capsule with approximate 400 mm sealing element having 321.688 kg of mass with 3155.7593 N normal force, while capsule with approximate 500 mm sealing element have a mass of 469.6968 kg with 4607.7256 N normal force act to the capsule body. Results also show that there is a difference in pressure drop value of both capsules. Capsule with smaller diameter of sealing element experienced larger pressure drop than the capsule with larger diameter of sealing element. This state influenced by the velocity drop of the capsule due to surface area and normal force of the capsule's body. According to the calculations that were made, the leakage flow ratio visible to experience marked contrast where the smaller sealing element capsule only have 0.563 % of leakage compared to the larger sealing element capsule that have 11.24 % of leakage flow ratio. This condition also may influence by the velocity movement of the capsule and the fluid of pigging medium, while the value of velocity influence by normal force value and area of the contact surface. Therefore, to decrease the larger diameter capsule leakage flow ratio, the points can be controlled are the weight of the changeable sealing elements and the diameter itself. In comparing the drag coefficient value produce by formula using Kasugi's Equation and using fluid flow analysis using ANSYS both value differ so much this is because the Kasugi's Equation had already known that can predict Drag Coefficient with 20 % error besides it only consider the drag on the surface of capsule that touching with the pipe inner surface

compare with fluid flow analysis using ANSYS that considering the drag on the fully body of the capsule. Therefore, this cause visible marked contrast on the result.

### 8.3. Analysis Result on ANSYS

#### 8.3.1. Pressure Distribution

The red area in Fig. 5 shows the highest pressure contour  $1.607 \times 10^4$  where the air pressure supply to the capsule to move forward. The green and blue region shows the medium and low pressure contour. The figure clearly show that the high pressure area only at one side where the pressure inlet supplied.

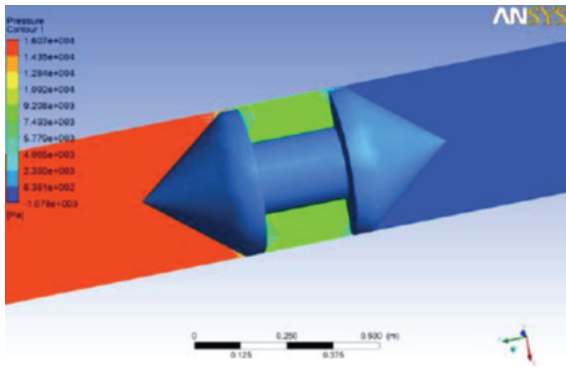


Fig. 5. Pressure distribution exists on the developed capsule.

#### 8.3.2. Steamline

It is found that, the developed module is capable in reaching the highest velocity which is up to  $5.687 \text{ms}^{-1}$  as shown in Fig. 6.

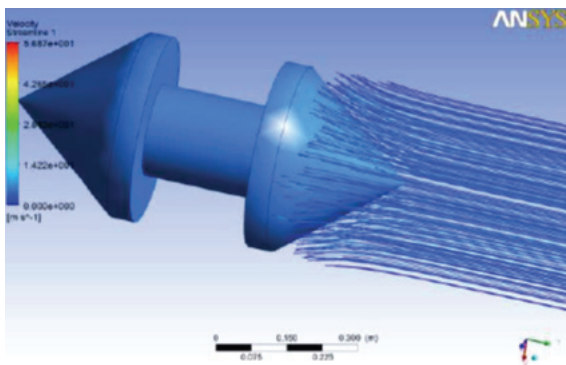


Fig. 6. Steamline simulation result of the developed capsule.

#### 8.2.3. Velocity Vector on the Capsule

The area in Fig. 7 that circled in red shows the vector that acts counters the inlet pressure resulted

leakage due to clearance between capsule and inner pipe diameter.

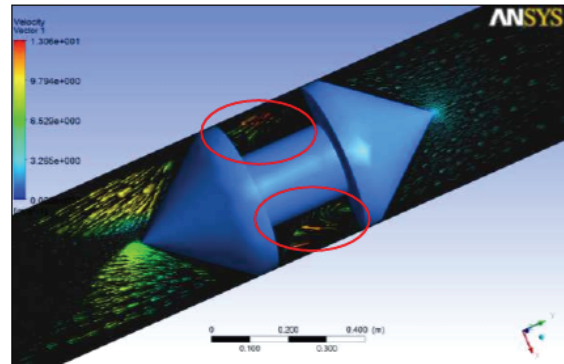


Fig. 7. Velocity vector which acts on the capsule.

#### 8.2.4. Pressure Distribution

The red area shown in Fig. 8 is the highest pressure contour  $1.607 \times 10^4 \text{Pa}$  where the air pressure supplied to the capsule to move forward. The green and blue region shows the medium and low pressure contour. The figure clearly shows that the high pressure area only at one side where the pressure inlet supplied.

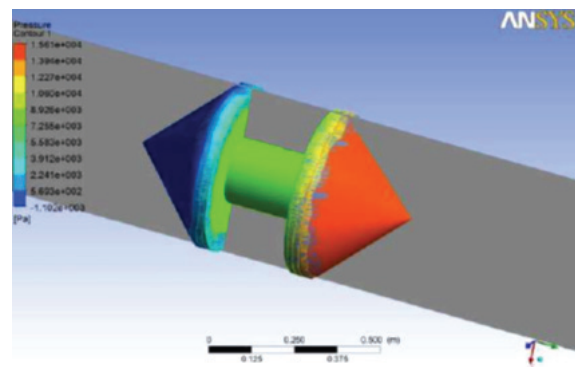


Fig. 8. Pressure distributions of the module in 3D view.

### 9. Conclusion

In conclusion, the objective of the project on design MFL capsule that can flow through different sizes of pipe ranging inner diameter from 400 mm to 500 mm analyzed motion of MFL Capsule flow using calculation and Computational Fluid Dynamic Software had been achieved. The MFL capsule is designed with a changeable sealing element which enable capsule to flow in 400 mm and 500 mm pipe's diameter. The analysis of obtaining the minimum force require by the capsule to move forward had resulted a minimum of  $1.1177 \text{ kN}$  air pressure to enable the capsule flow for 400 mm diameter sealing element and  $1.8687 \text{ kN}$  of air required to enable the

capsule of 500 mm diameter sealing element capsule to flow. So, the listed element had proved that the objective of the project had achieved.

## Acknowledgment

This work was supported in part by the Malaysian Government under FRGS Grant 9003-00285.

## References

- [1]. T. A. Bubenik et al., Magnetic Flux Leakage (MFL) Technology for Natural Gas Pipeline Inspection, Battelle, Report Number GRI-91/0367 to the *Gas Research Institute*, November 1992.
- [2]. Magnetic Flux Leakage Retrieved 11 November 2011, ([http://en.wikipedia.org/wiki/Magnetic\\_flux\\_leakage](http://en.wikipedia.org/wiki/Magnetic_flux_leakage)).
- [3]. H. Liu, Pipeline engineering, Vol. 1, *Lewis Publisher*, United States of America, 2003.
- [4]. M. L. Nayyar, Piping handbook, 7<sup>th</sup> edition, *McGraw-Hill*, 1999.
- [5]. G. Dobmann, P. Holler, Physical analysis method of magnetic flux leakage, in *Research Techniques in Nondestructive Testing*, Vol. IV, edited by R. S. Sharpe, *Academic Press*, 1980.
- [6]. W. Hoke, Principles of magnetic particle testing, edited C. E. Benz, *Magnaflux Corporation*, Chicago, 1967.
- [7]. A. V. Deforest, Magnetic testing of iron and steel, *Iron & Steel Engineer*, Vol. 9, 1932.
- [8]. F. B. Doane, Magnaflux inspection for cracks and seams, *Iron Age*, September 1933.
- [9]. Batelle (<http://www.battelle.org/pipetechnology/mfl/LinksMFLHistory.htm>).
- [10]. G. J. Posakony, V. L. Hill, Assuring the integrity of natural gas transmission pipelines, *GRI Report* 91/0366, 1992.
- [11]. J. B. Nestleroth, T. A. Bubenik, Magnetic flux leakage (MFL) technology for natural gas pipeline inspection, Battelle, Report Number GRI-00/0180, *Gas Research Institute*, February 1999.
- [12]. G. Dobmann, P. Holler, Physical analysis methods of magnetic flux leakage, in *Research Techniques in Nondestructive Testing*, Vol. IV, edited by R. S. Sharpe, *Academia Press*, 1980.
- [13]. J. B. Nestleroth, Implementing current in-line inspection technologies on crawler systems (Technology Status Report), Battelle: *Gas Research Institute*, April 2004.
- [14]. R. Davidson, An introduction to pipeline pigging, *Pigging Products and Services Association*, p. 9, 2002.
- [15]. McGraw-Hill Professional (<http://www.mhprofessional.com/downloads/products/0071743898/0071743898ch1.pdf>).
- [16]. P. Guieze, A. Scheffler, V. Afanasyev, B. Theuven, B. Pingue, Multiphase fluid samples: a critical piece of the puzzle, p. 39, 2009.
- [17]. M. R. Baxter, Product design, Cheltenham, *Stanley Thornes*, UK, 1999, pp. 76-79.
- [18]. Y. A. Cengel, J. M. Cimbala, Fluid mechanics fundamental and application, 2<sup>nd</sup> Edition, *Mc Graw Hill*, 2010.
- [19]. Computational fluid dynamics ([http://en.wikipedia.org/wiki/computational\\_fluid\\_dynamics#P\\_DF\\_methods](http://en.wikipedia.org/wiki/computational_fluid_dynamics#P_DF_methods)), (8 October 2011).
- [20]. K. Oenoki, Forces and Newton's Law, *ORACLE ThinkQuest*, Vol. 2012, 1997.

## Using BP Neural Network and Kalman Filter to Signal Processing of MEMS Inertial Sensors

<sup>1</sup>Wenxian XIAO, <sup>2</sup>Hao ZHANG, <sup>1</sup>Xiaoqin MA

<sup>1</sup>Henan Institute of Science and Technology,  
Henan Xinxiang, 453003, China

<sup>2</sup>Dept. of Computer Science and Technology, Henan Mechanical and Electrical Engineering College,  
Henan Xinxiang 453003, China  
Tel.: 13849382972  
E-mail: wenxianxiaoedu@163.com

*Received: 3 July 2013 / Accepted: 25 August 2013 / Published: 30 September 2013*

---

**Abstract:** The paper put forward using BP neural network and Kalman filter to signal processing of MEMS inertial sensors. This paper uses Kalman filter value for information fusion of gyroscope and accelerometer, and the attitude angle is accurate. The state and observation equation of attitude angle measuring system with characteristic of BP neural network, and the design of the Kalman filter is simple and gyroscope measurement information data fusion, the preparation of the corresponding MATLAB program Kalman filter is designed. Through the simulation results of the image, this method can compensate the zero drift of gyroscope, improves the measurement precision of the attitude angle. *Copyright © 2013 IFSA.*

**Keywords:** BP neural network, Kalman filter, Inertial sensors, MTALAB.

---

### 1. Introduction

With the development of inertial sensor technology, inertial navigation system (INS) is independent, not susceptible to interference, real-time output and other excellent characteristics so that it is widely applied in military, commercial and related fields. INS depends on the accuracy of inertial sensor, gyroscope and accelerometer accuracy. There is a large amount of random noise and inertial sensor of the measurement data, to measure the carrier through the gyro attitude angle, its stability and short-term advantages of high precision, is suitable for the measurement of fast changing information, but the carrier attitude gyro measuring angle error will be rapid accumulation (drift), when the long time work when the drift infinite increase, cause the system to not work [1]. The accelerometer and magnetometer can also be used for measuring the attitude, and the

measuring error is not accumulated with time, its static performance is good, suitable for measuring the slow changes in the information, but when the acceleration is larger this method cannot be used.

Inertial sensors including accelerometers (or acceleration sensors) and angular velocity sensor (gyroscope) and their single, double, three axis combined IMU (inertial measurement unit), AHRS (attitude reference system includes a magnetic sensor). MEMS accelerometer sensor is measured using inertial force sensing quality, generally by the standard mass (sensor) and detection circuit. According to the sensing principle is different, mainly piezoresistive, capacitive, piezoelectric, tunnel current, resonant, thermoelectric coupling and electromagnetic.

MEMS (Micro Electro Mechanical System) inertial sensor chip using inertial sensor manufacturing microelectronic processing

technology, system integration is the micro devices composed of micro sensor, micro actuators, signal processing and control circuit, communication interface and power supply and other components of the system. The goal is to capture, processing and implementation of integrated information, composed of multifunctional micro system integration system, so as to greatly improve the system automation, intelligence and reliability level.

Although MEMS devices precision has not yet reached the limit, by improving the hardware design and manufacturing method can improve the accuracy, but by hardware manufacturing high precision gyroscope is not nearly technology difficult, and its cost is high. Method for collecting and handling the signal of the inertial sensor output signal to improve the precision of gyroscope, can reduce the needs of inertial sensor precision of hardware, and then achieve the goal of reducing the cost, this is the inertial circles has been an important research direction. According to the characteristics of these two kinds of sensors need to be fused the measurement information, improve the signal precision inertial sensors, to obtain more reliable information of attitude. Kalman filter has the ability to suppress the interference of strong, and can make the control method has good dynamic performance, has been very good application in nonlinear optimal estimation. The paper put forward using BP neural network and Kalman filter to signal processing of MEMS inertial sensors.

## 2. Application of MEMS Inertial Sensors Analysis by BP Neural Network

The low accuracy of MEMS inertial sensors for consumer electronic products mainly used in mobile phone, portable game machine, music player, wireless mouse, digital camera, PD, hard disk protection device, intelligent toys, pedometer, anti-theft system, GPS navigation. Because of the acceleration measurement, inclination measurement, vibration measurement and measurement of rotation and other basic measuring function, to consumer electronics application of mining will continue to occur [2]. Intermediate of MEMS inertial sensors for industrial and automotive products, mainly used in automotive electronic stability program (ESP or ESC) GPS aided navigation system, automobile airbags, vehicle attitude measurement, precision agriculture, industrial automation, medical equipment, robotics, instrumentation, engineering machinery and so on.

Problems of BP neural network prediction ability and training ability: prediction generalization ability also known or generalization ability, training ability also known approximation ability or learning ability. Under normal circumstances, training ability, predictive ability is poor, and to a certain extent, with the ability to improve the predictive ability of the

training, will be improved. But the trend is not fixed; it has a limit, when reaching the limit, as the training ability, predictive ability will decline, also is the so-called "fitting" phenomenon. Reasons for this phenomenon is the network learning too much detail in the sample, the learning model cannot reflect the sample contains the rules, so how to grasp the important research content of learning, problem solving contradiction prediction ability network and training ability and BP neural network.

The development trend of MEMS inertial sensors are mainly in the following aspects: Technology: precision will continue to improve, with the top as an example, there are alternative low precision of fiber optic gyro trend. For consumer applications, more seek to further simplify the manufacturing process, reduce the cost of the trend. At the same time, the integration is the future trend of development, not only the module manufacturers go software, hardware integration approach, more and more upstream chip manufacturers also walk route technology integrated block. Thus constantly biaxial, three axis accelerometer, and gyroscope chip is published.

Using the inertia element can be on the moving body attitude measurement, inertial MEMS (Micro-Electro-Mechanical System) is the inertial component appears in recent years, it has low cost, high reliability, low power consumption, small size and other advantages, but the precision is relatively low, the gyroscope in the motion body attitude angle measurement, with increasing the measurement time will drift, so that the measured attitude angle is not accurate. In the vertical take-off and landing aircraft, aircraft can be regarded as a fixed base device, which can electrically equivalent angle measurement of aircraft with an accelerometer, and because the accelerometer drift angle is small, the long time measured are accurate. Therefore, the compensation and correction is in order to inclination measurement of gyroscope, as is shown by equation 1.

$$E_{jB}^{\xi}(m, n) = \sum_{m' \in J, n' \in K} W_B^{\xi}(m', n') [D_{jB}^{\xi}(m + m', n + n')]^2 \quad (1)$$

Due to the single on continuous improvement of instrument design and processing, to improve the method of debugging accuracy of inertial instrument accuracy, in practice, due to the cost, complexity and other issues encountered more and more difficulties, which makes the inertial sensor and components of the signal processing technology more attention in error compensation and the application, from the original one-sided pursuit of lower instrument absolute error, to focus on ensuring the instrument performance stability, random error compensation using signal processing technology as much as possible to reduce the instrument [3]. Gyro signal processing research mainly concentrated in the static error model, the dynamic error model and error

compensation of these three aspects. Gyro static model and dynamic model because of its error trends are identified, so the error modeling has formed a fixed mode.

Modern inertial sensors are using tuning fork and piezoelectric vibratory silicon micromachining. Their sensitivity to small rotation of moving objects by reciprocating vibrating tuning fork based on Coriolis acceleration. Modern inertial sensors are widely used in such as a digital camera anti-shake, vehicle rollover airbag.

$$\frac{\partial^2 f}{\partial y^2}(i, j) \approx \frac{1}{h_2} [f(i, j+1) - 2f(i, j) + f(i, j-1)] \quad (2)$$

The gyro can measure positive, reverse direction angle speed ratings range. The rated range, gyro scale factor nonlinearity satisfies the requirements. (1). the scale factor (mV / deg / S) Scale Factor (Sensitivity) also known as the scale factor, scale factor, gradient, sensitivity. Refers is to the ratio of output and input angular rate gyro. The ratio is based on the input; output data of the whole input angular rate was measured over the range, slope straight line by least square method to fit the calculated. (2). the scale factor nonlinearity (%) Scale Factor Nonlinearity refers to the input angular rate gyro output range, relative to the least squares fitting linear maximum deviation and the maximum output ratio. (3) At zero bias and zero bias stability (V; V, deg / h or deg / S) Bias and Bias Stability bias refers to the output of gyroscopes in zero input condition. The output set time measured mean to represent. The bias stability is a measure of the gyroscope output around its mean zero input state (bias) discrete degree of ups and downs, get used to the RMS value representation, and the equivalent input corresponding angular rate. The industry is also known as the bias stability of zero drift, as is shown by equation 3 [4].

$$\hat{f}_n = f(u_n) = f\left[\sum_{k=1}^K w_k \sum_{m=1}^M x_m \psi\left(\frac{x_m - b_k}{a_k}\right)\right] \quad (3)$$

Analysis of variance has been recognized as the practical method of fiber optic gyro random error standard analysis. This is because the output of fiber optic gyro random drift data with statistical characteristics and frequency fluctuation is very similar, the noise of the Allan variance and power spectrum density has the quantitative relationship between, can be directly from the output data of fiber optic gyro type and amplitude of each error source in fiber optic gyroscope in the time domain. Allan variance analysis with standard identification method for white noise, bias instability in high frequency, angle random walk and quantization noise not only results in low frequency band, to identify the rate ramp is not the only. So the improvement of Allan variance also emerged.

BP neural network in training can through the study of automatic extraction of output, output data

between “rule of reason”, and adaptive learning content on the network weights in memory. BP neural network with a high degree of self-learning and adaptive ability. Generalization ability: generalization ability refers to the design of a pattern classifier, namely to consider the network in the guarantee of the required classification on the correct classification, but also concerned about the network after training, can not seen mode or noise pollution model, were correctly classified. The BP neural network has the ability of learning achievements are applied to the new knowledge.

The training process of BP network are as follows: (1) network initialization, assignment of the network parameters and the weight coefficient, the coefficient should take random number; (2) the input training samples, each layer of the value prediction, and compared with the true value, the network output error (3); on the basis of error back propagation rules, weight coefficient between hidden layer between input layer and hidden layer and is shown by equation 4.

$$C(t) = \frac{E[B(t), B(-t)]}{E[B(t)^2]} = 2^{2H-1} \quad (4)$$

In the gyro signal demising, wavelet transform has been widely applied because of its excellent characteristics of multiresolution. The fog signal was decomposed into multi-scale, signal reconstruction on each scale is after, multiscale gyros drift data. Time series modeling on scales of the drift data reconstruction, can get the multi-scale time series model of gyro random drift [5]. Then the model based on, on scales of the gyro random noise are filtered using the Kalman filter, which can effectively improve the signal-to-noise ratio of fiber optic gyro. Some domestic researchers' wavelet neural network technology is applied to the gyro random drift model.

THELMA is a non - integrated MEMS manufacturing process, than the polysilicon surface micromachining process is complex, but has unique advantages, to achieve a thicker structure, this is extremely useful for capacitive inertial sensors. Although the THELMA process for the realization of capacitive inertial sensors, but the technology is very flexible, but also can be used for manufacturing the accelerometer, gyroscope and other MEMS devices.

$$I = -\sum_{t=0}^T q(t) \log q(t) - \left(-\sum_{t=0}^T p(t) \log p(t)\right) \quad (5)$$

Micro mechanical acceleration score for drape / displacement type or resonant using closed loop capacitive sensing and static electricity. The restoring force of micro machined accelerometer is a kind of typical structure, the accelerometer as silicon structure of a single, consisting of one can read the capacitance of the torsion pendulum and electrostatic torque device, device size was about

300 μm × 600 μm. Supported by a pair of crankshaft torsional pendulum, below inclined plate as output and torque electrode, while the integrated output angle sensor, used to drive torque to maintain the initial position of the modified inclined plate. Output balance required torque and acceleration in a certain proportion. Performance index (Revised) of the error is about 100 μg, at the same time scale factor error is 100 \* 6, silicon accelerometer has a wide application prospect in the commercial domain, can also be used in military field and independent of traffic industry market. It can be applied to the measurement of acceleration extreme, such as the projectile velocity measurement in gun.

While the gyro random drift due to the random noise sources, compensation error is more complex difficulties. The gyro drift test and modeling has done a lot of work [6]. The mathematical and physical model is established from the physical structure of the fiber optic gyroscope fog layer, and then to compensate for gyro mechanical structure and other physical compensation. But the traditional IIR filtering, smoothing filtering and other classical digital filtering technology has been used as auxiliary analysis method used in gyro signal processing.

$$\binom{\delta}{k} \equiv \frac{\delta!}{k!(\delta-k)!} = \frac{\Gamma(\delta+1)}{\Gamma(k+1)\Gamma(\delta-k-1)} \quad (6)$$

The attitude angle based on MTi inertial sensors to measure the angular velocity gyroscope, which is used to measure the angular velocity vector, the integral processing to obtain the attitude angle vector angle, but accumulated error, when the long time work accumulated error will be increased indefinitely, the relevant control system leads to the measured attitude information is not trusted which causes the carrier will not work properly. Attitude angle measurement vector with the accelerometer, its static performance is good, suitable for measuring the slow changes in the information, not suitable for tracking dynamic angle movement.

In BP network, transfer function derivation is very important, Tansig, logsig and purelin have guiding function dtansig, dlogsig and dpurelin correspondence. In order to get more transfer derivative function, transfer function, you can take the character “derive”: Tansig (‘deriv’) the first step of ANS = dtansig network construction and initialization of training a feed forward network is to establish a network object. The function newff is to set up a training feed forward neural network. 4 input parameters that need to be. The first parameter is an Rx2 matrix to define R input vector of the minimum and maximum values. The second parameter is an array of weakly each layer neuron number. The third parameter is an array containing the cells in each layer transfer function name. The last parameter is the name of the training function used in the.

Micro mechanical gyroscope MTi system in this paper refers to the vibrating gyroscope (vibratory

gyroscope, VG). Micro mechanical gyroscope working principle: the use of mass of the high frequency vibration produced by Coriolis acceleration in the base is driven to rotate, which uses the vibration mass made of monocrystalline silicon or polysilicon, rotation will cause the energy conversion between the two vibration modes. Vibration vibration gyroscope is driven to work in the first vibration mode (drive mode), when the direction of vibration modal and the first vertical rotating angular rate input, the vibration parts due to brother’s effect produced second vibration modes of a vertical to the first vibration mode (also called sensitive mode), this mode is directly proportional to and the angular velocity of rotation. To detect the sensitive mode, you can detect the angular velocity.

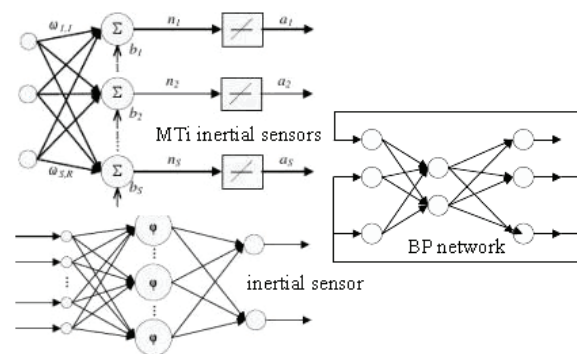


Fig. 1. The information processing of MEMS Inertial Sensors Analysis by BP Neural Network.

The basic principle of the information processing model of BP network is: input signal Xi through intermediate nodes (hidden layer) effect on the output node, through non – linear transformation, generates the output signal Yk, each sample for training the network comprises an input vector X and expected output T, the output value of the network Y and the expected output value deviation between T by adjusting the input nodes, and the nodes in the hidden layer connection strength value of Wij and the hidden layer nodes and the output nodes of the connection strength Tjk and threshold, the error decreases along the gradient direction, after repeated training, determine the network parameters corresponding to the minimum error phase (weights and thresholds), training is stopped [7]. The trained neural network can input information of similar samples, dispose of output error is minimized by non – linear transformation information.

The accelerometer is in accordance with the principle of inertia relative to inertial space work. Acceleration itself is difficult to directly measure, the actual existing accelerometer are the sensitive quality into force of indirect measurement, accelerometer measurement principle of Newton based on the second law: the force which acts on an object is equal to the object’s mass times acceleration. In other words, the acceleration effect in the sensitive quality

formation of inertial force gauge can not distinguish between the forces of inertia and gravity, so the output of accelerometer is reflected by the quality unit force detection of inertial space, namely the inertial force and gravitational force and it.

MTi has two kinds of data output mode: raw data output mode and the corrected data output mode; the corrected data are effectively compensate the original data of non-orthogonal error, installation error, temperature transform on silicon micro machined devices, the effect of scale factor error based on the acquired data. The corrected data for decimal data, corrected data is not after the filtering and other real-time processing and only the physical calibration model is applied to the data obtained from the A/D converter. Data output format corrected as shown in equation 7. Inertial sensor experimental data used in this paper are corrected data.

$$u'(x_1, x_2) = \sum_{s=-n}^n \sum_{t=-n}^n w(s, t) u(x_1 + s, x_2 + t) \quad (7)$$

In summary, the neural network has four kinds of structure, hierarchical network layer hierarchical network, connecting the feedback hierarchical network, interconnection network connection, the neural network model of a sensor network, linear neural network, BP neural network, radial basis function network, feedback neural network, BP neural network is mainly studied in this paper to study, BP neural network and the approximate inertial sensor function and the estimation of sample size of two examples of application.

### 3. Inertial Sensor Signal Processing Based on Kalman Filter

Due to the random drift in inertial navigation system using the method cannot simply be compensation, so it becomes the most important measure of the gyroscope precision index. Our research on MEMS gyro noise reduction system is for MEMS Gyroscope Random Drift. In addition, the long-term stability of the gyro drift and characterization of a random drift rate, called drift uncertainty or successive drift rate. Drift uncertainty reflected in successive start in the random variations in drift rate of the system, it will affect the precision of inertial navigation system of compensation for gyro drift.

The main error sources of accelerometer in the following aspects: (1) fixed deviation: under the condition of constant acceleration, constant value deviates from the standard acceleration voltage nominal value. (2) Scale factor error: the change in output voltage and the input acceleration change ratio. Can a simple table show a proportional form, also can be expressed as a percentage of the full-scale measurements [8]. (3) Cross coupling error: error in the accelerometer output value is due to the

accelerometer to orthogonal to the input shaft of the acceleration is extremely sensitive to the cause.

In the inertial navigation system, gyro is the key of its sensitive element. So the error of the MEMS gyroscope has become the main source of error in inertial navigation system. Precision gyro azimuth reference mainly depends on the size of the gyro drift error. In general, the gyro drift rate refers to the time variation of gyroscope output relative deviation from the ideal output rate, and the corresponding input relative to inertial space with unit time angular displacement [9]. Gyroscope drift will in open-loop state caused by range of deviation over time, even if the main factors in closed loop work shift are caused by the measurement error. Gyro drift error of the size of the drift angular velocity value, usually called the drift rate.

According to the characteristics of these two kinds of sensors need to be fused to the acquisition of information, to get the attitude information reliable. Kalman filter has the ability to suppress the interference of strong, and can make the control method has good dynamic performance, in the field has been well applied to estimate the nonlinear optimal. Fig. 2 is the research content of this article briefly structure diagram, which uses Kalman filter value for information fusion of gyroscope and accelerometer to get by, the attitude angle is accurate.

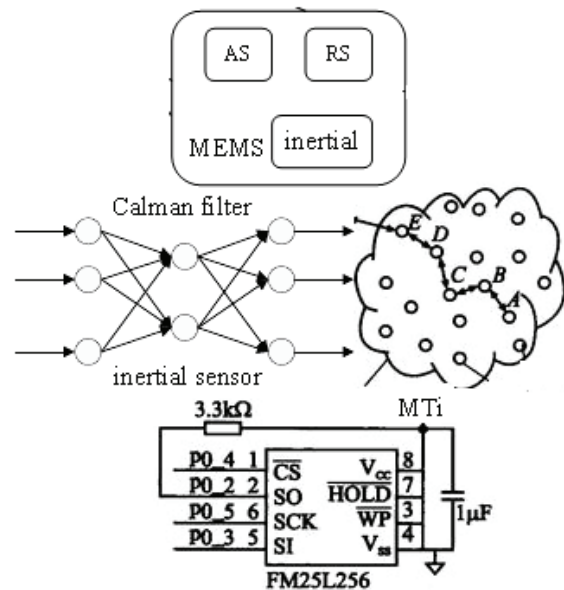


Fig. 2. The Inertial Sensor Signal Processing based on Kalman Filter.

For a specific application, Kalman filter state equation and measurement equation design problem. We must consider the actual process and the operation is simple and easy to use, so that the design of the filter is feasible. In the design process, to the amount of selected affect the entire state equation of the structure is a key part of Kalman filter design. Taking into account the existence of derivative

relations angle and angular acceleration, angle can be used to make a state vector, and the angular acceleration is not suitable as a state vector, because its derivative is not given, a feasible choice is not directly estimate the angular acceleration of the true value, and estimate the gyroscope zero offset B, and this deviation as the state vector established as the system of equations.

$$MEAN = \sum_{i=0}^{M-1} \sum_{j=0}^{N-1} F(i, j) / (M \times N) \quad (8)$$

Using the gravity magnetic field between the geographic coordinate system and body coordinate direction cosine transform is absolute angle solution, get the attitude angle. Drawback is the slow dynamic response of the accelerometer, and it is not suitable for tracking dynamic angle movement, interference and is very interested, so it cannot be used for dynamic measurement of vehicle attitude.

Method using gyros and accelerometers integrated attitude determination method, is one of the above two and method together, acceleration information method of the attitude determination to output accelerometer use in computing the attitude of the MTi is used as the measurement value to compensate the gyro drift, this algorithm can guarantee the alignment of the MTi inertial sensor precision, and can guarantee by the gyro dynamic and stability of system has higher [10]. In this manner, the gyroscope, accelerometer integrated attitude determination fixed integrating gyro angle after drifting through the Kalman filter, improve the precision of inertial sensors.

Kalman filter is used to estimate a time, coupled with the real-time measurement of real-time estimation. Kalman filter is a recursive linear minimum variance estimation, because the estimation of time is measured using a moment before and the quantity, so the real-time estimation of the recursion is measured data obtained by all volume; secondly, Kalman filter to estimate the state of the system is used, with the system state equations to describe the transfer process, state thus, state correlation function between each time, can according to the transfer characteristic equation of state to describe the non-stationary random process, solve the difficulty in estimating. Kalman filter optimal criterion and linear minimum variance estimation, estimation of every moment to estimate the minimum mean square error. The state equation of the system is used, must be linear Kalman filtering.

Kalman filtering algorithm with two loops: gain loop and filter loop. The calculation of loop gain is calculated independently, filter loop depends on the gain calculation circuit. On 8 basic equations for linear discrete is stochastic system of Kalman filter. As long as the given initial value based on the observed K values of Z (k), can be recursive calculation of K moment state estimation. In a filter cycle, from the Kalman filter in the use of

information and information of observation sequence, Kalman filter has two obvious information renewal processes: time update process and the observation update process. Type (9) shows that with the k-1 time state estimation and prediction K.

$$\frac{\partial u}{\partial x_1} = u(x_1 + 1, x_2) - u(x_1, x_2) \quad (9)$$

By using the statistical characteristics of the system noise and observation noise, the measured values as the input filter system, the estimation (system state or parameter) as the output of the filter, between the input and output filter is composed of time updating and the observation update algorithm together, according to estimate all need treatment the signal system and observation equations. It with conventional filter completely different meaning and method is actually an estimation method for the optimal [11]. The Kalman filter is applied to the error of inertial sensor attitude angle compensation, first needs to determine the measurement and state transition matrix.

The output signal data of the inertial sensor in stationary and motion is obtained by experiment, data analysis in Matlab 7.0 software platform, in the stationary state was observed in drift of gyroscope, and through the Kalman filter in gyroscope and accelerometer data fusion, effectively inhibit the accumulated drift of gyroscope, and improve the measurement accuracy of inertial sensor. In the state of motion as the accelerometer slow dynamic response is not suitable for tracking dynamic angle movement, and measure the attitude gyroscope angular and cumulative error, by Kalman filtering fusion of accelerometer and gyroscope signals, through the simulation of the image can be seen, this method compensates the zero drift of gyroscope, improve the measurement precision measuring the attitude angle, to achieve the desired effect research.

#### 4. Using BP Neural Network and Kalman Filter to Signal Processing of MEMS Inertial Sensors

Inertial measurement unit composed of inertial sensor axis of this study, can find the pitch angle and roll angle of the vector of the output signal of the sensor, but the attitude angle of the random drift error, this paper proposed a Kalman filter to achieve fusion and gyroscope information on the acceleration, the filtering algorithm is simple and practical, to compensate the error of inertial sensors to obtain optimal estimation of attitude angle, so as to obtain more precise attitude information.

BP neural network is a kind of supervised learning, one-way communication, and multilayer feedforward neural network. Between the upper and lower BP network neuron implement the right

connection, namely each unit of each unit and the upper layer are implemented in connection, no connection between the same layer neurons. Because of the network, the weight adjustment using back propagation (Back Propagation) learning algorithm, so called BP network. BP neural network is the core part of front network, embodies the essence of artificial network [12]. BP neural network through iterative gradient algorithm for solving network between the actual output and the expected output of the minimum mean square value, and can reverse transfer and modify the error.

In this paper, the design data of the inertial sensor output signal in stationary and moving down through the experiment, by using Kalman filtering in the MATLAB program, the simulation obtained gyro and accelerometer data fusion of the pitch angle and roll angle of the image signal and eliminate the simulation image of gyro's drift by Kalman filter using MATLAB software.

$$\tilde{W}_{j,k} = \sum_{l=0}^{L_j-1} \tilde{h}_{j,l} X_{k-l \bmod N} \quad (10)$$

In this paper, the use of MTi is the MEMS structure, composed of micro inertial measurement unit system and the three axis magnetometer. Micro inertial measurement unit 3 silicon micro accelerometer sensitive to X, Y, Z three directions of the linear acceleration; angle of rotation speed of 3 silicon micro machined gyroscope sensitive around the X, Y, Z three direction; the 3 axis magnetometer measurements of the earth's magnetic field strength. Gyro, accelerometer and magnetometer fixedly connected on the bracket of micro inertial measurement unit of the device, in mutually perpendicular position to install [13].

The design of the BP network, the hidden layer number, hidden layer nodes (neurons) determination is a very important question. People usually think, the

simulation accuracy and complexity of the topological structure of network is proportional to, the network topology structure is more complex, more number of hidden layer nodes, the simulation precision is high, the smaller the possibility of getting into local minimum. But a large number of experimental results show that: the simulation accuracy does not vary with the complexity of network topology structure increased. Simulation for the same problem and it is network topology of the large difference.

The actual rate gyro drift is generally consists of two part system drift and random drift rate: (1) systematic drift rate: is defined with the specified operating conditions related to the drift rate component, it has nothing to do with acceleration by drift and drift and acceleration of the rate of group, represented by the angle displacement per unit of time. The system reflects the gyro drift rate under actual conditions of use and the working precision. Generally speaking, this kind of drift is systemic or regularly, it can be used to describe the relationship between the deterministic function, can use a certain method of compensation, and is a very mature approach of systematic drift compensation. (2) random drift rate: refers to the specified operating conditions drift rate in non systematic time-varying component, this kind of drift is random, such as disturbance torque electronic circuit noise, friction, temperature gradient caused by the nature of it.

The MTi inertial sensor data acquisition device is tied to the human leg, with the normal walking and acquisition of the signal data series, about 852 steps, the sampling frequency is 130 Hz, the data will be stored in the TXT file. The scene experiment as shown in Fig. 3. Will preparation good Kalman filtering program kalman11.m open in matlab7.0, signal output data and open the inertial sensor in the stationary state, simulation experiment is carried out and the corresponding movement in the state of TXT file into the Kalman filter program.

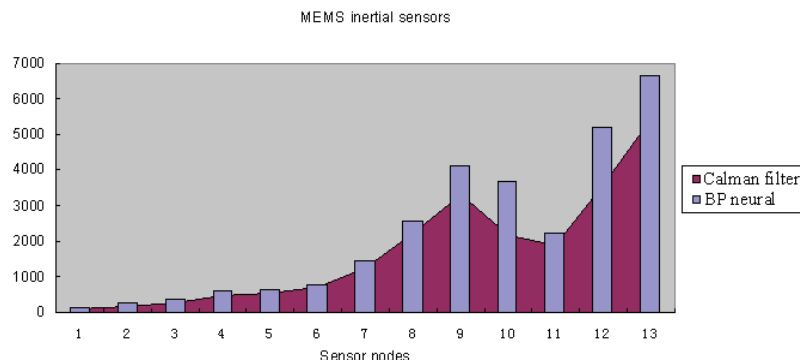


Fig. 3. Comparison signal processing of MEMS inertial sensors based on Kalman filter with BP neural network.

In the carrier in motion when the inertial sensor accelerometer and gyroscope signals sampled data, through the MATLAB maps, X axis and Y axis of gyroscope measured angular velocity gyroscope,

obtained by integral point of view, the green line to the X axis, Y axis blue dotted line. Can be seen from the chart, the existence of relatively large drift by the gyroscope points obtained angle, which rely on

untreated gyroscope output signal can not get a long time accurate carrier attitude angle.

BP neural network algorithm, the core idea is to reverse the spread of forward propagation and error signal information signal. The input signal from the input layer to the hidden layer, transmission, the final output layer obtained by converting output signal output, this is the forward propagating signal. The network output signal, obtained between the output signal and the expected output of the difference value of the error signal. The error signal from the output layer to reverse propagation, and according to the error signal correction output layer, and it is hidden layer and the threshold value matrix of input layer, in order to improve the output of the network effect. In every training session, positive signal propagation in the process of the network, the weights and thresholds are invariant.

## 5. Conclusions

Highlight the shortcomings of inertial navigation is the navigation accuracy decreases with the time increasing. Because of the existence of the core components of the gyro drift error of inertial navigation instrument, the carrier working time increasing, deviation from the reference position angle increases, the calculation error measurement and real-time location and speed increasing, the navigation accuracy decreases. In order to improve the precision of inertial navigation, the need to improve the measurement precision of gyroscope and accelerometer, but due to the manufacturing process, to improve the precision of the already difficult or increase micro inertial instrument accuracy, have to pay expensive cost. Therefore, the research of inertial sensor signal processing, mainly to complete the following several aspects: analysis of the gyroscope and accelerometer structure and working principle, and analyzes the source of error, the error model is suitable for it. The paper put forward using BP neural network and Kalman filter to signal processing of MEMS inertial sensors.

This paper uses BP neural network data forecast, we should first establish the BP neural network. The BP neural network construction, generally from the network level, the number of neuron and learning rate and other aspects of each layer are considered. For the BP neural network, there is a very important theorem. In addition, this paper also studies the implementation of Kalman filter, and based on the MATLAB7.0 environment prepared by the accelerometer and gyroscope won the attitude angle program.

## References

- [1]. Liu Meng, Sui Hulin, Wang Jun and Ma Qingbo, Firefighter indoor dead-reckoning system with inertial sensors, *International Journal of Digital Content Technology & its Application*, Vol. 5, No. 12, 2011, pp. 259-265.
- [2]. Yongbin Li, Prediction model of traffic based on wavelet analysis and BP neural network, *International Journal of Digital Content Technology & its Application*, Vol. 6, No. 22, 2012, pp. 775-784.
- [3]. Ren Ya-Fei, Ke Xi-Zheng, Selection of wavelet decomposition level in multi-scale sensor data fusion of MEMS gyroscope, *International Journal of Digital Content Technology & its Application*, Vol. 4, No. 8, 2010, pp. 209-215.
- [4]. Chen Limin, Chang Mingyu, Xu Shizhe, Liang Yin, Analysis of interference between multiple Kinect sensors and a noise reduction method for mobile robots, *Journal of Convergence Information Technology*, Vol. 7, No. 21, 2012, pp. 27-35.
- [5]. Xuejun Li, Xin Li, Lingli Jiang, Guangbin Wang, M. Ka Pickavet, AE signal fault recognition based on improved lifting wavelet denoising and BP neural network, *Journal of Convergence Information Technology*, Vol. 7, No. 22, 2012, pp. 719-727.
- [6]. Yue Wang, Qingquan Liu, Jiahong Zhang, Min Li, Solar Radiation Error Correction of Sounding Humidity Sensors, *Advances in Information Sciences & Service Sciences*, Vol. 4, No. 22, 2012, pp. 581-588.
- [7]. Yu Zhou, Jun Li, Xiaoming Zhou, Study on EEG password based on AR power spectrum and BP network, *Journal of Convergence Information Technology*, Vol. 7, No. 9, 2012, pp. 6-14.
- [8]. Paul C.-P. Chao, Chun-Yin Tsai and Chih-Kuo Chang, Hybrid high sensitivity MEMS microphone fabrication processes, *Research Notes in Information Sciences*, Vol. 5, 2010, pp. 1-5.
- [9]. Shengguang Peng, An experimental study of higher mathematics teaching based on Matlab software, *Journal of Convergence Information Technology*, Vol. 7, No. 18, 2012, pp. 473-480.
- [10]. Xiang Pengcheng, Luo Kun, The evaluation for the behavioral risk of principal participants in construction project based on BP neural network, *Advances in Information Sciences & Service Sciences*, Vol. 4, No. 14, 2012, pp. 97-107.
- [11]. Li Yang, Jinxue Sui, Zhilin Zhu, Burner flame recognition and combustion diagnosis based on back propagation neural network, *Advances in Information Sciences & Service Sciences*, Vol. 3, No. 6, 2011, pp. 13-22.
- [12]. Xu Wang, Kun-Li Wen, Zhong-Yu Wang, The development of Matlab toolbox in measurement error analysis, *Journal of Convergence Information Technology*, Vol. 6, No. 8, 2011, pp. 200-212.
- [13]. Deng Yao-Hua, Han Wei, Liao Qing-fu, Wu Li-Ming, Regression calculation model of flexible material processing deformation based on distributed sensors measurement, *Advances in Information Sciences & Service Sciences*, Vol. 3, No. 11, 2011, pp. 208-212.

## An Embedded-technology-based Security Monitoring System Design of Intelligent Building

Yuanyi ZHANG, Ying ZHANG

School of Architecture, Fuzhou University,  
Xueyuan Road No. 2, Fuzhou, 350108, China  
Tel.: (86)-591-22866392, fax: (86)-591-22866380  
E-mail: [yuanyifzu@gmail.com](mailto:yuanyifzu@gmail.com)

*Received: 18 June 2013 / Accepted: 25 August 2013 / Published: 30 September 2013*

---

**Abstract:** Security monitoring system is the important content of safety management in intelligent building. This paper aimed at the defects of security monitoring system in intelligent building, and used embedded technology, Internet technology, video compression/decompression technology, sensors technology to design a security monitoring system based on Internet. Users can detect the illegal intrusion and fire hazards indoors in real-time, through computers or mobile phones. The validity and efficiency of the system was validated via test-experiment. The results show that this system has several merits such as good safety, good generality, simple operation, easy maintenance, low cost and so on. As an indispensable part of digital home, this system has extremely important realistic meanings to the future's construction and development for intelligent building. Copyright © 2013 IFSA.

**Keywords:** Intelligent building, Internet technology, Security monitoring, Sensor technology.

---

### 1. Introduction

Intelligent building is a new discipline. It is a product which combined with information technology, automation technology, modern communications technology, microelectronics, building technology and other advanced technology. Meaning from the engineering, the intelligent building is to set building automation systems, communication network systems, office automation systems and security systems in the buildings, and to make a uniform management. It is a system engineering which combined with monitoring, service and management, and to achieve optimization. As the building intelligence is gradual increase with the development of science and technology, and its contents have been enriched. So, there is no uniform definition of the "intelligent building" in the international arena to now. With the development of social economy and promote high-tech applications,

due to negligence caused by various types of fire accidents have occurred, a variety of criminal means to become more subtle, more specialized. Therefore, to enhance monitoring efforts inside and outside of buildings is particularly important.

At present, the security monitoring program of intelligent building is mainly achieved through the two subsystems: video surveillance system and fire detection and alarm system. Video monitoring system, also known as closed circuit monitoring system, is mainly acquiring the signals through the front of the camera, monitor, intrusion detectors and other equipment, and sending all kinds of information to the matrix host computer of central control room through the decoder that field configuration and the transmission lines, then the host switch and display all kinds of signals to different output devices. Fire detection and alarm system is a controller which mainly consisted by the primary backup power

supply, fire alarm, and fault alarm. It collected the fire signal, and displayed the controller state via LED [1, 2]. Therefore, either from the video surveillance system or fire detection and alarm system, their structure is relatively complicated and the installation costs are high, it is not suitable for the needs of ordinary families. Thus greatly restricts the spread and development of intelligent building. In addition, the traditional video surveillance system used analog signal transmission, and it requires a lot of video recorders, video tapes to store image information, which is bound to bring a lot of wiring work, a large number of images stored in the work, a lot of image retrieval [3]. Moreover, in the operation, video surveillance system and fire detection and alarm system are two independent systems, when the fire hazards and illegal intrusion occurred simultaneously, they can not be controlled unity.

Therefore, this paper plans to use embedded technology, Internet technology, video compression/decompression technology and so on, integrated video surveillance system with fire detection and alarm system. Then through the Internet to transmit video signals and fire signals, use of computer hard disk system to store images, so that to save the system installation costs and reduce the workload of image storage and retrieval effort.

## 2. System Design Scheme

Security monitoring system consisted of the main controller AT91SAM9260, Internet interface circuit, memory circuit, video capture circuit, and sensors module (body sensors and smoke sensors). Among them, the video capture circuit and the body sensor mainly achieved the video monitoring of system. When the body sensors detected there were any illegal intrusions happened, the system will alarm and record the live video through video capture circuit. Smoke sensors main achieved fire detection and alarm function, when the fire hazards happened, the system will issue a warning signal and displays the location of the fire. Fig. 1 illustrated the structure diagram of system.

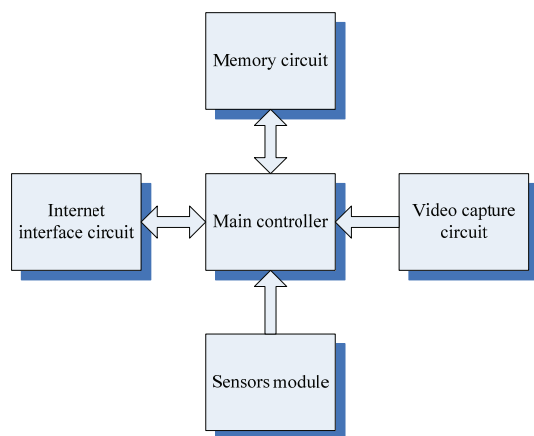


Fig. 1. The structure diagram of system.

## 3. Hardware Design of System

Considered the developing cost and the need of this system is to use Java language to develop embedded Web Server, we selected AT91SAM9260, the 32 bit micro-controller with ARM9EJ-S kernel [4], as the main controller. It has abundant system resources, and support Java language (ARM Jazelle Technology for Java Acceleration). It includes a 10/100M Base T Ethernet MAC, which can process TCP/IP protocol easily, and transmit IP packet. The system can access Internet via LAN, router or switch. And users can use Internet to detect the illegal intrusion and fire hazards indoors in real-time.

### 3.1. Internet Interface Circuit

As the video signal transmission is achieved through the Internet, so the design of Internet interface circuit is very important. Internet interface is composed of MAC controller and physical interface from the view of hardware. Since AT91SAM9260 has integrated Ethernet controller (EMAC), it only needs to realize the physical interface which can reduce the complexity of system design and improve its efficiency [5, 6]. In this system, it took DM9161 as Ethernet's physical interface. DM9161 connect with Internet through a network insulate transformer HR911105. It is very simple to connect Ethernet controller DM9161 with the network insulate transformer HR911105, so long as connected DM9161 receiving signal wire RX+, RX- and sending signal wire TX+ and TX- with HR911105 RD+, RD- and TD+, TD- respectively. Network insulate transformer HR911105 has integrated the RJ45 joint. Therefore it may access Internet directly through HR911105. Since HR911105 takes the work status indicator light itself, it can indicate the system's work status. The signal's sending end and receiving terminal access Internet through HR911105.

### 3.2. Memory Circuit

Taken into account that the system needs to take up a lot of memory resources in dealing with video images, the system extended a K9F1208UOM chip which is a 64 M NAND Flash memory produced by Samsung, and a HY57V561620CT-H chip which is a 32 M SDRAM memory produced by Hynix Semiconductor Inc.

### 3.3. Video Capture Circuit

Video capture circuit mainly constituted of the image sensor. The AT91SAM9260 has an Image Sensor Interface (ISI). So it can connect a CMOS Image Sensor to capture all kinds of images via ISI.

And the processor can transform data before it saving images to the memory through DMA channel. The principle of video capture circuit is illustrated in Fig. 2.

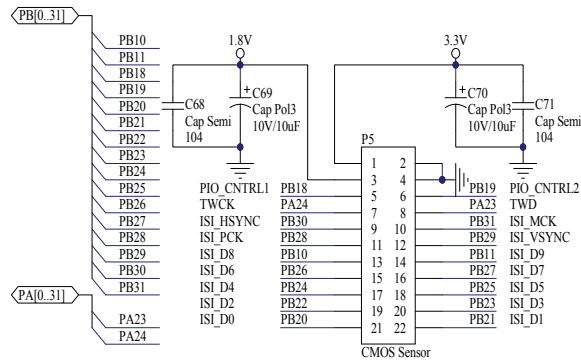


Fig. 2. The schematic diagram of video capture circuit.

### 3.4. Sensors Module

The sensors module consists of two parts: body sensors and smoke sensors. Fig. 3 illustrated the schematic diagram of sensors module. In this system, we designed two channels body sensors and two channels smoke sensors. The body induction module is mainly for the function of guard against theft. In this system we chose TDL718 which is a body induction module based on infrared technology. The module has many merits such as high sensitivity, reliable, and it can induce automatic. The second pin of TDL718 will output a high level when there were some people entering its inductive scope, and stop the high level then output a low level when people left the inductive scope. Therefore, the system can know whether there were any people enter the user's house illegal via detect the level signal of PC25 and PC26. The system will automatically alarm and notify the image sensor to record live video when there are some abnormal conditions happened.

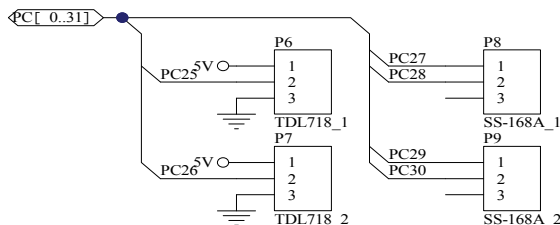


Fig. 3. The schematic diagram of sensors module.

The function of smoke sensors is to realize fire alarm. The system will detect the ions of smoke through smoke sensor. When the concentration of smoke indoor is exceeded the limit, it will automatically alarm and display the location of the fire on the home page of system. We chose SS-168A

as the smoke sensor in this system. SS-168A has two dry contacts (output pins), when it detects there are some fire risks happen, its buzzer will give alarm and the indicator light will display, then outputs signals to the host controller from the two dry contacts. AT91SAM9260 will call Embedded Web Server to display the location of the fire on the home page of system after it received and processed the signals.

## 4. Software Design of System

Security monitoring system used embedded Linux 2.6.19 as the software platform, and adopting modularity design. So that it has good portability and good expansibility. The kernel and root file system of Linux 2.6.19 was programmed in the Flash memory inside, so the boot process of embedded Linux 2.6.19 must be based on the target platform to prepare, and to plan the address space of memory.

### 4.1. Planning of Memory Address Space

In this system, the address space of flash memory was from 0x0200A000 to 0x0800A000, so we can divide the flash memory. The address space from 0x0200A000 to 0x0280A000 was the storage space of Boot-loader, from 0x0280A001 to 0x0400A000 was used to store the kernel image file, from 0x0400A001 to 0x0800A000 was used to store the root file system, and as a device file was loaded into the system. Fig. 4 illustrated the address space planning of flash memory.

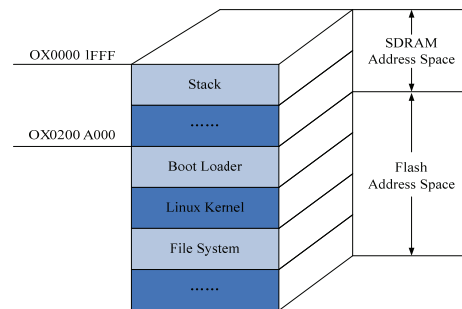


Fig. 4. The address space planning of flash memory.

After the system reset, according to the system's setting, system program counter (PC) points to the SDRAM address 0 at first, to complete the necessary system initialization. Then, the system program counter jump to flash address 0, that is 0x0200A000, to complete the system SDRAM initialization, and the Boot-loader code will be copied to the SDRAM address 0, which is 0x00001FFF. Subsequently, PC pointer will jump to the flash address 0x00001FFF again, to executive the Boot-loader kernel and load code in the internal of SDRAM memory. The reasons of executive Boot-loader within the SDRAM without

in flash memory, is because the speed of executive code in SDRAM is much faster than in the flash inside. So it can help to speed up the boot speed of system.

Then the work of Boot-loader was copied the compressed kernel image to SDRAM address 0x0000A004, and transfer the address parameters of the root file system to the kernel. After the kernel had copied to SDRAM, PC pointer will jump to 0x0000A004, to extract the kernel, and executive the kernel boot. The system will find the root file according to the address parameter which transferred from Boot-loader, and load to security monitoring system.

In accordance with the above arrangement, we download Boot-loader, kernel and root file system to the Flash in succession through the software SAM-BA1.11 and tftp, then we can start the system, embedded Linux can be boot up into the normal state.

#### 4.2. Design of Video Compression Algorithm

Embedded Web Server has unified interface and communication protocol, so it can provide unified operation mode and control interface based on Internet Explorer. In this system, there were four modules on the Embedded Web Server: Files module, HTTP request and process module, Java Applet data request and process module, and Monitoring module. Monitoring module is responsible for monitoring ports, and establishing a connection between the system and the Explorer of the client through three times handshake process of TCP protocol. When there is a request from the Internet Explorer, the monitoring module will judge whether it is a HTTP request or a Java Applet request according to the port number. Then call HTTP request and process module or Java Applet data request and process module to start the corresponding process. Files module was realized by the files system of Embedded Operating System. The Files module including GGI processing files (Common Gateway Interface), Static web page files and Applet code files. And the GGI processing files have two functions: one is to realize user authentication mechanism; another is to parse and process the parameters which come from HTTP message, when the users set up the parameters for control through Internet Explorer.

### 5. System Testing

In order to confirm the correctness of system design, we took a comprehensive test to the system functions (Including the communication interface, data transfer and overall performance.) and network performance. Before system testing, we should set up related parameters, such as IP address, gateway address, server address, the video frame size, number of frames per second acquisition, network bandwidth and so on.

### 5.1. System Functional Testing

First of all, we establish two hyper terminals in one personal computer, one is connected with the serial port another is connected with Socket. When we input some data on the first hyper terminal, the second hyper terminal was response immediately. It means the communication interface of system is well [8]. Secondly, we connected the system with the serial port of personal computer through electrical level transfer circuit, and verified the data transmission via hyper terminal. Thirdly, we establish a Web Server through Java Script language and PWS Server. As the embedded Web Server has a standard interface format and communication protocol, the web servers embedded in equipment can provide a unified browser-based operation and control interface, for any legitimate users who accessed the network [9]. Finally, used a net wire to connect this system with a router (or switch), and communicated with the Web Server through Internet Explorer. After several experiments, the results show that it is easy to establish connection between security monitoring system and Internet, and the users can detect the illegal intrusion and fire hazards indoors in real-time, through computers or mobile phones. Fig. 5 illustrated the operation interface of security monitoring system.



Fig. 5. The operation interface of security monitoring system.

The whole safety monitoring system can be set by monitor settings, including the storage path of video and the save format. At the same time, you can set that system to automatically record video and save it when someone illegally broken into the monitor area. And you can download the video which temporarily stored in the experimental system through the option of video download. Report print is mainly for intrusion detection and fire detection. It can print the monitoring data within a period of time, to print. As the intelligent building security monitoring system is based on B/S model, so the function of background management was to management and set the embedded Web Server. When the body sensors detected that someone had

entered monitor region, the system will display “1” in the corresponding position of intrusion detection. Similarly, when the corresponding location of the smoke sensor was displayed “0”, it means the system detected there was no fire hazards, displayed “1” to means detected fire hazards.

## 5.2. Network Performance Testing

Network performance testing was mainly for the video monitoring of system. It was necessary to install the WildPackets Etherpeek Nx software in the host before testing. Through the software, we can capture the network performance data of system. Here, we set to sample the network data packet every 10 seconds, the main network parameters which captured by the software are: the packet number and byte count of sending every 10 seconds, the utilization of network bandwidth and so on. We tested the system through setting different bandwidth. Table 1 illustrated the network performance situation of system in different bandwidth.

**Table 1.** Network Performance in Different Bandwidth.

Setting Bandwidth (Kbps)	The average bandwidth (Kbps)	Display Effect
100	131.5	More blurred, with Mosaic
200	211.4	Slightly blurred, no mosaic phenomena
600	605.8	Still images clear, motion images slightly blurred
1200	960.6	Still images clear, motion images is also clear

When the system was running at a steady state, and the setting bandwidth was 1200 Kbps, the resolution of video stream was  $640 \times 480$ , and the frame rate was 50. In this case, the network performance of the system was shown in Fig. 6.

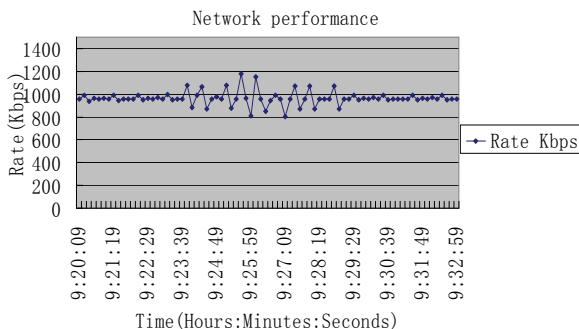


**Fig. 6.** The network performance of video monitoring system.

From Fig. 6 we can see clearly that before 9:23:39 and after 9:29:19, there were still image-based in monitor area, and the average rate of video transmission was to 960.6 Kbps. There were sharp moving objects in monitor area between 9:23:39 and 9:29:19, lead to a greater jitter of video transmission rate, the maximum rate was 1189 Kbps and the minimum rate was 806 Kbps. The tests found that, for still images or motion do not change much, the overall compression ratio was high, and using smaller bandwidth can obtain clear graphics. And motion pictures are required for higher bandwidth, the system can be based network bandwidths, automatically adjust the amount of data the size of the single frame to ensure picture fluency. When the network bandwidth is a serious shortage, the display screen will appear mosaic phenomenon. After several experiments, the results show that it is easy to establish connection between Security Monitoring System and Internet, and the users can detect the illegal intrusion and fire hazards indoors in real-time, through computers or mobile phones.

## 6. Conclusion

The information technology whose core is computer technology, control technology and measurement and control technique, is rapid development since the 1990's. It makes people to set a higher request to security, comfort and efficiency of building environment. As the important content of safety management in intelligent building, the design of security monitoring system will affects the performance of the entire intelligent building directly. There were many merits of this system, such as good safety, good generality, simple operation, easy maintenance, low cost and so on. As an indispensable part of digital home, this system has extremely important realistic meanings to the future's construction and development for intelligent building, it can meet the needs of security monitoring for an ordinary home.

## Acknowledgements

This work is supported by 2012 National Science and Technology Support Program of China (No.2012BAJ14B05), the National Natural Science Foundation of China (No.51278123), Natural Science Foundation of Fujian Province (No.2011J01303), and Education Department Foundation of Guangxi Province (No. 200808LX273).

## References

- [1]. R. R. Yager, Some measures relating partitions useful for computational intelligence, in *International Journal of Computational Intelligence Systems*, Vol. 1, No. 1, 2008, pp. 1-18.

- [2]. Fang Qiansheng, Experimental Guide to Intelligent Buildings, *China Communication Press*, 2003.
- [3]. Geng Jianjun, Design and application of video surveillance system in intelligent building, China, *Shandong University Master's Thesis*, 2007, 5.
- [4]. AT91 ARM Thumb Microcontrollers AT91SAM9260 Preliminary ([http://www.atmel.com/dyn/resources/prod\\_documents/6221s.pdf](http://www.atmel.com/dyn/resources/prod_documents/6221s.pdf)).
- [5]. Xiang Yang, Yuanyi Zhang, Rongyang Zhao, Study and design of home intelligent system based on embedded internet, in *Proceedings of the International Conference on Embedded Software and Systems Symposia (IEEE CS PRESS)*, 2008, pp. 344-349.
- [6]. M. V. C. Da Silva, N. Nedjah, M. de Macedo Mourelle, Optimal IP assignment for efficient NoC-based system implementation using NSGA-II and MicroGA, *International Journal of Computational Intelligence Systems*, Vol. 2, No. 2, 2009, pp. 115-123.
- [7]. Mei Dacheng, Yang Daqian, Zhou Yong, Embedded wireless video capture system design, *Microcomputer Information*, Vol. 23, No. 7, 2007, pp. 19-20.
- [8]. Yuanyi Zhang, Xiang Yang, Design of phone remote measurement and control system in intelligent building, in *Proceedings of the 9<sup>th</sup> International Conference on Electronic Measurement & Instruments (IEEE PRESS)*, 2009, pp. 392-395.
- [9]. M. Can Filibeli, O. Ozkasap, M. Reha Civanlar, Embedded web server-based home appliance networks, *Journal of Network and Computer Applications*, Vol. 30, Issue 2, 2007, pp. 499-514.
- [10]. Bu Chunyuan, Xu Dahua, Development of intelligent laboratory-monitoring system, *Experimental Technology and Management*, Vol. 24, Issue 7, 2007, pp. 145-147.

2013 Copyright ©, International Frequency Sensor Association (IFSA). All rights reserved.  
(<http://www.sensorsportal.com>)

**Easy and quick sensors systems development**

**Evaluation Kit CD**  
**EVAL UFDC-1/UFDC-1M-16**  
International Frequency Sensor Association  
OPTYS Corporation

- 16 measuring modes
- Frequency range from 0.05 Hz up to 7.5 MHz (120 MHz)
- Programmable accuracy from 1 % up to 0.001 %
- RS232 (USB optional)

[sales@sensorsportal.com](mailto:sales@sensorsportal.com)  
[http://www.sensorsportal.com/HTML/E-SHOP/PRODUCTS\\_4/Evaluation\\_board.htm](http://www.sensorsportal.com/HTML/E-SHOP/PRODUCTS_4/Evaluation_board.htm)

## Design of Novel Intelligent Transportation System based on Wireless Sensor Network and ZigBee Technology

Zhou YU, Weizeng GAO, Xiangang ZUO

School of Information and Engineering, Henan Institute of Science and Technology,  
Henan Xinxiang, 453003, China  
Tel.: 13598608819  
E-mail: eduzhouyu@163.com

*Received: 2 July 2013 /Accepted: 25 August 2013 /Published: 30 September 2013*

---

**Abstract:** Intelligent transportation system (ITS) applied in the city traffic is mainly reflected in the microscopic traffic information collection, traffic control and guidance, to improve the efficiency of traffic system. Wireless sensor network has excellent characteristics, and it can provide an effective means for information collection of intelligent transportation system and can monitor the intersection in all directions of the vehicle. ZigBee is a short distance data communication network protocol and network layer based on 802.15.4. This design uses the mesh model and builds a ZigBee personal network by using ZigBee network coordinator and PAN ID. The nodes of wireless sensor network on the ZigBee module of the physical network address is sole, and it can be sent to the ITS through the physical address information. This design can improve the signal controller and intelligent public traffic system is effective and intelligent. *Copyright © 2013 IFSA.*

**Keywords:** Intelligent transportation system (ITS), ZigBee, Wireless Sensor Network.

---

### 1. Introduction

Wireless sensor networks usually have the following characteristics: 1 self organization. Node sensor network system with automatic networking function, nodes can communicate with each other to coordinate the work of more than 2 routes [1]. The communication distance, power control and energy constraints, when a node cannot communicate directly with the gateway, required by other nodes to forward data transmission, so the network data transmission route is a multi-hop and dynamic topology; 3. In some special applications, wireless sensor networks are mobile, sensor nodes may terminate the work for energy or other fault, and these factors will make the network topology changes.

Intelligent transportation system (ITS) applied in the city traffic is mainly reflected in the microscopic

traffic information collection, traffic control and guidance, to improve the efficiency of traffic system by increasing the effective use and management of traffic information, mainly by the information acquisition input, control, output strategy execution, between each subsystem data transmission and communication subsystem.

Wireless sensor network is formed by a network of sensor nodes, can be all kinds of information the observer deployment area of real-time monitoring, sensing and collecting nodes interested in the perception of object (such as light, temperature, humidity, noise and harmful gas concentration phenomena), and after processing the information in a wireless way sent by the wireless network, finally sent to the observer.

Wireless sensor network is novel technology of integration of the short-range wireless communication technology, microelectronics, sensor,

embedded system, and it being used in related fields of intelligent transportation systems requires data collection and detection. Intelligent transportation system is from the system's concept, the vehicle and the road taken together, using a variety of high-tech system to solve the problem of ideas emerges as the times require. It is the advanced information technology, data communication transmission technology, electronic sensor technology, electronic control technology and computer processing technology used to effectively integrate the entire transportation management system, and built up a kind of in a large range, the role of comprehensive, integrated transportation management system with real time, accurate, efficient. It is currently abroad to solve city and highway traffic jam, main measures to improve the traffic safety and protect environment, but also solve the traffic construction limits, namely by the land resource constraints, to improve the international competition ability, breeding measures and emerging industry slightly.

ZigBee technology is a kind of to automation and wireless control of low rate, low power consumption, low price of wireless network solution. The communication rate it demands less than Bluetooth, wireless communication function provided by the battery power supply equipment. The ZigBee supports the mesh network topology, the wireless device to work in the public frequency band. Information acquisition subsystem through the sensor acquisition vehicle and road information, strategy control subsystem according to the set target (such as the traffic volume, maximum or average waiting time shortest etc.) use computational methods (such as fuzzy control, genetic algorithm and so on) to calculate the best scheme, and outputs a control signal to the execution subsystem (usually traffic the signal controller), to guide and control the passage of vehicles, to achieve goals. The paper presents design of novel intelligent transportation system based on wireless sensor network and ZigBee technology.

## 2. Application of Wireless Sensor Network in Development of ITS

With the development of social economy, traffic demand growth rate is still much higher than the road network capacity growth rate. The world city development is facing serious traffic congestion, pollution, accidents, environmental degradation and other obsession. Traffic problems have gradually become hot and difficult issues of universal social concern. However, blindly through the allocation of funds for construction, construction of multi-layer road, widen the road traffic, only limited vehicle use passive measures to solve the immediate as pressing danger, the long run, it is not feasible.

In the structure of wireless sensor networks, the sink node is installed on both sides of the road to form a self-organizing multi-hop mesh based on

Mesh network architecture, the sink node traffic information dedicated terminal sensor node and each adjacent collection consists of a star network communications, the final data will be gathered to the gateway node. The gateway node can be used as a module is installed in the traffic signal controller, through a proprietary network signal controller, sending data will be collected to the VTS center for further processing.

Most of the wireless sensor network is powered by battery, the working environment is bad. But the number of large, replace the battery is very difficult, so low power consumption is one of the most important criteria for the design of wireless sensor networks [2]. In the network nodes of some module does not work or is in a dormant state, it can be the power supply circuit is disconnected to save electricity, when the instruction to wake up, then connected to the power supply circuit in order to ensure the normal operation of the system. This can save energy effectively, prolong the battery power supply time and service life, but also to ensure the quality of the whole network system, prolong the service life, as is shown by equation 1.

$$I_{\sigma}(i, j) = \sigma_{\Omega_{ij}}, \Omega_{ij} = \{(i-1)l+1 \leq x < il, \\ (j-1)l+1 \leq y < jl\} \quad (1)$$

The application of wireless sensor network, the node location information is necessary during data acquisition; monitoring information without location information is usually meaningless. To determine the node position of the location of the incident or collection of data is one of the most basic functions of wireless sensor network. In order to provide location information effectively, the sensor nodes are randomly arranged in the network deployment is completed must be able to determine their location. Classification and localization algorithm generally for distance positioning algorithm and range-free localization algorithm based on.

GIS-T as the support system of geographic information and traffic data storage and application, has strong traffic information service and management function, can be applied in many fields of traffic planning, traffic construction, traffic management and information services, become one of the core system is indispensable in the construction of ITS current. The basic function of GIS-T and traditional GIS, including editing, graphics and display and measurement layer and other functions, mainly used for input, store, edit the spatial and attribute data, as well as the mapping and spatial analysis, as is shown by equation 2.

$$C = \sum_{i=0}^{L-1} p_i \log_2 \frac{p_i}{q_i} \quad (2)$$

Need to transform the existing traffic signal controller to implement bus priority function in intelligent transportation system. By adding sensors and other auxiliary equipment, traffic signal controller can estimate the bus arrived at the intersection of time (travel time), calculate the vehicle to give priority at intersections need (can choose the number of passengers as priority), then select the priority of appropriate control strategies, by adjusting the green signal ratio of bus priority release.

The practical application of the process technology in wireless sensor network, there exist the following factors: (1) the cost: the cost of sensor nodes is an important factor which restricts the large-scale application, according to specific application requirements the balance cost, data precision and energy supply time [3]. (2) energy: applications most need network using disposable independent power supply system, so the requirement of network low energy consumption, prolong the network life cycle, which is an important factor to expand the application of. (3) The miniaturization: in some areas, demand volume micromotion node, do not have any effect on the target itself, or can not be found to perform specific tasks.

The quality of road transport, the main road traffic flow, traffic capacity, saturation, and it is thereby reducing the network equilibrium utilization rate. Dependence of the main road is too large, the construction of roads and the slip road far lag, lack of general auxiliary relief way for the main road intersection, reduce traffic reliability. Layout of the road planning is not reasonable, the lack of overall planning and optimization of road construction, most of the provinces and cities administrative region as the center, partial weight to become a system oneself, does not meet the need of the lateral ties. From the national highway layout analysis, road network density distribution is uneven, and with the economic development in different regions is not coordinated.

$$E[(X(0) - \mu_x(0))(X(0) - \mu_x(0))^T] = P_x(0) \quad (3)$$

In this paper, the widely application of wireless sensor network are discussed, and introduce its typical applications in various fields, and summarize the factors restricting the application of wireless sensor network and the current research hot spot. Wireless sensor networks will eventually become contact information world and the objective physical world interface, which humans can learn the objective physical world through sensors network information and make corresponding measures.

In the design of ITS wireless sensor networks, network nodes according to different functions, need to separately design. The terminal node, the sink node and gateway node software function. The terminal nodes equipped with different sensors for motor vehicle information acquisition and road information acquisition.

Each part of the power system mainly realize the following functions: power supply is composed of

2 blocks of 12 V lead-acid batteries in series, providing a DC voltage of 24 V for the system; battery detection module mainly carries on the sampling via the output voltage of the power supply, in order to get the battery power consumption information, to ensure the real-time charging the battery the normal work of the entire system; the various power switch control module is mainly according to the working state of the system load, controlled by a switch to decide whether the load power supply, in order to reduce standby power consumption, prolong the using time of the battery; power converter module is mainly used as DC-DC converter module conversion construction unit to realize power supply voltage to provide the appropriate voltage for load.

$$W_{2,j} f(n) = 2^{-j/2} \int_{-\infty}^{\infty} f(x) \psi(2^{-j} x - k) dx \quad (4)$$

The problem of mobile positioning of wireless sensor network node can be described in the following state space. In order to  $\mathcal{L}$  said discrete time, It said the location distribution of  $f$  time node,  $Dt$  node in  $t-1t$  moment to moment from the observation of  $T$  beacon node receives the value. Conversion equation  $P(t|t-1)$  estimation of the position of the node previously said the current location based on it [4]. The observation equation  $P(LT, Ot)$  said in a given observation probability under the Condition node at the location of  $Lt$ . The goal is to filter algorithm of the node location distribution of  $P(t|O0, O1... Over time, Ot)$  iterative estimation. The value of  $Lt$  by a group of sampling ( $N$ ) indicates the position distribution of  $LT$  node, and each time algorithm to iteratively calculate on the sampling sequence, because  $Lt-1$  is in all previous observations of a concentrated reflection, so using only  $Lt-1$  and  $Ot$  can calculate  $Lt$ .

The gateway node is required in the network coordinator, responsible for the initiation of the network, configuration of the network address, network maintenance, maintenance of member node binding table, is also responsible for the collecting preliminary data processing and delivery of traffic signal controller is transmitted to the upper level information center, need more storage space, computation and communication ability.

Time-varying and spatial characteristics of road traffic are linked, are indispensable. Time-varying contains spatial relations, spatial expression of implicit time on traffic. Therefore, the paper before the prediction of road traffic flow, considering the traffic data of the time-varying and spatial characteristics, the fusion of adjacent space object subsequence in time series theory, construct some combination of the two time series models, a full table of factors influencing road traffic, in order to improve the prediction accuracy of road traffic flow.

The application of application of wireless sensor network in development of ITS is shown in Fig. 1.

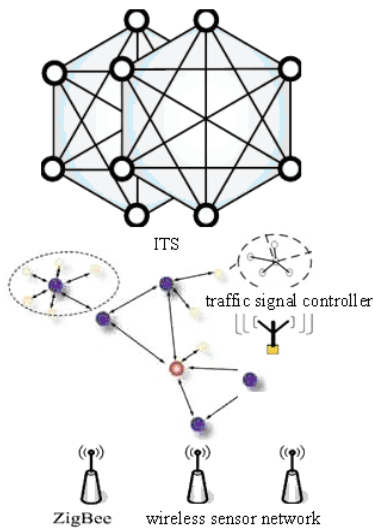


Fig. 1. Application of Wireless Sensor Network in Development of ITS

The nodes of wireless sensor network using modular design method, each node includes a wireless transceiver module, main control module and the function module. System receives the master sent by wireless transceiver module command code, main control module to the command decoding, complete control of each function module (open acquisition, timing reset). System to complete the repeated test, so each test is completed to the experimental data (shock wave data, environment variables, timing and positioning information) stored in the data storage management, at the same time to prepare for the next test.

Information is the use of text, numbers, symbols, language, image and other media to represent events, things, phenomena such as content, or the number of features, and thus to the people (or system) provides a new facts and the real world, as the production, construction, operation, management, analysis and decision-making. As a kind of information, traffic information is directly reflect the public travel status, is the key to reflect and traffic related phenomena in nature, characteristics and the motion state of knowledge, it reveals is the essence of traffic entities and their relationship, this solution is all kinds of traffic data, as is shown by equation 5.

$$R(W_j^\sigma, F_e) = \frac{E[(\xi_{W_j^\sigma} - E(\xi_{W_j^\sigma}))(\xi_{F_e} - E(\xi_{F_e}))^T]}{\sqrt{D(\xi_{W_j^\sigma})D(\xi_{F_e})}} \quad (5)$$

Physical layer communication protocol: Research on sensor network transmission media, band selection, modulation. The data link layer protocol: To study the network topology, channel access methods, topology includes planar structure, hierarchical structure, hybrid structure and Mesh structure, channel access includes mixing fixed allocation, random competition or the. The network layer protocol: study routing protocol, routing

protocol is divided into plane and cluster two, plane protocol node equal status, easy to expand, but lack of management; cluster routing that cluster as the cluster head and the cluster members, convenient maintenance and management, research focus is integrated two routing mode.

The power conversion circuit chip mainly used is the DC/DC module power of Jin Shengyang, and with 78 series of three terminal voltage power supplies. The DC / DC module power supply product features are: wide input voltage range (2:1 to 4:1), efficiency as high as 85 %, high and low temperature performance is good, can meet the requirements of industrial products, technical working temperature: -40 ~ +85°C, isolation voltage of 1500 V DC, dual output, metal shielding package, international standard pin, MTBF>1 000000 H.

In order to meet the system test task, the wireless sensor node uses the modular design, each functional module through a SPI interface link. Because the system functional requirements make a module and a plurality of modules link communication, the interface circuit of SPI working in master-slave mode different, using a single SPI interface switch, is bound to reduce intermeddle communication speed and flexibility [5]. On the basis of the programmable logic device CPLD has its programming flexibility, expansibility, extended SPI interface inside the module, the test results show that SPI interface circuit design, a simplified block connections, improve the speed, system scalability, and improves the overall performance of the system.

Sensor nodes in terms of computational resources and storage resources is shortage, the testing method of polygon approximation to determine the direction of first node, the method is completely based on the connectivity between nodes, only need the beacon node hops position broadcast information, so no extra power consumption and hardware requirements for node. In this paper, a test method inside polygon point, hop between hypotheses M and A is 4, then hops between nodes 1 and A is 3, 2 and A hops between nodes is 5; M and hop count between B is 3, then the number of hops between 2 and B is 2, hops between nodes 1 and B is 4.

This paper introduces the basic concepts of wireless sensor network, analyzes the power module for the crucial importance of wireless sensor network, the system can work safely and reliably, introduced the realizing process of the power system of wireless sensor network and the module of the circuit structure and function, and through the experiment to prove its performance to reach the scheduled performance.

$$\begin{cases} D_{j,F}^\xi(m,n) = D_{j,A}^\xi(m,n) & E_{j,A}^\xi(m,n) \geq E_{j,B}^\xi(m,n) \\ D_{j,F}^\xi(m,n) = D_{j,B}^\xi(m,n) & E_{j,A}^\xi(m,n) < E_{j,B}^\xi(m,n) \end{cases} \quad (6)$$

Time-varying traffic information refers to information traffic flow characteristics change over time. The transportation system is a complex

nonlinear system by the people involved, the traffic flow over time; according to the people's travel activities have a significant change of flow. Time rotation, alternating seasons, reincarnation seven days a week, will play a role can not be ignored for transportation. According to the observation of the traffic information, the annual traffic flow will reach a peak during the holidays, then dropped to the bottom; weekly traffic flow over the weekend on Monday rose, the rapid decline; commuting time traffic flow is far higher than other time. All of these changes in traffic flow, there have all kinds of connections with time varying contact with it.

The spatial and temporal characteristic of the traffic information determines its ambiguity. Fuzzy traffic information are the main operation of space position of traffic flow is influenced by many factors, such as rain and snow weather, road maintenance, fuzziness of roadside parking, fuzzy attributes, fuzzy relationship between fuzzy time as well as the three Traffic accidents [6]. These factors caused the transport uncertainty, such as the link capacity degradation, link travel time fluctuation, the traffic flow change etc. Traffic information to describe the performance of traffic flow and therefore is uncertain.

The sensor is an important device for information collection, data collection by the sensor, known as "how nervous tentacles" it achieve its network, is the current hot research problem. Most of the current measurement and control system, sensors are wired, but in some special cases, wired cable connection will certainly cause a lot of inconvenience, can not meet the needs of reality. With the emerging wireless technologies (such as Bluetooth Technology) development and reduce the price of chip, wireless way on many occasions are used to replace the original cable interface. Wireless sensor networks will become an important direction of sensor development.

### 3. Novel Intelligent Transportation System based on ZigBee Technology

Usually, the ZigBee node's IEEE64 address is defined by the users themselves, they are written in the node EEPROM. Each terminal node network, the center node will assign it a 16 network short address. For the terminal node used for the first time, can through the process and center node binding so that the binding table terminal node address information appears in the center node, the data transmission more stable. For smaller networks, since sent directly to the central node, you can direct the use of 0x00 as a target.

Traffic flow forecasting is an important problem in ITS study and transportation planning. In the present road traffic flow measurements have done many researches, prediction technology is mainly divided into two categories: one category is the qualitative forecasting techniques; one is the quantitative prediction technology. Qualitative

prediction technique is in the extensive collection, understand the objective background, basic data objects based on the law of the development of object, research and analysis, and, in a certain period of time to determine the object of development trend, forecast the development object. The common qualitative forecasting methods are empirical method, analogy method.

ZigBee is a short distance data communication network protocol network layer based on 802.15.4. ZigBee in the union, when the protocol development to the latest version and it is each layer of the protocol have been intended to improve. ZigBee network is applied to the region within the scope of coverage, through the gateway equipment, seamless connection and implementation of Ethernet /GPRS network, to achieve the perfect low cost remote monitoring application [7].

ZigBee is a short distance, low rate, low power consumption, low cost and low complexity wireless transmission technology, which works in no need to register for 2.4 GHz ISM band, the transmission rate of 100 ~ 250 Kb/s, the transmission distance is 10 ~ 75 m, the typical distance of 30 m. ZigBee is an extension to the IEEE 802.15.4 standard, which is based on the 7 layer of the open systems interconnection standard (OSI) model. The network layer (NWK) and application layer (APL) the design of the framework is responsible for making ZigBee alliance, IEEE is making the physical layer (PHY) and medium access control layer (MAC) standard. Among them, the APL framework includes application support sublayer (APS), ZigBee device object (ZDO) as well as the application object specified by the manufacturer. System structure as is shown in Fig. 2 of the ZigBee.

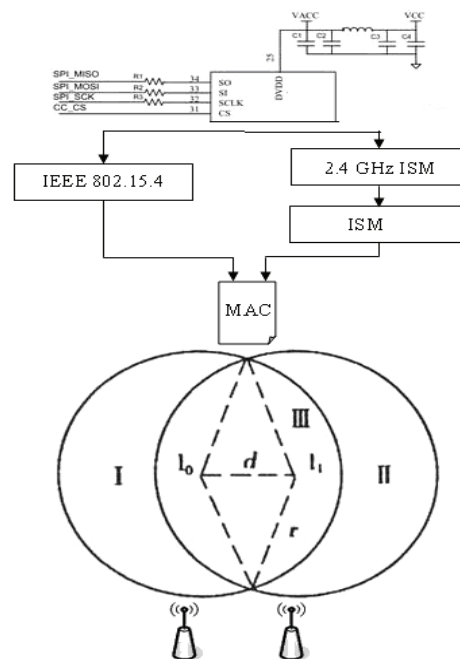


Fig. 2. Intelligent Transportation System based on ZigBee Technology Figure.

The IEEE802.15.4 specification based on ZigBee technology, have the following characteristics: low power consumption, 2 5 number batteries can support a node 6~24 months; the network capacity, network up to a node, and to support the tree, star, mesh and other networking mode; the transmission distance, the two node room the outside transmission distance can reach several hundred meters, increasing transmit power of up to several thousand meters; the reliability is high, with multilevel security model; the cost is low, the simplified ZigBee protocol stack open, working in the 2.4 GHz unlicensed ISM band.

The geographic information data set contains the spatial relationship between abstract space sequence is the first step to traffic flow time series modeling based on prediction. The spatial relationship between spatial objects with complicated shape representation and abstraction is the main goal of building a space sequence [8]. Effects of spatial relation of traffic activity in the geography space is obvious, such as: traffic activity frequency of two adjacent city is higher than the activity of traffic frequency two city distance between, say two adjacent city traffic more closely linked, as is shown by equation 7.

$$Cov\{X, Z\} = E[(X - \mu_X)(Z - \mu_Z)^T] = C_{XZ} \quad (7)$$

ZigBee technology adopts IEEE 802.15.4-2003 standards of physical layer and media access control layer as ZigBee physical layer and media access control layer, ZigBee alliance in the provisions of the framework of network layer and application layer; ZigBee technology has powerful function of the equipment of the Internet, he supported the star structure (Star), reticular formation (Mesh) and cluster (Tree) three kinds of self-organizing wireless network type, especially the network, he has the reliability of network robustness, strong.

With the rapid development of domestic economy, the city scale is expanding constantly, especially all kinds of traffic tools is growing more rapidly, which makes the contradiction of city traffic supply and demand have become increasingly prominent, and rely on the expansion of the road traffic infrastructure to alleviate the contradiction is difficult to continue. In this case, the intelligent transportation system (Advanced Public Transportation Systems, APTS) also emerge as the times require, and become a research hotspot in recent years. In the various technologies involved in intelligent transportation system, wireless communication technology is particularly attract sb.'s attention. ZigBee is a new short-range, low-rate wireless communication technology, has gained more and more attention and application.

The main services of GIS-T spatio-temporal data mining is to predict the traffic activities between regions, belonging to the regional traffic data mining areas, therefore, in accordance with the definition of the field of spatial sequence, in view of the influence of regional spatial relations between traffic in the

field of transport activities, the regional spatial relationship and communication abstraction.

In the traffic information collection, terminal nodes can be used non-contact magnetic sensor to collect and sensing area of vehicle speed, vehicle distance information. When the monitoring range of vehicles entering the sensor, important information terminal nodes through the magnetic sensor to collect the running speed of vehicles, and send that information to the next node timing wake up. When a node induction to the vehicle, with the vehicle driving time between two sensor nodes estimate, we can estimate the average speed of the vehicle, as is shown by equation 8.

$$W_{j,k} = \sum_{l=0}^{L_j-1} h_{j,l} X_{2^{l(k+1)-l-1} \bmod N_j - 1} \quad (8)$$

ZigBeeRFIC+MCU are ZigBee protocol stack. Use of this product is the advantage of relatively low cost, disadvantage is the need to be familiar with ZigBee architecture, called the underlying protocol, so the development cycle is long, need to have high frequency circuit design experience such as TICC2420+MSP430 [9]. Containing RF MCU, the advantage of low cost, circuit design are relatively less. The disadvantages are needed to be familiar with ZigBee protocol such as FreescaleMC1322X, long development cycle.

The function of this system is to collect data, and transmits the data to the multi-hop manner to the sink node. The sensor node consists of a sensor module, a processor module, wireless communication module and power supply module is composed of 4 parts, as shown in Fig. 2. Among them, the processor module is responsible for the control and management of the entire node; sensor module is responsible for the acquisition of the predetermined monitoring regional information, and do some data conversion; wireless communication module is responsible for communication protocol between nodes according to a certain mutual communication; energy supply module for the node power supply, provide the required parts run electricity.

#### 4. Design of Novel Intelligent Transportation System based on Wireless Sensor Network and ZigBee

The technology of wireless sensor network is a wireless technology with short distance, low complexity, low power consumption, low data rate, low cost, is a set of development based on IEEE 802.15.4 Wireless Standard Development of the network, security and application software technology [10]. It supports 3 kinds of self-organized wireless network types, namely the star network, cluster tree network and mesh network topology. Mesh is a high reliability Ad Hoc network.

In a wireless sensor network deployment, the sink node can transport facilities installed at the roadside column, bar and so on, gateway nodes can be integrated to the intersection traffic signal controller inside, special terminal sensor node can fill in the road or installed on the side of the road, the movement of vehicles on the road can also install node dynamic sensor to sensor networks.

Time and space has been the focus problem in traffic field, two major factors also affect traffic activities. Temporal-spatial fusion sequence modeling, is the core of this prediction method of traffic, the basic idea is to consider the spatial and temporal characteristics of significant road traffic information, combined with road traffic complexity, take the time as the factors and space are equally important to the method in GIS-T space, construction sequence space object forecast target and its adjacent, Sorama Ko sequence as an element of time series into time series, form a time series model of space-time elements fusion, and on the basis of this research and Trend prediction.

$$S_t = \frac{1}{M} \sum_{i=1}^M \tilde{x}_i \tilde{x}_i^T = \frac{1}{M} \Phi_t \Phi_t^T \quad (9)$$

In the stop there are usually many bus arrive at the same time, a corresponding number of bus stops, suitable for the use of the star network wiring network [11]. But in order to ensure the reliability of the network, when the bus stop outside the channel is blocked, can be forwarded to other bus stop by the routing node, this design uses the mesh (Mesh) network model. The distribution in the bus lines on the electronic bus stop board is configured as a coordinator, and will reach the bus configuration for the router. When a channel and PAN ID and start selecting stop coordinator ZigBee network, the establishment of a ZigBee network (PAN). Once the

coordinator has launched PAN, allows routers and terminal node join PAN.

The router to join PAN, will receive a 16 network address, and can send and receive PAN data from other devices. The PAN coordinator of the network address is always 0. The bus stop on the ZigBee module of the physical network address is the only, can be sent to stop by physical address information.

A plurality of terminal nodes will each collection and initial processing of information by the sink node convergence to the gateway node, data fusion, get traffic and road vehicles, vehicle velocity and other information, so as to provide accurate information for the control of input traffic signal. Through the installation of temperature and humidity, light intensity, gas detection sensor etc. to the terminal node, also can detect road condition, visibility, vehicle exhaust pollution.

This paper introduces the application of performance characteristics of Xbee Pro module of ZigBee / IEEE802.15.4 protocol compatible and in the intelligent transportation system in wireless communication. At present, the system is released for Xbee Pro module mesh version of firmware, greatly enhance the network function. With the increasing popularity of ZigBee technology, Xbee Pro module will be applied more widely in the wireless sensor network.

Wireless sensor network has many solutions, including the chip manufacturers introduced external single-chip RF chip and integrated RF, single chip microprocessor. ZigBee RF chip is often used in design of node in Atmel AT86RF230, TI CC2420, Freescale MC1319x and MC1320x, Microchip MRF24J40 etc. In addition, chip manufacturers introduced a single chip solution, such as TICC2430 to use the CC2420 chip architecture, in a single chip integrated ZigBee RF front-end, memory and micro controller; JN5121/JN513x single chip Freescale of MC1321x/MC1322x and Jennic solutions.

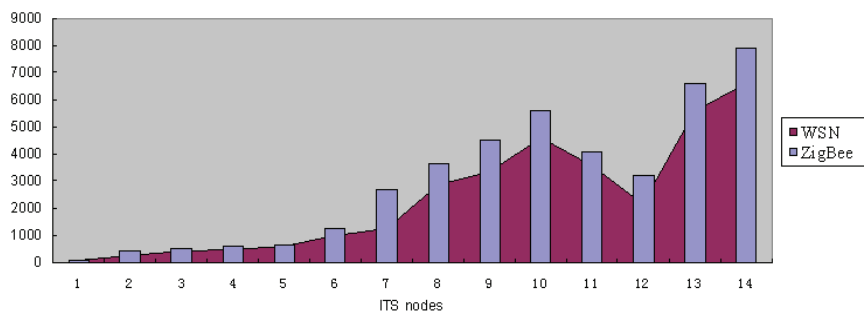


Fig. 3. Comparison of novel intelligent transportation system based on wireless sensor network with ZigBee.

The following considerations in the design of intelligent traffic system for wireless sensor network node: low power design of node. The terminal nodes are battery (available solar battery) power supply; the node to low cost. In large-scale traffic information acquisition and deployment, node costs will be the

key project; data processing and storage capacity of the node. Some nodes need high-speed information acquisition and recognition algorithm, so the need for data processing ability. Also need to consider in the limited space of the storage procedures, data, and online update function code.

Wireless sensor network has excellent characteristics, can provide an effective means for information collection of intelligent transportation system, can monitor the intersection in all directions of the vehicle, according to monitoring results, improved to simplify, improve the signal control algorithm, improve transport efficiency. The control system of wireless sensor network can be applied to the execution subsystem and guidance subsystem.

## 5. Conclusions

This system combines electronic technology, information technology, communication technology and system engineering in transportation applications in attracted attention, began to carry out large-scale test on road transportation intelligent. At first, this kind of research is called intelligent vehicle highway systems (IVHS), mainly research the road function and the intelligent vehicle, system function and gradually extended to the whole process of road transportation and related services, to become the impetus of intelligent transportation system of the road transportation modernization. The paper presents design of novel intelligent transportation system based on wireless sensor network and ZigBee technology. In the design of wireless sensor network gateway, need strong data processing ability, is used to realize the complex routing protocol and information processing. Imote2 Crossbow node using the MarvellPXA271 high performance, low power processor. The processor uses dynamic voltage scaling technique.

## References

- [1]. Li Dong, Gong Zhe, An Baoyu, Ou Yangxi, Cui Wei, Zhu Hongliang, A novel security management scheme in wireless sensor networks, *International Journal of Digital Content Technology & its Application*, Vol. 4, No. 10, 2012, pp. 36-44.
- [2]. Zifu Fan, Xiaoyu Wan, Research of on-demand multipath distance vector routing protocol based on QoS and node movement speed in wireless sensor network, *International Journal of Digital Content Technology & its Application*, Vol. 4, No. 10, 2012, pp. 306-314.
- [3]. CaiQian Zhang, Lei Ge, Using decision tree algorithm to construct intelligent traffic management system, Research of on-demand multipath distance vector routing protocol based on QoS and node movement speed in wireless sensor network, *International Journal of Digital Content Technology & its Application*, Vol. 4, No. 21, 2012, pp. 346-353.
- [4]. Lin Yong, Research on an wireless sensor network streaming media transmission based on the improved Rayleigh wavelet algorithm, *Journal of Convergence Information Technology*, Vol. 7, No. 11, 2012, pp. 52-59.
- [5]. Chun-Cheng Lin, Wen-Ping Chen, Shan-Chih Hsieh, Song-Shyong Chen, Design and implementation of ZigBee wireless controller module, *Advances in Information Sciences & Service Sciences*, Vol. 4, No. 18, 2012, pp. 106-115.
- [6]. Ouyang Xi, Li Dan, Zhang Jianyi, Liu Hongwei, Zhu Hongliang, Xin Yang, Malicious node detection in wireless sensor networks using time series analysis on node reputation, *Journal of Convergence Information Technology*, Vol. 7, No. 15, 2012, pp. 8-16.
- [7]. Jiping Li, Shouyin Liu, Shixun Wu, A design of remote computer house monitoring and control system based on ZigBee WSN, Research of on-demand multipath distance vector routing protocol based on QoS and node movement speed in wireless sensor network, *International Journal of Digital Content Technology & its Application*, Vol. 4, No. 12, 2012, pp. 233-240.
- [8]. Qian XiaoJun, Fan Dongping, Chen Congyan, Chu Qingsheng, Jiang Naisong, The vehicle positioning system based on the ZigBee technology of wireless sensor networks, *Journal of Convergence Information Technology*, Vol. 8, No. 7, 2013, pp. 383-391.
- [9]. Lu Yang, He Xin, Research on key technologies to target coverage algorithm in wireless sensor networks, *International Journal of Digital Content Technology & its Application*, Vol. 6, No. 17, 2012, pp. 542-550.
- [10]. Xian Feng Yang, Zhen Liu, The application of association rules mining in building intelligent transportation systems, *Journal of Convergence Information Technology*, Vol. 7, No. 20, 2012, pp. 575-582.
- [11]. Xiaoyong Yan, Huanyan Qian, Multivariate regression for location estimation in wireless sensor network, *Journal of Convergence Information Technology*, Vol. 7, No. 21, 2012, pp. 278-286.

## Method for Identifying Mechanical Vibration Source Based on Detected Signals by Optical Fiber

<sup>1</sup> Hongquan QU, <sup>1</sup> Guoxiang LI, <sup>2</sup> Liping PANG

<sup>1</sup> College of Information Engineering, North China University of Technology, Beijing, 100041 China

<sup>2</sup> School of Aviation Science and Engineering, Beihang University, Beijing 100191, China

<sup>2</sup> Tel.: +86-10-82313186, fax: +86-10-82316654

<sup>2</sup> E-mail: pangliping@buaa.edu.cn

Received: 6 July 2013 /Accepted: 25 August 2013 /Published: 30 September 2013

**Abstract:** A Optical Fiber Vibration pre-Warning System (OFVWS) has an ability to detect and identify vibration signals by using a optical fiber cable lain along with pipes, hence it has been widely applied in some safety fields, such as the pipeline transportation, national defense, military base and so on. In the application of the OFVWS, one of the key issues is to identify harmful mechanical vibration sources quickly and efficiently. In this paper, we analyzed vibration signal produced by mechanical vibration sources and extracted the signal features transmitted by the OFVWS. A conclusion was drawn that most of mechanical vibration sources have an obvious feature of fundamental frequency. Based on this conclusion, we developed a method to detecting and recognizing a mechanical vibration source based on a variation coefficient of fundamental frequency periods. This method is able to accurately judge if the detected vibration signals having a feature of fundamental frequency or not by calculating and analyzing its variation coefficient of fundamental frequency periods. Field test results showed that this method can identify various harmful mechanical vibration sources, and have a high probability of detection and recognition, and a low probability of false alarm. *Copyright © 2013 IFSA.*

**Keywords:** Optical fiber sensor, Fundamental frequency, Mechanical vibration model, Variation coefficient.

### 1. Introduction

With the rapid development of pipeline transportation, the construction and ground-breaking around the pipeline can be seen everywhere, and they threaten the security of the pipeline seriously. The OFVWS can monitor the long-distance soil vibration information by using the fiber lain along with the pipeline as a distribute sensor. This system can warn the staff the destroying pipeline events happening as soon as possible, so it plays a role of safety early warning.

The common harmful mechanical vibration signals are generated by some working mechanical equipments and construction machines, such as the excavators, broken road machines and so on, which have a high power and exist for a long time. They have very high probability of damaging the pipeline and threaten the safety of the OFVWS seriously because they may break the surface of road and damage the fiber and pipeline quickly. Therefore, it is a key to detecting and identifying a mechanical vibration source accurately and quickly by using the OFVWS.

At present, researches on the recognition of vibration signals include: linear classifiers [1], neural network [2], support vector machines [3, 4], etc. These methods all need to study and train on a large number of samples, hence have some issues, such as a large amount of calculation and a convergence of training.

In addition, there also exist some harmless interfering vibration sources in the fiber-optic warning area even through their power are high and their duration time are long, for example, a train passing vibration source. These vibration sources just pass through the area covered by optical fiber frequently, and do not generate any harmful action to threat the warning area. However, conventional vibration detection method might confuse these harmless vibration sources with the harmful mechanical vibration sources so as to send the staffs a false alarm of harmful vibration source frequently. This can influence the recognition badly, and is unfavorable for the reliability of the system running.

In this paper, a method to identifying mechanical vibration source is presented by using a vibration source feature model and the detected vibration signal data by the OFVWS. This method can distinguish between a harmful mechanical vibration source and a harmless train vibration source, and identify the mechanical vibration source automatically without using a learning and training process. Therefore, its amount of computation is reduced greatly. This method can reduce the probability of error identification by improve the correct recognition probability.

## 2. Working Principle of OFVWS

Fig. 1 shows the working principle of a vibration source measuring and locating system [4]. A distributed optical fiber sensor, which is laid along with the pipeline, can detect a vibration signal along the pipeline.

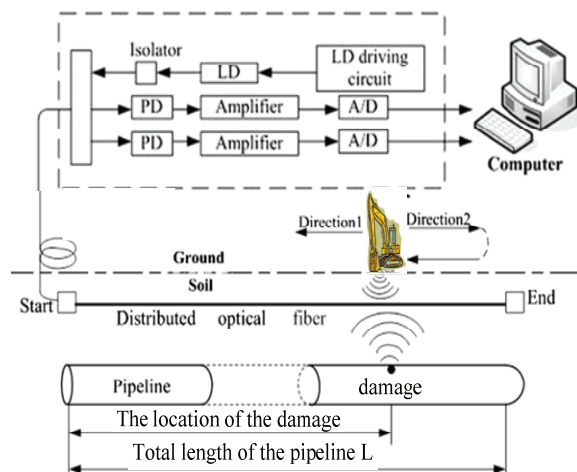


Fig. 1. Working principle of OFVWS.

The detected vibration signals will be transported by the optical fiber sensor to photoelectric detectors, and then is transmitted through photoelectric conversions, Amplifications and AD conversions, and finally to a computer for further process and analysis. In this way, the OFVWS can monitor the vibration signals in its coverage areas in real-time.

The sampling frequency of the OFVWS is 25 kHz and every 1024 sampling data form a frame. Because of an interference caused by low frequency signal and high frequency signal in the signal transmission, such as the power supply (220 V, 50 Hz), the OFVWS uses an 800-order FIR band-pass filter to pre-process all the collected data. Its pass-band range from 100 Hz to 3 kHz and its frequency response is shown in Fig. 2.

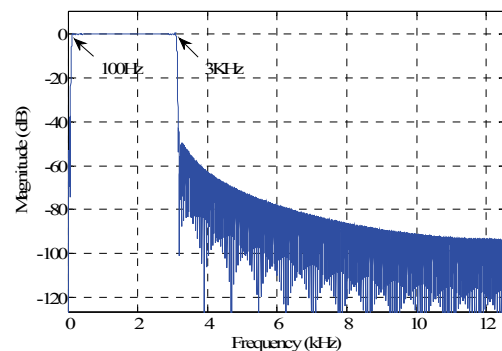


Fig. 2. Frequency response of the FIR filter.

## 3. Time and Frequency Domain Analysis of Vibration Signal

Generally, a vibration source will turn to be a harmful vibration source when the power of signal is high enough and its duration time is long enough. However, there exist two kinds of this vibration sources which have the above features in the nature, one may be a passing train, and another be a working construction machine. The former vibration source does no harm to a safety of the pipeline and the OFVWS, hence it dose not need to send alarm to the safety staffs. But the later may be harmful. Therefore, it is very important to distinguish between the train vibration signal and the mechanical vibration signal.

The traditional vibration signal analysis method is a time domain and frequency domain analysis. Here, we also use this method to analyze a mechanical vibration signal and a train vibration signal detected from some oil pipelines, respectively.

### 3.1. Signal Power and Time-domain Waveform Analysis

We analyze the signal power by using one-minute vibration signal data and calculate their single power, as shown in Fig. 3. Then we choose 20 frames data

(about 0.8 seconds), which have relative higher power than the other chosen signal. We will analyze their amplitude and observe their time-domain waveforms. Fig. 4(a) and Fig. 4(b) show the time-domain waveforms of the corresponding mechanical and train vibration signals.

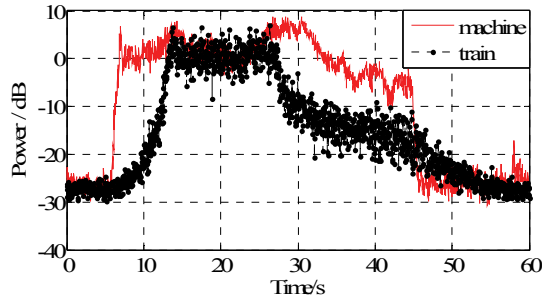
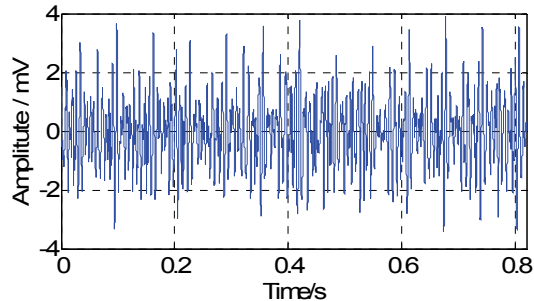
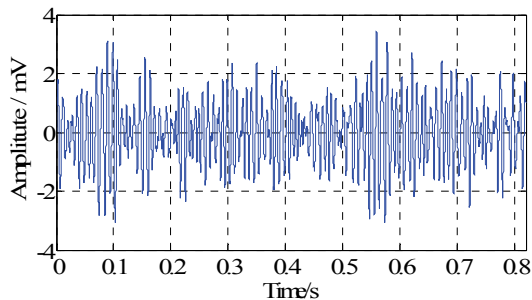


Fig. 3. Single power analysis results.



(a) Mechanical vibration signals.



(b) Train vibration signals.

Fig. 4. Time-domain waveforms.

From Fig. 3-4 we can observe that:

(1) The signal power and duration time of the mechanical and train vibration source are very similar. It is very difficult to distinguish them by using the signal power feature, as shown in Fig. 3.

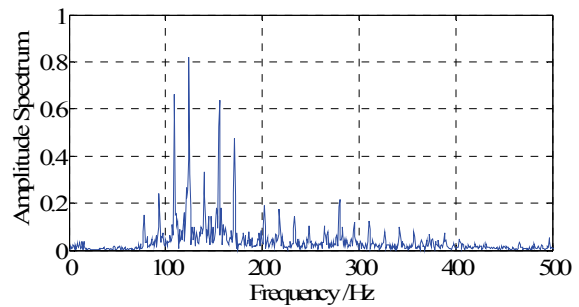
(2) Their time-domain waveforms in Fig. 4(a) and Fig. 4(b) are also very similar, and their amplitudes are about 2 mV.

A conclusion can be drawn that it is difficult to distinguish between the mechanical and train vibration signals by only using signal power and time-domain waveform analysis.

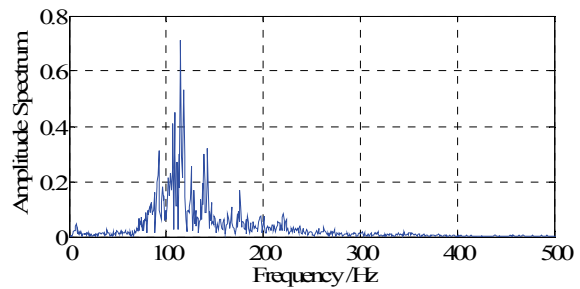
Next, we will analyze their frequency features of these vibration signals.

### 3.2. Fundamental Spectrum Analysis

Because the low frequency part of signals is filtered by the band-pass filter as shown in Fig. 2, the signals lower than 100 Hz frequency are filtered. The frequency of filtered data is as shown in Fig. 5.



(a) Mechanical vibration signals.



(b) Train vibration signals.

Fig. 5. Frequency spectrum analysis.

We can observe a difference between these signals from Fig. 5. The frequency spectrum of the mechanical vibration signals contains multiple discrete spectral lines, and the intervals between adjacent spectral lines are almost a fixed value. This feature is clearly different from the train vibration signals. Therefore, a mechanical signal has a periodical change feature. We infer that this feature can be used as a basis to distinguish between the mechanical and train vibration signals.

### 4. Feature Extraction of Mechanical Vibration Source

In section 3, we infer that the studied harmful vibration signals have a periodical change feature in its frequency spectrum. We can use a complex periodic mechanical signal model to represent the studied signal [5-7], as shown in Equation (1):

$$x(t) = \sum_{n=1}^{\infty} A_n \cos(2\pi nft - \theta_n) \quad (1)$$

where  $x$  is the amplitude of a vibration signal;  $f$  is the fundamental frequency of a vibration signal, which can represent a feature of spectral line intervals, Hz;  $A_n$  and  $\theta_n$  are the amplitude and an phase of the  $n^{\text{th}}$  Harmonic waves, respectively;  $t$  is the time, s;  $n$  is the order of harmonic wave.

For the studied vibration signals, we suppose  $n=13$ ,  $f=15$  Hz, and then obtain the simulation results, as is shown in Fig. 6(a) and Fig. 6(b). The simulation signals are processed by a band-pass filter further, as shown in Fig. 6(c) and Fig. 6(d).

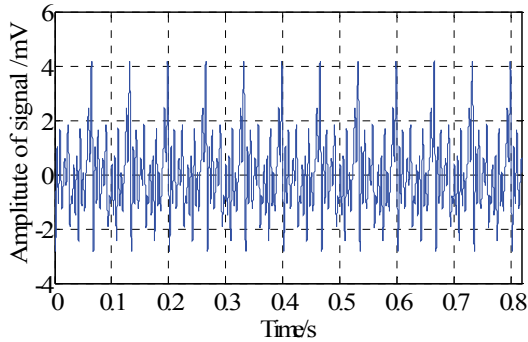


Fig. 6 (a). Frequency domain waveform of the simulated mechanical vibration signals.

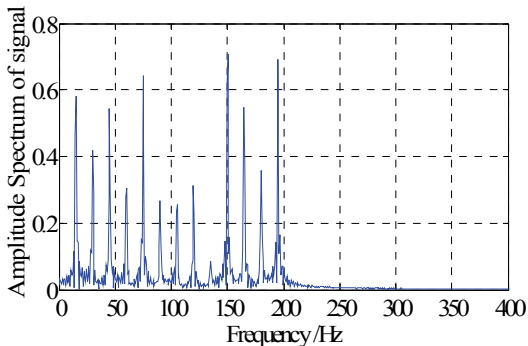


Fig. 6 (b). Frequency domain waveform of the simulated mechanical vibration signals.

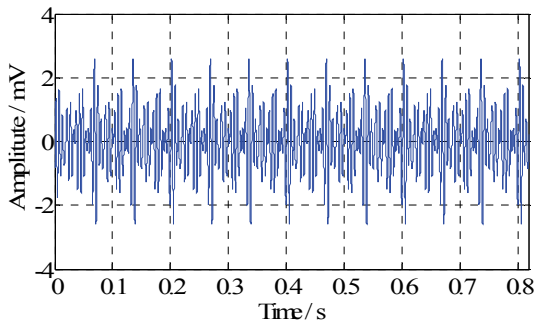


Fig. 6 (c). Frequency domain waveform of the filtered vibration signals.

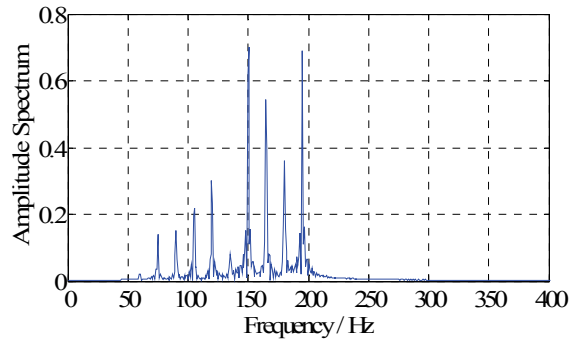


Fig. 6 (d). Frequency domain waveform of the filtered vibration signals.

Comparing Fig. 4(a) and Fig. 6(c), Fig. 5(a) and Fig. 6(d), separately, we can know that the identification model, as shown in Equation 1, is correct. Therefore, we can extra the feature of fundamental frequency of signal,  $f$ , to identify a harmful mechanical vibration source. If a vibration signal has its fundamental frequency feature, then it is inferred to be a mechanical vibration signal; otherwise to the contrary.

## 5. Mechanical Vibration Source Identification Method

From the above analysis, we know that the key of identification is to extract a fundamental frequency feature of vibration signals. Therefore, we will develop a method to identify a kind of high-power mechanical vibration source existing for long time. The presented method is based on a variation coefficient of fundamental frequency. First, we will extract fundamental frequency information of vibration signals from their autocorrelation coefficients. From this result, we can infer if the vibration signals have fundamental frequency feature or not. Second, we measure the stability of fundamental frequency periods by calculating a variation coefficient of peak value intervals in an autocorrelation coefficient curve. This index can directly reflect if the curve having a periodicity or not. At last, we establish a strategy to identify a mechanical vibration source automatically.

### 5.1. Extraction of Fundamental Frequency Information

Autocorrelation is the cross-correlation of a signal with itself, and it can find repeating patterns, such as the presence of a periodic signal which has been buried under noise, or identifying the missing fundamental frequency in a signal implied by its harmonic frequencies. Therefore, we use the autocorrelation coefficient to extract fundamental frequency information.

The sampling frequency of the OFVWS system is 25 kHz, which means a huge calculation load. In order to reduce the amount of calculation, we use a down-sampling method to sample the vibration signal data.  $X = \{x_1 \dots x_{10} \dots x_{20} \dots x_{30} \dots x_{20n}\}$  represents an observed vibration signal sequence and its length is  $20 \times n$ . We down-sample signal data  $X$  from every 10 samples. The down-sampling of  $X$  is  $Y$ :

$$Y = \{y_1, y_2, y_3, \dots, y_{2n}\} = \{x_{10}, x_{20}, x_{30}, \dots, x_{20n}\}, \quad (2)$$

where  $Y$  is the observed down-sampled sequence of  $X$  and its length is  $2 \times n$ .

We can obtain a short-time autocorrelation coefficient [8] of  $Y$  with Equation (3):

$$R(k) = \frac{\sum_{i=1}^n \left( y_i - \frac{1}{n} \sum_{m=1}^n y_m \right) \left( y_{i+k} - \frac{1}{n} \sum_{m=k+1}^{n+k} y_m \right)}{\sqrt{\sum_{i=1}^n \left( y_i - \frac{1}{n} \sum_{m=1}^n y_m \right)^2} \sqrt{\sum_{i=1}^n \left( y_{i+k} - \frac{1}{n} \sum_{m=k+1}^{n+k} y_m \right)^2}} \quad (3)$$

where  $k=1,2,\dots,n$ ,  $R$  is the short-time autocorrelation coefficients and  $R = \{r_1, r_2, \dots, r_n\}$ .

By using Equation (3) we can obtain  $R(k)$ ,  $1 \leq k \leq n$ . A autocorrelation coefficient curve figure of  $R(k)$  can be formed. In this curve figure, there will be some local maximal peaks. Here we record the number of these local maximal peaks,  $d$ , and the time interval of the adjoined two maximal peaks,  $\Delta T$ . A time interval sequence will be obtained,  $\Delta T = \{\Delta T_1, \Delta T_2, \dots, \Delta T_{d-1}\}$ .

The coefficient of variation is a statistical magnitude which is used to measure the degree of variation of the measurement value. The value of the

coefficient of variation can illustrate the degree of dispersion of the samples. The smaller of the value means the smaller degree of variation of the measured values, which means more stable of the measured value. Since the coefficient of variation is a dimensionless number, it can represent the significance level of the local maximal peak intervals of the autocorrelation coefficients. Hence this index can directly reflect if the observed vibration signals having a periodicity or not. The formula of a coefficient of variation [9, 10] is defined as follow:

$$cv = \frac{\sigma}{|\mu|} \times 100\%, \quad (4)$$

$$\mu = \frac{1}{d-1} \sum_{i=1}^{d-1} \Delta T(i) \quad (5)$$

$$\sigma = \sqrt{\sum_{i=1}^{d-1} [\Delta T(i) - \mu]^2}, \quad (6)$$

where  $cv$  is the  $\mu$  coefficient of variation of the measurements, and  $\sigma$  are the mean and standard deviation of the measurements, respectively;  $d-1$  is the number of the measurements.

### 5.2. Implementation of Identification Strategy

We establish a strategy to identify a vibration source by using Equation 2-6. Fig. 7 shows the implementation of this identification strategy.

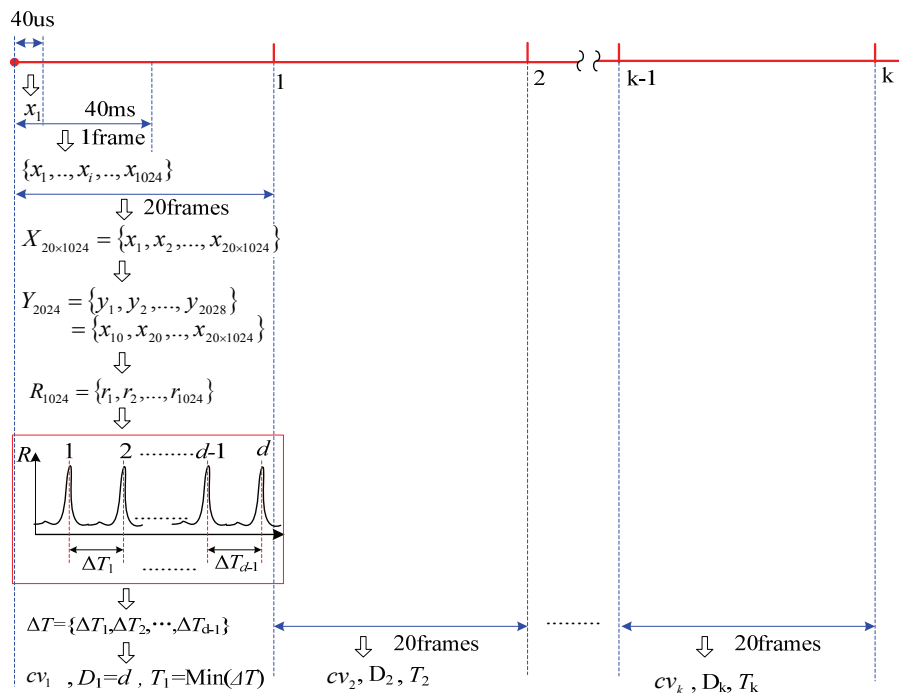


Fig. 7. Implementation of identification strategy.

The steps of the strategy are as follows:

(1) The OFVWS detects a vibration signal,  $x_1$ , every  $40 \mu\text{s}$ . Every 1024 data of the signals comprise one frame. The signal power ( $P_1$ ) and the duration time ( $Time_1$ ) for these vibration signals will be calculated. Only when  $P_1$  and  $Time_1$  are both bigger than their thresholds,  $P_0$  and  $Time_0$ , respectively, then the presented identification strategy is started. We will process the vibration signal data every 20 frames (about 0.8 s), that is,  $X = \{x_1, x_2 \dots x_{20 \times 1024}\}$ .

(2) Down sample the signal data  $X = \{x_1, x_2 \dots x_{20 \times 1024}\}$  with Equation (2), and obtain its down-sampled sequence,  $Y = \{y_1, y_2 \dots y_{2048}\}$  in this 20 frames.

(3) Calculate the short-time autocorrelation coefficients of  $Y$ , and obtain the corresponding short-time autocorrelation coefficient sequence,  $R = \{r_1, r_2 \dots r_{1024}\}$ , and a curve figure of  $R$  will be formed. From this curve, we can observe the number of the frequency spectrum intervals,  $d$ , and  $\Delta T = \{\Delta T_1, \Delta T_2, \dots, \Delta T_{d-1}\}$  by setting the autocorrelation coefficient threshold as a floating value. Let  $D_1 = d$ . The minimum interval of the periodical frequency spectrum is the minimum value of  $\Delta T$ , that is,  $T_1 = \text{Min}(\Delta T_1, \Delta T_2, \dots, \Delta T_{d-1})$ . Only when  $D_1$  and  $T_1$  are both larger than their set values  $d_0$  and  $T_0$ , respectively, the presented identification strategy is continued.

(5) Calculate the variation coefficient of the intervals  $\Delta T = \{\Delta T_1, \Delta T_2, \dots, \Delta T_{d-1}\}$  for this 20 frames, that is,  $cv_1$ .

(6) Repeat the above step (1)-(5) to process the other 20-frame signals, then a variation coefficient sequence will be formed,  $CV = \{cv_1, cv_2, \dots, cv_k\}$ .

(7) If the minimum value of  $\{cv_1, cv_2, \dots, cv_k\}$  is less than a given threshold value,  $cv_0$ , then this indicates that the vibration signals have a periodicity and are generated by a mechanical vibration source. Otherwise it is not a mechanical one.

### 5.3. Identification Results

We analyze four kinds of signal data collected by the OFVWS from the pipeline of the China Petroleum Pipeline Bureau. The signal data of 'machine<sub>1</sub>' and 'machine<sub>2</sub>' are two different kinds of mechanical vibration signals. One was produced by an excavator and the other by a broken road machine. The signal data of 'train<sub>1</sub>' and 'train<sub>2</sub>' were produced by trains passing through the Lan-Zheng-Chang oil pipeline.

We will process these vibration signals by using the presented identification method, and evaluate its reliability. The autocorrelation coefficients waveforms of the mechanical and train vibration signals are shown in Fig. 8(a) and Fig. 8(b), respectively, and Fig. 8(c) and Fig. 8(d) show the intervals extracted in the autocorrelation coefficients of the mechanical and train vibration signals.

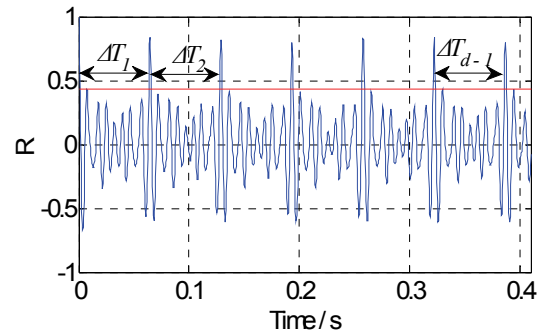


Fig. 8(a). Autocorrelation coefficients waveform of vibration signals and their intervals for mechanical vibration signals.

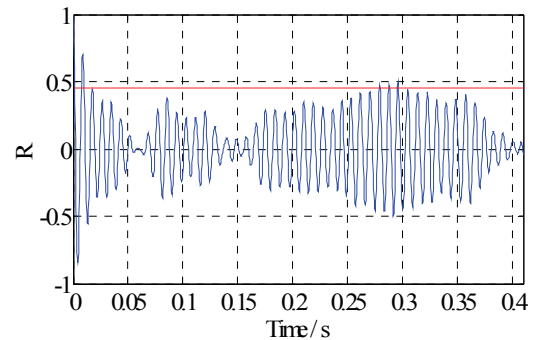


Fig. 8(b). Autocorrelation coefficients waveform of vibration signals and their intervals for train vibration signals.

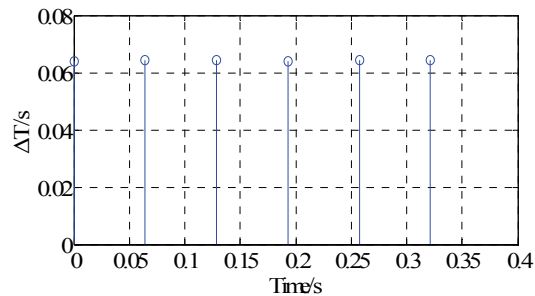


Fig. 8(c). Autocorrelation coefficients waveform of vibration signals and their intervals, extracted in the mechanical signals.

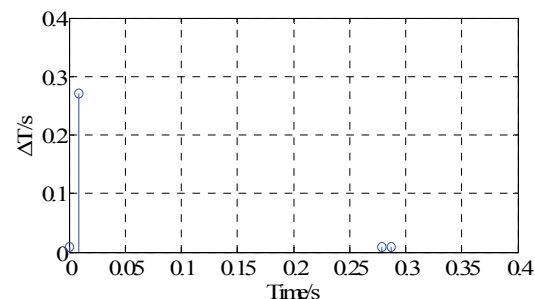


Fig. 8(d). Autocorrelation coefficients waveform of vibration signals and their intervals, extracted in the train signals.

From Fig. 8 we can observe that: the short-time autocorrelation coefficients of mechanical vibration signals have a stable periodicity, which is obviously different from the train vibration signal. We can extract the fundamental frequency period,  $\Delta T = \{\Delta T_1, \Delta T_2, \dots, \Delta T_{d-1}\}$ , with a suitable set threshold, as shown in Fig. 8(a).

Then we can calculate a variation coefficient ( $cv_k$ ) of the fundamental frequency intervals to measure the fundamental frequency stability of vibration signals. We set the power threshold,  $P_0$ , as -20 dB, and the duration time threshold,  $T_0$ , as 4 seconds. After extracting the local maximal peak intervals of the autocorrelation coefficients, we set  $d_0=5$  and  $T_0=60$  s, respectively. The floating threshold will adapt itself in order to obtain the effective intervals and let  $cv_0=10$ . Fig. 9 shows the results of  $cv$ .

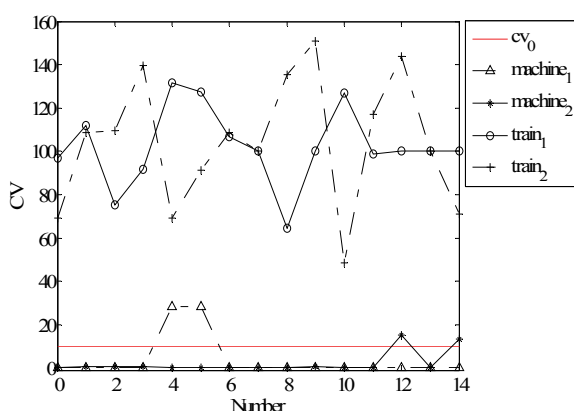


Fig. 9. Result of recognition.

From Fig. 9, we can observe that:

(1) Most of the variation coefficients of the mechanical vibration signals are stable and lower than  $cv_0$ .

(2) All of the variation coefficients of the train vibration signals are unstable and higher than  $cv_0$ .

(3) There are a large number of redundancy in the actual data, hence it can be determined as mechanical vibration source as long as there exists one of the variation coefficient of fundamental frequency lower than the given threshold  $cv_0$ , and the coefficients which are above the threshold don't affect the final determination.

From the above studies, we can conclude that this identification strategy can detect and identify mechanical vibration signals accurately.

## 6. Conclusions

For the safety of pipeline running, it might be harmful for a kind of vibration source, which has high vibration power and exists for long time. A frequently passing vehicle, such as a passing train, also has these features, but this vibration source is harmless. At this time, an OFVWS will send the staff

a false alarm, which will decrease the working reliability of the OFVWS badly.

In order to improve the identification performance and reduce the probability of false alarm for the OFVWS, we analyzed the fundamental frequency features of the vibration signals, and present a method for identifying harmful mechanical vibration sources, which have high power and long existing duration. This method can extract the fundamental frequency periods of the vibration signals, then evaluate its stability by calculating the variation coefficients of fundamental frequency periods ( $cv$ ), and finally identify the harmful mechanical vibration sources from the other vibration sources.

In order to investigate the performance of the presented method, we process some vibration signal data detected by an OFVWS of the China Petroleum Pipeline Bureau. The results show that this method can distinguish the harmful mechanical vibration sources accurately from the high-power and long-duration sources by analyzing the stability of variation coefficients of fundamental frequency.

This presented method based on the variation coefficients of the fundamental frequency periods can identify the harmful mechanical vibration sources accurately in real-time and reduce the false alarm rate. At the same time, it needn't a process of learning and training, so can reduce the calculation amounts greatly.

## References

- [1]. Alexander Kostin, A simple and fast multi-class piecewise linear pattern classifier, *Pattern Recognition*, Vol. 39, Issue 11, 2006, pp. 1949-1962.
- [2]. P. N. Suganthan, E. K. Teoh, D. P. Mital, Pattern recognition by homomorphic graph matching using Hopfield neural networks. *Image and Vision Computing*, Vol. 13, Issue 1, 1995, pp. 45-60.
- [3]. Zhenfeng Zhu, Xingquan Zhu, Yuefei Guo, Inverse matrix-free incremental proximal support vector machine, *Decision Support Systems*, Vol. 53, Issue 3, 2012, pp. 395-405.
- [4]. Zhigang Qu, Hao Feng, A SVM-based pipeline leakage detection and pre-warning system, *Measurement*, Vol. 43, Issue 4, 2010, pp. 513-519.
- [5]. Li Li, Mechanical vibration signal process and application, *Huazhong University of Science and Technology*, Wuhan, China, 2007.
- [6]. Tingting Liu, Xingmin Ren, Application of independent component analysis to vibration signal separation of rotational machine, *Journal of Vibration, Measurement & Diagnosis*, Vol. 29, Issue 1, 2009, pp. 36-41.
- [7]. Tingting Liu, Xingmin Ren, Mechanical vibration signal separation using blind de-convolution technology, *Journal of Vibration, Measurement & Diagnosis*, Vol. 29, Issue 4, 2009, pp. 419-423.
- [8]. Raymond Kan, Xiaolu Wang, On the distribution of the sample autocorrelation coefficients, *Journal of Econometrics*, Vol. 154, Issue 2, 2010, pp. 101-121.
- [9]. H. Albrecher, S. A. Ladoucette, J. L. Teugels, Asymptotics of the sample coefficient of variation and the sample dispersion, *Journal of Statistical*

Planning and Inference, Vol. 140, Issue 2, 2010, pp. 358-368.

- [10]. Wan Kai Pang, Bosco Wing-Tong Yu, Marvin D. Troutt, Shui Hung Hou, A simulation-based

approach to the study of coefficient of variation of dividend yields, *European Journal of Operational Research*, Vol. 189, Issue 2, 2008, pp. 559-569.

2013 Copyright ©, International Frequency Sensor Association (IFSA). All rights reserved.  
(<http://www.sensorsportal.com>)

Promoted by IFSA

## Status of the CMOS Image Sensors Industry Report up to 2017

The report describes in detail each application in terms of market size, competitive analysis, technical requirements, technology trends and business drivers.

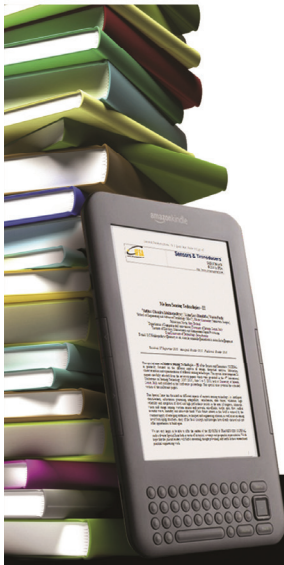
Order online:

[http://www.sensorsportal.com/HTML/CMOS\\_Image\\_Sensors.htm](http://www.sensorsportal.com/HTML/CMOS_Image_Sensors.htm)



## International Frequency Sensor Association Publishing Call for Books Proposals

Sensors, MEMS, Measuring instrumentation, etc.



**Benefits and rewards of being an IFSA author:**

### 1 Royalties

Today IFSA offers most high royalty in the world: you will receive 50 % of each book sold in comparison with 8-11 % from other publishers, and get payment on monthly basis compared with other publishers' yearly basis.

### 2 Quick Publication

IFSA recognizes the value to our customers of timely information, so we produce your book quickly: 2 months publishing schedule compared with other publishers' 5-18-month schedule.

### 3 The Best Targeted Marketing and Promotion

As a leading online publisher in sensors related fields, IFSA and its Sensors Web Portal has a great expertise and experience to market and promote your book worldwide. An extensive marketing plan will be developed for each new book, including intensive promotions in IFSA's media: journal, magazine, newsletter and online bookstore at Sensors Web Portal.

### 4 Published Format: printable pdf (Acrobat).

When you publish with IFSA your book will never go out of print and can be delivered to customers in a few minutes.

You are invited kindly to share in the benefits of being an IFSA author and to submit your book proposal or/and a sample chapter for review by e-mail to [editor@sensorsportal.com](mailto:editor@sensorsportal.com). These proposals may include technical references, application engineering handbooks, monographs, guides and textbooks. Also edited survey books, state-of-the art or state-of-the-technology, are of interest to us. For more detail please visit: [http://www.sensorsportal.com/HTML/IFSA\\_Publishing.htm](http://www.sensorsportal.com/HTML/IFSA_Publishing.htm)

## Increasing Geometric Resolution of Data Supplied by Quickbird Multispectral Sensors

**Claudio PARENTE and Raffaele SANTAMARIA**

Department of Sciences and Technologies, University of Naples "Parthenope"

Directional Centre of Naples, Isle C4, Naples, 80143, Italy

Tel.: 081-5476608, fax: 081-5476514

E-mail: [claudio.parente@uniparthenope.it](mailto:claudio.parente@uniparthenope.it)

*Received: 8 August 2013 /Accepted: 25 August 2013 /Published: 30 September 2013*

---

**Abstract:** On board of Quickbird satellite two types of sensors are present: panchromatic and multispectral. The first acquires earth images within spectral range  $0.405 \mu\text{m} - 1.053 \mu\text{m}$ ; the second acquires simultaneously four images of the same scene, each of them within shorter range of spectrum (Blue, Green, Red, Near-Infrared). Panchromatic images present geometric resolution  $0.60 \text{ m}$  while multispectral ones  $2.40 \text{ m}$ . For many applications, detailed data are welcome, so in the last decades several methods have been elaborated in Remote Sensing to transfer pixel dimensions of pan images into multispectral images. Included in data fusion techniques, they are named pan-sharpening methods and one of the principal problems they are called to resolve is to define weights to attribute to each multispectral component in fusion operations. The aim of this paper is to consider the application to Quickbird imagery of two efficient pan-sharpening methods, IHS and Brovey transformation, demonstrating that multispectral weights can be easily derived by analysis of sensors relative spectral radiance response. *Copyright © 2013 IFSA.*

**Keywords:** Quickbird images, Panchromatic and multispectral sensors, Geometric resolution, Pan-sharpening, Relative spectral radiance response.

---

### 1. Introduction

The successful launch of the first very high resolution (VHR) satellites, such as IKONOS in September 1999 or Quickbird in October 2001, marked the beginning of a wholly new age in remote sensing; in fact, VHR satellites are able to capture images of the earth's surface with a ground sample distance (GSD) of  $1 \text{ m}$  and even less [1].

Because of their high resolution, those images are used for many applications: IKONOS scenes (pan:  $1 \text{ m} \times 1 \text{ m}$ , multispectral  $4 \text{ m} \times 4 \text{ m}$ ) are used to establish accurately variation of shorelines in presence of coastal erosion [2].

Recently cell size of  $50 \text{ centimeters}$  has been achieved for panchromatic data, such as in the cases of GeoEye-1 and WorldView-2 [3].

To reduce effects of noise on signals, multispectral sensors capture data with lower resolution than panchromatic ones. For consequence intense research activities in the last decades have been focused on the possibilities for integrating different images to produce more information than that can be derived from a single sensor [4].

Multispectral (MS) images are conducted to higher spatial resolution by exploiting panchromatic ones that frequently are acquired simultaneously by sensors on the same satellite. This fusion process is called pan-sharpening of MS images [5].

A large number of pan-sharpening methods are present in the literature: in this work the attention was focused on IHS (Intensity-Hue-Saturation) and Brovey transformation, remarking the possibilities to enhance quality of results using for both methods

weights that were derived by operative characteristics of panchromatic and multispectral sensors.

## 2. Data and Methods

### 2.1. Quickbird Sensors

Launched on October 18, 2001, Quickbird satellite has a polar sun-synchronous orbit at an altitude of 450 km with a period of 93.6 minutes. On board of it there are two types of sensors (both with a swath width of 16.8 km) that respectively supply at nadir 61 centimeters panchromatic images (0.405  $\mu\text{m}$  – 1.053  $\mu\text{m}$ ) and 2.44 meters multispectral images (Blue: 0.430  $\mu\text{m}$  – 0.545  $\mu\text{m}$ ; Green: 0.466  $\mu\text{m}$  – 0.620  $\mu\text{m}$ ; Red: 0.590  $\mu\text{m}$  – 0.710  $\mu\text{m}$ ; Near-Infrared: 0.715  $\mu\text{m}$  – 0.918  $\mu\text{m}$ ). Pixel dimensions become respectively 0.66 and 2.64 meters when images are collected with an acquisition angle of 15°. Commercially data are supplied with geometric resolution of 0.60 m for panchromatic and 2.40 m for multispectral ones. Radiometric resolution for both is 11 bit (BV=0÷2047) [6-7].

### 2.2. Study Area and Data

Pan-sharpening methods were applied to a clip of Quickbird imagery concerning San Francisco (Fig. 1), courteously supplied by Digital Globe as product samples available for download. Set includes panchromatic as well as multispectral data and was collected on June 8, 2012 [3].

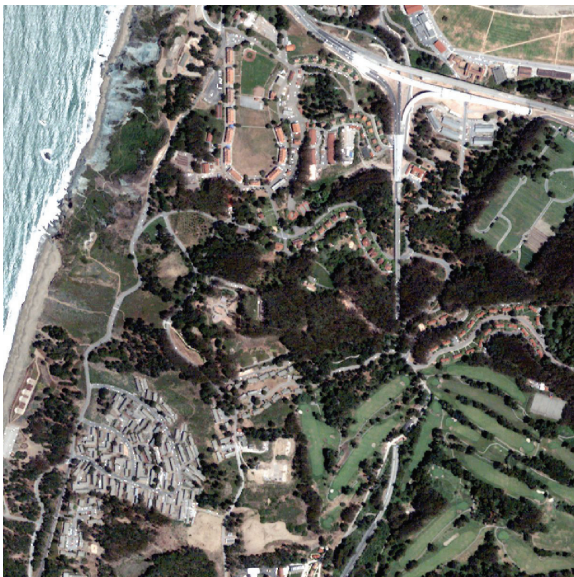


Fig. 1. The RGB true color composition of the considered area (San Francisco, California).

The clipped scene extends 1,800 m  $\times$  1,800 m. In reference to UTM-WGS84 cartographic system (10 S

zone), limits for East and Nord coordinates are:  $E_1=545,474.4$  m,  $E_2=547,274.4$  m,  $N_1=4,182,511.2$  m,  $N_2=4,184,311.2$  m. For consequence the original panchromatic image consists of 3,000 columns and 3,000 rows, while for the other four bands matrices are constituted by 750  $\times$  750 pixels because of lower geometric resolution (2.4 m  $\times$  2.4 m rather than 0.6 m  $\times$  0.6 m).

### 2.3. IHS Method

IHS method [8-10] transforms RGB colour composite of bands into Intensity-Hue-Saturation colour space. Similarity of Intensity component (I) to panchromatic image is used to produce data fusion preserving the higher spatial resolution and radiometric resolution. The Intensity component is replaced by the pan image and the scene is reverse transformed: for consequence R'G'B' composition with higher geometric resolution is produced.

Because Quickbird multispectral images are four, Intensity is supplied by the mean of them. Better results can be achieved introducing weights:

$$I = \frac{a*B + b*G + c*R + d*NIR}{a+b+c+d} \quad (1)$$

Weights can be established in universal way considering series of images that cover different areas. In this application we propose to use coefficients that can be derived by Relative Spectral Radiance Response (RSRR) of the Quickbird system (Fig. 2): it was determined by the producer using analysis of laboratory measurements [11].

In this work the contribution of each multispectral band in percentage to the sum of the contributions of all multispectral bands to panchromatic one was calculated considering the areas of the respective polygons in the RSRR. Every polygon is generated by the correspondent graph and X-axis. The resulting weights are reported in Table 1.

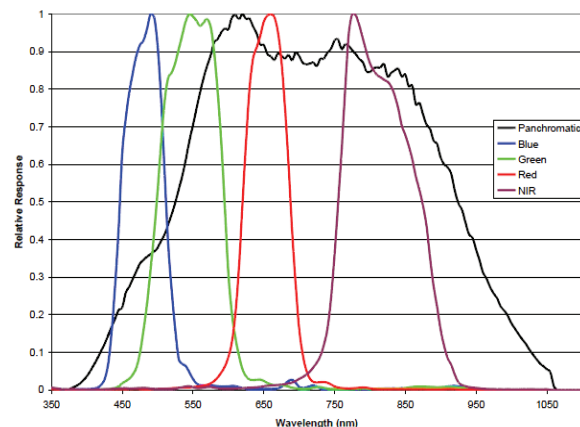


Fig. 2. Relative Spectral Radiance Response (RSRR) of QuickBird sensors.

**Table 1.** Weights that were derived by Relative Spectral Radiance Response.

Bands	Blue	Green	Red	NIR
Weights	0.11	0.26	0.24	0.39

## 2.4. Brovey Transformation

Brovey transformation [12] is included in *Modulation-based fusion methods* (MBFM) that research spatial details multiplying the multispectral (MS) data by the ratio of the pan image to a synthetic image which generally presents lower resolution [13]. The fused image is supplied by:

$$fusion_i = \frac{Pan}{Syn_p} \cdot Mul_i, \quad (2)$$

where  $fusion_i$  is the fused  $i^{\text{th}}$  band;  $Mul_i$  is the original MS  $i^{\text{th}}$  band;  $Syn_p$  is the synthetic band;  $Pan$  is the higher resolution panchromatic band.

Particularly with Brovey transformation the synthetic image is the average of the multispectral bands that are included in panchromatic one:

$$Syn_p = \frac{\sum_{i=1}^n Mul_i}{n} \quad (3)$$

Similarly to IHS method, weights may be introduced, so the fused image is supplied by the following formula:

$$Syn_p = \frac{\sum_{i=1}^n p_i Mul_i}{\sum_{i=1}^n p_i} \quad (4)$$

In this work we used the same weights above mentioned for IHS and derived by RSRR.

## 3. Results and Discussion

In Fig. 1 a particular of the RGB composition with pan-sharpened bands by IHS with weights is shown in comparison with the analogous supplied by the original imagery.

Advantage of pan-sharpening is evident: more details are visible and the resulting imagery can support further studies. To establish the similarity of pan-sharpened bands to those obtainable by real sensors with same high resolution, quality indices must be considered. According with that reported in literature, to establish the quality of results and verify the efficiency of the calculated weights, two indices were considered:

*Universal Image Quality Index (UIQI);*  
*Relative Dimensionless Global Error in Synthesis.*



(a)



(b)

**Fig. 3.** Particulars of comparison between RGB true color composition with pan-sharpened bands by IHS with calculated weights (a) and the correspondent one with original bands (b).

*Universal Image Quality Index (UIQI)* was introduced by Wang and Bovik (2002) [14] and can be calculated as:

$$UIQI = \frac{Cov_{AB}}{\sigma_A \sigma_B} \cdot \frac{2\mu_A \mu_B}{\mu_A^2 + \mu_B^2} \cdot \frac{2\sigma_A \sigma_B}{\sigma_A^2 + \sigma_B^2} \quad (5)$$

where:  $A$  is the original multispectral image;  $B$  is the correspondent multispectral image after pan-sharpening;  $\sigma_A$  is standard deviation of image  $A$ ;  $\sigma_B$  is standard deviation of image  $B$ ;  $Cov_{AB}$  is covariance between  $A$  and  $B$ ;  $\mu_A$  is the mean values of images  $A$ ;  $\mu_B$  is the mean values of images  $B$ .

In (5) the first term is the correlation coefficient, the second term is about mean shifting, and the third term is about contrast similarity. Good quality of Pan-sharpened images is certified by  $Q$  value close to one.

*Relative Dimensionless Global Error in Synthesis* is indicated as *ERGAS*, the abbreviation of *Erreur Relative Globale Adimensionnelle de Synthèse*. Introduced by Wald [15], it is supplied by the formula:

$$ERGAS = 100 \frac{h}{l} \sqrt{\frac{1}{K} \sum_{k=1}^K \left( \frac{RMSE(k)}{\mu(k)} \right)^2}, \quad (6)$$

where  $h/l$  is the ratio between pixel sizes of pan and original multispectral images;  $RMSE(k)$  is the RMSE of the  $k^{\text{th}}$  band;  $\mu(k)$  is the mean of the  $k^{\text{th}}$  band.

A small value of ERGAS means good image quality.

Values of those indices are shown in Tables 2, 3, 4, 5 in reference to each applied method.

**Table 2.** Quality indices for IHS.

	UIQI	ERGAS
Blue	0.838	5.420
Green	0.843	
Red	0.842	
NIR	0.929	

**Table 3.** Quality indices for IHS with weights.

	UIQI	ERGAS
Blue	0.907	4.242
Green	0.908	
Red	0.906	
NIR	0.935	

**Table 4.** Quality indices for Brovey transformation.

	UIQI	ERGAS
Blue	0.901	4.644
Green	0.885	
Red	0.887	
NIR	0.895	

**Table 5.** Quality indices for Brovey transformation with weights.

	UIQI	ERGAS
Blue	0.935	3.732
Green	0.931	
Red	0.929	
NIR	0.913	

Comparing results, advantages that are introduced by calculated weights are evident. Mean value of UIQI increases from 0.863 to 0.914 for IHS, and from 0.892 to 0.927 for Brovey transformation. ERGAS rises of about 27 % for IHS and 24 % for Brovey transformation.

## 4. Conclusions

Calculation of weights in consideration of RSRR of Quickbird pan and multispectral sensors is an efficient approach to effort IHS and Brovey transformation. In fact, introducing those weights in the calculation of Intensity as well as Synthetic image, improvement of results is generated as confirmed by both quality indices UIQI and ERGAS. In other approaches these weights are calculated

considering series of images: in this application they are directly derived by RSRR and can be used in any case in presence of Quickbird data.

## Acknowledgements

This paper synthesizes results of works performed within the project PRIN 2010-11 financed by *MIUR (Ministero dell'Istruzione, dell'Università e della Ricerca)* - Italy and developed at University of Naples "Parthenope" (Coordinator: Prof. Raffaele Santamaria).

## References

- [1]. M. A. Aguilar, M. M. Saldana and F. J. Aguilar, GeoEye-1 and WorldView-2 pan-sharpened imagery for object-based classification in urban environments, *International Journal of Remote Sensing*, Vol. 34, 2013, pp. 2583-2606.
- [2]. M. Basile Giannini, C. Parente, P. Maglione, R. Santamaria, Cartography and remote sensing for coastal erosion analysis, in *Proceedings of the Coastal Process II*, Naples, Italy, 27-29 April 2011, WIT Transactions on Ecology and the Environment, WIT Press, 2011, pp. 65-76.
- [3]. Digitalglobe Web Portal (<http://www.digitalglobe.com>).
- [4]. J. Yang, J. Zhang, H. Li, Y. Sun, P. Pu, Pixel level fusion methods for remote sensing images: a current review, in *Proceedings of the ISPRS TC VII Symposium – 100 Years ISPRS*, Vienna, Austria, 5-7 July 2010, IAPRS, Vol. XXXVIII, Part 7B, ed. by W. Wagner, B. Székely, pp. 680-686.
- [5]. L. Alparone, L. Wald, J. Chanussot, C. Thomas, P. Gamba, L. Mann Bruce. Comparison of pan-sharpening algorithms: outcome of the 2006 GRS-S data-fusion contest, *IEEE Transactions on Geoscience and Remote Sensing*, Vol. 45, Issue 10, 2007, pp. 3012-3021.
- [6]. DigitalGlobe, Quickbird – Data sheet: <http://www.digitalglobe.com>
- [7]. L. Rossi, Satellite high resolution new applications: Quickbird, in *Proceedings of the EFITA Conference* 5-9 July 2003, Debrecen, Hungary, pp. 388-392.
- [8]. R. Haydn, G. W. Dalke, J. Henkel, Application of the IHS color transform to the processing of multisensor data and image enhancement, in *Proceedings of the International Symposium on Remote Sensing of Arid and Semi-Arid Lands*, Cairo, Egypt, 19-25 January 1982, pp. 599-616.
- [9]. R. Welch, M. Ehlers, Merging multiresolution SPOT HRV and Landsat TM data, *Photogrammetric Engineering and Remote Sensing*, Vol. 53, Issue 3, 1987, pp. 301-303.
- [10]. W. Carper, T. Lillesand, R. Kiefer, The use of intensity-hue-saturation transformations for merging SPOT panchromatic and multispectral image data, *Photogrammetric Engineering and Remote Sensing*, Vol. 56, Issue 4, 1990, pp. 459-467.
- [11]. K. Krause, Radiometric use of QuickBird imagery – technical note, *DigitalGlobe*, Longmont, Colorado, USA, 2005.

- [12]. J. Vrabel, Multi-spectral imagery advanced band sharpening study, *Photogrammetric Engineering and Remote Sensing*, Vol. 66, Issue 1, 2006, pp. 73-79.
- [13]. J. Zhang, Multi-source remote sensing data fusion: status and trends, *International Journal of Image and Data Fusion*, Vol. 1, Issue 1, 2010, pp. 5-24.
- [14]. Z. Wang, A. C. Bovik, A universal image quality index, *IEEE Signal Processing Letters*, Vol. 9, Issue 3, 2002, pp. 81-84.
- [15]. L. Wald, Data fusion: definitions and architectures – fusion of images of different spatial resolutions, Les Presses, *Ecole des Mines de Paris*, Paris, France, 2002, 200 p.

---

2013 Copyright ©, International Frequency Sensor Association (IFSA). All rights reserved.  
(<http://www.sensorsportal.com>)

## Universal Sensors and Transducers Interface (USTI)

for any sensors and transducers with frequency, period, duty-cycle, time interval, PWM, phase-shift, pulse number output



- \* Input frequency range:  
0.05 Hz ... 9 MHz (144 MHz)
- \* Selectable and constant relative error:  
1 ... 0.0005 % for all frequency range
- \* Scalable resolution
- \* Non-redundant conversion time
- \* RS232, SPI, I2C interfaces
- \* Rotational speed, *rpm*
- \* Cx, 50 pF to 100  $\mu$ F
- \* Rx, 10  $\Omega$  to 10 M $\Omega$
- \* Pt100, Pt1000, Pt5000, Cu, Ni
- \* Resistive Bridges
- \* PDIP, TQFP, MLF packages

**Just make it easy !**

<http://www.techassist2010.com/>    [info@techassist2010.com](mailto:info@techassist2010.com)

## Research on Infrared Small Target Detection and Tracking Algorithms Based on Wavelet Transformation

Liping LU

School of Computer Science and Engineering, Xi'an Technological University,  
Xi'an 710032, China  
E-mail: llp21@126.com

*Received: 5 June 2013 /Accepted: 25 August 2013 /Published: 30 September 2013*

---

**Abstract:** In dynamic targets tracking measure system, a new detection algorithm on infrared small target is put forward. The algorithm is base on wavelet transformation, and by using it we can gain clear characteristics of target image and decrease mistake of tracking target. In paper, the principle of infrared small target detection was introduced, and the infrared small target detection system is designed. According to the theory of wavelet transformation, the method of Butter worth wavelet low-pass filtering was applied to filter noise and eliminate high frequency single. Multi-resolution wavelet filter on infrared target was studied to improve image quality, and make the target edge more clear. By setting up the track detection model, the Mean Shift target tracking algorithm is applied to analyze the key technology of the dynamic target tracking algorithm. The method of image segmentation and edge detection on dynamic targets were analyzed. Through experiment and calculation, the detection algorithm meets the measure need. *Copyright © 2013 IFSA.*

**Keywords:** Infrared small target, Tracking and detection, Wavelet transformation, Image processing, Image segmentation.

---

### 1. Introduction

In dynamic targets tracking test system, with development of the infrared imaging technology, the infrared imaging technology has been widely applied to optical remote sensing, target detection, fire control, night navigation and missile guidance [1-2]. Because infrared technology has the advantages of good concealment, strong anti-jamming performance, long distance and work double, so it plays a vital role in those fields. As a key technology in the guidance fields, homing infrared search tracking fields and warning fields, infrared small target tracking and detection technology become a long history and energetic research topic [3-5]. Due to factors such on the detection distance, a smaller field of view,

complicated background, there are some difficulties, such as no obvious characteristics of target, external thermal disturbances in infrared small target detection system, so conventional algorithms already cannot be used to the detection system under complex background [6-7]. In the paper, wavelet transformation is used to infrared small target detection. By using the wavelet transformation, we can solve these questions: the firstly, using the energy characteristics image method based on wavelet transformation, the original image can be divided into two zone i.e. target zone and natural texture background zone [8-10], the more smoother the target zone is and the more detailed the background texture is, the more higher target detection accuracy is, the secondly, the target detection method is

adapted to situations such as air, on land, sea and other natural texture context, selection of energy characteristics has nothing to do with the direction of background texture, finally, because the target change has rotation, translation invariance and the method is suitable for the same type of target detection under different circumstances.

## 2. The Principle of the Infrared Small Target Detection

In wild environment, because the dynamic small target tracking based on the principle of optical imaging is often affected by the external environment, so there are some difficulties in tracking system. The infrared background (especially the sky, the sea, clouds of natural background and waves) often showed a large area continuous distribution, gradual transition state in the intensity of infrared radiation [11]. Thus the infrared images are greater relativity in image gray spatial distribution, it is a slowly varying two-dimensional and non-stationary random process, and the background of the infrared images is undulate [12-13]. In fact, the intensity of infrared target radiation is no relativity with the intensity of natural background radiation, and is higher than the intensity of natural background radiation. So the background is in the low-frequency part of the image signal, the target is in the high frequency part of the image. By using the wavelet transformation the infrared image is separated into low frequency and high frequency part. Then the high frequency image is analyzed, thus the targets can be detected.

The multi-resolution characteristics and decorrelation in wavelet transformation mainly distill infrared small target point [14-16]; it can improve target image quality. Firstly Wavelet transformation is used to denoising, it can improve the image contrast. Secondly, Mallet algorithm is used to multi-scale decomposed by the image signal; it can enhance the information of small target. Lastly, the image segmentation is used to determine the target. Fig. 1 is the principle of algorithm target detection.

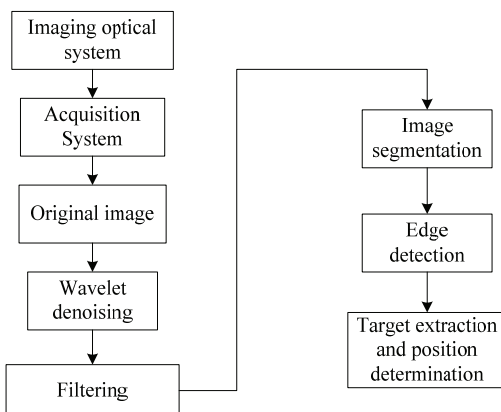


Fig. 1. The work principle of the target detection algorithm.

## 3. Principle of Wavelet Transformation

Suppose,  $\psi(t) \in L^2(R)$ ,  $\hat{\psi}(t)$  is the Fourier transformation, when  $\hat{\psi}(t)$  meet formula (1).

$$C_{\psi} = \int_R \frac{|\hat{\psi}(\omega)|^2}{|\omega|} d\omega < \infty \quad (1)$$

We consider  $\psi(t)$  is a basic wavelet, or mother wavelet, the function of  $\psi(t)$  is out spread and level moved, and gain a wavelet sequence [17], it can expressed by formula (2):

$$\psi_{a,b}(t) = \frac{1}{\sqrt{|a|}} \psi\left(\frac{t-b}{a}\right) \quad (2)$$

In formula (2),  $a, b \in R$ ,  $a \neq 0$ ,  $a$  is the expansion factor,  $b$  is the translation factor.

If the wavelet is discrete, its sequence can be expressed by formula (3):

$$\psi_{j,m}(t) = 2^{-j/2} \psi(2^{-j}t - m) \quad (3)$$

where  $j$  is the scale index,  $m$  is the position index.

To random function  $f(t)$ , if  $f(t) \in L^2(R)$ , its continuous wavelet transform can be expressed by formula (4).

$$\psi_{a,b} \gg = \frac{1}{\sqrt{|a|}} \int_R f(t) \psi\left(\frac{t-b}{a}\right) dt \quad (4)$$

## 4. Small Target Detection Algorithm based on the Wavelet Transformation

### 4.1. Denoising Wavelet Transformation

In infrared target detection system, those images coming from computer contain many noises. If we want to gain idea image, the original image must be preprocessed by wavelet transformation denoising. The preprocessed is mainly to improve the image SNR, inhibit the background, and meet the requirement of image real-time process. If the process can not meet the requirement, it will directly affect the feature extraction and matching of target. The method of Butter worth wavelet low-pass filtering was used to eliminate noise and make the image is proportion to target detection [18]. The Butter worth wavelet low-pass filtering can be expressed by formula (5).

$$G(u, v) = H(u, v) F(u, v), \quad (5)$$

where  $F(u, v)$  is the transformation image, which has noise.  $H(u, v)$  is transfer function, if we select appropriate  $H(u, v)$ , the High frequency components of  $F(u, v)$  will be attenuated and obtain  $G(u, v)$  that is transformed function by smooth processing. We will obtain the smooth image  $g(x, y)$  by the inverse transformation of  $G(u, v)$ . The transformation function  $H(u, v)$  can be expressed by (6):

$$H(u, v) = \frac{1}{1 + (\sqrt{2} - 1) \cdot \left| \frac{D(u, v)}{D_0} \right|^{2*3}} \quad (6)$$

In formula (6),  $D_0$  is the Cutoff frequency,  $D(u, v) = \sqrt{u^2 + v^2}$ .

#### 4.2. The Wavelet Filter of the Multi-Resolution Infrared Target

After the target image was preprocessed, if we want to obtain specific target features, and make the edge more clear. It is necessary to process infrared target image by using multi-resolution wavelet filter.

If  $\phi(x)$  is a one-dimensional scaling function, and  $\psi(x)$  is a corresponding wavelet function, we can get a two-dimensional wavelet basis function.

$$\psi^1(x, y) = \phi(x)\psi(y) \quad (7)$$

$$\psi^2(x, y) = \psi(x)\phi(y) \quad (8)$$

$$\psi^3(x, y) = \psi(x)\psi(y) \quad (9)$$

Track image can be viewed as two-dimensional matrix, generally, we assume the size of the image matrix is  $N \times N$ , here  $N$  equals to  $2n$ ,  $n$  is the non-negative integer. After transformation, the image will be divided into four region, their size is 1/4 original picture, those picture contain correspond frequency band coefficients.

To improve the processing speed, we apply Matlab algorithm to dispose picture. This kind algorithm has merits, it can speed for decomposed and disposed of image.  $f(x, y)$  is the two-dimensional image, it can be divided into two one-dimensional wavelet transforms along directions  $x$  and  $y$ , when it is processed by wavelet decomposition. That is,  $\phi(x)$  is scaling function,  $\psi(x)$  is wavelet function,  $f(x, y)$  is decomposed into two parts when we analyze  $\phi(x)$  and  $\psi(x)$  along the  $x$  direction. Those two parts are profiles and details. Along the  $y$  direction we can analyze  $f(x, y)$  in the same way. Ultimately we can obtained 4-outputs, the first output is two-dimensional profiles of  $f(x, y)$ . The remaining 3 outputs are the wavelet details along  $x$  direction,  $y$  direction and  $xy$  diagonal direction. The reconstruction of image can also be treated as of two one-dimensional direction, from which obtained the Matlab algorithm of two-dimensional signal. The algorithm is expressing by Fig. 2.

#### 4.2 Infrared Target Image Segmentation and Edge Detection Base Wavelet Transforms

Technology of image segmentation is got by wavelet transformation. It is a threshold selection method of the discrete binary wavelet transformation, it can automatically selected threshold in different scales, and effectively separate Image.

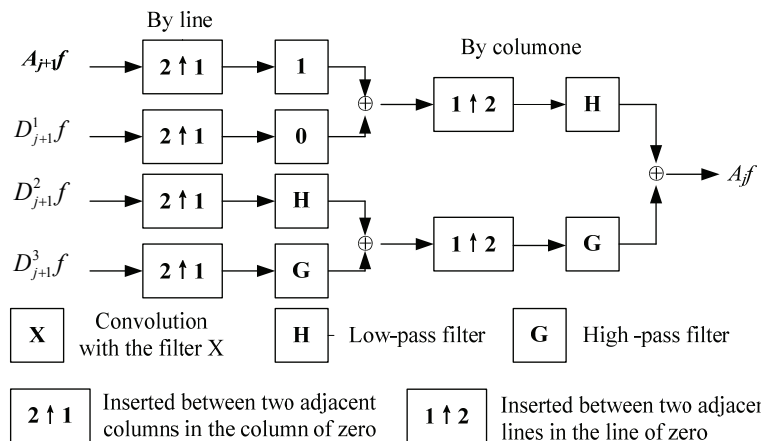


Fig. 2. The wavelet reconstruction algorithm of the image.

We know, the image is formed by the background and objectives, their gray-level histogram chart has two peaks corresponding to gray-level, if we select a threshold, the two peaks was separated, and image is divided. We can get a meaningful valley value from the two peaks in the histogram. The valley value is an effective threshold of image segmentation. Because of low sensitivity of infrared thermal imaging devices and high-gain of follow-up amplifier, the collected infrared image have noises, there is difficulty to distinguish obviously the histogram peaks and valleys, and select the threshold. Wavelet transform image segmentation can overcome this shortcoming; the specific algorithm was described as follow:

Assume,  $\theta(x)$  is the surface smooth function that is suitable for infrared target, and satisfy bellow condition:

$$\int_{-\infty}^{\infty} \theta(x) dx = 1, \lim_{x \rightarrow \infty} \theta(x) = 0, \quad (10)$$

where  $\theta(x)$  is the Gaussian function, it can be expressed by formula (11).

$$\theta(x) = \frac{1}{\sqrt{2\pi}\sigma} e^{-x^2/2\sigma^2} \quad (11)$$

If  $\psi(x) = \frac{d\theta(x)}{dx}$ , and  $\int_{-\infty}^{\infty} \psi(x) dx = 0$ ,  $\psi(x)$  is a basic wavelet or mother wavelet function. To random  $g(x)$ , we can introduce,  $g_s(x) = \frac{1}{s} g(\frac{x}{s})$ , the wavelet transformation of  $f(x)$  can be expressed by formula (12):

$$W_s f(x) = f * [\frac{sd\theta_s}{dx}](x) = s \frac{d}{dx} (f * \theta_s)(x) \quad (12)$$

We can acted  $f * \theta_s(x)$  as the function smoothed by the Gaussian function in the scale  $s$ , when  $S$  is very small, and the  $f(x)$  is smoothed by  $\theta_s(x)$ , the mutation general features of  $f(x)$  is not affected. From view of the frequency domain,  $f(x)$  is filtered by  $\hat{\theta}(s\omega)$ . When  $S$  is smaller,  $\omega$  can be extended,  $\hat{\theta}(\omega)$  has bigger bandwidth than  $\hat{\theta}(s\omega)$  and the waveform feature of the  $f(x)$  is little effect. Otherwise, when  $S$  is bigger,  $\omega$  can be expressed,  $\hat{\theta}(\omega)$  has smaller bandwidth than  $\hat{\theta}(s\omega)$ , some small changes of  $f(x)$  will eliminate, and some larger size characteristics of  $f(x)$  is left. From above all, when we select the appropriate  $S$ , the noise of image is eliminated.

The zero crossing of wavelet transformation  $W_s f(x)$  is extreme point of  $f(x)$ . We only study the corresponding point of  $W_s f(x)$  from negative to zero, because those points can reflect local valley points positions of  $f(x)$ . If we select valley points as threshold to process the wavelet transformation on image, the two peaks of image are parted, and the image segmentation is done.

If we want obtain the edge feature of the infrared small target, the image must be detected about edge after image segmentation. Assume,  $f_x$  and  $f_y$  are two functions in two-dimensional direction on image. If  $i$  and  $j$  are a position point coordinate in image. [19] We use the difference between two adjacent pixels in diagonal direction to instead gradient value in order to find outer edge of image. Their relation can be expressed by formula (13) and (14).

$$f_x = f(i, j) - f(i+1, j+1) \quad (13)$$

$$f_y = f(i, j+1) - f(i+1, j) \quad (14)$$

Convolution operator of  $f_x$  and  $f_y$  is expressed by formula.

$$f_x : \begin{pmatrix} 1 & 0 \\ 0 & -1 \end{pmatrix} \quad f_y : \begin{pmatrix} 0 & 1 \\ -1 & 0 \end{pmatrix} \quad (15)$$

Gradient amplitude is approximately expressed by formula (16):

$$R(i, j) = \sqrt{f_x^2 + f_y^2} \quad \text{or} \quad (16)$$

$$R(i, j) = |f_x| + |f_y|$$

When the threshold of  $\tau$  is selected, if  $R(i, j) > \tau$ , point  $(i, j)$  is the edge point. According to the formula (16), the edge detection of infrared target can be processed.

## 5. The Algorithm of the Small Target Tracking Detection

The target shadow value must be quantitatively analyzed to debase quantity of calculating and satisfy need for real time. Suppose the track point is  $y$ , the detection area is a rectangle area which center is  $y$ , breadth is  $h$ , and pixels point is expressed by  $\{x_i\}_{i=1..n}$  and its value is  $m$ , that is, the function  $b(\square) : R^2 \rightarrow \{1..m\}$  is shadow index of pixels point  $x_i$ . the Mean Shift target track algorithm is applied to obtain the character value of the dynamic

target. It uses the character value of the shadow and texture of image to represent the target, the gradient-Descent search algorithm of mean shift vector to track the object [20].

Suppose the center of object area is  $x_0$ , in which there are  $n$  pixels points expressed  $\{x_i\}_{i=1\dots n}$ , the quantity of character value is  $m$ , the probability density of the character value  $u$  of target is expressed by formula (17).

$$\hat{q}_u = C \sum_{i=1}^n k\left(\left\|\frac{x_0 - x_i}{h}\right\|\right)^2 \delta[b(x_i) - u] \quad (17)$$

In formula,  $k(x)$  is profile function of kernels function, because the effect of the background and shadow, the pixels point of target model center about is more credible than the others, by the function  $k(x)$ , weight calculation of the center pixels point is bigger, weight calculation of the point apart from center pixels is smaller. The function  $k(x)$  can eliminate effects which come from calculating the different size target, make the ellipse target normalize the unit round through  $k(x)$ .  $\delta(x)$  is Delta function. Using  $\delta[b(x_i) - u]$ , we can judge the gray value of the pixels point in the target area whether belong to the number  $u$  characteristic value, if the value belongs to the number  $u$  characteristic value, the value is 1, otherwise, the value is 0.  $C$  is a standardization constant coefficient which can produce  $\sum_{u=1}^m q_u = 1$ , the kernels consistency expression of the profile function on kernels function can be expressed by formula (18).

$$C = \frac{1}{\sum_{i=1}^n k\left(\left\|\frac{x_0 - x_i}{h}\right\|\right)^2} \quad (18)$$

The area in which the dynamic target possibly is of the second and the subsequence frame image is candidate area. The center coordinate of it is  $y$ ,  $y$  also is center coordinate of the kernels function. The pixels point of the area is expressed by  $\{x_i\}_{i=1\dots n_j}$ , when the character value of the candidate model is  $u$ , the value of  $u$  is between 1 and  $m$ , the probability consistency of  $u$  can be expressed by formula (19).

$$\hat{P}_u(y) = C_h \sum_{i=1}^{n_k} k\left(\left\|\frac{x_0 - x_i}{h}\right\|\right)^2 \delta[b(x_i) - u] \quad (19)$$

The similitude function represents the similitude degree between the target model and the candidate target model. Bhattacharyya coefficient is used the similitude function.

$$\hat{\rho}_u(y) = \sum_{u=1}^m \sqrt{\hat{P}_u(y) \hat{q}_u} \quad (20)$$

The value of Bhattacharyya is between 0 and 1.

The bigger the value of  $\hat{\rho}(y)$  is, the bigger the similitude degree is between the two models. We can obtain the different candidate model in different candidate area by calculating, the candidate model in which  $\hat{\rho}(y)$  is the biggest is the target position.

To make  $\hat{\rho}(y)$  biggest, suppose, the place of center  $y_0$  in the front frame image is the center place of the nonce frame image, from the point, we search the optimization matching target. Firstly, we calculate Taylor from  $\hat{\rho}(y_0)$  in the target candidate model to gain the biggest value of  $\hat{\rho}(y)$ , using the biggest  $\hat{\rho}(y)$  to find the target point of the place. By using Mean Shift method, from the point  $y_0$ , according to gray changing big direction in two model, we can calculate to find the target place.

## 6. Calculation and Analysis

To validate infrared small target detection algorithm using wavelet analysis, we can select two infrared images that include noise to process. In the Fig. 3, there has noises in the target image; the target is almost submerged in the background and noise. In the Fig. 4, after the image denoising, the multi-resolution wavelet transform, and filtering, the low-frequency background of image is basic blurring, the small target detected appears is clear, and some of the background image has been suppressed. In the Fig. 5, the image of edge detection is showed. View from analysis of theory, the algorithm can meet the small target detection in complex background and lay a sound basis for dynamic target tracking system. View from the results the experiment; the noise of images is essentially removed.

Fig. 6 also is a small track. In the Fig. 6, there has noises in the target image in the field background; the target is almost submerged in the background and noise. After the image to be preprocessed, the low-frequency parts of image is filtrated basically, and figure of the background image is correspondingly clear. In the Fig. 7, the image processed by method of edge detection is showed. View from the results the experiment, the algorithm can essentially removed noise of complex background, recognize the small target, and lay a sound basis for dynamic target tracking system.

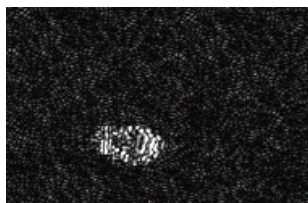


Fig. 3. Pretreatment.



Fig. 4. Multi-resolution wavelet transformation processing.

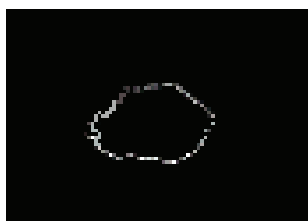


Fig. 5. Edge processing.

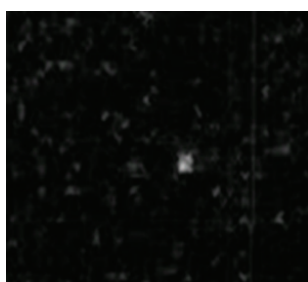


Fig. 6. Target original image.

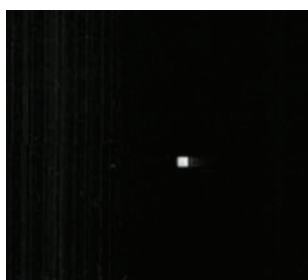


Fig. 7. The image by segmentation and edge processing.

## 7. Conclusion

In order to get the dynamic infrared target characteristic in the complex background, the image is denoised by the wavelet transformation. Then the

flooding wave and noise of the image is weakened, the image of the background and target is strengthened. Although the small target and the background image is still mixed together, but the edge feature has been exposed relatively to the original target. The noise of the image is reduced, but the loss of target is very small, which proved that the method of denoising is feasible. Base on the multi-resolution wavelet filtering, the background of the image is suppressed, the small target is outstanding. On the basis, the edge detection of the image is done, and the contour of the small target is outstanding. The detected effect of algorithm is affected and can not detect the target when the interference information is more, and the complexity is on the increase, although it can detect accurately the small target of the infrared image in the complicated background. Because the algorithm can only detect the single target. In order complete the detection task, we can add the multi-frame detection, which can achieve perfect results, the study of this paper provide reliable detection method and theory for Follow-up multi-target detection, and has practical significance.

## References

- [1]. Zhang Yurong, Tao Chenli, Test and analysis on intersection measurement precision of CCD for the target in the air, in *Proceedings of the 6<sup>th</sup> International Symposium on Test and Measurement*, 2005, pp. 1108-1112.
- [2]. Sano Mutsuo, Meguro Shinichi, Ishii Akira, Gray-level image recognition based on multiple cell-features, *Systems and Computers in Japan*, Vol. 22, Issue 5, 1991, pp. 81-93.
- [3]. J. Fischer, T. Radil, Simple methods of edge position measurement using shadow projected on CCD Sensor, *Measurement Science Review*, Vol. 3, Issue 3, 2003, pp. 37-40.
- [4]. L. Zhang, Y. X. Li, X. J. Li, Synchronous control analysis of TDI-CCD imaging system, in *Proceedings of the SPIE*, Vol. 6, 2007, pp. 279-206.
- [5]. Thomas W. McCurnin, Larry C. Schooley, Gary R. Sims, Signal processing for low-light-level high-precision CCD imaging, in *Proceedings of the SPIE*, Vol. 1448, 1991, pp. 225-236.
- [6]. Masahiro Ohbo, Ikuo Akiyama, Takanori Tanaka, A new noise suppression method for high-definition CCD cameras, *IEEE Transactions on Consumer Electronics*, Vol. 35, Issue 3, 1989, pp. 367-374.
- [7]. Plemmons Robert, Horvath Michael, Leonhard Emily, Computational imaging systems for Iris recognition, in *Proceedings of the SPIE, The International Society for Optical Engineering*, 2004, pp. 346-357.
- [8]. V. V. D. Shah, Image processing and its military application, *Defence Science Journal*, Vol. 37, Issue 4, 1987, pp. 457-468.
- [9]. L. A. Johnston, V. Krishnamurthy, Performance analysis of a dynamic programming track before detect algorithm, *IEEE Transactions on Aerospace and Electronic Systems*, Vol. 38, Issue 1, 2002, pp. 228-242.
- [10]. Chen Xiang-Wei, Wang Long-Shun, Liu Qing-Min, Research on measurement of roundness errors based

- on CCD Image, *Semiconductor Optoelectronics*, Vol. 25, Issue 4, 2004, pp. 312-316.
- [11]. J. L. Davidson, F. Hummer, Morphology neural network: an introduction with applications, *IEEE Transactions on Signal Processing*, Vol. 12, Issue 2, 1993, pp. 177-210.
- [12]. Geoffrey Dougherty, Effect of sub-pixel point spread function of a CT image system, *Medical Engineering and Physics*, Vol. 22, 2000, pp. 503-507.
- [13]. L. Varsano, V. Adler, S. R. Rotman, Algorithms for tracking point targets in infrared sequences, in *Proceedings of the SPIE*, 5987, 2005, pp. 271-278.
- [14]. L. Yang, J. Yang and K. Yang, Adaptive detection for infrared small target under sea-sky complex background, *Electronics Letters*, Vol. 40, Issue 17, 2004, pp. 1083-1085.
- [15]. You Hong-Jian, Hu Yan-Feng, Zhang Shi-Qiang, New method to recognize buildings from airborne CCD image, *Optoelectronic Engineering*, Vol. 32, Issue 9, 2005, pp. 8-11.
- [16]. Yu Nong, Wu Chang-yong, Li Fan-Ming, et al., Morphological neural networks for automatic target detection by simulated annealing learning algorithm, *Science in China*, Vol. 46, Issue 4, 2003, pp. 262-288.
- [17]. H. Sh. Li, Z. Y. Lei, Z. M. Wang et al., Principle and analysis of high altitude projectile location measurement using multi-screen target method, *Chinese Journal of Scientific Instrument*, Vol. 30, Issue 3, 2009, pp. 621-624.
- [18]. Hua Jianjun, Zhang Jianqiang, Calculation method of infrared signature of aerial target, *Laser and Infrared*, Vol. 31, Issue 3, 2001, pp. 166-169.
- [19]. M. Diani, G. Corsini and A. Baldacci, Space-time processing for the detection of airborne targets in IR image sequences, in *IEE Proceedings on Vision, Image and Signal Processing*, Vol. 148, Issue 3, 2001, pp. 151-157.
- [20]. M. Z. Tidrow, New infrared sensors for ballistic missile defense, in *Proceedings of the SPIE*, 2005, 5732, pp. 217-224.

---

2013 Copyright ©, International Frequency Sensor Association (IFSA). All rights reserved.  
(<http://www.sensorsportal.com>)

## International Frequency Sensor Association



**International Frequency Sensor Association (IFSA)** is a professional association, created with the aim to encourage the researches and developments in the area of quasi-digital and digital smart sensors and transducers.

**IFSA Membership is open to all organizations and individuals worldwide who have a vested interest in promoting or exploiting smart sensors and transducers and are able to contribute expertise in areas relevant to sensors technology.**

More than 600 members from 63 countries world-wide including ABB, Analog Devices, Honeywell, Bell Technologies, John Deere, Endevco, IMEC, Keller, Mazda, Melexis, Memsis, Motorola, PCB Piezotronics, Philips Research, Robert-Bosch GmbH, Sandia Labs, Yokogawa, NASA, US Navy, National Institute of Standard & Technology (NIST), National Research Council, etc.



For more information about IFSA membership, visit  
<http://www.sensorsportal.com>

## The Design of Check Control System of Strip Steel Deviation Correction and the Heat Structure Coupling Analysis on Relative Sensor

Hong-Yu LIU, Ze-Ning XU

School of Mechanical Engineering and Automation, University of Science and Technology Liaoning, Anshan, Liaoning Province, 114051, China  
Tel.: 15241277551, fax: 0412-5929777  
E-mail: lhy\_12@126.com

*Received: 23 June 2013 / Accepted: 25 August 2013 / Published: 30 September 2013*

---

**Abstract:** Anneal process must be made before strip steel figuration handling. The strip steel length passed anneal furnace can reach thousands of meters. Strip steel is easy off tracking. So, strip steel deviation correction sensor must be set in anneal furnace. Strip steel deviation correction check control system must be set on strip steel production line. Electromagnetic inductance strip steel deviation correction sensor was designed independently by electromagnetic induction principle in this paper to work in anneal furnace. Its structure form is centring check form. The technique quotas of this sensor are same as similar product of Germany EMG Company. SolidWorks software was adopted to construct the right half part model of sensor metal frame. Transient state heat analysis and heat structure coupling analysis were made on relative model by ANSYS software. The influence rules of temperature field and gravity field on sense structure deformation were found. Strip steel deviation correction check control system was designed. Prepositive amplification rectification circuit was designed. Second order infinite gain multiple circuit feedback lowpass smoothing circuit was designed. This research provides important reference base on realizing nationalization of import electromagnetic induction deviation correction sensor and enhancing automation level of inland cold rolling strip steel equipments. Copyright © 2013 IFSA.

**Keywords:** Strip steel deviation correction, Check control system, Sensor, Transient state heat analysis, Heat structure coupling analysis.

---

### 1. Introduction

In recent years, the requirement for cold rolling strip steel is very large on many industries in China. Anneal process must be made before strip steel figuration handling. The temperature in anneal furnace can reach 600 °C to 1000 °C. The influence of high temperature on strip steel deviation correction sensor is big. Inaccurate collection information and low check precision will emerge

probably which will cause the error actions engendered by check control system and executive system. The strip steel length passed anneal furnace can reach thousands of meters. Strip steel is easy off tracking on transport process. These will cause strip steel damage, strip steel break and stop production. The continuous, fast and stable work of strip steel production line will be influenced accordingly. Electromagnetic inductance strip steel deviation correction sensor and strip steel deviation correction

check control system can adapt to each position on strip steel production line. This kind of sensor has strong antijam capability. The influences of dirt accumulated on sensor, static electricity field, steam engendered by rolling process and metal fog of anneal furnace inner on electromagnetic inductance strip steel deviation correction sensor are all small [1-5]. In various sensors, only electromagnetic inductance strip steel deviation correction sensor can work normally under the high temperature environment in anneal furnace. This kind of sensor has long working life. It does not need artificial maintenance after installation and adjustment [6]. So, Inductance strip steel deviation correction sensor and strip steel deviation correction check control system are key links to ensure the continuous, fast and stable work of strip steel production line. The main products of Germany EMG Company are electromagnetic inductance sensor, camera sensor and photoelectric sensor. The main products of America FIFE Company and North America Company are photoelectric sensor, camera sensor and capacitive sensor. The main product of Japan Yokogawa Company is photoelectric sensor. The main products of Beijing Aritime Company are photoelectric sensor, camera sensor and capacitive sensor [7]. Electromagnetic inductance deviation correction sensors imported directly from abroad were widely adopted on cold rolling strip steel production line of many Chinese iron and steel enterprises currently. Eight sets of electromagnetic inductance deviation correction sensors were applied on pickling and cold rolling strip steel production line of Benxi Iron and Steel Company. Fourteen sets of electromagnetic inductance deviation correction sensors were applied on relative continuous anneal production line. It is very difficult in using and maintaining this kind of sensor. The price of this kind of sensor is very expensive [8, 9]. So, the independent research and development on electromagnetic inductance strip steel deviation correction sensor and strip steel deviation correction check control system have important significance on enhancing automation level of inland cold rolling strip steel equipments.

## 2. The Design of Strip Steel Deviation Correction Sensor

### 2.1. The Structure Design of Strip Steel Deviation Correction Sensor

The structure form of mutual inductance strip steel deviation correction sensor was designed as centring check form, based on the characteristics of mutual inductance sensor. The sensor can adapt the high temperature environment in anneal furnace. The relative work sketch map of this sensor was shown as Fig. 1.

The sensor contains two transmission coils and two receiver coils. After alternative sinusoidal

voltage was acted on transmission coil 1 and transmission coil 3, alternative magnetic field will be engendered around them. Induction electromotive force  $\mathcal{E}$  will be engendered on receiver coil 2 and receiver coil 4 accordingly which was shown in formula (1).

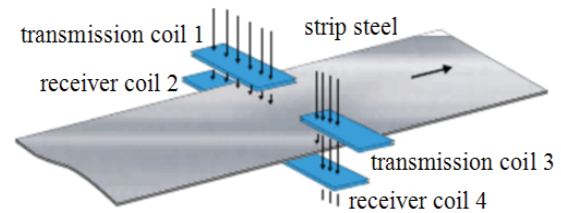


Fig. 1. The work sketch map of mutual inductance strip steel deviation correction sensor.

$$\mathcal{E} = K_1 N \frac{d\phi}{dt}, \quad (1)$$

In formula (1),  $K_1$  represents coil structure constant.  $N$  represents receiver coil circle number.  $\phi$  represents the magnetic flux of receiver coil.  $t$  represents time. When strip steel passes two transmission coils and two receiver coils, some magnetic induction lines will be covered by strip steel. Induction electromotive force  $\mathcal{E}$  obtained by two receiver coils will decrease accordingly which were shown in formula (2) and formula (3) respectively.

$$\phi = \frac{K_2 B}{hb}, \quad (2)$$

$$\mathcal{E} = \frac{K_1 K_2 N B}{h(db/dt)}, \quad (3)$$

In above formulae,  $K_2$  represents constant.  $B$  represents magnetic induction strength.  $h$  represents strip steel thickness.  $b$  represents strip steel width. When strip steel conveying is normal, strip steel centre line superposes with sensor centre line. When strip steel conveying is towards the left, receiver coils 2 signals will be weakened. Receiver coils 4 signals will be strengthened accordingly. Above signals will be amplified prepositively, rectified, filtered and inputted into controller. Finally, strip steel deviation correction controls were accomplished by controller and execution system.

### 2.2. The Electromagnetic Inductance Coil Design of Strip Steel Deviation Correction Sensor

Strip steel width scope is 300 mm to 1000 mm. Strip steel deviation scope is  $\pm 30$  mm. Sensor coil

form was designed as rectangle. Relative length is 865 mm. Relative width is 120 mm. Relative thickness is 44 mm. The polyester varnished wires used as electromagnetic inductance coil must have good insulation property and tensile strength. High temperature will enlarge the thermal expansivity coefficient and resistance of copper line. Sensor check precision will be influenced accordingly. Therefore, QZ high strength polyester varnished wires were wound into rectangle electromagnetic inductance coil directly by automatic numerical control winder in this paper.

### 2.3. Strip Steel Deviation Correction Sensor Technic Quotas

The technic quotas of strip steel deviation correction sensor designed independently in this paper are same as similar product of Germany EMG Company. Relative technic quotas are as follows. Work temperature is 600°C to 1000°C. Surroundings temperature is 0°C to 85°C. Checkable strip steel thickness is 0.3 mm to 2.5 mm. Centring precision is  $\pm 5$  mm.

## 3. Heat Structure Coupling Analysis of Strip Steel Deviation Correction Sensor

### 3.1. Model Construction

The work map of strip steel deviation correction sensor in anneal furnace was shown as Fig. 2. The unpacked strip steel deviation correction sensor was shown as Fig. 3. Sensor metal frame will engender structure deformation under the common actions of temperature field and gravity field. It will cause the position change of coils fixed on sensor metal frame. Sensor can not accurately check strip steel deviation accordingly. Executive system will engender error actions. Strip steel can not be normally conveyed. Production accident will be engendered. Sensor metal frame was regarded as beam in this paper. The bottom up model construction mode was adopted. Because relative model is symmetrical, only right half part model of sensor metal frame was constructed by SolidWorks software in this paper.

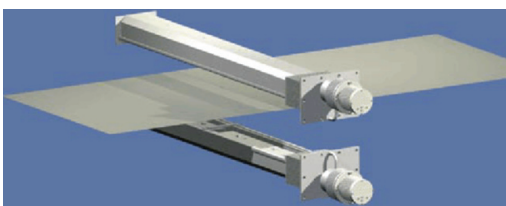


Fig. 2. The work map of strip steel deviation correction sensor in anneal furnace.



Fig. 3. The unpacked strip steel deviation correction sensor.

### 3.2. Grid Division

Because relative model length is too long, only a section of relative model grid division result was shown as Fig. 4.

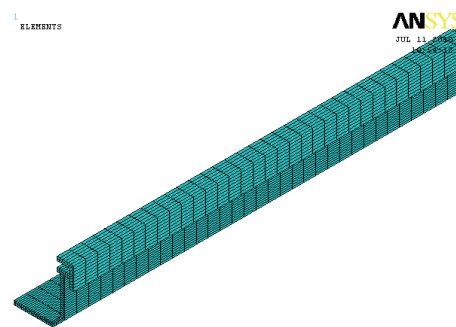


Fig. 4. A section of relative model grid division result.

### 3.3. Boundary Condition Definition

GH3030 high temperature alloy steel was adopted as sensor metal frame material. Only heat conduction in model inside was considered. Relative model was divided into left section, middle section and right section. Corresponding temperatures were loaded on them. Model material diathermancy was regarded as isotropy. The latent heat influences engendered by high temperature phase change were not considered.

### 3.4. Transient State Heat Analysis Result

The heat influences of sensor in anneal furnace are synthetical processes combining heat conduction, heat convection and heat radiation. Transient state heat analyses were made on relative model under three typical working conditions by ANSYS software in this paper. The displacement distribution picture of sensor metal frame at certain time can be obtained. In working condition 1, middle section temperature is 350 °C, left section temperature and right section temperature are all 300 °C. In working condition 2, middle section temperature is 800 °C, left section temperature and right section temperature are all 600 °C. In working

condition 3, middle section temperature is 1000 °C, left section temperature and right section temperature are all 800 °C. The displacement distribution picture of sensor metal frame under working condition 1 was shown as Fig. 5.

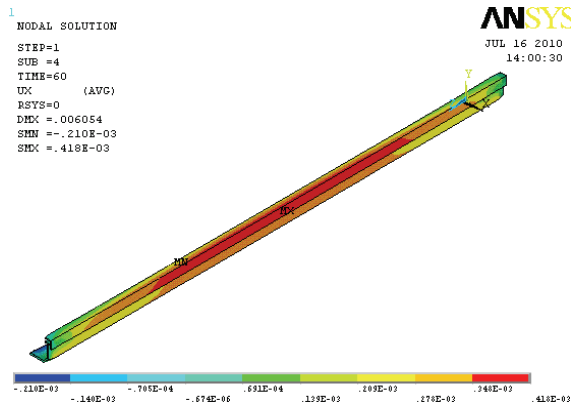


Fig. 5. The displacement distribution picture of sensor metal frame under working condition 1.

Fig. 5 shows that the maximal displacement of sensor metal frame on X direction is 0.418 mm under working condition 1. The displacement distribution picture of sensor metal frame under working condition 2 was shown as Fig. 6.

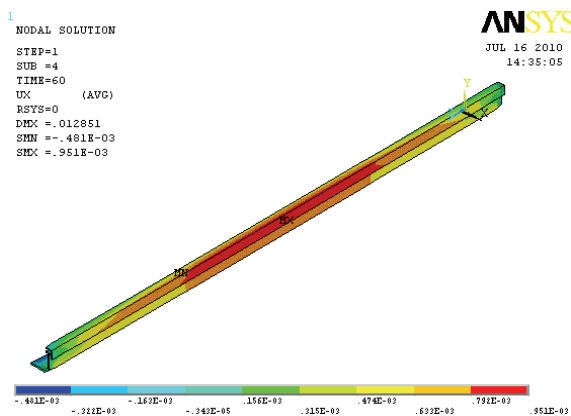


Fig. 6. The displacement distribution picture of sensor metal frame under working condition 2.

Fig. 6 shows that the maximal displacement of sensor metal frame on X direction is 0.951 mm under working condition 2. The displacement distribution picture of sensor metal frame under working condition 3 was shown as Fig. 7.

Fig. 7 shows that the maximal displacement of sensor metal frame on X direction is 1.191 mm under working condition 3. From Fig. 5 to Fig. 7, it shows that the middle position displacement of sensor metal frame on X direction is maximal. Temperature gradient and deformation will increase with temperature increase.

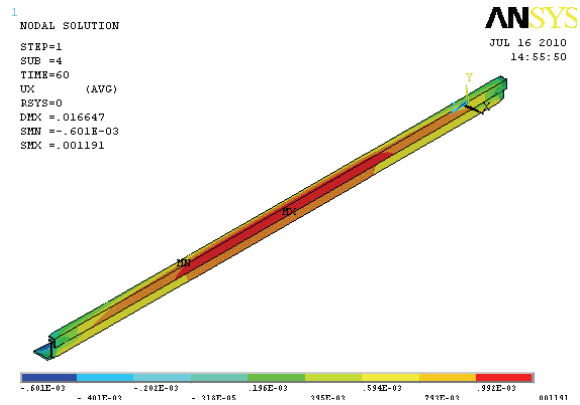


Fig. 7. The displacement distribution picture of sensor metal frame under working condition 3.

### 3.5. Heat Structure Coupling Analysis Result

Relative displacement distribution pictures of sensor metal frame under above mentioned three typical working conditions can be obtained by heat structure coupling analysis. The displacement distribution picture of sensor metal frame under working condition 1 was shown as Fig. 8.

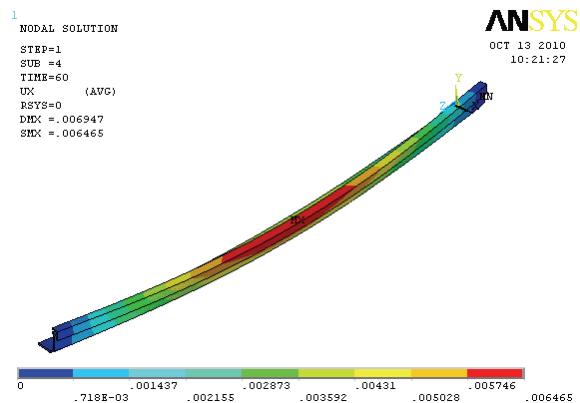


Fig. 8. The displacement distribution picture of sensor metal frame under working condition 1.

Fig. 8 shows that the maximal displacement of sensor metal frame on X direction is 6.465 mm under working condition 1. The displacement distribution picture of sensor metal frame under working condition 2 was shown as Fig. 9.

Fig. 9 shows that the maximal displacement of sensor metal frame on X direction is 8.933 mm under working condition 2. The displacement distribution picture of sensor metal frame under working condition 3 was shown as Fig. 10.

Fig. 10 shows that the maximal displacement of sensor metal frame on X direction is 10.608 mm under working condition 3. From Fig. 8 to Fig. 10, it shows that the middle position displacement of sensor metal frame on X direction is maximal. Temperature gradient and deformation will increase with temperature increase. Relative displacements

become bigger under the associated actions of temperature field and gravity field.

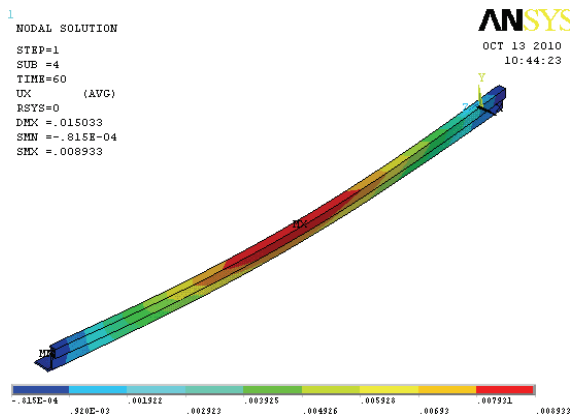


Fig. 9. The displacement distribution picture of sensor metal frame under working condition 2.

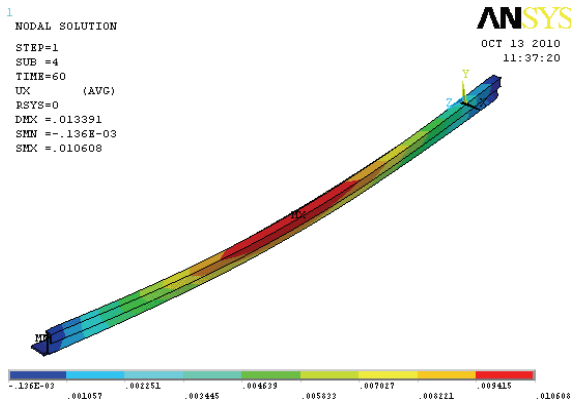


Fig. 10. The displacement distribution picture of sensor metal frame under working condition 3.

## 4. Strip Steel Deviation Correction Check Control System Design

### 4.1. Strip Steel Deviation Correction Check Control System Formation

Strip steel deviation correction check control system contains sensor, first order amplification, second order amplification, rectification, smoothing, A/D switch, controller, electric and hydraulic servo valve, hydraulic cylinder and deviation rectification roller frame. It was shown as Fig. 11.

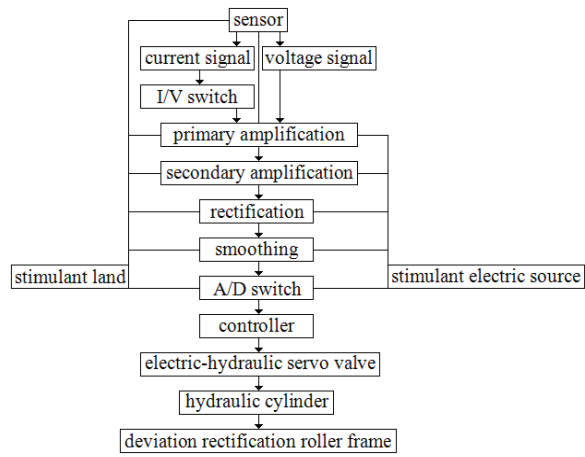


Fig. 11. Strip steel deviation correction check control system.

### 4.2. The Design of Prepositive Amplification Rectification Circuit

The output signals of sensor are differential signals. In order to eliminate common mode disturbances and noises, differential voltage amplifier was added into test circuit. Differential amplification circuit was shown as Fig. 12. The alternating signals after first order amplification are still very weak. It is very difficult in showing, analyzing and applying these signals directly. Thus second order amplification and rectification treatments were made on relative signals. Second order amplification rectification circuit was shown as Fig. 13.

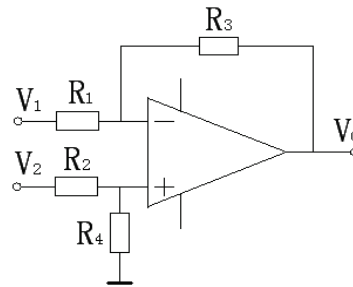


Fig. 12. Differential amplification circuit.

### 4.3. Lowpass Smoothing Circuit Design

First order lowpass smoothing circuit can not satisfy the requirement of quick amplitude frequency characteristics decrease. Thus second order infinite gain multiple circuit feedback lowpass smoothing circuit was applied in this paper. It was shown as Fig. 14.

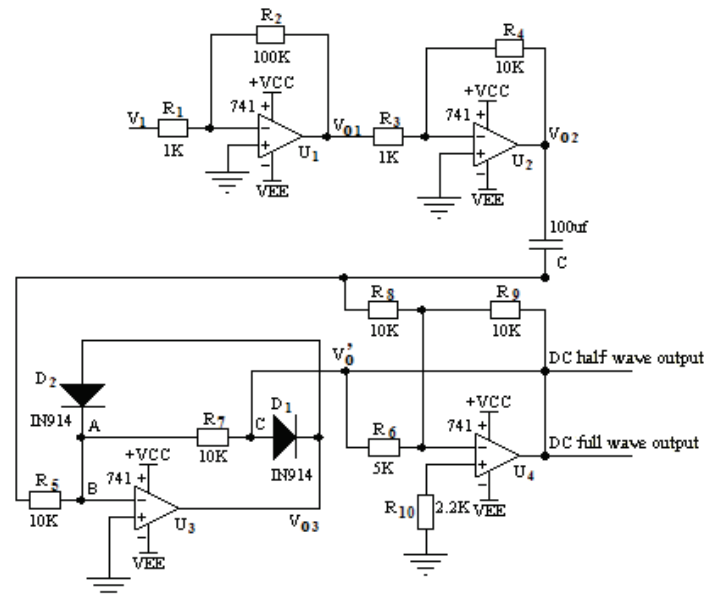


Fig. 13. Second order amplification rectification circuit.

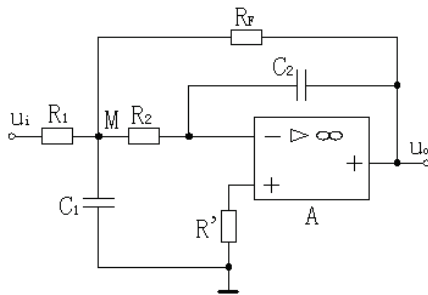


Fig. 14. Second order infinite gain multiple circuit feedback lowpass smoothing circuit.

## 5. Conclusions

Electromagnetic inductance strip steel deviation correction sensor was designed independently by electromagnetic induction principle in this paper to adapt the environment in anneal furnace. QZ high strength polyester varnished wires were wound into rectangle electromagnetic inductance coil directly by automatic numerical control winder. The technic quotas of strip steel deviation correction sensor designed independently in this paper are same as similar product of Germany EMG Company. Relative technic quotas are as follows. Work temperature is 600 °C to 1000 °C. Surroundings temperature is 0 °C to 85 °C. Checkable strip steel thickness is 0.3 mm to 2.5 mm. Centring precision is  $\pm 5$  mm. GH3030 high temperature alloy steel was adopted as sensor metal frame material.

The right half part model of sensor metal frame was constructed by SolidWorks software in this paper. Transient state heat analyses were made on relative model under three typical working conditions by ANSYS software. Relative displacement distribution pictures show that the middle position displacement of sensor metal frame on X direction is

maximal. Temperature gradient and deformation will increase with temperature increase. Heat structure coupling analysis was made on relative model by ANSYS software. Relative displacement distribution pictures show that the middle position displacement of sensor metal frame on X direction is maximal. Temperature gradient and deformation will increase with temperature increase. Relative displacements become bigger under the associated actions of temperature field and gravity field. The method of adding reinforce ribbed slabs on sensor metal frame can enhance sensor deformation resistance.

Strip steel deviation correction check control system was designed in this paper. Differential amplification circuit was adopted as first order amplification to eliminate common mode disturbances and noises. Second order amplification and rectification treatment was made on weak signals after first order amplification by second order amplification rectification circuit. Second order infinite gain multiple circuit feedback lowpass smoothing circuit was adopted on smoothing. Relative smoothing effects are good.

## Acknowledgements

This work was supported by the National Natural Science Foundation of China (No. 51144007), the Scientific Research Foundation for the Returned Overseas Chinese Scholars of State Education Ministry (No. 20111139).

## References

- [1] J. Y. Xu, H. Shi, R. L. Zhang, The application of deviation rectification system in cold rolling production, *Silicon Valley*, Vol. 10, Issue 20, 2011, pp. 154-155.

- [2]. Y. M. Wen, The application of strip steel deviation rectification system in cold rolling production, *Journal of Anhui University of Technology (Natural Science Edition)*, Vol. 27, Issue S1, 2010, pp. 24-27.
- [3]. F. X. Zou, X. L. Yang, Z. X. Gao, The control method of strip steel deviation rectification based on inductive position test principle, *Metallurgy Automation*, Vol. 30, Issue 4, 2006, pp. 37-39.
- [4]. W. Wan, Z. M. Qiu, Z. P. Wu, Analysis and simulation of hoop corrects an error system, *Journal of Wuhan Institute of Technology*, Vol. 32, Issue 3, 2010, pp. 100-102.
- [5]. L. L. Wang, D. Z. Chao, The design and application research of strip steel deviation rectification equipment in continuous strip steel treatment set, *Machinery & Electronics*, Vol. 27, Issue 12, 2010, pp. 46-48.
- [6]. J. Ma, The analysis of strip steel deviation rectification system in continuous annealing set furnace, *Sichuan Metallurgy*, Vol. 34, Issue 2, 2012, pp. 52-55.
- [7]. S. H. Sun, The development direction of modern sensor, *Journal of Electronic Measurement and Instrument*, Vol. 23, Issue 1, 2009, pp. 1-10.
- [8]. D. W. Dong, The application and development condition analysis of China sensor, *Radio Frequency Universal Journal*, Vol. 5, Issue 3, 2010, pp. 35-38.
- [9]. X. Ding, The development of intelligent sensor was promoted by enterprise requirement, *Maschinen Markt*, Vol. 29, Issue 3, 2010, pp. 21-23.

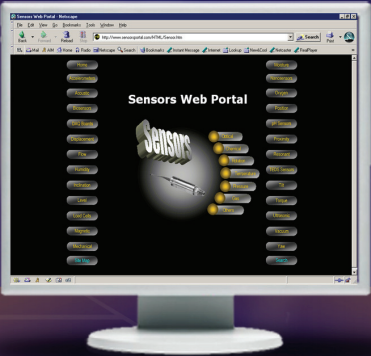
---

2013 Copyright ©, International Frequency Sensor Association (IFSA). All rights reserved.  
(<http://www.sensorsportal.com>)



**SENSORS WEB PORTAL** 

- **MEMS**
- **NEMS**
- **NANOSENSORS**
- **SMART SENSORS**



**All about SENSORS**  
<http://www.sensorsportal.com>

## Multi-sensor Target Recognition Based on VIKOR

<sup>1</sup> Haiping REN, <sup>2</sup> Lianwu YANG

<sup>1</sup> School of Software, Jiangxi University of Science and Technology,  
330013, P. R.China

<sup>2</sup> School of Mathematics and Computer Science, Yichun University,  
Yichun 330060, P. R. China

<sup>1</sup> Tel.: 15979014223

<sup>1</sup> E-mail: [chinarhp@163.com](mailto:chinarhp@163.com)

*Received: 1 June 2013 /Accepted: 25 August 2013 /Published: 30 September 2013*

---

**Abstract:** Aiming at the target recognition problem of multi-sensor with multiple characteristic indexes, a new fusion method is proposed. The method firstly substitutes the distance of confidence for the ordinary attribute values, and the weights of attributes are derived by solving the optimal programming of maximizing the total square deviation of the confidence distance for all attributes. Then according to the basic ideology of traditional VIKOR method, the rule of target recognition is given. The method may avoid the subjectivity of the weight of characteristic indexes and improve the objectivity and accuracy of target recognition. Numerical simulation illustrates the effectiveness and exercisable of the proposed method. *Copyright © 2013 IFSA.*

**Keywords:** Multi-sensor, Data fusion, Target recognition, VIKOR.

---

### 1. Introduction

Sensors are the devices used to make observations or measurements of physical quantities such as temperature, range, angle, etc. A certain relationship of mapping exists between this measured quantity and the state of nature, and thus necessary information is provided. In this regard, the interpretation of sensor measurements and sensor environment is extremely important. However, physical descriptions of sensors (sensor models) are unavoidably only approximations owing to incomplete knowledge and understanding of the environment. This, coupled with the varying degrees of uncertainty inherent in a system itself and the practical reality of occasional sensor failure, results in the lack of coincidence in sensor measurements. The fact is that despite any advances in sensor technologies, no single sensor is capable of obtaining all the required information reliably, at all times, in often dynamic environments. The obvious solution in

this case is to employ several sensors thus extracting as much information as possible.

In multi-sensor systems these sensors can be used to measure the same quantities, which is especially helpful in the case of sensor failure. Alternatively, different quantities associated with the same state of nature can be measured by different sensors. In addition, various sensor technologies can be employed. In all these cases the uncertainty is significantly reduced thus making the system more reliable.

Multisensor information fusion is being applied to a wide variety of fields such as automated target recognition, battlefield surveillance, guidance and control of autonomous vehicles, robotics, industrial process control, medical diagnostics, image processing and pattern recognition. The basic task of the target recognition is the use of the characteristics of a sample to compare with the target library known target characteristics to identify the sample, and divides it into the corresponding target type. Multi-

sensor data fusion (MSDF) is defined as the process of integrating information from multiple sources to produce the most specific and comprehensive unified data about an entity, activity or event [1]. In recent years, the multisensor data fusion has become an important means of target recognition. For multi-sensor target recognition problem, many authors have developed many fusion methods. For example, papers [1-6] proposed target recognition method based on the Dempster – Shafer evidence theory, papers [7-10] proposed target recognition method based on the theory of fuzzy, etc. These fusion methods all work well. However, methods based on Shafer-Dempster evidence and fuzzy theories excessively depend on the selection of basic probability assignment and the membership function. Papers [11-13] studied the problem for multi-sensor object recognition with several characteristic indexes, and proposed variable fuzzy method [11], extension method [12] and maximum likelihood method [13], respectively. However, characteristic weights in these methods are artificially determined, which is influenced greatly by the subjective factors. To overcome these difficulties, avoid the subjective randomness of selecting weights of the characteristic indexes, and improve the trustworthy and scientific degree of the object recognition result, this paper uses confidence distance, which propose by [14] as the characteristic attribute value, and then use optimization method to determine the objective characteristics of the weights of indicators, and based on the basic idea of the VIKOR, a new sensor target recognition method is proposed. As close to ideal point, the TOPSIS method in terms of attributes aggregation cannot actually reflect the close degree of each scheme and ideal solution, Opricovic (1998) [15] proposed a multicriteria compromise solutions for sorting (VIKOR) method, which is a compromise between sorting method, its biggest characteristic is to provide the maximum group interests and minimize the individual regret of the opposition, with other traditional methods, such as TOPSIS, PROMETHEE method and ELECTRE decision has strong superiority compared [16, 17].

A target recognition database contains  $n$  different target recognition category, noted as,  $\pi = \{\pi_1, \pi_2, \dots, \pi_n\}$ , each target has  $m$  a characteristic parameters, recorded as,  $o = \{o_1, o_2, \dots, o_m\}$ . Set  $\theta_{ij}$  and  $\sigma_{ij}^2$  are respectively said to the first  $j$  category  $\pi_i$  feature parameters (attributes) of the features (attributes) value and variance. The system has a characteristic vector matrix  $X = (\theta_{ij})_{m \times n}$ . In target recognition, always through the identified target of each characteristic parameters, and the observation and target database known target characteristic parameters matching to determine the identified target category. We use  $n$  different sensors to an unknown target object of study of each characteristics were observed. The first  $i$  set a sensor to detect the object first  $j$  a feature index of the

observed value  $\theta_{0j} (j=1,2,\dots,n)$ , and the task of data fusion is according to the value of state  $\theta_{0j} (j=1,2,\dots,n)$  to determine the research object belongs.

## 2. Target Fusion VIKOR Method

### 2.1. Confidence Distance

Because characteristics observed value has many causes of random error uncertain factors, thus will feature observations using probability distribution to describe. For any characteristic value, might as well put obey the normal distribution. Will be identified target of each characteristic parameters of the observed value and the target database known target parameters matching, must first determine the matching measure, therefore define the concept of a distance measure. To check the consistency of the sensor, Luo (1998) introduced the definition of confidence distance measure, is as follows:

$$d_{ij} = \int_{x_i}^{x_j} \frac{1}{\sqrt{2\pi\sigma_i^2}} \exp\left(-\frac{(x-x_i)^2}{2\sigma_i^2}\right) dx, \quad (1)$$

$$= P(|Z| \leq \frac{|x_i - x_j|}{\sigma_i})$$

where  $Z \sim N(0,1)$ , and  $x_i, \sigma_i^2$  are the measured value of the sensor and the measurement variance respectively,  $d_{ij}$  is said the confidence distance of sensor  $i$  and  $j$ .

Suppose that  $X_{ij}, X_{0j}$  are target characteristic values of class  $i$  and general goals  $j$  respectively. The random variable  $X_{ij}$  is independent with  $X_{0j}$ ,  $X_{ij} \sim N(\theta_{ij}, \sigma_{ij}^2), X_{0j} \sim N(\theta_{0j}, \sigma_{0j}^2)$ , and then it is easily proved that

$$X_{ij} - X_{0j} \sim N(\theta_{ij} - \theta_{0j}, \sigma_{ij}^2 + \sigma_{0j}^2),$$

Let

$$Z = \frac{X_{ij} - X_{0j} - (\theta_{ij} - \theta_{0j})}{\sqrt{\sigma_{ij}^2 + \sigma_{0j}^2}},$$

then  $Z \sim N(0,1)$ .

By Luo confidence distance measure inspiration, [18] defines a new distance measure,

$$d_{ij} = d(\theta_{ij}, \theta_{0j}) = P(|Z| \leq \frac{|\theta_{ij} - \theta_{0j}|}{\sqrt{\sigma_{ij}^2 + \sigma_{0j}^2}}), \quad (2)$$

$$= 2\Phi\left(\frac{|\theta_{ij} - \theta_{0j}|}{\sqrt{\sigma_{ij}^2 + \sigma_{0j}^2}}\right) - 1$$

where  $\Phi(\cdot)$  is the distribution function of standard normal distribution.  $d_{ij}$  is the target class  $i$  and general goals for the first  $j$  a characteristic value of the distance measure. Thus we get the target class and general goals for confidence distance matrix  $D = (d_{ij})_{m \times n}$ .

**2.2. Weight of Characteristic Indexes**

If a attributes (features)  $k$  for all the target for a class are common, the attributes of target recognition will doesn't work, can make its weight is 0; Conversely, if the attribute  $k$  makes all target class and general goals for about the attributes of the characteristic value difference is bigger, the attributes of target recognition will play a great role, at this time, should give greater weight.

Target category  $i, j$  respectively with the target to know about attribute  $k$  confidence distance square deviation for  $w_k(d_{ki} - d_{kj})^2$ , the target class  $I$  and other target category about attribute  $k$  confidence distance square deviation for  $\sum_{i=1}^m w_k(d_{ki} - d_{kj})^2$ , all target category about attribute  $k$  confidence distance sum of squares of deviations for  $\sum_{i=1}^m \sum_{j=1}^n w_k(d_{ki} - d_{kj})^2$ . Therefore, the choice of attribute weights should make all attributes confidence distance deviation sum of squares is the largest, and the optimization model can be the structure is as follows:

$$\begin{aligned} \max & \sum_{k=1}^n \sum_{i=1}^m \sum_{j=1}^n w_k(d_{ki} - d_{kj})^2 \\ \text{s.t.} & \sum_{k=1}^n w_k = 1, w_k \geq 0, k = 1, 2, \dots, n \end{aligned} \quad (3)$$

To solve the above model, structure Lagrange function:

$$\begin{aligned} L(w, \lambda) = & \sum_{k=1}^n \sum_{i=1}^m \sum_{j=1}^n w_k(d_{ki} - d_{kj})^2 \\ & + 2\lambda(\sum_{k=1}^n w_k - 1) \end{aligned} \quad (4)$$

For partial derivative, and make it to zero, get:

$$\begin{cases} \frac{\partial L(w, \lambda)}{\partial w_k} = 2 \sum_{i=1}^m \sum_{j=1}^n w_k(d_{ki} - d_{kj})^2 + 2\lambda = 0 \\ \frac{\partial L(w, \lambda)}{\partial \lambda} = 2(\sum_{k=1}^n w_k - 1) = 0 \end{cases} \quad (5)$$

Then we have

$$w_k = \frac{1}{J_k \sum_{k=1}^n 1/J_k}, \quad (6)$$

where

$$J_k = \sum_{i=1}^m \sum_{j=1}^n w_k(d_{ki} - d_{kj})^2, k = 1, 2, \dots, n,$$

**2.3. Identification of the Target VIKOR Method**

The VIKOR method is first proposed by Opricovic (1998). It is one of the important methods for multi-criteria decision making problem. Its basic idea is to first determine the ideal solution and negative ideal solution, then according to each value of each alternative and ideal scheme's proximity to sorting and preferred alternatives. Its characteristic is to maximize the utility, minimizing individual regret, which is a compromise decision method. VIKOR method is developed with the measure

$$d_j^p = \left\{ \sum_{i=1}^n \left[ w_i \left( \frac{x_i^* - x_{ij}}{x_i^* - x_i^-} \right) \right]^p \right\}^{1/p}$$

to a decision-making method. When  $p = 1$  and  $p = \infty$  respectively are:

$$\begin{aligned} d_j^{p=1} &= S_j = \sum_{i=1}^n w_i \left( \frac{x_i^* - x_{ij}}{x_i^* - x_i^-} \right) \\ d_j^{p=\infty} &= Q_j = \max_i \left\{ w_i \left( \frac{x_i^* - x_{ij}}{x_i^* - x_i^-} \right) \mid i = 1, 2, \dots, n \right\} \end{aligned}$$

In this paper, the proposed objection recognition method based compromise ranking algorithm VIKOR is given as the following steps:

**Step1.** Define the ideal solution

$$d^* = \{d_1^*, d_2^*, \dots, d_n^*\} = \min_i \{d_{ij}, j = 1, 2, \dots, n\}$$

and the negative solution

$$d^- = \{d_1^-, d_2^-, \dots, d_n^-\} = \max_i \{d_{ij}, j = 1, 2, \dots, n\}$$

**Step2.** Compute the values  $S_i$  and  $R_i$ ,  $i=1, 2, \dots, m$ . by the relations

$$S_i = \sum_{j=1}^n w_j \frac{d_j^* - d_{ij}}{d_j^* - d_j^-}, \quad (7)$$

$$R_i = \max_j \{w_j \left( \frac{d_j^* - d_{ij}}{d_j^* - d_j^-} \right)\}, \quad (8)$$

where  $w_i, i=1,2,\dots,n$  are the weights of attribute given by (6).

**Step 3.** Compute the value  $Q_i, i=1,2,\dots,m$ , by the relation

$$Q_i = \lambda \frac{S_i - S^*}{S^- - S^*} + (1 - \lambda) \frac{R_i - R^*}{R^- - R^*}, \quad (9)$$

where  $S^* = \min_i S_i, S^- = \max_i S_i, R^* = \min_i R_i, R^- = \max_i R_i$ , and  $\nu$  is introduced as weight of the strategy of “the majority of criteria”(or “the maximum group utility”), where  $\nu = 0.5$ .

**Step 4.** Now, we give the following rule of object recognition is given as:

$$\text{If } K_0 = \arg \min_i \{C_i\},$$

$$\text{where } C_i = 1 - Q_i, i=1,2,\dots,m,$$

then judging the unknown object is target  $\pi_{K_0}$ .

### 3. A Simulation Example

In order to illustrate the effectiveness of the fusion method proposed in this paper. A simulation data described in [13] is considered. In order to realize intelligent robots to object to be automatic recognition and classification of the method is applied to the sensor in the robot system. The system by SCARA robot, the robot control and drive, sensor system, the main computer, etc, in the multisensor system equipped with six d force sleep, and close to sleep, and contact sleep and sliding sleep, and array touch, heat sensation for the sensor and the corresponding signal processor. In the experiment determined the six independent characteristics of the characteristic index to show the workpiece, they were shape factor, the section center moment, surface reflection ability, surface roughness of the workpiece, weight, material coefficient of thermal conductivity. A total of five kinds of different selection of the workpiece as the standard, the model of the characteristic value and variance (Table 1).

**Table 1.** The model of the characteristic value and standard variance.

Part	$\theta_1$	$\theta_2$	$\theta_3$	$\theta_4$	$\theta_5$	$\theta_6$
1	1.30	1.86	3.07	2.75	1.73	3.71
	(0.12)	(0.10)	(0.11)	(0.25)	(0.28)	(0.37)
2	2.43	3.71	2.28	2.34	2.87	1.57
	(0.37)	(0.17)	(0.37)	(0.07)	(0.17)	(0.19)
3	2.18	1.93	1.37	1.52	0.95	3.42
	(0.15)	(0.11)	(0.13)	(0.12)	(0.25)	(0.27)
4	1.85	2.52	2.97	1.93	1.90	2.70
	(0.19)	(0.23)	(0.25)	(0.19)	(0.340)	(0.23)
5	2.15	3.10	1.87	0.59	2.14	2.13
	(0.25)	(0.29)	(0.11)	(0.31)	(0.17)	(0.07)

The sensor signal through the data collect and input to the computer, and through the information analysis and characteristic level data fusion for some unknown characteristic of the data in Table 2.

**Table 2.** The sensor measurement value (M) and standard variance (SD).

Sensor	1	2	3	4	5	6
M	2.15	1.30	2.15	2.12	1.88	2.81
SD	(1.30)	(0.32)	(0.17)	(0.21)	(0.09)	(0.27)

This paper presents the use of the method to identify the unknown workpiece.

**Step 1.** Table 1, 2 of the data and (1), (2) type get feature matrix and confidence distance matrix is as

$$X = \begin{pmatrix} 1.30 & 2.43 & 2.18 & 1.85 & 2.15 \\ 1.86 & 3.71 & 1.93 & 2.52 & 3.10 \\ 3.07 & 2.28 & 1.37 & 2.97 & 1.87 \\ 2.75 & 2.34 & 1.52 & 1.93 & 0.59 \\ 1.73 & 2.87 & 0.95 & 1.90 & 2.14 \\ 3.71 & 1.57 & 3.42 & 2.70 & 2.13 \end{pmatrix}$$

$$D = \begin{pmatrix} 0.8377 & 0.2779 & 0.0378 & 0.3489 & 0 \\ 0.6125 & 0.9994 & 0.6633 & 0.9000 & 0.9788 \\ 0.9197 & 0.1404 & 0.8465 & 0.7942 & 0.4033 \\ 0.6471 & 0.3224 & 0.7073 & 0.2361 & 0.9661 \\ 0.1948 & 0.9478 & 0.8893 & 0.0243 & 0.3899 \\ 0.7394 & 0.9325 & 0.5935 & 0.1236 & 0.7565 \end{pmatrix}$$

**Step2.** Determine the ideal point and negative ideal point respectively are:

$$d^* = \{d_1^*, d_2^*, \dots, d_n^*\} \\ = \{0.8377, 0.9994, 0.9197, 0.9661, 0.9478, 0.9325\} \\ d^- = \{d_1^-, d_2^-, \dots, d_n^-\} \\ = \{0, 0.6125, 0.1404, 0.2361, 0.0243, 0.1236\}$$

**Step 3.** By section 2.2 of the given method to determine the weights of attributes vector:

$$w = (w_1, w_2, w_3, w_4, w_5, w_6) \\ = (0.0519, 0.2662, 0.1105, 0.2591, 0.088, 0.2243)$$

**Step 4.** Compute the values  $S_i, R_i$  and  $Q_i, i=1,2,\dots,6$ , and given as

$$S = (S_1, S_2, S_3, S_4, S_5)^T \\ = (0.4953, 0.6263, 0.5174, 0.3121, 0.7587)^T \\ R = (R_1, R_2, R_3, R_4, R_5)^T \\ = (0.1708, 0.2662, 0.1672, 0.1978, 0.2591)^T$$

$$Q = (Q_1, Q_2, Q_3, Q_4, Q_5)^T$$

$$= (0.2228, 0.8518, 0.2298, 0.1544, 0.9641)^T$$

**Step 5.** Compute the support degree  $C$ , and give the unknown target belong to category.

$$C = 1 - Q = (0.7772, 0.1482, 0.7702, 0.8456, 0.0259)^T$$

Due to the maximum  $C_4 = 0.8456$ , so the time to check the unknown workpiece as the fourth kind of workpiece. The [18] recognition results are consistent.

This paper presents to the VIKOR method and the literature [18] grey relational grade, improved grey correlation method and maximum likelihood method [13] comparison. That will be all kinds of methods of the evaluation of target value as the support degree. Then despite their recognition results for the fourth kind of the workpiece, but four methods for all kinds of target recognition degree are different. Table 3 reflects the four methods support degree of difference. The table of the gap is the fourth kind of the workpiece support and other kinds of workpiece support difference.

**Table3.** Three methods support degree comparison

Part	1	2	3	4	5
Improved GRD method	0.4446	0.4745	0.4454	0.6080	0.4301
	0.1634	0.1335	0.1626		0.1779
GRD method	0.5012	0.5662	0.5661	0.6239	0.6055
	0.1227	0.0577	0.0578		0.0184
ML method	0.1390	0.1190	0.1260	0.2580	0.0200
	0.1190	0.1390	0.1320		0.2380
The paper	0.7772	0.1482	0.7702	0.8456	0.0359
	0.0684	0.6974	0.0754		0.8097

Can be seen from Table 3, this paper uses the method to get the category 4 support for 0.8456 more than other methods support, and if use of the workpiece and the fourth class to other workpiece support degree difference to sum, then get four methods to support the total gap are: 0.6374, 0.2566, 0.6280 and 1.6500, so the VIKOR method get support always the biggest gap. Obviously, the greater the gap to target recognition that the distinction between the higher level of recognition results, and the higher the credibility.

#### 4. Conclusions

The confidence distance as a new attribute value, by solving the attributes confidence distance deviation square sum to maximize the objective optimization model to determine the weights of attributes, and thereby reducing the human subjective factors of interference, give full consideration to the

different attribute value itself to the importance of information fusion degree, so as to enhance the target recognition results of objectivity and differentiate. This method is simple and easy to use Matlab software such as program operation, to solve the problem of target recognition provides a new way.

#### Acknowledgements

This work is partially supported by Natural Science Foundation of Jiangxi Province of China (No. 2010GZS0190), Science and Technology Project of Jiangxi province educational department in China (No. GJJ116 00 and GJJ11479).

#### References

- [1]. Y. J. Pang, Z. F. Du, A new method of the basic probability assignment, *Journal of Fushun Petroleum Institute*, Vol. 14, 1994, pp. 52-54.
- [2]. P. L. Begler, Shafer-Dempster reasoning with application to multi-sensor target identification system, *IEEE Transactions on SMC*, Vol. 17, 1997, pp. 968-977.
- [3]. X. Yu, C. Z. Han, Q. Pan, et al., Method based on evidence theory for multi-source target recognition, *Systems Engineering and Electronics*, Vol. 29, Issue 5, 2007, pp. 788-790.
- [4]. K. J. Cao, Z. G. Zhao, H. Jiang, Target identification based on D-S theory and rule of conditioning, *Systems Engineering and Electronics*, Vol. 28, Issue 8, 2006, pp. 1169-1172.
- [5]. Y. Yang, Z. R. Jing Zhang, Multi-sources information fusion algorithm in airborne detection system, *Journal of Systems Engineering and Electronics*, Vol. 18, Issue 1, 2007, pp. 171-176.
- [6]. T. L. Chen, P. W. Que, Object recognition based on modified combination rule, *Journal of Systems Engineering and Electronics*, Vol. 17, Issue 2, 2006, pp. 279-283.
- [7]. S. Y. Chen, J. M. Hu, Variable fuzzy method and its application in parts recognition, *Systems Engineering and Electronics*, Vol. 28, Issue 9, 2006, pp. 1325-1328.
- [8]. H. Odeberg, Fusion sensor information using fuzzy measures, *Robotica*, Vol. 31, 1989, pp. 217-242.
- [9]. J. S. Liu, R. H. Li, Y. L. Liu, et al., Multi-sensor data fusion based on correlation function and fuzzy integration function, *Systems Engineering and Electronics*, Vol. 28, Issue 7, 2006, pp. 1006-1009.
- [10]. J. Chanussot, G. Mauris, P. Lambert, Fuzzy fusion techniques for linear features detection in multi-temporal SAR images, *IEEE Transactions on Geoscience and Remote Sensing*, Vol. 37, Issue 3, 1999, pp. 1292-1305.
- [11]. S. P. Wan, Multi-sensor target recognition based on entropy weight, *Systems Engineering and Electronics*, Vol. 31, Issue 3, 2009, pp. 500-502.
- [12]. L. W. Diao, C. W. Wang, J. Y. Shang, etc., Improved and generalized consensus data fusion method, *Systems Engineering and Electronics*, Vol. 24, Issue 9, 2002, pp. 60-62.
- [13]. Y. Shao, F. C. Shi, J. Peng, An approach of robot non-vision multi-sensor fusion, *Acta Electronica Sinica*, Vol. 24, Issue 8, 1996, pp. 94-97.

- [14]. R. C. Luo, M. Lin, P. S. Scherp, Dynamic multi-sensor data fusion system for intelligent robots, *IEEE Journal of Robotics and Automation*, Vol. 4, Issue 4, 1998, pp. 386-396.
- [15]. S. Opricovic, Multicriteria optimization of civil engineering systems, *Faculty of Civil*, Belgrade, Jugoslavia, 1998.
- [16]. S. Opricovic, G. H. Tzeng, Compromise solution by MCDM methods: A comparative analysis of VIKOR and TOPSIS, *European Journal of Operational Research*, Vol. 156, Issue 2, 2004, pp. 445-455.
- [17]. S. Opricovic, G. H. Tzeng, Extended VIKOR method in comparison with outranking methods, *European Journal of Operational Research*, Vol. 178, Issue 2, 2007, pp. 514-529.
- [18]. S. P. Wan, Method of improved grey relational degree for multi-sensor target recognition, *Computer Engineering and Applications*, Vol. 45, Issue 24, 2009, pp. 25-27.

2013 Copyright ©, International Frequency Sensor Association (IFSA). All rights reserved.  
(<http://www.sensorsportal.com>)

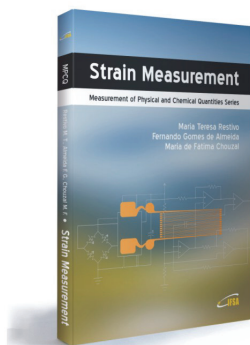


International Frequency Sensor Association (IFSA) Publishing

Maria Teresa Restivo, Fernando Gomes de Almeida, Maria de Fátima Chouzal

## Strain Measurement

Measurement of Physical and Chemical Quantities Series



Formats: printable pdf (Acrobat) and print (hardcover), 106 pages

ISBN: 978-84-616-0067-0,  
e-ISBN: 978-84-615-9897-7

'*Strain Measurement*' deals with measurement of stresses and strains in mechanical and structural components. This topic is related to such diverse disciplines as physical and mechanical sciences, engineering (mechanical, aeronautical, civil, automotive, nuclear, etc.), materials, electronics, medicine and biology, and uses experimental methodologies to test and evaluate the behaviour and performance of all kinds of materials, structures and mechanical systems.

The material covered includes:

- Introduction to the elementary concepts of stress and strain state of a body;
- Experimental extensometry measurement techniques;
- Basic instrumentation theory and techniques associated with the use of strain gauges;
- Optical fibre based extensometry;
- Uncertainty estimation on the measurement of mechanical stress;
- Supplemented multimedia components such as animations, simulations and video clips.

The different subjects exposed in this book are presented in a very simple and easy sequence, which makes it most adequate for engineering students, technicians and professionals, as well as for other users interested in mechanical measurements and related instrumentation.

[http://sensorsportal.com/HTML/BOOKSTORE/Strain\\_Measurement.htm](http://sensorsportal.com/HTML/BOOKSTORE/Strain_Measurement.htm)

## Design of Wireless Sensor Network Security and Solution by MAC Protocol and Topology Control Technology

<sup>1</sup> Zhen LIU, <sup>2</sup> Yanhao CHEN, <sup>1</sup> Xiaoqin MA

<sup>1</sup> Henan Institute of Science and Technology,  
Henan Xinxiang, 453003, China

<sup>2</sup> Network Center, Henan Normal University,  
Henan Xinxiang, 453000, China

<sup>1</sup> Tel.: 13613738850

E-mail: eduliuzhen@163.com

*Received: 2 July 2013 / Accepted: 25 August 2013 / Published: 25 September 2013*

---

**Abstract:** Wireless sensor network security is the guarantee of the task execution confidentiality, data reliability, data fusion, and the security of data transmission. This paper analyzes security problems in wireless sensor network MAC protocol at present. The aim of topology control is through the transmission range control nodes to generate network topology satisfying certain properties, in order to extend the network life cycle, reduce network interference, improve the throughput. The paper proposes design of wireless sensor network security and solution by MAC protocol and topology control technology. Finally, this paper discusses a new security design of WSN based on more energy-efficient MAC protocol, and the simulation experiment is carried out in NS2 network. *Copyright © 2013 IFSA.*

**Keywords:** Wireless sensor network, MAC protocol, Topology control, Network security.

---

### 1. Introduction

Wireless sensor network (WSN) technology is a kind of integrated network system for monitoring, control and wireless communication technology. Sensor network nodes generally equipped with one or more sensors, the perception of the physical world. It adopts multi-hop propagation and no infrastructure network, acquisition and node is the issue of information, as well as the routing of information, has large scale, self-organization, dynamic, application, based on the data center etc. Wireless sensor network is different from the traditional one: the number of nodes in wireless sensor network, many network, generally do not have a globally unique identifier, wired, wireless network transmission system, each node has a unique address for the route.

Wireless sensor networks are the monitoring and management of the surrounding environment temperature, humidity, light, acceleration and other information technology. This wireless sensor nodes with sensor, sensor, control circuit, CPU wireless communication module, antenna, power supply device, through the Ad-Hoc communication technology, and the sensor nodes around the together to transmit data to the sink node. This paper introduces a wireless sensor network consists of a sink node and multiple sensor nodes by the sink node, uploaded to the remote host.

Wireless sensor network is composed of three parts: nodes, gateway and system. Measurement of spatial node distribution through connected with sensor to monitor the surrounding environment. The monitoring of the wireless data is sent to the gateway,

the gateway can be connected with the cable system, so you can use the software to finish data collecting, processing, analysis and display [1]. The router is a kind of special measuring node, you can use it to extend the distance in WSN and increase reliability.

In WMSN, the media access control (Medium, Access Control, MAC) protocol in wireless sensor network protocol stack, the main function is to allocate the limited wireless channel resource among sensor nodes competing, determines the wireless channel utilization and network performance, and is an important technology to ensure the normal operation of the whole network. According to the characteristics of complex WMSN limited hardware resources, audio and video media and abundant in information processing task, this paper summarizes the characteristics and challenges of the current MAC protocol design, the existing protocols are classified according to the channel access methods, focuses on the analysis of several typical protocol, and the protocol of WSN security support capabilities are discussed in detail. The paper proposes design of wireless sensor network security and solution by MAC protocol and topology control technology.

So it is not necessary to update the routing table information. Because of wireless, battery-powered, coverage and node lifetime is limited. A practical problem is how to extract data from a wireless sensor network deployed in the distance, a method of connecting WSN and existing network infrastructure, including the internet. Today most of the network using the IP protocol as the basic technology, therefore, how to achieve the WSN and IP network has become a hot research topic. Because WSN uses multi-hop propagation and no infrastructure network group, in the field or the battlefield and other harsh and remote environments, that are not covered in the power system and the operation of the local communication network, but often there is a big play sensor network, real-time monitoring to the field on target detection sensor control and remote access wireless sensor network is not realistic computer equipment, large power, using low power single chip and composition of the system, using Power-over-Ethernet technology can expand the Ethernet in a certain range covering range.

## 2. Analysis Security of Wireless Sensor Network by MAC Protocol

Wireless sensor network is a new research hot point crossed by many scientific fields of current international concern. Simply put, wireless sensor networks is a resource-constrained integrated sensing and driving control ability, computing ability, communication ability in a body (refers to the computation, storage and energy constraints) embedded node through the wireless way interconnected network. Also refers to the sensor nodes arranged in a specific application in the environment by means of wireless communication

networking, sensor node collecting data specified, node sends the data to the network through the wireless sensor network, and ultimately received by a particular application.

Network node software includes data acquisition and wireless sensor. Data acquisition includes temperature and humidity sensor, light sensor, infrared sensor, the analog quantity acquisition luminance sensor, infrared sensor data is directly input into the digital quantity, software design is relatively simple, only temperature and humidity sensor SHT as an example to introduce the data acquisition software. Wireless communication adopts ZigBee technology acquisition.

The WSN Ethernet gateway connected to the Windows controller or real-time controller based on LabVIEW. The Windows controller is based on PC, and can also be embedded PC; Need to install the LabVIEW software based on Windows operating system. That is to say, you can easily add any Windows system based on wireless data recording function. If the connection to the LabVIEW real-time controller, such as NI CompactRIO or other programmable automation controller (PAC), you can put the wireless measurement placed next to the cable measurement and control application. The operation of LabVIEW software in the main controller can be collected, and it is the measured data from the sensor network processing, analysis and display.

Wireless sensor network architecture is shown in Fig. 1, a sensor network system usually consists of sensor nodes, sink node (sink node) and the management node [2]. A large number of sensor nodes are randomly deployed in (sensor node) detection region (sensing region), on the self-organizing way constitute a network, data transfer by multi-hop relay will be detected to the sink node, finally through the Internet or satellite to a management node. The user through the management node configuration and management of sensor networks, detection task and collect test data release.

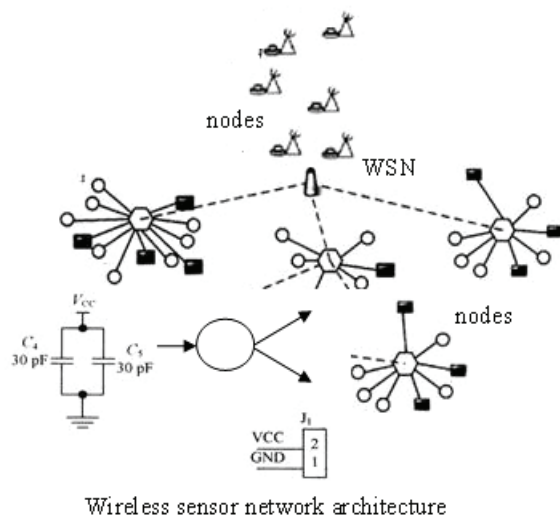


Fig. 1. Wireless sensor network and nodes architecture.

General description of the routing protocol is to choose a path from the source node to the target node, and then through some rules this path for transmitting information packet. Wireless sensor network routing protocol is to design objectives especially special requirements, no matter what kind of routing protocol, mostly including route discovery, maintenance of routing and routing (delete) process, and it is in the sleep state of the sensor node is far lower than the work or open for energy dissipation, state. In general, in order to save energy, sensor nodes are in the sleep state in before the data transmission, in need of data transmission, began to shift to the routing establishment (found) process.

Design of WSN key management protocol is a complex and difficult problem, in recent years, people from the natural biological systems (Natural biological systems) in a lot of inspiration, use some mechanism of natural biological systems to solve the problems of complex network [3]. Such as the use of genetic algorithm with self evolution characteristics, improve the performance of WSN routing protocol, the circulatory system method, a large number of sensor nodes to make the artificial node by node deployment is almost impossible, by modifying the code of each sensor node, or to each node storing key material, as is shown by equation 1.

$$C = \sum_{i=0}^{L-1} p_i \log_2 \frac{p_i}{q_i} \quad (1)$$

Designs of wireless sensor network MAC protocol traditional mainly consider the following three aspects: save energy; deployment of nodes and the network topology to be scalable; network efficiency, including fairness, throughput and bandwidth utilization. The current sensor network MAC protocol basically does not support QoS, can not provide multimedia communication services.

MAC (Schedules MAC) protocol is a time scheduling protocol based on energy saving technology, which combines the wireless network of almost all the. The main purpose of S - MAC protocol is energy saving, its main idea is by sleep periodically to make the RF low duty-cycle operation. In addition it also incorporates energy-saving technology of other, such as avoiding collision avoidance and crosstalk, and message passing and adaptive sensing mechanism.

CSMA mechanism is to provide a competitive channel function. With the establishment of IEEE 802.15.4 standard, the radio frequency chip manufacturers have also launched a better performance, more powerful radio frequency chip. TI (formerly Chipcon) launched the CC2420 instead of the wireless sensor network to use most of the RF chip CC1000. Because the radio frequency chip characteristics of different functions, in order to make the CSMA protocol to achieve better performance, according to the specific characteristics of RF chip to design optimization of CSMA mechanism becomes very necessary, as is shown by equation 2.

$$I_{\sigma}(i, j) = \sigma_{\Omega_{ij}}, \Omega_{ij} = \{(i-1)l+1 \leq x < il, \\ (j-1)l+1 \leq y < jl\} \quad (2)$$

Increase the defense mechanism in the existing routing protocols are difficult to implement, the best way is the routing protocol, designed to make the wormhole attack invalid for example: routing protocol based on geographic location, defense witch attacks on sensor networks outside the witch can attack method use certification and effective organization, but is invalid for the internal network witch attack [4]. You can use a trusted base station and each node sharing a different asymmetric key, between two nodes can be mutual authentication, and establish a shared secret key. In order to prevent insider attacks around the network gradually with the nodes in the network to establish a shared secret, the base station can reasonably limit the number of its neighboring nodes. The use of wireless resource detection to find the witch attack source, and it is use the identity registration and random key distribution node to build secure connection between the old witch attack prevention methods. In a geographic routing protocol in use, can attack witch security positioning technology.

Because of this, the symmetric key mechanism because it is simple and easy to use, complicated computation is introduced into as the main encryption in wireless sensor networks. With the development of wireless sensor network routing protocol, there have been many good routing protocol, such as hierarchical routing protocol and multi-path routing protocol.

The symmetric key mechanism was introduced to the routing protocol to guarantee the security of data transmission, the symmetric key mechanism in wireless sensor networks is mainly divided into shared keys, cluster keys and rent key. But the key and authentication security solutions cannot resist the legitimate nodes from certified attack based on internal attacks, i.e. Trust is the main solution methods to solve open internal attack in the network; it can resist malicious nodes from the network in all kinds of malicious attacks. According to the different ways to achieve secure routing protocol for wireless sensor networks, the secure routing protocol in wireless sensor network classification.

$$G(x, y, \sigma) = (2\pi\sigma^2)^{-\frac{1}{2}} \exp\left(-\frac{x^2 + y^2}{2\sigma^2}\right) \quad (3)$$

In the NI WSN system, the gateway is equivalent to a network coordinator, responsible for the management of node authentication, message buffer, and to build bridges between IEEE 802.15.4 Wireless Network and wired Ethernet network, the Ethernet networks, you can make a collection, processing, analysis and display of measuring data using NI software. You can use multiple gateways in WSN and communication in the wireless channel in

different software provided by each gateway. You can connect 8 WSN terminal node (in a star topology) or WSN (up to 36 nodes in a mesh topology) to the WSN gateway. You have your choice of two for the NI WSN gateway.

MAC protocol design needs to strike a balance between various properties, the balance between the performance is often more important than individual performance. Multimedia sensor network MAC how to strike a balance in terms of QoS, network efficiency, scalability, energy consumption, but also an important issue. Tradeoff problem is complexity and performance optimization. The MAC protocol to maximize the performance of WMSN is optimized, but often the protocol design too complex. Sensor nodes energy, computing and storage capacity is limited, can not be too much calculation, so the protocol should be designed as simple as possible and efficient.

Method of S – MAC is the long message into many small pieces, and then transmits them. But only in the beginning with an RTS group and a CTS group. Each transmission of a data segment packet, wait for the receiver to the sender sent ACK. Each data segment and the ACK comes with a surplus of time domain, its significance is to inform the neighbors also need how long channel, which is equivalent to the entire message transmitting channel reservation time required [5]. So if you don't receive ACK, nodes can extend the transmission time, and it is fast retransmission existing fragment, as is shown by Fig. 2.

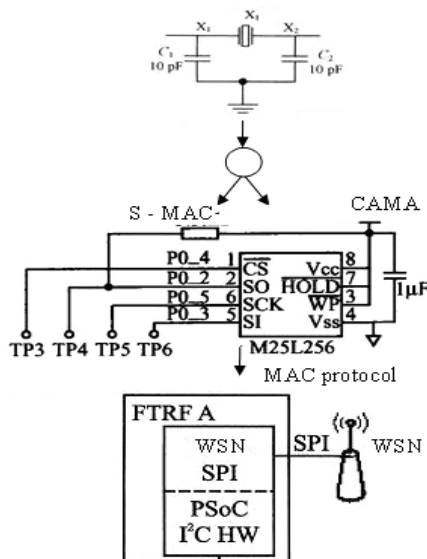


Fig. 2. The design of Security of Wireless Sensor Network by MAC Protocol.

CC2420 provides a CSMACA function, called CCA (Clear Channel Assessment, clear channel assessment), which uses a register to set the threshold value. When the CC2420 receives a CCA command, began sampling RSSI value, only the sample to RSSI to send data to allow less than register threshold.

Although CCA has realized the basic function of channel monitoring, but also has its own disadvantages: less flexible and open degree is not enough, only one complete channel monitoring, and cannot set sampling times. It has limited its use in other protocols, such as LPL (Low Power Listening, low power listening) protocol, only one time of sampling as a listener.

In addition, decision mechanism of it and not perfect, only one threshold, so developers are difficult to find a suitable threshold.

CAMA protocol is a widely used non-persistent CSMA protocol based on nodes, namely before sending packets to monitoring channels, if the channel is idle, the node will start sending data packets. Conversely, if the monitoring results for the busy channel, the channel has been occupied by the neighbor nodes, the node rollback for a random period of time after, began monitoring again, repeat the above operation.

Hello flood attack defense to rely on local information exchange between neighbor nodes for topology maintenance and flow control routing protocol is vulnerable to Hello flood attack, flood attack methods for Hello is the effective communication between the parties to take effective measures for authentication or confirm each neighbor node identity through trust base station, and use the node position limits the range of neighbor nodes. Methods against fraudulent information can use the identity authentication and digital signature to ensure the legitimacy of the identity of communicating parties [6]. Due to limited resources, in the sensor network must be built for sensor network identity authentication scheme reasonable compromise the efficiency and performance of a comprehensive consideration of safety.

Programming wireless sensor node needs not only the programmer with embedded system knowledge, but also understand some suppliers selected text based programming language. But with the LabVIEW WSN Pioneer, you only need to use the same kind of graphical programming method can add smart wireless sensor node NI, this method has become the development of data acquisition and processing industry standard applications. LabVIEW WSN Pioneer can also be flexible code C and graphical code directly binding, and running on the node, which can realize the algorithm reuse, as is shown by equation 4.

$$\bar{w}(m) := [\bar{w}^T(m,1), \bar{w}^T(m,2), \dots, \bar{w}^T(m,M)]^T \quad (4)$$

The symmetric key and asymmetric key management based on the use of cryptography, WSN key management can be divided into symmetric key and asymmetric key management two. In the symmetric key management, communication both use the same key and encryption algorithm for data in encryption, decryption, symmetric key management key length is not long, computation, communication

and storage overhead is relatively small, compared with the use of WSN, a major research direction in the current WSN key. In the aspect of asymmetric key management, node has different encryption and decryption keys, are generally used in the encryption algorithm to calculate the sense of security.

Node localization in wireless sensor network technology, according to whether the node known its position, the sensor nodes are divided into anchor nodes (anchor node) or beacon node (beacon node) and unknown node (unknown node). The anchor node is the reference node unknown node location. The anchor node in the network nodes can be set according to the specific location of the proportion of demand, the positioning method including through carrying GPS positioning equipment and other means to obtain accurate unknown itself or in some cases are set in advance to the corresponding position.

In WMSN, the MAC protocol in wireless sensor network protocol stack, wireless channel resource allocation among sensor nodes competing, determines the wireless channel utilization and network performance. According to the channel access mechanism, these protocols can be divided into three categories: non competitive occupation, occupation and occupation competition hybrid scheme [7].

In the S - MAC protocol can not according to the network load adaptively adjusting the duty cycle of the problem, TMAC protocol based on keep listening and sleeping time summation invariant, the agreement sets a minimum idle listening time  $T_A$ , after waking from sleep, if in the  $T_A$  time period no activation events, then again to enter the sleep cycle, or continue to add a  $T_A$  to keep the listening state. In this way, the nodes can end early interception time to sleep so as to reduce the energy consumption, but also brought to the problem, although the proposed future requests and full buffer priority method to solve these problems, but the result is not ideal.

$$\sigma_j = \sum_k \delta_k v_{jk} b_j (1 - b_j) \quad (5)$$

Therefore, closely related to positioning technology and system to attack the, concrete analysis is as follows: Based on the location of the attack based on ranging and positioning are especially vulnerable to occur in the physical layer and link layer ranging interference or spoofing attacks, resulting in deviation from the actual results ranging result than the normal range. The attacker can not only move, isolation of beacon nodes to reduce the positioning accuracy, but also can initiate radio jamming attack.

Non competitive MAC protocols are usually based on TDMA mode; mode channel also can use FDMA or CDMA access. Proposed by Sohrabi et al. SMACS is a TDMA based MAC protocol. In the absence of synchronization in the network circumstances, SMACS can find the neighbor nodes, build the transmit / receive link, and the neighbor

node discovery and channel allocation for the merger. Communication chain routing on random selection at a fixed frequency (or frequency hopping sequence) constitute a communication node. Random wake-up through the link is established, and the idle time slot closed emission mechanism effectively reduces the energy loss.

$$g(n) = (-1)^{n-1} \tilde{h}(-n+1) \quad (6)$$

Analysis of sensor network node positioning system security measures and compared with conventional security mechanisms such as anti compromised hardware, software technology, spread spectrum and code technology and symmetric and asymmetric encryption algorithm, and the vulnerability of the attack to defense the different positioning properties of technical physics or the positioning process. Therefore, emerge as the times require some sensor node localization system customized security measures. According to the safety goal is different, 4 aspects of these security measures can be divided into the distance definition, security, intrusion and anomaly detection and isolation and robust node localization algorithm. There is big difference exists between different protocols or algorithms, but also have a certain correlation.

### 3. Research of Wireless Sensor Network Security and Solution by Topology Control

As a communication key and must be in the calculation condition; communication complexity, amount of information transport in a communication key generation process. Key connectivity: the probability to establish communication keys between nodes, maintaining a sufficiently high key connection probability is a necessary condition for the WSN to bring its function into play. Needs to be emphasized is almost impossible, WSN nodes and other nodes distance communication directly, therefore does not need to guarantee that a node with the other nodes to maintain a secure connection, only need to ensure that the connection between the connected nodes maintain a high key, impaired ability to withstand node; survivability (resilience) in the link exchange information not to link exposure of any security information.

Topology control technology is one of the most important technologies in wireless sensor networks. In the topology generated by the wireless sensor network, between two nodes can communicate directly with the presence of a topological edge. If there is no topology control, all nodes will work with the maximum transmission power. In this case, on the one hand, the limited energy of nodes will be the communication component fast consumption, reduce the network life cycle. At the same time, the wireless

signal of each node in the network will cover a number of other nodes, wireless signal caused by the conflict, affects the quality of wireless communication nodes, reduce the throughput of the network, as is shown by equation 7 [8].

$$S_i = \frac{1}{M} \sum_{i=1}^M \tilde{x}_i \tilde{x}_i^T = \frac{1}{M} \Phi_i \Phi_i^T \quad (7)$$

First put forward the random key pre-distribution scheme in WSN (referred to as E-G), which consists of 3 stages. The first stage is the key pre-distribution phase, before deployment, deployment server first generates a number of keys for the key pool and key identification P, each node from the key pool randomly selected K and different key, the random allocation such that any two nodes can present with a certain probability a shared key; second stage is the shared key discovery phase, random deployment, two adjacent nodes if there exists a shared key, randomly selected one of them as a key pair both (pair-wise key); otherwise, entered into the third stage, third stage establishment stage for the key path, node with other existing in shared neighbor node key through the establishment of a key path both sides after several jump. According to the theory of random graphs classic, there are several relations in total D and the network node n: among them, Pc is the connectivity probability.

The aim of topology control is through the transmission range control nodes to generate network topology satisfying certain properties, in order to extend the network life cycle, reduce network interference, improve the throughput. The general hypothesis node distribution in the two-dimensional plane, all the nodes are isomorphic, all without the use of directional antenna. The directed graph model of wireless sensor network, if the transmission power is greater than Pi node i from node i to node transmission power Pij J; between the node i to node j has a directed edge. The topology of all nodes is at maximum power when the generated called UDG (Unit Disk Graph), as is shown by equation 8.

$$C_i = \frac{\sum_{k=1}^n \mu_{ik} x_{i,k}}{\sum_{k=1}^n \mu_{ik}}, \quad (1 \leq i \leq c) \quad (8)$$

The key idea of E-G random redistribution scheme provides a feasible solution for the distribution strategy of the WSN key, the development of follow-up many schemes and protocols are based on the framework, they were from the shared key threshold, key pool structure, key pre-distribution, key path establishment methods, improve the performance of random key redistribution formula.

Connectivity to achieve mutual communication among the nodes, the topology generated must ensure connectivity; from any one node can send a message

to another node. Connectivity is any topology control algorithm must ensure a property. As defined by the UDG graph can know, connectivity of UDG graphs is maximum connectivity network can provide, therefore assume that UDG graph is connected. So, any topology control algorithm to generate the topology is UDG sub graph.

$$\tilde{Q}(m) = \text{diag}[Q(mM), Q(mM+1), \dots, Q(mM+M-1)]^T \quad (9)$$

Properties of symmetric polynomial random key pre-distribution scheme Blumdo scheme using two symmetrical polynomial and  $f(x, y) = f(y, x)$  to establish pair-wise key for any two nodes in the network. Random key pre-distribution scheme is put forward on the basis of Liu to a plurality of two symmetrical polynomials. Before deployment, and it is the deployment server in the adjacent nodes if the same polynomial sharing, directly establish pair-wise key [9]. Experiments show that, when the damaged fewer nodes, invulnerability of the scheme is better than the E-G scheme and q-composite scheme, but when the damaged nodes exceeds a certain threshold value (such as 60 % node damage), safety link the damaged quantity more than the two solution.

The combinatorial design theory is used to design the WSN identify key pre-distribution scheme. The total number of nodes in the network for the N hypothesis, n order finite projective space (finite projective (symmetric n generates a parameter for  $(n^2+n+1, n+1, 1)$  BIBD, plane) to meet the  $n^2+n+1 \geq N$  primes) number of network nodes support for  $n^2+n+1$ , key pool size  $n^2+n+1$ , can generate  $n^2+n+1$  size as the key ring of  $n+1$ , any two key ring has at least 1 public key, and each key in  $n+1$  a key ring. Thus, any two nodes key connectivity probability is 1, but the coefficient of N does not support any network scale. For example, when the  $N > n^2+n+1$ , n must be a prime number next, while the large prime number will cause the key ring increases rapidly, the storage space through node but not applicable to WSN.

#### 4. Design of Wireless Sensor Network Security and Solution by MAC Protocol and Topology Control Technology

Random key pre-distribution scheme or agreement is considered to be the most suitable for WSN; the present is a main research direction of WSN key management. Higher key connectivity probability means secure connectivity adjacent nodes and even the whole network can achieve higher; and the probability of key is exposed more small; it means the survivability of the better. The key pool design is structured, improve the shared key threshold, using geographic information or deployment knowledge, can effectively improve the key invulnerability, random key pre-distribution

scheme or protocol connectivity probability and node deployment density, the theoretical basis for the random graph model, model of random graph model is not suitable for WSN at the same time, also points out how to select the key pool and key ring size appropriate, obtain higher to ensure that key connection probability.

Random key pre-distribution schemes or protocols cannot provide the best key connectivity probability, but its computation, storage and communication overhead is more ideal, and has the characteristics of a good distribution, while the key pre-distribution or asymmetric key management schemes and protocols identified although can guarantee that any two nodes can establish a key connection.

The plane is generated topologies in no two sides. From the graph shows, meet the plane must satisfy the sparsely. Geographic routing is a routing protocol for wireless sensor node is very limited computing and storage capacity of it does not need to maintain routing tables and make complex routing calculation, need according to certain rules for forwarding message [10]. But when the underlying topology is not planar graph, geographic routing protocol can't ensure accessibility message forwarding. Therefore, when the node is running geographic routing protocol, the requirements generated topology must meet the plane, as is shown by equation 10.

$$\Delta w_{jk}(k) = mc\Delta w_{jk}(k-1) + \eta(d_k - o_k)o_k(1 - o_k)y_j \quad (10)$$

In wireless Ad Hoc network, competitive occupation and carrier sensing based on MAC protocol. Due to the similarity of the wireless medium, the algorithm is also suitable for wireless sensor networks. IEEE 802.11e made the stipulation to the MAC layer to distinguish between service levels is the main basis for competitive occupation scheme design.

In these schemes, according to the packet priority, differentiated service by changing the corresponding IFS duration and CW implementation. For example, Veres studied the distributed algorithm, the improved IEEE 802.11 DCF for differentiated services. Firstly, algorithm according to the packet priority determination contention window range of CWmin and CWmax, then according to its value determines the backoff time. This can be a high priority packet in the CWmin and CWmax values are set below the low priority packets, shortens backoff time, the sensor image coordinates.

$$\Lambda = \begin{bmatrix} S' & 0 \\ 0 & 0 \end{bmatrix}, \quad S' = \text{diag}(\lambda_1, \lambda_2, \dots, \lambda_r) \quad (11)$$

From the point of view of system structure, key management to provide services to other security mechanisms, the overall security solutions and the composition of WSN and the safety mechanism. We

believe that the implementation of cross layer design, key management will help to clear the design objectives and performance optimization, for example, the current key management scheme for the vast majority of and protocol communication key are just working to establish the relationship between neighboring nodes, and the solutions of some effective security, communication keys between nodes is necessary coupling, strengthen key management and secure routing, secure localization, secure data aggregation, security mechanism, and it is capable of handling of plan and agreement from the angle of whole system complexity, storage and communication complexity is optimized, which makes the key management scheme and protocol design more in line with the characteristics of WSN, has good adaptability.

Topology control technology has become the research hotspot in this field, there still exist many problems. First of all, for the modeling of wireless sensor network model is too ideal. In order to obtain quantitative results more consistent with practical, need to use more realistic model. Secondly, distribution hypothesis node is too ideal. The general studies assume that nodes are uniformly distributed. Although this assumption is reasonable in certain circumstances, but in most cases this assumption is too idealized. Finally, regional assumptions placed wireless sensor is too idealization. The general hypothesis placing wireless sensor area is two-dimensional flat, without considering terrain factors.

The use of the WSN characteristics of the theory analysis method for the study of key management is very necessary, it can avoid the mechanism and algorithm design have come to rely too much on intuition, experience and lack of rigorous, scientific, reliable theoretical basis, in order to avoid one-sided, local rigorous results, even not available. In order to provide more efficient solutions, we will rely on the mature theory and practical, such as random graph theory, information theory, using WatchDog, one-way hash function / chain, self-healing technology, security algorithms and techniques, combined with the WSN resources limited, topology change, deployment, self-organization, random characteristics large scale, without a fixed infrastructure support, design is feasible, reliable key management scheme or agreement, implementation of key management mechanism and algorithm can be modeled, measurable and computable, as is shown by Fig. 3.

Hybrid MAC scheme effectively combines the advantages of non competition occupation and occupation plan competition. The transmission cycle is divided into reservation (competition) cycle and send (non-competitive) cycle of two sub cycle. In the reservation period, sensor neighbor nodes according to the volume of business competition to send and transmit cycle. Once the acquisition transmission slots, between transmitter and receiver will communicate. The paper proposes design of wireless sensor network security and solution by MAC protocol and topology control technology.

Current research on topology control can be divided into two categories. One is the computational geometry method, with some geometric structure of topology construction network infrastructure, in order to satisfy certain properties. Another kind is the

method of probability analysis, the nodes according to a certain probability density distribution; calculation of the minimum transmission power to about topology satisfies some properties of nodes required and minimum neighbor number.

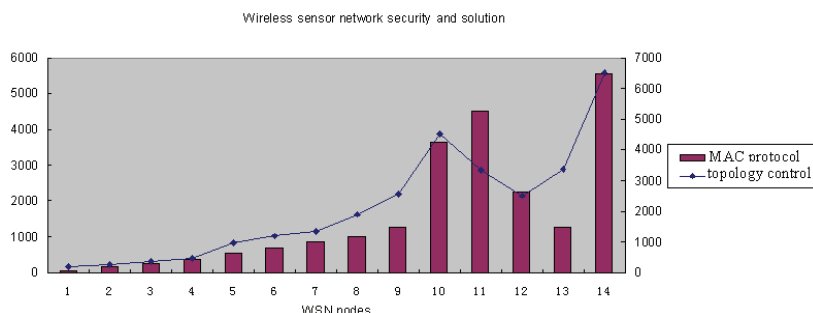


Fig. 3. Comparison results of wireless sensor network security and solution by MAC protocol with topology control technology.

## 5. Conclusions

In this paper, through the routing security protocol, the MAC protocol for wireless sensor networks, topology control technology three aspects of analysis, emphatically analyzed the key management protocol for wireless sensor network, a detailed analysis of several key management scheme is more important and the importance of security in wireless sensor network. Through the design and analysis of all kinds of security schemes, you can better understand the safety performance of the requirements of wireless sensor network, and makes further analysis and research, to strengthen the security of wireless sensor networks and feasibility. Energy efficient MAC protocol should get a balance between service guarantee two aspects of complexity and resource efficient application. These are the need to consider the future of wireless multimedia sensor MAC protocol design problems, hoping to promote the future research work.

## Acknowledgements

This paper is supported by Youth Foundation of Henan Normal University.

## References

- [1]. Hao Sun, Yongrui Chen, Binhua Wang, Weidong Yi, Dynamic count: an energy-efficient mechanism for WSN MAC protocol, *International Journal of Advancements in Computing Technology*, Vol. 5, No. 3, 2013, pp. 745-755.
- [2]. Yuan Jiang, Dongming Jiang, An approach to wireless sensor network security assessment with fuzzy number intuitionistic fuzzy information, *Advances in Information Sciences & Service Sciences*, Vol. 3, No. 9, 2011, pp. 140-146.
- [3]. Lu Qingmei, Research on the congestion control mechanism based on the cooperative AODV protocol in LTE, *International Journal of Digital Content Technology & its Application*, Vol. 6, No. 14, 2012, pp. 118-124.
- [4]. Bin Wang, Xiao Wang, Wangmei Guo, A secure scheme with precoding approach in wireless sensor networks, *Advances in Information Sciences & Service Sciences*, Vol. 5, No. 1, 2013, pp. 782-788.
- [5]. Zheng Gengzhong, Liu Qiumei, Energy-efficient topology evolution for scale-free wireless sensor networks, *Advances in Information Sciences & Service Sciences*, Vol. 4, No. 1, 2012, pp. 336-342.
- [6]. Shen Zihao, Liu Shufen, Security threats and security policy in wireless sensor networks, *Advances in Information Sciences & Service Sciences*, Vol. 4, No. 10, 2012, pp. 166-173.
- [7]. Lieping Zhang, Weili Wang, Zhaoliang Liao, Research on funneling-MAC protocol based on broadcast mechanism, *International Journal of Advancements in Computing Technology*, Vol. 5, No. 8, 2013, pp. 1311-1316.
- [8]. Tao Ma, Chunhong Zhang, Topology proximity and property-aware distributed hash tables based on network coordinates, *Advances in Information Sciences & Service Sciences*, Vol. 4, No. 7, 2012, pp. 308-316.
- [9]. Li Dong, Gong Zhe, An Baoyu, Ou Yangxi, Cui Wei, Zhu Hongliang, A novel security management scheme in wireless sensor networks, *International Journal of Advancements in Computing Technology*, Vol. 4, No. 10, 2012, pp. 36-44.
- [10]. Gang Jing, Lei Jia, A cross-layer tree routing protocol for multichannel wireless sensor networks, *Journal of Convergence Information Technology*, Vol. 7, No. 17, 2012, pp. 251-259.

## Real-Time Surveillance Performance under Different Sensing Models in Duty-Cycled Sensor Networks

Yanjun Li

School of Computer Science and Technology, Zhejiang University of Technology,  
288 Liuhe Road, Hangzhou 310023, China  
Tel.: +86-571-85290527, Fax: +86-571-85290668  
E-mail: [yjli@zjut.edu.cn](mailto:yjli@zjut.edu.cn)

*Received: 28 May 2013 / Accepted: 25 August 2013 / Published: 30 September 2013*

---

**Abstract:** In this paper, we derive closed-form expressions to describe the relationship between the surveillance quality and system parameters under different real-time requirements and arbitrary sensing models, where the surveillance quality is represented by real-time intrusion detection probability and the system parameters are represented by duty cycle factors and node density. Various sensing models are adopted in the numerical simulations, including Boolean disk model, exponential model, power-law model, staircase model and anisotropic model, to validate the analytical closed-form results. It is shown that under all these sensing models adopted, the numerical results always closely matches the analytical ones, which soundly verifies the correctness of our derivation. *Copyright © 2013 IFSA.*

**Keywords:** Real-Time, Sensing Model, Duty-Cycle, Sensor Networks.

---

### 1. Introduction

For many long-term unattended applications such as environmental monitoring, infrastructure protection and military surveillance, wireless sensor networks (WSNs) have become one of the most effective solutions, due to their pervasive sensing, computing and self-organizing capabilities. One common goal for these surveillance applications is the real-time detection of abnormal states or intrusion targets with minimal energy consumption. However, detection timeliness and energy efficiency are to some extent two contradictive objectives. For example, full duty-cycled sensing guarantees instant response to events, but it is not energy-efficient. On the contrary, low duty cycle can extend the network lifetime but makes the sensing ability intermitted, which will adversely affect the surveillance quality, e.g., increasing the detection delay. Sometimes

surveillance quality can be sacrificed within users' tolerable limits for prolonged lifetime. Therefore, it is required to understand the relationship that describes the tradeoffs between surveillance quality and system parameters, e.g., the relationship between the detection probability, the detection delay, the duty cycle factor and the node density etc. With this knowledge, an appropriate set of parameters can be selected to configure the network for achieving required surveillance performance.

In this paper, we aim to establish the relationship between the surveillance quality and system parameters under different real-time requirements and arbitrary sensing models. We make two major contributions in this paper. First, closed-form expressions are obtained to specify the above-mentioned relationship. The advantage is that we can now answer a variety of questions without simulations or experiments, e.g., under an arbitrary

sensing model and a specific detection delay bound, how much should we set the sensor's duty cycle factor or the node density to achieve a required detection probability? Second, different sensing models are adopted in the numerical simulations to validate the analytical closed-form results. It has been shown that under all these sensing models adopted, the numerical results always closely matches the analytical ones.

The remaining of the paper is organized as follows. Section 2 discusses related work. Section 3 derives the closed-form expressions for detection probability. Numerical simulations are conducted in Section 4. Finally Section 5 concludes the paper.

## 2. Related Work

Research on energy efficiency and real-time performance has been highly investigated by the sensor network community in recent years. We here briefly review only a handful of the most related work to this study. The work in [1] studies the quality and energy tradeoffs for mobile object tracking in WSNs. Various activation strategies are discussed. The work in [2-4] presents the real-time design and analysis of VigilNet, a large-scale sensor network system which detects and classifies objects in a timely and energy efficient manner. It provides a design framework to guarantee the requested end-to-end deadline. The power management system composes of both sentry and non-sentry nodes where non-sentry nodes are sleep unless sentry nodes activate them. The work in [5] analyzes the accuracy of tracking vs. response latency to the tracking queries, as well as the effect of duty-cycle parameters on the quality metrics. The sensors assumed in previous work [1, 3-6] are binary detectors, i.e., Boolean disk sensing model, except in [2], anisotropic sensing model is also considered. However, none of the above work incorporates the fading effect of sensing ability into consideration. The contribution of our work compared to previous derivation is in obtaining a general result for real-time surveillance performance in duty-cycled WSNs for arbitrary sensing models, including Boolean disk model, exponential model, power-law model, staircase model and anisotropic model. We believe our work a necessary complement towards thorough understanding of the detection performance.

## 3. Detection Performance Analysis

In this section, we analyze the probability distribution of the detection delay  $t$  for any given delay bound  $\tau$ .

### 3.1. Notations and Assumptions

Some notations and assumptions for analysis are presented here. First of all, we assume the nodes are

independently and identically distributed conforming to homogeneous Poisson point process (P.P.P.) with intensity  $\lambda_A$ , where  $\lambda_A$  is defined as the node density  $d$  multiplying the area in which nodes are deployed, denoted by  $A$ . In our analysis, we first assume the probability that an event at point  $P$  be sensed by sensor  $S_i$  to be  $p(x)$ , where  $p(x)$  can be an arbitrary function depending on the distance  $x$ , which means  $p$  can be viewed as a function  $p: \mathbb{R} \rightarrow [0, 1]$ . In fact, besides the distance between the sensor and the actual event, the sensing quality also depends on other factors, for example, the directionality and the environmental noise. However, to make the problem less complicated, we mainly focus on the distance aspect and assume omnidirectional sensing and no random noise, just as most of the sensing models in the literature do. However, in the simulation part, we also take anisotropic sensing model into consideration. Based on the above assumptions, the average number of nodes within the coverage area of a sensor can be calculated as:

$$\lambda_c = d \cdot \int_{x \in \mathbb{R}} 2\pi x p(x) dx, \quad (1)$$

Taking Boolean disk sensing model for example:

$$p(x) = \begin{cases} 1, & x \leq R, \\ 0, & x > R, \end{cases} \quad (2)$$

Therefore, under Boolean disk model,  $\lambda_c = \pi R^2 d$ . Given an arbitrary sensing model, the value of  $\lambda_c$  can be analogically calculated following equation (1).

Each sensor node is assumed to have a scheduling period of  $T$  and working time  $T_w$ ,  $0 < T_w \leq T$ ; thus  $\beta = T_w / T$  is the duty cycle ratio. Each node can choose its wake-up point  $t_s$  within  $[0, T)$  and wakes up for a period of time  $T_w$ , and then goes back to sleep until  $T + t_s$ . We assume all the events are stationary and persistent, e.g., a localized fire. It is required that the events be detected within a delay bound  $\tau$ .

### 3.2. Detection Analysis

*Proposition 1:* Suppose duty-cycled sensor nodes are deployed conforming to homogeneous P.P.P. in an area  $A$  and the event arrival follows uniform distribution, the probability that any event be captured within delay bound  $\tau$  is:

$$P_s(t < \tau) = \frac{1 - e^{-\lambda_c(\frac{\tau}{T} + \beta)}}{1 - e^{-\lambda_A}}, \quad 0 < \beta \leq 1 - \frac{\tau}{T}, \quad (3)$$

*Proof:* First, the probability that there are  $k$  nodes in the area  $A$  is  $\frac{\lambda_A^k}{k!} e^{-\lambda_A}$ ,  $k = 0, 1, 2, \dots$ . The

probability that no nodes are in the area ( $k = 0$ ) is  $e^{-\lambda_A}$ . Therefore, the probability that there is at least one node in the area is  $1 - e^{-\lambda_A}$ . Second, if the probability of an event occurring in a sensor's coverage area is  $g$ , and since the average number of nodes within the coverage area of a sensor is  $\lambda_c$ , the probability of an event being captured at least by one sensor is:

$$P_o = 1 - e^{-g\lambda_c}, \quad (4)$$

Now we consider an arbitrary point of interest to be monitored. Suppose node  $S$  is the only node covering the point. The duty cycle of node  $S$  is stated in Section 3.1. Since the sensor has a probability  $\beta$  of being awake, we have  $P_o(t = 0) = \beta$ . The probability density function (PDF) of the detection delay  $t$  is  $f(\tau)$ , where  $0 < \tau \leq T - \beta T$ , which conforms to a uniform distribution, thus  $f(\tau) = \frac{1}{T}$ , as long as the event occurs uniformly anywhere within the duty cycle. Therefore, when there is only one sensor covering the point, the cumulative probability distribution for the detection delay is:

$$P_o(t < \tau) = \beta + \frac{\tau}{T}, \quad 0 < \tau \leq T - \beta T, \quad (5)$$

When there are  $k$  nodes covering the point, we substitute the  $g$  in equation (4) with equation (5) and get the probability that an event is captured within an interval time no larger than  $\tau$ :

$$P_o = 1 - e^{-\lambda_c(\frac{\tau}{T} + \beta)}, \quad (6)$$

Since we focus on those points that are in the area, the cumulative density function (CDF) of the detection delay for such points is

$$P_s(t < \tau) = \frac{1 - e^{-\lambda_c(\frac{\tau}{T} + \beta)}}{1 - e^{-\lambda_A}}, \quad \text{where } \lambda_c \text{ is given in equation (1).}$$

### 3.3. Discussions

We now discuss the implications of our analytical results. When the delay bound  $\tau = 0$ , it means the event should be instantly detected. With the increase of  $\tau$ , the real-time detection probability becomes larger on average. This is because more events can be captured with relaxed detection deadline. In order to save energy, the duty cycle factor  $\beta$  should not be set large. If it is larger than  $1 - \frac{\tau}{T}$ , the delay bound  $\tau$  will lose all meaning. With the increase of node density, both  $\lambda_A$  and  $\lambda_c$  become larger. The real-time detection probability approaches 1 when the node

density is sufficiently large, independent of the duty cycle  $\beta$ .

## 4. Numerical Simulations

In this section, numerical simulations are conducted under various sensing models to check whether simulation results match analytical predictions. The regular sensing models adopted include Boolean disk model, power-law model, exponential model and staircase model. For Boolean disk model,  $p(x)$  is given in equation (2). For power-law model, exponential model and staircase model, the expressions of  $p(x)$  are respectively given in equations (7), (8) and (9), and their examples are demonstrated in Fig. 1(a).

$$p(x) = \begin{cases} 1, & x \leq r_s, \\ \frac{\alpha}{x^\eta}, & r_s < x \leq r_u, \\ 0, & x > r_u. \end{cases}, \quad (7)$$

$$p(x) = \begin{cases} 1, & x \leq r_s, \\ e^{-\omega(x-r_s)^\beta}, & r_s < x \leq r_u, \\ 0, & x > r_u. \end{cases}, \quad (8)$$

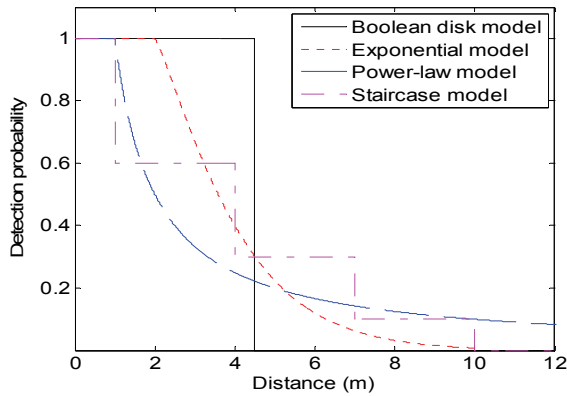
$$p(x) = \begin{cases} 1, & x \leq r_s, \\ p_1, & r_s < x \leq l_1, \\ p_2, & l_1 < x \leq l_2, \\ p_3, & l_2 < x \leq r_u, \\ 0, & x > r_u. \end{cases}, \quad (9)$$

With the expressions of  $p(x)$ , respective  $\lambda_c$  for each sensing model can be calculated by equation (1).

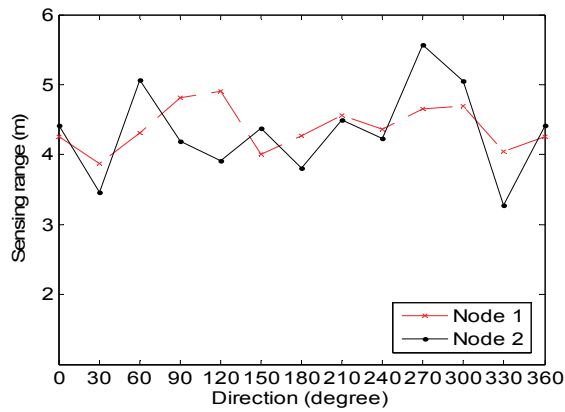
Experimental tests show that the realistic sensing range is anisotropic. Therefore we also incorporate the anisotropic sensing model into simulations to test the robustness of the performance predictions. It is concluded from the experimental data set of ExScal Mote [7] that the sensing range in one direction can be approximated by a normal distribution  $N(217, 32^2)$ (inches). We scaled the normal distribution  $N(217, 32^2)$ (inches) to  $N(4.5, 0.7^2)$ (m) to fit the simulation settings. For simplicity, we use linear interpolation to specify the boundary of the sensing area. As an example, the approximation of the two representative nodes based on this model are shown in Fig. 1(b), which accurately reflects the fluctuations of sensing ranges in different directions. We use the same formulas as the previous idealistic experiments.

In the simulations, locations of nodes are generated over an area of the size  $50\text{m} \times 50\text{m}$ , conforming to a homogeneous P.P.P. The period  $T$  is

chosen to be 1 s. The waking points of the nodes are generated according to a uniform distribution over [0 s, 1 s). The parameters for different sensing models are listed in Table 1.



(a) Regular sensing models.



(b) Anisotropic sensing models.

Fig. 1. Illustration of different sensing models.

Table 1. Parameter settings for different sensing models.

Sensing Models	Parameter Settings
Boolean disk model	$R = 4.5$ m
Power-law model	$r_s = 1$ m, $r_u = 14$ m, $\alpha = 1$ , $\eta = 1$
Exponential model	$r_s = 2$ m, $r_u = 10$ m, $\omega = 0.4$ , $\beta = 1.2$
Stair-case model	$r_s = 1$ m, $l_1 = 4$ m, $l_2 = 7$ m, $r_u = 10$ m, $p_1 = 0.6$ , $p_2 = 0.3$ , $p_3 = 0.1$
Anisotropic model	$R \sim N(4.5, 0.72)$ m

We choose 200 random points each time to be the target locations and run the simulation. The simulation repeats 50 times and we calculate the average values. In the first set of simulations, the parameter  $\lambda_A$  is set to 250 with node density  $d = 0.1$ . We record the average detection probability given the detection delay bounds equal to 0s, 0.1s, ..., 0.9 s, and 1 s. Various  $\beta$  values are also considered (0.1, 0.2, 0.3 and 0.4). We then compare these simulated

detection probabilities with the analytical results obtained by equation (3). The comparison results are shown in Fig. 2 (a)–(e), under respective sensing models. From Fig. 2 we can see that the simulation results conform to the analytical ones very well, which validate our proposition in Section 3.2.

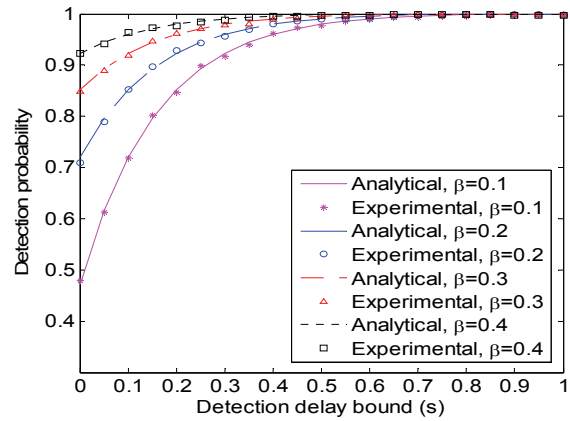


Fig. 2 (a). Detection probability vs. delay bound with different duty cycles, node density  $d = 0.1$  – Boolean disk model.

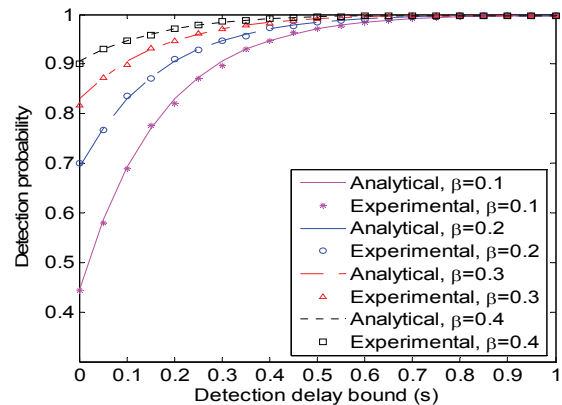


Fig. 2 (b). Detection probability vs. delay bound with different duty cycles, node density  $d = 0.1$  – Exponential model.

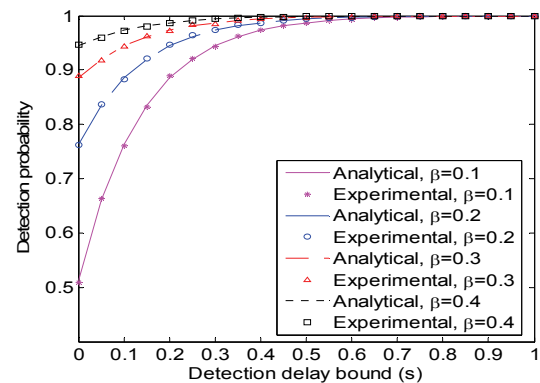
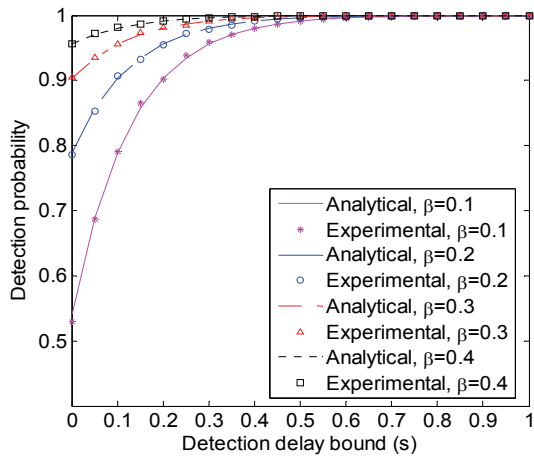
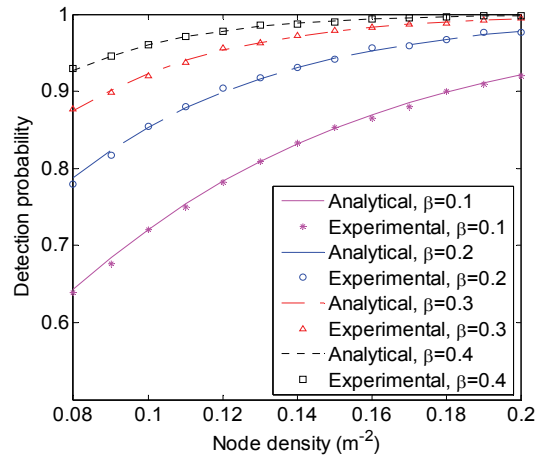


Fig. 2 (c). Detection probability vs. delay bound with different duty cycles, node density  $d = 0.1$  – Power-law model.



**Fig. 2 (d).** Detection probability vs. delay bound with different duty cycles, node density  $d = 0.1$  – Staircase model.



**Fig. 3 (a).** Detection probability vs. node density with different duty cycles, delay bound  $\tau = 0.1$  – Boolean disk model.

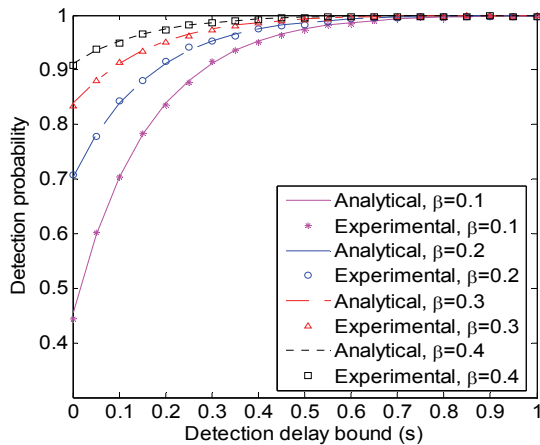


**Fig. 2 (e).** Detection probability vs. delay bound with different duty cycles, node density  $d = 0.1$  – (c) Anisotropic model.

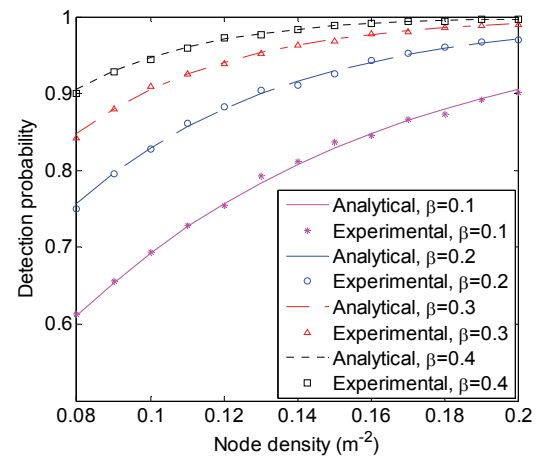


**Fig. 3 (b).** Detection probability vs. node density with different duty cycles, delay bound  $\tau = 0.1$  – Exponential model.

In the second set of simulations, we choose various node density values (0.08, 0.1, ..., 0.2) and  $\beta$  values (0.1, 0.2, 0.3 and 0.4), and run the simulations to gather the average detection probabilities. Other settings are the same as the previous set of simulations. We compare the average detection probabilities with the analytical probabilities obtained by equation (3) and plot Fig. 3. The figures show that under arbitrative sensing models, the average detection probabilities obtained by simulations are very close to the analytical results.

Regarding these results we have two major observations. First, sensing irregularity has a very small effect on the final results. One reason is that even though the sensing ranges vary with different directions, the overall degree of coverage for the area remains almost the same, approximated by  $\lambda_c$ . Therefore, the overall detection delay distribution is almost not affected. Second, the maximal error relative to analytical predictions is no more than 2.4 %.

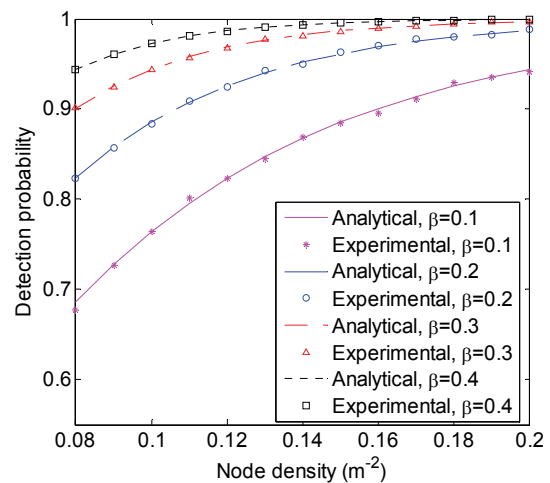


**Fig. 3 (c).** Detection probability vs. node density with different duty cycles, delay bound  $\tau = 0.1$  – Power-law model.

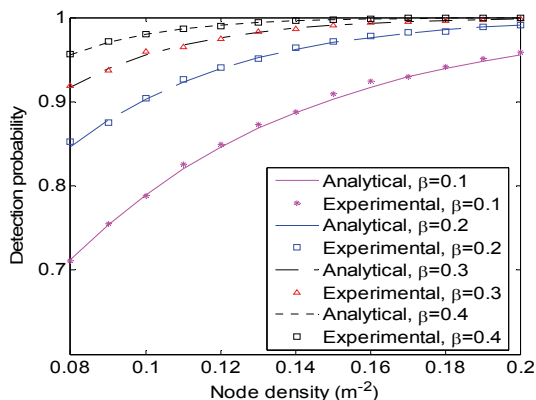


**Fig. 3(d).** Detection probability vs. node density with different duty cycles, delay bound  $\tau = 0.1$  – Staircase model.

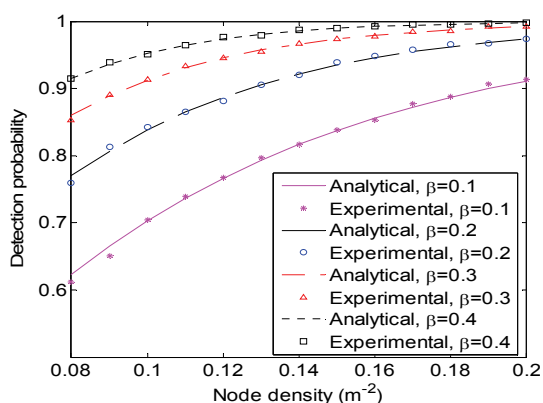


**Fig. 3(e).** Detection probability vs. node density with different duty cycles, delay bound  $\tau = 0.1$  – Anisotropic model.

That is, suppose we have a set of system parameters that guarantee 99 % successful detection within the delay bound. Then, the actual detection rate should be no less than 96 %. Based on the above observation, we conclude that our model is quite robust to most sensing conditions. However, there are still types of sensors which may exhibit different characteristics and may have varied effect on the detection performance. However, we envision that with a relatively large system with considerable density, the effect of sensing irregularity will be considerably limited.

## 5. Conclusions

In this paper, closed-form expressions are derived for distribution of real-time detection delay. Various sensing models are adopted in the numerical

simulations to validate the analytical closed-form results. It is shown that under all these sensing models adopted, the numerical results always closely matches the analytical ones. The analytical results are highly important for understanding the relationship between the surveillance quality and system parameters under different real-time requirements and arbitrary sensing models. Designers can apply these analytical results to predict the detection performance without costly deployment and testing. They can make decisions on key system or protocol parameters, such as the network density and the duty cycle, according to the detection requirements of the system.

## Acknowledgements

The authors acknowledge the support from the National Natural Science Foundation of China (No.61003264) and Zhejiang Provincial Natural Science Foundation of China (No. LY13F020028).

## References

- [1]. S. Pattem, S. Poduri, and B. Krishnamachari, Energy-quality tradeoffs for target tracking in wireless sensor networks, in *Proceedings of the 2<sup>nd</sup> International Conference on Information Processing in Sensor Networks*, Palo Alto, California, USA, April 22-23, 2003, pp. 32-46.
- [2]. Q. Cao, T. Yan, J. Stankovic, and T. Abdelzaher, Analysis of target detection performance for wireless sensor networks, *Lecture Notes in Computer Science*, Vol. 3560, 2005, pp. 276-292.
- [3]. T. He, P. Vicaire, T. Yan, L. Luo, L. Gu, G. Zhou, R. Stoleru, Q. Cao, J. A. Stankovic, and T. Abdelzaher, Achieving real-time target tracking using wireless sensor networks, in *Proceedings of the 12<sup>th</sup> IEEE Real-Time and Embedded Technology and Applications Symposium*, April 4-7, San Jose, California, USA, pp. 37-48.
- [4]. P. Vicaire, T. He, Q. Cao, T. Yan, G. Zhou, L. Gu, L. Luo, R. Stoleru, J. A. Stankovic, and T. F. Abdelzaher, Achieving long-term surveillance in VigilNet, *ACM Transactions on Sensor Networks*, Vol. 5, 2009, pp. 1-39.
- [5]. S. Zahedi, M. Srivastava, L. Kaplan, and C. Bisdikian, Quality tradeoffs in object tracking with duty-cycled sensor networks, in *Proceedings of the 31<sup>st</sup> IEEE Real-Time Systems Symposium*, San Diego, CA, November 29-December 2, 2010, pp. 160-169.
- [6]. Y. Zhu, Y. Liu, and L. M. Ni, Optimizing event detection in low duty-cycled sensor networks, *Wireless Networks*, Vol. 18, Issue 3, 2012, pp. 241-255.
- [7]. ExScale mote. (<http://www.cast.cse.ohio-state.edu/exscal/>)

## A General Robust Key Management Scheme for Wireless Multihop Communication Network

<sup>1</sup> Danyang QIN, <sup>2</sup> Renheng XU, <sup>3</sup> Lin MA and <sup>1</sup> Qun DING

<sup>1</sup> Electronic Science and Technology Post-Doctoral Research Center, Heilongjiang University, Harbin 150080, P.R.China

<sup>2</sup> Harbin Research Institute of Electrical Instruments, Harbin 150028, P.R.China

<sup>3</sup> Communication Research Center, Harbin Institute of Technology, Harbin 150080, P.R.China

<sup>1</sup> Tel.: +86-451-86359280

<sup>1</sup> E-mail: [qindanyang@hlju.edu.cn](mailto:qindanyang@hlju.edu.cn)

*Received: 10 August 2013 / Accepted: 25 August 2013 / Published: 30 September 2013*

---

**Abstract:** Wireless multihop communication network is an important part of modern communication network, because of its flexible forms of networking, not relying on any fixed infrastructure to achieve network connectivity and data transfer, but through the mobile nodes' collaboration and self-organization. The negative impact of network partitions on the availability of key management services in wireless multihop communication network will be alleviated by a robust key management scheme based on the traditional distributed certificate authority (DCA) proposed in this paper. Auxiliary shares are used to increase the redundancy of shares in the networks thereby ensuring robustness and security at the same time. Simulating results show that the average failure ratio for DCA requests is reduced by more than 5 %, and the successful rate of establishing secure link is greatly improved. Security analysis and simulations show that the approach ensures system robustness and thwarts common attacks. *Copyright © 2013 IFSA.*

**Keywords:** Multihop Communication, Key Management, Data Security, Threshold Cryptography, Lagrange Interpolation.

---

### 1. Introduction

Wireless multihop communication network usually consists of many static or moving nodes in self-organized and multi-hop style with the purpose of detecting, processing and transmitting the monitoring information of sensing objects in the network coverage area, as well as reporting it to the users [1]. Over the past several years, this kind of communication style, has gained tremendous popularity due to the user mobility and flexibility they offer in accessing information. In addition, the

cost of wireless networking equipment has dropped, and there have been significant improvements in performance. The enormous flexibility offered by wireless multihop communication network, however, presents a number of potential security challenges. The network security is always one of the most important elements in network technology. Encryption, authentication, firewall, intrusion detection and physical isolation are principal means of network security. Wireless multihop communication network transmits data using radio waves, which makes the transmission signal available

to anyone within the range of the transmitter, posing a high security risk to wireless networks. A higher security demand is required based on the character of typical application scenario and openness of itself. A reliable key management, as the precondition of providing sorts of security service, is considered to be one of the core problems in security research of wireless multihop communication network [2].

Distributed certificate authority (DCA) [3], based on threshold, has become the main trend of technology in wireless multihop communication network key management, for single points of failure have been avoided and the degree of difficulty in stealing system key has been increased [4, 5]. There are still a lot of problems, however, needing to be solved. In a typical application scenario of wireless multihop communication network, such as military and emergency rescue, frequent movement of nodes and environmental changes cause various network topology structures and even partitions [6]. Key management service should be always on line required by characters of wireless multihop communication network allowing nodes to enter and leave the coverage frequently, while network partition will make number of sub-keys below threshold value so as to invalidate the service, which has proved that network partition harms key management service seriously, thereby how to improve robust and reduce impact of partition at the same time is critical in key management scheme design for wireless multihop communication network [7, 8]. Although existing solutions have improved the system robustness in some degree, security has always been sacrificed and the system suffers from single points and Sybil attack much easily. There are not any effective schemes that can solve this problem perfectly as known.

A novel key management scheme based on the traditional DCA has been proposed, including an extended key update protocol and a series of algorithms for auxiliary sub-key management. Effective management on auxiliary increases the redundancy of sub-keys in wireless multihop communication network strategically, thereby ensuring robustness and security at the same time.

## 2. Summary of the Scheme

### 2.1. Distributed Certificate Authority

Wireless multihop communication network nodes can be classified as server nodes and common nodes according to the traditional DCA approach, which possesses a pair of public/private key. The private key is used to generate the signature, in order to achieve a certificate distribution, updating and revocation list publication. In DCA based on  $(n, t)$  threshold scheme, the private key is shared as sub-key by  $n$  server nodes. The public key is used by all network nodes to verify the signature. Every server

node has a public/private key pair for each, to verify signature, confer session keys and set up safety links. To avoid attackers, Proactive Secret Sharing (PSS) is adopted to update the sub-keys periodically. When a node submits requisition to DCA, only if there are  $t$  (or more than  $t$ ) server nodes passing the authentication and accepting the requisition, the certificate will be validated.

### 2.2. Introduction of Auxiliary Sub-keys

Being unsatisfied, the node will submit again, when the appearance of network partitions makes the number of server nodes smaller than  $t$ , and retry will fail to succeed and the key management service is invalid. Auxiliary network nodes are introduced in this paper to solve this problem. They never ask for preset certificate and system sub-keys, but auxiliary ones. Moreover, the auxiliary sub-keys don't have the ability to participate in DCA signature generation. Controlled by DCA, they can transform to temporary ones in some condition, and obtain signature ability temporarily. Once unneeded, they will be reduced to auxiliary sub-keys. Therefore the system is able to increase sub-keys temporarily to improve robustness.

### 2.3. Security Target

Although the redundant sub-keys could improve system robustness, security of the system will reduce accordingly. It has already been proved that system always suffers from Sybil attack in environment without centralized authority. In wireless multihop communication network with redundant sub-keys, Sybil is quite easily adopted by attackers. In order to avoid similar attacks, all identities of server nodes should be validated by authority, known as preset certificate. Other network nodes, such as auxiliary nodes and client nodes, can join in flexibly in using certificate, nodes guaranteeing, and many other ways [9, 10]. The security targets that the scheme presented should be achieved [11]: (1) To resist single points attack, that is to say, to encroach only one node is far less enough to forge certificate or obtain system keys; (2) To avoid multi server nodes identities to be obtained dynamically by masquerading; (3) To prevent attackers from carrying Sybil attack into execution to key management service.

## 3. Realization Mechanism

In traditional DCA approach, server nodes make up of a server group (SG) to establish secure communication connection between by the preset certificate. Protocols can be used to achieve update inside SG, query and other operations.

Auxiliary sub-key management comprises generation, activation, reduction and revocation.

Only when the whole server nodes are available, candidate auxiliary nodes could submit to SG to generate auxiliary sub-keys, and those succeed have the opportunity to transform the auxiliary nodes, in process of which SG selects an associated server node  $S_i$  for each auxiliary node  $A_k$ , denoted as  $S_i \leftarrow A_k$ . When there are less than  $t$  accessible nodes, SG will select a certain number of auxiliary nodes and activate their auxiliary sub-keys. After transforming to temporary sub-keys, the activated nodes, along with available servers, compose temporary DCA to achieve the certificate management operation. SG will reduce the temporary sub-keys to the very original state after self-recovery of the network. The auxiliary nodes under this circumstance no longer possess ability to participate in certificate management operation. Revocation protocol makes it possible for SG to revoke the auxiliary sub-keys of those nodes which appear malicious behavior. Obviously, the auxiliary sub-key management is always initiated and supervised by SG.

An Extended Key Update Protocol (EKUP) has been proposed in this paper to realize the effective management on auxiliary sub-keys. It is also an extension of the Secret Renewal Protocol (SRP), the main idea of which is to renew the sub-keys of the trustable server nodes without changing the original system keys. Since the sub-keys of the new and old edition cannot renew the system keys together, the hostile nodes will be excluded effectively. Not only generating new edition sub-keys, EKUP can also provide an activation increment.

The whole life period has been divided into several time segments in EKUP. At the beginning of each segment  $r$ , the server node  $S_i$  ( $i=1,2,\dots,n$ ) participating in initiating EKUP, assumes that there are  $n$  server nodes in all and has to take operations as follows. Firstly,  $S_i$  respectively generates  $(t-1)$ -order polynomial  $g_i^{(r)}(z)$  in  $Z_q$  independently to satisfy  $g_i^{(r)}(0)=0$ .  $S_i$  calculates activated information  $g_i^{(r)}(w_k)$  of auxiliary sub-keys for node  $A_k$ , at the same time with calculating  $g_i^{(r)}(v_j)$  for  $S_j$  ( $j=1,2,\dots,n$ ). Subsequently,  $S_i$  transmits  $g_i^{(r)}(v_j)$  and  $g_i^{(r)}(w_{k'})$ ,  $k' \in \{k' | S_j \leftarrow A_{k'}\}$ , to  $S_j$  in a safe way. After  $S_j$  has received  $g_i^{(r)}(v_j)$  and  $g_i^{(r)}(w_{k'})$ , updated the sub-key  $x_{j'}$ , the activated increment  $I_k$  of  $A_k$  will be respectively:

$$x'_i = x_i + \sum_{j=1}^N g_j^{(r)}(v_i) \pmod{q}, \quad (1)$$

$$I_k = -\sum_{i=1}^n g_i^{(r)}(w_k) \pmod{q}, \quad (2)$$

The old edition sub-keys will be preserved in EKUP, and the system can activate the auxiliary sub-

keys with the activated increment. Actually, EKUP renews the sub-key for some temporary reasons, which doesn't ask the entire server nodes to join in, so that it will not bring in too much burden of communication.

### 3.1. Generation

There are two sub-key generation protocols generally used at present, the aim of which are using  $t$  sub-keys existing to generate new sub-keys. The newly generated sub-key  $x_r$  is visible to the applicant node  $A_r$ . Since the auxiliary sub-key doesn't possess the ability of signature before being activated, there are some points need to be improved in the traditional sub-key generation protocol, which can also be shown in Fig. 1.

One of the most important parameters is the relevance limit  $A_q$ , which is the upper limit number of all the possible auxiliary nodes associated with a single server node. Generally,  $A_q+1$  need to be smaller than the threshold  $t$  to keep Sybil attack away.  $A_q$  depends on the nodes of SG, which means SG has the ability to confer, and it will supervised by SG according to the first step. The selection strategy of  $S_j$  depends upon the consideration about the security and robustness. A high security needed means a random selection of  $S_j$ , while a high robustness will be obtained by selecting the server nodes approaching to the applicant node mostly.

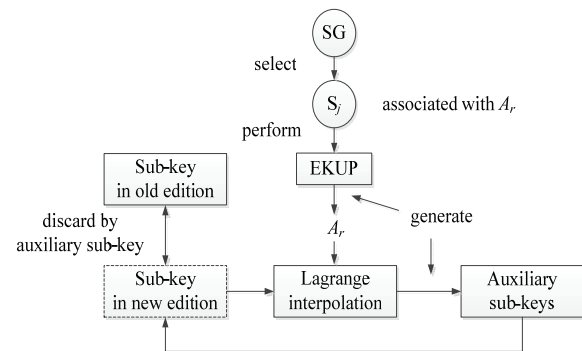


Fig. 1. Improvements in generation.

### 3.2. Activation

The main idea of an activating operation is to use the temporary sub-keys generated by the activated increment and auxiliary sub-keys. Assume the number of nodes available in SG is  $n'$ , the main steps of the activated algorithm will be as follows: (1) SG selects  $l'$  auxiliary nodes which are needed to be activated; (2) EKUP is initiated by parts of the server nodes to update the sub-key  $x_j$  ( $j=1,2,\dots,n'$ ) of the server node in present SG and the selected activated increment  $I_k$  ( $k=1,2,\dots,l'$ ) of the auxiliary node to

be  $x'_j$  and  $I'_k$ , in process of which, there is no new activated increment generated; (3) The server node transmits  $I'_k$  to the corresponding auxiliary node  $A_k$  through a secure link, and the auxiliary sub-key of which is  $h_k$ ; (4)  $A_k$  will calculate  $h'_k = h_k + I'_k \pmod{q}$  to get a temporary sub-key, and then  $A_k$  becomes the temporary server node.

### 3.3. Reduction and Revocation

When there is no need of temporary server nodes, the management certificate authority of the temporary nodes could be invalidated. Reduction is a kind of imperative operation initiated by SG. Since the updating operation is firstly performed for activated increment of the server nodes and the specific auxiliary nodes, the server nodes in SG only need to reduce  $x'_j$  and  $I'_k$  to  $x_j$  and  $I_k$ . This will naturally invalidate the temporary sub-keys, and they can be activated again only by  $h_k$  instead of  $h'_k$ . If the associated server node is still available, it is possible to finish invalidating just by deleting its activated increment.

## 4. Security Analysis

In the key management service of this paper, an effective attack indicates to forge certificate successfully or obtain the system keys. DCA based on the threshold scheme ensures that the attacker cannot forge certificate or obtain the system key by invading only one node, so as to keep the single node attack away. To launch an effective attack, the attacker needs to obtain multi server nodes identities or to embezzle multi server nodes gradually. Though preventing mobile attackers effectively, PSS is not able to keep Sybil attacker away.

Since off-line certificate is asked to be provided as identity authenticating for the server nodes in this paper, if the certificate is reliable, the attackers will have no chance to obtain multi server nodes identities and sub-keys dynamically. While in approach with redundant sub-keys, if the signature authority has been obtained by those generated dynamically, the attackers will be able to launch Sybil attack through masquerading as nodes with redundant sub-keys. Consequently, the authority of auxiliary sub-keys has been limited in this paper, so the premise of an effective attack is to obtain at least  $t$  sub-keys or temporary sub-keys. In case of the sub-keys not being activated, an effective attack will be launched only when the following two conditions are satisfied simultaneously: (1) At least  $\lceil t/(A_q+1) \rceil$  server nodes are under control; (2) Total number of the controlled server node  $S_c$  and auxiliary node  $A_c$  is no less than  $t$ , and should satisfy  $S_c \leftarrow A_c$ .

Therefore, the scheme proposed in this paper will make much more difficulty for attackers to steal the system keys. Moreover, with the parameters correctly set up, since  $A_q+1 < t$ , this scheme is able to prevent Sybil attack effectively.

## 5. Simulation Test

### 5.1. Simulation Model

The scheme has been simulated by Network Simulator (NS2.89) [12]. Simulating parameters of the typical scenario are set as in Table 1. The scenario simulates a wireless multihop communication network with the network partitions appearing frequently, and the average velocity of the nodes can be adjustable, in order to measure the effect of nodes mobility on the proposed scheme without loss of generality.

Table 1. Simulating parameters settings.

Parameters	Values	Parameters	Values
Size of Scenario	1 km×1 km	Mobile Model	Random Way-Point
Number of Nodes	100	Number of Server Nodes	10
Threshold Parameter	(10,4)	Number of Auxiliary Nodes	0,5,10,15,20,25,30,35,40,45,50
Transmission Range	20 m	Simulating Duration	600s
Average Velocity	5 m/s, 15 m/s	Reference Protocols	EKUP, SPR, tradition DCA

### 5.2. Simulating Results

The comparison of average failure rate with different number of auxiliary nodes and different velocities can be seen in Fig. 2.

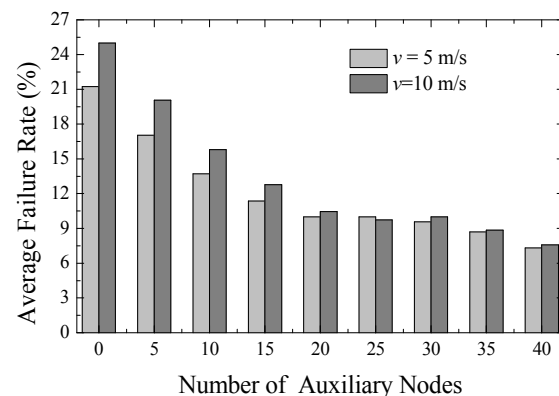


Fig. 2. Comparison of the average failure rate.

It can be seen that DCA application failure rate will descend remarkably with the number of auxiliary nodes increasing, which indicates that the robustness of system has been improved greatly with EKUP proposed in this paper. When number of auxiliary nodes drops to 0, it actually equivalents to traditional DCA with average failure rate in each scenario being 21.19 % and 25.10 % respectively. When the number of auxiliary nodes rises to 20, the average failure rate will drop to 9.24 % and 10.63 % respectively, and are both reduced by more than 50 %.

The advantage of establishing secure links by EKUP has been clarified through the mathematic model set up above. To prove the correctness of the mathematic model and the applicability of EKUP, the traditional DCA and SPR have been adopted as comparisons to simulate the improvement of EKUP on successful rate of establishing secure link with different number of auxiliary nodes, when the attack frequency reaches to 1 link per second. The parameters of scenario will be set as Table 1. Simulating results can be seen in Fig. 3.

It can be observed from Fig. 3 that the successful rate of establishing secure link will increase with the number of the auxiliary nodes rising. In the network environment with frequent attack, however, the successful rate of establishing secure link will be improved much more rapidly when the number of auxiliary nodes is small with EKUP proposed in this paper than that with the traditional DCA and SPR. What is more, when there are 12 auxiliary nodes, it will achieve the probability of up to 96 % to establish the secure links with EKUP, and that will be 56 % and 17 % with SPR and the traditional DAC respectively. In contrast, the successful rate will be increased by 71.43 % with EKUP instead of SPR.

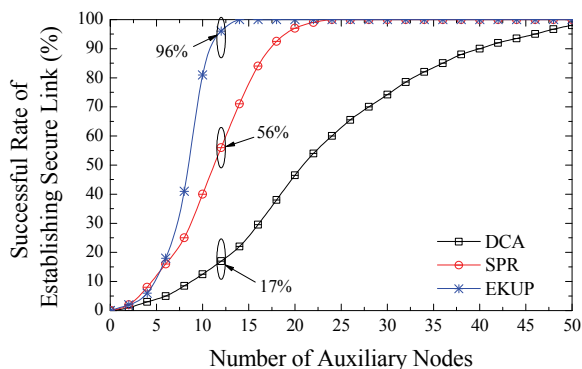


Fig. 3. Comparison of the successful rate of establishing secure link by different key management protocols.

## 6. Conclusion

Wireless multihop communication network, like WSN, Ad Hoc, Mesh, etc, as a key component of the next generation network, has attracted intensive public attention as an empowering technology in a wide variety of military and commercial applications

including national defense, public security and environmental technology. An Extended Key Update Protocol has been proposed in this paper to realize the effective management on auxiliary sub-keys based on the traditional DCA. The mathematic model has been established with auxiliary sub-keys brought in. Security analysis indicates that the scheme proposed in this paper is able to prevent common attacks in wireless multihop communication network effectively, such as Sybil attack and so on. Simulating results on NS2.89 prove that the deployment of this scheme will the reduce failure rate of operations related to key management service by more than 50 %, and will greatly increase the successful rate of establishing secure link, which is quite important for wireless multihop communication network. Consequently, the scheme presented is able to enhance robustness of key management service in wireless multihop communication network effectively without loss of generality. Future research direction will focus on the global key updating management mechanism to provide a safety certificate and confidentiality protection for message broadcasting in wireless multihop communication network.

## Acknowledgements

This work was support by Specialized Research Fund for the Doctoral Program of Higher Education under Grant No.20122301120004, China Postdoctoral Science Foundation under Grant No.2012M520778, Heilongjiang Province Postdoctoral Science Foundation under Grant No.LBH-Z12217, Research Foundation of Education Bureau of Heilongjiang Province under Grant No.12531480 and the Youth Science Fund Project of Heilongjiang University under Grant No.QL201110.

## References

- [1]. C. Alcaraz, J. Lopez, R. Rodrigo and C. Hsiaha, Selecting key management schemes for WSN applications, *Journal of Information Science and Engineering*, Vol. 31, Issue 18, 2012, pp. 956-966.
- [2]. D. Manivannan and P. Neelamegam, WSN: Key issues in key management schemes – A review, *Research Journal of Applied Sciences, Engineering and Technology*, Vol. 4, Issue 18, 2012, pp. 3188-3200.
- [3]. L. Changyuan, L. Wei, L. Hailin and J. Bo, Measurement method for space networks authenticated key security under distributed CA, *Journal of Electronics and Information Technology*, Vol. 31, Issue 10, 2009, pp. 2316-2320.
- [4]. L. Ming, Study on secret key management project of WSN on ECC, *Journal of Networks*, Vol. 7, Issue 4, 2012, pp. 652-659.
- [5]. J. Yang, L. L. Sun, C. Biyun and Y. Min, Key management scheme in WSN based on grid deployment model, *Lecture Notes in Electrical Engineering*, Vol. 127, Issue 4, 2012, pp. 623-629.

- [6]. D. Qi and L. Donggang, Using auxiliary sensors for pairwise key establishment in WSN, *Transactions on Embedded Computing Systems*, Vol. 11, Issue 3, 2012, pp. 251-262.
- [7]. R. Kishore, S. Radha and L. Chelyflar, Improving connectivity and resilience using ECC based key predistribution for deployment knowledge based WSN, *WSEAS Transactions on Communications*, Vol. 11, Issue 9, 2012, pp. 309-320.
- [8]. S. Rehman, B. Muhammad, A. Basharat and Y. Khawajaa, Comparison based analysis of different cryptographic and encryption techniques using message authentication code in WSN, *International Journal of Computer Science Issues*, Vol. 9, Issue 1, 2012, pp. 96-101.
- [9]. Z. Zhonghua, W. Huanfu, S. Limin and Z. Xinyun, Non-intrusive backplane-based testing platform for wireless sensor networks, *Journal of Software*, Vol. 23, Issue 4, 2012, pp. 878-893.
- [10]. V. Jelcic, M. Magno, D. Brunelli, P. Giacomo and B. Luca, Context-adaptive multimodal wireless sensor network for energy-efficient gas monitoring, *IEEE Sensors Journal*, Vol. 13, Issue 1, 2013, pp. 328-338.
- [11]. Z. Zhichu, G. Jianghong and Z. Haifeng, Data aggregation scheme for WSN with privacy protection, *Applied Mechanics and Materials*, Vol. 268, Issue 1, 2013, pp. 1671-1674.
- [12]. The Network Simulator ns-2, (<http://www.isi.edu/nsnam/ns/>), 2011.

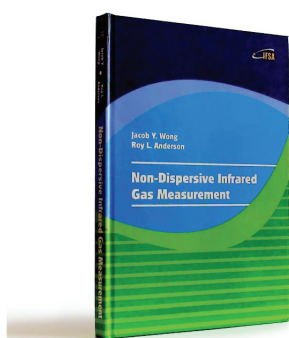
2013 Copyright ©, International Frequency Sensor Association (IFSA). All rights reserved.  
(<http://www.sensorsportal.com>)



International Frequency Sensor Association (IFSA) Publishing

**Jacob Y. Wong, Roy L. Anderson**

## **Non-Dispersive Infrared Gas Measurement**



Formats: printable pdf (Acrobat) and print (hardcover), 120 pages

ISBN: 978-84-615-9732-1,  
e-ISBN: 978-84-615-9512-9

Written by experts in the field, the *Non-Dispersive Infrared Gas Measurement* begins with a brief survey of various gas measurement techniques and continues with fundamental aspects and cutting-edge progress in NDIR gas sensors in their historical development.

- It addresses various fields, including:
- Interactive and non-interactive gas sensors
- Non-dispersive infrared gas sensors' components
- Single- and Double beam designs
- Historical background and today's of NDIR gas measurements

Providing sufficient background information and details, the book *Non-Dispersive Infrared Gas Measurement* is an excellent resource for advanced level undergraduate and graduate students as well as researchers, instrumentation engineers, applied physicists, chemists, material scientists in gas, chemical, biological, and medical sensors to have a comprehensive understanding of the development of non-dispersive infrared gas sensors and the trends for the future investigation.

[http://sensorsportal.com/HTML/BOOKSTORE/NDIR\\_Gas\\_Measurement.htm](http://sensorsportal.com/HTML/BOOKSTORE/NDIR_Gas_Measurement.htm)

## System Dynamics Modeling and Intelligent Tracking Control Based on Wireless Sensor Networks for Robot

<sup>1</sup>Qu Xiao-Yuan, <sup>1,2</sup>Zhang Feng, <sup>1</sup>Zhang Yong-Heng, <sup>1</sup>Dong Jian-Gang

<sup>1</sup>School of Information Engineering, Yulin University,  
Yulin 719000, China

<sup>2</sup>School of Automation, Northwestern Polytechnical University,  
Xi'an 710072, China

<sup>1</sup>Tel.: +8613509122121

E-mail: 282307708@qq.com

*Received: 10 August 2013 / Accepted: 25 August 2013 / Published: 30 September 2013*

---

**Abstract:** In order to improve robot arm intelligent tracing control accuracy and make the robot move in the environment autonomously, the robot must be capable of calculating its pose, the nominal system dynamics model based on orientation parameters of moving plant of shoulder is developed. Pose localization problem is a key researching domain in the mobile robot community and get much attention around the world. This dissertation is focused on the multi-sensor fusion based pose calculation problem for mobile robot. Application results show that the intelligent tracking has a significant effect in improving the tracing efficiency and reducing the tracking and monitoring cost, improving the capability of environment perception, co-operating and autonomous navigation of mobile robot. *Copyright © 2013 IFSA.*

**Keywords:** Target tracking, Wireless sensor network, System dynamics model, Intelligent control, Dynamic modeling.

---

### 1. Introduction

The robot is a kind of joint and complex systems with redundant degree of freedom. It focuses on the latest research results of machinery and electronics, automatic control, artificial intelligence, bionic and many other disciplines, and represents the latest scientific achievements in mechatronics [1]. Research on the robot, not only to promote the development of multi-disciplinary, but also can be coordinated through robots and humans working together to bring more value to human society.

Throughout the various types of robots, there are two main focuses its development faces, one is from the institutional perspective to develop robot. If this type of robot and human structure similar to the

structure, it is called a humanoid robot [2]. Humanoid robot is mainly composed of the mechanical arm, hand, clever eyes, waist and shoulder humanoid walking leg [3] humanoid components. If the structure similar to the other biological structure, it is called biomimetic robots, such as the snake robot, robot fish, dog, horse and other machine. On the other hand: Simulation of human and other biological behavior from the behavior perspective. Such studies including visual [4], touch [5] and smell [6] and other information acquisition and processing, humanoid thinking [7], the dynamic environment adaptive abilities, double arm [8], hand-eye and head coordinated action and the mutual exchange of realization, and even to drive the robot with consciousness also caused some people's interest [9].

With the further research, these two faces are constantly focusing on integration.

One of important mechanical arm actuator humanoid robot in addition to cooperate with other humanoid component to achieve capture, handling and throwing a series of human behavior, but also can be used as system application independent in industry, agriculture, medical, aerospace and other fields, replace human tasks such as machining, taking feeding, welding, surgery, space operations, fire, rescue and other sophisticated, heavy and dangerous task, so manipulator has been a large domestic and foreign experts, scholars and business units of the research topic, its research and applications have been ahead of the bionic humanoid robots and other components. In order to distinguish applied to different areas of robotics, when its application as a standalone system, called the industrial robot, humanoid robot when it is used as the "arm" for undertaking the study, called anthropomorphic robotic arm.

At the end of the nineteen fifties, the United States of America J. F. Eagleburger and G. C. Devol jointly developed the world's first [10] manipulator. Its body is installed on a rotary arm, top with the work piece pick-and-place mechanism, the control system is the teaching type. In 1962, the first robot made on the basis of a CNC tried teaching and playback type robot, named Unimate, take the "universal automatic" means. The motion of the system modeled on the turret, the arm can rotate, pitch, expansion, driven by hydraulic; drum as a storage device control system. In 1962, the U.S. machinery manufacturing company successful experiment called Vewrsatran robot. The robot can turn a central column, lifting hydraulic drive and control system is also teaching and playback type. Both robots laid a foundation for the development of industrial robots. Germany from the beginning of 1970 application machinery in the lifting and transport equipment, welding and cutting operation in hand.

To sum up, the domestic and international development process of mechanical arm, looked from the structure that is a simple series, parallel to the hybrid process; from the task analysis is a simple positioning operation to the realization of trajectory tracking, intelligent learning control; from the technical point of view, is a simple logic control to high precision adjustment to the kinetics of intelligent control.

## 2. Overview of Robot Control Technology

It can be divided into two categories of manipulator job tasks. One for the point to point movement, such as handling, welding, etc. Another along a given trajectory, such as welding, painting and so on. No matter what kind of exercise, start are given end-effector in Descartes coordinates of point and track, so how is obtained according to the change

law of motion of each joint end-effector in Descartes coordinate system in which the location or trajectory, and through the drive mechanism to adjust the joint position enables the robot to track a given trajectory or stable in the specified position, is the most important problems to be solved in kinematics, namely the inverse kinematics problem. Inverse kinematics plays an important role in robotics, is the foundation of robot dynamics and control of robot, and directly related to the motion analysis, off-line programming. The kinematics of second important issue is the error correction. The manipulator is a complex series, parallel or hybrid mechanism, the assembly error accumulated through the levels of transmission, greatly affected the total accuracy. To solve this problem, the best solution is the introduction of spatial position measurement, it is very difficult to implement. Another option is to pre-establish a model to correct the error.

To sum up, in order to achieve a more precise control of the robot, at least need to consider two aspects: fast and accurate to calculate the problem of inverse kinematics, the kinematic control problem; consider the design problem of the uncertainty of the robot dynamics modeling and trajectory tracking controller, the dynamic control problem.

### 2.1. Robot Dynamics Modeling Methods and Mathematical Models

As the basis of robot dynamics analysis and control, dynamic model has been the primary problem to solve the robot research. The dynamical model of the robot has two models, respectively is the dynamic model and inverse dynamics. Positive dynamics model of the robot driving each actuator force or torque as a variable to the robot joint angle trajectory in the joint variable space or end effectors trajectory in Cartesian space mathematical model for the response variable.

Inverse dynamics model of the robot in the joint variable space trajectory is a variable, or end effectors trajectory in the Cartesian space as a variable to each robot actuator driving force or torque as the dependent variable mathematical model. Current Analysis robot inverse dynamics methods are Newton-Euler method, Lagrange method, Kane method, least restrictive principle of law and the generalized Gaussian Dhahran Bell law. The basic way to derive robot dynamics algorithm has two kinds: one is the inverse dynamics algorithm as the basic calculation subroutine, n order equations for solving problems with symmetric coefficient matrix; the two is from the point of view of the robot model using Newton -Euler equation, recursive formula is derived directly for generalized acceleration Q. The robot inverse dynamics control, usually the following mathematical model.

$$M(p)\ddot{p} + C(p, \dot{p})\dot{p} + G(p) = \tau, \quad (1)$$

where  $\bar{p}$  - the position vector of each joint robot, velocity vector, acceleration vector;  $M(p)$  - robot inertia matrix;  $C(p, \dot{p})$  - robot matrix Coriolis force and centrifugal force;  $G(p)$  - the robot's gravity term vector.

Load change, existing external disturbance, friction and other uncertain factors in the robotic system has brought great difficulties to the robot research.

### 2.2. Robot Control System Structure

The end effectors through instruction signal generating device, the expected position and the desired trajectory, and through the target trajectory generation device to convert it into the robot drive displacement or track mechanism, as the mechanism driving the desired output. The control algorithm of the controller feedback signal and the desired output signal processing, calculates the volume control and transported to the actuator. The actuator according to the type and the size of the output torque control drive robot, ultimately makes the system stable and localization error less than the allowable error and tracking error converges to a region of zero or near zero, and can meet the dynamic performance index of certain.

### 3. Shoulder Dynamics Modeling

#### 3.1. Shoulder Member Kinetic Calculation

Assuming all side chain density uniform, regular shape. Article  $i$ -th branched diagram as shown in Fig. 1. Let  $r_c$  is the length of the  $a_i u_i$  and  $b_i d_i$  section,  $r_u$  is the length of the segment,  $r_D$  is the length of the segment. In the  $a_i u_i$  segment,  $a_i c_i$  segment,  $c_i b_i$  segment and  $b_i d_i$  segment each pick a point, the centric vector is denoted as  $P_{i1}$ ,  $P_{i2}$ ,  $P_{i3}$  and  $P_{i4}$ . Set the line density is  $\rho_1$ , then  $a_i u_i$ ,  $a_i c_i$ ,  $c_i b_i$ ,  $b_i d_i$  kinetic energy are

$$\begin{cases} V_{iau} = \rho_1 \int_0^{r_c} (p_{i1}^T p_{i1}) dx \\ V_{iac} = \frac{1}{2} \rho_1 \int_0^{r_u} (p_{i2}^T p_{i2}) dx \\ V_{ibc} = \frac{1}{4} \rho_1 r_c^2 r_d (C_i^T \bar{C}_i) \\ V_{ibd} = \frac{1}{8} \rho_1 r_c^3 (C_i^T \bar{C}_i) \end{cases} \quad (2)$$

By equation (2) the kinetic energy of all branched sum is

$$V_L = \sum_{i=1}^3 (V_{iau} + V_{iac} + V_{icb} + V_{ibd}) \quad (3)$$

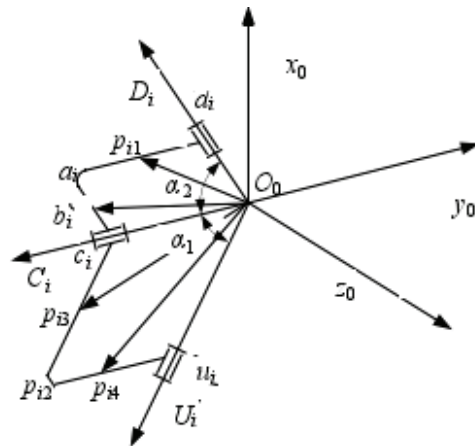


Fig. 1. Structure of the  $i$ -th branch.

#### 3.2. Shoulder Joint Component Calculation of Potential Energy

Set the link I quality is  $m_1$ , the centroid vector is  $h_{i1}$ . Even rod I quality is  $m_2$ , the centroid vector is  $h_{i2}$ , so we can write

$$\begin{cases} h_{i1} = \begin{bmatrix} X_i Z_i \frac{X_i \times Z_i}{|X_i \times Z_i|} \\ 0 \end{bmatrix} \begin{bmatrix} x_1 \\ x_2 \\ 0 \end{bmatrix} = x_1 X_1 + x_2 Z_1 \\ h_{i2} = \begin{bmatrix} X_i U_i \frac{X_i \times U_i}{|X_i \times U_i|} \\ 0 \end{bmatrix} \begin{bmatrix} y_1 \\ y_2 \\ 0 \end{bmatrix} = y_1 X_1 + y_2 U_1 \end{cases} \quad (4)$$

where,  $(x_1, x_2)$  is the centroid coordinates in the  $X_i O U_i$  plane of the connecting rod I.  $(y_1, y_2)$  is connecting rod I in the  $X_i O U_i$  plane of the centroid coordinates. Let the moving platform quality is  $m_3$ , then the total potential energy of the system is

$$P = m_1 g \left( \sum_{i=1}^m h_{i1} \right) + m_2 g \left( \sum_{i=1}^m h_{i2} \right) + m_3 g (h_m) \quad (5)$$

Using the Lagrange equation

$$\frac{\partial}{\partial t} \left( \frac{\partial L}{\partial q} \right) - \frac{\partial L}{\partial q} = u \quad (6)$$

where,  $L = V - P$  is a generalized coordinates, generalized coordinates  $q = [\alpha \ \beta \ \gamma]^T$ ,  $\mu$  is a

generalized force corresponding to the generalized coordinates  $q$ . Equation (2) to equation (5) into equation (6), so we can write

$$u = \frac{\partial}{\partial t} \left( \frac{\partial V_L}{\partial \dot{q}} \right) - \frac{\partial V_L}{\partial q} + \frac{\partial}{\partial t} \left( \frac{\partial V_c}{\partial \dot{q}} \right) - \frac{\partial V_c}{\partial q} \quad (7)$$

## 4. Mobile Robot System Model

### 4.1. Coordinated System

In mobile robot navigation study, the main use of three types of coordinate systems, the first category is the Cartesian coordinate system; second polar coordinate system, the majority of the distance / direction sensors, such as sonar, laser range finder, etc., are using this coordinate system; third is DIN70000 coordinate system in Europe widely used within the field of mobile robotics. Cartesian coordinate and DIN70000 coordinate system is the two representations of the Cartesian coordinate system, the Descartes coordinate system in general as Cartesian coordinate representation.

Study of the mobile robot, the main use of three coordinate systems: global coordinate system  $X_w O_w Y_w$ ,  $X_r O_r Y_r$  coordinate system of the robot and the sensor coordinate system  $X_s O_s Y_s$ , their relationship as shown in Fig. 2. In general, the system model of the robot are the three coordinate system based on the defined. Sometimes the sensor coordinate system to the robot coordinate system, using only the global coordinate system and the robot coordinate system.

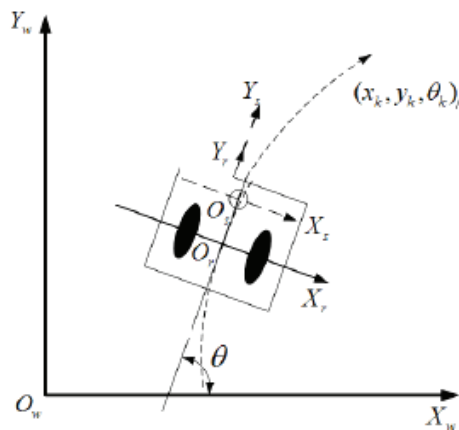


Fig. 2. Coordinate system for mobile robot.

### 4.2. The Environment Map Model

A typical characteristic environment map representation maps, raster maps and topological maps. The robot's map-based calculation method to pose environmental features map-based,

environmental characteristics are often assumed stationary. Characteristic map with a series of characteristic points of the environment in which the robot, each feature point in the global coordinate system to use it in the position  $L_i = (x_i, y_i)^T$  to the indication, and by a  $2 \times 2$  matrix represents the variance of its position uncertainty. The environment map can be expressed as  $m = (L_1, L_2, \dots, L_i)^T$ .

As a map-based computing is to solve the pose unknown environments positioning and navigation problems, so the map is essentially the process of creating a series of feature point calculation, and the map is constantly updated, because the position of the feature point and the robot together pose calculation and update. When the robot at time  $k$ , observed a new signpost  $L_{i,k}$ , you need to add new signs observed a map has been constructed, and its representation on the map based on the robot's current position as the origin of the local coordinate observables converted to the global coordinate system function, so we can write

$$L_{i,k} = \begin{bmatrix} x_{i,k} \\ y_{i,k} \end{bmatrix} = \begin{bmatrix} x_k + r_{i,k} \cdot \cos(\theta_k + \phi_{i,k}) \\ y_k + r_{i,k} \cdot \sin(\theta_k + \phi_{i,k}) \end{bmatrix} + v_k \quad (8)$$

where, the robot sensors was the first  $I$  measurements in polar coordinates are expressed as  $z_{i,k} = (r_{i,k}, \phi_{i,k})^T$ ,  $v_k$  is expressed in stochastic landmark model uncertainty,  $(x_k, y_k, \theta_k)^T$  were expressed in global coordinates of the robot pose.

### 4.3. The Sensor Observation Model

Observation model describes the relationship between  $z_{i,k}$  and the position of the robot sensors  $p_k$

$$z_{i,k} = h(p_k, l_i) + v_k, \quad (9)$$

where  $v_k$  represents the random measurement noise and uncertainty of the model itself, generally assumed to be Gaussian noise,  $N(0, R_k)$ ,  $L_i$  is the characteristic map of the  $i$ -th position. The different sensors have different forms observation equation. Assuming the distance sensor of observations as Equation (10), the time  $k$  obtained in the  $i$ -th concept of measurement  $z_{i,k}$  by the following observation equation

$$z_{i,k} = \begin{bmatrix} r_{i,k} \\ \phi_{i,k} \end{bmatrix} = \begin{bmatrix} \sqrt{(x_k - x_i)^2 + (y_k - y_i)^2} \\ \arctan \left( \frac{y_k - y_i}{x_k - x_i} \right) - \theta_k \end{bmatrix} + v_k, \quad (10)$$

where,  $L_i = (x_i, y_i)^T$  is the detected coordinates of the  $i$ -th feature,  $p_k = (x_k, y_k, \theta_k)^T$  is the robot pose observation time  $k$ .

## 5. Simulation Testing and Analysis

In order to verify the effectiveness of the passive controller, to simulation research. We take the  $\gamma = 2200$ ,  $\beta = 2.1232$ , the measurement noise variance  $\sigma = 5 \times 10^{-6}$ , sensor nodes are randomly arranged, spacing of about 50 m. Objective to (50, 50) as a starting point, the initial velocity, acceleration are 0 state begins to move, process noise  $\text{var}(w_i) = 0.43$ . Specific as shown in Fig. 3.

**Table 1.** Sensor nodes parameters of shoulder joint.

Parameters	Values	Parameters	Values
$r$	0.21 m	$r_S$	0.093
$r_D$	0.125 m	$\rho_1$	1.453 kg/m
$r_U$	0.075	$m_1$	0.56 kg
$r_C$	0.035	$\rho_2$	1.235 kg/m <sup>2</sup>

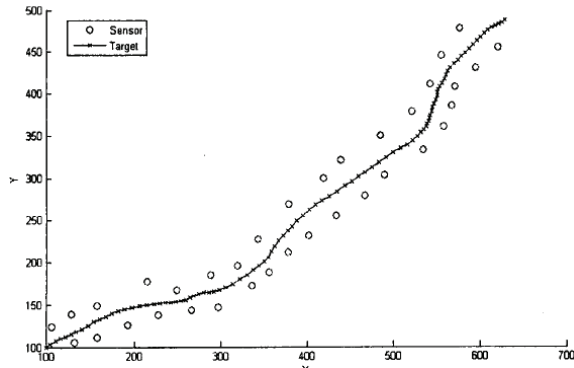


**Fig. 3.** Simulation results of mobile robot sensor nodes.

## 6. Conclusions

In this paper, the theory and application of technology based on wireless sensor network of shoulder joint research, around of shoulder joint in wireless sensor networks in recent years carried out research work, focused on the multi-sensor fusion based pose calculation problem for mobile robot.

The intelligent tracking has a significant effect in improving the tracing efficiency and reducing the tracking and monitoring cost, improving the capability of environment perception, co-operating and autonomous navigation of mobile robot.

## Acknowledgements

This work is partially supported by Natural Science Basic Research Plan in Shaanxi Province of China (Program No. 2013JM8005), Funding Project for Department of Education of Shaanxi Province in 2013 #2013JK1167, #2013JK1151, Research and Cooperation Project for Department of Yulin city in 2012 #2012CXY3-26. Thanks for the help.

## References

- [1]. Elif Derya Übeyli, Implementing eigenvector methods/probabilistic neural networks for analysis of EEG signals, *Neural Networks*, Vol. 21, Issue 9, 2008, pp. 1410-1417.
- [2]. T. Bailey, Mobile robot localisation and mapping in extensive outdoor environments, *University of Sydney*, Ph. D. Dissertation, 2002.
- [3]. S. Thrun, A system for volumetric robotic mapping of abandoned mines, in *Proceedings of the IEEE International Conference on Robotics and Automation (ICRA)*, Taipei, Taiwan, 2003, pp. 4270-4275.
- [4]. J. Yang, M. Xu, W. Zhao, et al., A multipath routing protocol based on clustering and ant colony optimization for wireless sensor networks, *Sensor*, Vol. 10, Issue 5, 2010, pp. 4521-4540.
- [5]. H. Alemdar, C. Ersoy, Wireless sensor networks for healthcare: A survey, *Computer Networks*, Vol. 54, Issue 15, 2010, pp. 2688-2710.
- [6]. J. Du, Sh. W. Chao, A study of information security for M2M of IoT, in *Proceedings of the Third International Conference on Advanced Computer Theory and Engineering*, 2010, Chengdu, August 20-22, 2010, v3-576-v3-579, New York: IEEE Press, 2010.
- [7]. Ilkka Kivelä, Design of networked low-cost wireless noise measurement sensors, *Sensors and Transducers*, Vol. 10, February 2011, pp. 171-190.
- [8]. Y. Jing, X. Mai, Zh. Wei, et al., A multipath routing protocol based on clustering and ant colony optimization for wireless sensor networks, *Sensor*, Vol. 10, 2010, pp. 4521-4540.
- [9]. Q. Liu, I. Cui, h. M. Chen, Key technologies and applications of Internet of Things, *Computer Science*, Vol. 37, Issue 6, 2010, pp. 1-4.
- [10]. R. Siegwart, I. R. Nourbakhsh, Introduction to autonomous mobile robots, *MIT Press*, 2004.

## WSN Message Authentication Code Based on Chaos and XOR-Encryption

<sup>1,2</sup> Bai EN-JIAN, <sup>1</sup> Zhu JUN-JIE, <sup>1</sup> Wu LIANG-CHENG

<sup>1</sup> College of Information Science & Technology, Donghua University,  
Shanghai 201620, China

<sup>2</sup> Engineering Research Center of Digitized Textile & Fashion Technology, Donghua University,  
Shanghai 201620, China

<sup>1</sup> Tel.: +8618621181309

E-mail: baiej@dhu.edu.cn

*Received: 5 June 2013 / Accepted: 25 August 2013 / Published: 30 September 2013*

---

**Abstract:** Wireless sensor network (WSN) is a kind of energy-constrained network. If any fake communication request is not recognized, that will lead to network security problems and additional energy consumption of the nodes. A good message authentication code (MAC) will help to solve this problem effectively. In this paper, we improve the MAC algorithm by using the technology of chaos and XOR-encryption. The advanced MAC generator can be divided into the sub-key generator and the MAC structure. The advanced MAC algorithm provides not only high data confidentiality but also message authentication functions. The sub-key generator provides excellent random performance and solves the periodicity defects of RC4. That extends the lifetime of “Seed-Key” and to further reduce the energy consumption. The structure is designed for the advanced MAC specially to meet the needs of WSN applications. It can avoid “Replay Attack” effectively when compared with CBC-MAC. The improved MAC algorithm provides simpler calculation and sufficiently reliable security performance. We have also tested the advanced MAC generator by using “Pearson’s Chi-squared goodness-of-fit test”. The test results reveal that the MAC sequences generated by the advanced MAC can provide enough security performance. *Copyright © 2013 IFSA.*

**Keywords:** WSN, Message authentication code (MAC), Chaos, XOR-encryption, Chi-squared goodness-of-fit test.

---

### 1. Introduction

Wireless sensor networks (WSN) have been developing rapidly in the last years. It’s an intelligent and private network organized by a large number of sensor nodes themselves with wireless communication. These sensor nodes with specific functions transmit information each other, to accomplish a specific function cooperatively. Currently, sensor nodes are promoted to be used in a wide spectrum of applications such as in military, healthcare and environmental applications.

Compared to the traditional wireless networks, WSNs have such characteristics as the large scale of deployment, power limitation, limited computing ability and memory capability, the limitation of communication bandwidth and range and the dynamic characteristic. Due to these limitations, WSN is faced with the challenge of security in such applications as military fields, environment monitoring, medical treatment and hazardous area. In order to keep communication secure, sensitive data should be encrypted and authenticated. Therefore, security is the critical issue in the WSN.

WSN is a kind of energy constrained wireless network. This makes the energy consumption level to be an important index in the design of WSN protocols and algorithms. Therefore, as an important part in WSN communication protocol, MAC algorithm is not only needed to consider the security performance, but also its energy consumption level.

Many energy-saving algorithms for WSN were put forward, but most of them are about energy efficient routing or networking. What they have in common is that both of them consume large energy while working. Therefore, almost every simplified algorithm of them provides high energy saving efficiency. But most of them take the method of reducing their working frequency to reduce the energy consumption further. Harvest seems small if we continue studying on these two kinds of algorithms. So we focus on studying energy-saving algorithms about link-layer algorithms. They are commonly used in WSN communication. Every time of message transmission need to call the related link-layer algorithms. As a result, studies on link-layer algorithms will provide same energy-saving efficient as well as routing or networking.

Meanwhile, link-layer algorithms have high portability and transparency. This makes link-layer algorithms have the very high research value.

Since the frequent calls of link-layer encryption algorithm during the data transmission, the energy research on the link layer security strategy can achieve good energy saving effect.

The link-layer security strategy is mainly composed of encryption algorithm, decryption algorithm and Message Authentication Code (MAC). An improved sub-key generator is invented for the lightweight MAC generator. The improved sub-key generator helps us proposing a WSN link-layer encryption algorithm based on the combination of stream-cipher and block-cipher. And then, we build a MAC algorithm suitable for WSN by studying the link-layer security protocol built-in TinyOS and combining the new WSN encryption algorithm.

In [1], the author mentioned that the security requirement of WSN includes Authentication, Confidentiality, Integrity and Non Repudiation.

Study on MAC is an important part in link-layer security algorithms. As we mentioned above, link-layer algorithms have the very high transplantation ability. Therefore, we can find MAC algorithm in almost all studies of WSN link-layer security strategy. Considering the energy consumption limits in the design of WSN, researchers use symmetric encryption as a mainstream design idea [2].

Most WSN link-layer MAC algorithms use CBC-MAC as the main structure, such as TinySec [3] and WSNSec [4]. The CBC mode is adopted in the encryption part of these two protocols and the MAC algorithm as well (CBC-MAC). CBC-MAC provides a simple structure and conforms to the requirements of the WSN application very much. But CBC-MAC is not safe enough. It provides a low security

performance in the face of "Birthday Attack", which is proved in the previous studies [5].

Meanwhile, some researchers have also tried some other MAC structures, such as MIC (Message Integrity Code) in WSNSec we introduced above. And they called it "CTR". But the CTR needs more calculation than CBC-MAC and increases the energy consumption.

As we can see, there are few MAC algorithm specially designed for WSN. Even if the CMAC in ContikiSec [6] is also the continue use of OCB mode in WLAN. In this paper, we designed a lightweight WSN link-layer encryption algorithm, and then present an advanced MAC algorithm.

The rest of this work is organized as follows. The advanced MAC algorithm is described in Section 2. We analysis the proposed MAC algorithm in Section 3. Conclusions are made in Section 4.

## 2. MAC Algorithm Design

### 2.1. The TinySec Protocol

TinySec is a WSN link-layer security protocol built-in TinyOS (a component-based WSN Operating System), which is developed by UC Berkeley (University of California, Berkeley). The TinySec protocol is also developed by UC Berkeley and defines the packet formats. It also includes data encryption & decryption algorithm, and MAC algorithm as well.

There's no link-layer security protocol in the earliest version of the TinyOS. Although this saves the energy consumption of the encryption and authentication calculation, it has brought a great security risk. Therefore, UC Berkeley added TinySec in the TinyOS as the link-layer protocol.

TinySec uses RC5 [7] or SkipJack [8] as the encryption algorithm. Both of the two algorithms are symmetric encryption types. The encryption algorithm uses CBC mode. The block size of RC5 can be switched among 32, 64 or 128 bits, and fixed 64bits for SkipJack. It uses CBC-MAC as the structure of MAC algorithm, which largely reduces the computation amount of MAC.

To calculate the CBC-MAC of message/plaintext  $P (P=P_1||P_2||\dots||P_n)$ , one encrypts in CBC mode with zero IV (Initialization Vector). The Fig. 1 sketches the computation of the CBC-MAC of a message  $P$  using a secret Key  $K$  and a block cipher  $E$ .

Researchers from UC Berkeley also provide the packet formats of the TinyOS version with TinySec. All three TinySec packet formats are shown in Fig. 2.

TinySec provides several operation modes. They are TinySec-off mode, TinySec-Auth mode and TinySec-AE mode, respectively. The TinySec protocol uses the existing information security technology and makes a dramatically streamlining.

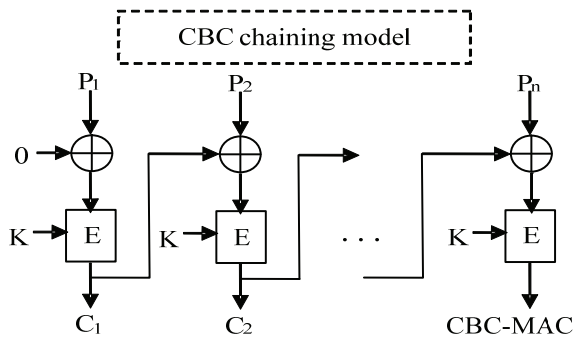


Fig. 1. CBC-MAC structure.

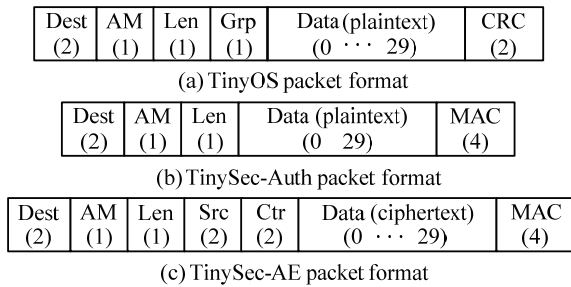


Fig. 2. The TinySec packet formats.

From the packet formats of TinySec, we can find that the earliest version of TinyOS only provides CRC check and does not provide any authentication function.

Compared with TinyOS packet format, TinySec-Auth and TinySec-AE just increase the length of 1 byte and 5 bytes. And it is important to note that TinySec-Auth mode can not save the energy consumption of encryption since it uses CBC-MAC. TinySec-Auth mode gives up the confidentiality to reduce the transmission energy consumption of 4 bytes. Certainly, that's still very considerable for the WSN.

These streamlining procedures help reducing the energy consumption, but also lead to some security loophole.

Firstly, the length of WSN communication data is always shorter than what is in traditional network, which means WSN has a smaller plaintext space and will be easier to be deciphered even using the same encryption algorithm.

Secondly, although Bellare et al. [9] proved that CBC-MAC is secure for fixed-length messages, CBC-MAC is still not secure enough for WSN. Bellare et al. [5] proves CBC-MAC can't provide adequate security performance when the length of data is variable, which would be deadly in WSN.

The last and most important is CBC-MAC only intercept the last cipher block as the Hash value, which leads to additional energy consumption when faced with Replay-Attacks.

Meanwhile, it's inevitable to call encryption algorithm while constructing MAC since TinySec uses CBC-MAC. And there's still possibility for

simplifying the link-layer encryption algorithm. We are committed to build an advanced link-layer MAC generator. So we present an improved sub-key generator, then present a lightweight MAC using XOR-cipher. In Section III, we test the advanced MAC algorithm and prove its security.

## 2.2. Sub-key Generation Algorithm Based on Chaos

In order to improve the security and energy-conservation performance of the WSN link-layer protocol, we have presented a sub-key generation algorithm based on standard RC4 and chaotic maps.

The improved sub-key generator inherits the stable structure from the RC4. It also uses chaotic maps to improve the randomness of the generated sequences.

Chaos is an ascertainable but unpredictable kinestate. Here's unpredictable means even a tiny change in a certain state will also lead to great deviation in the followed states. This is so-called "One false step will make a great difference". Chaos theory is a branch of mathematics and physics that deals with the behavior of certain nonlinear dynamical systems. By using the characteristics of chaos, we were able to build a pseudorandom sequence with excellent random performance.

The improved sub-key generation algorithm is composed of modified RC4. We use the chaotic mapping value to intervene the generation of pseudorandom sequences, which improves the random performance of the sequences and solve the periodicity defects in RC4.

The RC4 can be divided into Key Schedule Algorithm (KSA) and Pseudo Random Generation Algorithm (PRGA). We transform the PRGA part of RC4 by inserting a chaotic mapping value as the offset value. This makes full use of RC4's security architecture and improves the uncertainty of the output sequences at the same time. The improved sub-key generation algorithm increases the difficulty of deciphering successfully.

The random offset principle of the improved sub-key generator is shown in Fig. 3.

Sequences generated in this method possess excellent random performance. This provides premise for the lightweight design of WSN link-layer protocol and related algorithms. The new generating algorithm supports the block cipher algorithm that is commonly used in WSN. In this way, we can achieve "one-time pad" for all blocks. It is lightweight and secure as well. We have presented a WSN link-layer encryption algorithm based on this technique.

We use Logistic Mapping in the improved sub-key generator. The Logistic Chaos Model is shown in (1):

$$\begin{cases} X_{n+1} = \mu X_n (1 - X_n) \\ \mu \in [0, 4], X \in (0, 1) \end{cases} \quad (1)$$

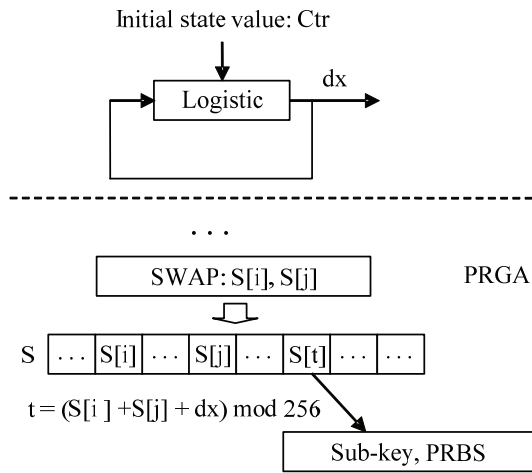


Fig. 3. Random offset principle of improved RC4.

Algorithm 1 shows the pseudo-code of the improved sub-key generator.

**Algorithm 1.** The improved sub-key generation algorithm.

```

u = 4; x = T[ IV mod 16 ]/128;
for i = 1: 4
    x = u * x * ( 1 - x );
end
i = j = dx = 0 ;
for round = 1: (Len/8)
    i = ( i + 1 ) mod 256 ;
    j = ( j + S[ i ] ) mod 256 ;
    x = u * x * ( 1 - x );
    dx = x * 256 ;
    swap ( S[ i ], S[ j ] );
    t = ( S[ i ] + S[ j ] + dx ) mod 256 ;
    Key[ round ] = S[ t ];
end

```

In the generator, we set the control parameter  $\mu$  as  $u=4$ .  $Len/8$  means the packet numbers of block cipher.

From Algorithm 1, we can find that the initial value  $X_0$  of Logistic map insert in the PRGA part is defined by the IVth element of T (the Seed-Key). IV mod 16 is due to the length (16 bytes) of the Seed-Key. Since the Ctr value is included in the IV, the  $X_0$  will be updated as IV together. That realizes the auto-updating function of the sub-key generator.

The iterative value is insert in the penultimate step ( $t = (S[i] + S[j] + dx) \bmod 256$ ;  $Key[round] = S[t]$ ).

This kind of modification method can increase the randomness of the output sequence and keep the stable structure of the standard RC4 at the same time.

The improved WSN link-layer sub-key generation algorithm skillfully uses the update of Ctr value from the packet format. This makes the key generation algorithm has the ability to update automatically, so we can improve the security performance while

lightweight the MAC algorithm. In this paper, we present an advanced MAC algorithm in this way.

### 2.3. The Advanced MAC Structure

We use XOR-cipher and CBC mode as the chaining model. The encryption part is a block cipher in essence. The main structure is the same as CBC block cipher shown in Fig. 1. The difference is we use XOR-cipher as the encryption function.

The block size is 8 bits (1 byte). This helps saving the padding process in most cases and provides better energy saving effect for short messages.

But this comes at a price. If we still use CBC-MAC, the MAC generator will not be able to provide MACs with enough length (4 bytes for WSN). So we propose a new MAC structure.

The improved sub-key generation algorithm has a higher random performance for generating sequences and has solved the periodicity defects in RC4. That will extend the lifetime of "Seed-Key", and then save the energy consumption caused by the key update. We use this to improve the MAC algorithm of WSN. Because of the excellent random performance from the sub-key generation algorithm, the encryption part is able to use "XOR-Encryption" to lightweight the encryption calculation. Using CBC mode as the cipher block chaining mode and the encryption/decryption algorithms can be expressed as in (2):

$$\begin{aligned}
 C_i &= (P_i \oplus C_{i-1}) \oplus K_i \\
 P_i &= (C_i \oplus C_{i-1}) \oplus K_i
 \end{aligned} \quad (2)$$

Based on this encryption algorithm, we have built an advanced MAC algorithm still using CBC-MAC as the main principal part that retains the lightweight structure feature. Researchers proved the length of MAC in WSN should be at least 4bytes (32bits) to ensure the security, but the advanced MAC uses 8 bits block cipher. So the structure of advanced MAC will be different from CBC-MAC or any other advanced CBC-MAC before. The advanced MAC algorithm structure is shown in Fig. 4.

Message Authentication Code can be considered as an encrypted hash value. In order to lightweight the algorithm calculation, the advanced MAC uses last 4 bytes ciphertext ( $C_{n-3}, C_{n-2}, C_{n-1}, C_n$ ) as the hash value and "XOR-Encryption" as encryption part.

We also considered the situation when the length of ciphertext is shorter than 4 bytes. If that happens, the advanced MAC will use Pseudorandom Binary Sequence (PRBS) generated by the sub-key generation algorithm to pad the hash value W, so as to make the length  $|W| = \sum C_i + |PRBS| = 4$  (bytes).

After get the hash value W, we introduce an Interleaving algorithm to disrupt the new hash value W, so that the PRBS can be fully involved in the MAC algorithm. All these operations ensure the security of MAC.

Algorithm 2 shows the pseudo-code of the advanced MAC.

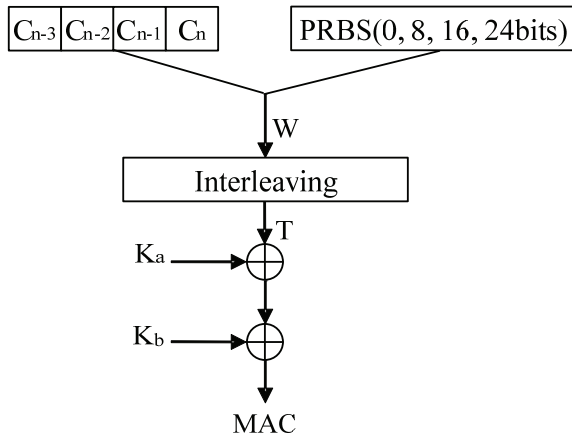


Fig. 4. The advanced MAC structure.

**Algorithm 2.** The advanced MAC algorithm.

```

C := E ( P, Key );
partition C into C1, C2, ..., Cn;
if ( |C| >= 4 )
  W = Cn-3||Cn-2||Cn-1||Cn;
else
  {
  switch ( |C| )
  {
  case 1: generate 3bytes PRBS ; break ;
  case 2: generate 2bytes PRBS ; break ;
  case 3: generate 1bytes PRBS ; break ;
  }
  W = C||PRBS ;
  }
T=Interleave ( W )
MAC = T ⊕ Ka ⊕ Kb;
  
```

It is necessary to note that PRBS,  $K_a$  and  $K_b$  are all generated by the sub-key generation algorithm. The PRBS is a variable-length sequence, and is needless if the length of plaintext is 4 bytes or longer.  $K_a$  and  $K_b$  are a length of 4 bytes (32 bits) sequence and provided with automatic updates as well as the PRBS.

Moreover, using  $K_a$  and  $K_b$  to encrypt the hash value  $T$  two times is not a redundant computation. That will be explained in Section 3.

### 3. Algorithm Analysis

#### 3.1. Security Analysis

The advanced MAC algorithm is similar to ECBC [10] in structure. ECBC is an improved algorithm of CBC-MAC, which uses “two times encryption” in the calculation. The MAC algorithm we present in this paper also uses “two times encryption” to provide adequate security performance. Then we will prove it.

First, unlike other algorithm variants of CBC-MAC, the new MAC uses PRBS to pad the sequence  $W$ . The padding process can ensure an effective 4-bytes output from the advanced MAC. What’s more, the padding process can increase the difficulty of MAC forgery and improve the security of MAC algorithm. That’s because the difficulty for the attacker will not be reduced when the length of plaintext is less than 4 bytes.

Second, the encryption processing of hash value  $T$  can solve the security problem of CBC-MAC when faced with “Replay Attack”. In combination with the improved random sequence generator we presented, the MAC will be widely divergent even if processing two same sequences. Therefore, the attacker will not be able to expend the energy of nodes by using Replay Attack. By using the advanced MAC and supporting encryption algorithm, the ciphertext for transmission will be widely divergent even processing the same plaintext. And the MAC will be quite so when processing the same ciphertext. In this way, the advanced MAC can identify the Replay Attack easily, then saving the energy of message deciphering.

Finally, it should be noted that the “two times encryption” is not a redundant computation. Since we use XOR-encryption in the MAC, “one time encryption” will reveal the Keys because the ciphertext and MAC are known. That will lead to great security problem of the whole link-layer security system. This is the weakness of “XOR-encryption” and can be solved by introducing “two times encryption” successfully.

Through the discussion above, we can fully prove that the advanced MAC can provide enough security performance. The structure is safe and stable, and it can resist attacks such as “Replay Attack” effectively. Meanwhile, it is really lightweight.

#### 3.2. Security Test Methods

Through the discussion above, we can prove that the advanced MAC generator’s structure can provide sufficient security. Then, we will use some scientific quantitative method for several tests to prove its security.

We implemented the sub-key generator, the encryption algorithm and the MAC generator in MATLAB. Test method we use is the “Pearson’s Chi-squared goodness-of-fit test”. The details will be mentioned in the following paragraphs.

The “Pearson’s Chi-squared test” uses a measure of goodness of fit which is the sum of differences between observed and expected outcome frequencies (that is, counts of observations), each squared and divided by the (3).

The “Pearson’s Chi-squared test” can be used in statistical tests for the block cipher. In this paper, it will be used to test the security performance of the advanced MAC generator. It is important to note that “Pearson’s Chi-squared test” requires the expected

frequencies not too small (greater than or equal to 5). The sample size  $M$  also has requirements (more than 50 best). Therefore, we take large number of samples in the tests in order to ensure the accuracy of the results.

Actually, we have already tested the security performance of the improved sub-key generator and the encryption algorithm by "Pearson's Chi-squared test". The test results show the excellent randomness performance of the sequences generated by the improved sub-key generator. The encryption algorithm combined with block cipher and XOR-generation also provides sufficient security. But due to limited space of this paper, we will just introduce the tests of the advanced MAC generation algorithm.

### 3.3. Security Tests

By using "Pearson's Chi-squared goodness-of-fit test" (Hereinafter referred to as "Pearson's Chi-squared test") [11], we have tested the security performance of the sub-key generator and proved the sequence it generates provide excellent random performance. In this paper, we still use "Pearson's Chi-squared test" to test the security performance of the advanced MAC algorithm.

According to the requirement of "Pearson's Chi-squared test", the sample capacity  $M$  should meet the condition:  $M \geq 50$ , and the theoretical frequency:  $E_i \geq 5$ . So we tested a large number of MAC samples to made  $M = 5 \times 2^{32} \gg 50$ , and  $E_i = C_{32}^0 \times M / 2^{32} = 5$ . The fitting value should be calculated as in (3):

$$\chi^2 = \sum (F_i - E_i)^2 / E_i, \quad (3)$$

where  $F_i$  is the observed frequency and  $E_i$  is the theoretical (expect) frequency.

Compare the value of the calculated  $\chi^2$  and threshold value of "Pearson's Chi-squared test" (significant level=5 %, degree of freedom=31 or 32).

If the calculated value is less than the threshold value, the sample will pass the "Pearson's Chi-squared test". That means the MAC sequence provide an excellent random performance that can be equivalent to the security performance.

#### 1) Randomness Test

Except using loophole in algorithms and protocols, the attackers usually use statistical analysis methods to forge a MAC code. That means, if a MAC algorithm can construct a sequence with good random performance, it can also provide good security performance because the advanced MAC is hard to be cracked in statistical analysis methods. The randomness test is spilt into frequency test and following test. Both of them use "Pearson's Chi-squared test" method.

##### Frequency test:

The frequency test is to test the 0-1 balance of the MAC. It need to count the number of sequences whose Hamming Weight is  $i$  ( $i = 0, 1, 2, \dots, 32$ ) from  $M$  samples and record it as  $F_i$ . The theoretical frequency  $E_i$  is calculated by the formula:  $E_i = C_{32}^i \times M / 2^{32}$ , ( $n=32$ ). Calculate the fitting value, then compare it with the threshold value (significant level=5 %, degree of freedom= 32) and get the test result.

##### Following test:

The following test is to test the performance of adjacent bits. During the following test, we exclusive-OR every adjacent bit in  $M$  MAC sequences. Then we have  $M$  31 bits long sequences. Count the number of sequences whose Hamming Weight is  $i$  ( $i=0, 1, 2, \dots, 31$ ), record it as  $F_i$ . The theoretical frequency  $E_i$  here is calculated by:  $E_i = C_{31}^i \times M / 2^{31}$ , ( $n=32$ ). Calculate the fitting values and compare them with the threshold value (significant level=5 %, degree of freedom= 31).

We took samples randomly and did each test for 10 times and the test result is showed in Table 1.

Table 1. Security test.

Project	Fitting value of Pearson's Chi-squared goodness-of-fit test										Threshold value
Frequency test	33.16	20.08	23.68	14.52	16.72	30.04	35.00	31.12	24.20	33.40	46.19
Following test	31.48	29.28	23.16	36.28	28.36	38.16	14.60	24.92	25.98	14.68	44.99
Diffusivity test	11.92	21.88	21.60	14.80	6.44	16.64	13.52	12.04	13.52	17.84	46.19

The test result shows that the message authentication codes constructed by the advanced MAC fit the binominal distribution and its following test also fits the requirement. The MAC sequence provides excellent random performance.

#### 2) Diffusivity Test

MAC generation algorithm can be considered as a Hash algorithm with key. Hash algorithm has an important security index, avalanche characteristic. Therefore, whether fits the avalanche characteristic is

one of the evaluation standards in MAC's security tests.

Using the "Pearson's Chi-squared test", we can have a diffusivity test for testing the avalanche performance of the advanced MAC. In the test, we chose  $M$  sequences of plaintext  $P_i$  ( $i=1,2, \dots, M$ ), then do the MAC calculation and get  $M$  sequences of MAC:  $MAC_i$  ( $i=1,2, \dots, M$ ). Then we invert the plaintext bit by bit and calculate the MAC codes  $MAC_{ij}$  ( $4 \leq j \leq 4*29$ ). Calculate the Hamming distance:

$d = W(\text{MAC}_i + \text{MAC}_{i,j})$ , count the number of  $d=k$  ( $k=0,1,2, \dots, 32$ ), record them as  $F_k$ . The theoretical frequency is  $E_i = C_n^i \times M/2^n$ , ( $n=32$ ), then calculate the fitting values and compare them with the threshold value (significant level=5 %, degree of freedom= 31).

The result is also enumerated in Table 1. We can find that the advanced MAC has a good diffusivity and fits the avalanche criterion.

#### 4. Conclusions

The advanced MAC uses CBC mode as its chaining mode like TinySec, so it's secure enough to use last 4 bytes ciphertext as the hash value. When the length of plaintext is shorter than 4 bytes, the advanced MAC pads the hash value with PRBS and uses an interleave process to ensure the security of the MAC generator.

The advanced MAC makes full use of the improved sub-key generator to improve the safety performance of the MAC generator. Without the periodicity defects brought from RC4, we can use "one-time pad" and XOR-Encryption to lightweight the calculation that won't reduce any security performance.

Using XOR-encryption two times after CBC-MAC, we can avoid the security loophole of XOR-encryption. That can also provide sufficient security and save the energy consumption form when faced with "Replay Attack". The advanced MAC also has an "Auto-updating" ability that can increase the difficulty of forging MAC.

After the statistical test (Pearson's Chi-squared test), we prove that the advanced MAC algorithm provides an excellent security performance. The codes it generates fit 0-1 distributions perfectly. That means codes generated by the advanced MAC algorithm can defend attacks using statistical analysis methods. In the "Diffusivity Test", we also proved the generator fits the avalanche criterion.

The advanced MAC algorithm can fit the security requirements and decrease the energy consumption effectively. That's quite suitable for link-layer security strategy of WSN.

#### Acknowledgments

We are grateful to the anonymous referees for their valuable comments and suggestions to improve the presentation of this paper. This work was

supported by National Natural Science Foundation of China under Grant 61201249 and Shanghai Municipal Natural Science Foundation under Grant 10ZR1401400.

#### References

- [1]. Byunggil Lee, Seungjo Bae and Dongwon Han, Design of network management platform and security framework for WSN, in *Proceedings of the IEEE International Conference on Signal Image Technology and Internet Based Systems (SITIS' 08)*, Bali, Indonesia, 30-03 December 2008, pp. 640-645.
- [2]. Sadaqat Ur Rehman, Muhammad Bilal, Basharat Ahmad, et al., Comparison based analysis of different cryptographic and encryption techniques using message authentication code (MAC) in wireless sensor networks (WSN), *International Journal of Computer Science Issues*, Vol. 9, Issue 1, No. 2, 2012, pp. 96-101.
- [3]. C. Karlof, N. Sastry, D. Wagner, TinySec: a link layer security architecture for wireless sensor networks, in *Proceedings of the 2<sup>nd</sup> ACM Conference on Embedded Networked Sensor Systems*, Baltimore, USA, 3-5 November 2004.
- [4]. Necla Bandirmali, Ismail Erturk, WSNSec: a scalable data link layer security protocol for WSNs, *Ad Hoc Networks*, Vol. 10, No. 1, 2012, pp. 37-45.
- [5]. M. Bellare, J. Kiliany, P. Rogaway, The security of the cipher block chaining message authentication code, *Journal of Computer and System Sciences*, Vol. 61, No. 3, 2000, pp. 362-399.
- [6]. Lander Casado, Philippas Tsigas, ContikiSec: a secure network layer for wireless sensor networks under the Contiki operating system, in *Proceedings of the 14<sup>th</sup> Nordic Conference on Secure IT Systems*, Oslo, Norway, 14-16 October 2009.
- [7]. Ronald L. Rivest, The RC5 encryption algorithm, Fast Software Encryption, LNCS 1008, *Springer-Verlag*, 1995, pp. 86-96.
- [8]. NIST. SKIPJACK and KEA Algorithm Specifications. (<http://csrc.nist.gov/encryption/skipjack-kea.htm>).
- [9]. M. Bellare, J. Kilian and P. Rogaway, The security of the cipher block chaining message authentication code, *Journal of Computer and System Sciences*, Vol. 61, No. 3, 2000, pp. 362-399.
- [10]. J. Black, P. Rogaway, CBC-MACs for arbitrary-length messages: the three-key constructions, in *Crypto 2000*, *Springer-Verlag*, Heidelberg, 2000, pp. 197-215.
- [11]. David M. Glover, William J. Jenkins, and Scott C. Doney, Least squares and regression techniques, goodness of fit and tests, non-linear least squares techniques, *Woods Hole Oceanographic Institute*, 2008.

## Three Dimensional Acoustical Imaging Based on Isosurface Technique for Bulk Material

<sup>1a</sup> He GUOCHAO, <sup>1b</sup> Ding JINWEN, <sup>2</sup> V. M. LEVIN, <sup>1a</sup> Dong LANFANG,  
<sup>2</sup> A. N. BOGACHENKOV, <sup>3</sup> Li KANG, <sup>1c</sup> Yao CHUANMING,  
<sup>2</sup> K. V. ZAKUTAILOV, <sup>2</sup> Yu. S. PETRONYUK, <sup>4</sup> Li FENG,  
<sup>2</sup> E. S. MOROKOV

<sup>1a</sup> School of Computer Science and Technology;

<sup>1b</sup> CAS Key Laboratory of Materials for Energy Conversion,  
Department of Materials Science and Engineering;

<sup>1c</sup> School of nuclear Science and Technology, University of Science and Technology of China,  
96 Jinzhai Road, Hefei, 230026, China

<sup>2</sup> Emanuel Institute of Biochemical Physics, Russian Academy of Sciences,  
4 Kosyгина Street, Moscow, 119334, Russia

<sup>3</sup> Anhui Province Coal Science Research Institute, 81 Xuancheng Road, Hefei, 230001, China

<sup>4</sup> 16<sup>th</sup> Research Institute of China Electronic Technology Group Corporation,  
439 Suixi Road, Hefei, 230043, China

E-mail: [jwding@ustc.edu.cn](mailto:jwding@ustc.edu.cn), [jinwending@hotmail.com](mailto:jinwending@hotmail.com)

*Received: 26 June 2013 / Accepted: 25 August 2013 / Published: 30 September 2013*

**Abstract:** The paper introduces the methods with time-resolved technique and isosurface display technique to get two- and three-dimensional (3D) acoustical imaging for scanning acoustic microscopy. Time-resolved technique presents the way to realize two-dimensional (2D) acoustical imaging – A- (O-), B- and C-scan, and a discrete combinatorial 3D image; and isosurface display technique realizes a 3D image with continuous distribution in full direction. The paper proposals a transitional model of square column, which consists of the data of echo signal pattern extracted from volume database, to construct the imaging cube and depict an isosurface using isovalue of internal boundaries in the cube, for the evaluation of internal defects in bulk specimen – Boron Nitride. 3D acoustical imaging has the advantage to show the position, size, appearance, distribution, and tendency of internal structures (voids, inclusions and defects) with complex shapes in non-transparent bulk material. The results show that 3D acoustical visualization presents more affluent, overall and intuitive pattern than 2D imaging for micro-sized structure investigation. *Copyright © 2013 IFSA.*

**Keywords:** Scanning Acoustic Microscope, Echo Signal Pattern, A-scan, B-scan, C-scan, Three Dimensional Acoustical Imaging, Isosurface Technique, Internal Defects, NDT/E, Boron Nitride.

### 1. Introduction

The technologies of Scanning Acoustic Microscopy (SAM) and their applications are based on the raster principle, which was proposed by

C. F. Quate and R. A. Lemons in 1974. High-frequency ultrasound usually more than 20 MHz is employed to produce a focused probe beam in immersion, with a focal spot diameter in tens of micrometers [1-3]. This ultrasound probe beam

penetrates into the bulk material, and its response radiation makes it possible to imaging micro-sized structure of a bulk specimen with micron or submicron resolution.

Ultrasound wave is very sensitive to the varieties in focal spot. Response radiation coming from the focal region of the probe beam output as an ultrasound signal, which is formed by the interaction between the ultrasound probe beam and the internal structure elements inside local insonified region. It can be employed to investigate some physics elastic properties – calculating acoustic wave velocities (longitudinal wave and transversal wave) by the time interval between various ultrasound signals, and investigating acoustical phenomena by analyzing signal formation in echo signal pattern [4, 5]. Another utility of response radiation is a means to form acoustical imaging. Acoustical imaging possesses its own mechanisms of acoustical contrast – specific ways to represent structural peculiarities of objects. Variations of signal parameters coming from diverse points of bulk material are displayed in the screen as a pixel of acoustical image.

At present, acoustic microscopy provides the mature two-dimensional (2D) imaging techniques, including A-(O-), B- and C-scan image, to evaluate the micro-sized structures in non-transparent solid bulk material.

In many modern high-tech industrial fields, the micro-sized internal defects inside the solid bulk material hide extreme risk in some applications. The material of Boron Nitride (BN) is a very modern and popular bulk material [6, 7]. It has wide range of application in the fields of aerospace and aviation industry, semiconductor and metal processing. Boron Nitride is used in wear-resistant and erosion-resistant coatings and thermal barriers in thermal spray coatings on the turbine engines, as dynamic friction materials in brake pads, as well as thermal management fillers in high-performance plastic components. Its elastic properties determine it is a fragile material, once in which there is any internal defects, the defects spread to the whole bulk and lead to full fracture. Hence, the microscopical inspection of internal defects for Boron Nitride material is prerequisite for some vital applications.

Scanning acoustic microscopy just provide the technology to detect the internal defects for this purpose in a non-destructed testing/evaluation (NDT/E) way [3, 8]. However, the traditional 2D acoustical imaging only presents internal structure information discontinuously, individually, and lack of affluent, intuitive and overall view. In the application of NDT/E field, the three dimensional (3D) acoustical imaging become more attractive for visualization of micro-sized structure. There are two techniques to realize 3D visualization – volume rendering and isosurface rendering [9-11]. Volume rendering sums the weighted contributions of all voxels along the line extended from the viewer's eye through the data volume. It is only used for visualization, and cannot obtain the 3D model of the

structures. Isosurface rendering is a high-resolution 3D interface construction technique proposed by W. E. Lorensen and H. E. Cline in 1987. It displays an interface representing the locus of a collection of points in the volume corresponding to a given constant – isovalue. The authors propose a model – ‘square column’ to match isosurface rendering technique specifically for 3D imaging of scanning acoustic microscopy. Along with the progress of graphic process unit (GPU) technology, the speed of 3D visualization is promoted effectively [12]. Under this background, based on the model of square column and isosurface techniques, and cooperating with the traditional 2D imaging techniques, the 3D acoustical imaging of scanning acoustic microscopy becomes more operable and powerful means, to investigate the micro-sized structure inside bulk materials.

## 2. Experimental

The specimen is an anisotropic material – Boron Nitride (hexagonal BN), with the sonic velocity of longitudinal wave along  $x$  or  $y$  plane is about  $18.05 \text{ mm}/\mu\text{s}$  and along  $z$  direction is about  $3.44 \text{ mm}/\mu\text{s}$  [8]. This specimen is treated into the cuboids' shape – the size with the length is  $5.53 \text{ mm}$ , the width is  $4.8 \text{ mm}$ , and the thickness is  $4.08 \text{ mm}$ . The specimen is put in immersion (water) and implemented by acoustic lens.

Acoustic lens is the kernel of acoustic microscope, carried by a mechanical motion system to realize the scanning and focusing function over the specimen surface. It excites a focused probe beam in immersion and collects the response radiation caused from the micro-sized structure at various depths of the bulk object. The transducer of the acoustic lens receives the reflected ultrasound radiation with the style of mechanical oscillation, and converts it into electrical ultrasound signals, which carry the micro-sized structure information. So, a series of electrical ultrasound signals emerge in an ultrasonic echo signal pattern, named A-(O)-Scan. See the picture a) of Fig. 1.

The picture a) is an experimental pattern, which displays the signals obtained at one scanning point, as the focused probe beam is driven by the mechanical scanning system over the specimen. The ultrasound signals with various amplitudes are distributed along the temporal axis of echo signal pattern, which are corresponded to various structures in vertical direction at a local region on/inside the object. Intensive signal stands for the existence of a boundary (interface) of an internal structure inside the bulk object, and arbitrary background signal means the uniform material inside this bulk object. In the Fig. 1, the symbol A represents that the signal is reflected from the front surface of an object, the symbol B reveals a boundary of internal defect inside this object, and the symbol C reveals the background noise caused by the uniform material.

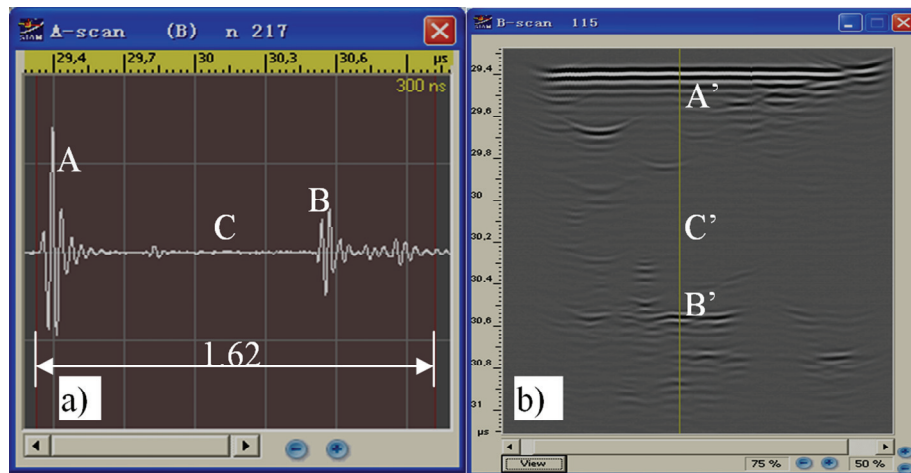


Fig. 1. Echo signal pattern and its scanning result B-Scan image along x direction.

Echo signal pattern is a fundamental data resource for imaging. Under the time-resolved technique, by setting the width of electrical gate in echo pattern, as the focused probe beam is driven along x or y direction by the mechanical scanning system, the microscopy system acquires the 2D cross-section image – B-scan image. The picture b) of Fig. 1 shows a B-Scan image as the lens is driven along x direction, and the width electrical gate is set to 1.62  $\mu\text{s}$ , in which the pixels marked by symbol A', B' and C' are the scanning results corresponding to the signal A, B and C in the picture a) individually.

In echo pattern, the velocity value in z direction of this BN can be derived from the thickness of the specimen, and the time interval between the front surface and bottom. The longitudinal velocity value is 3.03 mm/ $\mu\text{s}$ . Meanwhile, the time interval between signal A and B in the picture a) is 1.14  $\mu\text{s}$ , therefore, the depth of the defect inside the specimen can be deduced in 3.45 mm.

As the electrical gate width is set to 340 ns in echo signal pattern, and the acoustic lens is driven along x and y direction coordinately, Fig. 2 displays a 2D image – C-scan image, the profile of an internal structure at the depth is 3.45 mm inside this bulk specimen. The bright area with label B'' in different contrast shows this internal interface and its distribution along x or y plane.

Based on 2D acoustical image display techniques, logically, a group of slices consist of 2D images may form a discrete 3D image arranged in parallel as Fig. 3. It presents the simulation of this 3D image with a series of B-Scan images. Every slice is a B-Scan image produced along x direction and z direction, and the slices are arranged along y direction. The set of these pictures provides an approach to characterize the tendency and distribution of internal microstructures. But, between any two adjacent slices, it lost the characterization of some structures.

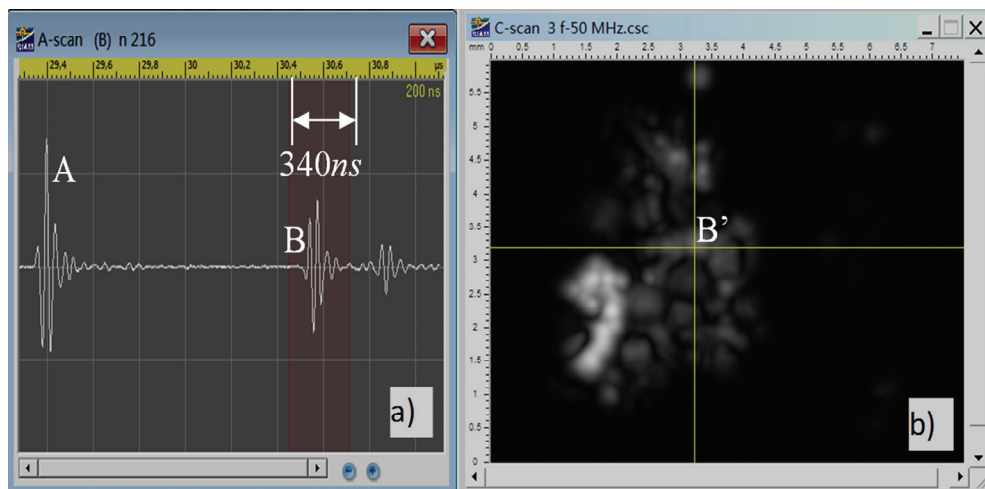


Fig. 2. Selected electrical gate in echo signal pattern and its C-Scan image along x and y plane.

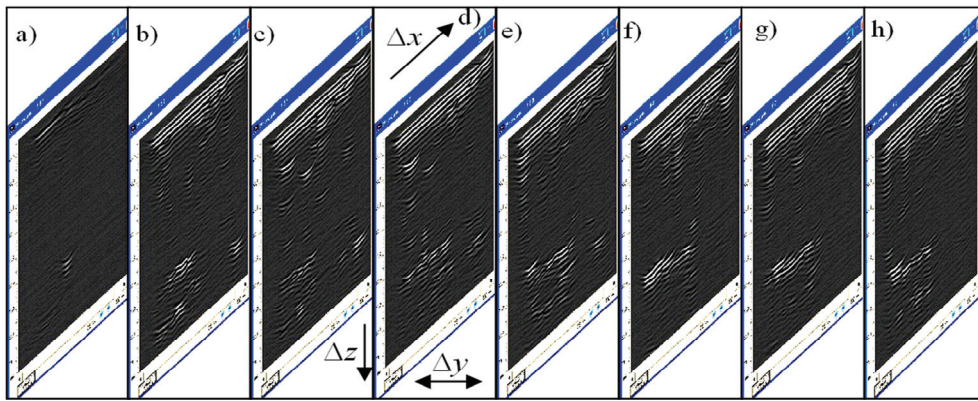


Fig. 3. Internal structures distribution shown in a series of B-Scan images (3D).

Furthermore, our concern is how to construct 3D image employing echo patterns for the real internal structure display in full direction, instead of the display mode with discrete 3D images. The authors build a model of imaging processing unit – square column to realize the 3D visualization, specifically for acoustical imaging.

Within mechanical scanning region, as the acoustic lens moved along  $x$  or  $y$  direction, the focused probe beam excites the specimen along a series of excitation points – point A, B, C and D ... over the specimen front surface. See the Fig. 4. The scanning points create a series of parallel tracks over the surface of specimen. The minimal scanning region is limited within a square grid with the four incident points on the surface of the object. The focused probe beam excites the incident point on the front surface. The spatial distances between these four incident points are  $\Delta x$  or  $\Delta y$ , which are determined by the mechanical scanning precision in two directions. The projections of the incident points A, B, C and D form a square column with four vertical edges -  $E_{i,j}$ ,  $E_{i+1,j}$ ,  $E_{i,j+1}$  and  $E_{i+1,j+1}$  hidden in the bulk specimen. The vertical edge is wave propagation trajectories, along which the focused probe beam penetrates through and goes back in this minimal local region. Digitalization of echo signal pattern satisfies the demand, to build a square column as a manipulation data unit, which is for constructing 3D image of the real internal structures in full direction using isosurface technique.

### 3. Methods and Results

Standard isosurface display technique visualizes any structures with various complex shapes, by a way to march through each cube (grid) in turn from the volume data, and to generate a triangulated approximation of the isosurface in each cube [9]. For isosurface display technique, a collection of P is defined to describe the spatial point in volume database, as shown in equation (1):

$$P = (x_i, y_j, z_k), i = 0, 1, \dots, m-1; j = 0, 1, \dots, n-1; k = 0, 1, \dots, s-1 \quad (1)$$

The pair of symbol  $x$ ,  $y$  and  $z$  is the spatial position located at coordinate  $(i, j, k)$ , the scale value of this position is used for 3D display in the bulk.

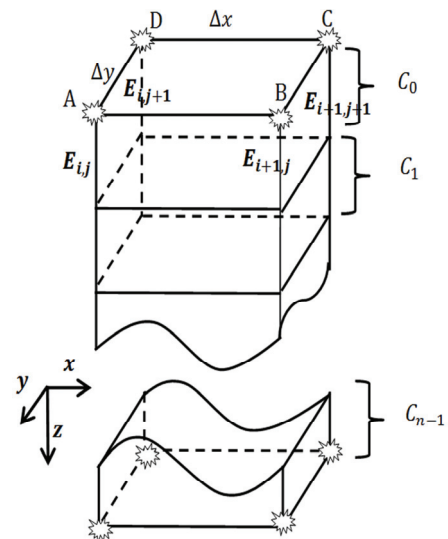


Fig.4. The scanning tracks along A-B and D-C in a minimal scanning region, and the model of a square column.

The model of square column is such a transitional framework, which meets the demand of isosurface display technique specifically for acoustical imaging. According to the physical structure of square column in Fig.4 – a minimal scanning region of SAM, The authors defined this square column in equation (2):

$$C_k = (x_i, y_j, t_k), i = 0, 1, \dots, m-1; j = 0, 1, \dots, n-1; k = 0, 1, \dots, s-1 \quad (2)$$

As the scanning position located at coordinate  $(i, j)$  over the object, symbol  $t$  is the temporal axis of

echo signal pattern; variant  $k$  is the sampling serial number in echo signal pattern of the square column. The label  $C_k$  refers an imaging cube in a square column with the section serial number  $k$ . Based on the model of square column and the needs of isosurface rendering technique, there are three steps to realize 3D imaging for the application of scanning acoustic microscopy.

### 3.1. Build all Square Columns from Volume Database

The first is to build all square columns from vast digital volume database. As the acoustic lens marched over the object, the variant of signal amplitude change along with the independent variant  $t$  of the echo signal pattern. The digital data of echo signal pattern is saved for the bulk information as a basic set, involving all ultrasound signals reflected

from all boundaries (interfaces) of the bulk material. See the picture a) – d) of Fig. 5.

The parallel scanning traces of acoustic lens form a series of slices. Logically it produces a series of square columns, coincided with the framework of the model in Fig. 4. Two adjacent scanning points (point A and B) along one scanning track are neighbor with another two points (point D and C) in an adjacent track. These four scanning points form a local scanning region with a pair of coordinates  $x$  and  $y$  for imaging position. According to four excitation point – A, B, C and D, search four adjacent sets of echo signal pattern from the bulk database synchronously, and build all individual square columns along the scanning track of the lens. The picture e) of Fig. 5 is one section of this square column. Physically, the echo signal pattern with the symbol A-A', B-B', C-C' and D-D' in the picture a) – d) corresponds to four edges of a cube in the picture e) of Fig. 5 individually.

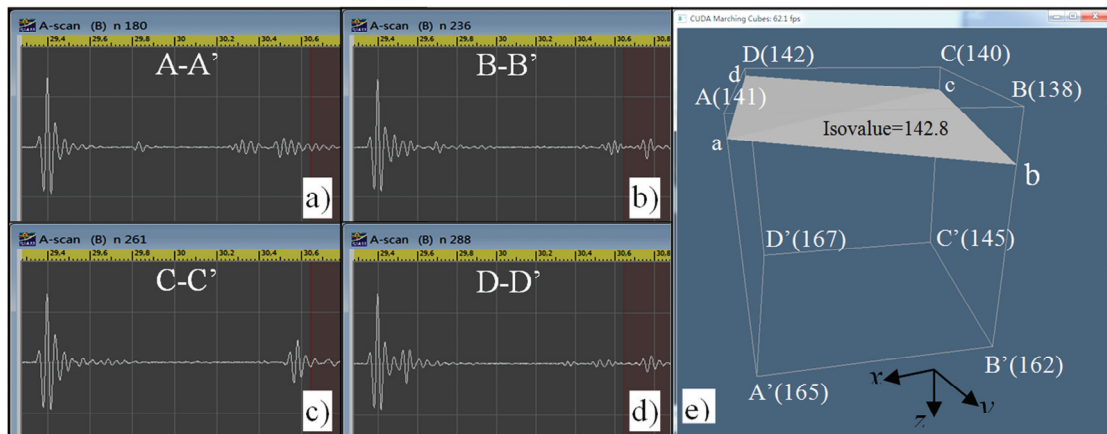


Fig. 5. Synchronistical digital signal in four sets of echo signal pattern of a square column and an imaging cube – P (140, 10, 50), and a local boundary inside the cube.

### 3.2. Build all Cubes in Every Square Column

The temporal axis of echo signal pattern coincide with the  $z$  direction of the square column, provides the potential to mapping reconstruction along  $z$  direction of the bulk. Extract synchronistical digital data from four sets of echo signal patterns to build an imaging cube. The picture a) – d) of Fig. 5 is extracted individually from the bulk database, according to four excitation positions – point A, B, C and D in Fig. 4.

The framework of square column and the equation (2) gives the infer to divide the square column into a series of cubes, in which choosing four neighbor points from one slice and another four neighbor points from the next adjacent slice. The group of eight points is convenient logical block to divide the square column, according to the variant  $t$  of temporal axis of echo signal pattern. The spatial

position is located at coordinate  $(i, j)$  over the object, and the label  $C_k$  is an imaging cube in a square column with the section serial number  $k$ . According to the equation (2), a series of cubes are blocked out with the front plane obtained at time  $t_k$ , and basal plane at time  $t_{k+1}$ .

The picture e) in Fig. 5 gives an experimental example – an imaging cube extracted from a square column, whose position is located at  $P(140, 10)$ . The pair coordinates of eight vertices points of the cube – couple of point A, B, C and D is located individually at the position  $P(140, 10)$ ,  $P(141, 10)$ ,  $P(141, 11)$  and  $P(140, 11)$ . The distance between these four vertices is variant  $\Delta x$  or  $\Delta y$ , which is the scanning step along  $x$  and  $y$  direction determined by the scanning precision of mechanical system. Its spatial position is 140 steps in  $x$  direction and 10 steps in  $y$

direction. The vertical position in  $z$  direction is determined by the sequence of sampling time. The cube in Fig.5 is located between  $t_{50}$  (100 ns, 50th sampling point) and  $t_{51}$  (102 ns, 51<sup>th</sup> sampling point) in the square column (the sampling frequency of ADC is 500 MHz).

### 3.3. Boundary Reconstruction in Every Cube by Isosurface

Each scanning spatial position  $P$  has its own scalar value, determined by the signals intensity from the acoustical interaction between internal boundaries and the focused probe beam. The scalar value of the cube vertices in the picture e) of Fig. 5, are used for presetting an isovalue to calculate the isosurface inside this cube. Full direction reconstruction in this local region is obtained by rendering the triangles inside this cube with a constant – isovalue. The surface-edge intersections are calculated, which are used as the triangle vertices in the cube, via linear interpolation at each edge by comparing the eight intensity value of the cube vertices with this isovalue. The isosurface is built as some triangles in the cube, which is an approximate micro appearance (surface) of the boundary in this local spatial region.

The picture e) shows the isosurface (a boundary) in this cube as the isovalue is 142.80. The isosurface

– triangle vertex in this cube is constructed with the four vertices –  $a$ ,  $b$ ,  $c$  and  $d$ . The same procedure is repeated to construct boundaries in every cube continuously and individually, by replacing the value  $t_k$  with  $t_{k+1}$  along the square column, and by moving the sequence of point A, B, C and D to an adjacent square column.

By extension, the system can get all internal boundary spatial distribution in each square column by constructing each cube. This square column only corresponds to one scanning point with the position  $x$  and  $y$  – a local region of bulk object.

Point by point and track by track in turn as scanning system marching, all adjacent square column units are constructed along the scanning direction. As the result, all internal structures and the spatial distributions in full direction are obtained and displayed in the 3D image – the picture c) in Fig. 6. There are many individual structures (defects, inclusions or voids) with various appearances, distributed below the surface of bulk specimen.

Some structures expand along some directions, presenting a belted distribution inside the bulk marked by a pointed arrow. The picture also presents various complex appearances of structure at subsurface. The 3D results provide an overall and intuitive view than the discrete 3D visualization with a series of B-Scan image slices as Fig. 3.

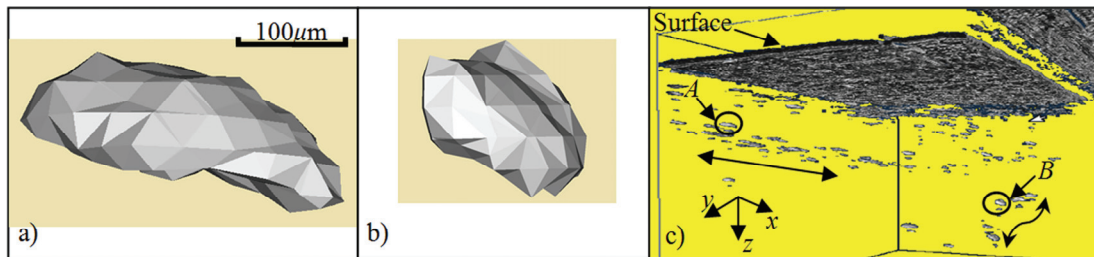


**Fig. 6.** a) 3D construction result of an internal structure marked by symbol A; b) 3D construction result of an internal structure B; c) 3D overall review of a BN bulk specimen in full direction.

The picture a) and b) of Fig. 6, which are a magnified micro-sized structure with a ragged margin boundary embedded in bulk specimen. This local internal microstructures marked by the symbol A in bulk specimen is completely reconstructed with 4,500 pieces of cubes ( $\Delta i = 15$ ,  $\Delta j = 20$  and  $\Delta k = 15$ ) in full direction, with length is 0.308 mm, width is 0.231 mm, height is 0.091 mm, and its depth is 0.171 mm in the bulk. The structure in the picture b) marked by the symbol B is constructed by 1,125 cubes ( $\Delta i = 15$ ,  $\Delta j = 5$  and  $\Delta k = 15$ ), with length is 0.077 mm, width is 0.231 mm, height is 0.091 mm, and its depth is 0.303 mm in the bulk.

Reflected intensive ultrasound signals produce a strong contrast for boundary imaging; and the arbitrary signals are ignored to take part in the imaging process through isosurface display

technique, presenting a transparent display in the cube.

## 4. Discussion

For the application of SAM, the difference and the relation between spatial and temporal domain should be taken into account. All data of echo signal pattern used for time-resolved technique, is based on the variation response distributed along the temporal axis. The variant  $t$  of temporal axis of echo signal pattern is the indication to divide the square column into a series of cubes for 3D reconstruction.

Thus, based on the concept of isosurface technique and square column, for the spatial distribution specifically for SAM, an improved

collection  $P$  is proposed as the equation (3) to instead of the equation (1) and (2):

$$P = (x_i, y_j, C_k), i = 0, 1, \dots, m-1; j = 0, 1, \dots, n-1; k = 0, 1, \dots, s-1 \quad (3)$$

In the equation (3) and the structure in Fig. 4, the pair of  $x$  and  $y$  is the scanning direction, coordinate  $(i, j)$  is the scanning position over the object, the label  $C_k$  refers an imaging block (cube) in a square column with the section serial number  $k$ . The variant  $t$  is a unique reference to divide the square column into a series of basic imaging unit – cube. Digital ultrasound signals of the echo signal pattern just satisfy the condition to block out these imaging cubes from the square column, by counting the sampling time interval of data converter. At each scanning position, the spatial point along the paraxial beam has its own scalar value with various signals intensity reflected from internal microstructures. Therefore, the spatial variant  $z$  is indirectly transformed from the temporal variant  $t$  of echo signal pattern.

Technically, all digital data of square column (echo signal pattern) are obtained discretely at the node of sampling time. There is no any signal converted in the blind of sampling interval of system. However, the natural spatial distributions of internal structures are expanded continuously in the bulk, with an irregular shape included in a micro-sized cube in full direction, not only limited on eight vertices of the cube. Hence, it is necessary to infill the continuous distributions of internal structures into all space of the cube, by employing isosurface display technique. It is significant to reconstruct the boundary of a structure among the space of this micro-sized imaging cube, to infill the continuous elements of the structure or its continuous varieties in the midst of eight vertices of the cube. Meanwhile, it is possible to simulate it by trilinear interpolation using eight known vertices data of the cube.

## 5. Conclusion

Digitalization of ultrasound signal provides the chance to save echo signal patterns into a database for huge data storage of a 3D visualization. The authors propose a model – square column, which is used to organize volume data for 3D acoustical imaging. The square column consists of four sets of digital echo signal pattern, and is used to construct a series of imaging cubes. The cube is a basic processing unit and derived from the square column by the sampling time interval of system. Based on it and isosurface technique, the local micro boundary is depicted to fill the space of the cube with the triangles, obtained by calculating the isovalue from the signal intensity of eight vertices in the cube. All elements appearance and distributions in full direction are depicted by the construction of all cubes

in all square columns. Intensive signal reflected from the boundary of internal structure in the bulk takes part in the triangle construction in the bulk. The uniform material in the bulk provides a transparent display in bulk imaging, for an arbitrary signal – background noise is absent to the boundary construction. These two facts let the real internal microstructures behind (through) non-transparent material can be displayed in 3D image. The experiment result shows that 3D acoustic image provides an overall view, continuous spectacle to investigate internal microstructures for bulk material than 2D imaging. It provides the information of the position, sizes and the appearance of internal structures (voids, inclusions and defects) with complex shapes, and the distribution and tendency of these internal structures in bulk specimen. Based on the model of square column and isosurface display techniques, 3D acoustical imaging is a practical visualization tool for scanning acoustic microscopy to investigate small scale, non-transparent bulk specimen in NDT/E field.

## Acknowledgements

This work was supported by the National Natural Science Foundation of China under Grant No. 61271403 and Grant No. 10932010/A0204.

## References

- [1]. R. A. Lemons, C. F. Quate, Acoustic microscopy – scanning version, *Applied Physics Letter*, Vol. 24, Issue 4, 1974, pp. 163-166.
- [2]. G. S. Kino, Acoustic waves: devices, imaging and analog signal processing, *Prentice-Hall*, Englewood Cliffs, New Jersey, 1987.
- [3]. A. Briggs, Acoustic microscopy, *Clarendon Press*, Oxford, 1992.
- [4]. J. G. Harris, Edge diffraction of a compressional beam, *Journal Acoustical Society America*, Vol. 82, Issue 2, 1987, pp. 635-646.
- [5]. J. W. Ding, V. M. Levin, Y. S. Petronyuk, Edge diffraction phenomena in high-resolution acoustical imaging, *Acoustical Imaging*, Vol. 31, 2012, pp. 299-312.
- [6]. S. L. Rumyantsev, M. E. Levinshtein, A. D. Jackson, S. N. Mohammad, G. L. Harris, M. G. Spencer, M. S. Shur, Properties of advanced semiconductor materials GaN, AlN, InN, BN, SiC, SiGe, Eds. M. E. Levinshtein, S. L. Rumyantsev, M. S. Shur, *John Wiley & Sons, Inc.*, New York, 2001, pp. 67-92.
- [7]. A. Bosak, J. Serrano, M. Krisch, Elasticity of hexagonal boron nitride. Inelastic x-ray scattering measurements, *Phys. Rev. B*, Vol. 73, 2006, pp. 041402.
- [8]. P. V. Zinin, O. V. Kolosov, O. I. Lobkis, K. I. Maslov, Imaging of spherical objects in a reflecting acoustic microscope, *Acoustical Physics*, Vol. 39, Issue 4, 1993, pp. 343-346.
- [9]. W. E. Lorensen, H. E. Cline, Marching cubes: A high resolution 3D surface construction algorithm,

- SIGGRAPH Computer Graphics, Vol. 21, Issue 4, 1987, pp. 163-169.
- [10]. M. Levoy, Display of surfaces from volume data, *IEEE Computer Graphics and Applications*, Vol. 8, Issue 3, 1988, pp. 29-37.
- [11]. J. Wilhelms, A. van Gelder, Topological considerations in isosurface generation – extended abstract, *Computers Graphics*, Vol. 4, Issue 5, 1990, pp. 79-86.
- [12]. Gunnar Johansson and Carr Hamish, Accelerating marching cubes with graphics hardware, in *Proceedings of the Conference of the Center for Advanced Studies on Collaborative Research CASCON'06*, ACM Press, NY, USA, 2006, p. 39.

---

2013 Copyright ©, International Frequency Sensor Association (IFSA). All rights reserved.  
(<http://www.sensorsportal.com>)



## Handbook of Laboratory Measurements and Instrumentation

Maria Teresa Restivo  
Fernando Gomes de Almeida  
Maria de Fátima Chouzal  
Joaquim Gabriel Mendes  
António Mendes Lopes

The Handbook of Laboratory Measurements and Instrumentation presents experimental and laboratory activities with an approach as close as possible to reality, even offering remote access to experiments, providing to the reader an excellent tool for learning laboratory techniques and methodologies. Book includes dozens videos, animations and simulations following each of chapters. It makes the title very valued and different from existing books on measurements and instrumentation.

  
International Frequency Sensor Association Publishing

Order online:  
[http://www.sensorsportal.com/HTML/BOOKSTORE/Handbook\\_of\\_Measurements.htm](http://www.sensorsportal.com/HTML/BOOKSTORE/Handbook_of_Measurements.htm)

## Design and Simulation of Two Stage Pressure-controlling Anti-overflow Breathing Valve in Tanker

<sup>1</sup>Yonggang Zuo, <sup>1</sup>Zhuxin Li, <sup>1</sup>Jun Chen, <sup>2</sup>Jing Yang, <sup>1</sup>Zhen Zhang

<sup>1</sup>Department of Petroleum Supply Engineering, Logistic Engineering University,  
Chongqing, China, 401311

<sup>2</sup>Department of mechanical and electrical Engineering, Logistic Engineering University,  
Chongqing, China, 401311  
Tel.: 13996388046  
E-mail: zyg938@163.com

Received: 6 July 2013 / Accepted: 25 August 2013 / Published: 30 September 2013

---

**Abstract:** The effect of breathing and anti-overflow of the breathing valve mounted on petroleum tank have great influences on the safety of the whole truck. This paper designs one kind of new two stage pressure-controlling anti-overflow breathing valve. The 3D model of the breathing valve is built in Pro/E, and the kinetics analysis of the key point of the breathing valve is done in ADAMS, which can provide theoretic guidance for designer to optimize structural design. Copyright © 2013 IFSA.

**Keywords:** Breathing valve, Anti-overflow, Simulation.

---

### 1. Introduction

The functions of the breathing valve are as below [1]: the first is inhaling or discharging air to insure the pressure in safe range when the liquid level in the petroleum truck changes, the second is preventing the oil gases or other poisonous gases from diffusing in the air, the third is insulating the flame and the medium in petroleum tank on condition of occasional fire, decreasing the pressure caused by the ascending temperature to prevent explosion. The spring type breathing valve (shown in Fig. 1) or steel ball type breathing valve (shown in Fig. 2) mounted on petroleum tank only has function of breathing but cannot prevent petroleum spillover from tanker, normal anti-overflow breathing valve (shown in Fig. 3) can prevent petroleum spillover while petroleum truck tanker tilt by means of closing the channel of the breathing valve, but the breathing

valve cannot breathe simultaneously. With these breathing valves, petroleum is easy to spill when the truck mounting petroleum tank is bumping on the load and it is dangerous [2-5]. To solve this problem, a new two stage pressure-controlling spill-protecting breathing valve is designed in this article, this breathing valve can protect the oil from spillover while the petroleum tanker tilt forward or backward, the left or the right, bump or turn on rough road. And the valve can breathe simultaneously to control the pressure in the oil can to guarantee the security.

### 2. Structural Design

The structure of two stage pressure-controlling anti-overflow breathing valve is shown in Fig. 4. It is composed of breathing valve body, exhaust valve spring, inlet valve spring, etc. It has function of

protecting spillover and two stage breathing. The principle of the first stage breathing is when the petroleum tanker is refueled (or the temperature increase), the pressure increase, when the pressure difference between the air in the petroleum tank and the air out of the petroleum tank is greater than 6 – 8 kPa, the pressure in the petroleum tank overcome the spring force of the exhaust valve, jack up the breathing valve plate and the exhaust valve

core, discharge the gas. When the petroleum is drawn out of the petroleum tank (or the temperature decrease), the pressure decrease, when the pressure difference between the air out of the petroleum tank and the air in the petroleum tank is greater than 2 - 3 kPa, the atmospheric pressure overcome the spring force of the inlet valve and open the breathing valve plate downward to draw in the air.

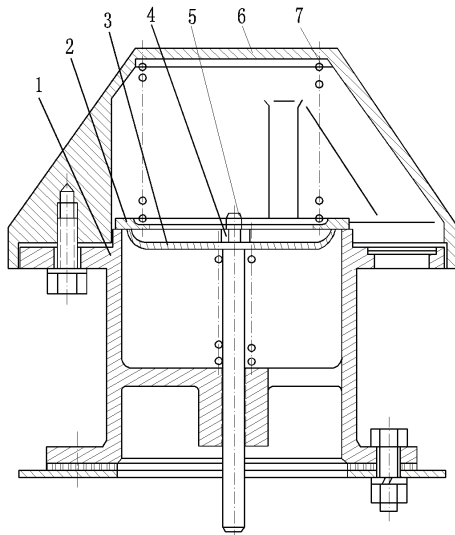


**Fig. 1.** Spring type breathing valve.

1. Valve body, 2. Upper valve plate, 3. Lower valve plate,
4. Inlet spring, 5. Valve bar, 6. Safeguard cover,
7. Outlet spring.

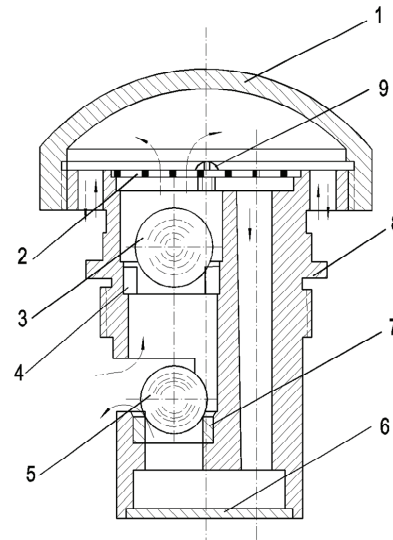


**Fig. 2.** Steel ball type spring breathing valve.

1. Valve body, 2. Filter board, 3. Outlet steel ball,
4. Press valve seat, 5. Inlet steel ball, 6. Bottom plate,
7. Inlet valve seat, 8. Valve body, 9. Bolt .

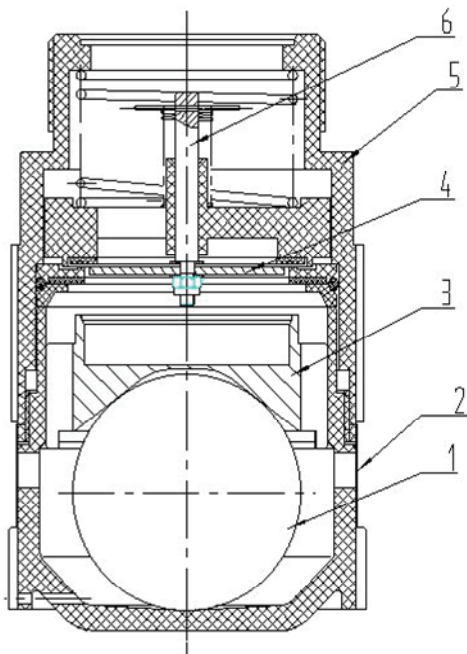


**Fig. 3.** Anti-overflow type breathing valve.

1. Ball body, 2. Anti-fire net, 3. Tilting valve plate, 4. Press
- valve seat, 5. Valve body, 6. Valve bar.

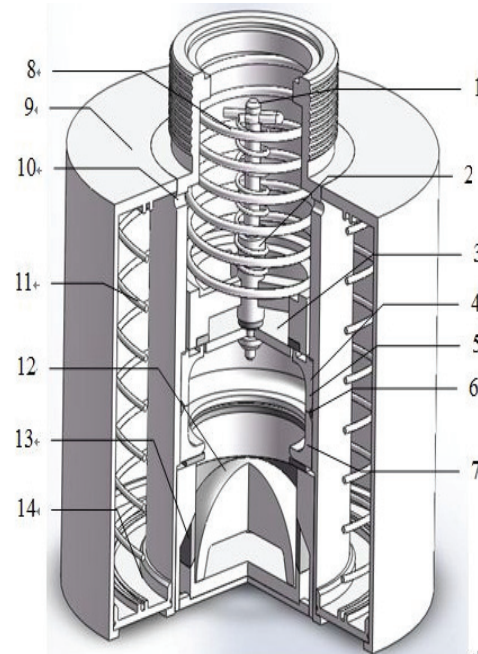


**Fig. 4.** Two stage pressure control anti-overflow breathing valve structure.

1. Valve bar, 2. The intake valve spring, 3. Breathing valve plate, 4. Upper valve seat, 5. "O" type ring, 6. Lower valve
- seat, 7. Sealing gasket, 8. Exhaust valve spring, 9. Valve body, 10. Air outlet, 11. Plate spring, 12. Sealing hemisphere, 13. Fire resistance, 14. Bottom plate.

The first stage anti-overflow principle of the breathing valve (shown in Fig. 5) is when the tanker drive in the steep slope or uneven off-road conditions, tanker tilt in a certain angle, the sealing hemisphere rotates, its sealing surface seal lower valve seat, shutting off first stage breathing ventilator, so petroleum cannot overflow out of tanker.

The second stage breathing principle (shown in Fig. 6) is when the sealing hemisphere seal lower valve seat, the first level of respiratory ventilator is

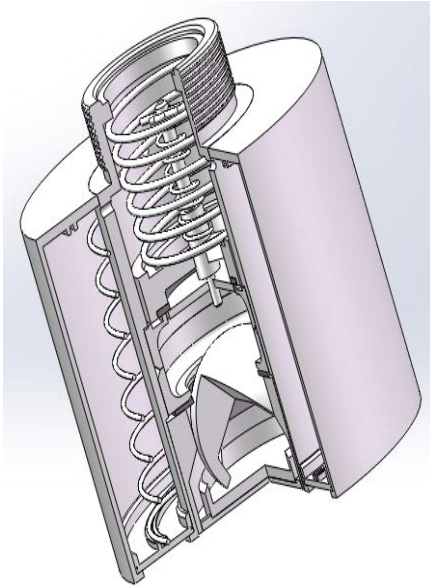


Fig. 5. The first stage anti-overflow breathing principle structure.

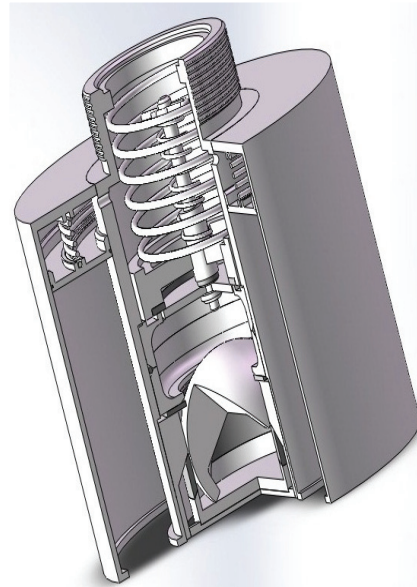


Fig. 6. The second stage anti-overflow breathing principle structure.

### 3. Analysis

In order to explain the influence of the vary amplitude of temperature and vary time on the breathing flow, two heat power course are used to simulate the process of the petroleum tank discharging gas while temperature is rising. The first course is with constant volume but rising temperature. Suppose that the initial pressure in the petroleum tank is critical air suction pressure  $P_1$ , the initial temperature is  $T_1$ , close the petroleum tank, the temperature ascend to  $T_2$  and the pressure is  $P_2$ , the constant volume course has the function (1).

$$P_2 = P_1 \frac{T_2}{T_1} \quad (1)$$

The second course is with constant temperature but volume expansion. The pressure in the petroleum tank is  $P_2$  after the first course, suppose that the petroleum tank volume expand and the pressure lower to critical discharge pressure  $P_3$ . The initial volume of the petroleum tank is  $V_1$ , the volume after expansion is  $V_3$ , the constant temperature expansion course has the function (2).

closed. When pressure in the tank rises to 8 kPa higher than the outside atmospheric pressure, the bottom plate overcome spring pressure and gradually rise, the air in the outer cavity of the breathing valve is expelled out of tank through the second stage air outlet and the first stage breathing channel, and then petroleum flows into the bottom of the cavity space, thereby increasing the available space in the tank to reduce the pressure in the tank.

$$V_3 = V_1 \frac{P_2}{P_3} \quad (2)$$

According to function (1) and function (2), we have:

$$V_3 = K \frac{T_2}{T_1} V_1, \quad (3)$$

where K is the ratio of breathing pressure,

$$K = P_1 / P_3.$$

The whole intake air volume of the petroleum tank with temperature ascending from  $T_1$  to  $T_2$  is:

$$\Delta V = V_3 - V_1 = V_1 \left( K \frac{T_2}{T_1} - 1 \right) \quad (4)$$

From function (4) we can see that when  $\frac{T_2}{T_1} = \frac{1}{K}$ ,  $\Delta V = 0$ . So the pressure in the petroleum tank varies from  $P_1$  to  $P_2$  while the temperature ascended, the petroleum tank shouldn't

discharge air, if the temperature has risen greatly and  $\frac{T_2}{T_1} > \frac{1}{K}$ , the petroleum tank should discharge air.

The higher the temperature rose, the more gas should be discharged.

When the petroleum tanker with full petroleum stop on the slope road or turn over, the petroleum tank with normal breathing valve will spill, the petroleum tank with spill-protecting breathing valve will close the petroleum tank to prevent petroleum from spillover, if the atmospheric temperature rise, the pressure in the petroleum tank should increase and cause risk. The atmospheric temperature vary is usually 20<sup>l</sup> from day to night. Suppose that the temperature of the air in the petroleum tank rise from 20□ to 40□, the volume of petroleum tank is 4000L, the top volume of air is about 200L, when the temperature rise, the whole volume of gas space discharged is:

$$\Delta V = V_1(K \frac{T_2}{T_1} - 1) = 300 \times (0.992 \times \frac{273+40}{273+20} - 1) = 11.94L$$

#### 4. Simulation

The 3D model of two stage pressure-controlling anti-overflow breathing valve is built in Pro/E, the assembling model is saved as paraboloid (.x\_t) type, and is imported in ADMAMS (shown in Fig. 7).

The material is chosen as carbon steel. A glide pair is built between the valve bar and the bottom plate, two spring dampers are built between the bottom plate and the top of the valve body, the stiffness of the spring is 1.8 Newton/mm, the damper coefficient is 3.1 Newton-sec/mm. 287.83 Newton is exerted on the bottom plate along the valve bar which simulates the force operating on the bottom plate. Associate simulation parameters are set and the simulation is done on the bottom plate MARKER\_49, MARKER\_53 and MARKER\_55, the results of

kinematics and dynamics simulation are shown in Fig. 8 - Fig. 10.

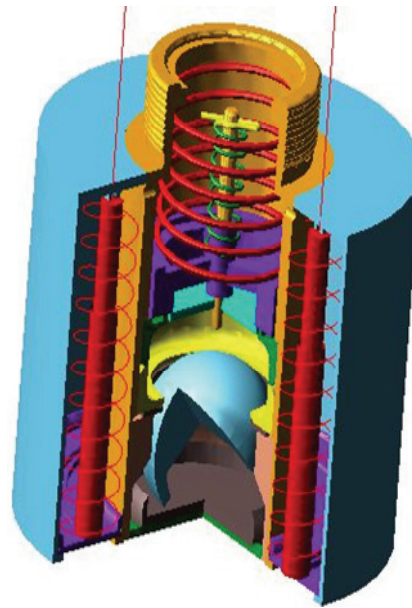


Fig. 7. ADMAMS model of the breathing valve.

#### 5. Conclusions

We can see from the above simulation results, when the tanker drive in the steep slope or uneven off-road conditions, causing tank tilting in a certain angle, the sealing hemisphere rotate and close first respiratory passage, when the tank pressure continues to rise to 8 KPa higher than the external pressure, the bottom plate overcome spring pressure and gradually rise, the air in the outer cavity of the breathing valve is expelled out of tank through the second stage air outlet and the first stage breathing channel, and then petroleum flows into the bottom of the cavity space, thereby increasing the available space in the tank to reduce the pressure in the tank.

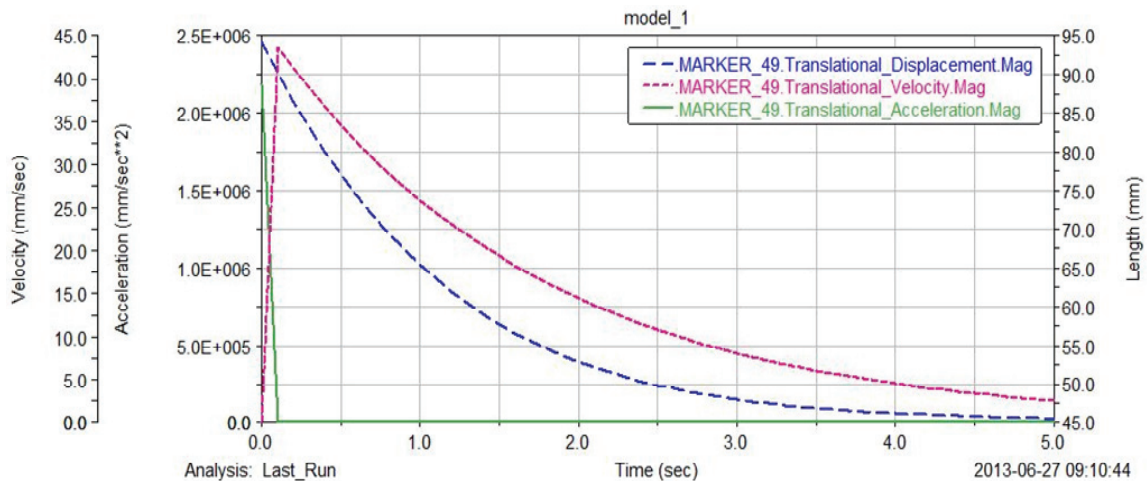


Fig. 8. Displacement, velocity and acceleration curve of the point Marker\_49.

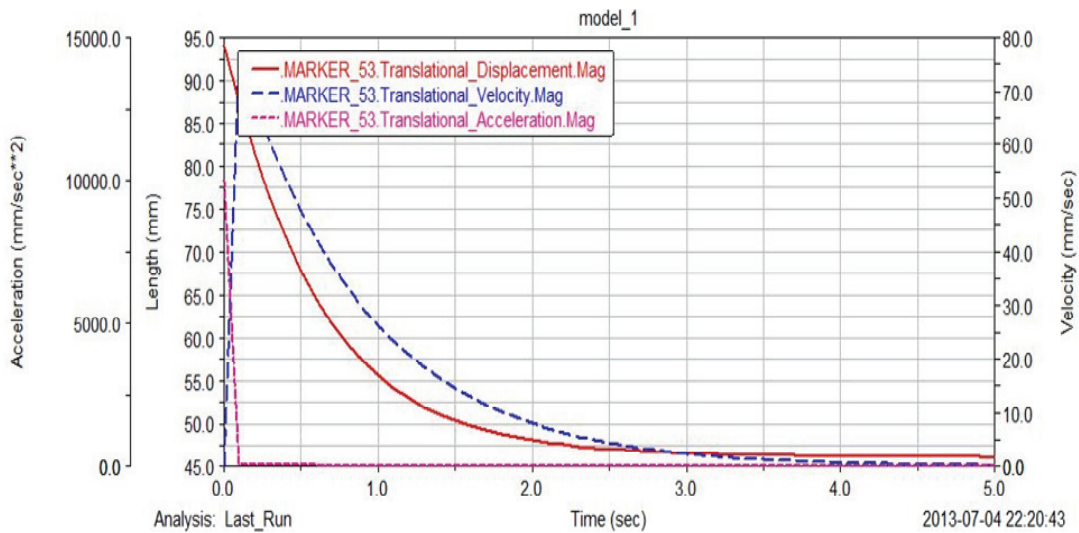


Fig. 9. Displacement, velocity and acceleration curve of the point Marker\_53.

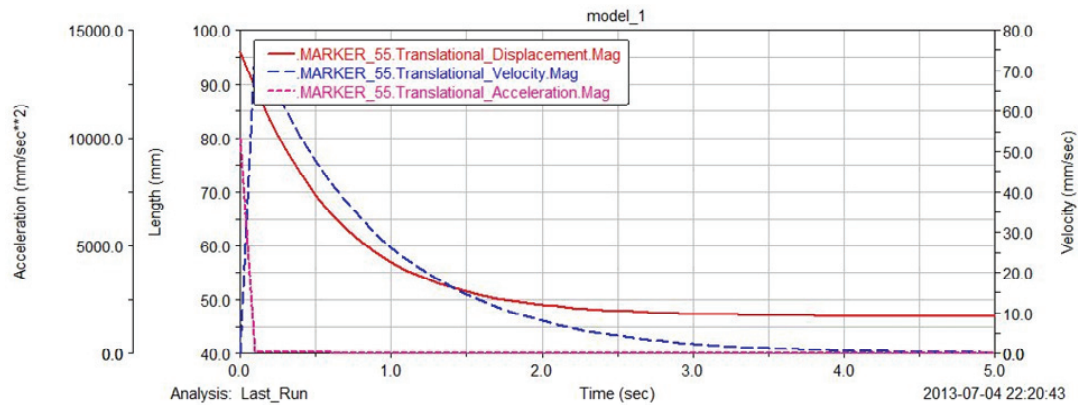


Fig. 10. Displacement, velocity and acceleration curve of the point Marker\_55.

The distance that bottom plate move is about 75 mm, because the cross-sectional area of valve body cavity is 267 mm<sup>2</sup>, so the volume of the exhausted gas from second stage breathing outlet for 12.84 L. It is more than theoretical exhaust total value 11.94 L, meeting the design requirement. So the design of two stage pressure-controlling anti-overflow breathing valve is accurate and effective.

## References

- [1]. API-2000 Venting Atmospheric and Low-Pressure Storage Tanks, *US Standard*, USA, Washington, 1998.
- [2]. Using ADAMS/Solver, *Mechanical Dynamics Inc*, 2002.
- [3]. Zeng Gang Li, Introduction and Example of ADAMS, *National Defense Industry Press*, 2006, pp. 96-99.
- [4]. Yu Qing, Cao Yuanwen, Vehicle Dynamic Loads Caused by the Road Roughness, *Journal of Chongqing Jiaotong University*, Vol. 22, 2003, pp. 32-34.
- [5]. Tong Wei, Guo Kong-Hui, Huang Xiang-Dong, Simulation research on handling and stability of global-coupled torsion-eliminated suspension, *Machine Tool & Hydraulics*, Vol. 36, 2008, pp. 137-138.

## Research on Key Technology of Cloud Design for Mechanical Equipment

<sup>1,2</sup> Jun Chen, <sup>1</sup> Gang Guo, <sup>2</sup> Yonggang Zuo

<sup>1</sup> College of Mechanical Engineering, Chongqing University, Chongqing, 400030, China

<sup>2</sup> Department of Petroleum Supply Engineering, Logistic Engineering University, Chongqing, 401311, China

<sup>1</sup> Tel.: 13983455823, fax: 023-86731148

E-mail: chenjun657@163.com, zyg938@163.com

*Received: 4 July 2013 / Accepted: 25 August 2013 / Published: 30 September 2013*

---

**Abstract:** In order to carry out rapid response of design of products, aimed at problems existed in realm cooperation during the design process of mechanical equipment, this paper proposes design mode of mechanical equipment based on cloud environment, implementation method of cloudy domain analysis on design demand and mapping technology, serial expand strategy on discrete design resource and strategy integrated design task with resource in time, it can implement reasonable allocation and delivery in the resource demand domain DR, the state control domain T and feasible resource domain R. Correctness and feasibility of model and method is analyzed and verified with examples. *Copyright © 2013 IFSA.*

**Keywords:** Mechanical equipment, Cloud design, Mapping.

---

### 1. Introduction

The characteristic of mechanical equipment is usually including specialization, complex structure, high performance requirement, multidisciplinary integrated technology, complex manufacturing process, etc. Its organization form is mostly stage dynamic alliance. Converse option to high – quality resource is usually lost with multiple rigid constraints and incomplete information when Core research entities develop mechanical equipment. In recent years many scholars have conducted many research in the field of cloud design and manufacturing, Reference [1-4] analyze typical characteristics and key technology of cloud manufacturing, study the manufacturing resources optimization deployment in cloud manufacturing environment, etc. The present study mostly concentrated in manufacturing resources with explicit characteristic and ability assessment etc. Design of key business processes for

manufacturing industry is an important support and cloud manufacturing precursor. Its knowledge attribute has decided to design concept, design principles design experience with the strong implicit feature, the corresponding research is insufficient. Aiming at the design of emergency equipment products, the design model and related key technical problems in design is solved using the cloud environment as the basis to achieve fast response.

### 2. Cloud Design Mode of Mechanical Equipment

Cloud design mode of mechanical equipment is different from traditional products design mode, because of the use of virtualization technology, what the user can use is no longer a single physical resources about the resource scheduling and sharing, design environment containing design knowledge,

technique and ability is obtained mostly by VMware / Xen/Citrix virtualization platform in some physical resource construction, its characteristics is highly complex, dynamic, uncertain, etc. In the collaborative design process, there are manufacturing mode of group organization regional cloud and private cloud product design characteristics, the mixed cloud characteristics of the industry chain department or enterprise collaborative innovation and public cloud and professional cloud feature model,

government cloud mode of the administrative resources. Its characteristic is obvious cloudy domain interaction, mapping and integration etc. Therefore, this paper puts forward emergency equipment product design mode which contain analysis and mapping in the demand of cloud environment, serialization integrating discrete design resource and induced chain drive demand lead by design demand shown in Fig. 1.

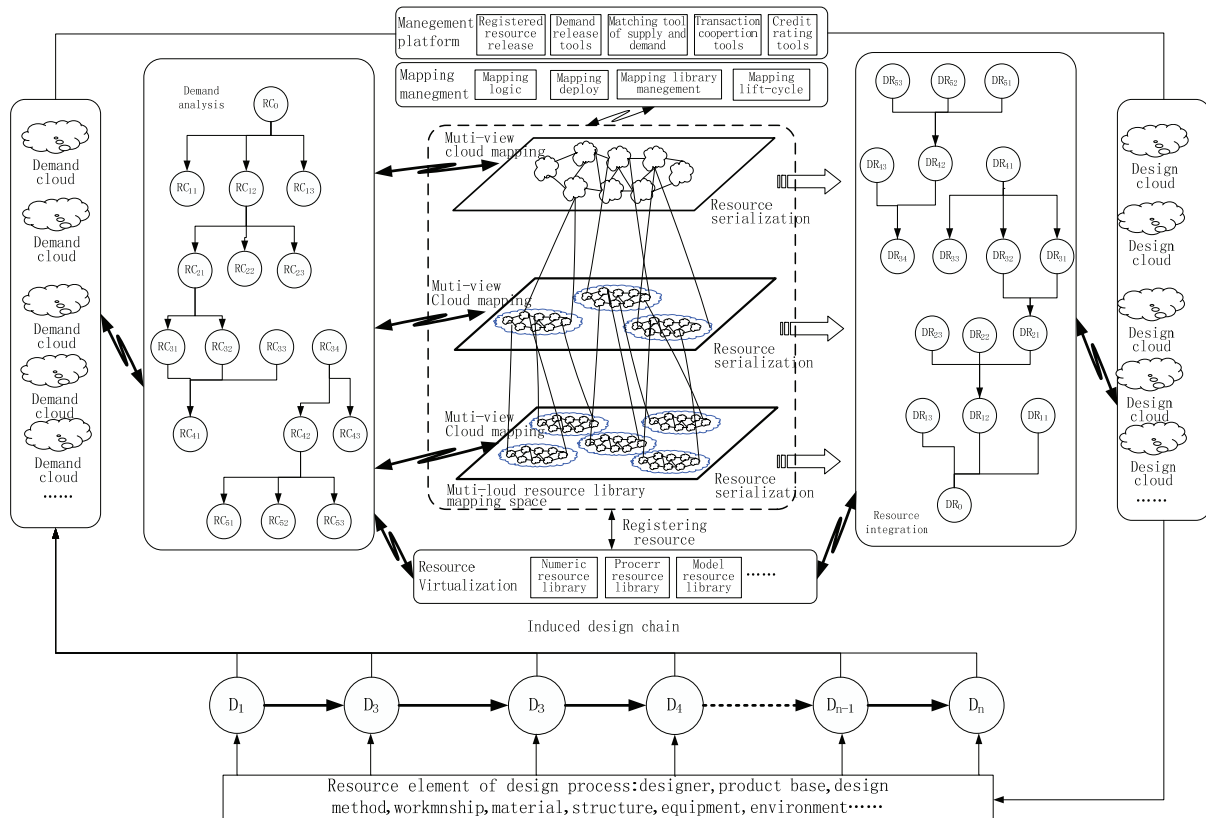


Fig. 1. Cloud design pattern of product for mechanical equipment.

The basic strategy of this model is driving design induction chain is the center of the core entity or the host factory, cloudy domain resource access based on the expression of different views and mapping of product design can spread out quickly own information and resource demand, When the cloud environment product is observed and analyzed in their point of view, the structure is more objective, more precisely, the circulation of information is more convenient, interactive resources is more symmetrical, decision-making errors and unstable factors is relatively reduced, design risk is greatly reduced. Design patterns by using serialization extended cloud resource and the collaborative design process is integrated, the configuration and design resources quickly was put forward with the premise using the least management and having minimal interaction with the service provider.

1) Cloudy domain data dependencies is established by analyzing the information of the design demand, loose information is placed in cloud data center domain, forming the demand cloud, so the high cohesion between different information sets and the low coupling and similar information is maintained, the tool is provided and the information is released or pushed through the platform management set;

2) Mapping strategy is scheduled to cloud domain with the biggest data dependence by mapping management, the new data is set into the high correlated data center to form the design cloud by discrete resource serialization;

3) Design resources which drives next design stage by design induced chain is integrated from the design cloud, subsequent design process is recursively affected, design interaction between clouds or in clouds is built, the cloud design mode for cloudy domain is achieved.

### 3. Cloudy Domain Analysis and Mapping Technology

It is necessary for design demand of cloud solution analyze mapping deployment demand, supporting generally public cloud, area cloud and various mixed cloud, on the other hand the case that leading party (demand side) effectively push or release information through the corresponding mapping logic and multi-domain mapping operation to solve the clouds is implemented.

1) Requirements analysis completes the combination and extension of resource requirements by the existing scenarios and domain knowledge and technical background, in the cloud resource pool deriving cloudy domain requirements set. Analytical model of requirement cloud is shown in Fig. 2.

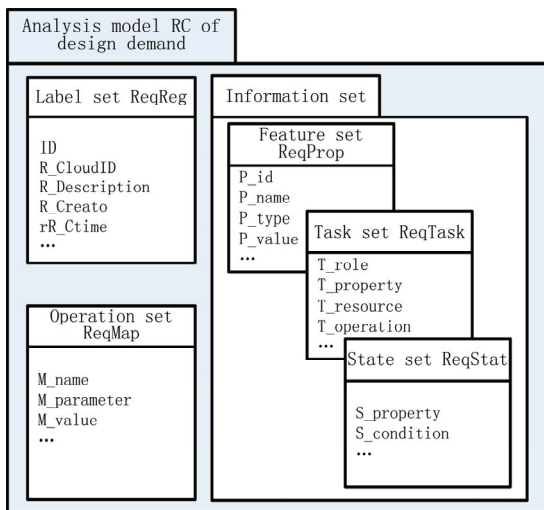


Fig. 2. Analysis model of demand.

Where ReqReg describes the identity property of demand, on behalf of the basic registration information need, ReqMap describes the mapping operation of demand, ReqProp is the demand feature set describing the characteristics property of requirements including functional requirements, structural demand, appearance requirements from customer expectation target and the engineering characteristic parameters, detection index, design technical requirements etc, analysis and processing of the statistical information can also be expressed, ReqTask describes the task set, demand produce many task execution sequence through the analysis and mapping, ReqStat describes the state set of demand, describing a collection of state information on demand, including demand process state, correlation constraints. The formal model of demand cloud is described for quintuple:

$$RC = (ReqReg, ReqMap, ReqProp, ReqTask, ReqStat)$$

$$ReqReg = (ID, R\_CloudID,$$

$$R\_Description, R\_Creator, R\_CTime)$$

$$ReqMap = (M\_name, M\_parameter, M\_value) \quad (1)$$

$$ReqProp = (P\_id, P\_name, P\_type, P\_value)$$

$$ReqTask = ($$

$$T\_role, T\_property, T\_resource, T\_operation)$$

$$ReqStat = (S\_property, S\_condition)$$

ID is the identification of RC, R\_CloudID describes the identification of demand cloud which is the qualitative for demand cloud scope, divided into the public cloud, hybrid cloud, private cloud mapping identifier, R\_Description describes the general demand, R\_Creator is founder of demand, R\_CTime describes the creation time of demand. M\_name is operating name of mapping, M\_parameter is operation parameters of mapping, M\_value is return value of operations. P\_id is characteristics identification of demand, P\_name is feature name, P\_type is type of feature, P\_value is feature or attribute. T\_role describes role set involved in task, T\_property describes attribute set of the task, T\_resource describes resources set executing the task. T\_operation describes the methods set that operate task attributes or resource. S\_property describes the state set in their current attribute, S\_condition is constraint condition set when the state occurs migration.

2) Mapping logic provides a mapping operation on the demand set, completing multi-view structure on the RC model.

Mapping decomposition is operation that one demand is decomposed into several sub one which decomposes mapping with function RC\_decompose (R\_CloudID, {ID, P\_id}), its mapping features is as follows:

The parameter R\_CloudID is the cloud property identification decomposing demand, ID is demand identification, P\_id is signature decomposing demand, after the demand is decomposed sub-demand inherit cloud properties of father-demand, the return value is the list signature of sub-demand {P\_id1, P\_id2, P\_id3, ..., P\_idn}.

3) Aggregation mapping is the mapping operation that aggregates two or more demand into a new demand which is described with function RC\_aggregate (R\_CloudID, {ID1, ID2, ID3, ..., IDn}), its mapping features is as follows:

The parameter R\_CloudID is cloud properties, ID is identification of aggregated demand, feature ReqProp of new demand of RC\_aggregate produced by the polymerization inherits all the features in RC polymerization, and can combine these features into a new feature of its own, the return value of polymerization is the signature of RC\_aggregate.

4) Derived mapping is the operation which expand characteristics of a set of RC ReqProp sion and map as a new demand which is described with function RC\_derive (ID, {P\_id1, P\_id2, ..., P\_idn}), its mapping features is as follows:

The new derived requirements RC\_derive produce new features of its own through a combination, new generation, expansion, in

addition to inherit all the characteristics of the original demand, parameter is the characteristic properties of ID and the expansion of RC {P\_id1, P\_id2,..., P\_idn}, derived return value is ID of RC\_derive.

5) Instance mapping is the operation that use the existing product case directly to solve RC which is described with RC\_instance (ID), its mapping features is as follows:

Instance demand must map RC in the demand system for solution as RC instance, according to the objective demand information content, RC\_instance can use the entity relationship model, object model, the XML document as a physical carrier. The parameter is ID of RC, the return value is ID of RC\_instance.

#### 4. Serialization Integration of Discrete Design Resources

Demand mapping solution not only have levels of granularity because the particle size of information itself is different, but also have complex, dynamic, decentralized and uncertain characteristics because the scene and the environment of cloud properties are different. Serialization integration of discrete design resources on amount of cloud "fragmentation" is basic ways to focus distributed resources and service.

1) Resource definition and description.

Design Resource Cloud, DRC is available information collection composed of discrete knowledge resources, intellectual resources, design tools, design, material, design field, service

resources in various cloud domain, the design resources is divided into knowledge resources, technical resources, design ability, DRC (ResReg[], KnoRes[], TecRes[], SerRes[]), where ResReg[] is the cloud registration information of resources, because the resources are favorable for the clouds and provide product cloud collaborative design service, knowledge resources KnoRes[] contains design principles, design experience, design specifications, design process, and the model of existing products, test and inspection data, market and customer feedback information [9]; technical resources TecRes[] includes software resources, equipment resources, patent resources, technical service; design capacity SerRes[] includes the design qualification, credit grade, intellectual resources, design site, design efficiency etc.

2) Resource Serialization integration strategy.

Design of emergency equipment is generally divided into the design concept, principle, scheme, assembly equipment, key parts according to the task level, and each level design can be divided into the overall design, system design, assembly and parts design, the whole process of product design and the design hierarchy or design stage not only exist resource serialization, but also they are associated with the corresponding integrated real-time design tasks. Task level extends longitudinally, design domain serializes design resources through the mapping with feasible domain of cloud resource, expanding vertically, and design domain and design stage of task level expand horizontally which is mapped to feasible domain of cloud resource and serializes design resources with horizontal expansion, Resource Serialization mode is shown in Fig. 3.

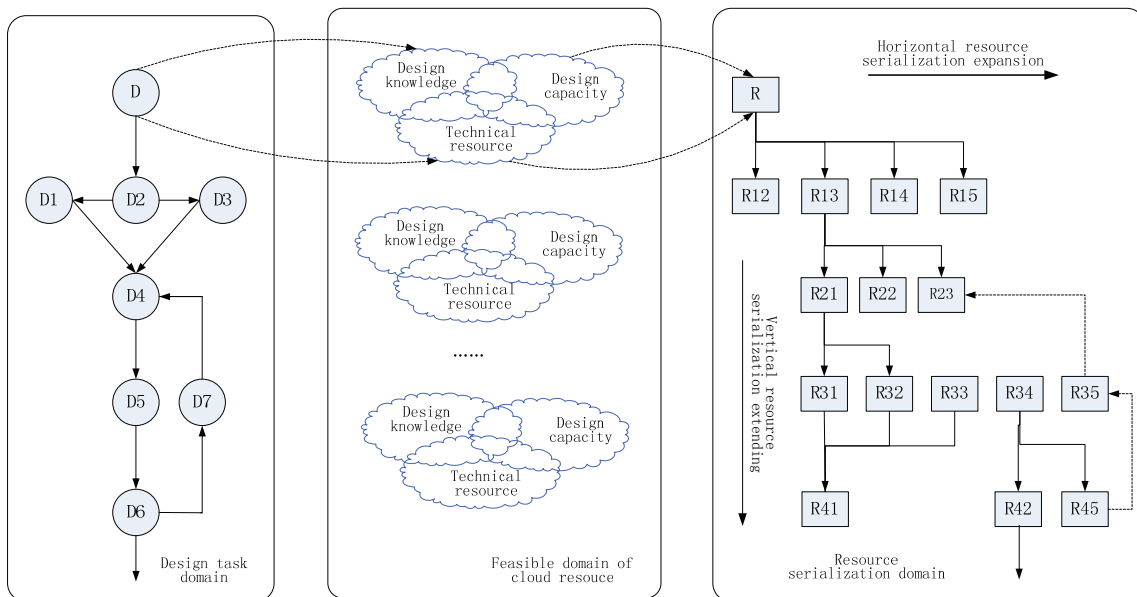


Fig. 3. Resource serialization model.

Resource Serialization model description:  
 Sort(DRC) // Resource Serialization solution  
 {i=0 // Vertical expansion  
 Do  
   {i=i+1;  
   j=0; // Horizontal expansion  
   (a)  $\forall rc \in RC, RC\_decompose(rc)=R$   
   //Decomposition mapping  
   j=j+1;  
   If  $R \neq \phi$  then  $R_{ij}=R$  goto (a)  
   else j=j-1;goto (b)  
   (b)  $\forall rc \in RC, RC\_aggregate(rc)=R$   
   // Aggregation mapping  
   j=j+1;  
   If  $R \neq \phi$  then  $R_{ij}=rc$  goto (b)  
   else j=j-1;goto (c)  
   (2)  
   (c)  $\forall rc \in RC, RC\_derive(rc)=R$   
   // derived mapping  
   j=j+1;  
   If  $R \neq \phi$  then  $R_{ij}=rc$  goto (c)  
   else j=j-1;goto (d)  
   (d)  $\forall rc \in RC, RC\_instance(rc)=R$   
   // instance mapping  
   j=j+1;  
   If  $R \neq \phi$  then  $R_{ij}=rc$  goto (d)  
   }  
 until  $\forall rc \in RC, \exists Sort(DRC)=FALSE$   
 }

“i” is design level; “j” is design phase process of each level.

3) The feasible region of serialization resource forms resource serialization matrix R[] after resource serialization is completed shown in Fig. 4.

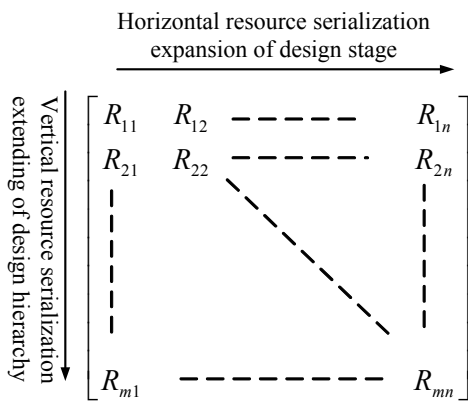


Fig. 4. Resource serialization matrix.

The time-varying control of resource state is introduced after the sequence of tasks on cloud resource mapping completing resource serialization form feasible domain resource, resources is pushed and drawn reasonably between the requirement domain DR of design resource, state control domain

T and feasible resource domain R, integration of the final serialization resources and design tasks is completed. Analysis expression of serialization resource integration:

$$DR[ ] = T[ ] \bullet R[ ], \quad (3)$$

where DR[] is the demand domain of design resource, T[] is state change control domain, R[] is Sequence of cloud resource feasible domain of serialization resource matrix DR[] is collection of requirement of design task resource, which is issued by design resource requirements. T[] is time control vector sequences executing design task, defined formally as T[T1, T2,... , Tn], which is task sequence vector set mapped by task sequence of RC task set ReqTas and task state feature of ReqStat.

### 5. Example Analysis

The task list of one mechanical equipment design project is shown in Table 1 as an example, there are 8 design tasks coordinated, including 6 task required precursor collaborative tasks.

Table 1. Analysis with design project.

Design task sequence set			Feasible domain of design task	Expected time
Design task	Precursor task	Sub-task		
A		A1, A2	$R_A[ ]$	4
B	A	B1, B2, B3,	$R_B[ ]$	3
C	B	C1, C2	$R_C[ ]$	8
D	B	D1, D2, D3	$R_D[ ]$	9
E		E1	$R_E[ ]$	2
F	C, D	F1, F2	$R_F[ ]$	4
G	E	G1, G2, G3, G4	$R_G[ ]$	8
H	F, G	H1, H2, H3	$R_H[ ]$	6

Double time-scaled network diagram of the design task is drawn, shown in Fig. 5, which constitutes the task sequence, corresponding time-varying state control domain T[] without loss of generality, example assumes feasible region of the design resource is not empty, i.e. full resources, there are resources set  $DRC[] = \{R_A[ ], R_B[ ], R_C[ ], R_D[ ], R_E[ ], R_F[ ], R_G[ ], R_H[ ]\}$  to meet every mapping the minimum requirements, and there are no conflict for resource state, namely the state change control only consider the temporal association, a total length of 27 time units, corresponding resource requirement periods are  $t_a = (0,4)$ ,  $t_b = (4,7)$ ,  $t_c = (7,15)$ ,  $t_d = (7,17)$ ,  $t_e = (0,2)$ ,  $t_f = (17,21)$ ,  $t_g = (2,10)$ ,  $t_h = (21,27)$ , if the time relaxation problem is not considered, execution time of each activity is fixed, and time interval during handover of the activities is ignored, time zone is divided into  $T1 \in [0,2]$ ,  $T2 \in [2,4]$ ,  $T3 \in [4,7]$ ,  $T4 \in [7,12]$ ,  $T5 \in [12,15]$ ,  $T6 \in [15,17]$ ,  $T7 \in [17,21]$ ,  $T8 \in [21,27]$ , take the

previous task as sequence,  $T[] = \{T1, T2, T3, T4, T5, T6, T7, T8\}$  is available.

Resource feasible domain spread serially shown in formula (2):

$$\begin{cases} Sort(R_A[]) = \{R_{A1}, R_{A2}\} \\ Sort(R_B[]) = \{R_{B1}, R_{B2}, R_{B3}\} \\ Sort(R_C[]) = \{R_{C1}, R_{C2}\} \\ Sort(R_D[]) = \{R_{D1}, R_{D2}, R_{D3}\} \\ Sort(R_E[]) = \{R_{E1}\} \\ Sort(R_F[]) = \{R_{F1}, R_{F2}\} \\ Sort(R_G[]) = \{R_{G1}, R_{G2}, R_{G3}, R_{G4}\} \\ Sort(R_H[]) = \{R_{H1}, R_{H2}\} \end{cases} \quad (4)$$

To obtain the Resource Serialization matrix  $R[]$ .

$$R[] = \begin{bmatrix} R_{A1} & R_{A2} & 0 & 0 \\ R_{B1} & R_{B2} & R_{B3} & 0 \\ R_{C1} & R_{C2} & 0 & 0 \\ R_{D1} & R_{D2} & R_{D3} & 0 \\ R_{E1} & 0 & 0 & 0 \\ R_{F1} & R_{F2} & 0 & 0 \\ R_{G1} & R_{G2} & R_{G3} & R_{G4} \\ R_{H1} & R_{H2} & R_{H3} & 0 \end{bmatrix} \quad (5)$$

## 6. Conclusion

Mechanical equipment product design have typical multidisciplinary cooperative and temporary customization features with amount of resource

demands and rigid time constraints, this paper research the design of cloudy domain requirements analysis and mapping method through cloud design theory model studying emergency equipment products, constructing formal concept model, the discrete design resource serialization and task integration strategy induce design process to promote cooperatively by controlling push and configuration of design resource in the process, which provides an effective means to realize the rapid response of product design. It is verified preliminarily by example.

## References

- [1]. Li Bohu, Lin Zhang, Typical characteristics, technologies and applications of cloud manufacturing, *Computer Integrated Manufacturing Systems*, 18, 7, 2012, pp. 1345-1355.
- [2]. Jingsheng Li, Aimin Wang, Tang Cheng-Tong et al. Distributed coordination scheduling technology based on dynamic manufacturing ability service, *Computer Integrated Manufacturing Systems*, 18, 7, 2012, pp. 1562-1573 (in Chinese).
- [3]. Nan Zhao, Zhanwen Niu, Wei Guo, Quantum harmony search method for design knowledge resource serialization combination in cloud manufacturing environment, *Computer Integrated Manufacturing Systems*, 18, 7, 2012, pp. 1435-1443 (in Chinese).
- [4]. Qian Zhang, Deyu Qi, Service-oriented collaborative design platform for cloud manufacturing, *Journal of South China University of Technology: Natural Science*, 39, 12, 2011, pp. 75-81.

2013 Copyright ©, International Frequency Sensor Association (IFSA). All rights reserved. (<http://www.sensorsportal.com>)



### Universal Frequency-to-Digital Converter (UFDC-1)

- 16 measuring modes: frequency, period, its difference and ratio, duty-cycle, duty-off factor, time interval, pulse width and space, phase shift, events counting, rotation speed
- 2 channels
- Programmable accuracy up to 0.001 %
- Wide frequency range: 0.05 Hz ... 7.5 MHz (120 MHz with prescaling)
- Non-redundant conversion time
- RS-232, SPI and I<sup>2</sup>C interfaces
- Operating temperature range -40 °C... +85 °C

[www.sensorsportal.com](http://www.sensorsportal.com)    [info@sensorsportal.com](mailto:info@sensorsportal.com)    SWP, Inc., Canada

## The Experimental Study of the Plateau Performance of the F6L913 Diesel Engine

<sup>1</sup> Weiming Zhang, <sup>2</sup> Jiang Li

<sup>1,2</sup> Dept. of Petroleum Supply Engineering, Logistical Engineering University,  
Chongqing, 401311, China

<sup>1</sup> Tel: 13908308569, fax: 023-86731156,

<sup>2</sup> Tel: 18523130833, fax: 023-86736137

E-mail: [zwm50262@163.com](mailto:zwm50262@163.com), [lijiang830@163.com](mailto:lijiang830@163.com)

*Received: 5 June 2013 / Accepted: 25 August 2013 / Published: 30 September 2013*

---

**Abstract:** The FST2E engine test bed was applied to carry out the simulation tests of the F6L913 diesel engine's plateau performance, to obtain the data of the engine at different altitudes and in various conditions, including torque, power, fuel consumption rate and oil consumption, and to generate the external characteristic curve and the load characteristic curve of the engine by fitting. The test result shows that the engine power and torque is decreased by 15 % to 20 % and the fuel consumption rate is increased by 15 % to 30 % whenever the altitude is increased by 1000 m, and the higher the altitude is, the faster this increase rate becomes. The stable working range of the engine becomes narrower and drifts to the high revolution area. *Copyright © 2013 IFSA.*

**Keywords:** Engines, Plateau simulation test, External characteristic, Load characteristic, Data analysis.

---

### 1. Introduction

The mobile pipeline can be used for oil transportation in the whole territory and under all weather conditions, so it is an important meaning for emergency oil transportation [1]. The prime motor of a certain type of pipeline pump unit uses the F6L913 air-cooled diesel engine, with the air intake way of natural aspiration. With the risen of elevation, the charging efficiency of the engine decreases, its working conditions become poor, its fuel consumption rate and oil consumption increases and its torque and power decreases. The decline in the power performance of the engine results in a reduction in the lift of the fuel pump and a decrease in the amount of oil, thus affecting the transportation performance of the pipeline. In order to make a quantitative analysis of the decreased performance of

the diesel engine at different altitudes and under different working conditions, the engine test-bed experiment that simulates the plateau environment was made.

### 2. Test Device and Method

#### 2.1. Test Device

The object of the test is the diesel engine of the pump unit, and its main performance indicators are shown in Table 1 [2]:

The experiment was made on the FST2E engine test bed which includes three parts, the engine bed system, the computer control system and the data acquisition system [3], with the butterfly valve as the air intake throttling part and the vacuum gauge to

measure the vacuum degree of the intake system, to simulate the air-intake pressure of the engine at different altitudes by controlling the opening degree of the butterfly valve, while measuring the air inflow

of the engine through the glass rotor flow meter. The simulation process of the intake of the device is shown in Fig. 1.

**Table 1.** F6L913 diesel engine performance parameters.

Number of cylinders	Rated power (kW)	Rated revolution (r/min)	Maximum torque (N · m)	Rated fuel consumption (g / kW · h)	Piston displacement (L)	Compression ratio
6	74	2200	384	238	6.128	17:1

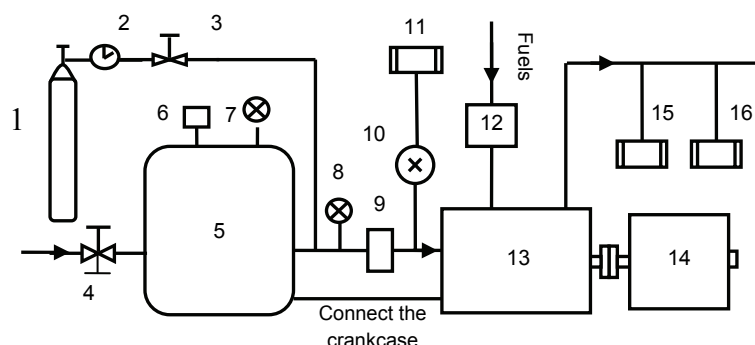


**Fig. 1.** The flow chart of the FST2E intake simulation:

- (1) - Oxygen bottles; (2) - Pressure reducing valve; (3/4) - Butterfly valve; (5) - Pressure stabilizing box; (6) - Temperature sensor; (7/8) - Vacuum gauge; (9) - Filter; (10) - Sampling vacuum pump; (11) - Oxygen analyzer; (12) - Fuel mass flow meter; (13) - Engine; (14) - Electric dynamometer; (15) - Exhaust gas analyzer; (16) - Opaque photometer.

## 2.2. Test Methods

The experiment is made based on Performance Test Code for Road Vehicle Engines [4], Reliability Test Methods for Motor Vehicle Engines [5], Measurement Methods of Net Power for Automotive Engines [6] and other national standards.

### 2.3. Test Method of External Characteristic [7]

Fix the opening degree of the engine throttle at 100 %, and measure power, torque, fuel consumption and fuel consumption rate and other parameters at the engine revolutions of 1300 r/min, 1400 r/min, 1500 r/min, 1600 r/min, 1700 r/min, 1800 r/min, 1900 r/min, 2000 r/min, 2100 r/min, 2200 r/min, 2300 r/min, 2400 r/min, 2500 r/min and 2600 r/min.

### 2.4. Test Method of Load Characteristic [8-9]

Select the rotation speed of the engine at low speed (1400 r/min), medium speed (2000 r/min) and high speed (2400 r/min), and increase the load of the engine under the fixed revolutions, starting from 20 % of the load, and then gradually increase to the load of 30 %, 40 %, 50 %, 60 %, 70 %, 80 %, 90 %

and 100 %, to separately measure the engine parameters under various loads such as engine power, fuel consumption rate, etc.

## 3. Test Results

With the above methods, parameters of the engine such as power, torque, fuel consumption rate and fuel consumption working at the altitudes of 0 m, 2000 m, 2500 m, 3000 m, 3500 m, 4500 m and 5000 m were tested, and the related data were obtained. Method in Reference [10] was used to correct the power and torque and to obtain the external characteristic curves and the load characteristic curves of the engine at various altitudes, as shown in Fig. 2 to Fig. 15.

## 4. Data Analysis

Through the analysis of the external characteristic curve graphs 2 to 8, the engine of this type has the inflection points of a sharp drop in power and torque appear in the revolutions between 2400 r/min and 2500 r/min. In order to ensure the reliability of the data analysis, the data in the revolutions from 1300 r/min to 2400 r/min are to be analyzed.

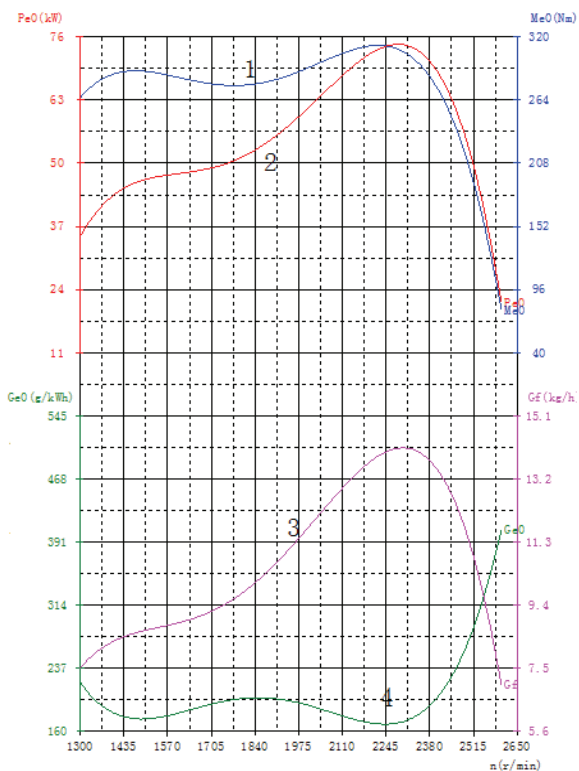


**Fig. 2.** 0 m External characteristic curve:  
 1 - Corrected torque;  
 2 - Corrected power;  
 3 - Fuel consumption;  
 4 - Corrected fuel consumption rate.

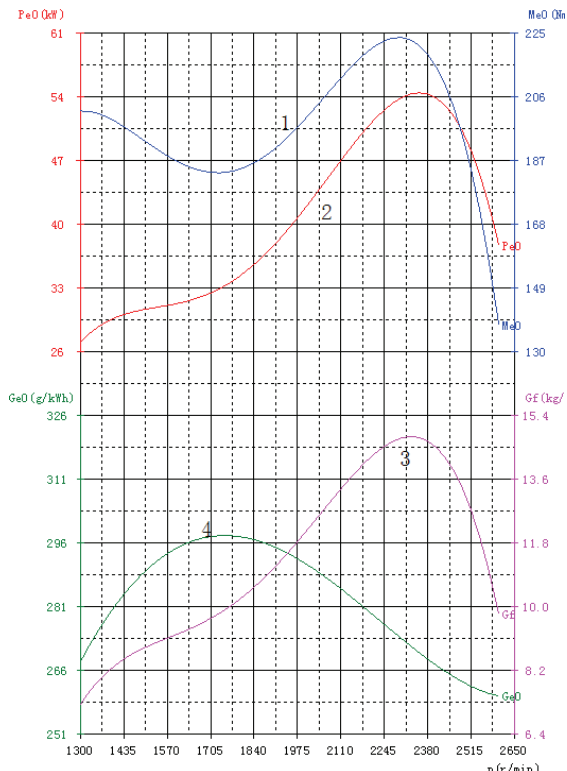


**Fig. 3.** 2000 m External characteristic curves:  
 1 - Corrected torque;  
 2 - Corrected power;  
 3 - Fuel consumption;  
 4 - Corrected fuel consumption rate.

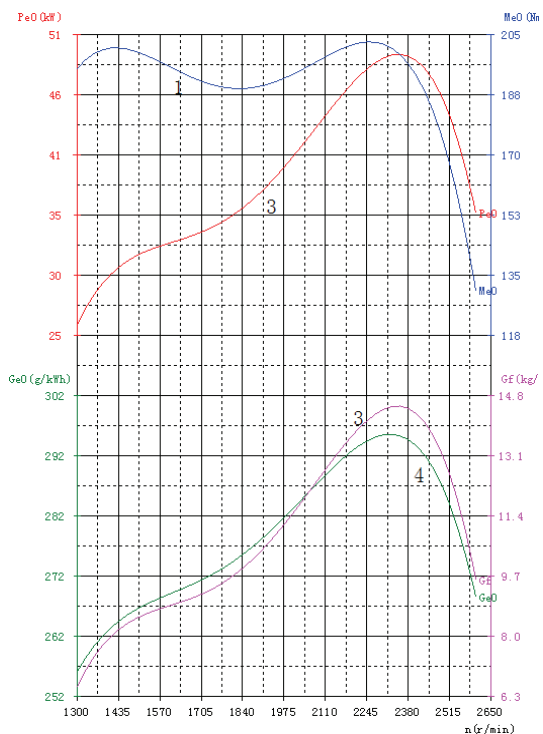


**Fig. 4.** 2500 m External characteristic curve:  
 1 - Corrected torque;  
 2 - Corrected power;  
 3 - Fuel consumption;  
 4 - Corrected fuel consumption rate.

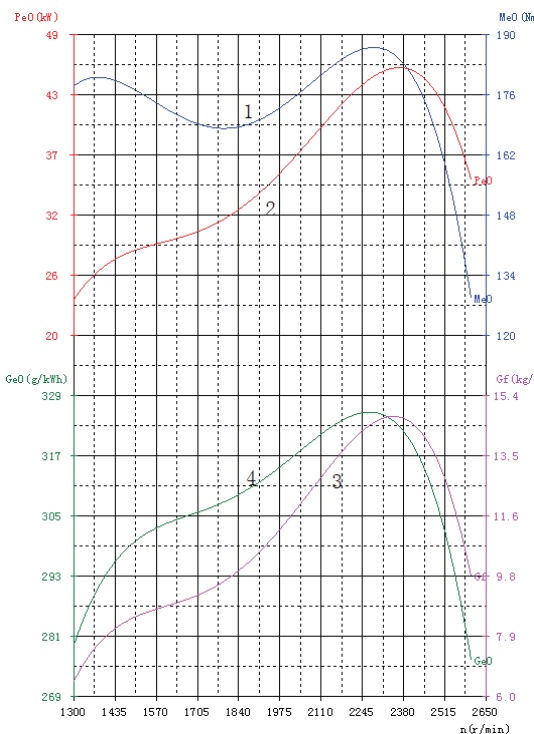


**Fig. 5.** 3000 m External characteristic curve:  
 1 - Corrected torque;  
 2 - Corrected power;  
 3 - Fuel consumption;  
 4 - Corrected fuel consumption rate.

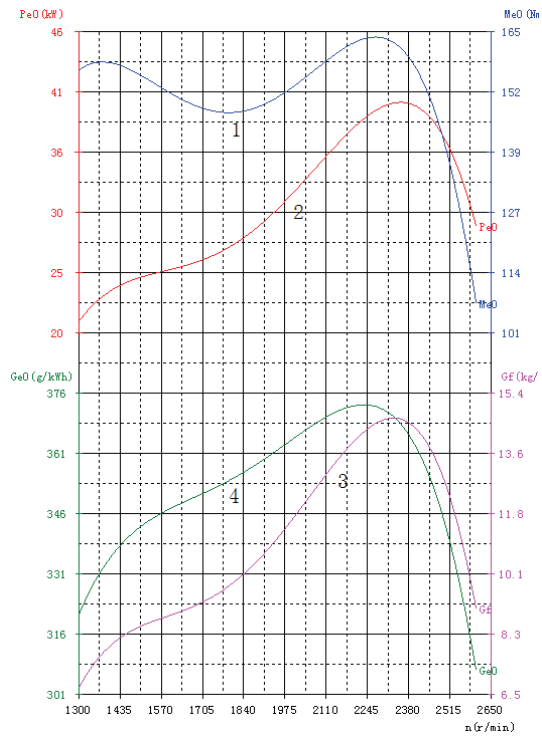


**Fig. 6.** 3500 m External characteristic curve:  
 1 - Corrected torque;  
 2 - Corrected power;  
 3 - Fuel consumption;  
 4 - Corrected fuel consumption rate.

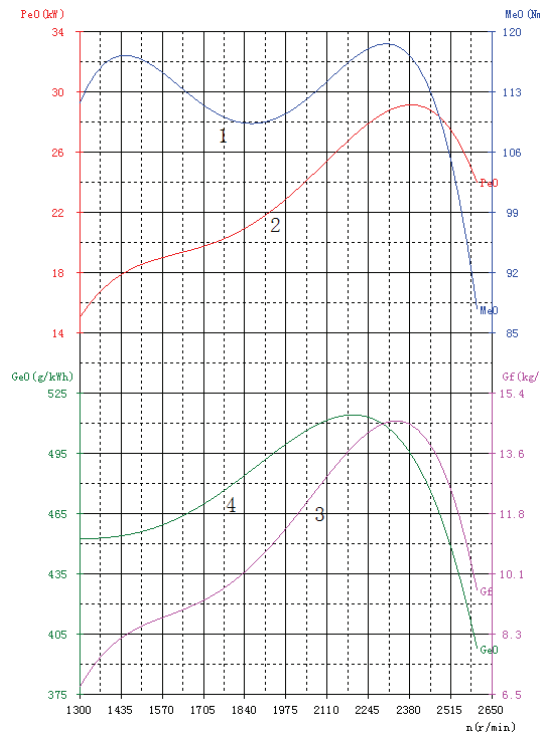


**Fig. 7.** 4500 m External characteristic curve:  
 1 - Corrected torque;  
 2 - Corrected power;  
 3 - Fuel consumption;  
 4 - Corrected fuel consumption rate.

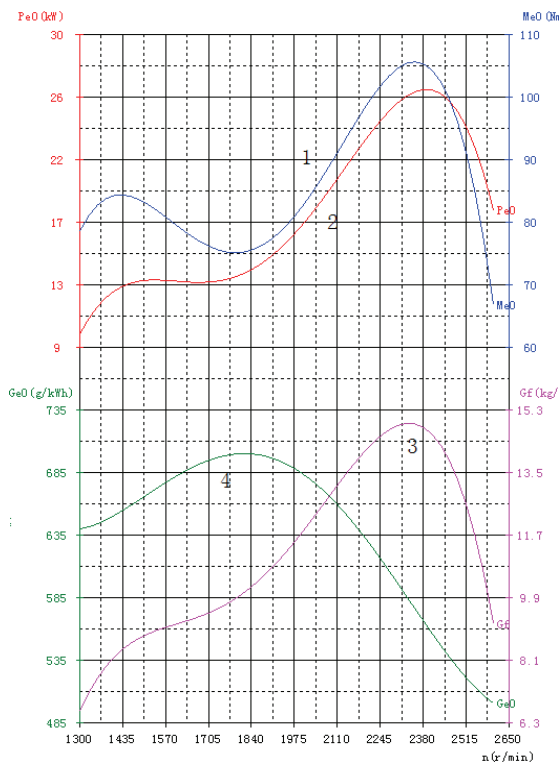


**Fig. 8.** 5000 m External characteristic curve:  
 1 - Corrected torque;  
 2 - Corrected power;  
 3 - Fuel consumption;  
 4 - Corrected fuel consumption rate.

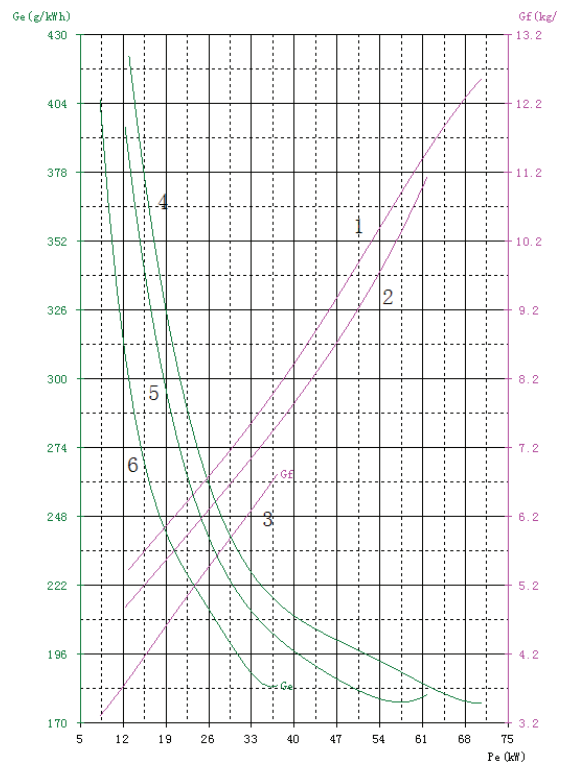


**Fig. 9.** 0 m Load characteristic curve:  
 1. 4-2400 r/min Fuel consumption (rate);  
 2. 5-2000 r/min Fuel consumption (rate);  
 3. 6-1400 r/min Fuel consumption (rate).

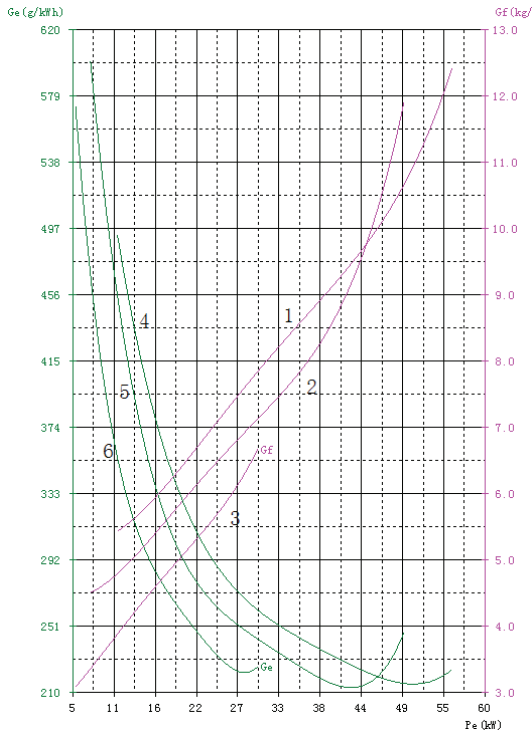


**Fig. 10.** 2000 m Load characteristic curve:  
 1. 4-2400 r/min Fuel consumption (rate);  
 2. 5-2000 r/min Fuel consumption (rate);  
 3. 6-1400 r/min Fuel consumption (rate).

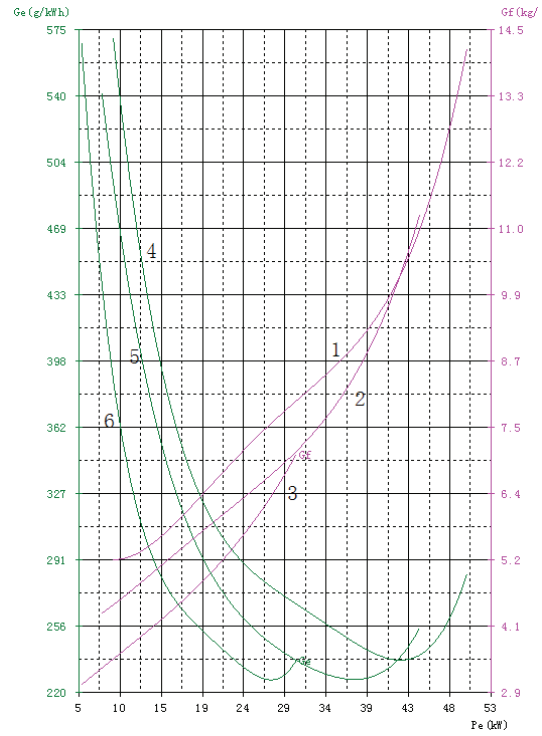


**Fig. 11.** 2500 m Load characteristic curve:  
 1. 4-2400 r/min Fuel consumption (rate);  
 2. 5-2000 r/min Fuel consumption (rate);  
 3. 6-1400 r/min Fuel consumption (rate).

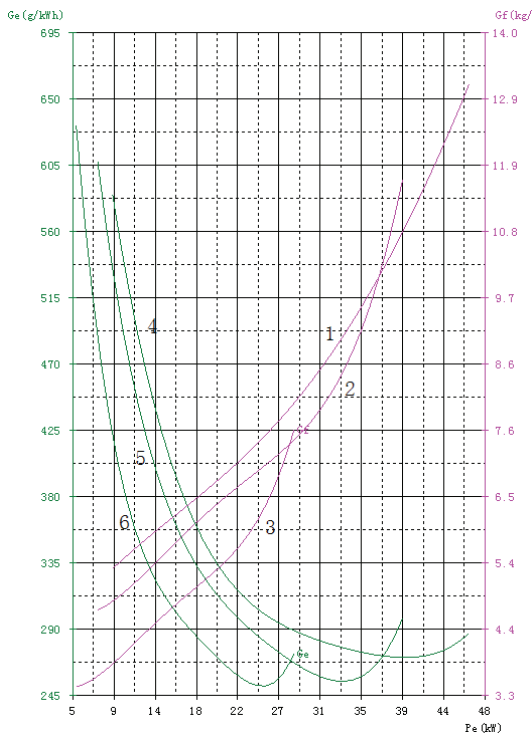


**Fig. 12.** 3000 m Load characteristic curve:  
 1. 4-2400 r/min Fuel consumption (rate);  
 2. 5-2000 r/min Fuel consumption (rate);  
 3. 6-1400 r/min Fuel consumption (rate).

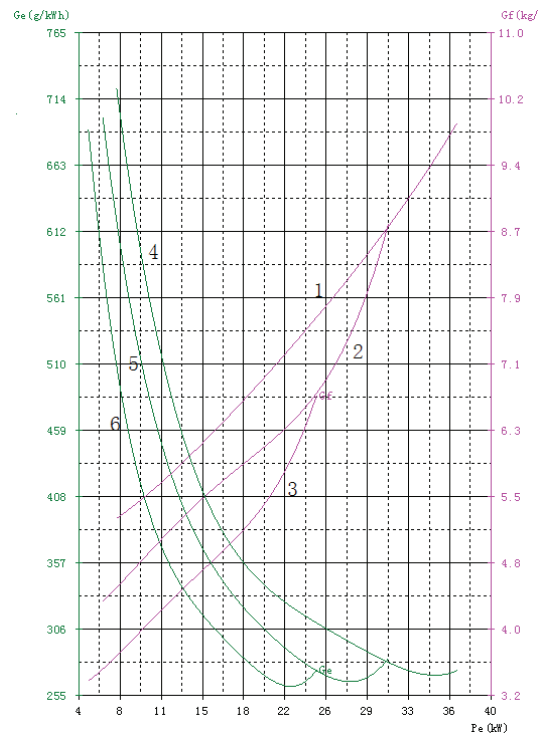


**Fig. 13.** 3500 m Load characteristic curve:  
 1. 4-2400 r/min Fuel consumption (rate);  
 2. 5-2000 r/min Fuel consumption (rate);  
 3. 6-1400 r/min Fuel consumption (rate).

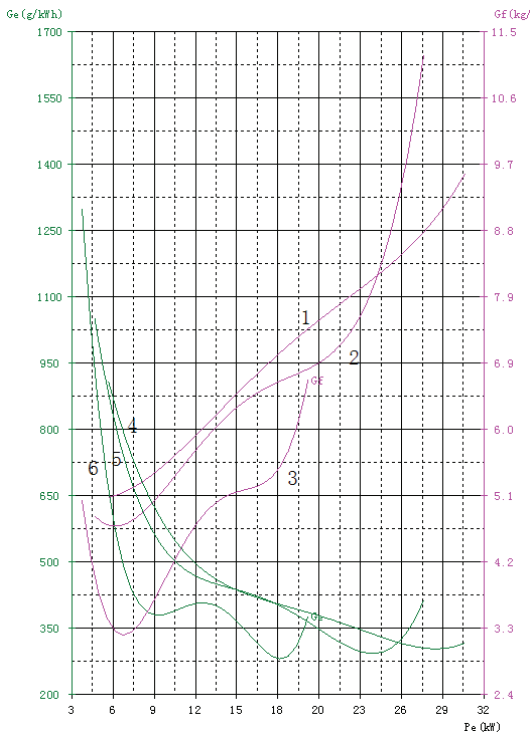


**Fig. 14.** 4500 m Load characteristic curve:  
 1. 4-2400 r/min Fuel consumption (rate);  
 2. 5-2000 r/min Fuel consumption (rate);  
 3. 6-1400 r/min Fuel consumption (rate).

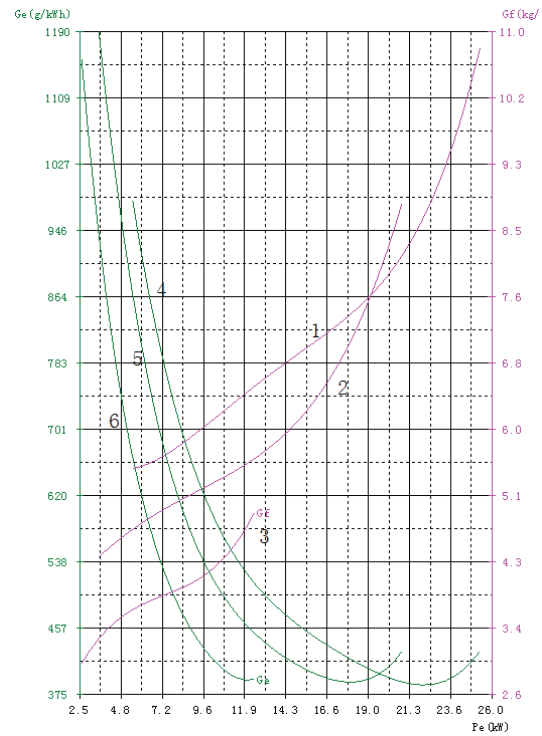


**Fig. 15.** 5000 m Load characteristic curve:  
 1. 4-2400 r/min Fuel consumption (rate);  
 2. 5-2000 r/min Fuel consumption (rate);  
 3. 6-1400 r/min Fuel consumption (rate).

#### 4.1. Impact on Power and Torque

In order to obtain the variation rule for engine power and torque at different altitudes, calculating the decrease rate of the maximum power and torque as well as the minimum power and torque of the engine under various revolutions and at various altitudes, compared with the data of 0 m, and take the mean value, the data are shown in Table 2 below.

The analysis of the data in Table 2 shows that with the rising of altitude, the power and torque provided by the engine have different degrees of decline, and the decline rate of the minimum power

and torque is lower than that of the maximum power and torque; the altitude of 3000 m is an inflection point for the decline of the power and torque of this type of engine. When the altitude is lower than 3000 m, the engine power declines by about 12 % and the torque by about 14 % compared to the altitude of 0 m per 1000 m; when the altitude is higher than 3000 m, the engine power declines by about 20 % and the torque by about 17 % compared to the altitude of 0 m per 1000 m. Altitude has a great impact on the power and torque of this type of engine and the impact degree will be deepened and speeded up along with the rising of the altitude.

**Table 2.** Variation rule for engine power and torque at different altitudes.

Altitude (m)	Maximum / minimum power (kW)	Maximum / minimum power decline rate (%)	Average power decline rate (%)	Maximum / minimum torque (N • m)	Maximum / minimum torque decline rate (%)	Average torque decline rate (%)
0	74/35	0	0	315/265	0	0
2,000	55/27	25.6/22.8	24.2	223/200	29.2/24.5	26.9
2,500	48/26	35.1/25.7	30.4	203/186	35.6/27.3	31.5
3,000	45/23	39.2/34.2	36.7	188/169	40.3/36.2	38.2
3,500	40/21	54.1/40	47	165/146	47.6/44.9	46.2
4,500	29/15	60.8/57.1	58.9	119/109	62.2/58.9	60.6
5,000	26/10	64.9/71.4	68.1	105/75	66.7/71.7	69.2

## 4.2. Impact on the Fuel Consumption Rate

Fig. 2 shows that the engine fuel consumption rate is basically stable at about 230 g / (kW · h) at the altitude of 0 m and in the revolutions of less than 2400 r/min. By comparing with data in Table 3 and Curve 4 in Fig. 3 to Fig. 8, it can be seen that the rising of altitude, the decrease of atmospheric pressure and the decline of the charging coefficient result in the continuous rising of the engine's fuel consumption rate, and in the altitude of 5000 m, the fuel consumption will grow by 203.5%. By comparing Fig. 9 to Fig. 15, it is known that the engine fuel consumption rate is the highest in the case of low loads, which is followed by the case of medium load, and the increase of the fuel consumption rate in the case of the high-load area is minimal.

The analysis of the relationship among curves 1, 2 and 3 in Fig. 9 to Fig. 15 also shows that the three fuel consumption curves are nearly parallel without intersection in the altitude of 0m, while there is at least one group among curve 1 and curve 2 or curve 2 and curve 3 at the other altitudes with an intersection. These present such a tendency that the higher the altitude is, the more frequently the cross curves becomes and the cross points appear in advance, e.g., as shown in Fig. 10. Only curve 1 and curve 2 are intersected, and the crossover point occurs in the vicinity of the power 45 kW, while in Fig. 12, the intersection occurs between both curve 1, curve 2 and curve 3, and the point of intersection of curves 1 and curve 2 occurs in the position of power 37 kW, which

suggests that the engine fuel consumption increases under the same power and torque in the plateau situation, thus leading to the increase in the rate of fuel consumption.

## 4.3. Impact on the Engine's Stable Working Range

As shown in Table 4, the maximum load is 38 kW when the altitude is 0m and the engine revolution number is 1400 r/min; the maximum load is 61 kW when the number of revolutions is 2000 r/min and the maximum load is 74 kW when the number of revolutions is 2400 r/min. With this as a standard, the following conclusions can be drawn from the comparison of the engine load characteristics at other altitudes, that is, every 1000 m increase in altitude will cause the maximum load of the engine to fall within the range of 10 % to 30 %, but its downward trend varies. In the case of 1400 r/min, the maximum load of the engine declines slowly in the beginning, but after the altitude is over 3500 m, a sharp decline occurs in the maximum load of the engine while in the case of 2000 r/min and 2400 r/min, the engine has the sharpest decline in the maximum load at the altitude from 2500 m to 3500 m. In addition, by comparing Curve 1 in Fig. 2 to Fig. 8, it can also be found that in the case of 1700 r/min to 1800 r/min, the inflection point is featured by "first drop and then rise of the torque", and a phenomenon can be seen that the higher altitude is, the steeper the curve becomes, and the position of the inflection point moves to the high revolutions area.

**Table 3.** Variation rule for engine fuel consumption rate at different altitudes.

Altitude (m)	Fuel consumption (g / kWh)	Minimum fuel consumption rate (g / kWh)	Maximum fuel consumption rate of growth (%)	Minimum fuel consumption rate of growth (%)	Average fuel consumption rate of growth (%)
0	240	200	0	0	0
2,000	280	240	16.7	20	18.4
2,500	300	260	25	30	27.5
3,000	325	280	35.4	40	37.7
3,500	370	324	54.2	62	58.1
4,500	510	450	112.5	125	118.8
5,000	700	630	192	215	203.5

**Table 4.** Variation rule for engine load characteristics at different altitudes.

Altitude (m)	1400 r/min maximum load (kW)	2000 r/min maximum load (kW)	2400 r/min maximum load (kW)	1400 r/min load decline rate (%)	2000 r/min load decline rate (%)	2400 r/min load decline rate (%)
0	38	61	74	0	0	0
200	30	49	56	21	19.7	24.3
2,500	29	47	50	23.7	23	32.4
3,000	28	39	46	26.3	36.1	37.9
3,500	25	31	36	34.2	49.2	51.4
4,500	19	27	30	50	55.7	59.5
5,000	12	21	24	68.4	65.6	67.6

It follows that with the rising of the altitude, the effective power that the engine can provide is getting smaller and smaller, and when it drops to a certain level, the engine at the low revolution area will be unable to output enough power to get out of the stable working range, which results in the stable working range of the engine drifting to the high revolution area, i.e. the stable working range of the engine is narrowed.

## 5. Conclusions

Through a series of simulation experiments of engine plateau performance, the rule of engine plateau performance decline is found and the external characteristic curve and the load characteristic curve are generated for engines. The following conclusions are drawn from the data analysis:

The engine has a significant reduction in its power and torque, and its downward trend speeds up along with the rising of the altitude. The experiment shows that the altitude of 3000 m is the inflection point of the decline in the power and torque of this type of engine. In the case of lower than 3000 m, every 1000 m increase in the altitude will decrease the engine power and torque by approximately 10 % to 15 %; in the case of higher than 3000 m, every 1000 m increase will cause the engine power and torque to fall by approximately 15 % to 20 %.

Fuel consumption increases, and the higher the altitude is, the greater the rate of growth becomes. The growth rate of the fuel at an altitude of 3500 m is maintained at an increase by 15 % for every 1000 m, and the rapid growth sharpens once exceeding 3500 m. The fuel consumption of the engine low load area has the highest growth rate, and the growth rate of the medium load area is higher than that of the high-load area.

The stable working range of the engine narrows and drifts to the high revolution area. Take the revolution of 1400 r/min for example, in the altitude

of 3000 m, the maximum power that the engine can obtain is only 27 kW and the fuel consumption increases dramatically and intersects with the load characteristics curve of 2000 r/min, at which the engine has drifted out of stable working range.

In order to ensure the safe and stable operation of the engine, this type of engine must be improved accordingly after the altitude exceeds 3000 m, in order to improve its plateau adaptability.

## References

- [1]. W. M. Zhang, Introduction to Pipeline Engineering, *Logistical Engineering University*, 2003.
- [2]. J. N. Pu, The Military Pipeline, *Logistical Engineering University*, 2001.
- [3]. M. S. Wei, X. Q. Cheng, Y. L. He, etc., Development of Turbocharged Diesel Engine Plateau Performance Simulation Program, *Internal Combustion Engine Engineering*, Vol. 28, Issue 4, 2007, pp. 40-42.
- [4]. GB/T 18297 - 2001 Automotive Engine Performance Test.
- [5]. GB/T 19055 - 2003, Automotive Engine Reliability Test Method.
- [6]. GB 17692 - 1997 Automotive Engine Net Power Test Methods.
- [7]. Y. X. Huang, Introduction to Plateau Engine Performance Test and Study, *CF Technology*, Vol. 28, Issue 3, 2000, pp. 14-20.
- [8]. J. L. Lei, L. Z. Shen, Y. H. Bi, The study of Turbocharged Diesel Engine Performance at Different Altitudes, *Small Internal Combustion Engine and Motorcycle*, Vol. 34 Issue 6, 2005, pp. 9-13.
- [9]. L. Z. Shen, Y. Z. Yang, J. L. Lei, etc., Study of the Turbocharged Intercooled Diesel Engine Performance and Emissions at Different Altitudes, *Internal Combustion Engine Journal*, Vol. 24, Issue 3, 2006, pp. 250-255.
- [10]. S. H. Ren, R. X. Li, Calculation Simulation of the Diesel Engine Speed Characteristic in the Plateau Conditions, *Internal Combustion Engine*, Vol. 24, Issue 1, 2007, pp. 25-28.

## The Diagnosis of Tool Wear Based on EMD and GA-B-Spline Network

\* Weiqing Cao, Pan Fu, Xiaohui Li

School of Mechanical Engineering, Southwest Jiaotong University, Chengdu, 610031, China

\* Tel.: 15882258040,

\* E-mail: caoweiqing@swjtu.cn

*Received: 5 June 2013 / Accepted: 25 August 2013 / Published: 30 September 2013*

**Abstract:** In view of the strong background noise involved in vibration signal of tool wear and the difficulty to obtain fault frequencies, this paper proposed a tool wear fault feature extraction method based on morphological filters-singularity value decomposition (SVD) with empirical mode decomposition (EMD). Firstly, an experiment system of the cutting tool wear monitoring was set up and a variety of data coming from vibratory sensor were collected, then, the pulse components from the original signal were inhibited by morphological filters and the signal sequences removed outlier were reconstructed, the attractor track matrix was decomposed using SVD for further noise reduction, and then we got weak signal failure frequency after the de-noise signals were decomposed with EMD. Finally, tool wear was identified by GA-B-spline neural network. B-spline networks were trained using genetic algorithms to search for global optimization. The experimental results shown that the diagnosis approach put forward in this paper could identify tool wear fault patterns effectively in noise background. *Copyright © 2013 IFSA.*

**Keywords:** Empirical mode decomposition; Morphological filtering; Singularity value decomposition; Genetic algorithm; B-spline Neural Networks.

### 1. Introduction

Online monitoring of the tool wear condition is very crucial in order to improve the quality of the unmanned manufacturing systems. In tool wear monitoring process, it is very important for tool wear early fault diagnosis how to extract the weak signal characteristics. Tool wear is a very complex phenomenon and the vibration signal is non-stationary signal with strong noise, so FFT and Wavelet analysis is not suitable for it. Empirical mode decomposition (EMD) is empirical, intuitive, direct, adaptive and is used widely in many areas [1, 2].

EMD is a good signal processing technique capable of decomposing a signal into several single

stable components at different time scales by sifting process. In view of the vibration signal from the sensors contains a lot of interference noise, which can affect the result of EMD, so, the signals must be denoising before implementing the EMD. Hao Rujiang [3] applied morphology filters to remove the noise in the signal and got obvious periodic fault impact characteristics. Wang Taiyong [4], Shin [5] proposed that the signal was pretreated by SVD before EMD decomposition and obtained better effect. Tang Baoping [6], applied singular value decomposition-morphology filter to reduce noise and got better fault characteristics. Morphological filtering can inhibit impulse noise signal and SVD can restrain random noise obviously. So, we can construct a confederative filter by

combining the morphological filtering and SVD as the signal pre-processing unit before implementing the EMD and achieve weak signal fault frequency well.

In order to realize the intelligent identification based on the weak signal feature extraction, this paper puts forward that intelligent diagnosis of the tool fault based on GA-B-spline network. B-spline network is a three-layer system, and is traditionally trained by using gradient-based methods [7], this may fall into local minimum during the learning process. Genetic algorithms (GAs) have drawn significant attentions in various fields due to their capabilities of directed random search for global optimization [8-9]. So, in this paper, the weighting factors and the knot points are searched by using a genetic algorithm. The experimental results show that the diagnosis approach put forward in this paper can effectively identify tool wear fault patterns in noise background.

## 2. Empirical Mode Decomposition

Empirical mode decomposition (EMD) can decompose a signal into several single stable components at different time scales by sifting process and it is empirical, intuitive, direct and adaptive with the a posteriori defined basis derived from the data. The components are referred to as Intrinsic Mode Functions (IMFs), subject to the following conditions:

1) In the whole data set of IMFs, the number of extremes and the number of zero crossing must either be equal or differ at most by one.

2) At any point, the mean value of the envelope defined by the local maxima and the envelope defined by the local minima must be zero.

At the end of the algorithm, the signal  $x(t)$  can be expressed as:

$$x(t) = \sum_{i=1}^n c_i + r_n, \quad (1)$$

where  $c_1, c_2, \dots, c_n$  is the intrinsic mode function from high frequency to low frequency and  $r_n$  is the residue of the decomposition.

Because of the fault information mainly in the high frequency region, therefore, we can calculate energy percentage of the pre- $n$  IMF component to show sign fault information [10].

The total energy  $E_i$ ,

$$E_i = \int_{-\infty}^{+\infty} |c_i|^2 dt \quad (2)$$

$i = 1, 2, \dots, n;$

We can structure vector characteristics using the percentage of energy to represent the characteristics of signal

$$E = \sqrt{\sum_{i=1}^n |E_i|^2}, \quad (3)$$

$$T = [E_1/E, E_2/E, \dots, E_n/E] \quad (4)$$

## 3. Signal Noise Reduction Analysis

In tool wear monitoring process, the vibration signal from the sensors contains a lot of interference noise. It will increase the number of spline interpolation and EMD layers which can increase cumulative error [11]. At the same time, because of the noise, IMF component can not be decomposed effectively and even increase aliasing modal. So, the signals must be de-noising before implementing the EMD.

### 3.1. Morphological Filtering

Morphological filtering is a nonlinear filtering technology based on mathematical morphology. Its advantage is fast and simple, generally containing only Boolean operations, including subtraction but not multiplication. Based on the geometric characteristics of the signal, morphological filtering uses pre-defined structure elements (SEs) to match the signal in order to extract it, maintaining the details and reducing the noise, it is used widely in the mechanical fault diagnosis [12]. Mathematical morphology's basic operations are: dilation, erosion, opening operation and closing operation. To get a good filtering result, in the process of fault diagnosis, the average value of the opening-closing (OC) and closing-opening (CO) filters is applied, which can restrain both positive and negative impulse noise. It can be defined as:

$$y(n) = \frac{1}{2} [F_{oc}(f(n)) + F_{co}(f(n))] \quad (5)$$

In morphological filtering, the results of the operations depend on not only the form of morphological transformation but also the size and shape of the SE. There are various kinds of SEs, such as flat SE, triangular SE and semicircular SE etc. The attributes of the SE are controlled by its shape and the selected SE should be as close as possible to the signal that being analyzed. In theory, a more complex SE will have a much stronger de-noising ability. Through the processing vibration signal using of different SE, the sine SE should first be consideration in the treatment of the vibration signal and the best filter effect can be got while the SE width is sampling points 1/12 and the SE high is selected 0.22-0.26 times of the signal amplitude [13].

### 3.2. Method of Signal Processing Based on Singularity Value Decomposition

Though morphological filtering can inhibit impulse noise signal well, it is not better than Singularity Value Decomposition (SVD) to filtering random noise. SVD de-noising is a method to increasing the signal-to-noise ratio based on the reconstructed attractor track matrix.

Supposing there is a sampled time series from a sensor:  $x_1, x_2, \dots, x_N$ , an  $m \times n$  dimension matrix can be reconstructed based on it:

$$H = \begin{bmatrix} x_1 & x_2 & \cdots & x_n \\ x_2 & x_3 & \cdots & x_{n+1} \\ \vdots & \vdots & \vdots & \vdots \\ x_m & x_{m+1} & \cdots & x_N \end{bmatrix} \quad (6)$$

In the formula,  $N=m+n-1$ ,

$$H = UDV^T = S + W, \quad (7)$$

where  $D = \text{diag}(\sigma_1, \sigma_2, \dots, \sigma_r)$ ,  $r = \min(m, n)$ , and  $\sigma_1 \geq \sigma_2 \geq \dots \geq \sigma_r > 0$  is called singularity value of matrix H. S is the track matrix of attractor corresponding to the smooth signal in reconstructed vector space; W is the track matrix corresponding to the noise or the abrupt information from abrupt fault [14].

SVD is a new and effective way to reduce noise. The order of singular spectrum will influence the effectiveness of de-noising directly. If the order is too small, the information in original signals is short of lose and even to cause the waveform distortion. If the order is too high, one part noise in original signals has been retained. The effect of de-noising is not very ideal. So, we will define the concept of singular energy difference spectrum which is normalized for easy of comparing [15]:

$$\rho(i) = \frac{\sigma_i^2 - \sigma_{i+1}^2}{\sigma_{\max}^2 - \sigma_{\min}^2}, i = 1, 2, \dots, r \quad (8)$$

It shows that there must be a peak in the parting between signal and noise. Behind the peak, spectrum peaks caused by noise are smaller. So,  $k$  - non-zero singular values can be achieved by it.

### 3.3. Simulation

To illustrate the effects of noise on EMD decomposition, we simulated signal  $x(t)$  added noise defined as follows:

$$x(t) = (1 + \cos(20\pi t))\sin(30\pi t) + \sin(70\pi t) + n(t) + \delta(t) \quad (9)$$

where  $n(t)$  is a white noise with effective value equal to 1,  $\delta(t)$  is an impulse noise signal. The sampling frequency of the signal  $x(t)$  is 1000 Hz, the length of the time series is 1024 points. The time domain wave form of the signal  $x(t)$  is shown as Fig. 1, Fig. 2 is the results of EMD implementing on  $x(t)$  directly.

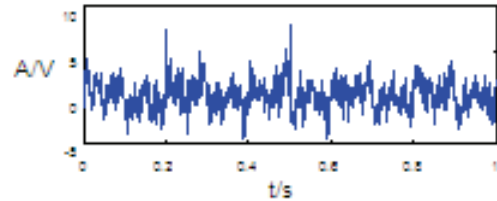


Fig. 1. Simulation signal.

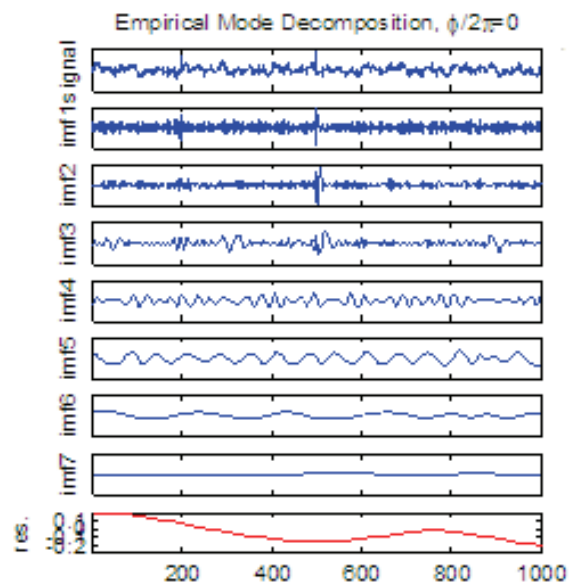


Fig. 2. The EMD of Simulation signal.

It is clear that the first three orders of IMFs are high frequency noise and the useful components are decomposition out on IMF4, IMF5 and IMF6, but the distinct frequency aliasing happened because of the noise interference. In order to improve the quality of EMD decomposition, the original signal contained noise has to be suitably pre-processed. The results of pre-processing by morphological filtering, SVD and confederative filter of them are shown as Fig. 3 - Fig. 5.

It can be seen, morphological filtering can inhibit impulse noise signal well and SVD can restrain random noise obviously. So, we can construct a confederative filter by combining the morphological filtering and SVD as the signal-pre-processing unit before implementing the EMD. From the Fig. 6, it can be seen that IMF has no frequency aliasing because the pulse signal and random signal are effectively controlled and the quality of EMD decomposition can be improved.

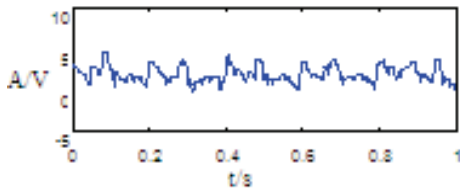


Fig. 3. Signal based on morphological filtering.

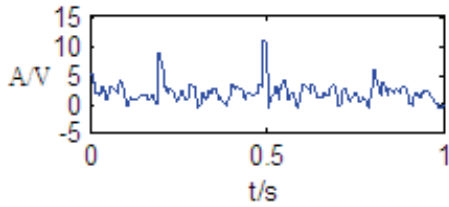


Fig. 4. De-noised signal based on SVD.

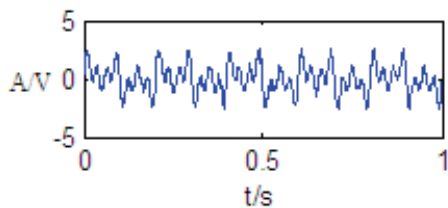


Fig. 5. De-noised signal based on confederative filter.

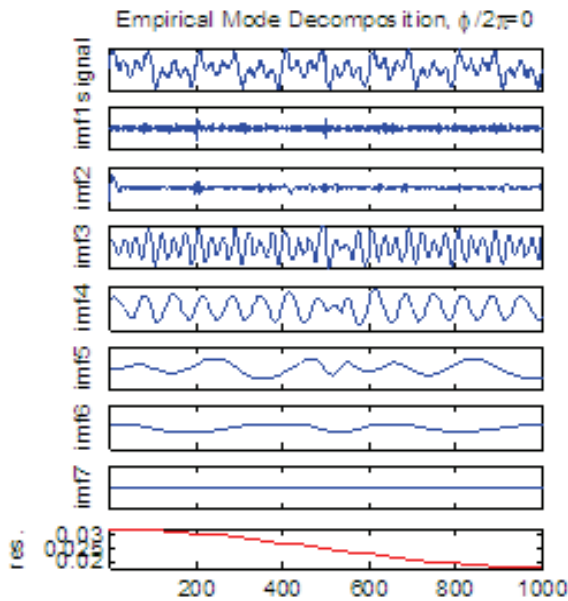


Fig. 6. EMD result of De-noised signal based on morphological filters and SVD.

#### 4. Weak Feature Extraction in Tool Wear Process

The experiments were carried out on a CK6143/100 CNC machine tool made in Wuhan Hankou Machining Centre, the spindle speed: 40-2500 rpm, spindle motor power: 5.5 kW, a Kistler 8702B50MI vibration sensor installation is shown in Fig. 7. The material of the workpiece: 45# (average

hardness 220 HB), the tool is PVD TiAlN coating blade (KC5010), main parameters:  $K_r=90^\circ$ , the speed of the tool is  $V_c=95\text{ m/min}$ , the feed rate of tool is  $f=0.2\text{ mm/r}$ , the depth of cut is  $a_p=1\text{ mm}$ . The sampling frequency of AD board is 2 MHz, the sampling point is  $2^{18}$ . We adopt the low temperature cold wind cooling in the experiments, as shown in Fig. 8.

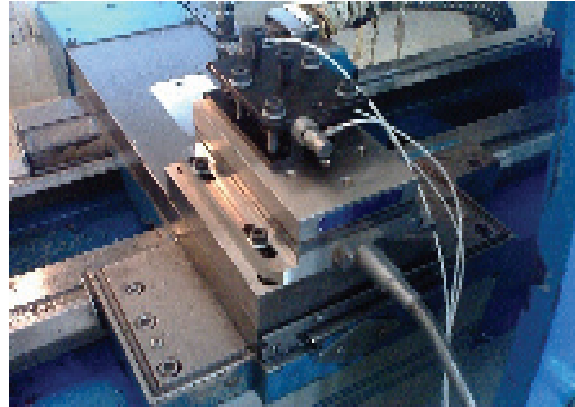


Fig. 7. Sensor installation.

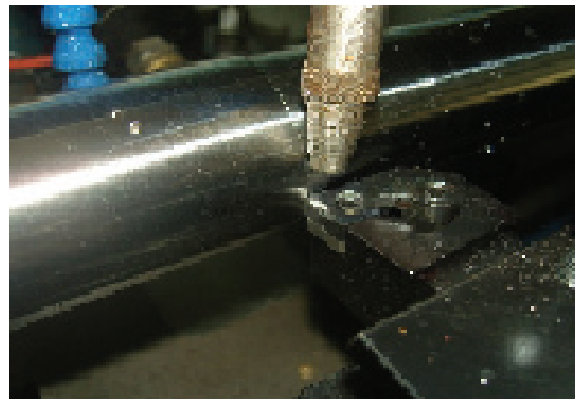


Fig. 8. Low temperature air cooling cutting.

In the experiment process, the tool wear status was divided into 3 patterns (shown in Table 1).

Table 1. The classification of tool wear.

Tool wear value (mm)	0-0.1	0.1-0.3	>0.3
Tool state	Mild wear	Moderate wear	Severe wear

300 samples were selected wear in the experiment and 120 samples were picked as testing samples. Fig. 9 shows the recognized results of tool mild wear and severe wear.

It can be seen that the signals were decomposed with EMD after the de-noising and the fault characteristic lay in the first five orders of IMFs. So, we calculate the energy percentage of them. Part test samples are shown in Table 2.

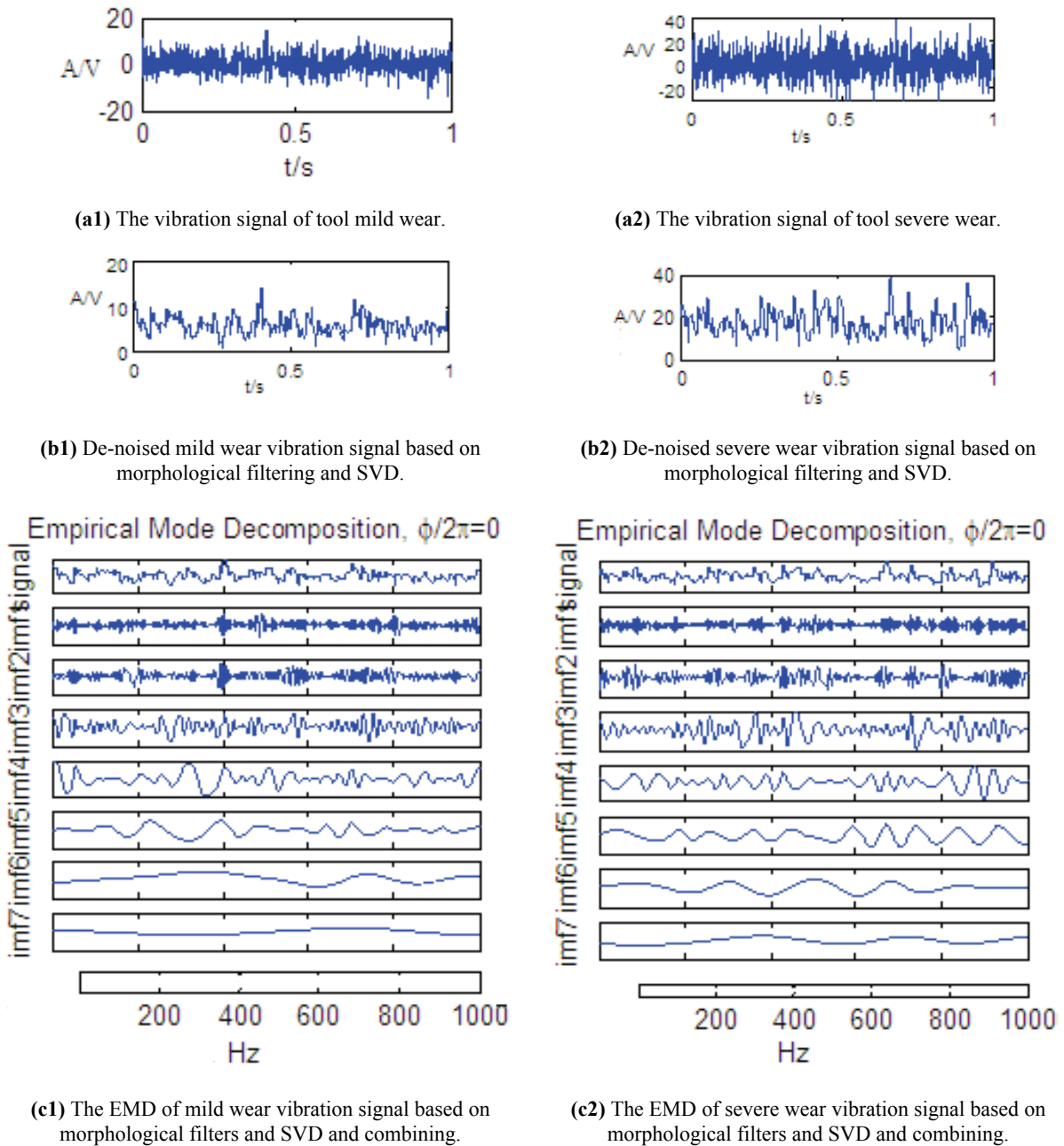


Fig. 9. Signal analysis of Tool wear.

Table 2. Part test samples of networks.

Samples (N)	Status of tool wear	The energy percentage of IMFs				
		E1/E	E2/E	E3/E	E4/E	E5/E
1	Mild wear	0.9527	0.2567	0.0823	0.0156	0.0089
2	Mild wear	0.9316	0.4752	0.0789	0.0571	0.0076
3	Mild wear	0.8525	0.5217	0.1273	0.0234	0.0065
4	Moderate wear	0.9572	0.3214	0.1003	0.0832	0.0076
5	Moderate wear	0.9532	0.2147	0.0756	0.0241	0.0095
6	Moderate wear	0.8726	0.4211	0.2103	0.1002	0.0024
7	Severe wear	0.9777	0.1245	0.0874	0.0541	0.0086
8	Severe wear	0.9587	0.2735	0.0789	0.0259	0.0019
9	Severe wear	0.9810	0.1403	0.0523	0.0122	0.0034

## 5. GA-B-Spline Neural Network

In tool wear monitoring process, in order to realize the intelligent identification based on the weak signal feature extraction, this paper puts forward that intelligent diagnosis of the tool fault based on GA-B-spline network.

B-spline network is a member of the class of lattice Associative Memory Networks (AMN). It can be represented as a three-layer system: a normalized input space layer, a basis functions layer and a linear weight layer. The structure illustrated in Fig. 10.

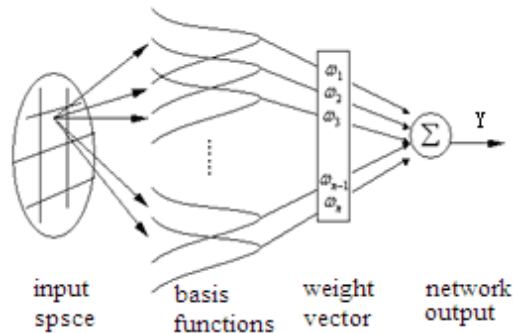


Fig. 10. B-spline network.

B-spline functions are composed of a linear combination of basis functions. The  $j^{\text{th}}$  B-spline basis function of order  $k$  and the internal knot point number  $r$  is defined as follows:

$$B_j^1(x) = \begin{cases} 1, & \text{if } x \in I_j \\ 0, & \text{otherwise} \end{cases} \quad (10)$$

$$I_j = \begin{cases} [\lambda_{j-1}, \lambda_j] & j = 1, 2, \dots, r \\ [\lambda_{j-1}, \lambda_j] & j = r + 1 \end{cases} \quad (11)$$

$$B_j^k(x) = \frac{x - \lambda_{j-k}}{\lambda_{j-1} - \lambda_{j-k}} \cdot B_{j-1}^{k-1}(x) + \frac{\lambda_j - x}{\lambda_j - \lambda_{j-k+1}} \cdot B_j^{k-1}(x) \quad (12)$$

When the B-spline fuzzy neural network is used for a modeling, there are some problems, such as how to select the appropriate weighting factors  $w$ , and how to choose the knot points  $r$  optimally, these problems are very important in achieving good approximation. B-spline neural networks are traditionally trained by using gradient-based methods [7], and may fall into local minimum during the learning process. Genetic algorithms (GAs) have drawn significant attentions in various fields due to their capabilities of directed random search for global optimization. So, in this paper, the weighting factors and the knot points are searched by using a genetic algorithm.

GA is powerful search optimization algorithm, which maintains a population of individuals (chromosomes) for iteration [16]. Each chromosome represents a potential to the problem. It forms a new population by selecting the more fit individuals with its fitness. After some numbers of generations, it is hoped that the system converges with a near-optimal solution.

Here, the initial chromosomes are randomly generated within the feasible ranges. A chromosome is defined as follows:

$$Z_p = (w_1, \dots, w_m, r_1, \dots, r_m), \quad (13)$$

where  $Z_p$  is the  $p^{\text{th}}$  chromosome for  $p=1, 2, \dots, k$ .  $k$  is the fixed number of population size and is used to prevent the unlimited growth of population. A set of the weighting factors  $w$  range from within the interval:  $[\omega_{\min}, \omega_{\max}] \subseteq R$ , and  $r$  range from within the interval  $[r_{\min}, r_{\max}] \subseteq R$ .

The performance of each chromosome is evaluated according to its fitness. After generations of evolution, it is expected that the genetic algorithm converges and a best chromosome with largest fitness representing the optimal solution to the problem is obtained. The fitness function is defined as follows:

$$fitness = \frac{1}{1 + E_i}, \quad (14)$$

where  $E_i$  is an estimation error function of  $i^{\text{th}}$  sample defined as follows:

$$E_i = \frac{1}{2} \|y_i - y_i'\|^2, \quad (15)$$

where  $y_i$  is the current outputs of  $i^{\text{th}}$  sample,  $y_i'$  is the desired outputs of  $i^{\text{th}}$  sample.

Two primary groups of genetic operators are crossover and mutation. Crossover combines the features of two parent chromosomes to form two similar offspring by swapping corresponding segments of the parents. Mutation, on the other hand, arbitrarily alters one or more genes of a selected chromosome, by a random change with a probability equal to the mutation rate.

When the number of iterations is the maximum or the fitness is smaller than setting accuracy, the optimization is terminated.

## 6. Tool Wear Intelligent Diagnosis

In this section, the better characters from the vibration signal (got in Section 4) are put into GA-B-spline neural network (got in Section 5). The network with 5 inputs and one output was adopted and the output of network is the diagnosis value of the tool

wear. Each input of network has 7 knot points and each order of B-spline basis functions is 2. The network is trained with GA, and the classification accuracy is 0.001, the largest number of iterations is 600, the crossover rate  $p_c=0.8$ , the variation rate  $p_m=0.1$ . Part of the identification results are shown in Table 3. It can be seen that the recognition rate achieves 98 % within the scope of the error is 0.01.

**Table 3.** The identification results of networks.

Sample (N)	1	2	3	4	5
Actual wear value (mm)	0.028	0.076	0.135	0.250	0.356
Diagnosis result (mm)	0.022	0.075	0.130	0.254	0.351
Sample (N)	6	7	8	9	10
Actual wear value (mm)	0.390	0.412	0.500	0.515	0.552
Diagnosis result (mm)	0.390	0.400	0.500	0.510	0.551

The same datasets of the tool wear are trained with the different learning algorithms, the error curves of training using the gradient-based methods and GA are illustrated in Fig. 11 and the results are compared each other, the average result can be shown in Table 4. It can be seen that the GA-B-spline is the best choice to identify tool wear with a lower average error and the higher diagnosis rate.

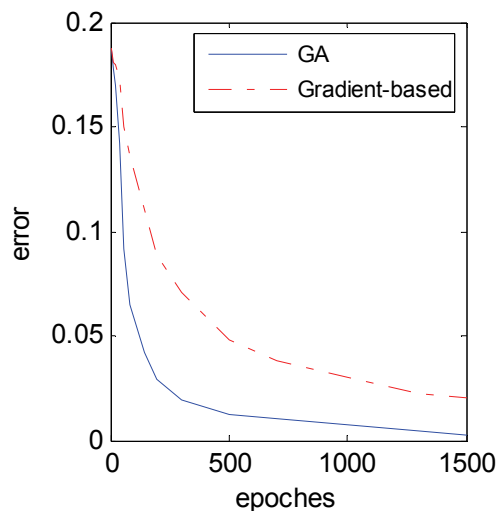


**Fig. 11.** Error curves of training the B-spline neural network using the different algorithms.

**Table 4.** The results for tool wear with different methods.

Learning algorithms	Average Error	Average Diagnosis rate
Gradient-based	0.0302	94.6 %
GA	0.0107	98.7 %

## 7. Conclusions

An intelligent tool wear monitoring system has been established. On the basis of the study, the following conclusions can be made.

1. In the tool wear monitoring process, it is difficult to extract tool wear feature information because of noise interference. The paper proposed a confederative filter by combining the morphological filtering and SVD as the signal-pre-processing unit before implementing the EMD. This can effectively remove the noise and reduce modal aliasing of the EMD. At last, the weak signal fault frequency was achieved.

2. The fault characteristic lay in the first five orders of IMFs. So, we calculate the energy percentage of them and put them into GA-B-spline networks. It simplifies the structure of the network and does not affect tool fault diagnosis.

3. The advanced GA-B-spline networks are applied in the tool wear monitoring process. Because the B-spline network with traditionally trained by using gradient-based methods may fall into local minimum during the learning process, this paper applied Genetic algorithms (GAs) to search the weighting factors and the knot points and got better results. It can improve the accuracy of tool wear and adapt to online monitoring.

## Acknowledgment

This work is supported by the Fundamental Research Funds for the Central Universities (SWJTU12CX039).

## References

- [1]. Sun Bin, Huang Shengquan, et al., Identification method of gas liquid two phase flow regime based on empirical mode decomposition, *Chinese Journal of Scientific Instrument*, 29, 5, 2008, pp. 1011-1015.
- [2]. Xing Hongyan, Xu Ruiqing, Wang Changsong, Pulse signal feature research based on empirical mode decomposition, *Chinese Journal of Scientific Instrument*, 30, 3, 2009, pp. 596-602.
- [3]. Hao Rujiang, Lu Wenxiu, Chu Fulei, Morphology filters for analyzing roller bearing fault using acoustic emission signal processing, *Journal of Tingshua University*, 48, 5, 2008, pp. 812-815.
- [4]. Wang Taiyong, Wang Zhengying, Xu Yonggang, et al., Empirical mode decomposition and its engineering applications based on SVD de-noising, *Journal of Vibration and Shock*, 24, 4, 2005, pp. 96-98.
- [5]. Shin K., Hammond J. K., White P. R., Iterative SVD method for noise reduction of low-dimension chaotic time series, *Mechanical Systems and Signal Processing*, 13, 1, 1999, pp. 115-124.
- [6]. Tang Baoping, Jiang Yonghua, Zhang Xingchun, Feature extraction method of rolling bearing fault based on singular value decomposition- morphology

- filter and empirical mode de-composition, *Journal of Mechanical Engineering*, 46, 5, 2010, pp. 37- 42, 48.
- [7]. Fan Junbo, Hao Jisheng, An Adaptive Learning Algorithm for B-spline Networks, *Acta Electronica Sinica*, 27, 8, August 1999, pp. 90-93.
- [8]. Sang Haifeng, He Dakuo, Zhang Dapeng, Soft-sensing modeling of a fermentation process through support vector machines and genetic algorithms, *Journal of North Eastern University (Natural Science)*, 28, 6, 2007, pp. 781-784.
- [9]. Li Shichao, Shi Xiuhua, Fault Diagnosis Based on Genetic Algorithms Wavelet Neural Network in Dual-Redundancy Brushless DC Motor, *Journal of Vibration, Measurement & Diagnosis*, 29, 2, June 2009, pp. 223-226.
- [10]. Lin Ruilin, Zhou Ping, Fault diagnosis of valve train based on EMD and neural network, *Journal of Naval University of Engineering*, 20, 2, 2008, pp. 48-51.
- [11]. Hu Aijun, An Liansuo, Tang Guiji, New Process Method for End Effects of Hilbert-Huang Transform, *Journal of Mechanical Engineering*, 44, 4, 2008, pp. 154-158.
- [12]. Du Biqing, Wang Songling, Tang Guiji, Application of Morphological De-noising in Rotor Fault State Identifying by Fractal Method, in *Proceedings of the CSEE*, 28, 26, 2008, pp. 71-76.
- [13]. Du Biqing, Wang Songling, Tang Guiji, Morphological filter design for vibration signals from rotor system, *Chinese Journal of Construction Machinery*, 6, 2, 2008, pp. 243-248.
- [14]. Sanliturk Y., Cakay O., Noise elimination from measured frequency response functions, *Mechanical Systems and Signal Processing*, 15, 3, 2005, pp. 615-631.
- [15]. Xu Feng, Liu Yunfei, Song Jun, Feature extraction of acoustic emission signals based on median filter-singular value decomposition and empirical mode decomposition, *Chinese Journal of Scientific Instrument*, 12, 32, 2011, pp. 2712-2719.
- [16]. W. Y. Wang, Y. H. Li, Evolutionary Learning of BMF Fuzzy-Neural Networks Using a Reduced-Form Genetic Algorithm, *IEEE Trans. Syst., Man, Cybern. B*, 33, 2003, pp. 966-976.

2013 Copyright ©, International Frequency Sensor Association (IFSA). All rights reserved.  
(<http://www.sensorsportal.com>)



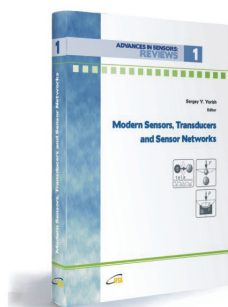
International Frequency Sensor Association (IFSA) Publishing

ADVANCES IN SENSORS:  
REVIEWS

1

## Modern Sensors, Transducers and Sensor Networks

Sergey Y. Yurish, Editor



Formats: printable pdf (Acrobat) and print (hardcover), 422 pages  
ISBN: 978-84-615-9613-3,  
e-ISBN: 978-84-615-9012-4

*Modern Sensors, Transducers and Sensor Networks* is the first book from the Advances in Sensors: Reviews book Series contains dozen collected sensor related state-of-the-art reviews written by 31 internationally recognized experts from academia and industry.

Built upon the series Advances in Sensors: Reviews - a premier sensor review source, the *Modern Sensors, Transducers and Sensor Networks* presents an overview of highlights in the field. Coverage includes current developments in sensing nanomaterials, technologies, MEMS sensor design, synthesis, modeling and applications of sensors, transducers and wireless sensor networks, signal detection and advanced signal processing, as well as new sensing principles and methods of measurements.

*Modern Sensors, Transducers and Sensor Networks* is intended for anyone who wants to cover a comprehensive range of topics in the field of sensors paradigms and developments. It provides guidance for technology solution developers from academia, research institutions, and industry, providing them with a broader perspective of sensor science and industry.

[http://sensorsportal.com/HTML/BOOKSTORE/Advance\\_in\\_Sensors.htm](http://sensorsportal.com/HTML/BOOKSTORE/Advance_in_Sensors.htm)

## Risk Assessment on Railway Signal System Based on Fuzzy-FMECA Method

You-Peng Zhang, Zheng-Jie Xu, \* Hong-Sheng Su

School of Automation and Electrical Engineering Lanzhou Jiaotong University,  
88 West Anning Road, 730070, China

\* Tel.: 13359492512

E-mail: shsen@163.com

*Received: 5 June 2013 / Accepted: 25 August 2013 / Published: 30 September 2013*

---

**Abstract:** Risk assessment is becoming increasingly important for railway signal system in order to safeguard their passengers and employees while improving safety and reducing maintenance costs. However, the application of risk assessment methods in railway signal system may not give satisfactory results because the risk data are incomplete or there is a high level of uncertainty involved in the risk data. This article presents a new risk assessment method for railway signal system using Failure Mode, Effects and Criticality Analysis (FMECA) and Fuzzy Analytical Hierarchy Process (FAHP). A case study on risk assessment of Interval Signal Control Function for Train Control Center is used to illustrate the application of the proposed risk assessment method. FMECA is firstly employed to summarize the potential failure modes of this function. And then based on the expert scoring for each failure mode in terms of Probability of Occurrence, Severity, and Detectability. FAHP is used to determine the relative importance of the risk contributions. The risk assessment results show that the application of Fuzzy-FMECA method can identify the failure modes and evaluate the potential risk of the Railway Signal System more objectively and effectively, which will provide railway risk analysts, engineers with a method to improve their safety management of Railway Signal System and set safety standards. Copyright © 2013 IFSA.

**Keywords:** Risk assessment, Railway signal system, FMECA, FAHP, Interval signal control function.

---

### 1. Introduction

China has experienced a large number of railway construction projects at an astonishing speed in both high-speed mainline railways and metro systems in the past few years. A major railway accident occurring on 23 July 2011 has brought the Chinese railway industry to almost a halt on new development. The accident investigation report concludes that the accident was due to serious design flaws in control equipment and improper handling of the lightning strike [1]. For this reason, The Railway Ministry stressed to strict with the security

assessment of the equipments for high speed railway. And professional testing for high speed railway equipments and risk assessment are carried out. Since China does not have the perfect security certificate. In order to complete the security certificate, it is urgent to study the risk assessment methods for equipments of high speed railway [2]. The Train Control Center is the core equipment of the train operation control system, which is widely used in line for passenger transportation and plays a crucial role in protecting the safety of the train [3]. The requirement of risk analysis is to demonstrate that if risks associated with a Railway Signal System are

high, risk reduction measures must be applied or operation and maintenance have to be reconsidered to reduce the occurrence probabilities or to control the possible consequences. If risks are negligible, no actions are required but the information produced needs to be recorded for audit purpose [4-6]. Therefore, railway engineers, managers and safety analysts need to develop and employ risk assessment approaches for their safety management and set safety standards.

Researchers have conducted many studies on the risk assessment of Railway Signal System. Failure Mode, Effects and Criticality Analysis (FMECA) combined with fault tree analysis contains a considerable amount of estimation and prediction, which can obtain the possible probability of failure modes [3, 7]. Analytical Hierarchy Process (AHP) is frequently criticized for its inability to adequately accommodate the inherent uncertainty and imprecision associated with mapping decision-maker perceptions to extract number [8, 9]. It is therefore difficult to response to the preference of decision-makers by assigning precise numerical values. Fuzzy Analytical Hierarchy Process (FAHP) can not identify the failure modes of systems or the equipments fully if it is used alone [10, 11]. Moreover, many risk assessment methods heavily rely on the availability and accuracy of the risk data. However, in many circumstances, these methods often do not cope with uncertainty of information. Furthermore, the statistic data does not exist and it must be estimated on the basis of expert knowledge and experience or engineering judgment. Therefore, railway risk analysts often face the circumstances where the risk data are incomplete or there is a high level of uncertainty involved in the risk data. Therefore, these methods can not assess the risk of the Railway Signal System effectively and scientifically.

This paper presents a new risk assessment method for Railway Signal System using FMECA combined with FAHP. FMECA is firstly employed to summarize the potential failure modes of the function. And then based on the expert scoring for each failure mode in terms of Probability of Occurrence, Severity, and Detectability, fuzzy comprehensive evaluation method is applied to map the investigation data to the corresponding fuzzy

judgment matrix of each failure mode, the weight distribution of every failure mode can be obtained using AHP. Through combined quantitative and qualitative methods, we had made a comprehensive evaluation method for FAHP to assess the risk of Railway Signal System. We try to identify risk factors and construct a comprehensive and reasonable, scientific and effective risk assessment analysis model.

## 2. Fuzzy-FMECA Theoretical Basis

This paper presents a new risk assessment method for Railway Signal System using FMECA combined with FAHP, which is Fuzzy-FMECA method. The purpose of the Fuzzy-FMECA is to quantify the FMECA analysis results and perform a security evaluation of the Railway Signal System.

### 2.1. Application of FMECA in the Security Analysis

FMECA can be divided into two procedures, Failure Mode and Effects Analysis (FMEA) and Criticality Analysis (CA). In FMEA, a procedure which covers identification for function of the system, analysis for each potential failure mode, and severity evaluation is performed to determine effects thereof in the system and to classify effects of each failure mode according to its severity. FMEA is the base of CA. At the beginning of this part, we give the closed-loop work analytical procedure of FMECA as shown in Fig. 1 [12].

In CA, based on results of FMEA, each failure mode needs to be evaluated and prioritized so that appropriate corrective actions can be taken for different failure modes. The priority of a failure mode is determined through the Risk Priority Number (RPN), which is defined as the probability of the Occurrence, Severity and Detectability, namely  $RPN = \text{Occurrence} \times \text{Severity} \times \text{Detectability}$  [13]. The three factors are all evaluated using the ratings (also called rankings or scores) from 1 to 10, as described from Table 1 to Table 3 [14]. Failures with higher RPNs are assumed to be more important and should be given higher priorities.

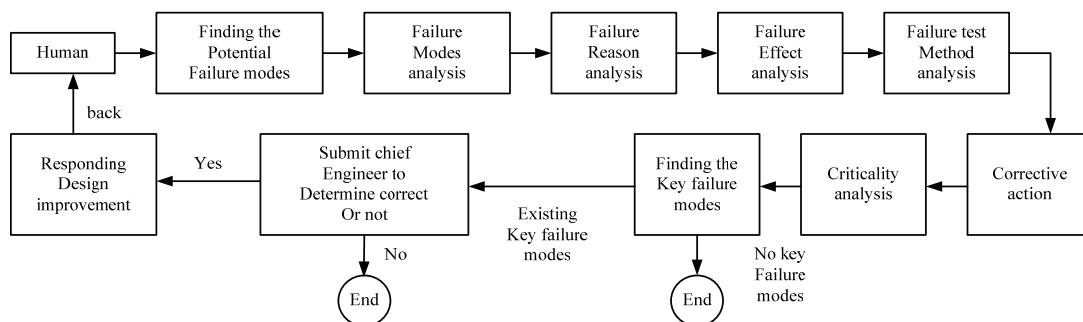


Fig. 1. The closed-loop work procedure of FMECA.

**Table 1.** Evaluation criterion for occurrence of certain failure.

Rank	Criteria: Probability of Occurrence	Probability
9, 10	Failure is almost inevitable	Very high
7, 8	Repeated failures	High
5, 6	Occasional failures	Moderate
3, 4	Relatively few failures	Low
1, 2	Failure is unlikely	Remote

**Table 2.** Evaluation criterion for severity of certain failure.

Rank	Criteria: Severity of Effect	Effect
9, 10	System inoperable with destructive failure	Very high
7, 8	System inoperable with equipment damage	High
5, 6	System inoperable with minor damage	Moderate
3, 4	System inoperable with damage	Low
1, 2	No effect	Remote

**Table 3.** Evaluation criterion for detection of certain failure.

Rank	Criteria: Likelihood of Detection	Detection
9, 10	Remote chance	Remote
7, 8	Low chance	Low
5, 6	Moderate chance	Moderate
3, 4	High chance	High
1, 2	Very high chance	Very high

FMECA has function analysis and hardware analysis, function analysis is used in this paper, which lists the functions of the systems or produces one by one and analyzes the causes, influence and harmfulness of each failure modes for the systems or products. The risk analysis of Interval Signal Control Function is a very complicated subject, which is determined by numerous relevant failure modes. It is impossible for a single engineer or manager to consider all relevant failure modes. Therefore, risk identification of the Interval Signal Control Function involves a number of experts with different background or discipline regarding the railway safety. By referring to these judgments of experts and historical data, the failure modes of Interval Signal Control Function can be identified comprehensively.

**2.2. Principles of FAHP**

AHP was proposed by American scholar T. L. Saaty in the 1970s [15], a certain scale which changes subjective judgments into objective ones and solves qualitative problems with quantitative analysis. It is a simple and practical multi-criteria evaluation method, applied in many fields.

Fuzzy comprehensive evaluation is a branch of fuzzy mathematic which is created by a well-known cybernetics expert L. A. Zadeh, deal with the fuzzy phenomenon with mathematical method [16]. Fuzzy is one of the characteristics of human thinking and fuzzy sets theory; it is an effective tool for fuzzy phenomenon treatment, while the evaluation is a general view of things that the nature of thinking determines its fuzziness. As a result, the fuzzy mathematic method has been widely used in the field of systematic evaluation.

When the evaluation covers a number of indexes of things, it should be integrated various demands to more realistic assessment. Thus, fuzzy set theory can be used to achieve the level of the integrated index, and make a comprehensive evaluation in accordance with standard limited.

1) Establishment of Evaluation Factor Set.

$U = \{u_1, u_2, \dots, u_m\}$  is the evaluation factor set, that is the evaluation index system ( $u_i (i = 1, 2, \dots, m)$  shows the  $i^{\text{th}}$  factor which is influential to evaluation objects). The establishment of index system must follow the principles: systematic, scientific comparability and feasibility. After Delphi questionnaires repeatedly surveys, index system is divided into a number of levels according to their attributes. In general, the levels can be classified into three categories.

The highest level: Only one element factor is in this level, which is usually the intended target or desired results in analyzing problems, so also known as the target layer.

The middle level: This level includes intermediate links used for the realization of target level. It can be composed of a number of levels, including the criteria and the sub-criteria, thus, also known as criteria level.

The lowest level: This level includes a variety of measures and decision-making schemes for achieving the target, thus, also known as scheme level.

2) Determination of Weight Set.

The weight set  $W = \{w_1, w_2, \dots, w_m\}$  is determined by AHP, the steps are as follows.

A. Design Delphi questionnaires and compare the index in pairwise at each level, and form comparison matrix. A judgmental matrix, denoted as  $A$ , will be formed using the comparisons. Each entry  $a_{ij}$  of the judgmental matrix is formed comparing the row element  $A_i$  with the column element  $A_j$ .

$$A = (a_{ij})_{n \times n} = \begin{bmatrix} a_{11} & a_{12} & \dots & a_{1n} \\ a_{21} & a_{22} & \dots & a_{2n} \\ \vdots & \vdots & \dots & \vdots \\ a_{n1} & a_{n2} & \dots & a_{nn} \end{bmatrix} \quad (1)$$

The use of the Saaty's 1-9 scale [17] to transform the verbal judgments into numerical quantities representing the values of  $a_{ij}$ . The scale is explained

in Table 4. The judgmental matrix is a reciprocal matrix with  $a_{ij} > 0, a_{ij} = 1/a_{ji}, a_{ii} = 1$ .

**Table 4.** The Fundamental Scale.

The relative important scale	The definition of scale
1	Two activities contribute equally to the objective, Elements $A_i$ and $A_j$ are equally important
3	Experience and judgment slightly favor $A_i$ over $A_j$
5	Experience and judgment strongly favor $A_i$ over $A_j$
7	$A_i$ is favored very strongly over $A_j$ ; its dominance demonstrated in practice
9	The evidence favoring $A_i$ over $A_j$ is of the highest possible order of affirmation
2, 4, 6, 8	Sometimes one needs to interpolate a compromise judgment numerically because there is no good word to describe it
Reciprocals of above	If $A_i$ has one of the above judgments assigned to it when compared with $A_j$ , then, $A_j$ has the reciprocal value when compared with $A_i$

B. Once the judgmental matrix of comparisons of criteria with respect to the goal is available, the local priorities of criteria are obtained and the consistency of the judgments is determined. It has been generally agreed that priorities of criteria can be estimated by finding the principal eigenvector  $\omega$  of the matrix A. That is,

$$Aw = \lambda_{max}\omega, \tag{2}$$

when the vector  $\omega$  is normalized, it becomes the vector of priorities of the criteria with respect to the goal.  $\lambda_{max}$  is the maximum eigenvalue of the matrix A and the corresponding eigenvector  $\omega$  contains only positive entries.

The consistency of the judgmental matrix can be determined by a measure called the consistency ratio (CR), defined as

$$CR = \frac{CI}{RI}, \tag{3}$$

where CI is called the consistency index and RI is called the Random Index.

CI is defined as

$$CI = \frac{(\lambda_{max} - n)}{(n - 1)} \tag{4}$$

RI is the consistency index of a randomly generated reciprocal matrix from the Saaty's

1-9 scale, with reciprocals forced. The RI values for matrices of different sizes are shown in Table 5.

**Table 5.** The average consistencies of random matrices

Size	1	2	3	4	5
RI	0.00	0.00	0.58	0.90	1.12
Size	6	7	8	9	10
RI	1.24	1.32	1.41	1.45	1.49

If CR of the matrix is higher, it means that the input judgments are not consistent, and hence are not reliable. In general, a consistency ratio of 0.10 or less is considered acceptable. If the value is higher, the judgments may not be reliable and have to be elicited again.

3) Establishment of the Evaluation set.

All kinds of total judgment results given by judges form the evaluation set which can be expressed as V, denoted as  $V = \{v_1, v_2, \dots, v_n\}$ .

4) Construct Each Fuzzy Judgment Matrix.

Evaluation of single index is a set of fuzzy mapping  $f : U \rightarrow V$ . The different methods should be taken to determine membership because of the quantitative and qualitative index in the index system which has been established. Find some relevant experts, and evaluate each element of the second layer in the evaluation index system. After the collation of the survey results, it gets single-factor fuzzy judgment matrix.

$$R = \begin{bmatrix} r_{11} & r_{12} & \dots & r_{1n} \\ r_{21} & r_{22} & \dots & r_{2n} \\ \vdots & \vdots & \dots & \vdots \\ r_{m1} & r_{m2} & \dots & r_{mn} \end{bmatrix} \tag{5}$$

5) Comprehensive Evaluation.

Fuzzy comprehensive evaluation matrix can be described as follows

$$B = W \circ R, \tag{6}$$

where “ $\circ$ ” is synthetically computing operator, which uses weighted average based such as  $M(\bullet, \oplus)$ . Fuzzy Mathematics has four models such as  $M(\wedge, \vee)$ ,  $M(\bullet, \vee)$ ,  $M(\wedge, \oplus)$  and  $M(\bullet, \oplus)$  for membership degree conversion, long-term results show  $M(\bullet, \oplus)$  that is widely accepted [18].

### 3. Model Application

This article presents a new risk assessment method for Railway Signal System using FMECA and FAHP, namely Fuzzy-FMECA method. A case study on risk assessment of Interval Signal Control Function for Train Control Center is used to illustrate

the application of the proposed risk assessment method. The procedure of this method is presented in Fig. 2.

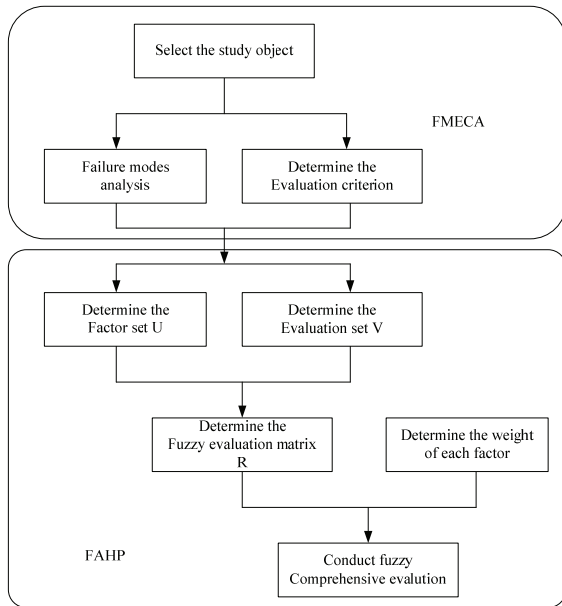


Fig. 2. The procedure of Fuzzy-FMECA.

### 3.1. Application of FMECA

FMECA method is used to identify the risk of Interval Signal Control Function, Based on the characteristics of signal transmission between the functions and the knowledge and expertise of the

expert, the failure modes of Interval Signal Control Function are summarized as four: Lighting control information can not be output, the lighting control output information is incorrect, Lighting control information lags behind seriously, always output the same light control information.

Based on results of failure modes analysis, each failure mode needs to be evaluated and prioritized so that appropriate corrective actions can be taken for different failure modes. The priority of a failure mode is determined through the RPN, which is defined as the probability of the Occurrence, Severity and Detectability. The three factors are all evaluated using the ratings (also called rankings or scores) from 1 to 10, as described from Table 1 to Table 3.

### 3.2. Application of FAHP

#### 1) Establish Evaluation Factor Set.

Based on the above FMECA analysis, the evaluation index set is divided into two levels: the first level, goal set is determined as  $U = \{U_1, U_2, U_3\}$ ,  $U_1$  denotes the Probability of Occurrence,  $U_2$  denotes the Severity, and  $U_3$  denotes the Detectability. The second level, sub goal set is determined as  $U_i = \{u_1, u_2, u_3, u_4\}$ ,  $U_i (i=1,2,3)$ .  $u_1$  denotes the lighting control information can not be output,  $u_2$  denotes the lighting control output information is incorrect,  $u_3$  denotes lighting control information lags behind seriously, and  $u_4$  denotes always output the same light control information. The evaluation index is described in Fig. 3.

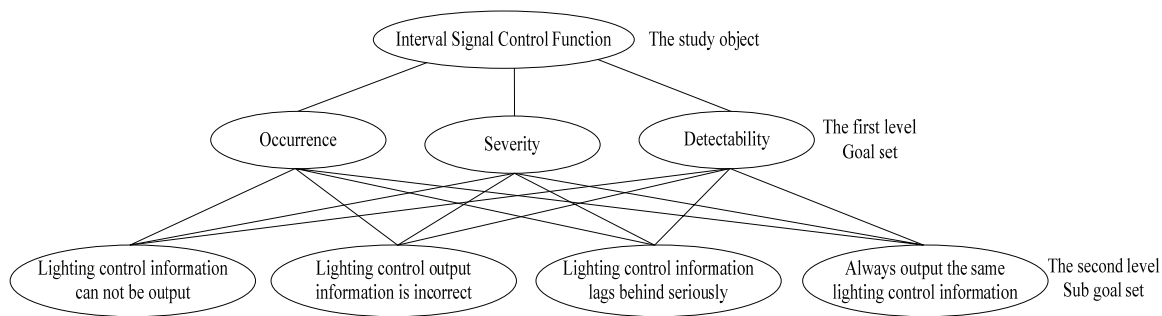


Fig. 3. The procedure of Fuzzy-FMECA.

#### 2) Establish Evaluation Set.

Based on the ratings from 1 to 10, as described from Table 1 to Table 3. The Occurrence, Severity and Detectability are all evaluated.

The evaluation set of factor  $U_1$  is determined as  $V_1 = \{v_{11}, v_{12}, v_{13}, v_{14}, v_{15}\}$ ,  $v_{1j} (j=1,2,\dots,5)$  denote very high, high, moderate, low, remote respectively in terms of probability of the Occurrence.

The evaluation set of factor  $U_2$  is determined as  $V_2 = \{v_{21}, v_{22}, v_{23}, v_{24}, v_{25}\}$ ,  $v_{2j} (j=1,2,\dots,5)$  denote

very high, high, moderate, low, remote respectively in terms of Severity.

The evaluation set of factor  $U_3$  is determined as  $V_3 = \{v_{31}, v_{32}, v_{33}, v_{34}, v_{35}\}$ ,  $v_{3j} (j=1,2,\dots,5)$  denote remote, low, moderate, high, very high respectively in terms of Detectability.

#### 3) Construct Fuzzy Judgment Matrix.

10 experts are found to evaluate the RPNs in terms of these four failure modes, Based on the collation of the questionnaires, the fuzzy judgmental

matrix  $R_1$  can be obtained by the set of fuzzy mapping  $f:U_1 \rightarrow V_1$ , the fuzzy judgmental matrix  $R_2$  can be obtained by the set of fuzzy mapping  $f:U_2 \rightarrow V_2$ , the fuzzy judgmental matrix  $R_3$  can be obtained by the set of fuzzy mapping  $f:U_3 \rightarrow V_3$ .

$$R_1 = \begin{bmatrix} 0.1 & 0.9 & 0 & 0 & 0 \\ 0.3 & 0.6 & 0.1 & 0 & 0 \\ 0.1 & 0.6 & 0.3 & 0 & 0 \\ 0 & 0.5 & 0.5 & 0 & 0 \end{bmatrix}$$

$$R_2 = \begin{bmatrix} 0 & 0.1 & 0.9 & 0 & 0 \\ 0.4 & 0.5 & 0.1 & 0 & 0 \\ 0 & 0.4 & 0.4 & 0.2 & 0 \\ 0.3 & 0.1 & 0.6 & 0 & 0 \end{bmatrix}$$

$$R_3 = \begin{bmatrix} 0 & 0 & 0.5 & 0.3 & 0.2 \\ 0 & 0.7 & 0.3 & 0 & 0 \\ 0 & 0.4 & 0.6 & 0 & 0 \\ 0 & 0.4 & 0.6 & 0 & 0 \end{bmatrix}$$

4) Determine the Weight Set.

Weight Set reflect the magnitude that every factor influences the evaluated target, According to the AHP, pairwise comparisons are used to compare factors based on the Saaty's 1-9 scale, The results of the pairwise comparisons can be used to construct a judgmental matrix, as is shown in Table 6.

**Table 6.** Judgmental matrix and priorities of each failure mode of interval lighting control function.

Intensity of importance	$u_1$	$u_2$	$u_3$	$u_4$	weights
$u_1$	1	1/9	5/21	1/9	0.0382
$u_2$	9	1	29/5	1	0.4314
$u_3$	21/5	5/29	1	5/29	0.0989
$u_4$	9	1	29/5	1	0.4314

According to the formula (2), the maximum eigenvalue  $\lambda_{max}$  can be calculated,  $\lambda_{max} = 4.1264$ . Based on the formula (3) and (4), the results show that the CR of comparison matrix is smaller than 0.1, which satisfies the consistency of the comparison matrix.

Similarly, the weight set  $W$  corresponding to the goal set  $U = \{U_1, U_2, U_3\}$  can be calculated as  $W = \{0.343, 0.351, 0.306\}$ , the weight set  $w$  corresponding to the sub goal set  $U_i = \{u_1, u_2, u_3, u_4\}$ ,  $U_i (i=1,2,3)$  can be calculated as  $w = \{0.0538, 0.6438, 0.0538, 0.2486\}$ .

5) Fuzzy Comprehensive Evaluation

A. Fuzzy Comprehensive Evaluation of First Grade.

The fuzzy comprehensive evaluation of first grade is also called the fuzzy comprehensive assessment of the single factor. It synthesizes contribution to the evaluated value of each grade of a factor, and makes assessment of single factor.

According to the formula (6), the fuzzy comprehensive evaluation of first grade can be obtained as follows,

$$B_1 = w \circ R_1 = (0.2039, 0.59128, 0.20482, 0, 0)$$

$$B_2 = w \circ R_2 = (0.3321, 0.37366, 0.28348, 0.01076, 0)$$

$$B_3 = w \circ R_3 = (0, 0.57162, 0.40148, 0.01614, 0.01076)$$

According to the results of the first grade fuzzy comprehensive evaluation, we can get the conclusions. The Occurrence of the Interval Signal Control Function is taken into account, Based on the calculation, the risk ratio are as follows: 20.39 %, 59.13 %, 20.48 %. According to the maximum membership principle, the Occurrence for the failure modes of the Interval Signal Control Function is high, and the distribution situation of evaluation criterion for probability of the Occurrence is shown as in Fig. 4.

Probability of the Occurrence

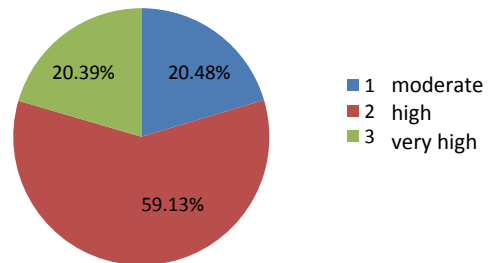


**Fig. 4.** The procedure of Fuzzy-FMECA.

The Severity of the Interval Signal Control Function is taken into account, Based on the calculation, the risk ratio are as follows: 33.21 %, 37.37 %, 28.35 %, 1.08 %. According to the maximum membership principle, the Severity for the failure modes of the Interval Signal Control Function is high, and the distribution situation of evaluation criterion for Severity is shown as in Fig. 5.

The Detectability of the Interval Signal Control Function is taken into account, Based on the calculation, the risk ratio are as follows: 57.16 %, 40.15 %, 1.61 %, 1.08 %. According to the maximum membership principle, the Detectability for the failure modes of the Interval Signal Control Function is low, and the distribution situation of evaluation criterion for Detectability is shown as in Fig. 6.

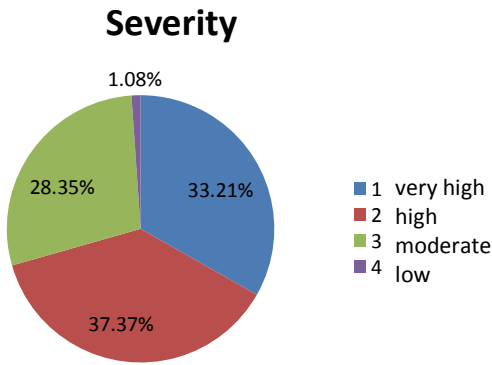


Fig. 5. Distribution situation of evaluation criterion for Severity.

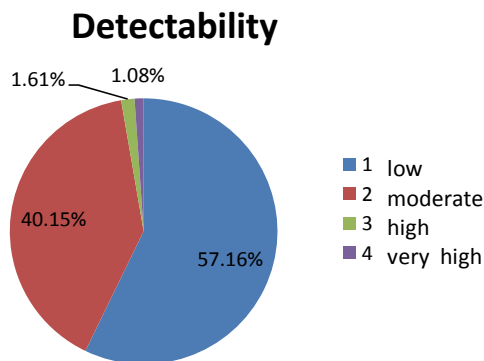


Fig. 6. Distribution situation of evaluation criterion for Detectability.

Based on the results of the first grade fuzzy comprehensive evaluation, the Occurrence for the failure modes of the Interval Signal Control Function is high and the failure modes will lead to the equipment damage, the likelihood of detection is low. Railway maintenance departments should attach importance to the failure moods of the Interval Signal Control Function, the detailed inspection and test plan should be made to ensure that its work is under safe state. However, each failure modes for the risk level of this function is different, in order to integrate the effects of each failure modes on this function and make the results of the risk analysis reliable, the comprehensive risk assessment about this function should be conducted to sequence the failure modes and find out the key failure mode.

B. Comprehensive Risk Assessment

Judgmental matrix can be obtained by conducting the fuzzy comprehensive evaluation of first grade, each fuzzy judgmental matrix can be obtained by extracting the row vectors of the judgmental matrix of each factor. For example, the first row of the judgmental matrix  $R_1$  can be obtained by the set of fuzzy mapping  $f : u_1 \rightarrow V_1$ . By extracting the corresponding row of the judgmental matrix, fuzzy judgmental matrix of each failure mode can be obtained. For example, in view of the failure mode  $u_1$ , the fuzzy judgmental matrix of failure mode  $u_1$  can be obtained after extraction

$$R^1 = \begin{bmatrix} 0.1 & 0.9 & 0 & 0 & 0 \\ 0 & 0.1 & 0.9 & 0 & 0 \\ 0 & 0 & 0.5 & 0.3 & 0.2 \end{bmatrix}$$

The weights of each factor about goal set is calculated as  $W = \{0.343, 0.351, 0.306\}$ , the fuzzy comprehensive evaluation of the failure mode  $u_1$  is obtained as

$$B^1 = W \circ R^1 = (0.0343, 0.3438, 0.4699, 0.0908, 0.0612)$$

In order to integrate the effect of each failure mode on this function, the weighted average model is used to calculate comprehensive risk level of failure mode  $u_1$

$$C^1 = \sum_{i=1}^5 b_i v_i,$$

where  $v_i = i (i = 5, 4, 3, 2, 1)$  and  $b_i = i (i = 1, 2, 3, 4, 5)$  are each element of the matrix  $B^1$ . The comprehensive risk level of failure mode  $u_1$  about this function can be calculated as  $C^1 = 2.89$ .

The same method can be used to calculate comprehensive risk level of other failure modes of Interval Signal Control Function; hence the vector of comprehensive risk level of other failure modes is populated as following

$$C = (C^1, C^2, C^3, C^4) = (2.89, 6.46, 3.47, 3.54)$$

The results show that the failure mode  $u_2$  has the highest risk, which should be prioritized for inspection, the overall risk priority ranking of the four failure modes for Interval Signal Control Function is assessed as  $u_2 > u_4 > u_3 > u_1$ , namely the risk ranking from high to low is the lighting control output information is incorrect, always output the same light control information, lighting control information lags behind seriously, lighting control information can not be output. The ranking of the four failure modes is showed in Fig. 7.

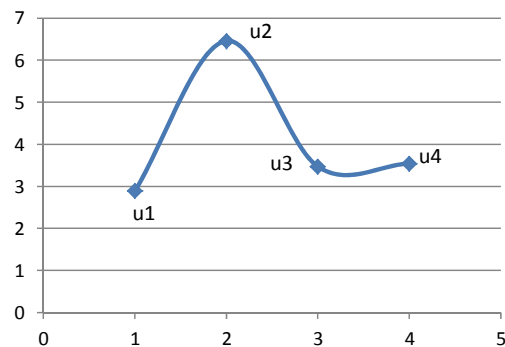


Fig. 7. The overall risk priority ranking of the four failure modes.

In order to verify the reliability of evaluation results, a number of experts who have nothing to do with this algorithm were selected to evaluate this function, the expert scoring results consistent with the calculation results, which confirm the feasibility of this method.

#### 4. Conclusions

Risk assessment results demonstrate the effectiveness of the Fuzzy-FMECA method, through ranking the results of the risk, the risk order of each failure mode can be found on this basis, design personnel and maintenance personnel can master more information of this function, the corresponding improvement measures should be made in connection to the higher risk of the failure mode.

By means of establishing the fuzzy-FMECA comprehensive evaluation model of the Interval Signal Control Function for Train Control Center, The risk assessment results show that the application of Fuzzy-FMECA method can identify the failure modes and evaluate the potential risk of the Railway Signal System more objectively and effectively, which will provide railway risk analysts, engineers with a method to improve their safety management of Railway Signal System and set safety standards.

#### Acknowledgements

This project is supported by Railway Ministry Science and Technology Research and Development Program (2010X003-B).

#### References

- [1]. Simon Zhang, Weihang Wu Human, Factors in the Development of Safety-Critical Railway Systems, *International Railway Safety Conference*, London, 2012, pp. 2-4.
- [2]. Li Cong, The Research of Train Positioning System Security Based on Fault Tree and Petri Net, *Southwest Jiaotong University*, Chengdu, 2012, pp. 1-2.
- [3]. Zhao Yuanzhe, Research on Application of Function Safety Analysis of Train Control Center, *Southwest Jiaotong University*, Chengdu, 2009, pp. 23-56.
- [4]. M. An, W. Lin, A. Stirling, Fuzzy-reasoning-based approach to qualitative railway risk assessment in: *Proceedings of the Institution of Mechanical Engineers, Part F: Journal of Rail and Rapid Transit*, Vol. 220, Issue 2, 2006, pp. 153-167.
- [5]. Health and Safety Executive, Railways (safety case) regulations, *HMSO, HSE Book*, London, 2000.
- [6]. F. Herrera, S. Alonso, F. Chiclana, E. Herrera-Viedma, Computing with words in decision making: foundations, trends and prospects, *Fuzzy Optimization and Decision Making*, Vol. 8, Issue 4, 2009, pp. 337-364.
- [7]. Ben Swarup Medikonda, P. Seetha Ramaiah, Anu A. Gokhale, FMEA and Fault Tree based Software Safety Analysis of a Railroad Crossing Critical System, *Global Journal of Computer Science and Technology*, 2011, pp. 3-4.
- [8]. C. K. Kwong, H. Bai, Determining the important weights for the customer requirement in QFD using a fuzzy AHP with an extent analysis approach, *IIE Transaction*, Vol. 35, 2003, pp. 619-626.
- [9]. T. S. Chan, and N. Kumar, Global supplier development considering risk factors using fuzzy extended AHP-based approach, *Omega*, Vol. 35, 2007, pp. 417-431.
- [10]. Zhang Yadong, Guo Jin, Shan Na, Comprehensive Evaluation of Risk Severity Level of Railway Signal System, *Journal of Southwest Jiaotong University*, Vol. 10, 2010, pp. 1-3.
- [11]. Min An, Yao Chen, Chris J. Baker, A fuzzy reasoning and fuzzy-analytical hierarchy process based approach to the process for railway risk information, A railway risk management system, *Information Sciences*, 2011, pp. 6-7.
- [12]. Yu Pang, Qiang Liao, Ning-Cong Xiao, Hong-Zhong Huang, Fuzzy Criticality Assessment of FMECA for the SADA Based on Modified FWGM Algorithm & Centroid Defuzzification, *Quality, Reliability, Risk, Maintenance and Safety Engineering (ICQR2MSE)*, 2011, pp. 1-3.
- [13]. J. B. Bowles, An assessment of RPN prioritization in a failure modes effects and criticality analysis, in *Proceedings of the Annual Reliability and Maintainability Symposium*, 2003, pp. 380-386.
- [14]. EN50126, Railway Applications: The specification and demonstration of Reliability, Availability, Maintainability and Safety (RAMS).
- [15]. Saaty T. L., The analytic hierarchy process, Priority setting, resource allocation, *McGraw-Hill*, 1980.
- [16]. Zhu Xiaolei, Subjective evaluation of completed, *Southeast University Press*, 2005.
- [17]. Linstone H. A., Turoff M., The Delphi method-techniques and applications, *Addison-Wesley*, New York, 2001.
- [18]. Liu Kaidi, Pang Yanjun, Hao Jimei, Improved multi-level fuzzy comprehensive evaluation for mechanism selection, *Journal of Engineering Design*, Vol. 16, 2009, pp. 88-92.

## Study on Monte Carlo Simulation of Intelligent Traffic Lights Based on Fuzzy Control Theory

ZENG Shengda, \* WU Lurong, JING Lin, WU Bizhi

Computer and Information College, Fujian Agriculture and Forestry University,  
Fuzhou 350002, China

\* Tel.: +86 15005098168

E-mail: wulurong1@sina.com

*Received: 5 June 2013 /Accepted: 25 August 2013 /Published: 30 September 2013*

---

**Abstract:** Based on the traffic flow pattern in single intersection, this paper advances a design method for intelligent traffic lights in the state of stochastic dynamic change of traffic flow by employing the Fuzzy Control Theory. The application of fuzzy control technology to achieve the traffic lights control system not only breaks the traditional mechanical models but also manages to simulate intelligence control system in which the traffic is directed by the police, making possible signal conversion for different situations and optimum delay time of green light. It is proved that the fuzzy control system can effectively reduce the delay time length of waiting vehicles. In consideration of the randomness and robustness of traffic flow, this paper employs the Monte Carlo method in combination with MATLAB to simulate, which proved to be more effective than the traditional control method. It significantly increases the utilization rate of traffic, thereby generating considerable economic benefits. *Copyright © 2013 IFSA.*

**Keywords:** Single intersection, Fuzzy control, Intelligent traffic lights, Monte Carlo, Simulation.

---

### 1. Introduction

With the rapid development of automobile industry, more and more automobile enterprises began to set foot in the field of automobile intellectualization and apply cutting-edge Information Technology to the automobile and its control. According to relevant statistics, over 90 % of innovation in automotive industry is related to automobile intelligent system. Intellectualization is the trend of automobile's future development and is considered as a revolution in the process of automotive technology development. It is an important and effective means to gain a niche in the future automobile market. Although the automobile intelligent technology has reached a relatively mature stage, the road management cannot be reformed once

and for all. The congestion problem has become increasingly prominent and the intersection is the most congested section, where traffic jam is quite often seen. Phenomenon of 2~3 hours congestion is quite common in metropolis like Beijing, Shanghai and Shenzhen. Reform of traffic rules since this year particularly poses a grave challenge to the traffic control. As a result, ideas of using high-tech systems such as intelligent, fuzzy, automation to solve the problems of road traffic are emerging.

Referring to the realistic data of China's traffic situation, considering time difference of traffic flow in different regions with periodic regularity, taking into account of length of the waiting vehicles in stop way of intersection, based on the theory of intelligent fuzzy control and with the help of computer simulation, this paper sets up an automated multi-

phase intelligent traffic control system and establishes a more effective control system compared with the induction time control. The control system is designed to make the vehicle at the intersections wait for the shortest time, thereby reducing their passing time. The control system has the following characteristics:

- 1) Adopting statistical view, combining the past traffic volume and statistical analysis of computer data to predict real-time traffic;
- 2) Adopting fuzzy control method, taking prediction of real-time traffic flow as input condition to control the traffic lights;
- 3) The control methods used have feedback self-directed learning function, and have strong sensitivity to disturbance of special time quantum.

## 2. Analysis of Intelligent Traffic Signal Control

Time delay distribution of traffic light in single intersection is determined by traffic flow in different intersections. Fig. 1 is the single intersection traffic flow chart.

All of the 4 directions in the three-lane road single intersection have three kinds of traffic flow direction, namely, left, right, straight on [1]. In the control of time delay distribution of traffic light in single intersection, this paper takes into account the effect of queue length of detained traffic flow at intersection during red light and the passing number of vehicles during green light on time delay distribution and draws up corresponding fuzzy control rules, constructs the traffic light intersection

fuzzy controller, and achieved the delay timing control of intersections.

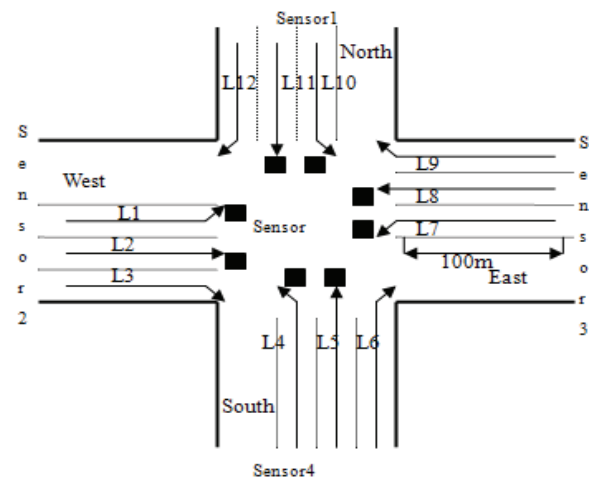


Fig. 1. Single intersection traffic flow chart.

According to the analysis of the above traffic flow structure chart of single intersection, considering the effect of queue length of detained traffic flow during red light and the passing number of vehicles during green light on time delay distribution, in realistic control, traffic flow in rush hours and in slack periods are in random change. Fig. 2 is flow chart of overall control feedback of traffic light, which enables the fuzzy controller of traffic light to accomplish intelligent artificial feedback timing regulation at different stages, so as to shorten the time of traffic congestion.

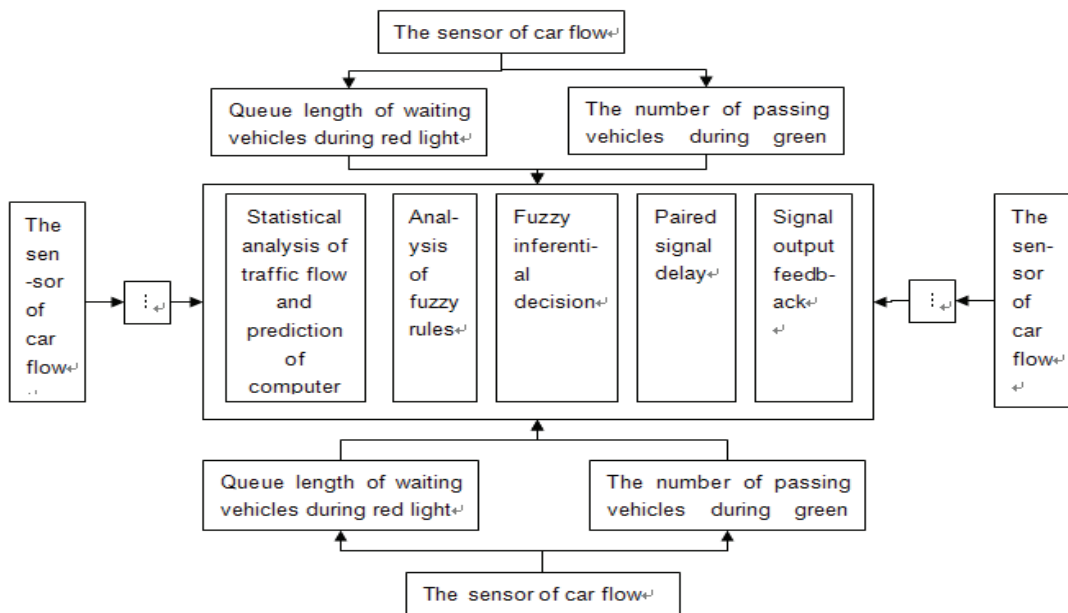


Fig. 2. Flow chart of overall control feedback of traffic light.

### 3. Model Design of Intelligent Traffic Light Control

#### 3.1. Analysis of Traffic Flow Phase and the Length of Queue

Since the signal control systems of traffic light in the past generally didn't consider the phase change, we take a periodic change control of "four phase" into consideration in order to cater to the random timing distribution of intelligent automation in different states. Fig. 3 is the traffic patterns of 4 phases. This paper adopts the improved control method of 4 phases in random sequence, based on the statistical analysis of sensor traffic flow, uses phase fuzzy optimization control to calculate and analyze to determine the execution phase of the next moment [3].

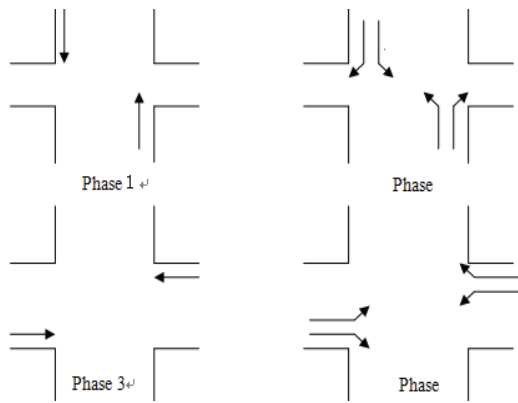


Fig. 3. Phase traffic patterns.

In Fig. 1,  $L_i, (i = 1, \dots, 12)$  represents the current length of fleet in different lanes. The maximal length

that passes the intersection in current moment is called length of passage and the maximal length of two fleets that pass in the phase next moment is called waiting degree.

Therefore, the length of passage and value of waiting length of 4 phases can be obtained according to the traffic patterns of 4 phases [2].

#### 3.2. The Fuzzy Delay Control Rule of Traffic Light and its Quantification

Use the theoretical achievements of fuzzy controller to turn the control strategy described by nature language into fuzzy control rules in order to realize fuzzy control.

In this regard, the variable that is used for fuzzy control has the following 3 parts: fuzzification, fuzzy control rules and defuzzification.

Use the theoretical achievements of fuzzy controller to turn the control strategy described by nature language into fuzzy control rules in order to realize fuzzy control.

In this regard, the variable that is used for fuzzy control has the following 3 parts: fuzzification, fuzzy control rules and defuzzification [4, 5].

In fuzzy control, input is decided through considering the queue length of the current phase and the next phase. The queue length consists of passing queue length and waiting queue length  $L$ ; Output is the delay time  $T$  of green light. Set the distance of sensor as 100 m, load length of every queue phase as 4m and the traffic flow of each phase as 50 vehicles. It follows that the domain of discourse of the passing queue length and waiting queue length in question is  $[0, 54]$ ; since the shortest delay time of green light is 8 seconds and the longest 90 seconds, the domain of discourse of delay time during green light is  $[8, 90]$ .

Table 1. Passing queue length and waiting queue length of four phases.

Phase	Traffic queue length	Wait length
1	Max $(L5+L11)$	Max $(L1+L3+L7+L9, L4+L6+L10+ L12, L2+ L8)$
2	Max $(L4+L6+L10+L12)$	Max $(L1+L3+L7+L9, L5+L11, L2+L8)$
3	Max $(L2+L8)$	Max $(L1+L3+L7+L9, L5+L11, L4+L6+L10+L12)$
4	Max $(L1+L3+L7+L9)$	Max $(L5+L11, L4+L6+L10+L12, L2+L8)$

Fuzzifying the input and output, we can get:

The basic domain of discourse of passing queue length is  $\{3, 6, 9, 12, 15, 18, 21, 24, 27, 30, 33, 36, 39, 42, 45, 48, 51, 54\}$ , the basic domain of discourse of waiting queue length is  $\{3, 6, 9, 12, 15, 18, 21, 24, 27, 30, 33, 36, 39, 42, 45, 48, 51, 54\}$ , the basic domain of discourse of delay time during green light is  $\{8, 12, 16, 20, 24, 28, 32, 36, 40, 44, 48, 52, 56, 60, 64, 68, 72, 76, 80, 84, 88, 90\}$ . When it comes to red light, compare the traffic flow of the east and west straight-on lanes and choose the larger one.

Then, if the traffic flow at last 8 seconds is less than 5 vehicles, reduce the next-round green light time quantum by 4 seconds [6-7]; if more than 10 vehicles, increase by 4 seconds; if within 5-10 vehicles, the next-round green time quantum remains unchanged. (As shown in Fig. 2)

On the amount of input and output, we set up the model of fuzzy subset:  $\{NB(\text{very few}), NS(\text{few}), ZE(\text{Medium}), PS(\text{many}), PB(\text{plenty})\}$ [8] and get Table 3.

**Table 2.** Time control of traffic flow before the end of green light.

Order number	Traffic flow	Green time of next round
1	Less than 5 vehicles	Reduced by 4seconds
2	5-10 vehicles	Unchanged
3	More than 10 vehicles	Increased by 4 seconds

**Table 3.** The rule table of fuzzy delay control.

		T				
		NB	NS	ZE	PS	PB
L	NB	NB	NB	NB	NB	NB
	NS	NS	NB	NB	NB	NB
	ZE	ZE	NS	NS	NB	NB
	PS	PS	ZE	ZE	NS	NB
	PB	PB	PS	ZE	ZE	ZE

### 3.3. The Rules of Fuzzy Delay Control and Analysis of Matlab Program

Based on the above principles, we can set the appropriate parameters and consider the probability distribution of traffic flow that accord with Queuing Theory. (Poisson distribution). Supposing that the traffic flow accords with the random quantity of Poisson distribution, then calculate the number of waiting vehicles and stopping length of time during red light in the west and the number of waiting vehicles and total stopping length of time in both the east and the west, generating the red light waiting time and number of waiting vehicles in each intersection. It's therefore defined that the next red light time quantum is the sum of green light time quantum of the rest three intersections.

This paper adopts the fuzzy inference method of Mamdani [6], the arithmetic of conjunctions "and", "or" and "also" of MATLAB fuzzy logic toolbox and fuzzy implication and comprehensive defuzzification are as follow [9]:

- 1) The calculation of "and"

$$\mu_{A \otimes B}(N, W) = \min(\mu_A(N), \mu_B(W))$$

- 2) The calculation of "or"

$$\mu_{A \oplus B}(N, W) = \max(\mu_A(N), \mu_B(W))$$

- 3) The calculation of Implication

$$\mu_{A \rightarrow B}(N, W) = \min(\mu_A(N), \mu_B(W))$$

- 4) The calculation of Aggregation

$$\mu_{A \times B}(N, W) = \max(\mu_A(N), \mu_B(W))$$

- 5) The calculation of Defuzzification

Employing Center of Area, that is, determine the fuzzy set membership function curve and center of abscissa surrounding area and choose the center's corresponding abscissa value as the representative value of the fuzzy set [10].

The following are some Matlab procedure codes:

```

while t1_WEST < x_1a
while v1_WEST <= x_1a
v1_WEST = v1_WEST + CAR1_WEST(i1_WEST)
T)
i1_WEST = i1_WEST + 1
while v1_WEST >= x_1a - m
if v1_WEST > x_1a
break
end
j1_WEST = j1_WEST + 1
v1_WEST = v1_WEST + CAR1_WEST(i1_WEST)
T)
i1_WEST = i1_WEST + 1
t1_WEST = t1_WEST + 1
end
end
t1_WEST = t1_WEST + 1
end
...
d = d1 + d2 + d3 + d4
s = s1 + s2 + s3 + s4
p = (y_1a + y_2a + y_3a + y_4a) / (d + s)
l = (d + s) * 60 / 7
y = y_1a + y_2a + y_3a + y_4a

```

Firstly, through the theoretical analysis and construction of traffic light fuzzy neural network of traffic flow, we establish the expert fuzzy control rule library; and by constant adjustment and learning in the MATLAB fuzzy system (FIS) [11]-[12], we achieve the queue length membership function and green light delay membership function value and map out the corresponding membership function diagram [4], as shown in Fig. 4:

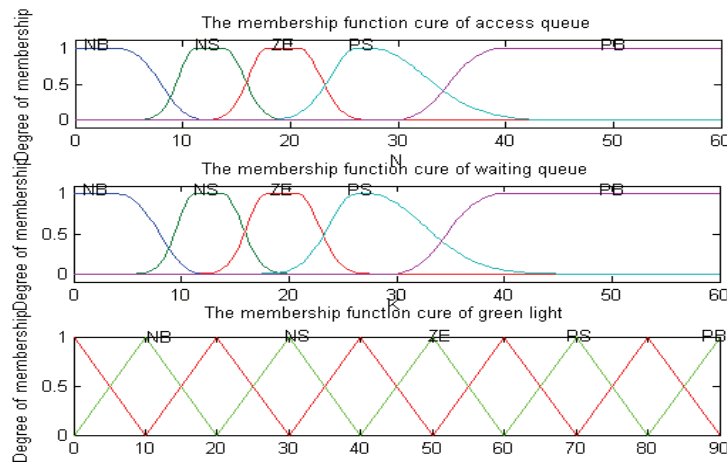


Fig. 4. The membership function diagram of queue length in traffic flow and the delay time during green light.

### 4. Monte Carlo Simulation

In order to reflect the advantages of intelligent traffic light control system, this paper proposes empirical method of control algorithm and combines real-time data to carry out Monte Carlo system simulation. According to the required intelligent control system features, this paper works out a Matlab simulated program and makes a simulation study on the traffic flow and control system, crystallizing the entire system to make a more direct and obvious comparison with the traditional traffic light.

At first, we use the date obtained from an intersection in Cangshan district of Fuzhou to carry out fuzzy control and compare the statistical data with the traditional control method, as shown in the following Table 4:

Table 4. Comparison of the number of waiting vehicles at the intersection for 20 minutes.

Intersection	Traditional traffic light	Intelligent traffic lights
East	50	38
South	15	12
West	128	112
North	39	30

Obviously, we find that the intelligent traffic light control is superior to traditional traffic light control. In order to reflect the uncertainty and mathematical regularity of traffic flow, we use Monte Carlo method in combination with MATLAB to carry out simulation data. Simulation of traffic flow is based on on-the-spot and long-time statistical traffic flow volume, MATLAB simulation and Poisson distribution rule, generating a large amount of simulation data. In MATLAB, we can use the function of POISSFIT (X) to obtain the sample X, and calculate the point estimate of parameter  $\lambda$  in Poisson distribution, thereby calculating the Poisson

parameter estimation function. We can use [LAMBDAHAT, LAMBDA CI] = POISSFIT(X, ALPHA) to get the value of sample X. Calculate the parameter point estimate of Poisson distribution LAMDA and its confidence coefficient and we get interval estimation  $100(1-ALPHA)$ . Use the sample data to replace X in matrix form and we get the sample value of ALPHA and then use the formula  $R = POISSRND(LAMBDA, M, N)$  to get Poisson distribution  $\lambda = LAMDA$  and random number matrix of line M and row N. Generally, the M in random number matrix is set as 1, then in the process of determine N, a certain amount of random number can be simulated. Here we set N as 10000, that is, there will be a random number of 10000 vehicles passing through the intersection.

According to the above simulation analysis, it is evident that no matter the input flow and output flow are known/certain or unknown/random, the traditional control is inferior to the intelligent fuzzy control.

### 5. Conclusion

The signal time delay controller of intelligent fuzzy traffic light, which is based on Monte Carlo theory and fuzzy mathematics control method, is practical in traffic control at single intersections. This paper puts forward a preferable intelligent control project of traffic light. Since this project is not subject to time, region or weather, strictly conforms to traffic rules, and has memory and learning function, it has universal practical applicability.

No matter in rush hours or slack hours of traffic, imbalance of traffic flow in different direction of the same phase will not increase the vehicle's waiting time in other phases or the average vehicle's delay time. This is a big advantage of this project. This paper just analyzes the traffic light situation at single intersections, and the design of traffic light at multiple intersections will be extended and taken as the future research.

Table 5. Monte Carlo simulation results.

The last N second of green light	Traditional traffic light		Intelligent traffic light	
	The number of stopping vehicles	The average vehicle stopping time	Number of stopping vehicles	Average stopping time
1	1086	189.3	924	147.4
2	919	148.4	813	129.5
3	853	125.4	787	108.7
4	732	109.6	642	106.3
5	658	94.7	532	84.4
6	692	95.2	586	93.5
7	774	112.1	667	90
8	832	123.2	795	109.8
9	982	152.8	960	134.6
10	1053	186.3	1024	162.4

## Acknowledgements

The research work was jointly supported by National Innovation Practice of Undergraduate (Grant No. 201210389017), and Fujian province Innovation Practice of Undergraduate in China (Grant No.111ZC1258).

## References

- [1]. Xiaoguang Yang, Bailei Chan, Guoxiong Peng, Study on pedestrian traffic control signal settings, *Journal of China Highway and Transport*, 14, 1, 2001, pp. 73-80.
- [2]. Zhiyong Liu, Intelligent traffic control theory and its application, *Science Press*, Beijing, 2000.
- [3]. Weikang Qiu, Weizhi Wang, Traffic signal control based on fuzzy neural network, *Jiangsu Electric*, 04, 2008, pp. 22-26.
- [4]. Xiaoli Wu, Zhehui Lin, MATLAB aided fuzzy system design, *Xi'an University of Electronic Science and Technology Press*, Xi'an, 2002.
- [5]. Jing Li, Fuzzy control and Simulation of traffic signal intersection, *Micro Computer Information*, 22, 7, 2006, pp. 33-35.
- [6]. Yassine Hadjadj Aoul, Ahmed Mehaoua, Charalabos Skianis, A fuzzy logic-based AQM for real-time traffic over internet, *Science Direct*, 6, 2007, pp. 4617-4633.
- [7]. Chou Chil-H Sun, Teng Jen-Chao, A fuzzy logic controller for traffic junction signals, *Information Sciences*, 143, 1, 2002, pp. 73-86.
- [8]. Hallapuro A., Lappalainen V., Hamalainen D., Performance Analysis of Low bit Rate H. 26L Video Encoder, in *Proceedings of the IEEE International Conference on Acoustics, Speech and Signal Processing (ICASSP'01)*, 2, May 2001, pp. 1129-1132.
- [9]. Tarte S. M., Talib H., Ballester M. Evaluating Partial Surface Matching for Fracture Reduction Assessment, in *Proceedings of the 3<sup>rd</sup> IEEE International Symposium on Biomedical Imaging: Macro to Nano*, USA, 4, 2006, pp. 514-517.
- [10]. Jee-Hyong Lee, Hyung Lee-Kwang, Distributed and Cooperative Fuzzy, Controllers for Traffic Intersection Group, *IEEE Transactions on System, Man and Cybernetics*, 29, 1999, pp. 263-271.
- [11]. Richardson B., Rodriguez D., ITS in developing countries: strategic opportunities, *ITS Quartely*, 5, 3, 1997, pp. 7-15.
- [12]. Carlsson C., Fuller R., Optimization under fuzzy if then rules, *Fuzzy Sets and Systems*, 11, 4, 2001, pp. 111-118.

## Computational-geometry-based Plant Organs Classification and Foliage 3D Reconstruction from Point Cloud Data

**Ting Yun, Mingxing Gao, Yanming Wang, Xiaofeng Liu**

Nanjing Forestry University, Longpan Road, No.159, Nanjing, 210037, China

Tel.: 13585100839, fax: 025-85427687

E-mail: njyunting@qq.com, liuxiaofeng.njfu@hotmail.com

*Received: 5 June 2013 / Accepted: 25 August 2013 / Published: 30 September 2013*

---

**Abstract:** In recent years Terrestrial Laser Scanner (TLS) is widely used in complex scene survey and space objects measurement, however, due to the trees' irregular and complex morphology, also the scanning results be effected by the wind blowing and occlusion effect, so quantifying the 3-D morphology structure and forestry index of an individual tree or a forest stand from Point Cloud Data (PCD) is a challenging task. In this paper, the computer theory is combined into our approach. Firstly the covariance matrixes based on neighborhood information are constructed to retrieve the feature vectors of every PCD, including normal vector, torsion and curvature from the scanning data. Secondly the LLE manifold-learning method is adopted for dimensionality reduction of PCD features, then identification and classification of different plant organs are achieved. Finally orthogonal least squares algorithm about three-dimensional surface fitting is presented to remove deviation caused by leaf jitter, then the whole PCD of single leaf are mapped onto one three-dimensional surface, next, many triangles are used to form the foliage area and Leaf Area Index (LAI) can be calculated based on the delaunay triangulation algorithm. In this paper we apply computer theory to overcome the shortcomings of TLS in forestry application, automatically and nondestructively achieve the classification of different plant organs and 3-D reconstruction of real foliage, most importantly, this work provide a theoretical foundation for retrieving LAI and forestry parameters from PCD obtained with a TLS. *Copyright © 2013 IFSA.*

**Keywords:** Terrestrial laser scanning (TLS), Point cloud data (PCD), Plant organs classification, Foliage 3-D reconstruction.

---

### 1. Introduction

The forest has an irreplaceable status in regulating the Earth's environment of human habitation and slowing down global environmental degradation trend, forest surveying and forestry information acquisition become an important issue in recent years, how to take fine measurement of quantitative forest inventories and provide an effective way to improve the accuracy and efficiency of

forestry data collection is the main task in forestry management.

In recent years, there are several methods of obtaining trees morphology structure and measuring trees parameter. Firstly, plant canopy analyses and traditional mechanical instruments for trees measurement are inefficient and be affected by leaf overlap and aggregation, the measurement results also be influenced by sun zenith angle and mathematics calibration. Hyper-spectral remote

sensing [1, 2] measure the canopy from top down and usually include a recorded reflection from the ground, it is capable of producing one-shot topographic and spectral intensity information, which will enable a simultaneous study of structural and biochemical vegetation parameters, but hyper spectral instrument be affected by atmospheric conditions and accuracy of aerial photography, also it is not theoretically support by modern physical model. Airborne LIDAR [3, 4] can monitor plant biomass and growth, but if only rely on the finitely waveform of echo signal with attenuation and noise, we can not accurately estimate individual vegetation features. The TLS scans [5, 6] pulse laser over the full upper hemisphere and part of the lower hemisphere by using a mirror rotating in the vertical plane (the zenith scan) and a rotation of the instrument to provide azimuthal coverage. The time-dependent intensity of reflected light from each laser pulse is recorded, providing a waveform that may include responses from multiple targets. The laser produces an energy pulse that is distributed in time. The shape of the outgoing pulse is consistent and has a well defined peak. Reflections from targets are time-delayed copies of this pulse, where the range to the target is simply inferred from the arrival time of the pulse peak relative to the peak of the outgoing pulse. TLS can mosaic the multi-view scanning data, thereby ensure scanning data completeness and reduce the impact of foliage cover, eventually get 3D point cloud model of real stumpage. Due to high precision and high density characteristics of TLS, the TLS-based method is taken as a most appropriate method for tree measurement, it can also serve as a calibration tool for airborne laser scanning and other measurement application with ground sampling.

In recent years, there are several ideologies to calculate tree parameters from TLS point clouds.

1) Different space partitioning method and projection strategy about PCD are used to calculate vegetation architecture and foliage assemblage in each space cell, then to indicate trees' growth index [7, 8]. Such as Zheng [9] presented a new voxel-based method with line quadrat direction to retrieve the biophysical characteristics of the forest canopy including extinction coefficient, gap fraction, overlapping effect along the direction of the line quadrat and estimated effective leaf area (ELA) from TLS point cloud data. Bélanda [10] investigated the use of a voxel-based approach to retrieve leaf area distribution of individual trees from PCD and provided vertical as well as radial distributions of leaf area in individual trees to estimate savanna vegetation structural parameters with a high level of detail. Zheng [11] developed circular point cloud slicing to explore the spatial variation of point density for both azimuthal angular and radial directions; the result showed comprehensive scan combination could fully represent the canopy structure and structural variation of the heterogeneous forest stand.

2) The physical model and forestry formula are applied to PCD analyzing for forestry index calculation. Such as Lovella [12] used Semi-analytic Pgap and Radiative Transfer (CanSPART) model to predict tree gap probability (Pgap) profiles, then a canopy structure model based on simple geometric forms and parameterized with plot-scale statistical biometric data were used to predict gap probability (Pgap) profiles. Experimental result showed that his mathematical model about PCD calculation performs better in clumped canopies than a simple exponential model. Zheng [13] combined beer laws to present a new method that using total least square fitting techniques to reconstruct the normal vectors, then indirectly and nondestructively retrieved foliage elements' orientation and distribution from PCD obtained using a terrestrial laser scanning (TLS) approach.

3) Computer graphics and computer vision theory are studied for TLS point cloud processing. Xu [14] presented a semi-automatic method for realizing the sparse point clouds of range scanned trees transform to full polygonal models, a skeleton of the trunk and main branches was produced based on the scanned point clouds, then steps were taken to synthesize additional branches to produce plausible support for the tree crown, subsequently, allometric theory was used to estimate appropriate dimensions for each branch, at last, leaves were positioned, oriented and connected to nearby branches. Liang [15] presented a fully automatic stem-mapping algorithm, he used a series of cylinders to built up trees' stem model, result show in a relatively dense managed forest, the majority of stems could be located by proposed automatic algorithm.

In summary, three questions are existed in tree's LAI calculation:

1) How to extracted and distinguished the leaf from the flourishing tree's PCD with enormous various leaf inclination angle and morphology.

2) The scanning PCD exist deviation and jitter due to disturbance and occlusion of external environmental conditions, so how to remove the measurement deviation and design the algorithm to get real deformation foliage data is to be considered.

3) TLS can obtain discrete point cloud data, while the manifestation of real leaves is in the form of three dimensional surfaces, so how to design a reasonable point to plane transform algorithm is to be solved.

Due to extreme complex morphology of trees, in order to retrieve the biophysical characteristics of real stumpage including LAI, branches location, crown density, tree trunk shape etc, it needs the combination of computer vision and graphics theory to explore hidden information from PCD. In this paper the manifold learning LLE method is adopted to classify and identify different tree organs, then the least squares surface fitting method with orthogonal distance is proposed to eliminate deviation which caused by wind and occlusion, then PCD projection on the Z axis without spatial morphology distortion is achieved. Finally,

triangulation algorithm for foliage modeling is designed to derive real tree leave 3D model.

## 2. Plant Organs Classification Based on Manifold Learning

### 2.1. Characteristics of PCD Calculation

In this section, the spatial distribution properties of the laser points are studied. Trees' PCD are defined by means of features calculation such as flatness, direction, and shape. Due to geometrical form difference, different organs of trees share dissimilar attributes, therefore, a robust feature extraction and classification method is needed to estimate stumpage parameters when branches or foliages points are present. In this step, the properties of point distribution, such as flatness and normal vector direction, are used to distinguish the trees' organs from the huge amounts of irregular PCD. Consequently, the method about feature calculation is given below.

For a point  $p_i = (x_i, y_i, z_i)^T$  in the point cloud  $P$ ,  $P \subset R^3$ , its surrounding finite space is defined by  $N$  nearest points  $p_j = (x_j, y_j, z_j)^T$  with mean  $u = (1/N) \sum_{j=1}^N p_j$ , the covariance matrix  $C_p$  of points  $p_j$  is defined by  $C_p = \frac{1}{N} \sum_{j=1}^N (p_j - u)(p_j - u)^T$ , the point set  $p_j$  itself

does not have context information. The eigenvalue & eigenvector approach is usually employed to study point distribution, by utilizing eigenvalue decomposition, a new coordinate system can be defined, where point directions are given by eigenvectors and point variances along axes are given by the corresponding eigenvalues. Let  $e_i$  be the eigenvector and  $\lambda_i$  be the corresponding eigenvalue, where  $i = 0, 1, 2, \dots$  and  $\lambda_0 \leq \lambda_1 \leq \lambda_2$ . In this new coordinate system,  $e_0$  gives the direction in which the points exhibit the least variance and  $e_2$  gives the one in which the points exhibit the most variance. Where a surface structure is spanned in the neighborhood,  $e_0$  approximates the normal vector at point  $p_i$ . For convenience,  $e_0$  is denoted as the normal vector in the following. The eigenvalue  $\lambda_i$  quantitatively shows the data variance along the axis  $e_i$ , or the compactness of the point distribution along the axis. Therefore, flatness  $F_l$  can be defined as  $F_l = 1 - \frac{\lambda_0}{\lambda_0 + \lambda_1 + \lambda_2}$ , which shows the significance of the point distribution in two main directions. A high value of  $F_l$  means that the point is approximately on a planar surface.

After the above analysis, a series of features about each point  $p_i$  is obtained, described as  $c_{p_i} = \{x_i, y_i, z_i, r_i, g_i, b_i, e_{ix}, e_{iy}, e_{iz}\}$ , where  $r_i, g_i, b_i$  is the color value and  $e_{ix}, e_{iy}, e_{iz}$  represent the normal vector of  $p_i$ , then these features are taken into the classification algorithm to realize different tree organs classification.

### 2.2. PCD Classification Based on LLE Framework

LLE [16] maps a data set  $C_p = \{c_{p_1}, c_{p_2}, c_{p_3}, \dots, c_{p_m}\}$ ,  $c_{p_i} \in R_d$  globally to a data set  $Y = \{y_1, y_2, y_3, \dots, y_n\}$ ,  $y_i \in R^m$ . In previous section calculating  $c_{p_i}$  has been described, assuming the data lies on a nonlinear manifold which locally can be approximated linearly, it uses two stages:

1) locally fitting hyper planes around each sample  $c_{p_i}$ , based on  $k$  nearest neighbors of point  $p_i$ , and calculating reconstruction weights;

2) finding lower dimensional co-ordinates  $y_i$  for each  $c_{p_i}$ , by minimizing a mapping function based on these weights. In stage 1, the cost function minimized is:

$$\min \varepsilon(W) = \sum_{i=1}^n \left| c_{p_i} - \sum_{j=1}^k w_j^i c_{p_{N(j)}} \right|^2 \quad (1)$$

i.e. how well each  $p_i$  can be linearly reconstructed in terms of its neighbors  $p_{N(1)} p_{N(2)} \dots p_{N(k)}$ . For one vector  $c_{p_i}$  and weights  $w_j^{(i)}$  that sum up to 1, this gives a contribution

$$\varepsilon_i(W) = \left| \sum_{j=1}^k w_j^{(i)} (c_{p_i} - c_{p_{N(j)}}) \right|^2 = \sum_{j=1}^k \sum_{m=1}^k w_j^{(i)} w_m^{(i)} Q_{jm}^{(i)}, \quad (2)$$

where  $Q^{(i)}$  is the  $k \times k$  matrix

$$Q_{jm}^{(i)} = (c_{p_i} - c_{p_{N(j)}})^T (c_{p_i} - c_{p_{N(m)}}) \quad (3)$$

Let  $R^{(i)} = (Q^{(i)})^{-1}$ . Solving the least squares problem (Eq. (2)) with constraint  $\sum_j w_j^{(i)} = 1$  gives:

$$w_j^{(i)} = \sum_{m=1}^k R_{jm}^{(i)} / \sum_{p=1}^k \sum_{q=1}^k R_{pq}^{(i)} \quad (4)$$

In practice, a regularization parameter  $r$  will have to be used for  $Q^{(i)}$  before inversion (as its rank is  $d$ , certainly for  $k > d$ ):  $R^{(i)} = (Q^{(i)} + rI)^{-1}$ .

Interestingly,  $Q^{(i)}$  can also be calculated based on just the squared Euclidean distance matrix  $D$  between all samples in  $C_p$ :

$$Q_{jm}^{(i)} = \frac{1}{2} (D_{i,N(j)} + D_{i,N(m)} - D_{N(j),N(m)}) \quad (5)$$

In stage II, the weights  $w$  are fixed and new m-dimensional vectors  $y_i$  are sought which minimize the criterion:

$$\min \varepsilon_{\Pi}(Y) = \sum_{i=1}^n \left| y_i - \sum_{j=1}^k w_j^{(i)} y_{N(j)} \right|^2 \quad (6)$$

The  $w_j^{(i)}$  can be stored in a  $n \times n$  sparse matrix  $W$ , where  $W_{i,N(j)} = w_j^{(i)}$ . Re-writing Eq. (6) then gives

$$\varepsilon_{\Pi}(Y) = \sum_{i=1}^n \sum_{j=1}^n M_{ij} y_i^T y_j = \text{tr}(YMY^T), \quad (7)$$

where  $M$  is an  $n \times n$  matrix found as  $M = (I - W)^T (I - W)$  and  $Y$  contains the  $y_i$ 's as its columns. To be able to solve this problem, the covariance matrix of the  $y$ 's can be constrained to be identity. Finding  $Y$  then becomes a well-known problem: minimize  $\text{tr}(YMY^T)$  with constraint  $\frac{1}{n} YY^T = I$ . All eigenvectors of  $M$  are solutions, the eigenvector with the smallest eigenvalue corresponds to the mean of  $Y$  and can be discarded to enforce  $\sum_{i=1}^n y_i = 0$ . The next  $m$  eigenvectors then give the  $Y$  that minimizes Eq. (7).

By LLE classification, the high dimensional PCD can be projected to a low-dimensional plane, on this plane we take finely classification according to the data distribution and distinguish the different plant organs through back projection to the original high dimension data space. In this way, classification and identification of one tree's PCD have finished, then, the results prepare for leaf three dimensional modeling.

### 3. Foliage Reconstruction Using Orthogonal Least Squares Fitting and Delaunay Triangulation Algorithm

#### 3.1. Surface Fitting Based on Least Squares Method

The method of least squares requires that the vertical distance from each observed data point to the

model surface be such that the sum of the squares of these distances is a minimum.

Given the data set:  $\{(x_1, y_1, z_1), (x_2, y_2, z_2), \dots, (x_n, y_n, z_n)\}$  calculate coefficients  $a_1, a_2, \dots, a_m$  in the fitting equation of quadric surface:

$$f_3(l_i) = f_3(x, y) = a_1 + a_2x + a_3y + a_4x^2 + a_5xy + a_6y^2 + a_7x^3 + a_8x^2y + a_9xy^2 + a_{10}y^3 \quad j = 1, 2, \dots, 10. \quad (8)$$

and the fitting equation of cubic surface is described as:

$$f_2(l_i) = f_2(x, y) = a_1 + a_2x + a_3y + a_4x^2 + a_5xy + a_6y^2, \quad (9)$$

where  $l_i = (x_i, y_i)$ , so the sum of squared errors

$$E(f) = \sum_{i=1}^n (f(l_i) - z_i)^2 = \sum_{i=1}^n \left( \sum_{j=1}^m a_j f(l_i) - z_i \right)^2 \quad (10)$$

is minimized. Then set up the equations:

$$\partial E(f) / \partial a_j = 0 \quad j = 1, 2, \dots, m \quad (11)$$

Re-writing Eq. (8) then gives

$$\begin{aligned} \frac{\partial E(f)}{\partial a_j} &= 2 \sum_{i=1}^n \frac{\partial f(l_i)}{\partial a_j} [f(l_i) - z_i] = 2 \sum_{i=1}^n b_i^j [f(l_i) - z_i] = 0 \\ &= 2 \sum_{i=1}^n [b_i^j (a_1 b_i^1 + a_2 b_i^2 + \dots + a_m b_i^m) - b_i^j z_i] \\ &= 2 \left[ a_1 \left( \sum_{i=1}^n b_i^j b_i^1 \right) + a_2 \left( \sum_{i=1}^n b_i^j b_i^2 \right) + \dots + a_m \left( \sum_{i=1}^n b_i^j b_i^m \right) - \left( \sum_{i=1}^n b_i^j z_i \right) \right] \end{aligned} \quad (12)$$

Solve for the coefficients  $a_1, a_2, \dots, a_m$ , the Eq. (12) becomes

$$\begin{cases} a_1 \sum_{i=1}^n b_i^1 b_i^1 + a_2 \sum_{i=1}^n b_i^1 b_i^2 + \dots + a_m \sum_{i=1}^n b_i^1 b_i^m = \sum_{i=1}^n b_i^1 z_i \\ a_1 \sum_{i=1}^n b_i^2 b_i^1 + a_2 \sum_{i=1}^n b_i^2 b_i^2 + \dots + a_m \sum_{i=1}^n b_i^2 b_i^m = \sum_{i=1}^n b_i^2 z_i \\ \dots \\ a_1 \sum_{i=1}^n b_i^m b_i^1 + a_2 \sum_{i=1}^n b_i^m b_i^2 + \dots + a_m \sum_{i=1}^n b_i^m b_i^m = \sum_{i=1}^n b_i^m z_i \end{cases} \quad (13)$$

Eq. (13) gives in matrix notation  $BB^T A = BZ$ ,

$$\text{where } B = \begin{bmatrix} b^1(l_1) & b^1(l_2) & \dots & b^1(l_n) \\ b^2(l_1) & b^2(l_2) & \dots & b^2(l_n) \\ \vdots & \vdots & \ddots & \vdots \\ b^m(l_1) & b^m(l_2) & \dots & b^m(l_n) \end{bmatrix}$$

$A^T = (a_1, a_2, \dots, a_m)$ ,  $Z^T = (z_1, z_2, \dots, z_n)$ ,  $B$  is the  $m \times n$  matrix,  $A$  and  $Z$  are the  $m, n$  vector. Based on the above matrix equation, the value of  $a_1, a_2, \dots, a_m$  can be estimated, then least squares method is finished.

### 3.2. The Least Squares Surface Fitting Method Using Orthogonal Distance

In this section we introduce our very efficient orthogonal distance fitting algorithm for implicit surfaces, the orthogonal distance or the modifications between measurement points to the fitting surface is

$$\begin{cases} x_p = x_p^0 + \delta_{x_p} \\ y_p = y_p^0 + \delta_{y_p} \\ a_{ij} = a_{ij}^0 + \delta_{c_{ij}} \end{cases} \quad (14)$$

$\delta$  represents correction coefficient, Eq. (14) is equivalent to

$$\begin{cases} v_{xp} = \delta_{x_p} + x_p - x_p^0 \\ v_{yp} = \delta_{y_p} + y_p - y_p^0 \\ v_{zp} = \sum_{i=0}^m \sum_{j=0}^{m-i} (a_{ij} x_p^i y_p^j - z_p^0) \end{cases} \quad (15)$$

From Eq. (14) and Eq. (15), we get

$$\begin{cases} v_{xp} = \delta_{x_p} + x_p - x_p^0 \\ v_{yp} = \delta_{y_p} + y_p - y_p^0 \\ v_{zp} = \sum_{i=0}^m \sum_{j=0}^{m-i} (a_{ij}^0 + \delta_{c_{ij}}) (x_p^0 + \delta_{x_p})^i (y_p^0 + \delta_{y_p})^j - z_p^0 \end{cases} \quad (16)$$

After Eq. (16) expansion, we obtained

$$\begin{cases} v_{xp} = \delta_{x_p} + x_p - x_p^0 \\ v_{yp} = \delta_{y_p} + y_p - y_p^0 \\ v_{zp} = \sum_{i=0}^m \sum_{j=0}^{m-i} \left\{ (a_{ij}^0 + \delta_{c_{ij}}) \left[ (x_p^0)^i + i(x_p^0)^{i-1} \delta_{x_p} + (\delta_{x_p})^i \right] \left[ (y_p^0)^j + j(y_p^0)^{j-1} \delta_{y_p} + (\delta_{y_p})^j \right] - z_p^0 \right\} \end{cases} \quad (17)$$

through calculation then get

$$\begin{cases} v_{xp} = \delta_{x_p} + x_p - x_p^0 \\ v_{yp} = \delta_{y_p} + y_p - y_p^0 \\ v_{zp} = \sum_{i=0}^m \sum_{j=0}^{m-i} \left\{ (a_{ij}^0 + \delta_{c_{ij}}) \left[ (x_p^0)^i (y_p^0)^j + i(x_p^0)^{i-1} \delta_{x_p} (y_p^0)^j + j(y_p^0)^{j-1} \delta_{y_p} (x_p^0)^i + i(x_p^0)^{i-1} \delta_{x_p} j(y_p^0)^{j-1} \delta_{y_p} + (\delta_{x_p})^i (\delta_{y_p})^j \right] - z_p^0 \right\} \end{cases} \quad (18)$$

In Eq. (18), the item including  $(\delta)^n$   $n \geq 2$  can be discarded because  $\delta$  is a small offset value, so the power of  $\delta$  can be ignored. Then derivatives of Eq. (18) lead to

$$\begin{cases} v_{xp} = \delta_{x_p} + x_p - x_p^0 \\ v_{yp} = \delta_{y_p} + y_p - y_p^0 \\ v_{zp} = \sum_{i=0}^m \sum_{j=0}^{m-i} a_{ij}^0 (x_p^0)^i (y_p^0)^j + a_{ij}^0 i (x_p^0)^{i-1} \delta_{x_p} (y_p^0)^j + a_{ij}^0 j (y_p^0)^{j-1} \delta_{y_p} (x_p^0)^i + \delta_{c_{ij}} (x_p^0)^i (y_p^0)^j - z_p^0 \end{cases} \quad (19)$$

The matrix form of Eq. (19) is described as:

$$V = \begin{bmatrix} I_{x_p} & 0 & 0 \\ 0 & I_{y_p} & 0 \\ B_x & B_y & J \end{bmatrix} \begin{bmatrix} \delta_{x_p} \\ \delta_{y_p} \\ \delta_{c_{ij}} \end{bmatrix} + \begin{bmatrix} L_1 \\ L_2 \\ L_3 \end{bmatrix} = GX + L, \quad (20)$$

where  $I_{x_p}, I_{y_p}$  are identity matrix with  $p$  dimension,  $B_x, B_y$  are diagonal matrix with  $p$  dimension,

$$B_x = \begin{bmatrix} \sum_{i=0}^m \sum_{j=0}^{m-i} i (x_1^0)^{i-1} (y_1^0)^j a_{ij}, 0, \dots, 0 \\ 0, \sum_{i=0}^m \sum_{j=0}^{m-i} i (x_2^0)^{i-1} (y_2^0)^j a_{ij}, \dots, 0 \\ 0, 0, \dots, 0 \\ 0, 0, \dots, \sum_{i=0}^m \sum_{j=0}^{m-i} i (x_n^0)^{i-1} (y_n^0)^j a_{ij} \end{bmatrix}$$

$$B_y = \begin{bmatrix} \sum_{i=0}^m \sum_{j=0}^{m-i} j (y_1^0)^{j-1} (x_1^0)^i a_{ij}, 0, \dots, 0 \\ 0, \sum_{i=0}^m \sum_{j=0}^{m-i} j (y_2^0)^{j-1} (x_2^0)^i a_{ij}, \dots, 0 \\ 0, 0, \dots, 0 \\ 0, 0, \dots, \sum_{i=0}^m \sum_{j=0}^{m-i} j (y_p^0)^{j-1} (x_p^0)^i a_{ij} \end{bmatrix}$$

$$J = \begin{bmatrix} \sum_{i=0}^m \sum_{j=0}^{m-i} (x_1^0)^i (y_1^0)^j \\ \sum_{i=0}^m \sum_{j=0}^{m-i} (x_2^0)^i (y_2^0)^j \\ \dots \\ \sum_{i=0}^m \sum_{j=0}^{m-i} (x_p^0)^i (y_p^0)^j \end{bmatrix}$$

$$L = \begin{bmatrix} x_p - x_p^0 = 0 \\ y_p - y_p^0 = 0 \\ a_{ij} (x_p^0)^i (y_p^0)^j - z_p^0 \end{bmatrix}$$

The indirect adjustment method is used to minimize the Eq. (20), then get  $\delta = (G^T G)^{-1} G^T L$ . Bring the  $\delta$  into the Eq. (14), the fitting surface answer is

$$z_p = \sum_{i=0}^m \sum_{j=0}^{m-i} (a_{ij} x_p^i y_p^j) \quad (21)$$

Through orthogonal least square fitting method, we can get jitter-free and non interference real leaves PCD, based on this; the triangulation algorithm is adopted to accomplish the conversion of discrete points to foliage surface.

## 4. Experimental Results

### 4.1. Experimental 1

We first collect a scan of a well-isolated individual tree, scanned from two side lateral locations, this preliminary data set is used to develop and illustrate the algorithm. The upper portion of the complete individual big-leaf tree's PCD is provided for our experiment, shown in Fig. 1 (a). The leaf orientation distribution and the direction of a solid angle originated from every PCD are shown in Fig. 1 (b). Fig. 1 (c) shows that K-means clustering of partitioning method are used, through this method; we examine similarities and dissimilarities of observations PCD, where the characteristics of points in the same cluster are same color and the characteristics of points in different clusters are

presented by different color. Seen from the Fig. 1 (c) the existing K-means clustering method can not effectively classify the plant organs; In Fig. 1 (d), curve drawing and description are adopted to analyze every inter-class variance, where curves of different colors represent different classes feature quantity, the black thick line represents the average value of this class. As seen from Fig. 1 (d), the curve of every class exist significant fluctuation and indicate the classification results are not optimal. Fig. 1 (e) shows the building low dimensional embedded space of the tree's PCD by the manifold learning LLE algorithm, we find a low dimensional basis for describing high dimensional tree PCD, then uncover the intrinsic dimensionality of the PCD. Fig. 1 (e) convert to the Fig. 1 (f) of three-dimensional space, in the Fig. 1 (f) XOY plane is corresponding with Fig. 1 (e), the Z axis keep the count of projective PCD numbers on the Fig. 1 (e) plane, through the selection of threshold value, classification results of tree's PCD are determined. Fig. 1 (g) shows the classification results of manifold learning LLE algorithm, as seen from the result, our method be able to identify different plant organs. It's clear from Fig. 1 (h) that each species have discernibly same characteristic quantity and every cluster characteristics are similar to its cluster centroid.

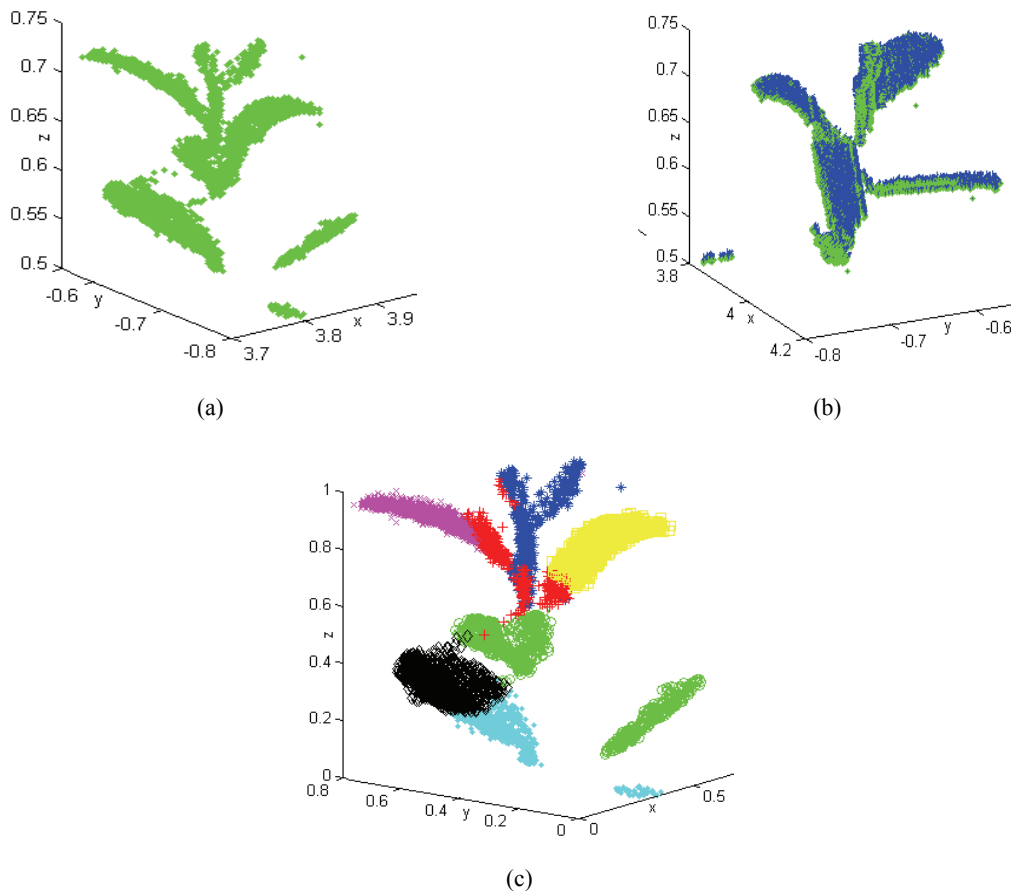
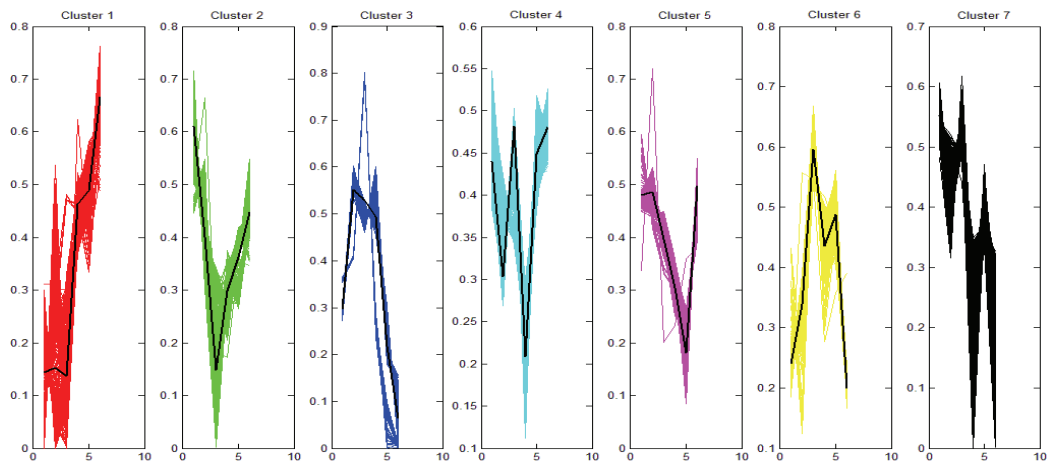
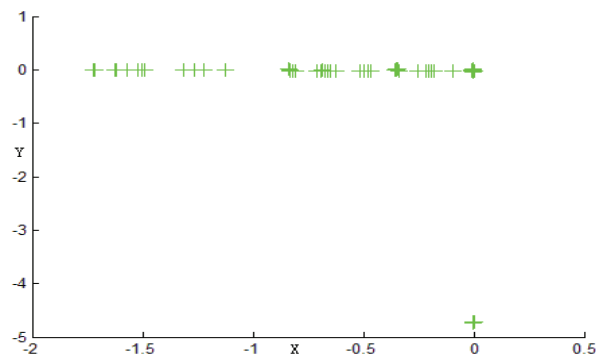


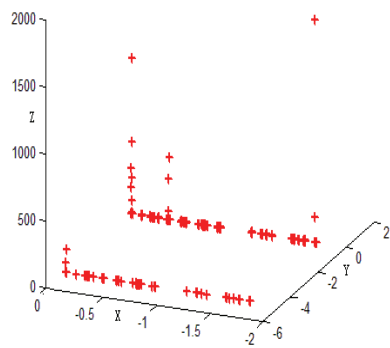
**Fig. 1 (a-c).** The classification result of different algorithm.



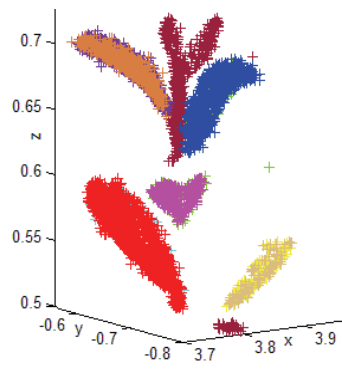
(d)



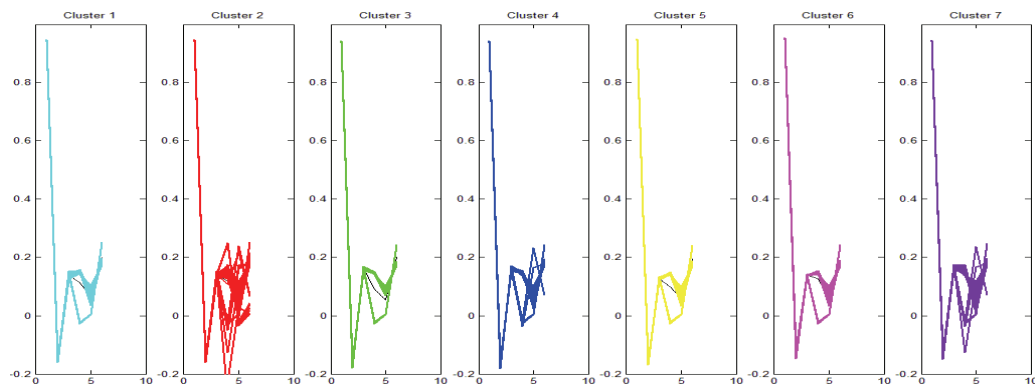
(e)



(f)



(g)



(h)

Fig. 1 (d-h). The classification result of different algorithm.

## 4.2. Experimental 2

Fig. 2 Schematic diagrams illustrate the tree leaves modeling process; Fig. 2 (a) Original PCD of an individual tree leaf; Fig. 2 (b) shows the fitting leaf surface after curve fitting method from PCD; we can see from Fig. 2 (c) that the fitting results by the curve fitting method can not construct a surface because an arbitrary surface can not contain all the leaf PCD, so the least squares estimation and orthogonal least square method are used to map all the PCD onto the approximating surface, the results are shown in Fig. 2 (d), Fig. 2 (e), Fig. 2 (f), where the red points represent the original foliar PCD, the

green points represent the results of original foliar PCD taking “projection” operation by least square approach, the blue points are the “projection” operation results by orthogonal least square method; Fig. 2 (g), Fig. 2 (h) describe the projection surface through least square approach and orthogonal least square method, just express in the color of black and pink, then we obtain a set of projection vertices about original foliar PCD at the projection surface and utilize delaunay triangulation algorithm to generate triangle meshes with highly quality (Fig. 2 (i)), finally, adaptive subdivision and mesh re-sampling based on distance field are provided (Fig. 2 (j), Fig. 2 (k)).

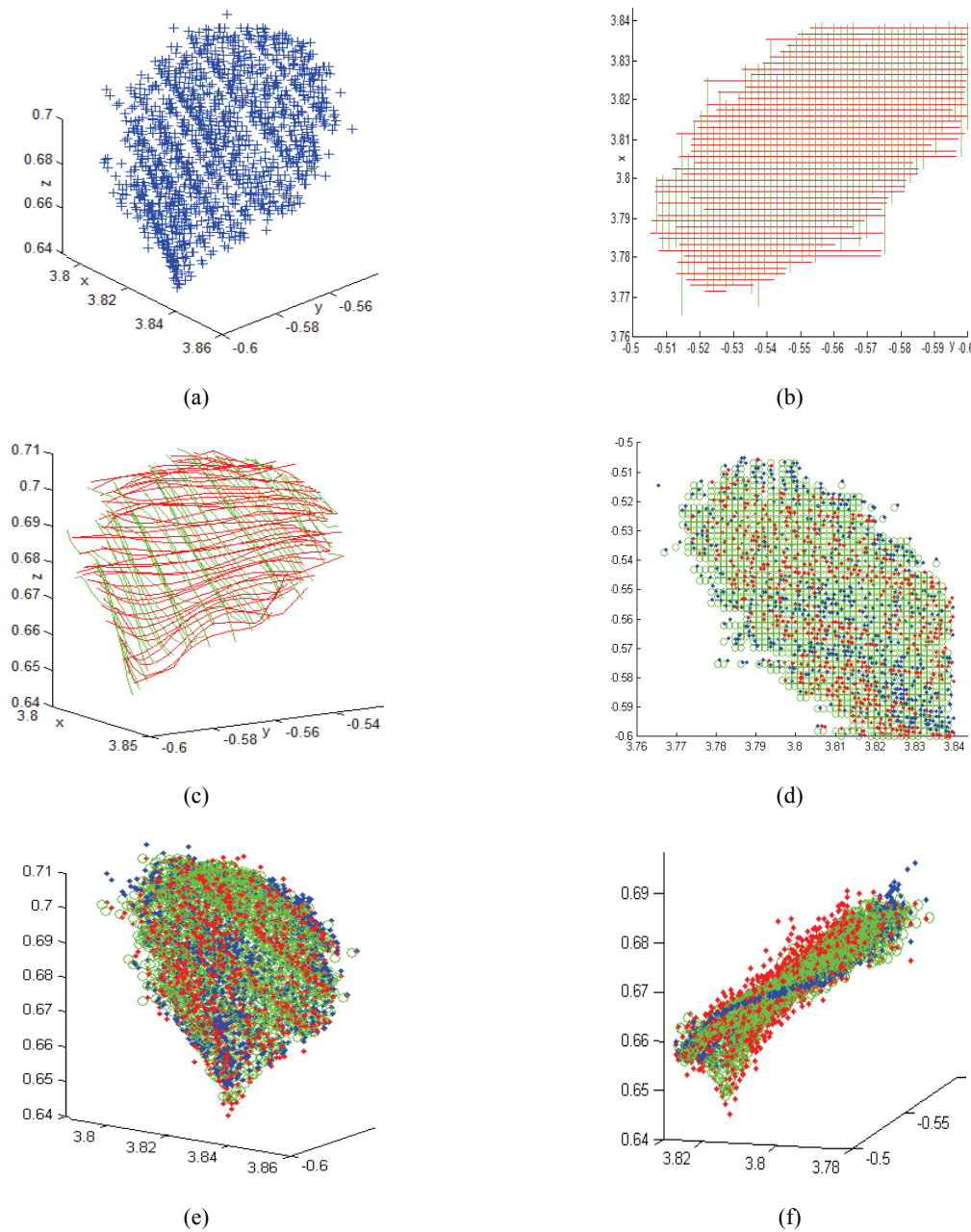


Fig. 2 (a-f). The experiment result of foliage reconstruction.

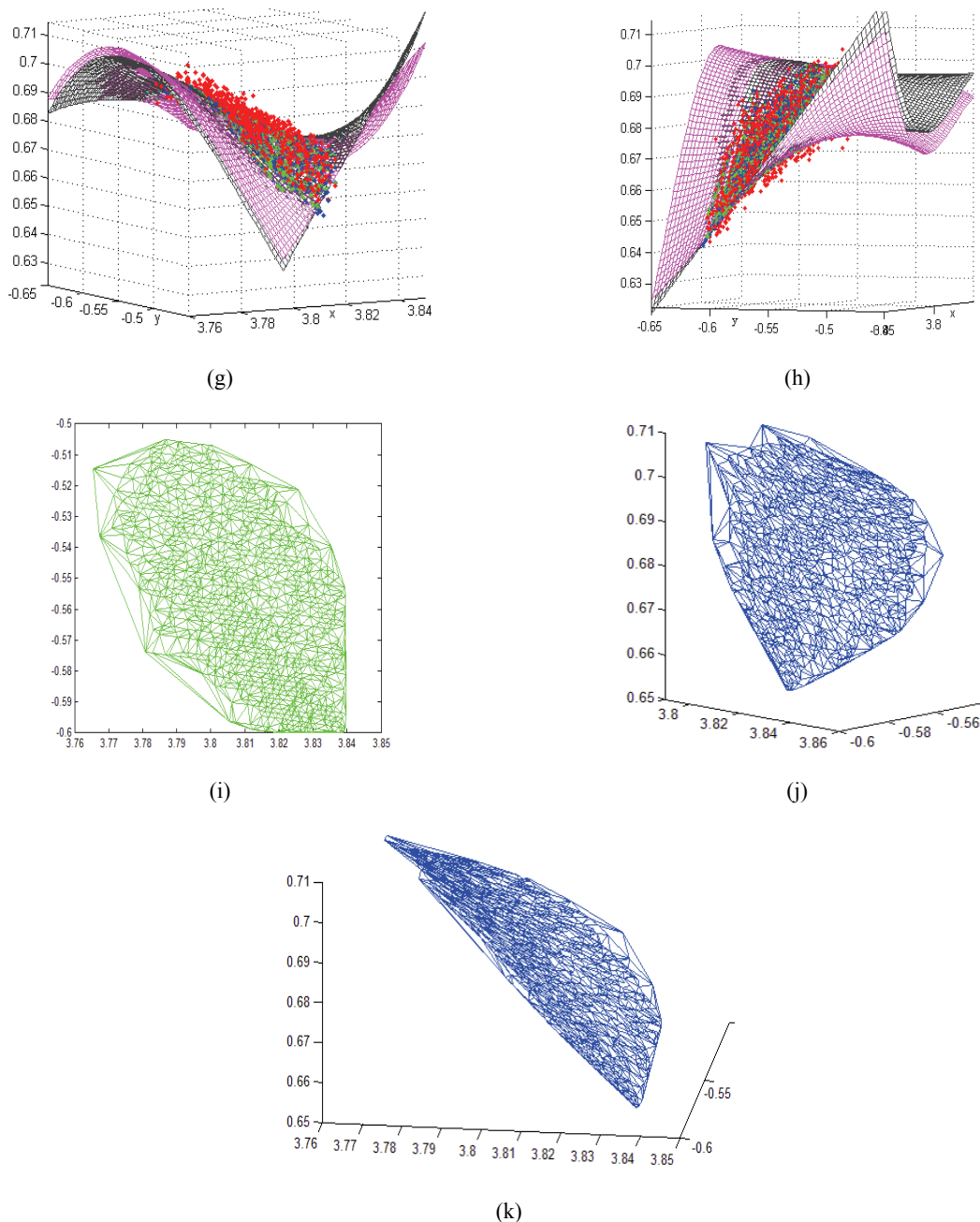


Fig. 2 (g-k). The experiment result of foliage reconstruction.

## 5. Conclusions

In recent years, TLS has been used in forestry parameter measurement, but the stumpage shape is non-rigid and irregular, and the scanning results are interfered by external environment, such as wind and occlusion effect, so the registration of multi-location scanning PCD exist deviation and can not fully capture 3-D structural information of forest stands. In this paper, we combine computer graphics and vision theory to provide a novel non-contact way for trees parameters calculation and real three dimension construction, our work mainly include:

1) Using the point and its neighborhood, we construct the covariance matrix to calculate the normal vector of every point, and take color

information, torsion, curvature to form multi-dimensional characteristics of PCD.

2) Nonlinear manifold learning method is explored for dimensionality reduction of the tree's PCD features and plant organs identification.

3) Due to foliar jitter caused by the wind, three-dimensional orthogonal least squares algorithm is designed to eliminate jitter, thus making the whole leaf's PCD can project onto single surface and obtain the real leaves surface, then delaunay triangulation algorithm is used to realize the conversion between the discrete PCD to the real leaf surface.

In brief, this paper use the latest measurement technology (TLS) to extend traditional tree index acquisition method, and combine computer science to identify different leaves organs, then proceed to

achieve leaf surface reconstruction. After this subject study, the mode innovation of broad-leaved trees measurement is proposed and the construction of forestry digitization process is developed.

## Acknowledgements

This work is supported by natural science foundation of Jiangsu Province (BK2012418), High academic qualifications fund of Nanjing Forestry University (163070052, 163070036). We also appreciate Advanced Analysis and Testing Center of Nanjing Forestry University that provide the Leica TLS for our measurement.

## References

- [1]. S. Hancock, P. Lewisb, M. Fosterd, et al., Measuring forests with dual wavelength lidar: A simulation study over topography, *Agricultural and Forest Meteorology*, Vol. 161, Aug. 2012, pp. 123-133.
- [2]. B. Koch, Status and future of laser scanning, synthetic aperture radar and hyperspectral remote sensing data for forest biomass assessment, *ISPRS Journal of Photogrammetry and Remote Sensing*, Vol. 65, Issue 6, Nov. 2010, pp. 581-590.
- [3]. A. Ferraz, F. Bretar, S. Jacquemoud, et al., 3-D mapping of a multi-layered Mediterranean forest using ALS data, *Remote Sensing of Environment*, Vol. 121, Jun. 2012, pp. 210-223.
- [4]. A. Peduzzi, H. R. Wynne, T. R. Fox, et al., Estimating leaf area index in intensively managed pine plantations using airborne laser scanner data, *Forest Ecology and Management*, Vol. 270, Apr. 2012, pp. 54-65.
- [5]. D. Seidela, S. Fleckb, C. Leuschner, Analyzing forest canopies with ground-based laser scanning: A comparison with hemispherical photography, *Agricultural and Forest Meteorology*, Vol. 154, Mar. 2012, pp. 1-8.
- [6]. J. L. Lovell, D. L. B. Jupp, G. J. Newnhamc, et al., Measuring tree stem diameters using intensity profiles from ground-based scanning lidar from a fixed viewpoint, *ISPRS Journal of Photogrammetry and Remote Sensing*, Vol. 66, Issue 1, Jan. 2011, pp. 46-55.
- [7]. I. Moorthy, J. R. Miller, B. Hu, et al., Field characterization of olive (*Olea europaea* L.) tree crown architecture using terrestrial laser scanning data, *Agricultural and Forest Meteorology*, Vol. 151, Issue 2, Nov. 2011, pp. 204-214.
- [8]. A. Iio, Y. Kakubari, H. Mizunaga, A three-dimensional light transfer model based on the vertical point-quadrant method and Monte-Carlo simulation in a *Fagus crenata* forest canopy on Mount Naeba in Japan, *Agricultural and Forest Meteorology*, Vol. 151, Issue 4, Apr. 2011, pp. 461-479.
- [9]. G. Zheng, L. Monika Moskal, Computational-Geometry-Based Retrieval of Effective Leaf Area Index Using Terrestrial Laser Scanning, *IEEE Transactions On Geoscience and Remote Sensing*, Vol. 50, Issue 10, Oct. 2012, pp. 3958-3969.
- [10]. M. Bélanda, J. L. Widlowskib, R. A. Fourniera, Estimating leaf area distribution in savanna trees from terrestrial LiDAR Measurements, *Agricultural and Forest Meteorology*, Vol. 151, Issue 5, Sep. 2011, pp. 1252-1266.
- [11]. G. Zheng, L. Monika Moskal, Spatial variability of terrestrial laser scanning based leaf area index, *International Journal of Applied Earth Observation and Geoinformation*, Vol. 19, Oct. 2012, pp. 226-237.
- [12]. J. L. Lovella, V. Haverdb, D. L. B. Jupp, et al., The Canopy Semi-analytic Pgap And Radiative Transfer (CanSPART) model: Validation using ground based lidar, *Agricultural and Forest Meteorology*, Vol. 158, Jun. 2012, pp. 1-12.
- [13]. G. Zheng, L. Monika Moskal, Leaf Orientation Retrieval From Terrestrial Laser Scanning (TLS) Data, *IEEE Transactions on Geoscience and Remote Sensing*, Vol. 50, Issue 10, Oct. 2012, pp. 3970-3979.
- [14]. H. Xu, N. Gossett, B. Q. Chen, Knowledge and Heuristic Based Modeling of Laser-Scanned Trees, *ACM Transactions on Graphics*, Vol. 26, Issue 4, Dec. 2007, pp. 1-19.
- [15]. X. I. Liang, P. Litkey, J. Hyypä, et al., Automatic Stem Mapping Using Single-Scan Terrestrial Laser Scanning, *IEEE Transactions on Geoscience and Remote Sensing*, Vol. 50, Issue 2, Feb. 2012, pp. 661-670.
- [16]. T. R. Sam, K. S. Lawrence, Nonlinear Dimensionality Reduction by Locally Linear Embedding, *Science*, Dec. 2000, pp. 2323-2326.

## Intelligent Model of Home Furnishing and Transportation Based on Improved RFID Web Fuzzy Clustering

<sup>1</sup> Xiaohong Luo, <sup>2</sup> Yali Wang

<sup>1</sup> School of Computer & Information Engineering, Nanyang Institute of Technology, Nanyang Henan, 473000, China

<sup>2</sup> Jiyuan Vocational and Technical College, Jiyuan HeNan, 459000, China

<sup>1</sup> Tel.: 18237770044

E-mail: luoxiaohongedu@163.com

Received: 25 June 2013 / Accepted: 25 August 2013 / Published: 30 September 2013

---

**Abstract:** This paper uses the fuzzy clustering method based on clustering path division, according to user access path. In the cluster, according to the access time and Agent classification of user, this method is then according to the user to all pages in order to visit division. The hardware of intelligent home furnishing controller by the advanced ARM9 embedded system, mobile phone module and RFID module. Intelligent transportation system through the sharing of traffic information, can realize the coordinated traffic signal control, effective traffic prediction and grooming. The paper presents intelligent model of home furnishing and transportation based on improved RFID web fuzzy clustering. Experiments show that RFID and fuzzy clustering can improve reliability of intelligent traffic and home furnishing and effectiveness. *Copyright © 2013 IFSA.*

**Keywords:** Intelligent home furnishing, Intelligent transportation, Fuzzy clustering, RFID.

---

### 1. Introduction

Mining field in the Web log, clustering analysis is an important research topic, with fuzzy processing ability of fuzzy clustering is introduced into fuzzy theory is the analysis of the existing data. The FCM algorithm is currently widely used fuzzy clustering algorithm. But it also exists some shortcomings, such as the FCM algorithm by the initial impact is relatively large; the iteration is easy to fall into local minimum. This article from the modified clustering objective function and the initial implosion of the class put forward a kind of improved FCM algorithm.

The RFID solution is RFID technology vendors for RFID application plan development characteristic industry, can be customized according to the actual

requirements of different enterprises. RFID solutions can be classified according to the industry, logistics, anti-theft security, identity recognition, asset management, animal management, fast payment, please click here to view the scheme.

Indoor Wi-Fi terminal positioning before the first planned in accordance with the actual situation of the indoor terminal maps stored in the database of information processing; AP access point is then set according to the indoor distribution, we need to set a fixed location reference tags as a measurement reference point to help position calibration, set the number of access points according to the specific indoor.

Electronic label vehicles is introduced, the fusion of multiple RF field and digital technology in the leading technology, using software radio technology,

unique micro power technology, anti-collision technology, response protocol, local activation of space access technology patent portfolio, can fully meet the demand of automatic recognition of the high speed development.

Intelligent home furnishing system can realize the communication of information through the GSM/GPRS/CDMA/ network, ZigBee network, Internet domain and community information network [1]. Users in the outdoor appliances and lighting device through the mobile phone control of home, also available anti-theft, fire, gas leakage alarm information home in a timely manner; at home through the regulation of home appliance remote controller. The indoor host controller also has a visual intercom system function, can refer to all kinds of information community released, can be issued a warning to the community security distress signal when necessary. The system is mainly composed of a smart home furnishing a controller and a plurality of indoor monitoring ZigBee modules.

To analyze a collection of data objects, usually to divide the class is unknown. In this case, the clustering is more appropriate, by clustering, we can identify the dense and sparse regions can discover user characteristics different access paths from the users of the site, to find the overall distribution patterns and data attributes between the interesting relationships. This paper uses a method of clustering W path planning based on EB log, by dividing the user access path, fuzzy C means clustering algorithm for peer-to-peer long path clustering, to obtain the optimal clustering number, greatly improving the W EB access patterns discovery efficiency.

Electronic label also known as radio frequency label, transponder, data carrier; the reader is also known as the readout device, scanner, communicator, reader (depends on whether the electronic tags can be wireless overwrite data). By coupling the RF signal components of the space between tag and reader (no contact) coupling, in the coupling channel, according to temporal relations, the exchange of, data to realize the energy. There are two types of coupling RF signal between the reader and the tag.

Work or life needs different pattern to match, no one by one to switch lights and light, just set according to your heart, you can achieve "one-click" scene mode and the scene can be "one-click" memory storage, which is the major force of China intelligent scene control and storage function let the work and life's advantage. Example: in the study on the Internet are tired, want to rest for a while, then as long as the press of a button, enter the rest mode, by a bright light will gradually darken and is particularly soft, can be a good nap for a while. Of course, such as theater mode, drawing pattern and other patterns can be preset and stored and the realization of "one-click" switch. The paper presents intelligent model of home furnishing and transportation based on improved RFID web fuzzy clustering.

## **2. Intelligent Home Furnishing and Transportation by Web Fuzzy Clustering**

Through the fuzzy membership to a data object is added to a weight value and to optimize the number of clusters  $C$  into fuzzy clustering validity function in the algorithm. To demonstrate the usefulness of the improved FCM algorithm, the algorithm is applied to two areas: network intrusion detection and Web log mining. Intrusion detection is a second line of defense of network security [2]. In this paper, analysis of the intrusion detection technology to point puts forward a method of Intrusion Detection Based on improved FCM algorithm. The advantage of this method is not need labeled training data sets. In this paper, it is using the KDD99 data set as the experimental data.

Intelligent controller can be pre-set zone, the security of the entire bedroom in the wireless security alarm system, infrared detectors for active human body to detect signal. Door sensor detectors switch control doors and windows. If the doors and windows are opened illegally broke into someone from the outside world the controller immediately by the siren's live sound and light alarm and press the set alarm phone number to send alerts to the owner and upload a warning to the alarm center.

To reduce the traffic accident system, increase traffic safety. Through the implementation of traffic control, can make the traffic flow conflicts were separated from time and space, so as to reduce traffic accidents, increase traffic safety. Traffic control and reasonable, can effectively guide and scheduling of traffic flow, the city traffic flow is maintained in a stable state, so as to avoid or mitigate traffic congestion, reduce the delay of vehicles in road traffic, improve the overall efficiency of transportation.

The basic method of clustering is often defined between the distance is defined between the two objects in the distance of two objects, but also the basic methods do not depend on the distance of the definition of the cluster distance between two objects: firstly, the definition of a optimization objectives, optimization is a local minimum first defines an optimal target first, define an optimization objective optimization is a local minimum [3]. Clustering and classification of difference: clustering is an unsupervised learning process is the observation of learning; learning process and classification is a supervised clustering and classification of the genus distinction between supervision, learning from examples.

The fundamental difference between them is the fundamental distinction, classification, need to know in advance in accordance with the fundamental difference between classification according to the attribute values and clustering is to find this classification attribute value. General attribute values

are of two kinds: numerical attributes and attribute values and symbolic attributes.

With the social and economic structure, the family structure and the development of information technology and the human of home furnishing environment safety, comfort, efficiency requirements increase, resulting in increased demand for intelligent home furnishing, at the same time, more and more families requirements of intelligent home furnishing products not only to satisfy basic needs, more requirements of intelligent home furnishing system function expansion, even in extension services can do simple, convenient, safe, as is shown by Equation 1.

$$E_{j,A}^{\xi}(m,n) = \sum_{m' \in J, n' \in K} w_A^{\xi}(m',n') [D_{j,A}^{\xi}(m+m',n+n')]^2 \quad (1)$$

Controller inside with 1 ZigBee module and it is communication through the monitoring device for ZigBee wireless network and home furnishing in, as the coordinator of ZigBee network (FFD) to use. It is responsible for the construction of intelligent home furnishing ZigBee network, sending and receiving control system and the command center and makes the corresponding processing. At the same time, from the routing node (FFD) or a terminal node (RFD) sends the data received to the system control center.

When a team has many intersections in a trunk road, coordinated control makes the vehicle in the main intersection always arrive at the beginning of green, so there is no need to stop the intersection, forming a traffic green wave band [4]. Green wave control can effectively improve the vehicle speed and traffic capacity, ensure that the road is smooth and

reduce the vehicle in the running process of the delay time and energy consumption. The control parameters of arterial traffic coordinated control are the cycle length. Green ratio and phase difference, the control goal is generally the average delay and the number of parking vehicles.

Although the concept of intelligent home furnishing appears very early, the market demand will always exist, but for a long time the development of intelligent home furnishing due to subject to the related technical breakthrough, has not been universal large-scale application. Intelligent home furnishing technology existing in the present market is introduced as follows: all control signals in this way must be connected through the cable, signal wire controller end is more formidable, but encountered problems are difficult. Cable faults are very prominent, wiring complexity, heavy workload, high cost and difficult maintenance, not easy to network. These shortcomings resulted in intelligent home furnishing of wired way just stays in the concept and the pilot phase, not a large-scale promotion.

Many methods of cluster analysis, it usually refers to the record in the database, according to the classification rules some classification rule, reasonable certain classification rules of a collection of records, where each record to determine the category (e.g., K - average algorithm, K - center algorithm, based on the hierarchical agglomerative clustering based on hierarchical clustering division etc.) [5]. In general, for the same data set, if using different clustering methods, may results in the different division, as is shown by Fig. 1.

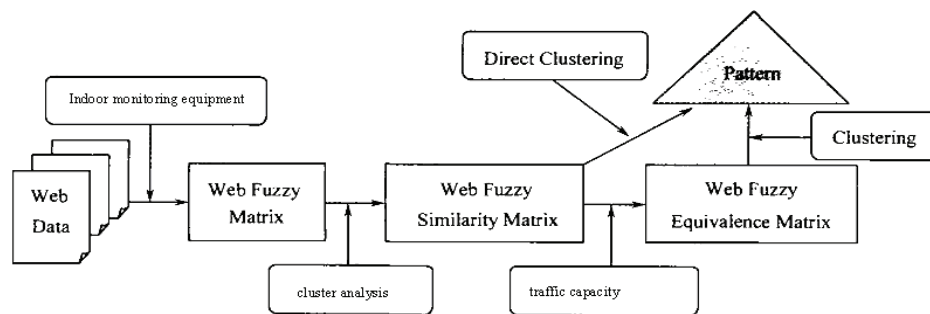


Fig. 1. Intelligent Home Furnishing and Transportation by Web Fuzzy Clustering storage.

Indoor monitoring equipment according to use can be divided into 3 categories: the first category is the switch and the socket, the socket of the most simple through the small electronic switch for household electrical appliances (such as electric rice cooker, water dispenser, TV, refrigerator, air conditioner, washing machine, electric curtains and does not require dimming the lamp) power switch control; intelligent switch and socket complicated with output power adjustable function, used for dimming or electric fan pendant lamp, floor lamp the speed etc.

Second types of sensor products, of which the piezoelectric infrared sensor and magnetometer sensor used for anti-theft, smoke sensor for fire, gas sensor for gas leakage and manual alarm button for emergencies (such as the elderly sudden onset). These nodes are equipped with ZigBee module, as the terminal nodes of the network (RFD). The third class for a handheld remote controller, in addition to the household electrical appliance switch control, dimming control, also has lighting scene setting and control function.

The rise of the Internet of things will bring a broad market space for ZigBee. Because of the Internet of things will be all kinds of information sensing transmission unit and the Internet combine to form a huge network, in the vast network, need for transmitting data between sensing transmission unit and a communication network, while the other wireless technology, ZigBee in the investment, construction, maintenance and other advantages, in the IOT intelligent home furnishing will be widely applied to the fields.

Timing control to the historical traffic flow data as the basis, find out the different traffic flow changes every day / week and for a period of time, by means of artificial method or computer simulation prepared different days / week and different time zone distribution scheme, which belongs to the open loop control, not easily according to the flow condition real-time adjustment control scheme. Because the timing control of traffic signal machine requirements low, no need of real-time traffic, which is still a control strategy for the city road traffic system is widely used in the.

Clustering and classification of different is clustering requires dividing the class is unknown. Clustering is a classification of the data into classes or clusters of such a process, so the objects in the same cluster is very similar and objects in different clusters have great dissimilarity. From a statistical point of view, cluster analysis is a method of simplifying data through data modeling [6].

Statistical cluster analysis method of the traditional system clustering method, decomposition, addition method, dynamic clustering, clustering ordered samples, there are overlapping clustering and fuzzy clustering. Cluster analysis tools using k-mean, k- center point algorithm has been added to many famous statistical analysis software package, such as SPSS, SAS etc. From a machine learning perspective, clusters correspond to hidden patterns. Clustering is an unsupervised learning process search clusters.

Cluster network ZigBee combination of the star and mesh structure, we use the intelligent home furnishing controller and ZigBee sensor nodes in real application cluster network. It has good scalability, for the small-sized apartment or villa users, can also increase the routing nodes to extend the network coverage for large-sized apartment; the user, can reduce the routing nodes into a star network, in order to save energy, to accelerate the speed of data transmission.

$$H(x, y) = \begin{bmatrix} \frac{\partial^2 f}{\partial x^2} & \frac{\partial^2 f}{\partial x \partial y} \\ \frac{\partial^2 f}{\partial y \partial x} & \frac{\partial^2 f}{\partial y^2} \end{bmatrix} \quad (2)$$

Clustering is according to certain requirements and rules for classifying things, set group of physical or abstract objects into the process is composed of

similar objects multiple classes. In this process, there is no teacher guide, didn't have any on the classification of prior knowledge, only rely on the things between the similarity criterions for dividing the class, which belongs to the unsupervised classification category, in many applications, can be a kind of image data as a whole to stay [7]. Clustering and classification are not the same, it divided the class is unknown. In the classification mode, for what classes of this information exists in the target database.

In the man-machine interface, it is using TFT 5 inch LCD screen and the configuration of the touch screen. Can be used to display various information visitor images and small transmitted and it is the user easily input data to control various home furnishing equipment. In addition to more flexible control, using the I2C bus interface design of keyboard interface processor, which can be extended in various control, alarm, as is shown by Fig. 2.

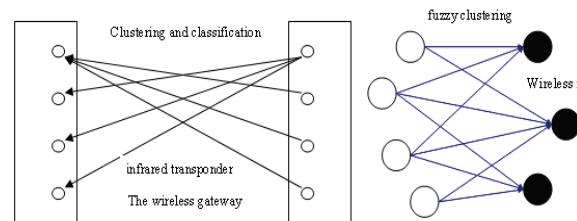


Fig. 2. The wireless gateway by fuzzy clustering architecture.

The wireless gateway: all wireless sensor and wireless linkage equipment information collection control terminal. All sensor, detector will collect the information to the mobile phone, tablet computer, the computer authority management device through the wireless gateway, in addition the control command by the management device through the wireless gateway sends to the linkage equipment [8]. Then if no one at home when the door is opened, the door to detect an intruder, the intrusion alarm through the wireless gateway is sent to the master mobile phone, mobile phone message is received send shock ringbone, master confirmation send the control command, electromagnetic lock automatically locks and trigger the wireless alarm device sends out alarm.

Multi-agent system is a front subject in artificial intelligence, is an important research branch of distributed artificial intelligence, its goal is to build a large complex system into small, communicating and coordinating, easy to manage subsystem, the subsystem of autonomous ability and the coordinated ability to solve complex system control problem. City area traffic network with real-time dynamic characteristics of the road traffic scale and complexity of the traffic flow, the multi-agent system is applied to the city traffic network control research issues concerned. To design the structure of city intelligent traffic control based on it.

The controller is equipped with Ethernet interface, with the controller on the Web server; users can monitor the home environment and various appliances by Internet. Fig. 3 RS-485 interface for communication with the district Wuguan (matched with the original cell network. Using MAX3232 two USART transceivers are ARM9, consisting of two RS-232 ports and one RS-485 ports.

Clustering is not know in advance the target database to the bottom with the number of class situation, hope will have some records into different clusters or "cluster" that is high in the same clustering, similarity and in different clustering between has low similarity. Clustering analysis is the method in mathematical research and treatment given to cluster image, is a kind of multivariate statistical analysis. It is a category of labeled samples set according to some criterion is divided into several subsets, have similar samples as far as possible to make the classified as a class, not similar samples as far as possible into different categories.

Select the middle strategy between the centric and based on the method of object based on the representative. It is not a single centric or objects to represent a cluster, but the choice of a fixed number of representative points in data space [9]. Chameleon is a dynamic model in a hierarchical clustering algorithm. The merge process dynamic model based on Clustering for natural and Isomorphism of discovery and as long as the similarity function can be applied to all types of data, as is shown by Equation 3.

$$\delta_{oj}(k) = -\frac{\partial E}{\partial Net_j(k)}; \frac{\partial E}{\partial w_{ij}} = \frac{\partial E}{\partial Net_j(k)} \cdot \frac{\partial Net_j(k)}{\partial w_{ij}} \quad (3)$$

Clustering analysis is one of the core technologies in the field of data mining; it is from a given data set search value exists between data objects of the data distribution model. Cluster analysis based on the principle that objects within the same cluster have similar as big as possible, but not the same object in the cluster has a different possible in clustering analysis, the main problem is how to without prior knowledge, we meet to seek the cluster aggregation.

Clustering analysis is also called unsupervised learning (Unsupervised Study), is mainly reflected in the clustering data object has no class label, required by the clustering algorithm of automatic calculation. Clustering analysis, spatial data has been widely used in the analysis of financial data, satellite images, medical image automatic detection, the relationship between experimental elements determining etc.

Wireless infrared transponder: This product is mainly used for equipment in the home can be infrared remote control, such as air conditioning, electric curtains, TV etc. Through the wireless infrared transponder, you can remote control air conditioning; you also can not get up close the curtains. This is a very meaningful products, it will be the traditional home appliance is immediately converted to intelligent home appliances.

The intelligent body except with segment agent the same function, such as acquiring traffic flow information, the control signal for the data support; their independent, can separate operation characteristics, regional agents can also according to the traffic flow operation, signal coordination of traffic intersection, with optimized control corresponding road network traffic, decide the corresponding control strategy and the signal timing results promptly issued parrot regions within each signal and transmits the traffic demand and control effect to a layer of decision-making layer, namely traffic management center.

$$SNR = 10 * \log_{10} \frac{\sum_{x=1}^M \sum_{y=1}^N P_{xy}^2}{\sum_{x=1}^M \sum_{y=1}^N (\tilde{P}_{xy} - P_{xy})^2} \quad (4)$$

Clustering or grouping, evaluate the output. Data preprocessing includes the choice of the number, scale and characteristics, it relies on the feature selection and feature extraction, feature selection to select the important feature, feature extraction feature transformation input for a new character, they are often used to obtain an appropriate feature set to avoid the curse of dimensionality "clustering", data pretreatment also includes outlier removal data, outlier is not attached to the general data or model of the data, so the isolated point often leads to the clustering results biased, so in order to get the correct clustering, we must put them out. Since similar is the definition of a class, then between the different data in the measure of the same feature space similarity for the clustering step is very important, because the diversity of types and characteristics of the scale, distance metrics must be cautious, it often depends on the application.

### 3. Using Improved RFID to Build Intelligent Home Furnishing and Transportation

Anti collision (collision) functions of RFID system, the price is more expensive than the system does not have the function to. When the individual users in the RFID system, if not necessary for a plurality of ID also know there is no need to select the collision resistant function of the reader.

Wireless intelligent socket: mainly used for switch control home appliances, such as it can automatically start the exhaust fan exhaust, in the hot summer for the airtight garage is an interesting application [10]. Of course, it also can control any you want to control home appliances, as long as the appliance plugs the wireless intelligent socket, such as drinking machine, electric water heater and so on.

A problem of radio frequency technology meets is reader collision, is received to a reader's information and another reader information conflict,

overlap. A method to solve this problem is to use TDMA technology, is simply the reader is directed at different times of the received signal, rather than at the same time, this will ensure that the reader will not interfere with each other. But in the same region of goods will be read two times, so it is necessary to establish the corresponding system to prevent this from happening, as is shown by Equation 5.

$$MEAN = \sum_{i=0}^{M-1} \sum_{j=0}^{N-1} F(i, j) / (M \times N) \quad (5)$$

The parking card according to different demands, issued monthly card (card), cards, special card (free card) and rent card (the temporary card) four types of cards: monthly cards and special cards in time limit; the stored-value card to balance limit; the temporary card along with a grab, simple convenient; in addition the monthly card and card of prepaid expenses, the yard management simple, active.

RFID can write another factor data is to distinguish the radio frequency identification system for RFID tag. The radio frequency identification system simple, RFID data are mostly simple (sequence) number, can be integrated into the processing chip, will never change. On the contrary, RFID tags can be written by a reader or a special programming device writes data. The RF tag data writing is generally divided into wireless is written with two forms and cable. The railway locomotive and it is lorry RFID application adopting a cable written work.

Wireless air quality sensor: the main sensor detecting the bedroom air quality is cloudy, it is very useful for you to go home and rest, especially families with infants is especially important [11]. It is through the detection of the air quality of indoor air is telling you the effect of health and related equipment optimization adjusting the air quality is initiated by the wireless gateway. Wireless doorbell: This is valuable for small-sized apartment or villa, as is shown by Equation 6.

$$\delta I_i = \begin{cases} I(P) - I(P_i), i = 0, 1, 2, 3 \\ I(P_i) - I(P), i = 4, 5, 6, 7 \end{cases} \quad (6)$$

Intelligent home furnishing controller operating system adopts the embedded Linux operating system with open source, through the reduction of transplanted to the hardware platform controller. The intelligent home furnishing controller Linux, ARM system, mobile phone and ZigBee module to form a whole, constitute an embedded system with complete functions, using ZigBee technology to realize wireless connection within the family of many nodes.

One of the important features of radio frequency identification system is to supply the RF tag. Passive RFID tags have no power. Therefore, the electromagnetic field energy obtained all passive RFID tag work must from reader to send in. In contrast, the active RFID tag contains a battery;

micro chip provides all or part of the work ("auxiliary battery") energy.

The low frequency RFID tag, referred to as low frequency tags, its operating frequency range is 30 kHz – 300 kHz. Typical operating frequency: 125 kHz, 133 kHz. LF tag is passive tags, its energy by inductively coupled mode from reader coupled coils in the near-field radiation. Data transfer between low frequency tags and reader, reader antenna radiation in low frequency tags for the near field zone. LF tag reading distance is generally less than 1 meter.

Wireless communication technology in intelligent home furnishing mainly include: IrDA infrared technology, Bluetooth technology and ZigBee technology. IrDA belongs to the point of the half-duplex communication of short distance, point, inconvenient use and high error rate, network mode is not applicable to the family; Bluetooth technology because of the limited network capacity, high cost, not suitable for home furnishing network application more nodes. The study adopted the transmission range is moderate, safe and reliable, high capacity of ZigBee network technology, intelligent home furnishing design of remote monitoring system, as is shown by Fig. 3.

RFID UHF and microwave band, referred to as the microwave radio frequency label, its typical operating frequency of 862 (902): 433.92 MHz, ~928 MHz, 2.45 GHz, 5.8 GHz. Microwave and radio frequency label can be divided into active and passive tag two tags. When working, RFID reader antenna radiation field in the far zone field, coupling between tags and reader for the electromagnetic coupling. Reader antenna for passive tags provides RF energy, the active tag wake [12]. The radio frequency identification system reading distance is generally larger than 1m, the typical case is 4-6 m, the maximum can reach more than 10 m. The reader antennas are usually of directional antennas, only in the reader antenna directional beam within the scope of the RFID tags can be read / write.

The topology of ZigBee network is mainly of 3 types: star, tree and mesh network. Mesh network fault tolerant ability, adaptive, long transmission distance, but its complexity is the highest; the star network has the characteristics of simple and low power consumption, simple to use, suitable for a family of small scale, low complexity of tree network is somewhere in between. Application of the star network in intelligent home furnishing, can obtain a higher price.

System matching electric block driveway gate is lifted, prevent to hit the car function; detection system using analog-to-digital advanced conversion technology, strong anti-interference ability, adapt to the harsh environment, has also increased the sensitivity and reliability of one's own knack in; the system can query cart, a yard full automatic light full words the red light and automatically stop the entrance into the car.

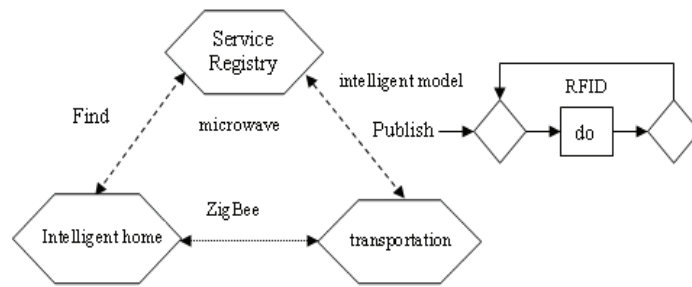


Fig. 3. Intelligent model of home furnishing and transportation based on improved RFID.

ZigBee technology for the low cost and it is low power consumption and low rate wireless communication market vacancy. The hardware of intelligent home furnishing controller by the advanced ARM9 embedded system, mobile phone module and ZigBee module; the embedded operating system Linux, the home network using ZigBee wireless network, security, system functions, to meet the needs of the future development of intelligent home furnishing.

Data storage capacity of microwave and radio frequency label generally confined within 2 kbits and large storage capacity does not seem to have much meaning, from technology and application perspective, microwave and radio frequency label is not suitable as a carrier of large amounts of data, its main function lies in identifying objects and completes the identification process without contact. Data capacity index typical: 1 kbits, 128 Bits, 64 Bits etc. Developed by Auto-ID Center of the electronic is product code EPC capacity: 90 Bits, as is shown by Equation 7.

$$\frac{\partial E}{\partial v_{ih}} = \frac{\partial E}{\partial Net_i(k)} \cdot \frac{\partial Net_i(k)}{\partial v_{ih}} \quad (7)$$

See the application of the every kind of RFID, the first problem enterprises want to ask is: "how do I put my existing system connected with the new RFID Reader?" The essence of the problem is the enterprise application system and the hardware interface problem. Therefore, the permeability is the key of application, correctly grasping the data, ensure the reliability of data read and effectively transmit data to the back-end system is a problem that must be considered. Between traditional applications and Applications (Application to Application) data transparent is solved by intermediate piece of architecture; similarly, architecture design middleware solutions will become the RFID application is a very important core technology.

The core controller system board for type S3C44B0X 32 bit microcontroller, processing and the discrimination of the data and through the MMS module and ZigBee module sends the information and instructions; extension plate is used to access the smoke, gas, infrared, home security state sensor; MMS module family security state information is

transmitted to the user mobile phone a system controller and receives a user message sent instructions; data crosslinked ZigBee module is responsible for the system board, between the expansion board and household appliances, as is shown by Equation 8.

$$MI_{FA}(f, a) = \sum_{f,a} P_{FA}(f, a) \ln \frac{P_{FA}(f, a)}{P_F(f)P_A(a)} \quad (8)$$

Software for the soul of the system, software design with friendly interface, convenient operation, simple maintenance as the basis and strive to practical function and improvement. Parking system software design includes: the system registry, system maintenance, archives management, card management, access control management, access management, query records, statistical statements, exit the system.

According to ABI Research Inc., before 2008, the global industry demand created by the RFID market size could reach \$20000000000, of which the software market accounted for about \$4700000000, integrated service revenue in 2010 will exceed RFID product revenue. With the development of hardware technology gradually mature, large software market opportunities to domestic and foreign information service producers who sustained attention and early input, RFID Middleware in the RFID industry applications in central nervous system, particularly by international companies concerned.

Service Oriented Architecture (SOA) target is to establish communication standard, breakthrough application-to-application communication barriers, to achieve business process automation, innovation and business model, make the IT more flexible and faster response to demand [13]. Therefore, the RFID Middleware in the future development will be in service oriented architecture based trend, provide enterprises with more flexible service.

The triple play in the network level is to unify existing expressway communication, monitoring, charging three electromechanical systems; at the operational level is the integration of data, audio, video three businesses. Triple play is the development trend of information is based on the expressway communication system for network transmission, transmission of voice, data and image

in the same network and can contain other traffic management information, providing network services to society.

#### 4. Intelligent Home Furnishing and Transportation by Improved RFID Web Fuzzy Clustering

Fuzzy clustering is due to the sample belongs to each category uncertainty degree; the sample expressed an intermediary category, which established the sample for the category uncertainty description, which can objectively reflect the real world, thus becoming the mainstream of clustering analysis. The concept of fuzzy partition was proposed by Ruspini, using the concept of people have proposed many kinds of clustering methods, typical are: method of relation and fuzzy relationship based on similar (including polymerization method and splitting method), based on the transitive closure method based on fuzzy equivalence relation, the fuzzy maximum tree method based on graph theory and data the convex decomposition, dynamic programming and is difficult to distinguish between method [14]. However, because the method is not suitable for large data volume, difficult to meet the requirements of real-time applications, so its application is not wide enough, so the research in this area is gradually reduced.

The algorithm is in the traditional C - means algorithm of fuzzy technology is introduced; based on the partition (Partition-Based) clustering method; based on the layer (Hierarchical-Based) clustering method based on density; (Density-Based) clustering method based on grid; (Grid-Based). Clustering method; and based on the model (Model-Based) Guo Xiujuan: Professor Yu Xianfa: phase angle relation method, most small method, arithmetic average minimum method, several He Ping were the most small method; absolute value index method.

Density clustering needs to scan the entire data set, the data space is divided into different squares, approximate representation of clusters and the use of small square and. The method may not be accurate, but this method for noise data and outlier insensitivity. This method can also be used for clustering spatial index structure, by calculating the super ball area density, but this method because of the need to maintain the index structure complex, so the efficiency problems of mass data; continuous based clustering: clustering objects mapped to model or hyper graph model, then according to the edges or hyper edges search connected node sets, as is shown by Equation 9.

$$\begin{cases} w_{j,\min}^{\xi}(m,n) = \frac{1}{2} - \frac{1}{2} \left[ \frac{1 - M_{j,AB}^{\xi}(m,n)}{1 - T} \right] \\ w_{j,\max}^{\xi}(m,n) = 1 - w_{j,\min}^{\xi}(m,n) \end{cases} \quad (9)$$

Clustering analysis is a very active research field in data mining and put forward many clustering

algorithm. Traditional clustering algorithms can be divided into five categories: partition method, hierarchical method, density based method, based on the grid method and the method based on model.

The 1 division method (PAM: PARTitioning method) to first create a K partition, K is the number of partition to create; and then use a circular positioning technology through an object from a partition to another division to help improve the classification quality. Including the partition method of typical: K-means, k-medoids, CLARA (Clustering LARge Application), CLARANS (Clustering Large Application based upon RANdomized Search). FCM 2 level methods (hierarchical method) are to create a hierarchy to decompose a given data set.

RFID middleware is a kind of Middleware Oriented message (Message-Oriented Middleware, MOM), information (Information) is based on message (Message) forms, are transmitted from one program to another or a plurality of program [15]. Information to be asynchronous (Asynchronous) transmission and it is so the sender does not have to wait for the response. The intermediate function contains a message oriented is not only transfer (Passing) information, must also include the interpretation of data, security, data broadcast, error recovery, cyber source, find the location information and the cost path, priorities and debugging work extends with services, as is shown by Equation 10.

$$\sigma_j = \sum_k \delta_k v_{jk} b_j (1 - b_j) \quad (10)$$

Intelligent home furnishing network communication system has the following characteristics: the amount of transmitted data is small, without the transmission speed is too high; the capacity of the network, to meet a variety of household appliances in the family; the good real-time information, short time delay. RFID technical characteristics determine its can well meet the demand of intelligent home furnishing network, especially with the self-organization, self-healing ability, wireless communication technologies such as intelligent home furnishing ideal way of communication system.

The paper presents intelligent model of home furnishing and transportation based on improved RFID web fuzzy clustering. The system is mainly composed of a smart home furnishing a controller and a plurality of indoor monitoring RFID modules. The system model is shown in Fig. 4. Intelligent home furnishing controller through the interconnection of 2 wireless communication network, Internet and 2 cable lines of communication with external equipment to achieve the information and intelligent home furnishing controller and can be regarded as the digital home gateway.

This part of the experiment mainly is for user session in clustering analysis. Experience using UCI data number MSNBC set in the real data set, the data set of MSBN network station after data preprocessing all session set by households, a total of 8564745 session

records and the site has a plurality of intelligent furniture and intelligent transportation system, the number according to the two dimension set of  $985545 \times 252$  sparse matrix, as is shown by Fig. 4.

The experimental results of different clustering threshold (A) of the experimental results of a collaborative filtering recommendation method based on fuzzy clustering firstly users need for fuzzy clustering for all users, each user membership degree of fuzzy cluster with respect to on the basis of fuzzy clustering, fuzzy clustering for fuzzy clustering

which will affect the accuracy of recommendation method. In order to choose an optimal clustering threshold and it is respectively. Found from the experimental results. In the implementation of proposed method are 3 different clustering thresholds; in the selected data set are respectively crossed do 4 experiments. The experimental results as shown in Fig. 3, where the abscissa is the nearest neighbor to the target user number, the ordinate is the corresponding MAE value, the experimental results were obtained from the 254, 856 and 1245 threshold.

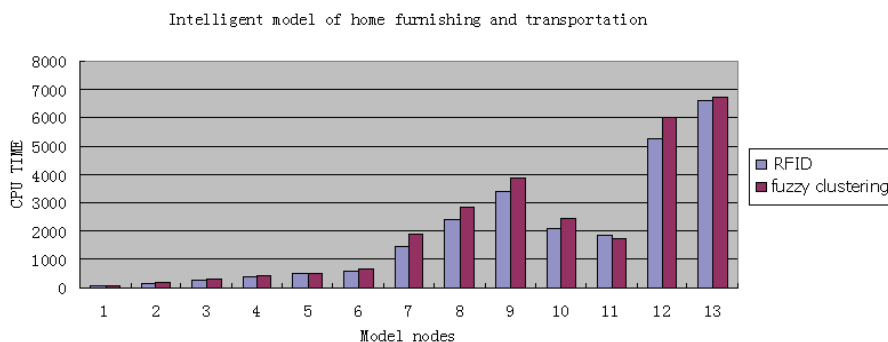


Fig. 4. Compare of intelligent model of home furnishing and transportation based on RFID with web fuzzy clustering diagram.

## 6. Conclusions

Architecture-centric (Infrastructure Centric) with the complexity of enterprise application systems, enterprise is unable to load Hot Code for each application programming Adapter, while facing the object standardization issues, enterprises can consider RFID middleware standard specifications provided by manufacturers. In this way, even if the storage RFID tag information database software by other software instead of, or read and write RFID tag and RFID Reader increase occurs, the application end without modification can handle it. The paper presents intelligent model of home furnishing and transportation based on improved RFID web fuzzy clustering.

FCM algorithm is the matter which belongs to the local search mountain climbing method, through clustering of raw P and dividing the alternating optimization between U matrix to find the local optimal solution, so it must start the iteration from a starting point for P or U, the problem that leads to an initialization algorithm. Research shows that the FCM algorithm strongly depends on the quality of parameter initialization, because the body is stored in two fatal weak points: the first one is the fuzzy clustering objective function is a non-convex function, stored in the local extreme points of large quantity, when properly will cause the algorithm to converge to a local extremism points and not to the data set of optimal fuzzy partition.

## References

- [1]. Minbo Li, Hua Li, Research on RFID Integration Middleware for Enterprise Information System, *Journal of Software*, Vol. 6, No. 2, 2011, pp. 218-226.
- [2]. Zhang Qiu-Yu, Yang Hui-Juan, Wang Peng, Ma Wei, Fuzzy Clustering based on Semantic Body and its Application in Chinese Spam Filtering, *JDCTA*, Vol. 5, No. 4, 2011, pp. 1-11.
- [3]. Jie Zeng, Meng Zhang, Hu Sheng, Jinxiu Luo, The Intelligent Video Playback System Based on RFID Technology, *Journal of Networks*, Vol. 7, No. 10, 2012, pp. 350-361.
- [4]. Shifei Ding, Chang Tong, Research and Comparison of Granularity Cluster Analysis Methods, *IJACT*, Vol. 3, No. 7, 2011, pp. 154-159.
- [5]. Junfei Chen, Zeyuan Huang, Huiming Wang, Drought Situation Evaluation of Crops Based on Integrated Gray Fuzzy-Clustering Method, *JCIT*, Vol. 7, No. 19, 2012, pp. 211-219.
- [6]. Jing Tian, Bing Yu, Dan Yu, Shilong Ma, A Semi-supervised Approach for Missing Data Imputation based on Fuzzy K-means Clustering, *IJACT*, Vol. 5, No. 7, 2013, pp. 480-487.
- [7]. Feng Xiao, Yajian Zhou, Jingxian Zhou, Hongliang Zhu, Xinxin Niu, Security Protocol for RFID System Conforming to EPC-C1G2 Standard, *Journal of Computers*, Vol. 8, No. 3, 2013, pp. 150-159.
- [8]. Guoying Liu, Wenyong Ge, Changqing Zhang, A Fuzzy Clustering Method for Image Segmentation Based on Hidden Markov Random Field Models, *JDCTA*, Vol. 6, No. 21, 2012, pp. 347-356.
- [9]. Bing Chen, Chengxiang Tan, Bo Jin, Xiang Zou, Yuebo Dai, RFID-based Electronic Identity Security

- Cloud Platform in Cyberspace, *Journal of Networks*, Vol. 7, No. 7, 2012, pp. 280-290.
- [10]. Hao Wang, Wireless Sensor Networks for an Extended City Intelligent Transportation System, *IJACT*, Vol. 3, No. 5, 2011, pp. 300-307.
- [11]. Huaibin Wang, Haiyun Zhou, Chundong Wang, Virtual Machine-based Intrusion Detection System Framework in Cloud Computing Environment, *Journal of Computers*, Vol. 7, No. 10, 2012, pp. 2397-2403.
- [12]. Ke Zheng, Ke Cheng Liu, The research of intelligent transportation system based on formal concept ontology models, *JCIT*, Vol. 7, No. 10, 2012, pp. 158-165.
- [13]. Wang Xinxin, Zhao Jianlin, Design of Wireless Intelligent Home Security System, *JDCTA*, Vol. 7, No. 6, 2013, pp. 282-289.
- [14]. Hao Chen, The Construction of Intelligent Home Based on Wireless Sensor Networks, *IJACT*, Vol. 4, No. 16, 2012, pp. 312-319.
- [15]. Haitao Zhang, Pu Miao, An Improved RFID Localization Algorithm Based on Layer By Layer Exclusion, *Journal of Computers*, Vol. 6, No. 12, 2011, pp. 58-93.

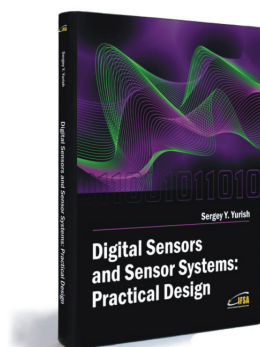
2013 Copyright ©, International Frequency Sensor Association (IFSA). All rights reserved.  
(<http://www.sensorsportal.com>)



International Frequency Sensor Association (IFSA) Publishing

## Digital Sensors and Sensor Systems: Practical Design

Sergey Y. Yurish



Formats: printable pdf (Acrobat) and print (hardcover), 419 pages

ISBN: 978-84-616-0652-8,  
e-ISBN: 978-84-615-6957-1

The goal of this book is to help the practitioners achieve the best metrological and technical performances of digital sensors and sensor systems at low cost, and significantly to reduce time-to-market. It should be also useful for students, lectures and professors to provide a solid background of the novel concepts and design approach.

### Book features include:

- Each of chapter can be used independently and contains its own detailed list of references
- Easy-to-repeat experiments
- Practical orientation
- Dozens examples of various complete sensors and sensor systems for physical and chemical, electrical and non-electrical values
- Detailed description of technology driven and coming alternative to the ADC a frequency (time)-to-digital conversion

*Digital Sensors and Sensor Systems: Practical Design* will greatly benefit undergraduate and at PhD students, engineers, scientists and researchers in both industry and academia. It is especially suited as a reference guide for practitioners, working for Original Equipment Manufacturers (OEM) electronics market (electronics/hardware), sensor industry, and using commercial-off-the-shelf components

[http://sensorsportal.com/HTML/BOOKSTORE/Digital\\_Sensors.htm](http://sensorsportal.com/HTML/BOOKSTORE/Digital_Sensors.htm)

## MEMS Multi-Fields Uniform Model Simulation and Optimization Method Research and Application

Gong Youping, Chen Huipeng, Liu Haiqiang, Li Zhihua, Chen Guojin

School of Mechanical Engineering Hangzhou Dianzi University Hangzhou, 310018, China

E-mail: [gypcad@163.com](mailto:gypcad@163.com)

Received: 10 August 2013 / Accepted: 25 August 2013 / Published: 30 September 2013

**Abstract:** To solve the coupling and optimizing problems in MEMS designing and analyzing process, the paper mainly put forward to the uniform model construction simulation method. The method adopt uniform constraints to describe MEMS multi-fields simulation model, firstly construct MEMS model library which includes structure, electricity, magnetic, thermal and fluid elements in multi-field uniform language modeling; through these elements, MEMS physics simulation model can be directly constructed; after model construction, some prosperities of the MEMS devices can be simulated. The aim of the method of paper is trying to conquer the computing efficiency of numerical simulation and abstraction problems of hardware describe language (HDL) and realizes MEMS multi-fields uniform constrained model construction and solving theory system. At last, an application example of the method has been realized, which shows that the method is effective to the early design of MEMS product. *Copyright © 2013 IFSA.*

**Keywords:** MEMS, Multi-fields simulation, Sensitivity analysis, Modelica.

### 1. Introduction

Micro-Electro-Mechanical Systems (MEMS) are the integration of mechanical elements, sensors, actuators, and electronics at the micron-scale or even at nano-scale through micro fabrication technology, which involves the mechanical, electronic, fluid, thermal, optical, magnetic and other disciplines [1]. Multi-energy domain coupling effect of MEMS can hardly be described perfectly, because in a micron-scale or even in a nano-scale working room, physical quantities of energy among the different domains interact with each other. So, in MEMS's design process, the comprehensive effects which have been made by a variety of physical phenomena must be taken into consideration. Along with electronics simulation theory, traditional MEMS simulation methods often carried out dynamic performance

analysis with equivalent circuit models, so VHDL-AMS and SPICE were widely used to design micro systems at system level, lacking a clear separation of function, complex and heterogeneous MEMS involving various other physical domains, such as mechanics, fluid, thermal and etc, can hardly be described by these circuit equivalent methods, how to quickly and accurately modeling and simulating the system has been a big problem for the design personnel, so it is a urgent need to study on the method to model and simulate the complex micro-electro-mechanical physical system which includes machinery, electronics, hydraulic control and other fields [2]. To support the modeling processes more effectively, a micro simulation components library (e. g. electro-thermal resistors, beams, plate masses, electrostatic gaps, and so on) is established based on uniform model language -modelica language. Using

these libraries, uniform constraints to describe MEMS multi-fields simulation model, represented simulation models can cascade from coupled multi-domain models to sub-models at each energy domain, then to the micro simulation components. Through the uniform constrained model, we can make comparison and validation to every link from design

to manufacturing, so as to optimize the design of MEMS devices, test the effectiveness of the manufacturing process, prevent unexpected errors shorten the development cycle, save the research funding, improve the quality of products. Fig. 1 is show the process of uniform constrained MEMS model construction and optimizing design process.

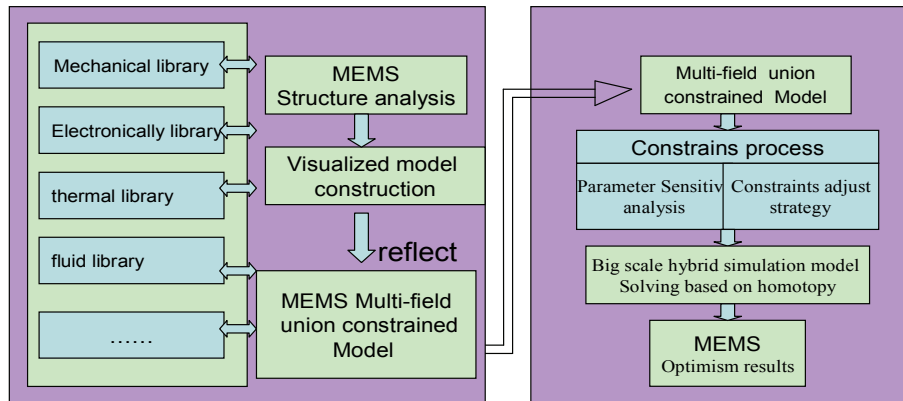


Fig. 1. MEMS uniform constrained model and optimizing process.

## 2. MEMS Simulation Method Preview

The scholars of the United States, Europe, Japan and other countries have realized the successful industrialization of MEMS and occupying the market largely depend on how to use the computer aided design, analysis and manufacturing methods (CAD/CAE/CAM) effectively. Currently, in the study of micro-electro-mechanical system, the development level of computer aided tools far behind the frontiers of the pace, most MEMS devices are designed by the analysis tools which have the similar functions and can not predict the execution situation of MEMS accurately. Therefore, we always use test troubleshooting methods, which often requires repeated trials to finalize the device equipment to meet the specific environment. For the development of MEMS devices and systems for commercial products, this backward design method has a long design cycle, low efficiency, high cost and impractical. Thus, there is an urgent need of advanced modeling tools and simulation methods for MEMS design. The multi-disciplinary nature of MEMS involves the complex coupling issues among the electric, mechanical, magnetic, thermal, fluid and optical physical multi-energy domain, and its integrated development trend needs a system simulation method of the device or system and circuit. At present, the simulation method that mainly used in MEMS, including numerical simulation, hardware description language method and the unified model of multi-domain simulation method, in which the hardware description language method develops into the signal flow analysis, nodal analysis, the bond graph method [3].

### 2.1. Numerical Simulation Method

Numerical simulation method includes the difference, finite element method, the boundary element, the finite volume method and other methods, the finite element method is the commonly used method, when we do the multi-energy domain coupling analysis of microelectromechanical system, we should seek the appropriate algorithm for the characteristics of each domain, and solve the coupling issues between different domains. Numerical simulation using ANSYS and other finite element software's or Intellisuite and other dedicated MEMS CAD software's to design and analyze MEMS structures. This method requires a pre-set of the structural parameters to make the model and simulation, then amend the original model according to the results of the simulation analysis until we get the satisfactory results. This simulation method has a greater progress than repeating trials, it reduce the costs and shorten the design cycle to a certain extent. Some well-known finite element software such as ANSYS has successfully introduced a coupling field calculation method to solve a variety of coupling issues [4, 5]. Li Jun and others have made a finite element modeling and analysis of the electrostatic micro-pump [6]. Ji Kexing and others have used the finite element method to study the influence of residual stress on the structural design of electrostatic feedback MEMS sensor with high temperature shear stress [7]. Field-based analysis of large-scale numerical simulation for different energy domain analysis needs to mesh, needs to achieve automatic mesh division which is very difficult and the calculation method has not reached a mature stage. The calculation is huge and there is a lack of efficient

method of calculating, so we can not achieve the simulation of system-level and circuit integration.

## **2.2. Signal Flow Analysis Method**

The signal flow analysis is also known as black-box analysis. The basic idea is to establish on the basis of numerical analysis to different energy domains of MEMS coupling field, selected a few parameters to describe the energy of the system, reduce the system's degrees of freedom and do not care about the local structure and characteristics of the system. Then, the system coupling field can be expressed by a black-box which has a few parameters. Generally we select the vibration modal of the sporty structures as the basic variables set, we use the generalized coordinates for the coefficient of linear superposition to get the approximate deformation of the sport structures, establishing the Lagrange equation of the system, converting it for the hardware description language model and having a simulation in circuit of the MEMS, then, the simulation time of system can be greatly reduced. This method can obtain a high precision and applies to any complex system [8, 9].

## **2.3. Nodal Analysis Method**

Using the node analysis to system modeling are in the form of the system unit geometry size and material constants components for simulation parameters, its ideology is similar to circuit analysis, considering the system is composed by the sub-structural units of the same energy domain or different energy domains, these component units with lumped parameter model description, interconnected by the nodes which have the same energy domain nature, equivalent to the circuit resistance, capacitance and so on. After converting it into hardware description language model, then link the units together, form a network topology structure, build the whole differential equations of system and implement the system simulation in the software of EDA. The advantage of the method is fully integrated with IC CAD tools, using the same software tools to solve MEMS and IC design problems at the same time, applying to the structures of lumped mass and stiffness can be decomposed, it is always used for the small displacement and small signal occasions. Jan E. Vandemeer has proposed nodal analysis for MEMS simulation and design [10], Q. Jing improved the nodal analysis method and applied it into the MEMS parametric analysis [11]. Yuan Weizheng used the improved nodal analysis method to solve the MEMS issues [12].

## **2.4. Bond Graph Method**

As a powerful theoretical tool for the interaction between the different energy domain systems, the

bond graph method makes the dynamic system as a system determined by the state variables, its relationship between the state variables and other system variables is established by a set of ordinary differential equations and algebraic equations. By using the bond graph language to describe the system model, different systems can exchange energy to achieve interaction. But the theory of the method is abstract, difficult to understand, incompatible with the electric network system simulator, it is difficult to achieve system-level simulation and optimization.

## **2.5. MEMS Multi-domain Uniform Modeling and Simulation**

To early design of MEMS, we often considered the MEMS device structure itself more and did less departure from a multidisciplinary point of view of technology, structure, fluid circuit, error to make the optimal design of the MEMS system. Even though the device itself achieves the best performance, once it is processed and used in conjunction with other peripheral subsystems, it can not achieve the optimal overall properties of the system, thereby increasing the number of iterations of the design, resulting in the improvement of product development costs. Therefore, it is necessary to study the MEMS simulation and optimization of design from the point of view of system, but there is still a lack of effective design methods to solve system design and optimization of MEMS. The method based on unified modeling language using a unified approach to describe the system components in different areas, it can achieve full realization of the seamless integration and data exchange between different areas of the model. The intrinsic component connection mechanism based on a unified language realizes the model composition and multi-domain integration; it can model and simulate all the problem which can be described by differential equations or algebraic equations.

The unified modeling studies of multi-domain physical system originated in the first object-oriented simulation modeling language Dymola by Elmquist in 1978 [13]. A series of object-oriented and equation-based simulation modeling language appeared in the later, for example, Omola, ASCEND, GPROMS, NMF, ObjectMath, Smile and so on [14]. Faced with the compatibility and standardization issues of many languages coexist, some experts and scholars in the simulation community in Europe had introduced a new generation of statement language Modelica on the basis of the previously summarized and unified a variety of modeling languages in 1997 [15]. Currently, the modeling based on the Modelica language has a wide range of applications in the automotive and electric vehicles, hydraulic systems, mechanical multi-body system, thermal power system, power systems, electromechanical systems, chemical systems and hardware in loop simulation, discrete event systems and other systems

of processes. The simulation application based on Modelica has been started in our country. For example, the simulation analysis of gas turbines, switched reluctance motor, synchronous motor, heat engine, engine, mechanical gearbox and turbofan engine [16-18].

### 3. Multi-fields Uniform Constrained Simulation Model

#### 3.1. Multi-domain Uniform Constrained Simulation Model Expression and Construction

Multi-domain uniform constrained simulation model's mainly strategy is to express every fields designing parameters, constraints conditions and solving aims in a uniform statement equations. Because of product's expression often are hierarchy model and MEMS' constraints relation model is also a part of product, so the uniform constrained simulation model also adopt hierarchy model like Fig. 2. According to classification of products, we divided MEMS constraints as product class constraints, components class constraints and parts class constraints and every class constraints have been divided constructive constraints, interface constraints and associated constraints and all the collects and relationship of the same class make up the constraints net. The constructive constraints express the MEMS's own characteristics, interface constraints express relationship between different fields and associated constraints express the

relationship between constructive constraints and interface constraints.

According to designing and analyzing of product should satisfy constraints, through grasp nature of different fields, we refine constraints as three elements: port, physical rule and element body, their relationship and expression are show as Fig. 3. The port was little circle of graph, the element bodies were linked by these ports and through object oriented and equation technology, make the constructive constraints, interface constraints and associated constraints as a union expression.

#### 3.2. Multi-domain Uniform Constrained Simulation Model's Parameters Sensitive Analyzing and Constraints Adjustment Strategy

Multi-domain constraint-based simulation model mapping the large-scale mixed constrained optimization system, corresponding to large-scale differential-algebraic and continuous-discrete hybrid equation and can not be directly solved. We should reduce the size and complexity of the problem before solving. Sensitivity analysis is one of the key technologies in the solving process of unified constrained optimization model, analyzing the sensitivity of the income can be used to determine the size of effect that the system design variables of parameters have been done on the objective function or constraint functions, it can also used to determine the coupling strength between the subsystems and ultimately used to guide the design [19, 20].

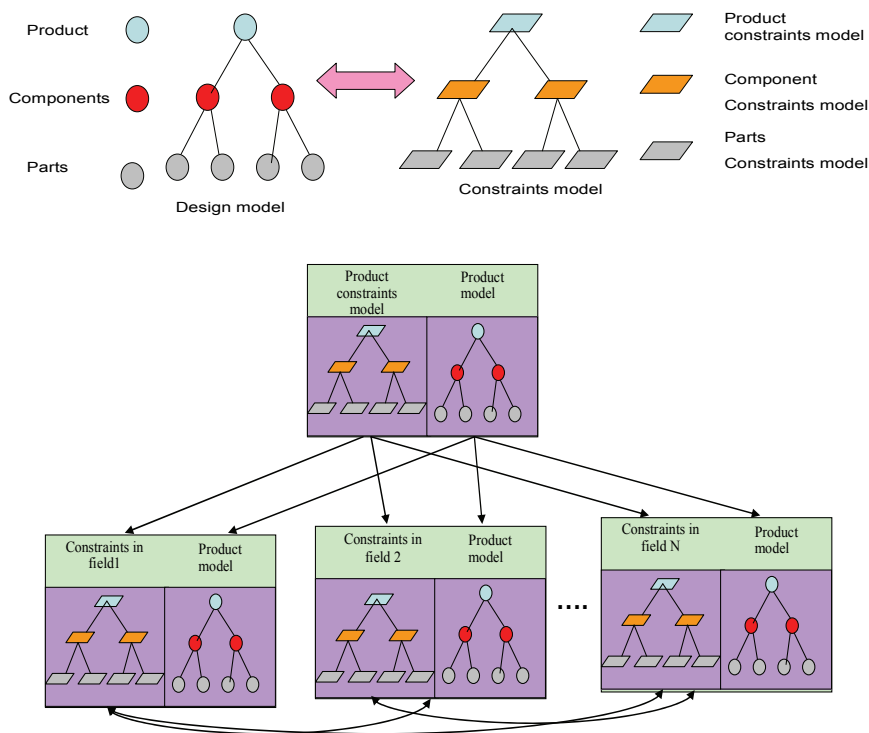


Fig. 2. MEMS Product constraints relationship model.

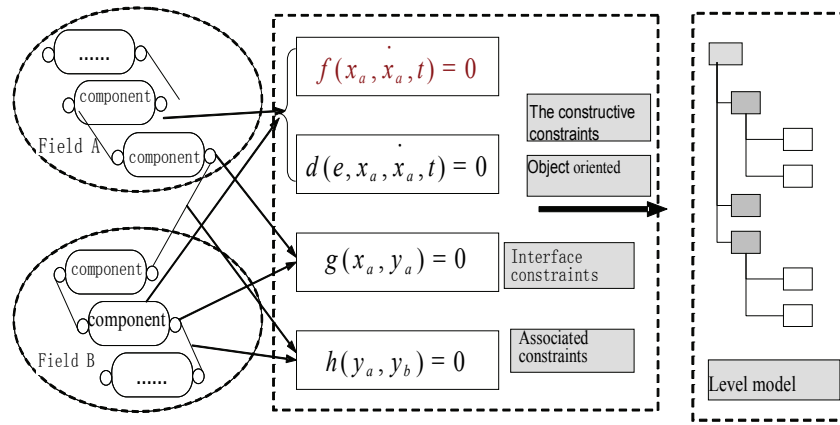


Fig. 3. MEMS union constraints model.

According to the sparse characteristics of the incidence matrix between the constraints (including the associated constraints, constitutive constraints, the matrix constraints and discrete constraints) and the variables, making coordination reduction partition processing of the large scale constraint system and getting the solution sequence or serialization of sub-problems, then selecting the appropriate iterative method to get the solution and get the best MEMS design program. According to the continuous

variables and discrete variables in the model, we can put forward the unified constrained optimization model generalized sensitivity analysis method, use the acquired information of the sensitivity to decouple the unified constrained optimization model and get a simplified processing of the constraint model. Fig. 4 shows the MEMS union constraints simulation model parameters sensitivity analyze method [19-21].

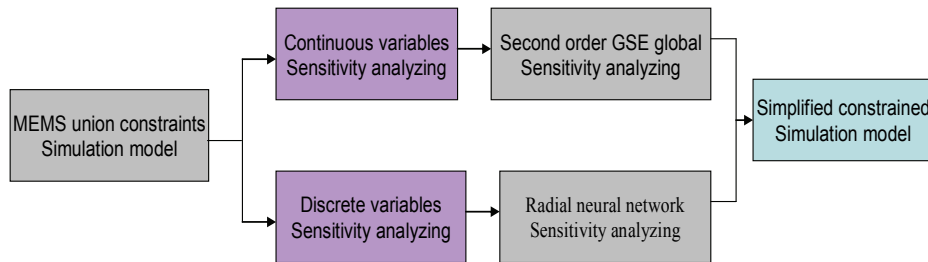


Fig. 4. MEMS union constraints simulation model parameters sensitivity analyze method.

From the angle of MEMS unified constrained optimization model, using the method of global integrated satisfaction to get the coordinated strategy of the MEMS unified constraint model, coordinating the constructed unified constraint network, seeking the design solution to optimize the overall satisfaction of the overall objective under the premise of achieving the target satisfaction level of all the areas. Fig. 5 shows the MEMS constraints adjustment strategy process [22, 23].

#### 4. Application Example

Modelica language, which provides a uniform multi-domain simulation model description method to construct the system dynamic models of such complex and heterogeneous micro-mechanical systems. Modelica is a general equation-based object-oriented language for multi-domain modeling of

physical systems and utilized in mechatronic models in robotics, automotive and aerospace applications involving mechanical, electrical, hydraulic and control subsystems and distribution of electric power. Among the various MEMS products available one important mechanical transducer is the accelerometer in which the sensor capacitance changes with input acceleration. The advantages of low cost, low power consumption, small size, reliability and batch fabrication make Micro-mechanical accelerometer have a wide range of applications in industry autoimmunization controls, automotive security systems, vibration and shock measurements, military markets. In the paper, we will try to find a way to construct the Micro-mechanical accelerometer uniform constrained simulation models. The typical Micro-mechanical accelerometer's structure is showing like Fig. 6, the moveable sensitive mass is a double comb micro-mechanical structure, linked with two folded flexure. Every comb extend to two sides

from middle moveable sensitive mass, every movable comb is a changeable capacity plate; fixed comb is fixing on the anchor point, every pair of movable comb and fixed comb constructs a differential capacity. The moveable sensitive mass moved along the sensitive orientation. When the system moves by the inertial force, the moveable sensitive mass moves

to another place, then change the distance from movable comb to fixed comb, through measuring the differential capacity's changing value, the inertial force can be derived and the acceleration also can be computed through the relationship between the inertial forces to movement.

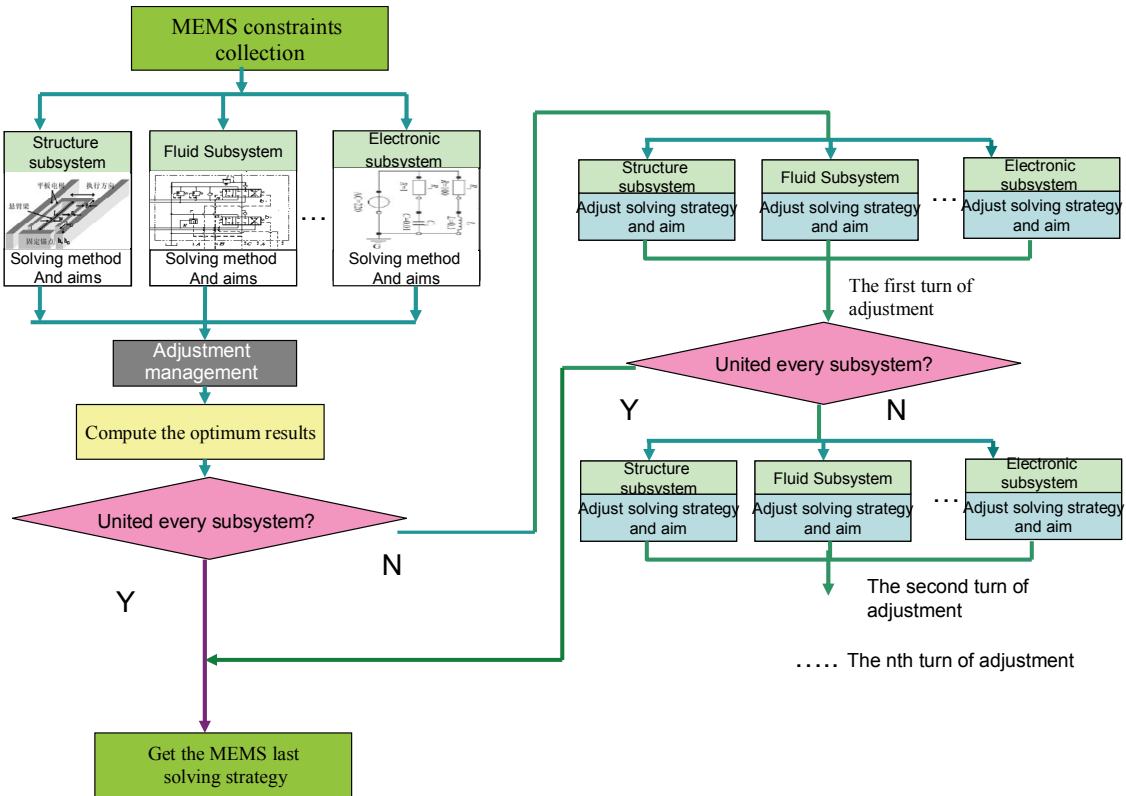


Fig. 5. MEMS constraints adjustment strategy process.

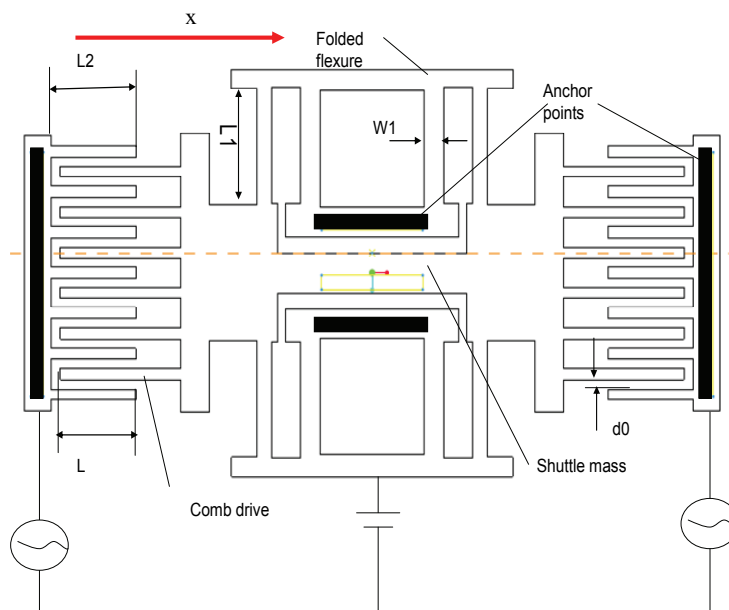


Fig. 6. The typical Micro-mechanical accelerometer's structure.

#### 4.1. Micro-mechanical Accelerometer Mechanical Model

Micro-mechanical accelerometer simplified dynamics model as shown in Fig. 7, it's working mode can be viewed as a spring-mass-damping vibration behavior of system under the action of periodic external force.

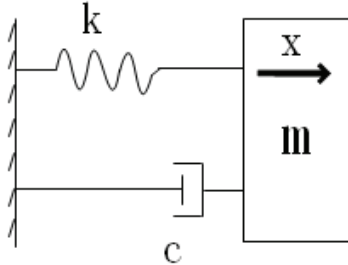


Fig. 7. Micro-mechanical accelerometer dynamic model.

Set quality pieces as shown in Fig. 7 in the X direction received force  $F$ , the movement of system can be described by the following equation.

$$m\ddot{x}(t) + c\dot{x}(t) + kx(t) = F \quad (1)$$

In the equation,  $m$  represents the quality of the quality mass,  $c$  represents the damping coefficient,  $k$  represents the beam stiffness coefficient,  $F$  represents the input force, the equation also can be converted to the following form equation.

$$m\dot{v}(t) + cv(t) + k \int v(t)dt = F \quad (2)$$

The differential capacity, as shown in the Fig. 8.

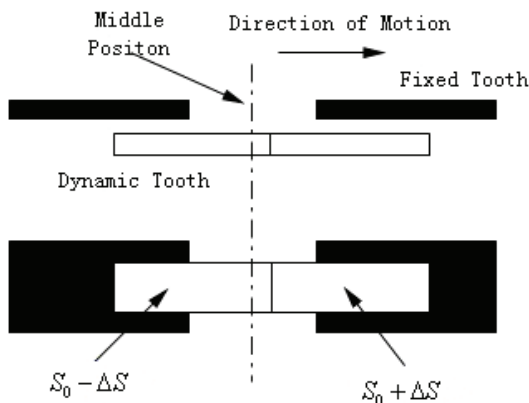


Fig. 8. Schematic diagram of the differential capacitance.

For the structure of the differential capacitance, as shown in Fig. 8, the capacitance can be divided into two parts, they can be expressed as:

$$C_1 = \frac{\epsilon_0 \epsilon_r (s_0 - \Delta s)}{d} \quad (3)$$

$$C_2 = \frac{\epsilon_0 \epsilon_r (s_0 + \Delta s)}{d}$$

In the last two equations,  $\epsilon_0$  represents the vacuum dielectric constant,  $\epsilon_r$  represents the relative dielectric constant of the medium,  $d$  represents the initial distance between capacitance boards,  $s_0$  represents the area of the capacitance between the plates,  $\Delta s$  represents the changes of the area.

So that you can produce differential capacitance, differential capacitance is obtained as below:

$$\Delta C = C_2 - C_1 = \frac{\epsilon_0 \epsilon_r (s_0 - \Delta s)}{d} - \frac{\epsilon_0 \epsilon_r (s_0 + \Delta s)}{d} = 2 \frac{\epsilon_0 \epsilon_r \Delta s}{d} \quad (4)$$

The changes of area  $\Delta s$  can be represented as:

$$\Delta s = b \times \Delta x \quad (5)$$

Among them,  $b$  represents the thickness of the finger,  $\Delta x$  represents the displacement change of the finger.

The equation 4 and 5 show that tiny displacement  $\Delta x$  due to acceleration of quality can be converted into the change of the differential capacitance and the differential capacitance variation  $\Delta C$  is proportional to the displacement variation  $\Delta x$ .

Due to external force  $F$  input, in the open loop, the inertial force on the quality mass is balance the elastic force caused by the beam.

$$F = ma = k\Delta x \quad (6)$$

Among them,  $F$  represents the external force,  $a$  represents the acceleration for the input,  $k$  represents the equivalent stiffness beam,  $m$  represents the quality of the mass, so we can obtain:

$$\Delta C = \frac{2m\epsilon_0 \epsilon_r b}{kd} a \quad (7)$$

The equation 7 shows that the differential capacitance variation is proportional to the input acceleration, so use the capacitance detection circuit converts the differential capacitance variation to voltage value that can be measured, so we can according to the output voltage to determine the size of the measured acceleration. After analyzing the micro-mechanical accelerometer in mechanical field and electric field, then we construct Micro-mechanical accelerometer united constrained model with modelica language, as shown in Fig. 9.

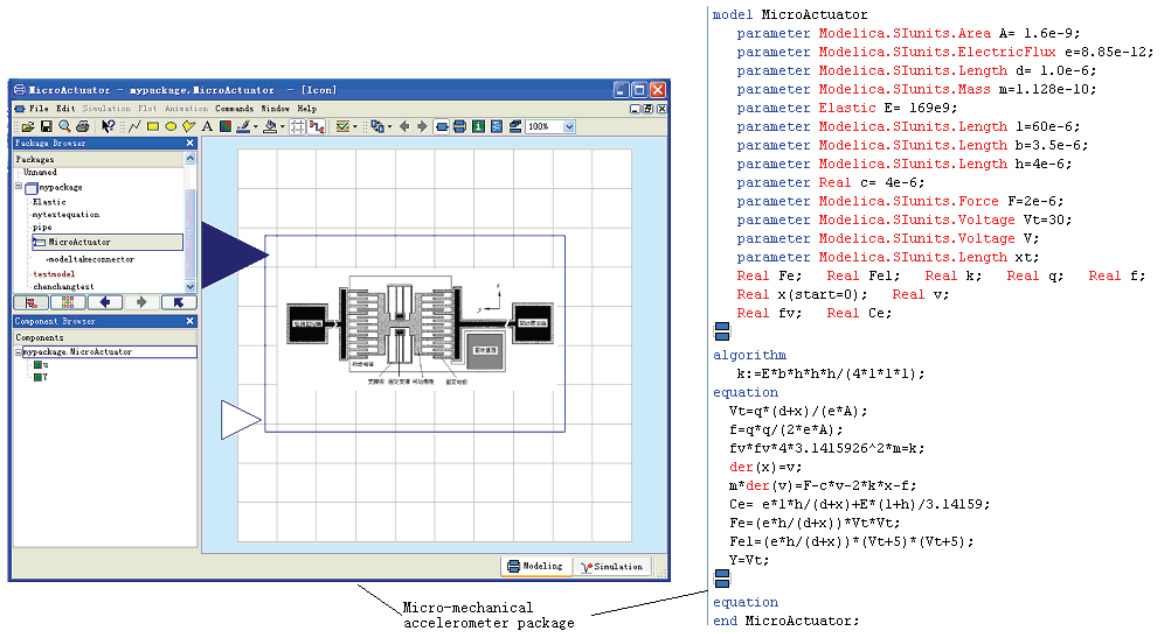


Fig. 9. Micro-mechanical accelerometer united constrained model with modelica language.

Exerting a harmonic force  $F = F_0 \sin(2\pi ft)$  along the horizontal direction to the accelerometer, the amplitude is  $F_0 = 7.2 \times 10^{-8} N$ , the frequency is  $f = 11933 Hz$ , taking the quality of the mass  $m = 4.58 \times 10^{-11} kg$ , the damping coefficient is  $c = 1.76 \times 10^{-7} Ns/m$ , stiffness coefficient of the beam is  $k = 0.2576 N/m$ , after simulate in Dymola for three millisecond, the test model is showing like

Fig. 10, we can get the speed characteristic curve as shown in Fig. 11, the quality mass reach steady state quickly. We can see from the Fig. 11 (a) the displacement of the from movable comb to fixed comb  $x = 60.8275 nm$ , the electric force between the movable comb and fixed comb is  $7.2653 \times 10^{-6} N$ , like the Fig. 11 (b).

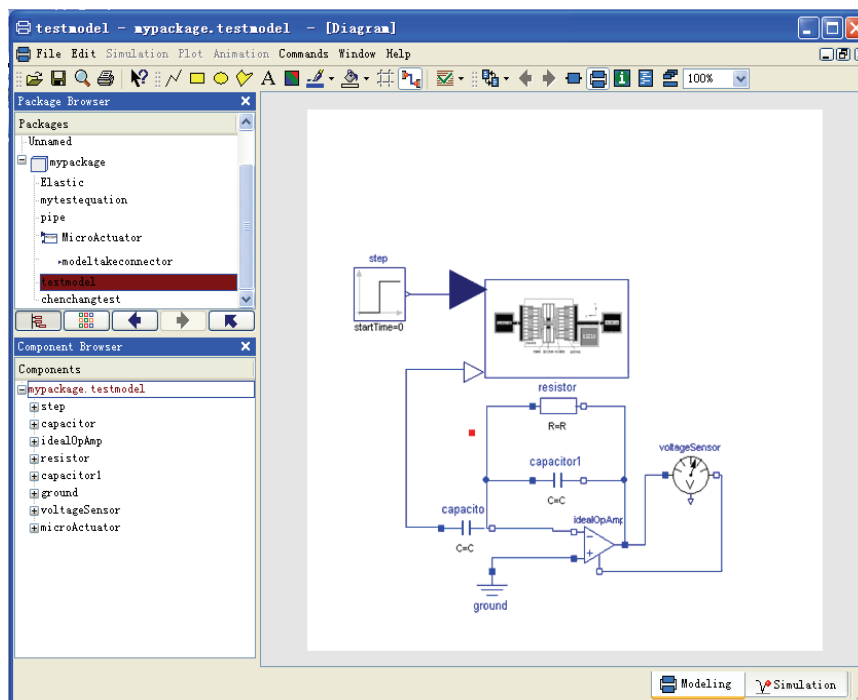
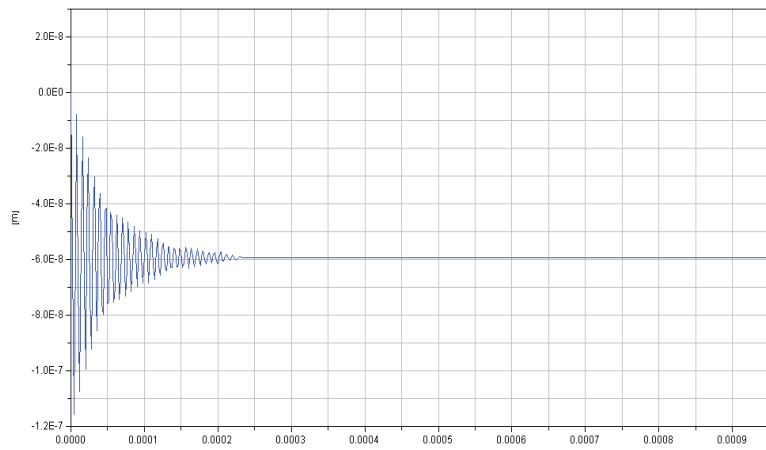
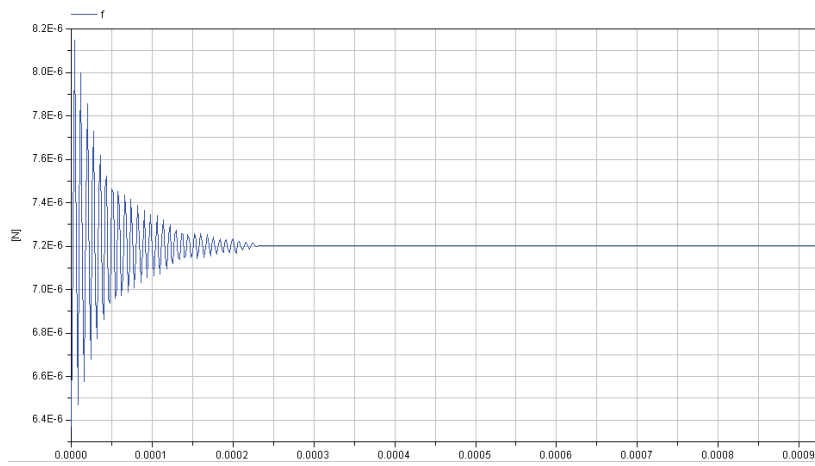


Fig. 10. Test model.



(a) The distance from movable comb to fixed comb.



(b) electric force between the movable comb and fixed comb.

**Fig. 11.** Simulation results.

## 5 Conclusions

The physical system modeling and simulation has been developed from a single field to the unified multi-domain modeling, has produced a number of criteria and has made a foundation to the study of the key technologies of multi-domain unified simulation optimization modeling and solving. Throughout the current MEMS simulation design methods, the study of multidisciplinary design optimization methods include single-discipline optimization, parallel optimization between the main systems and subsystems, whose role is to constantly improve multidisciplinary design of complex systems, until you find the optimal design. The simulation analysis method has a great progress than the trial and error, has reduced the costs and has shortened the design cycle to a certain extent. But to the analysis of different energy domains, the large scale numerical simulation based on the field analysis needs the corresponding grid partition. Realizing the automatic dividing grid is hard and computing method also did not reach the mature stage, the lack of efficient computational methods, the great amount of calculation, it is difficult to realize the system-level

simulation and circuit integration simulation. Hardware description language methods can get a high precision and can apply to any complex system, but it is just a abstract of the original system, it can not consider the local characteristics of system, can not show the influence that the structure size of the system parts have done on the performance of system, which is unfavorable for the design and optimization of MEMS. The MEMS optimal design method of the simulation optimization model based on multi-domain unified constraint expression use a unified constraint optimization model to describe the MEMS multi-domain optimization problem model. This model can embody the multi-field and hierarchical characteristics of MEMS; it has the unified constraint representation theory with the physical structure intrinsic and reusable characteristics. Before solving the situation, we should coordinate the coupling factors of each discipline, guide the optimal solution obtained under the unified constraint environment, improve the quality of solution, enhance the fault tolerance ability and improve the information exchange ability. Solving use the constraint mapping and structural reduction technology to achieve the solution of

multi-field optimizations design model under a large scale constraints environment and ultimately realize the solving theoretical system of MEMS unified constraint modeling and simulation optimization. Therefore, compared to other methods, multi-domain unified modeling and simulation optimization design method can better solve the MEMS simulation optimization problems.

## Acknowledgements

The paper was support by the National Natural Science Foundation of China “MEMS Multi-fields Uniform Simulation Model Construction and Optimism Research” (61100101, 51275141), the paper was also supported by Key Discipline of The Ocean Mechatronic Equipments Technology.

## References

- [1]. Li Desheng, MEMS Technology and its Application, *Haibin Industrial University Press*, 2002.
- [2]. L. S. Fan, Y. C. Tai, R. S. Muller, IC-processed electrostatic micromotor, *Sensors and Actuators*, 20, 10, 1989, pp. 41-47.
- [3]. Hu Wei, Hu Guoqing, Wei Xin and Xie Xiaozhu, MEMS CAD Research Development and the Present Situation, *Piezoelectrics and Acousto-optics*, 32, 4, 2010, pp. 682-691.
- [4]. Aluru N. R., White J., Multi-level Newton method for static and fundamental frequency analysis of electromechanical systems, in *Proceedings of the International Conference on Simulation of Semiconductor Processes and Devices (SISPAD)*, 1997, pp. 125-128.
- [5]. X. Rottenberg, P. Czarnecki, H. A. C. Tilmans, W. De Raedt, Multi-physics simulation and reliability analysis for RF-MEMS devices, in *Proceedings of the 9<sup>th</sup> Int. Conf. on Thermal, Mechanical and Multiphysics Simulation and Experiments in Micro-Electronics and Micro-Systems (EuroSimE)*, 2008, pp. 319-329.
- [6]. Li Jun, Ying Ji and Zhou Liangxing, Based on the MEMS Static Micropump Modeling and Simulation, *Journal of Engineering Design*, 16, 1, 2009, pp. 63-66.
- [7]. Ji Kexing, Song Hongwei and Fan Xuejun, Residual Stress Analysis of High-temperature MEMS Shear Stress Sensor, *Mechanics and Practice*, 32, 1, 2010, pp. 60-63.
- [8]. Robert L. Ewing, Technology Road Map to Methodologies for Mixed-Signal System Design and simulation, *Journal of VLSI Signal Processing*, 20, 1999, pp. 123-134.
- [9]. Wang Yongquan, Chen Hualing, Peng Bei and Zhu Zicai, MEMS Node Modeling and its Application of Integrated Microsystem Design, *Optical Precision Engineering*, 18, 1, 2010, pp. 198-203.
- [10]. Jan E. Vandemeer, Nodal Design of Actuators and Sensors (NODAS), Technical Report, *Carnegie Mellon University*, May 7, 1998.
- [11]. Q. Jing, T. Mukherjee and G. Fedder, Schematic-Based Lumped Parameterized Behavioral Modeling for Suspended MEMS, in *Proceedings of the Technical Digest of the ACM/IEEE International Conference on Computer Aided Design (ICCAD' 02)*, San Jose, California, 2002, pp. 367-373.
- [12]. Yuan Weizheng, Niu Haobin, Chang Honglong and Ma Binghe, Co-simulation Prototype System of MEMS devices and Circuit, *Optical Precision Engineering*, 18, 10, 2010, pp. 2206-2210.
- [13]. Gou Peng, Liu Wei and Gui Weicheng, A Comparison of Approximation methods for Multidisciplinary Design Optimization of Ship Structures, *Journal of Ship Mechanics*, 11, 6, 1978, pp. 913-922.
- [14]. Lee J. Y, K. Kim, Geometric Reasoning for Knowledge-Based Design Using Graph Representation, *Computer Aided Design*, 28, 19, 1998, pp. 831-841.
- [15]. Mattsson S. E., Elmqvist H., Otter M., Physical system modeling with Modelica, *Control Engineering Practice*, 6, 4, 1998, pp. 501-510.
- [16]. Zhou Xiangjun, Jin Shuang, Chen Yan, Lu Jun, Wang Hongjun and Liu Tianhu, Picking Manipulator Motion Control Modeling Based on the Modelica, *Journal of System Simulation*, 21, 18, 2009, pp. 5882-5885.
- [17]. Zhang Sheng, Cheng Wenke, Wang Hua and Tang Guojin, Ballistic Missile System Simulation Based on Modelica Language, *Journal of Missiles and Guidance*, 30, 5, 2010, pp. 20-25.
- [18]. Chen Qiongzong, Meng Guang, The Modelica Modular Modeling Method of Switched Reluctance Motor, *Motor and Control Applications*, 36, 12, 2009, pp. 1-5.
- [19]. Cui Jiuzheng, Sun Bo and Feng Qiang, Sensitivity Analysis of Factors Influencing MEMS Package Reliability, in *Proceedings of the Prognostics and System Health Management Conference*, 2011, pp. 1-7.
- [20]. A. Kohler, S. Reitz and P. Schneider, Sensitivity Analysis and Adaptive Multi-point Multi-moment Model Order Reduction in MEMS Design, *Design, Test, Integration and Packaging of MEMS/MOEMS*, 2011, pp. 64-71.
- [21]. Cheng J., Liao S. J., Mohapatrab R. N. and Vajravelu K., Series Solutions of Nano Boundary Layer Flows by Means of the Homotopy Analysis Method, *Journal of Mathematical Analysis and Applications*, 343, 1, 2008, pp. 233-245.
- [22]. Z. Li, B. Han, A Parameter Differential Regularization Algorithm for Solving Inverse Problems of GPR, *Journal of Computational Information system*, 4, 1, 2008, pp. 407-412.
- [23]. Gong Youping, Jin Tao and Tong Shuiguang, Application of Homotopy Method in the Reverse Engineering Constraint solving, *Journal of Image and Graphics*, 12, 4, 2007, pp. 727-731.

## Classification of Fatty Fat Acid in Palm Oil Using Near Infrared Spectroscopy

<sup>1</sup> Herlina ABDUL RAHIM, <sup>2</sup> Siti Nurhidayah Naqiah ABDULL RANI

<sup>1,2</sup> Process Tomography and Instrumentation Research Group (PROTOM-I), INFOCOMM Research Alliance, Universiti Teknologi Malaysia, 81310 Skudai, Johor

<sup>1</sup> Tel.: +609-7714208, fax: +607-5566272

<sup>1</sup> E-mail: [herlina@fke.utm.my](mailto:herlina@fke.utm.my)

Received: 21 June 2013 / Accepted: 25 August 2013 / Published: 30 September 2013

**Abstract:** This paper propose an experiment to determine compatibility of near infrared (NIR) application in crude palm oil (CPO) quality measurement, considering only the Free Fatty Acid (FFA). 100 samples were taken from Felda Johor Bulklers, Terminal 1 in 7 consecutive days of experiment. FFA reading from conventional wet chemical analysis is used as the reference and validation for NIR method. Partial Least Square Regression (PLSR) method is used for the linear analysis, generated from MATLAB software. However, the finding from this experiment not really support the application at which the accuracy percentage acquire is only 48.12 %. *Copyright © 2013 IFSA.*

**Keywords:** Palm oil, Fatty fat acid, Near infrared spectroscopy, Partial least square regression.

### 1. Introduction

Near-infrared spectroscopic is a well-known technique in agriculture and food engineering. Mid 1960, USDA had developed NIR method of analysis to detect internal qualities of apple crops. Besides, this technology too is used to predict fruit maturity level and sugar content. Nowadays, NIR is a popular method to perform rapid, non-destructive analyses especially across the agriculture and food industries [1].

In Malaysia palm oil (*Elaeis Guineensis*) is one of the important sources of revenue [2]. Two main oil yields from palm oil fruit are extracted from the mesocarp; Crude Palm Oil (CPO) and from the kernel; Palm Kernel Oil (PKO) [3, 4]. These two oils have different characteristic and properties. The properties of CPO make it suitable for food product (e.g. butter, cooking oil) while PKO is used for non-food product (e.g. cosmetic) [5]. However the usage

of CPO is more likely interested for this project. Thus, CPO has been chosen for the time being.

The main parameter for CPO quality can be classified in five term; Free Fatty Acid content (FFA), moisture level, Deterioration of Bleachability Index (DOBI), iodine value (IV) and carotene[6]. Among these internal quality attributes, FFA gave the most influence for consumer decision on trading purpose. The usage of analytical instrumentation in fats and oil is outdated and need adjustment to current technology development. Palm oil quality assessment need less time consuming method in order to preserve its quality [7].

### 2. Problem Statement

In Malaysia palm oil is one of the important sources of revenue. Yet, Malaysia too is the largest palm oil producer in the world [7]. Hence,

researchers have always finding ways of maintaining this sector to be at best performance and quality. Continuous studies have being developed in order to find ways to maintain and improved oil palm production in Malaysia.

A common problem occurred during harvesting is failure to determine the right ripe fruit. Fruit that is too ripe contain high fatty acid (FFA) which is lowering the quality of palm oil produced. While young fruit does not contain much oil. This will be a waste as for every 100 kilograms of right ripe fruit bunches, typically 22 kilograms of palm oil and 1.6 kilograms of palm kernel oil can be extracted.

Therefore, this project is proposing a method of determining the right ripe fruit to be harvested by using near-infrared spectroscopy. Thus, problems like harvesting too ripe or too young fruit can be avoided in future.

Mid 1960, USDA had developed NIR method of analysis to detect internal qualities of apple crops. Besides, this technology too is used to predict fruit maturity level and sugar content as shown in Fig. 1. Nowadays, NIR is a popular method to perform rapid, non-destructive analyses especially across the agriculture and food industries [1-5].



Fig. 1. Near infrared spectroscopy.

In 1998, Y. B Che Man and M. H Moh have developed a near-infrared spectroscopy calibration for determination of free fatty acid (FFA) in crude palm oil [4]. However, their objective is just to replace the common complex lab process to a simpler but reliable NIR method. A similar project was been done a year later by Y. B. Che Man et. al., this time by using FTIR spectroscopy. Both project shows positive improvement of conventional method and consistent results [7].

Conventionally, ripe palm oil fruit is determine by number of mature fruit fall from its bunches. In Malaysia, the fruit will turn from black to orange when ripen. The outer layer of the ripe fruit is oily and fleshy. Beside, when ripe, the intensity of fruit is increasing thus make it weighted around 40-50 kg per bunch.

Based on this characteristic, we are developing an analysis to recognize the ripe fruit by significant number of wavelength by applying NIR. This should be a promising yet reliable outcome from this project for an improvement in palm oil industry.

### 3. Materials and Method

The experiment took place at Felda Johore Bulkers-Terminal 1, Pasir Gudang, Johor from 1st December 2012 to 7th December 2012. 100 random selection of oil are collected from time to time in between these seven consecutive days. Wet chemical analysis is been done by qualified laboratory attendance immediately after the NIR scanning to preserve the same quality attributes of the chosen sample.

#### 3.1. Wet Chemical Analysis

Manual procedure for determining the acidity of CPO is being conducted based on the Malaysian Standard for Laboratory, MS 817:1989. (Standard of Test for Palm Oil & Palm Oil Products). From this standard, the acid value is defined as the amount (in milligram) of natrium hydroxide (NaOH) necessary to neutralize the free acids in 1 gram of sample.

Expression of result:

$$FFA\% = \frac{25.6 \times N \times V}{W}$$

where

- 25.6 is the weight for palmitic acid (palm oil and fractions);

- N is the normality of NaOH;

- V is the volume, in milliliters, of NaOH used;

- W is the weight, in gram, of the test portion.

For FFA below 0.15 %, FFA is expressed to three decimal places while for FFA above 0.15 %, two decimal places.

#### 3.2. Sample Preparation

100 oil samples received from random palm oil mills were used in this study. Each sample was divided into two parts to be used for chemical analysis and NIR scanning. The samples are collected in ambient temperature of 27 °C before inserted into water bath of 80 °C just before the analysis.

#### 3.3. Measurement

The NIR instrument used for this work is FOSS NIRSystem run by Vision Software. The wavelength measured range from 400 nm to 2500 nm but only 1600 nm to 1900 nm taken into account for the

analysis [6-9]. A single sample contained a total of 601 data points. Data were collected by absorbance spectroscopic and directly being used for the analysis.

#### 4. Results and Discussion

A data set comprising spectral intensities of 100 samples of CPO at region 1600 to 1900 nm wavelengths and their respective FFA value was loaded as matrix format into Matlab workspace [MATLAB 7.9.0 <R2009b>] [10]. Fig. 2 shows the raw absorbance spectrum of the CPO.

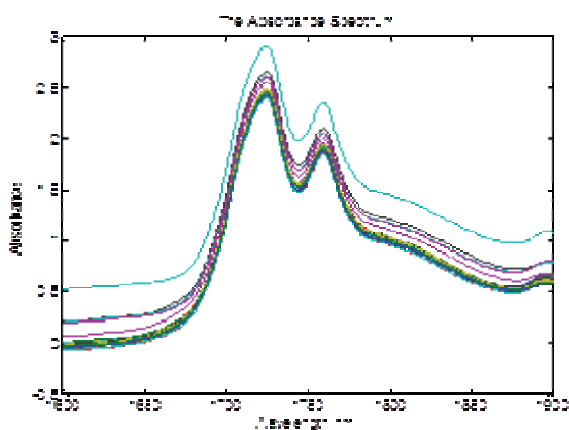


Fig. 2. Raw absorbance spectrum of the CPO.

The pattern shows in the graph is convincing that data were reliable for the analysis. Savitzky-Golay filter is applied to smooth the data before proceeds with the analysis.

Derivation is one of most widely used mathematical treatment for scatter in NIR spectra data [11, 12]. Fig. 3 and Fig. 4 show the first and second derivative respectively. After eliminating the scattering data by derivation, PLSR with 4 components was applied to it.

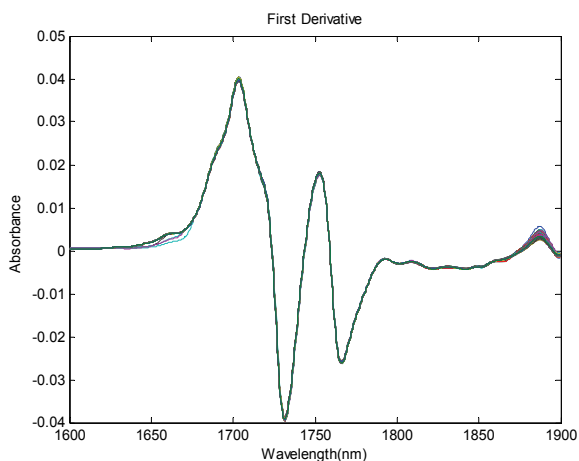


Fig. 3. First derivative for palm oil spectra data.

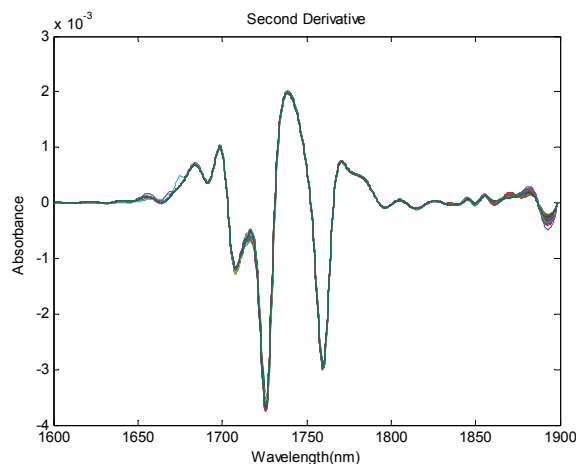


Fig. 4. Second derivative for palm oil spectra data.

Due to this result, it can be said that PLSR is not suitable to predict the FFA content of palm oil. The accuracy is only 48.12 % which is low as shown in Fig. 5. Hence, the data must undergo an advance analysis such as Artificial Neural Network for betterment in future [10].

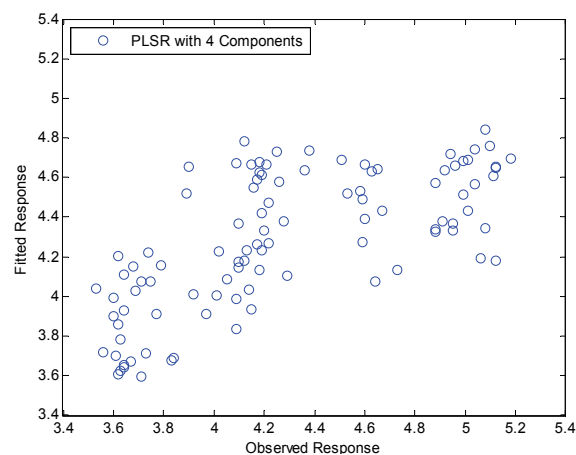


Fig. 5. Prediction of FFA.

#### 6. Conclusions

NIR spectroscopy is an easy, reliable and efficient instrument to measure the quality of rice and also other quality in food industries. The information within third overtone region, range 700 nm until 1100 nm is suitable for foods analysis since it is associated with hydroxyl bonds (O-H) and aliphatic chain (C-H). NIR Spectroscopy required further investigated on a large number of samples with different varieties, growing, cultivation methods, processing after harvesting and also the application on variety of chemometrics methods. The finding from this experiment not really support the application at which the accuracy percentage acquire is only 48.12 %. Next stage for further classification we will be used Artificial Neural Network for improving the accuracy.

## Acknowledgements

This work is partially supported by Ministry of Higher Education Malaysia and Universiti Teknologi Malaysia under research grant, with project number Q.J13000.2523.04H88.

## References

- [1]. Brodersen, K., Exloration of the Use of NIR Reflectance Spectroscopy to Distinguish and Measure Attributes of Conditioned and Cooked Shrimp (*Pandalus borealis*), *Lebensm.-Wiss u. Technol*, 34, 2001, pp. 533-541.
- [2]. Atinmo, T., Palm Fruit in Traditional African Food Culture, *Asia Pasific J. Clin Nutr*, 12, 3, 2003, pp. 350-354.
- [3]. Shaarani, S. M., A. Cárdenas-Blanco, M. H. G. Amin, N. G. Soon, L. D. Hall, Monitoring development and ripeness of oil palm fruit (*Elaeis guineensis*) by MRI and bulk NMR, *J. Agric. Biol*, 12, 2010, pp. 101-105.
- [4]. Mohd. Hudzairi Razali, A. S., M. A. Halim and Syazli Roslan, A Review On Crop Plant Production And Ripeness Forecasting, *International Journal Of Agriculture and Crop Sciences*, 4-2, 2012, pp. 54-63.
- [5]. Kalyana Sundram, R. S., Yew-Ai Tan, Palm fruit chemistry and nutrition, *Asia Pacific J Clin Nutr*, 12, 3, 2003, pp. 355-356.
- [6]. Osama Mohammed Ben Saeed, S. S., Abdul Rashid Mohamed Shariff, Helmi Zulhaidi Mohd Shafri, Reza Ehsani, Meftah Salem Alfatni, Mohd Hafiz Mohd Hazir, Classification of oil palm fresh fruit bunches based on their maturity using portable four-band sensor system, *Computers and Electronics in Agriculture*, 82, 2012, pp. 55-60.
- [7]. Man, Y. B. C., Determination of Free Fatty Acids in Palm Oil by Near-Infrared Reflectance Spectroscopy, *Journal of the America Oil Chemists' Society (JAOCS)*, Vol. 75, 5, 1998.
- [8]. El-Rahman, A. A., Ultraviolet, Visible and Infrared Wavelengths for Determination of Palm Oil Quality, *New Trends in Agricultural Engineering*, Nov. 2006, pp. 777-793.
- [9]. Tetsuo Sat, S. K., Mutsuo Iwamoto, Near Infrared Spectral Patterns of Fatty Acid Analysis from Fats and Oils, *Journal of the America Oil Chemists' Society (JAOCS)*, November 1991, Vol 68.
- [10]. Seng, C. K., Neural Network and principal component regression in non-destructive soluble solids content assessment : a comparison, *J. Zhejiang Univ-Sci B (Biomed & Biotechnol)*, 13, 2, 2012, pp. 145-151.
- [11]. Blanco, M., Critical Review: Near-Infrared Spectroscopy in the Pharmaceutical Industry, *Analyst*, August 1998, Vol. 123, pp. 135R-150R.
- [12]. Edward Szyk, A. S.-C., Agnieszka Kowalczyk-Marzec, NIR Spectroscopy and Partial Least-Squares Regression for Determination of Natural r-Tocopherol in Vegetable Oils, *Journal of Agriculture Food Chemistry*, 53, 2005, pp. 6980-6987.

2013 Copyright ©, International Frequency Sensor Association (IFSA). All rights reserved.  
(<http://www.sensorsportal.com>)

**Advertise in  
Sensors & Transducers Journal  
and Sensors Web Portal**

**TURN  
OUR VISITORS  
INTO  
YOUR CUSTOMERS  
BY THE SHORTEST WAY**

[http://sensorsportal.com/DOWNLOADS/Media\\_Planner\\_2013.pdf](http://sensorsportal.com/DOWNLOADS/Media_Planner_2013.pdf)  
[sales@sensorsportal.com](mailto:sales@sensorsportal.com)

## Near Infrared Spectroscopy Measurement: The Assessment of Amylose Content in Rice Grain

\* Herlina Abdul Rahim, Syahira Ibrahim

Process Tomography and Instrumentation Research Group (PROTOM-I),  
INFOCOMM Research Alliance, Universiti Teknologi Malaysia, 81310 Skudai, Johor

\* Tel.: +609-7714208, fax: +607-5566272

\* E-mail: [herlina@fke.utm.my](mailto:herlina@fke.utm.my)

*Received: 21 June 2013 / Accepted: 25 August 2013 / Published: 30 September 2013*

**Abstract:** There are several methods in assessing the traits of rice including destructive and non-destructive method. The objective of this study is to evaluate the amylose content (AC) on seven types of rice grain in Malaysia market by using the Near-Infrared (NIR) Spectroscopy. AC is one of the main criteria to determine cooked rice quality. Total of samples are 210, there are including two types of brown rice and basmati rice and three types of milled white rice where each of them was divided into 30 samples per group. Spectrums from 210 samples were collected from 680-1280 nm using a non-destructive, rapid and economical method. Reflectance spectra was converted into absorbance spectra and the baseline shift effect in the absorbance spectra was removed using first and second order derivative coupled with a first and second order Savitzky-Golay smoothing filter. Next, the spectral data were process and examine independently, by applying partial least square (PLS) analysis. Results show that NIR Spectroscopy help in determined the amylose content based on the spectra at 878 nm, 979 nm, 989 nm, 1100 nm and 1210 nm. The prediction on amylose content from Malaysia rice by using NIR Spectroscopy need to be further investigated on a large number of samples with different varieties, growing, cultivation methods and processing after harvesting. *Copyright © 2013 IFSA.*

**Keywords:** Near-infrared spectroscopy, Iodine colorimetric, Amylose content, Malaysia rice grain, Basmati rice, Milled rice, Brown rice.

### 1. Introduction

Food quality and safety are crucial issues throughout the world since it is closely related to consumers' growth and health. Staple food qualities are even more important issue because staple food gives massive contribution in gaining energy. Rice is the staple food in Asian countries because several countries like Thailand, Cambodia, Indonesia, Vietnam, Myanmar and China produce rice for world distribution [1]. Furthermore, rice has high carbohydrates that will turn into energy. However, compared to other Asian countries, the productivity

of rice cultivation in Malaysia is far lower so that Malaysia has to import rice from Thailand and others foreign country.

BERNAS (Malaysian National PaddyRice Corporation) report that rice production in Malaysia in 2009 was 1.91 million tons, while the annual requirement of rice was 2.19 million tones, this show that only 70 % the rice sufficiency level in Malaysia [2]. In 2010, due to flood and diseases, annual rice productions substantially decrease to 1.8 million [2]. Therefore, BERNAS has put some effort to increase paddy production at least enough for Malaysia population. In order to achieve their annual target,

BERNAS Rice Factory hire more workers in grading process section to ensure that all the rice are grade fairly and correctly [2]. However this effort is not efficient because it will increase the production cost since the workers need to get paid for every harvesting season. Therefore, the usage of simple, fast and low cost grading process technology is necessary such as Near-Infrared Spectroscopy.

Near Infrared spectroscopy is a form of overtones and vibrational spectroscopy utilizing absorption or reflection measurements in the near-infrared region of the electromagnetic spectrum [3]. The overtones makes NIR spectra complex and overlapping and it happens when the molecules reaches a vibrational states above the fundamental. Overtone was identified based on the arising of these chemical groups, C-H, S-H, N-H and O-H stretching modes [3, 4]. Besides, it

offers the non-destructive analysis even for intact solid or liquid samples and gives both chemical and physical information in development or production. Additional for their advantages are chemical free technique, required no sample preparation and the quality of the sample can assess in just one scan [5]. Usually it has been used in agriculture area to determine the amino acid [12, 6], protein [7], moisture [8] and it also will produce an accurate result for amylose content [9] in rice.

As illustrate in Fig. 1, amylose is made by a long carbohydrate molecule, it is insoluble in water, linear and long polymer of  $\alpha$ - (1  $\rightarrow$  4) linked D-glucose (IUPAC) units [10] and carry a few (< 0.5 %) occasional moderately long chains linked of  $\alpha$ - (1  $\rightarrow$  6) unit of starch [11, 12, 13] making up approximately 20 – 30 % of the structure.

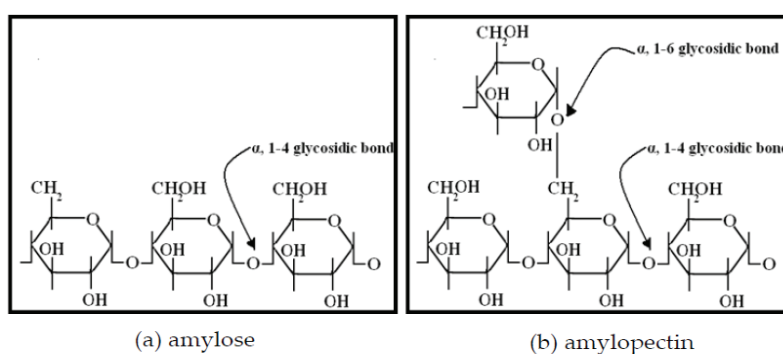


Fig. 1. The alpha link of amylose and amylopectin

Amylose content (AC) has a major influence on the characteristics or texture of cooked rice and it used for determining a processing quality [14, 15]. It is because; AC correlates negatively with taste panel scores for roughness, protein [15], cohesiveness, tenderness, color, gloss of the boiled rice but positively correlated to degree of milling, whiteness, adhesiveness and stickiness to lips [15]. Therefore, AC also gives an important trait in food industries, especially for analysis the ingredient, processing and product stage of production [16]. On the paper of William R. Windham *et al.*, [15] they conclude that NIR Spectroscopy is the best method to predict the texture characteristic of cooked rice by using uncooked rice as a sample. Then, they also stated the relationship between AC with the cooked rice characteristics.

Besides that, rice with high AC also will give extra advantages to human health, since high AC will reduce the digestion rate and as a results the postprandial glucose and insulin response become lower [14, 17]. Based on the formulation of diet for diabetes, the slower digestion and absorption rate of carbohydrate in human body, it will helps to maintain the regular levels of glucose in blood and reduce the insulin response [18]. So, rice with high AC is good for diabetic patient to sustain their regular blood glucose level.

## 2. Materials and Methods

### 2.1. Sample Preparation

A total of 210 samples of rice grain used in this experiment were obtained from the Factory of BERNAS, Kempas Johor, Malaysia. All rice in the factory was harvested and imported from local and foreign country. Seven types of rice were chosen randomly, there are including two types of brown rice and basmati rice and three types of milled white rice. Each types of rice will be divided into thirty groups and each group has 200 single rice grains. Then, all of the 210 samples has been packed in the plastic seal and labeled individually before the experiment began. After that, rice grain samples were stored in the laboratory (Robotic Laboratory, Faculty of Electrical Engineering, Universiti Teknologi Malaysia) at room temperature ( $\sim 27^\circ\text{C}$ ) before spectra acquisition. After the spectrum acquisition using NIR Spectroscopy was complete, each of the rice was grinded by using a dry blender (Philips, Model HR2001/70/AC, made in China) followed by crushing it with the white porcelain mortar and pestle to produce the soften rice powder. Lastly, before the conventional method of the amylose content measurement via iodine colorimetric was carried out, the rice powders were sieve using Laboratory test sieve, size of  $106\ \mu\text{m}$ .

## **2.2. Spectra Analysis**

A small ring cup was constructed using the OHP film (internal diameter 30 mm, depth 10 mm) on the transparency glass to place the sample of rice grains. The reflectance spectrum of each samples of rice was acquired using low cost portable NIR Spectroscopy (Ocean Optics USB4000 Miniature Fibre Optic Spectrometer (650-1300 nm), ORNET Sdn. Bhd., Selangor, Malaysia) from the surface of rice grains. The NIR energy source and the optical standard reference used in this work were a tungsten halogen light (360-2000 nm) (LS-1, Ocean Optics, USA) and a diffuse reflectance standard (WS-1, Ocean Optics, USA), respectively. A reflection probe (R400-7-VIS/NIR, Ocean Optics, USA) was positioned at a 45° angle at the top of rice samples and the distance to the surface of rice grain is 7 mm for the diffuse reflection measurement.

Both the spectrometer and the energy source were switched ON for at least 25 minutes to warm up the instruments before spectra acquisition began. The spectrometer was interfaced to a laptop computer by using software (SpectraSuite®, Ocean Optics, USA) for spectral data acquisition. One reflectance spectrum from the middle position of small ring cup of each rice sample was acquired. In order to increase the signal-to-noise ratio of the acquired spectrum, the acquired spectrum was smoothed with the boxcar value of 60. All the acquired spectral data were stored in the laptop computer and processed via MATLAB simulation software (MATLAB (R2012b)).

## **2.3. Chemical Analysis and Reference Measurement**

The iodine colorimetric method is a destructive and conventional method to determine the value of AC in rice. Firstly, for the extraction stage, 13 mg of rice flour in centrifuge tube was weighed on a microbalance. The samples were centrifuge with 5 ml methanol for 30 minutes at 60 °C and then discarded the supernatant liquors. Repeat the extraction step twice to get the trace of lipids. After that, added 2 ml of NaOH and 4 ml distil water to the lipid free samples, and heated it for 30 minutes in a water bath (or boiled water of 60 °C) - solution I. 0.1 ml of solution I and 5 ml of trichloroacetic acid (TCA) was added in a separate test tube. Next, added 0.05 ml of I2-KI solution and mixed it immediately. After 30 minutes, the blue color of the solution was read at 620 nm, using the UV/Vis Spectrophotometer, Lambda-25 by Perkin Elmers. The detail about these experiment methods can refer to [19].

## **2.4. Data Pre-processing**

Since there are big scattering effect at the beginning and the end of the spectrum, this study utilized the spectrum from 680 nm to 1280 nm and the wavelength beyond the range has been removed.

Next, NIR Spectroscopy data was transformed from reflectance value (R) to absorbance (-log (R)). After that, first and second order derivative coupled with a first and second order Savitzky-Golay smoothing filter was implemented to remove baseline shift effect and “smooth out” high frequency noises in the spectral data. And then, data has been examined by using partial least square analysis. Number of component was identified depend on the model parsimony.

## **3. Results and Discussion**

### **3.1. Assignment and Absorbance of NIR Spectroscopy**

Here is the results for non-destructive (NIRS) method and the results for colorimetric method. Time taken for NIR Spectroscopy measured the quality (diffuse reflection light) for 210 rice samples are three days. Refer to the Fig. 2 until Fig. 8, all data from three days has been separated into seven graphs which are based on their type. Each of them represented the absorption band from the NIR spectroscopy and the wavelength range is 680 nm until 1280 nm.

Let's evaluate on wavy point of the spectrum by referring to Table 1, the near infrared band assignment table and others research references for more understanding about the overtone of the stretching vibration for rice spectra. By searching all of the graphs with the assignment table of NIR spectra, there are a lots of information of overtone that was arise from the C-H, O-H and N-H bond on the wavelength range at 680 nm until 1280 nm. Some articles [4] state that absorption band from this range is suitable for foods analysis because it is suitable for measuring the moisture and sugar content since it is associated with hydroxyl bonds. Moreover, article on the [21] also state that the absorption band from the third overtones of the fundamental stretch bond is most suite for food analysis which have thick sample such as seed. Besides, it also states that this region is suitable for measuring the high moisture and fat content.

Refer to entire graph, there are some information's and the differentiation that can be recognize roughly. First, there have a similarity on their curvy shape accept Thailand brown rice and there are three important wavelengths around 960 nm, 1090 nm and 1220 nm where the curve is occur. Thailand brown rice has a different shape of spectrum because of the color of rice is dark brown, so it was effect on the reflection band on NIR Spectroscopy [22]. Next, the sequence of depression at 1090 nm and 1220 nm shown that there are dip depression for both of basmati rice compare with milled rice and follow by Malaysia brown rice. Lastly, the amplitude illustrate that both basmati rice has higher range of absorbance compare to milled rice and Malaysia brown rice.

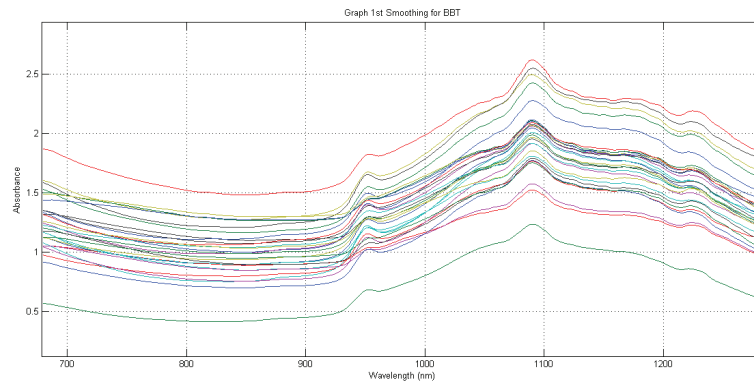


**Fig. 2.** Absorption band for Thailand brown rice.

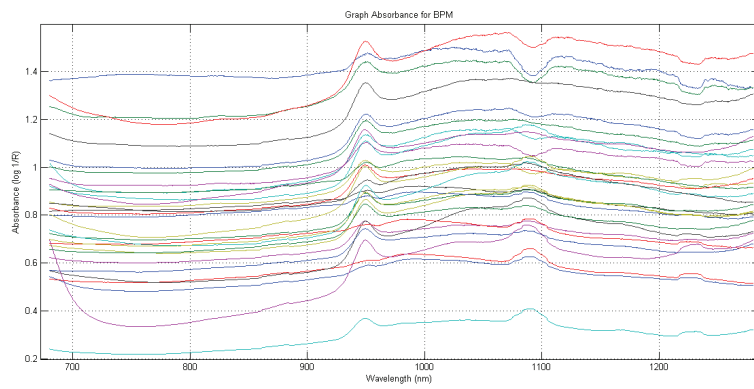


**Fig. 3.** Absorption band for Malaysia brown rice.

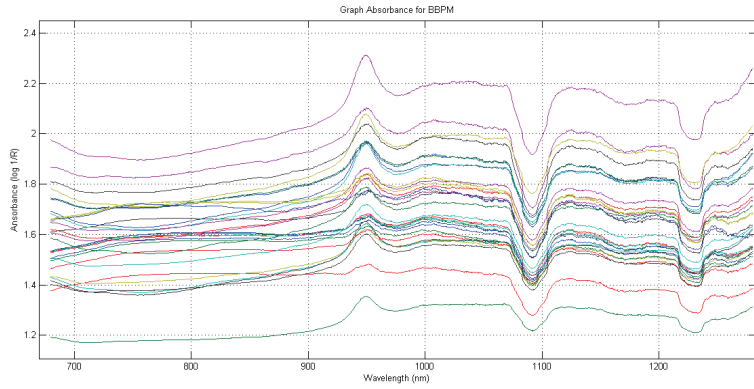


**Fig. 4.** Absorption band for Pakistan maharani basmati rice.

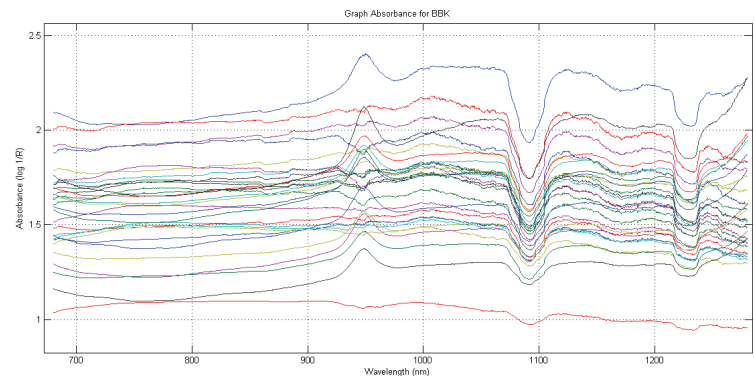


**Fig. 5.** Absorption band for Kainaat basmati rice.

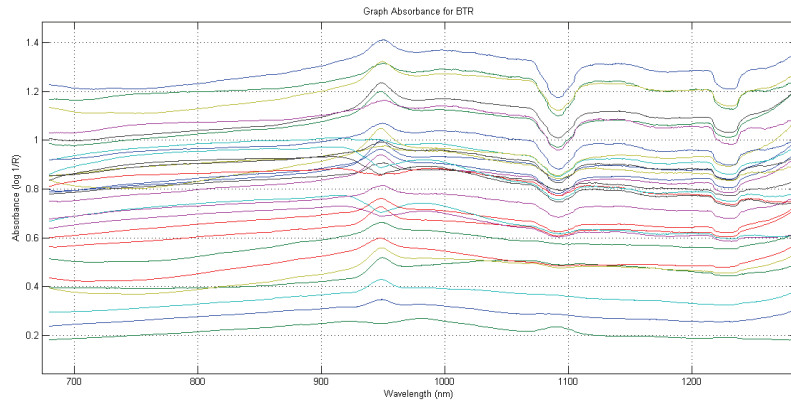


Fig. 6. Absorption band for local Milled rice from Pahang.

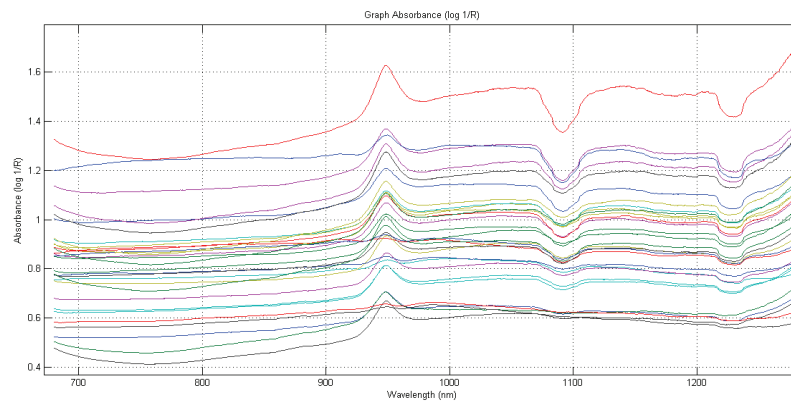


Fig. 7. Absorption band for local Milled rice from Selangor.

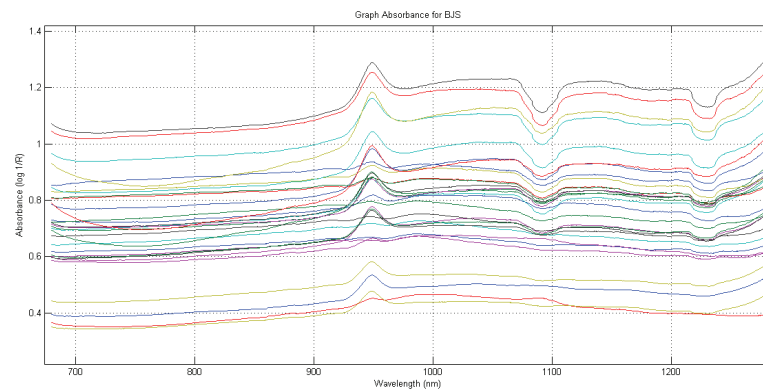


Fig. 8. Absorption band for local milled rice from Johor.

Start from the first peak of the graph around 958 nm to 960 nm, there are few chemical bonding that might be occur on it (Fig. 2 until Fig.8). However, most researchers prove that it was corresponding to the O-H second overtone of absorbance due to the moisture content [3, 15, 20, 23]. Hence, on the study of [23] and [15] shown that at wavelength around 878 nm, 979 nm and 985 nm, has indicate to the C-H stretch due to starch absorption. The next crucial point on the graphs is

near to the 1100 nm and it was indicate to the ArC-H second overtone band [20] where Ar was illustrate as an aromatic compound which have strong characteristic odour [24]. Last but not least, the wavelength around 1210 nm to 1222 nm also specify to the second harmonics for C-H stretching vibrations of CH<sub>2</sub> [25]. Since the chemical bonding of starch is made by a combination of the C-H and O-H bonding, so both of them is important for evaluating the amylose content in rice.



## 4. Conclusions

NIR spectroscopy is an easy, reliable and efficient instrument to measure the quality of rice and also other quality in food industries. The information within third overtone region, range 700 nm until 1100 nm is suitable for foods analysis since it is associated with hydroxyl bonds (O-H) and aliphatic chain (C-H). NIR Spectroscopy required further investigated on a large number of samples with different varieties, growing, cultivation methods, processing after harvesting and also the application on variety of chemometrics methods such as principle component regression and artificial neural network in analyzing data. Hopefully, this study is one step to enlarge the reference on Malaysia rice and in the same time, to ensure Malaysia be a one of leading country in science and technology fields especially in food analysis based on Malaysia rice.

**Table 3.** Summary of the coefficient of determination ( $r^2$ ) and the root mean square error (RMSE) of seven types of rice using partial least square (PLS) model.

Rice Variety	No. of PLS Components	Spectral Treatment	R <sup>2</sup>	RMSE
BPT	6	SG + 1 <sup>st</sup>	0.7171	1.1626
	5	SG + 2 <sup>nd</sup>	0.8504	0.8453
BPM	3	SG + 1 <sup>st</sup>	0.3132	3.5432
	4	SG + 2 <sup>nd</sup>	0.4452	3.1845
BBK	3	SG + 1 <sup>st</sup>	0.2024	1.6366
	3	SG + 2 <sup>nd</sup>	0.2820	1.5527
BBPM	3	SG + 1 <sup>st</sup>	0.3524	1.7743
	3	SG + 2 <sup>nd</sup>	0.4041	1.7020
BJS	3	SG + 1 <sup>st</sup>	0.3908	2.4069
	3	SG + 2 <sup>nd</sup>	0.4726	2.2394
BTR	4	SG + 1 <sup>st</sup>	0.2290	1.2931
	3	SG + 2 <sup>nd</sup>	0.2411	1.2829
BSBS	3	SG + 1 <sup>st</sup>	0.1738	3.4346
	3	SG + 2 <sup>nd</sup>	0.2646	3.2404

## Acknowledgements

This work is partially supported by Ministry of Higher Education Malaysia and Universiti Teknologi Malaysia under research grant, with project number Q.J13000.2523.04H88.

## References

- [1]. Fatimah Mohamed Arshad, Chapter 15: Pertanian, Evolusi dan Hala Tuju Sektor Pertanian di Malaysia, Asan Ali Golam Hassan, *Penerbit Universiti Utara Malaysia*, Sintuk, 2008, pp. 301-308.
- [2]. Padi Beras National Berhad, Annual Report 2009, Available From : <http://www.bernas.com.my>
- [3]. Glatt International Times, Fundamentals and pharmaceutical applications of near-infrared spectroscopy, 2007, 16 May 2013, Available from: [http://www.glatt.com/times/times23site/tms23\\_fundamentals\\_print.htm](http://www.glatt.com/times/times23site/tms23_fundamentals_print.htm)
- [4]. FOSS and Infrasoft International, A Brief Introduction to NIR Spectroscopy, 2005, Available from: [http://www.winisi.com/NIRS\\_theory.htm](http://www.winisi.com/NIRS_theory.htm)
- [5]. J. G. Wu and C. H. Shi, Prediction of grain weight, brown rice weight and amylose content in single rice grains using near-infrared reflectance spectroscopy, *Field Crops Research*, Vol. 87, No. 1, April 2004, pp. 13–21.
- [6]. Wu J. G., Shi C. H., Zhang X. M., Estimating the amino acid composition in the milled rice powder by near-infrared reflectance spectroscopy, *Field Crop. Res*, 75, 2002, pp. 1-7.
- [7]. Delwich S. R., McKenzie K. S., Webb B. D., Quality Characteristics in rice by near-infrared reflectance analysis of whole-grain milled samples, *Cereal Chem.*, 73, 1996, pp. 257-263.
- [8]. Iwamoto M., P. C. Williams and K. H. Norris, Near-infrared research in Asia, Near-infrared Technology in the Agriculture and Food Industries, *Cereal Chem*, 1987, pp. 223-226.
- [9]. J. Rash and J.-F. Meullenet, Apparent Amylose Content Prediction using Near Infrared Spectroscopy of Individual and Bulk Rice Kernels, *AAES Research Series*, 2010, pp. 312-321.
- [10]. M.-H. Chen and C. J. Bergman, Method for determining the amylose content, molecular weights, and weight- and molar-based distributions of degree of polymerization of amylose and fine-structure of amylopectin, *Carbohydrate Polymers*, Vol. 69, No. 3, June 2007, pp. 562–578.
- [11]. R. F. Tester, J. Karkalas and X. Qi, Starch-composition, fine structure and architecture, *Journal of Cereal Science*, Vol. 39, No. 2, March 2004, pp. 151–165.
- [12]. Y. Shao, Y. Cen, Y. He and F. Liu, Infrared spectroscopy and chemometrics for the starch and protein prediction in irradiated rice, *Food Chemistry*, Vol. 126, No. 4, June 2011, pp. 1856–1861.
- [13]. L. Copeland, J. Blazek, H. Salman and M. C. Tang, Form and functionality of starch, *Food Hydrocolloids*, Vol. 23, No. 6, August 2009, pp. 1527–1534.
- [14]. S. Nik Shanita, H. Hasnah, C. W. Khoo, Amylose and Amylopectin in selected Malaysian Foods and its Relationship to Glycemic Index, *Sains Malaysiana*, Vol. 40, No. 8, 2011, pp. 865-870.
- [15]. William R. Windham *et al.*, Prediction of Cooked Rice Texture Quality Using Near-Infrared Reflectance Analysis of Whole-Grain Milled Samples, *Cereal Chemistry*, Vol. 74, No. 5, 1997, pp. 626-632.
- [16]. David L. B. Wetzel, Analytical Near Infrared Spectroscopy, *Instrumental Methods in Food and Beverage Analysis*, 1998, pp. 141-194.
- [17]. Tilakavati Karupaiah, Chuah Khun Aik, Tan Choon Heen, Satiapoorany Subramaniam, Atiqur R. Bhuiyan, Parviz Fasahat, Abdullah M Zain and Wickneswari Ratnam, A transgressive brown rice mediates favourable glycaemic and insulin responses, *J Sci Food Agric*, 91, 2011, pp. 1951-1956.
- [18]. Cristiane C. Denardin, Melissa Walter, Leila P. da Silva, Gabriele D. Souto, Carlos A. A. Fagundes, Effect of amylose content of rice varieties on glycemic metabolism and biological response in rats, *Food Chemistry*, 105, 2007, pp. 1474-1479.
- [19]. Josept Chrastil, Improve colorimetric determination of amylose in starch or flours, *Carbohydrate Research*, Vol. 159, pp. 154-158.

- [20]. Z. Xiaobo, Z. Jiewen, M. J. W. Povey, M. Holmes and M. Hanpin, Variables selection methods in near-infrared spectroscopy, *Analytica Chimica Acta*, Vol. 667, No. 1–2, May 2010, pp. 14–32.
- [21]. Eric Bergles and William Yang, Profiting from telecom investments: Taking advantage of the NIR First Overtone and Raman's Spectral Fingerprints, *Bayspec Inc.*, 2009, Available from: <http://www.photonics.com/Article.aspx?AID=38689>
- [22]. D. Wang, F. E. Dowell and R. E. Lacey, Single Wheat Kernel Size Effects on Near-Infrared Reflectance Spectra and Color Classification, *Cereal Chemistry*, Vol. 76, No. 1, January 1999, pp. 34–37.
- [23]. F. E. Barton, D. S. Himmelsbach, A. M. McClung and E. L. Champagne, Two-Dimensional Vibration Spectroscopy of Rice Quality and Cooking, *Cereal Chemistry*, Vol. 79, No. 1, 2002, pp. 143-147.
- [24]. Glossary: Introduction to organic chemistry, General Chemistry Online!. Available from: <http://antoine.frostburg.edu/chem/senese/101/organic/glossary.shtml>
- [25]. Eric Dufour, Principle of Infrared Spectroscopy, Da-Wen Sun, Infrared Spectroscopy for Food Quality Analysis and Control, *Academic Press*, USA, 2009.
- [26]. Xiaoli Li, Yong He and Changqing Wu, Non-destructive Discrimination of Paddy Seed of Different Storage Age Based on Vis/NIR spectroscopy, *Journal of Store Products Research*, 44, 2008, pp. 264-268.
- [27]. Ozgur Yeniay and Atil Goktas, A Comparison of Partial Least Square Regression with Other Prediction Method, *Hacettepe Journal of Mathematics and Statistics*, Vol. 31, 2002, pp. 99-111.

2013 Copyright ©, International Frequency Sensor Association (IFSA). All rights reserved.  
(<http://www.sensorsportal.com>)

## Call for Books Proposals

### Sensors, MEMS, Measuring instrumentation, etc.

International Frequency Sensor Association Publishing



[www.sensorsportal.com](http://www.sensorsportal.com)

#### Benefits and rewards of being an IFSA author:

- 1) Royalties.**

Today IFSA offers most high royalty in the world: you will receive 50 % of each book sold in comparison with 8-11 % from other publishers, and get payment on monthly basis compared with other publishers' yearly basis.
- 2) Quick Publication.**

IFSA recognizes the value to our customers of timely information, so we produce your book quickly: 2 months publishing schedule compared with other publishers' 5-18-month schedule.
- 3) The Best Targeted Marketing and Promotion.**

As a leading online publisher in sensors related fields, IFSA and its Sensors Web Portal has a great expertise and experience to market and promote your book worldwide. An extensive marketing plan will be developed for each new book, including intensive promotions in IFSA's media: journal, magazine, newsletter and online bookstore at Sensors Web Portal.
- 4) Published Format: pdf (Acrobat).**

When you publish with IFSA your book will never go out of print and can be delivered to customers in a few minutes.

You are invited kindly to share in the benefits of being an IFSA author and to submit your book proposal or/and a sample chapter for review by e-mail to [editor@sensorsportal.com](mailto:editor@sensorsportal.com) These proposals may include technical references, application engineering handbooks, monographs, guides and textbooks. Also edited survey books, state-of-the art or state-of-the-technology, are of interest to us.



## Portable Synthetic Testing System Based on Information Fusion

<sup>1,2</sup> Zhao Li Ming, <sup>1</sup> Liu He Ping, <sup>2</sup> Zhang Bing

<sup>1</sup> Information Engineering College, University of Science and Technology Beijing, Beijing, 100083, China

<sup>2</sup> Institute of Information, Guangdong Ocean University, Zhanjiang, 524088, China  
E-mail: zhaolimingzb@126.com

Received: 5 June 2013 / Accepted: 25 August 2013 / Published: 30 September 2013

---

**Abstract:** In consideration of inconvenient to sinusoidal machine in naval vessels maintain to quick guarantee goal nowadays, a portable synthetic testing system has been designed in this paper which used for servo system based on information fusion. The testing system used a portable industrial computer as a core, which uses Windows as operating platform and C++Builder as programmable aid, and Native-XML database technique and dynamic access mechanism, and Win Driver technique and dynamic graphics display for accurate and coarse channels signal. Through developed and designed for hardware and software, it had extended function of conventional sinusoidal machine. It adopts NFE estimator to fusion multi-source information to diagnosis the instrument on-line and database technique for off-line. Application shows it possesses the advantage of simple operate and easy test, high efficiency. And it reduces the difficulty of equipment maintenance, conveniences to track and mastery the equipment for long time, and increases the quick guarantee capability. The static position precision of test overland gets 0.1 mil. It has great application value and promotion value.  
Copyright © 2013 IFSA.

**Keywords:** Portable design, Servo system, Synthetic testing system, Information fusion, Hardware design.

---

### 1. Introduction

Sinusoidal machine is indispensable as maintenance equipment for servomechanism in vessels. It provides all kinds of sine signal for detecting state of servomechanism. Traditional sinusoidal machine has only signal output function same as director modeling, has not or partial detection function. In order to master the overall state of equipment, it is necessary to maintain with the help of aided equipments, which raises the cost for maintenance and makes the intensity of maintenance enhanced. So it lacks the ability to rapidly maintenance.

In view of an increasing attention towards winning local wars is the ability to rapidly maintenance in high-tech conditions where the equipment maintenance cycle extends and reduces the work strength, this paper has designed a portable synthetic test instrument based on information fusion, which has not only signal output function as ordinary sine test, but also has automatic fault diagnosis and detection functions. It cans diagnostic analysis of related equipments on-line and off-line using multi-source information fusion technology, fusion diagnosis provides to workers serving as a rapid equipment support decision making. Also it has database functions such as data storage and query,

print, which is convenient for tracing the state of equipments long-term.

This paper will be structured as follows. Section 2 gives a brief overview of a related work. In Section 3 we will introduce the overall design of the system. In Section 4 we will expose the hardware design for testing system. In Section 5 we will describe the data processing and information fusion. In Section 6 we will describe our software design of testing system. In Section 7 we will show servo system testing.

## 2. The Related Work

As important equipment for servomechanism in vessels maintenance, it output all kinds of signal to servomechanism, such as static step signal, constant-velocity signal, and sine signal, small and larger angles turning over signal, which test the servo system response. Through the servo system response, we can diagnosis the state of servo system based on all kinds of technical standard of servo system. Currently, we often use some devices to observant and measure, analysis and save the response data. It is the key to our facing problems which is the larger number of devices required, the scarcity of whole servo system state, the larger time-consuming for diagnose.

For winning local wars under modern, especially high-technology conditions, Zhang [2, 3] design a sine machine with some functions. Zhao [1] design an integrated portable synthetic detection and testing instrument. WANG *et al.* [10] design a test device

for flack flowing systems based on virtual instrument technology.

For diagnosis technology and data base design, SHI *et al.* [5] use fuzzy information fusion in servo system for naval gun. Lian *et al.* [6] use SVM-ANN hybrid model to diagnosis fault of servo system of Naval gun. Guo *et al.* [9] use prognostics and health management technology for new-generation weapon.

Our work differs from the foregoing in that it fully considers the characteristic of quick maintenance, synthetic diagnosis and equipment maintenance standard and environment conditions. Hence, the proposed testing system is not only portable but also it provides synthetic performance guarantees.

## 3. The Overall Design of Testing System

According to the design requirements, the overall structure of testing servo system is as shown in Fig. 1. Through testing cable, field data is transferred to testing system from servo system. The testing system outputs data and command to servo system according to the test requirements. The test system saves the testing data to real time database and history database. Based on information fusion technology, testing data is processed and feature extracted and fused through the decision-making center, in the end, the decision-making is output through database reports as the state of servo system. The test system can print testing report on-line, and the history database can be used as diagnostic analysis off-line.

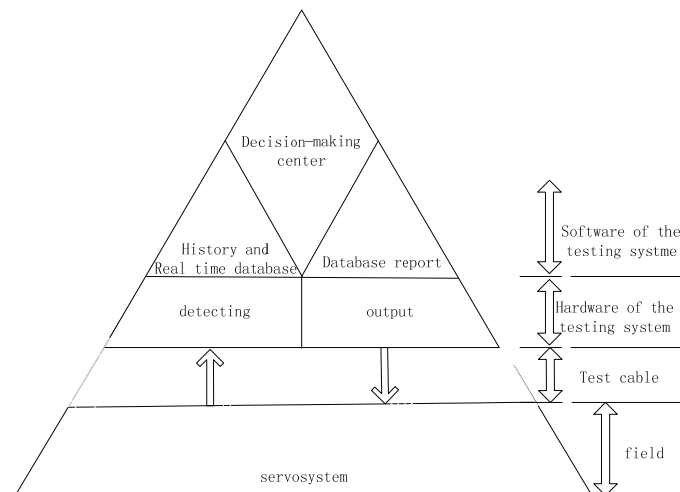


Fig. 1. The structure of testing system.

The testing system precede kinds of automatic measurement and test functions, such as multistep, constant-velocity, large and small angle arc rotary control. It can perform static error testing, constant-velocity tracing error testing, sine tracing error testing, large and small angle arc rotary tracing error.

It can display real-time waveforms for accurate channel and coarse channel, and forward feedback channel, negative feedback channel. Also it can display real-time error voltages, and overshoot, the degree of semi-resonance and reciprocating, the operating time [1-3].

## 4. Design of System Hardware

The hardware of system is as shown as Fig. 2. It include a portable industrial computer such as ACME8514P4V, 3 ISA cards which designed by us, 1 A/D card and 2 DI cards which made by Advantech

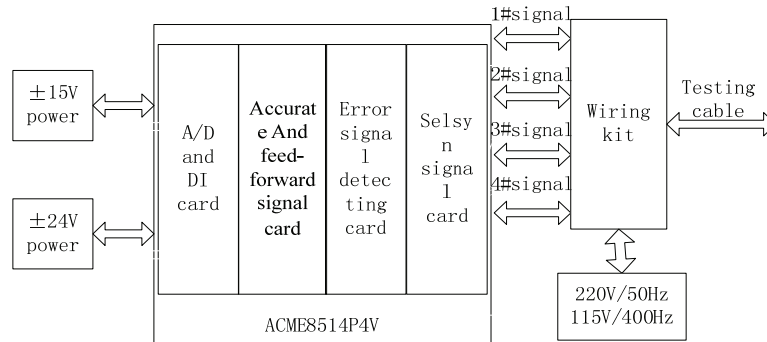


Fig. 2. The hardware structure of testing system.

### 4.1. Host Configuration

Host configuration of ACME8514P4V as follows: Intel Pentium4 2.4 B processor, FSB 533 MHz, Intel 845GV chipset, 80G hard disc, 64M display memory, 12 slots passive backplane. The working temperature is from  $-40^{\circ}\text{C}$  to  $+65^{\circ}\text{C}$ .

### 4.2. A/D and DI Card

A/D card adopts PCL818LA/D which transforms 16 channels single-in or 8 channels differential input analog signals to digital signal, which used as feed-forward output for servo system. And it adopts PCL733DI card as 32 channels digital input, which collect action characteristic of travel switches for servo system. Input of travel switches is DC24V. The standard pin of A/D card complies with ISA. The vacancy analog input must be grounded.

### 4.3. Accurate and Feed-Forward Signal Card

Accurate and feed-forward signal card output analog accurate voltage and analog feed-forward signal for servo system. Accurate voltage output is less than AC12V, and feed-forward voltage output is less than  $\text{DC}\pm 11.8\text{V}$ . The card include ISA bus interface, address decoder, linear solid selsyn signal module, voltage transformer and output interface. It adopts D25 pins as output. The core of card is the single channel digital-to-selsyn convertor and DAC convertor. The card output selsyn signal and feed-forward voltage. And the standard pins of A/D card comply with ISA. The vacancy analog input must be grounded.

company, 1#~4# signal wires, 1 wiring kit, and testing cables, accessory power. Except for peripheral cable, the full weight of the testing system is 15.7 kg. All card built in main board slot of portable industrial computer. The detailed description of the system configuration is as follows [4, 5].

### 4.4. Error Signal Detecting Card

The card is used as detecting card for servo system output double channel angle error. The error signal  $\Delta U$  is described by:

$$\Delta U = 57.2 \sin \omega t, \quad (1)$$

where 57.2 V is the maximum of linear rotating transformer output; and  $\omega t$  is the sum of accurate and coarse error angles.

The card includes ISA bus interface, address decoder, XXSZ linear rotate transformer-digital convertor, input interface. ISA bus interface driven by 74HC574. Address decoder adopts 74HC688. The selection signal for output module is generated by 74HC154, and 74HC138 for input module. The core of card is the single channel linear rotates transformer-to-digital convertor, which measure rotate transformer signal. The standard pins of A/D card comply with ISA. The vacancy analog input must be grounded.

### 4.5. Selsyn Signal Card

Selsyn signal card output mid frequency signal which is simulated as sinusoidal machine output. The mid frequency signal send to vessels servo system as driving signal. The card includes ISA bus interface, address decoder, selsyn signal output module, output interface. ISA bus interface is driven by 74HC574. The core of card is the single channel digital-selsyn convertor which power is 5 W. It output 2 channels selsyn signal that is accurate channel and coarse channel, which voltage is below AC90V. The two channels angle signal transfer is shown in Fig. 3. The digital quantity of accurate channel output  $A_{out}$  and

the digital quantity of coarse channel output  $R_{out}$  is described by:

$$\begin{aligned} A_{out} &= \theta \times n \times 2^m / 6000, \\ R_{out} / A_{out} &= 1/n \end{aligned} \quad (2)$$

where  $\theta$  is the output position angle, which is the sum of accurate channel output position angle and coarse channel output position angle.  $m$  is the module precision. And  $n$  is the ratio of the signal of accurate and coarse channel, which depends on the specific circumstances. In our design  $n$  is 30.

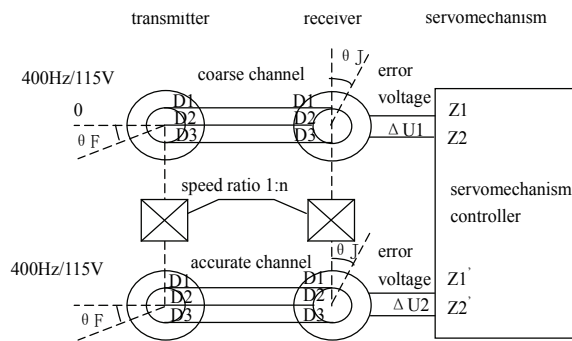


Fig. 3. A principle diagram of two signal transduction.

#### 4.6. The Wiring Kit and Other Peripheral Devices

The card signal and sinusoidal machine output signal and the error signal is pull in wiring kit, which is shown in Table 1.

1# ~ 4# signals is group of input and output signal for testing system, which max voltage is shown in Table 2.

Some peripheral devices include  $\pm 15$  V and  $\pm 24$  V power, and some testing cable. During the tests the mid frequency power is supplied by vessels with 220 V/50 Hz and 115 V/400 Hz.

Table 1. The main signal in signal box.

	Accurate/coarse signal	Max voltage, (V)
Card signal input	S1~S3	~90 V
	Z1, Z2	~12 V
Servomechanism	CS1~CS3	~90 V
Error input	S1/S2	$\pm 90$ V

Table 2. The max voltage of main signal in 1#~4#.

	Input signal (V)	Output signal (V)
1# signal	$\pm 90$	90
2# signal	18	$\pm 10$
3# signal	100	$\pm 12$
4# signal	30	---

#### 4.7. The System Design for Anti-interference

Due to various interferences can enter in servo system testing system, through space and earth wire, power line and other wire. In the design, we take measures to anti-interference which described as follows.

First, in order to restrain common mode interference, we link the IPC ground and signal ground and the shell ground to form one end line ground.

Second, in order to restrain series mode interference, we adopt filtering technique to restrain interference from servo system effectively.

Third, we adopt isolation technology to isolate high and low voltage, and shielding technology to anti-electromagnetic, and anti-power interference technology to power interference.

#### 5. The Data Processing and Information Fusion

It is important to pre-process signals such as estimate the multi-sensor states for data fusion [6]. In this paper, we use neural networks, fuzzy reasoning and expert system as multi-sensor state estimate method, which is NFE estimator. Because multi-source information fusion is a multi-attribute decision. The assessment procedure of evaluation is establishes one kind to correspond the multi-sensor information set and the confidence estimation mapping relations. The impact factors of sensor confidence estimate are sensor performance, electronic jamming, clutter intensity and natural environment. The single sensor confidence estimator is shown as Fig. 4.

The fusion step is as follows:

- 1) Establish the sensor confidence estimate system, fuzzy sensor attributes;
- 2) Define factors weight coefficient affected by sensor performance based on expert knowledge and unitary processing;
- 3) Modify the attributes using weight coefficient, which is confidence estimator input;
- 4) Choose fuzzy membership function using expert system based on input data;
- 5) Training data using comprehensive evaluation method, and carry through the evaluation using trained confidence estimator [7, 8].

NFE confidence estimator fusion algorithm is as shown as Fig. 5.

Expert knowledge and expert system include mainly the technical standard for servo system which is in common, and each servo system has its unique characters because of different service conditions for each vessel in a long term [9, 10].

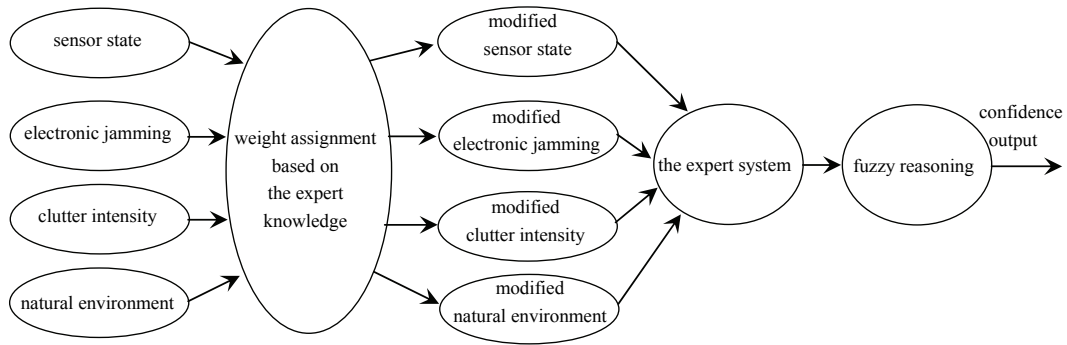


Fig. 4. A single sensor confidence estimator.

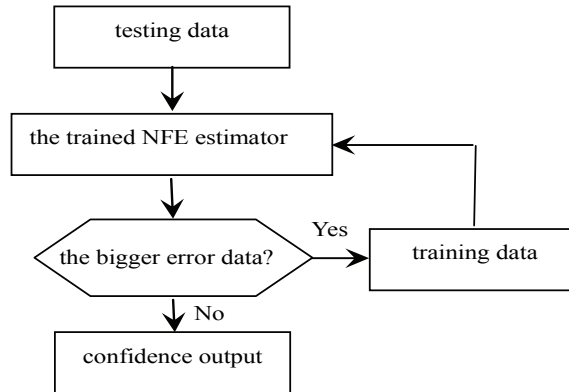


Fig. 5. The NFE estimator fusion algorithm.

## 6. The Design of System Software

The software structure is shown in Fig. 6. Edit program with C++ language, it is made up of main program, detection subprogram, testing subprogram, fusion and diagnosis subprogram, database. Because system is multitask operation and fast response with milliseconds, during software development process for testing instrument, it adopts multimedia timer and multiple threads control mechanism, the idea of modular design, Native-XML database techniques and dynamic access mechanism. And the key technologies for the designed cards include Win Driver technique and dynamic graphics display for accurate and coarse channels. With the features of independent to operation systems, system can be transplant to Linux operation system, which ensures the system excellent [11].

In operating software, some key modules is constructed, such as TEngle module, which visualized as the servo system electrical position directly in real-time.

The key to software is database, which includes dynamic database and static database. The static database records vessels administration, equipment's state and maintenance history. The dynamic database records testing project, testing time, testing data and maintenance decision.

Some details will be illustrated in the following.

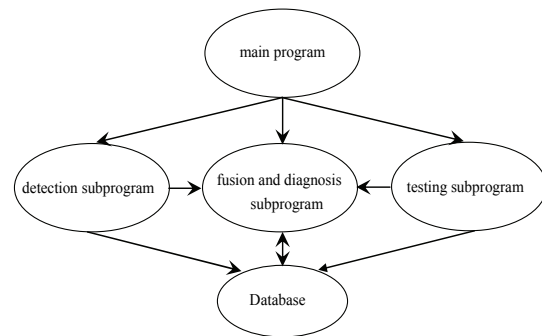


Fig. 6. A principle diagram of two signal transduction.

### 6.1. The Detecting and Testing Subprogram

A complete testing procedure for azimuth and elevation servo system is as shown as Table 3. All testing include accurate and coarse signal errors and error voltages. Besides, the angles turning over testing include turning over time testing, semi-oscillation testing, and overshoot testing.

As shown in Table 3, step 1 detects initial state which detect the initial position and related state. In step 2, static step testing defines initial position and amount of step. In step 3, a constant-velocity movement testing defines initial position, finished position, angular velocity, guiding time, feed forward coefficient, and the number of times for reciprocating movement.

**Table 3.** Testing for azimuth and elevation servo system.

No.	Content
1.	Detect initial state
2.	Static step testing
3.	A constant-velocity movement testing
4.	Sine movement testing
5.	Small angles turning over testing
6.	Larger angles turning over testing
7.	End

In step 4, sine movement testing defines initial position, guiding time and cycle and frequency, amplitude also. In step 5 and 6, small and larger angles turning over testing define initial position and turning over angles. A transform formula is described by:

$$1^\circ = \frac{50}{3} \text{mil} \quad (3)$$

The main performance index of each testing is left and right extreme position, minimum and maximum velocity and maximum acceleration. Each testing includes accurate and coarse channel static error measure and error voltage measure. In addition to, small angles turning over testing and larger angles turning over testing include tests such as turning over time and semi-oscillation and overshoot, etc.

There are some established content. Setting for the static testing is initial position and step. Setting for a constant-velocity movement testing is initial position and terminational position and angle velocity, and pilot time, and reciprocal time, positive feedback coefficient also. Setting for sine movement testing is initial position and cycle and amplitude, and the operating time, positive feedback coefficient also. Setting for small angles turning over testing and larger angles turning over testing are initial position and angle.

There are some characteristic of motion for each testing. For a constant-velocity movement testing, it output signal to driving servo system to achieve established velocity during pilot time. For sine movement testing, it output signal to driving servo system to achieve established characteristic of motion after n pilot time. And for other testing, it output signal to driving servo system to achieve the terminational position from initial position during the step time.

The established content of the testing system dynamic save the last setting. And system display the error voltage waveform in real-time.

Some key programs described as follows.

## 6.2. Sine Signal Output Subprogram

According to the design required, given the cycle and the operating time, the testing system output sine signal which amplitude is one-third of the established amplitude in first cycle and two-third of established

amplitude in second and next to last cycle, and the others output the established amplitude. Characteristic of sine signal output is shown in Fig. 7.

**Fig. 7.** The waveforms of sine signal output.

The main section of sine signal output subprogram is described as follows.

```
void CALLBACK Tfmsd::Time Procsfzx (UINT
uID, UINT uMsg, DWORD dwUser, DWORD dw1,
DWORD dw2)
{long izx=proctimei[3];double t,ty,zqxs;
switch(fwgdyxxz)
{case 0: t=StrToFloat(Edit22->Text);//cycle
ty=StrToFloat(Edit24->Text);//operating time
zqxs=StrToFloat(Edit25->Text);//positive feedback
coefficient
break;...default: break;}
static double y=0,thita;
double zxx0=StrToFloat(Edit20->Text);//initial
position
double A=StrToFloat>Edit23->Text;//amplitude
long sum1=(int)(1000/3);long sum2=(int)(2000/3);
long sum3=(long)(ty*60*1000/t)-2*(sum1+sum2);
long step0=sum1;long step1=sum1+sum2;
long step2=sum1+sum2+sum3;
long step3=sum1+2*sum2+sum3;
long step4=2*sum1+2*sum2+sum3;
if (izx<=step0)
{thita=2*M_PI/sum1;
y=zxx0+(A/3)*sinl(izx*thita);}
if((step0<izx)&&(izx<=step1))
{thita=2*M_PI/sum2;
y=x0+(A*2/3)*sinl((izx-step0)*thita)};
if ((step1<izx)&&(izx<=step2))
{thita=2*M_PI/1000;
y=zxx0+A*sinl((izx-step1)*thita)};
if((step2<izx)&&(izx<=step3))
{thita=2*M_PI/sum2;
y=zxx0+(A*2/3)*sinl((izx-step2)*thita);}
if((step3<izx)&&(izx<=step4))
{thita=2*M_PI/sum1;
y=zxx0+(A/3)*sinl((izx-step3)*thita);}
switch(fwgdyxxz)
{case 2:y=y*200/3;break;default: break;}
Kfz1->Port=0x332;Kfz1-
>Write("0x"+IntToHex((int)
(((long)y%6000+y-(long)y)*4*4096/6000),4));
Kfz1->Port=0x334;
```

```

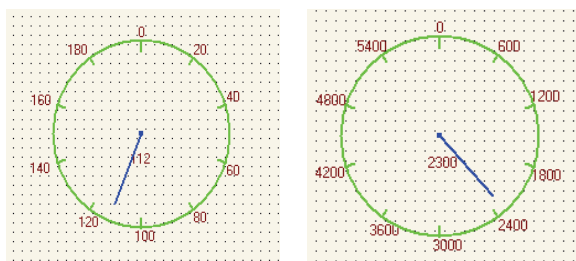
Kfz1->Write("0x"+IntToHex((int)(((long)y%200+y-
(longly)*4*4096/200),4));
double      qqdy=(int)(zqxs*y)%10+(zqxs*y-
(int)(zqxs*y)); Kfz1->Port=0x338;
if (qqdy>0)
{Kfz1-
>Write("0x0"+IntToHex(((int)qqdy*0x3ff/6000),3));
}
Else
{Kfz1-
>Write("0x0"+IntToHex(((int)qqdy*0x7ff/6000),3));
}
if(izx%10==0)
Edit53->Text=FormatFloat("###0.##",qqdy);
Engle1->Engle=y;Engle2->Engle=y;
Chart2->Series[0]->AddXY(izx,y);
Chart2->Series[1]-
>AddXY(izx,(zqxs*y)/1000.0);
if (izx>3000){Chart2->Series[0]->Delete(0);
Chart2->Series[1]->Delete(0);}
proctime[3]++;}

```

### 6.3. The Accurate and Coarse Channel Dynamic Output and Display Subprogram

In order to dynamic display the accurate and coarse channel error signal which is electrical angle that stand for the servosystem position directly, we construct the TEngle module.

As shown in Fig. 8, it looks like a clock which indicator stand for the actual electrical angle for the accurate channel (as shown in Fig. 8 (a)) and coarse channel (as shown in Fig. 8 (b)). The clock is divided into ten equal parts, which adopts 600 mil as increments for coarse channel and 20 mil as increments for accurate channel.



(a) The accurate channel, (b) The coarse channel

Fig. 8. The TEngle module.

The main section of the coarse channel TEngle module program is described as follows, which is similar to the accurate channel TEngle module program. In program, Brush is background color; Engle is angle; Font is style of the dial; Pen is the color of round frame and scale; and Ppen is the color of the indicator.

```

void __fastcall TEngle::Paint (
{ float rad,dir;float x1,y1,x2,y2;
(Width<Height)?Height=Width:Width=Height;
//boundary of square
(Width<Height)?dir=Width:dir=Height;
dir=dir-40;rad=dir/2;Canvas->Pen=FPen;
Canvas->Brush=FBBrush;Canvas->Font=FFont;
if(!JC) //draw dial
{Canvas-
>TextOutA(10+rad,35+rad,IntToStr(Engle%6000));
//display the angle
Canvas->Pen=FPen;Canvas->Brush=FBBrush;
Canvas->Font=FFont;x1=20+rad;y1=20;
x2=20+rad;y2=30;Canvas->MoveTo(x1,y1);
//draw the scale
Canvas->LineTo(x2,y2);
Canvas->TextOutA(x1-3,y1-13,"0");//draw the
label
x1=20+(rad+rad*sin(M_PI/5));y1=20+(rad-
rad*cos(M_PI/5));x2=20+(rad+sin(M_PI/5)*rad
*0.9);
y2=20+(rad-cos(M_PI/5)*rad*0.9);
Canvas->MoveTo(x1,y1);Canvas-
>LineTo(x2,y2);
Canvas->TextOutA(x1,y1-13,"600");
.....
x1=20+(rad+rad*sin(9*M_PI/5));
y1=20+(rad-rad*cos(9*M_PI/5));
x2=20+(rad+sin(9*M_PI/5)*rad*0.9);
y2=20+(rad-cos(9*M_PI/5)*rad*0.9);
Canvas->MoveTo(x1,y1);Canvas-
>LineTo(x2,y2);
Canvas->TextOutA(x1-20,y1-13,"5400");
Canvas->Ellipse(20,20,dir+20,dir+20);
Canvas->Pen=FPPen;
x1=20+rad;y1=20+rad;
Canvas->MoveTo(x1,y1);
Canvas->Ellipse(x1-2,y1-2,x1+2,y1+2);
x2=20+(rad+sin(Engle*0.06*M_PI/180)*rad
*0.8);
y2=20+(rad-
cos(Engle*0.06*M_PI/180)*rad*0.8);
Canvas->LineTo(x2,y2);} }

```

### 6.4. Diagnosis Subprogram for Travel Servo System

According to the characteristic of action for travel servo system, it divides the travel servo system into  $k$  intervals.  $k = (k_1, k_2, \dots, k_n)$ , which  $k_i (i = 1, 2, \dots, n)$  is an interval subset. Each interval subset has some travel switches which is different amount. For example,  $k_i = (x_1, x_2, \dots, x_m)$ ,  $x_j (j = 1, 2, \dots, m)$  is detection information of a single travel switch in  $k_i$  travel subset. Under the normal conditions,  $x_j$  fit the normal distribution. The diagnosis subprogram for travel servo system is described in Table 4. We use the data having

minimum variance as fault feature criterion in the end [12, 13].

**Table 4.** Diagnosis subprogram for travel servo system.

No.	Content
1.	Testing repeated many times
2.	Calculate the approximate unbiased estimation and variance
3.	Data process using Kalman Filter
4.	Calculate the minimum variance
5.	output

## 6.5. Design of Database

System database include static database and dynamic database, there are the table of user organization relationship and the table of administration authority, and table of equipment allocation, table of subservosystem testing, table of testing template, and the synthetic tests table, etc. The static database is used as saving information such as vessel subjection and administrative organization, and equipment and its state, history of maintenance, etc. It is convenient to master equipment state for the static database in long term. The dynamic database is used as saving information such as vessel code and equipment, testing system, testing item, testing time, testing data, maintenance decision-making, etc.

## 7. Testing for Servo System

The servo system testing wiring is shown in Fig. 9. Power of 220 V/50 Hz and 115 V/400 Hz during the tests the mid frequency power is supplied by vessels.

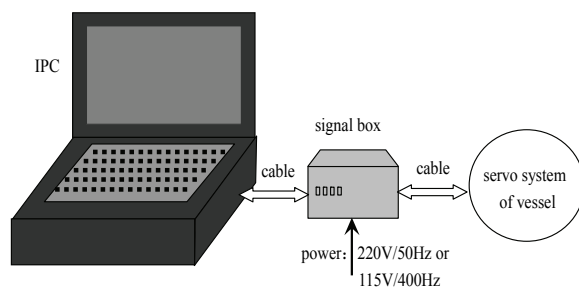


**Fig. 9.** The servo system testing wiring diagram.

The main section of calling programmer for PCL818 is described as follows.

```
if(DRV_DeviceOpen(0, &lDriverHandle)!=
SUCCESS)
{ShowMessage("Open Error!");return;} //open card
unsigned short x; //define a variable
Di.value=&x;
Di.port=A(0~32); //define a channel
```

```
if(DRV_DioReadPortByte(lDriverHandle,&Di)!=SU
CCESS)
```

```
{ShowMessage("Read error!");return;} //read data
The main section of detecting programmer for
static error is described as follows.
```

```
void CALLBACK Tfmsd::TimeProcjmw(UINT
uID,UINT uMsg, DWORD dwUser,DWORD
dw1,DWORD dw2)
{int imw=proctimei[7];float mw100ct0=0.0;static
long flagmw=0,mwctt=0,mwbzdc=0;double x1,x2;
double cjcs,jjcs,cjcsdy,jjcsdy,xc,xj,xcdy,xjdy;
fmsd-> Port=0x330;fmsd-> Write("0x0081");
fmsd-> Port=0x33c;cjwcinj=fmsd-> Read();
if(cjcs!=0&&jjcs==0){jjcs=200;}
//if accurate channel error is zero when coarse
channel error is not zero
cjcsdy=strtody(cjwcinj);jjcsdy=strtody(jjwcinj);
cjcs=strtojmw(cjcsdy);jjcs=strtojmw(jjcsdy);
if(imw%10==0)
{fmsd->Edit12-
>Text=FormatFloat("###0.###",jjcsdy);
fmsd->Edit10-
>Text=FormatFloat("###0.###",cjcsdy);
fmsd->Edit31-
>Text=FormatFloat("###0.###",jjcs);}
```

## 8. Conclusions

Through experiments overland, the servosystem has achieved the design requirements. Application shows it possesses the advantage of portable and simple operate and easy test, high efficiency. It reduces the difficulty of equipment maintenance, conveniences to track and mastery the equipment for long time, and increases the quick guarantee capability. The static position precision of test overland gets 0.1 mil. Based on above advantages it has great application value and promotion value.

In this paper, we design the hardware and software design for servosystem testing system, but there are some problems worth considering [14], such as how to qualitative describe characteristics of mechanical and electric of the whole equipment system, etc.

## Acknowledgements

The author wishes to thank the previously provided technical supported by science scheduled project of Zhanjiang which code is 2011C3108007 and 2011C3108008.

## References

- [1]. Zhao Liming, Liu Heping and Zhang Bing, Integrated Design of Portable Synthetic Detection and Testing Instrument for Servo System, *Computer Measurement & Control*, Vol. 12, December 2010, pp. 2904-2907.

- [2]. Zhang Bing, Study and design of sine servomechanism test instrument based on multi-source information fusion, in *Proceedings of the International Conference on Electronic Measurement & Instruments (ICEMI)*, Chinese Institute of Electronics (China), August 16-19, 2011, pp. 287-632.
- [3]. Zhang Xue-Han, Research on data comprehensive management of ship integrated logistics support, *Journal of Naval University of Engineering*, Vol. 18, No. 2, April 2006, pp. 74-78.
- [4]. Shi Yue-Dong, Wang De-Shi, Application of Fuzzy Information Fusion in Servo System Fault Diagnosis of Naval Gun, *Journal of Launch & Control*, Vol. 3, No. 1, September 2008, pp. 64-68.
- [5]. Lian Junqiang, Jiao Ziping, Ren Ting, Research on Fault Diagnosis of Servo System of Naval Gun Based on SVM-ANN Hybrid Model, *Ship Electronic Engineering*, Vol. 9, No. 28, September 2008, pp. 77-80.
- [6]. Slobodan Ribarić, Darijan Marčetić, Denis Stjepan Vedrina, A knowledge-based system for non-destructive diagnostics of façade isolation using the information fusion of visual and IR images, *Exper Systems with Application*, Vol. 36, No. 2, March 2009, pp. 3812-3823.
- [7]. Zong Hua, Zong Cheng-Ge, Yu Chang-Jun, and Quan Tai-Fan, Research and application on NFE model of multi-sensor information fusion, *Journal of Electronic & Information Technology*, Vol. 32, No. 3, 2010, pp. 525-527.
- [8]. Guo Yang-Ming, Cai Xiao-Bin, Zhang Bao-Zhen, and Zhai Zheng-Jun, Prognostics and health management technology for new-generation weapon, *Computer Engineering and Application*, Vol. 44, No. 13, December 2008, pp. 199-202.
- [9]. Yan Lin, Zhi Quan Feng, Bo Yang, Wei Gai and Xian Hui Song, Research on State Prediction Based on Multimode Fusion, *Journal of Software*, Vol. 7, No. 2, Feb. 2012, pp. 352-357.
- [10]. J. Garcia, J. Gomez-Romero, M. A. Patricio, J. M. Molina, Gala Rogova, On the Representation and Exploitation of Context Knowledge in a Harbor Surveillance Scenario, in *Proceedings of the 14<sup>th</sup> International Conference on Information Fusion*, 2011, pp. 1787-1794.
- [11]. Peter Hubinsky, Peter Hauptle, Reducing Oscillation During Positioning of A Servomechanism Having Flexibility, *Journal of Electrical Engineering*, Vol. 63, No. 4, July 2012, pp. 201-212.
- [12]. Qingle Pang, Information Fusion Based Fault Location Technology for Distribution Network, *Journal of Software*, Vol. 6, No. 5, May 2011, pp. 826-833.
- [13]. X. Luo, M. Kezunovic, Implementing fuzzy reasoning Petri-Nets for fault section estimation, *IEEE Transactions on Power Delivery*, Vol. 23, No. 2, Apr. 2008, pp. 676-685.
- [14]. Wang Jun-Zheng, Wen Zi-Yun, Zhao Jiang-Bo, and He Shi-Jun, Test Device for Flack Flowing Systems Based on Virtual Instrument Technology, *Transactions of Beijing Institute of Technology*, Vol. 10, No. 26, October 2006, pp. 540-545.

---

2013 Copyright ©, International Frequency Sensor Association (IFSA). All rights reserved.  
(<http://www.sensorsportal.com>)



**Sensors Industry  
News**

**FREE Monthly  
IFSA Newsletter**

ISSN 1726-6017

**SUBSCRIBE NOW**  
[subscribe@sensorsportal.com](mailto:subscribe@sensorsportal.com)

## Investigating the Fire Behavior of a Boiler Explosion in a Semiconductor Factory Using Computer Simulation and Verification

<sup>1</sup>C. S. Lin, <sup>2</sup>C. C. Yu, <sup>3</sup>T. C. Chen, <sup>4</sup>C. C. Lai, <sup>5</sup>S. C. Wang, and <sup>6</sup>H. C. Lu

<sup>1-5</sup> Department of Mechanical Engineering Yuan Ze University, Taiwan 32003, R. O. C

Tel.: 886-939-373643, fax: 886-3-4112231

E-mail: s958705@mail.yzu.edu.tw

*Received: 5 June 2013 / Accepted: 25 August 2013 / Published: 30 September 2013*

**Abstract:** This study reports the results of simulating a fire that occurred in a semiconductor factory in Taiwan in 2005. Based on the Fire Dynamics Simulator (FDS), this research investigated the risk factors involved in the semiconductor factory after undergoing the fire, and assessed the hazards caused by smoke. A factory fire of such magnitude shuts down operation and is damaging to the local society, economy, and the environment. The findings of this research are intended to enhance the engineering of the plant and mitigate the factors that negatively influenced the evacuation of people during the actual fire, to reduce risk and loss of the property fire. This paper provides specific parameters and quantitative data regarding planning and design, to serve as a reference for formulating countermeasures for the fire protection of industrial factories in Taiwan.

*Copyright © 2013 IFSA.*

**Keywords:** Computer simulation, Fire Dynamics Simulator (FDS), Fire, Semiconductor factory, Boiler.

### 1. Introduction

Each year, the loss caused by fires occurring in factories is far greater than that in city fires, and substantially hinders the competitiveness of the affected industries. Therefore, it is necessary to emphasize concerns about hazards, loss, casualties, and environmental disruption caused by fires occurring in factory buildings. When a fire occurs in a factory, raw, processed materials, products, equipment, and other objects that have stored in the plant area can be ignited by fire, thereby generating smoke and high temperatures. Staff inside the building seriously injured by inhalation of toxic gas produced, finally may be died on-site or the hospital. In recent years, some researchers have investigated fires that have occurred in buildings and have

conducted analyses using FDS [1-3], among including focusing on the effects of the venting on the fire to the smoke flow [4].

The Fire Dynamics Simulator (FDS) fire simulation software [5], developed by the Building and Fire Research Laboratory (BFRL), National Institute of Standards and Technology (NIST), was used in this research. The FDS Computational Fluid Dynamics fire simulation software is based on the Large Eddy Simulation (LES), which is applicable to a 3D fire scenario. FDS divides the space of the building into a fine grid and solves the governing conservation equations of each part of the grid by applying a numerical method. FDS accurately estimates physical data such as pressure, temperature, velocity, and smoke flow at the fire scene. FDS is particularly applicable to large buildings and

complex building space designs to fire simulations. Furthermore, it can calculate and describe in detail the temperature, pressure, and velocity at any location of a fire scene throughout the entire process of the fire, including to the fire phenomenon. FDS provides diverse information on the spread of flame, the movement of smoke, fuel, and heat transmission of the walls, and the actuation of the sprinkler system for the effects. FDS, which calculates variations of the heat flow field and heat transmission of the fire scene of a building space, is primarily based on the Navier-Stokes equations. The governing conservation equations are as follows [6]:

1) Conservation of momentum:

$$\frac{\partial}{\partial t} \rho \mathbf{u} + \nabla \cdot \rho \mathbf{u} \mathbf{u} + \nabla p = \rho \mathbf{g} + \mathbf{f}_b + \nabla \cdot \boldsymbol{\tau}_{ij} \quad (1)$$

2) Conservation of mass:

$$\frac{\partial \rho}{\partial t} + \nabla \cdot \rho \mathbf{u} = \dot{m}_b''' \quad (2)$$

3) Conservation of energy:

$$\frac{\partial}{\partial t} (\rho h_s) + \nabla \cdot \rho h_s \mathbf{u} = \frac{Dp}{Dt} + \dot{q}''' - \dot{q}_b''' - \nabla \cdot \dot{q}'' + \varepsilon \quad (3)$$

4) Conservation of state:

$$p = \frac{\rho R T}{W} \quad (4)$$

5) Conservation of Species (Combustion Material):

$$\frac{\partial}{\partial t} (\rho Y_i) + \nabla \cdot \rho Y_i \mathbf{u} = \nabla \cdot \rho D_i \nabla Y_i + \dot{m}''' \quad (5)$$

6) Equation in Diffusive Terms:

$$\begin{aligned} \Phi &\equiv \boldsymbol{\tau} \cdot \nabla \mathbf{u} \equiv \mu \left( 2(\text{def } \mathbf{u}) \cdot (\text{def } \mathbf{u}) - \frac{2}{3}(\nabla \cdot \mathbf{u})^2 \right) \\ &= \mu \left[ 2 \left( \frac{\partial u}{\partial x} \right)^2 + 2 \left( \frac{\partial v}{\partial y} \right)^2 + 2 \left( \frac{\partial w}{\partial z} \right)^2 + \left( \frac{\partial v}{\partial x} + \frac{\partial u}{\partial y} \right)^2 \right. \\ &\quad + \left( \frac{\partial v}{\partial x} + \frac{\partial u}{\partial y} \right)^2 + \left( \frac{\partial w}{\partial y} + \frac{\partial v}{\partial z} \right)^2 + \left( \frac{\partial u}{\partial z} + \frac{\partial w}{\partial x} \right)^2 \\ &\quad \left. + \frac{2}{3} \left( \frac{\partial u}{\partial x} + \frac{\partial v}{\partial y} + \frac{\partial w}{\partial z} \right)^2 \right] \quad (6) \end{aligned}$$

7) Equation of Radiative Transport:

$$\begin{aligned} s \cdot \nabla I_\lambda(x, s) &= -[k(x, \lambda) + \sigma(x, \lambda)] I(x, s) \\ &\quad + B(x, \lambda) + \frac{\sigma(x, \lambda)}{4\pi} \int_{4\pi} \Phi(s, s') I_\lambda(x, s') d\Omega' \quad (7) \end{aligned}$$

## 2. Research Method

This study investigated a fire in a semiconductor factory in Taiwan, which occurred in 2005. The sizes of the floors and their purposes are shown in Table 1.

**Table 1.** Case plant B1 ~ 4F floor area and use explains.

Floors	Areas	Purposes
1F - 4F	5,700 × 4 m <sup>2</sup>	Printed circuit plate production lines (BGA)
B1F	6,800 m <sup>2</sup>	

\* Ball Grid Array (BGA).

A fire, such as the case studied here, is one of the most harmful and dangerous disasters that can occur in a semiconductor factory. This is typically caused by large quantities of extremely dangerous, concentrated chemicals stored on-site. Examples of these chemicals, which are used in the manufacturing process, are hydrogen fluoride (HF), silane (SiH<sub>4</sub>), hydrogen (H<sub>2</sub>), and other substances. Such a disaster worsens when toxic or flammable gases and fluids are ignited. The diffusion of toxic substances causes injury to plant personnel and damages the surroundings. The smoke particle causes to machinery damage and equipment often costs as high as tens of billions of dollars (NTD). Therefore, establishing an effective fire protection mechanism for high-tech factories is critical to protect staffs from such danger.

The exterior dimensions of the building were 93 m (long) × 83 m (wide) × 50 m (high), in a rectangular block shape. The fire source was located on the first floor of the building. The fire was simulated in such a manner that it spread from the first floor to the fourth floor through the exhaust piping (see Fig. 1 for the model of the first to the fourth floors, as created in this study). The entire area of the first to the fourth floors, and the boiler chamber on the first floor, were explored.

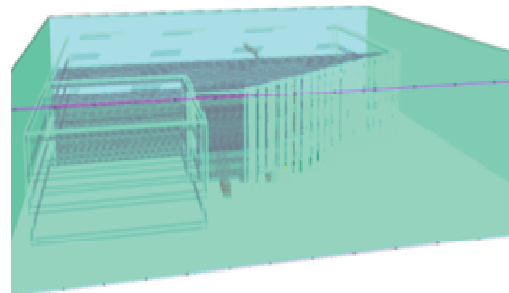


**Fig. 1.** The FDS software restructures factory model.

### 2.1. Fire Scene Verification and Analysis

This research collected information and data on the fire scene, and then verified the simulated results from the FDS software with the collected fire scene photographs. The results of a numerical simulation were added qualitatively and quantitatively, to describe the variations of temperature, smoke, and toxic gases over time. The method of using qualitative and quantitative analysis to determine and verify each of the regional variations, as well as the

trends of the physical parameters, are described as follows.

### 2.1.1. Verification I

This fire appears to have been caused by a boiler operator who turned on a boiler improperly, so that the boiler chamber exploded. The fuel oil and boiler water spilled out of the boiler body. The electrical equipment, and the hot boiler body, then ignited the fire. The fire spread to the exhaust piping above the boiler (Boiler A), and the exhaust piping was made of polypropylene (PP).

The temperature of Boiler A in the boiler chamber reached the melting point of the PP duct, above 150 °C, during the initial period of the fire. See Fig. 2 and Fig. 3 for the simulation results. The fire source was the diesel oil; hence, the fire spread rapidly. The CO concentration at this stage was between 2000 and 4000 ppm, and the air layer height was reduced to 1.5 m. An interview with the boiler operator revealed that the boiler operator had left the work site to inform the supplier of an abnormality observed while turning on the boiler. When the operator returned, had found that the rear of the boiler was full of thick smoke (see Fig. 4 and Fig. 5), which is consistent with the simulation.



Fig. 2. Boiler room in Boiler A upper ducts melting situation.

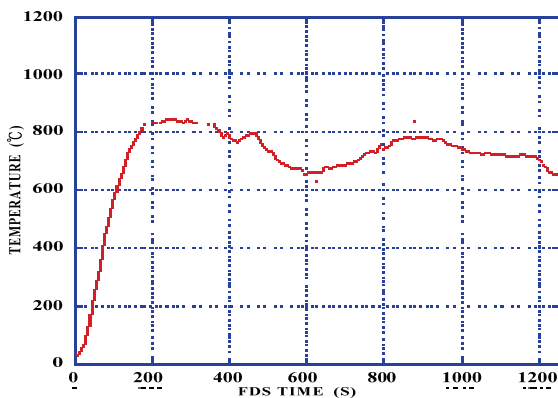


Fig. 3. The boiler chamber at Boiler A upper temperature the simulation results.

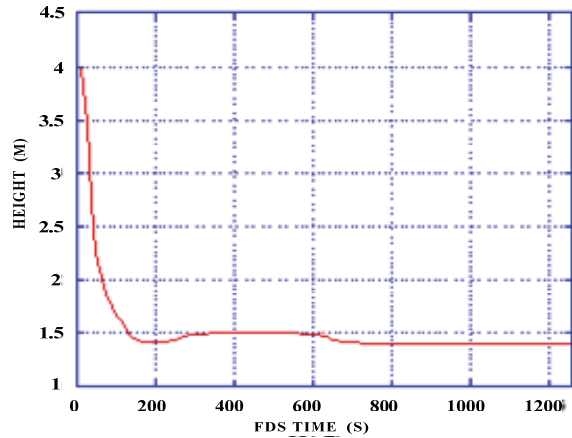


Fig. 4. The boiler chamber at Boiler A at the air layer height the simulation results.

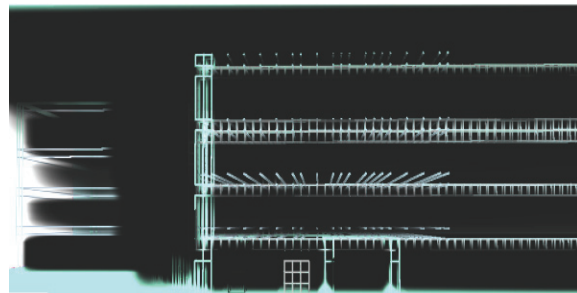


Fig. 5. The 600 s boiler chamber smokes to simulate transient.

### 2.1.2. Verification II

The plant was surrounded by a construction curtain wall. It was found, by analyzing a photograph of the fire site, that part of the aluminum partition plate was melted by the high temperature of the fire. An engineering study [7] stated that the curtain wall is made of alloy aluminum board, mostly 1100-H14 and 3003-H14, which 3003-H14 loses less mechanical strength when heated.

In terms of temperature resistance of the material, the melting point of aluminum is approximately 659 °C, which is insufficient to resist the high temperature of the fire scene. Aluminum begins to soften and deform at approximately 300 °C, and melts at approximately 600 °C. The comparison between the simulation result and photographs of the site shows that the entrance of the boiler chamber reached the threshold temperature of softening, deforming, and melting from the 200<sup>th</sup> to the 1260<sup>th</sup> seconds. This is consistent with the real situation, because it was under high temperature for a long duration, as shown in Fig. 6.

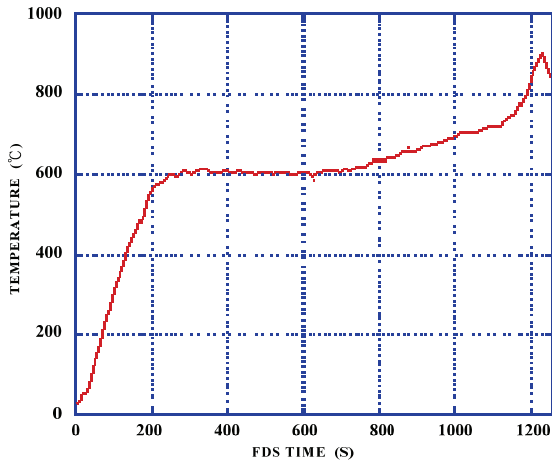


Fig. 6. Boiler chamber entrance temperature change simulation result and curtain wall aluminum partition plate melting situation.

### 3. Results and Discussion

This research simulated the real fire situation, and analyzed variations of upper layer temperature, CO concentration and air layer height of the first floor and the boiler chamber, as well as the effect of such variations on the fire scene. Table 2 lists the related settings of fire scene parameters.

Table 2. The fire parameters settings to explain.

Parameters	Setting conditions
Cause of ignition	The ignition of the boiler was caused by start abnormal factors
Number of boilers	5 sets
Boiler type	Tubular
Boiler leakage area	15 m <sup>2</sup>
Above the pipeline materials	Polypropylene (PP)
Main fire source	Diesel fuel
Heat release rate correction curves	Gasoline [8]
Vents	Full open

Indicators of three parameter limits, upper layer temperature, CO concentration, and air layer height are discussed below.

#### 3.1. Discussion Regarding the upper Temperature (°C)

Fig. 7 shows the temperature distribution of the upper layer of the boiler chamber, located on the first floor. The boiler chamber was designed so that five boilers were on the same side of Boiler A, which was the fire source. The investigation found that the boilers were a tubular-type. The initial determination stated that the cause of the fire was that the boiler was ignited because it was started improperly. Extremely high temperatures developed quickly during the initial period of fires. The oil and water leaking from the boiler covered approximately 15 m<sup>2</sup>. In addition, the ductwork above was made of combustible PP material and extended to the passageways and openings of other rooms. According to the interview, the doors of this area were mostly open, and so that the design of the passageway was set to open. Fig. 8 displays a simulated fire scenario for the boiler chamber. Diesel oil was the fire source. Because the heat value of this combustible liquid is extremely high, the heat release curve of this case is designed with reference to the calibration curve of the heat release rate, as described in the literature (TSAI, 2007, [8]).

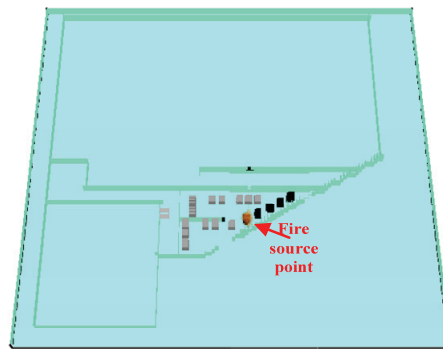


Fig. 7. The fire is an ignition point location diagram.

With advance of a time, the smoke had filled the interior of the boiler chamber quickly, and rapidly spread outside. This is consistent with the real situation when comparing photographs of the fire scene with those of the simulated scenarios, as shown in Fig. 9 and Fig. 10. Boiler A was burned, adjacent Boiler B and the ductwork above the other equipment were substantially scorched. The rest of the chamber facilities only suffered the surface of smoke damage. The fire did not reach a temperature that damage reduces the structural strength of the building, but did generate a considerable amount of smoke. Therefore, the structural damage caused by the fire can be repaired for continued use, as shown in Fig. 11.

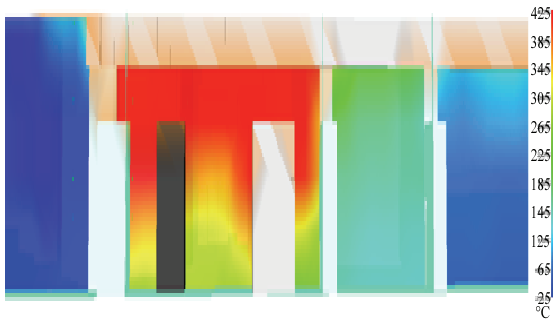
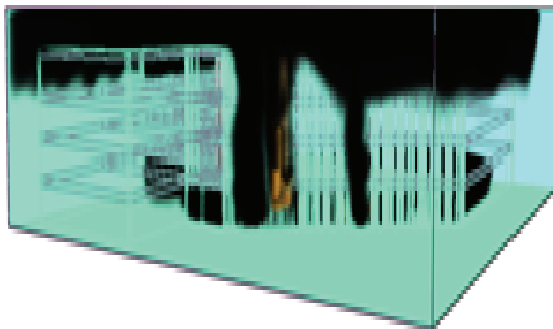


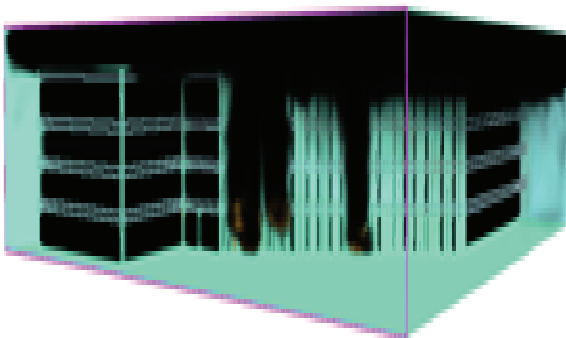
Fig. 8. The fire is the ignition point Boiler A y-section transient diagram.



Fig. 11. The boiler chamber inside photographs.



100 seconds



1260 seconds

Fig. 9. 100 - 1260 s fire transient diagram.



Fig. 10. Boiler chamber outside scene screens.

### 3.2. Discussion Regarding the CO Concentration (ppm)

The quantity of combustibles is closely related to the amount of smoke, temperature, and generated CO concentration. When a fire spreads, CO concentration reaches several thousand ppm over a short time. According to the research on this topic, when the CO concentration reaches 1,000-2,000 ppm, humans may experience unconsciousness, dyspnea, and coma, and may die within 2 hours. Therefore, CO concentration has an enormous effect on the survival of evacuees.

Fig. 12 shows the distribution of CO concentration in the boiler chamber on the first floor. The fire source was at the location of boiler A. The production of CO, from the dissociation caused by the combustion reaction, increased rapidly during the initial period of the fire. After reaching the peak at the 200<sup>th</sup> second, it stabilized in the range of 7000-8000 ppm. The PP acid-alkali exhaust piping from the boiler chamber is composed of combustible plastic materials, which are the source of the high CO values. In addition, because the spilled oil was extremely flammable, the operator was unable to quench the flames with the available extinguisher. Therefore, the fire spread rapidly. The firefighters attempted to extinguish the blaze with water, but failed, as shown in Fig. 13.

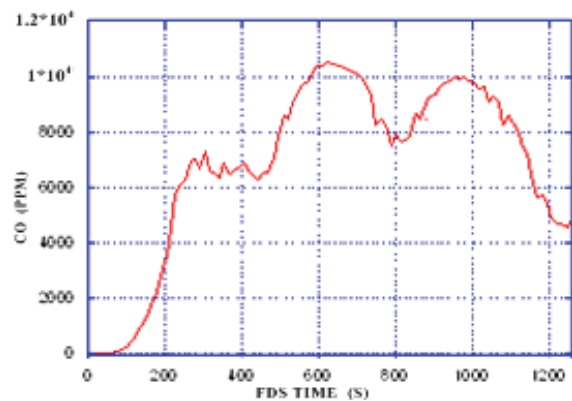
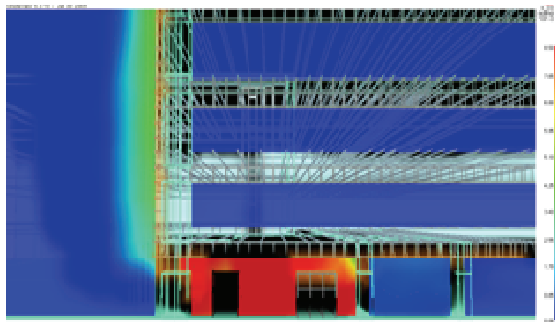
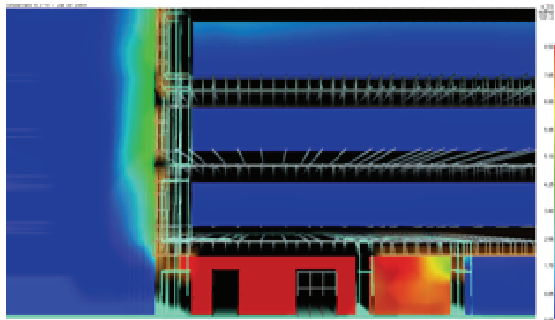


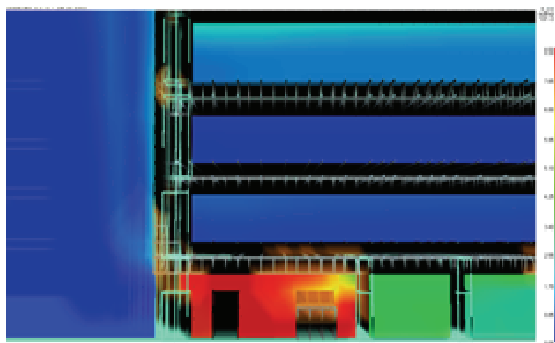
Fig. 12. The CO concentration location of Boiler A.



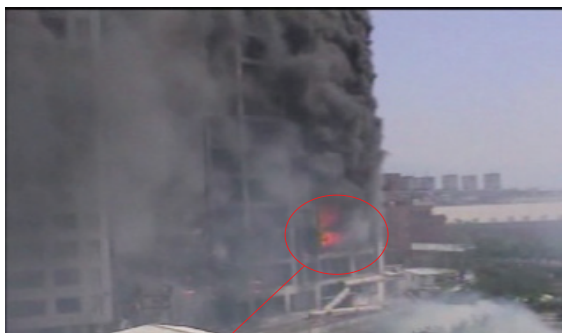
100 seconds



600 seconds



1260 seconds



Fire ignited point (Boiler chamber)

Fig. 13. Transient of the fire's CO concentration.

### 3.3. Discussion of the Layer Height (Meter)

Fire is often accompanied by a large amount of smoke. This is cause for concern, because the smoke contains toxic gases and has a high temperature; therefore, inhalation of such material causes the choking and burns in the airway and lungs of people in the area. According to previous research, an air

layer below 1.5 m is hazardous immediately to human life. The height of the air layer was declined by the accumulation of smoke under the ceiling, which also worsened the visibility. This condition may cause panic, and the people involved may not be able to identify the proper escape route.

Fig. 14 shows the air layer height of the boiler chamber. The height of the air layer in the boiler chamber was reduced to approximately 1.5 m at 200<sup>th</sup> second. This height was maintained to 1260<sup>th</sup> seconds the end of the simulation. From this, it may be inferred that the boiler chamber has the larger area; therefore, the accumulation of smoke requires longer time. Furthermore, a defect in the fire compartment allows the smoke to billow outwards. Consequently, the air layer height in the boiler chamber remained at approximately 1.5 m, as shown in Fig. 15.

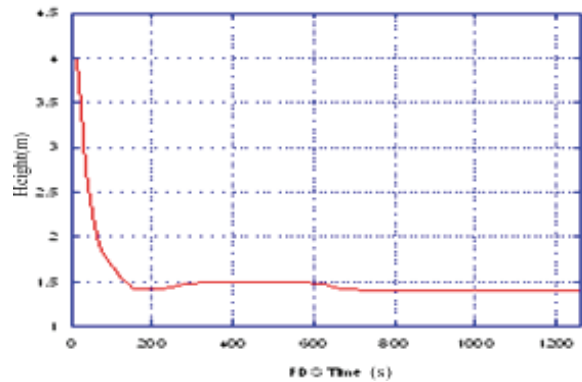
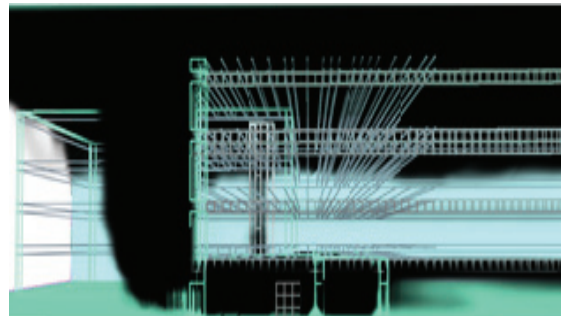
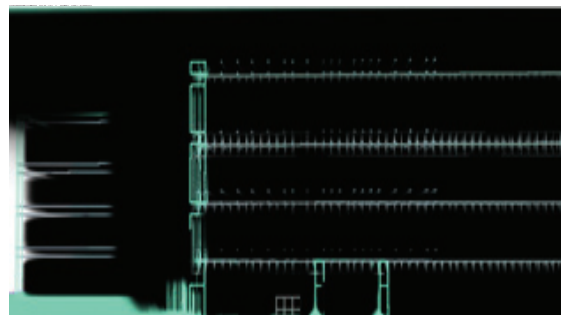


Fig. 14. Air layer height diagram of the Boiler A.



100 seconds



1260 seconds

Fig. 15. Transient of the boiler chamber at 100-1260 s.

In verifying the photographs, the part of the wall inside the boiler chamber that was blackened by smoke is found at approximately this height, as shown in Fig. 16.



Fig. 16. Photograph of the boiler chamber's smoke height.

Based on this analysis, the air layer height might vary significantly and depends on the amount of smoke from combustion, configuration of the room, vents, opening time, and the distance from where the fire started. If the air layer height of the major combustion region were to reach the lethal threshold, it would not have been possible to escape. By contrast, the production and parking areas were not burned by the fire directly, so the extent of influence is smaller.

#### 4. Conclusions

Based on a review of news reports, interviews, and FDS simulation results, the following conclusions about the fire scene of this case are inferred:

##### A. Fire Compartments

Although the floors and rooms have been at the designed stage of buildings, planning the fire compartments, but in the use of some equipment and ducts permitted through different compartments, in this case which leads to the fire to spread to other compartments.

##### B. Piping Materials

The manufacturing processes of the semiconductor factory require acid-alkali exhaust piping materials. The material used in the pipeline was initially PP. This material is a type of combustible plastic with a low melting point. Once a fire occurs, the loss can be substantial. In this case, along the PP exhaust piping burned, so that allowing the fire to expand.

##### C. Fire Source Heat Release Quantity

The amount of heat generated at the source of the fire influences the burn rate. This research simulated differential heat release rates under different conditions of boiler failure and various amounts of leaked oil. Research on how to prevent oil leakage, and an early warning mechanism, would help to prevent the expansion of fires.

##### D. Automatic Sprinkler Equipment

Automatic sprinkler equipment should be installed in boiler chambers. If the automatic sprinkler in the semiconductor factory case had worked during the initial period of the fire, it would have inhibited the fire and prevented it from expanding. This case exhaust pipes, with a diameter of at least 6 inches or more, has been equipped with the automatic sprinkler equipment, in order to facilitate extinguishing the fire during the initial period.

#### Suggestions

The simulation and analysis results can serve as a reference for planning and improving the design of related plants, which will be helpful for reducing the occurrence of fire disasters, and associated loss. This research proposes the following suggestions:

1) The requirements for engineering quality at any stage in the building of plants, including planning, design, construction, expansion, and equipment installation, should be more strengthened. In particular, the planning, design, and construction of the fire compartment should not be compromised by any previous stage. Once any one of the fire compartment units is broken, it can cause a domino effect when a fire disaster occurred.

2) Exhaust piping should be composed of non-combustible material. Even for building and equipment materials, non-combustible and combustion-resistant material should be the priority. If non-combustible and combustion-resistant materials are not used, then pipes with a diameter of at least 6 inches should be equipped with automatic sprinklers, according to NFPA guidelines.

3) In planning and designing plants, high-risk and high-heat equipment should be isolated from the major production manufacturing area. Such equipment should not be adjacent or connected to the production manufacturing area. However, the designs of old plants should also be examined critically to reduce the risks of disaster.

4) The body of the boiler and its surroundings should be upgraded by adding fault warning devices and a leakage detection device, which is capable of transmitting a warning signal to on-site personnel, so that any abnormal incidents can be promptly addressed.

## Acknowledgements

The authors would like to thank the National Science Council of the Republic of China, Taiwan, for financially supporting this research under Contract No. NSC 100-2221-E-155-076.

## References

- [1]. C. S. Lin, S. C. Wang, C. B. Hung and J. H. Hsu, Ventilation Effect on Fire Smoke Transport in a Townhouse Building, *Heat Transfer-Asian Research*, Vol. 35, No. 6, 2006, pp. 387-401.
- [2]. S. C. Wang, C. S. Lin and C. C. Yu, Effect of Wall Material and Ventilation on Flashover Phenomenon in a Compartment Fire, in *Proceedings of the 3<sup>rd</sup> International Symposium on Energetic Materials and their Applications (ISEM' 2008)*, Tokyo, Japan, 24-25 April 2008, p. 64.
- [3]. Y. He, Smoke Spread Experiment in a Multi-story Building and Computer, *Center for Environmental Safety and Risk Engineering Victoria University of Technology*, 1997.
- [4]. S. C. Wang, C. S. Lin and C. C. Yu, Dynamic Simulation of Backdraft Phenomena in a Townhouse Building Fire, *Heat Transfer-Asian Research*, Vol. 37, No. 3, 2008, pp. 153-164.
- [5]. N. L. Ryder, J. A. Sutula, C. F. Schemel, A. J. Hamer and V. V. Brunt, Consequence Modeling Using the Fire Dynamics Simulator, *Journal of Hazardous Materials*, 2004, pp. 149-154.
- [6]. K. McGrattan, S. Hostikka and J. Floyd, Fire Dynamics Simulator (Version 5) User's Guide, *NIST Special Publication 1019-5*, National Institute of Standards and Technology, 2010.
- [7]. W. Y. Chang, Preliminary Study on Fire Performance for UN-opening Aluminum Plate of Curtain Wall, Master thesis, *National Cheng Kung University*, 2003.
- [8]. M. J. Tsai, Development and Application of a Large Scales Fire Test Facility, Ph D. Thesis, *National Taiwan University of Science and Technology*, Appendix 2.3, 2007, pp. 135-141.
- [9]. "NFPA 101, Life Safety Code, Appendix C," *National Fire Protection Association*, Quincy, MA, 1981.

## Notation

Symbol	Description	Symbol	Description
$p; \rho; T$	Pressure; Density; Temperature	$\mu$	Dynamic viscosity
$R$	Universal gas constant	$\Phi$	Diffusion equation
$\bar{W}$	Molecular weight of the gas mixture	$\rho_\infty$	Surface constant density
$\mathbf{u} = (u, v, w)$	Velocity vector	$I$	Radiation intensity
$\dot{m}'''$	Production rate of species	$\lambda$	Wavelength
$\mathbf{g}$	Gravity vector, normally (0,0, -g)	$I_\lambda(x, s)$	Wavelength $\lambda$ radiation intensity
$\mathbf{f}_b$	External force vector (excluding gravity)	$\sigma_s(x, \lambda)$	Scattering coefficient
$\tau_{ij}$	Viscous stress tensor	$D$	Diffusion coefficient
$h$	Enthalpy	$s$	Unit vector in direction of radiation intensity
$\dot{q}'''$	Heat release rate per unit volume	$k$	Thermal conductivity; suppression decay factor
$\dot{q}_b'''$	The energy transferred to the evaporating droplets	$\sigma$	Stefan-Boltzmann constant
$\dot{q}''; \varepsilon$	Heat flux vector; Dissipation rate	$B(x, \lambda)$	Radiation source items
$Y_1$	The mass fraction of the chemical species 1	$\dot{m}_1'''$	The production rate of the chemical species 1 per unit volume

## The Design of an Embedded Video Data Acquisition System

<sup>1</sup>Chongyu Wei, <sup>2</sup>Weichen Wei, <sup>1</sup>Zuping Gu

<sup>1</sup>Qingdao University of Science & Technology, No.99 Songling road, Qingdao, 266061, P. R.China

<sup>2</sup>Melbourne University, VIC, Australia

<sup>1</sup>Tel.& fax: 86-532-88959036,

E-mail: weichongyu@sina.com

*Received: 5 June 2013 / Accepted: 25 August 2013 / Published: 25 September 2013*

**Abstract:** A video transmission system generally consists of three main parts: A video data acquisition unit, transmission networks and play back terminals. The video data acquisition unit is one of the main parts. This paper focuses on an embedded video data acquisition hardware and software design. In the design, a PXA310 is used as a primary processor. The software design is based on an Android operating system. First, the paper briefly introduces the hardware design including overall scheme and the selection of key components. Then, the software design of the video data acquisition unit is introduced more detail, which includes the transplant of an Android operating system and the application software implementations for video data acquisition and processing. The modifications of BLOB boot program, the modifications of the operating system kernel and the NAND FLASH driver transplantation are described in more detail. The description of the video data acquisition software design includes the use of the Android internal class “Mediarecorder”, the method of extracting frame data according to 3GP and H.264 protocol, and the use of the socket interface to transmit frame data to a 3G wireless network called TD-SCDMA. The designed acquisition unit has been tested in a video surveillance and monitoring system and the experiment results are given at the end of the paper. *Copyright © 2013 IFSA.*

**Keywords:** Networking video monitoring, Android, System transplant, Video data acquisition, H.264, Transmission unit.

### 1. Introduction

In recent years, the increasing market demands for network surveillance camera systems provide a good chance for the video data acquisition, processing and transmission technology development. And with the rapid increase in market penetration of 3G wireless cellular networks and their transmission bandwidths, wireless video surveillance and monitoring system can be deployed where a 3G network deployed. Under this condition, surveillance camera systems based on wireless networks and Internet becomes the mainstream of the monitoring

system [1, 2]. On the other hand, wireless video surveillance is also one of the main driving forces for 3G market development and will be an important growth of future mobile applications. Broadband wireless networks and the development of video compression coding techniques provided the necessary conditions for promotion of wireless video surveillance technology. In developing the surveillance camera systems above, how to design the unit for video data acquisition, processing and coding, and transmissions through a wireless network or Internet is a pivotal work, and have been becoming a hot point in technology development [12-15].

Video transmission based on the embedded system technology has features of low cost, compact size, easy to create and flexible applications. Android [3] is widely used embedded operating systems with open source code in recent years. Developing a video data acquisition and transmission unit based on an embedded system technology and for use in a 3G network is of great significance.

This paper describes the hardware and software design of the video data acquisition and processing.

## 2. Hardware Design of The Video Data Acquisition, Processing and Transmission Unit

The hardware platform mainly consists of a camera unit on the front end, a PXA310 [4, 5] processor module and a TM1902 wireless modem, as shown in Fig. 1. The Video camera OV7670 is an image sensor with 8 bits resolution data output and its frame rate is 30 F/s. The TM1902 modem supports TD-SCDMA HSUPA wireless transmissions. The Android platform is selected as the operating system.

Considering the minimum ROM size requirements for Android system to start up and run are respectively 105 MB and 128 MB and the minimum RAM size requirements are respectively 128 MB and 256 MB, the two in one chip MT29C2G24MAKJ, whose RAM and NAND FLASH sizes are 1 Gb and 2 Gb respectively, is used. The NAND-FLASH is used to store image files and configuration data needed to run the operating system. The OV7670 is connected to PXA310 via data and control bus respectively, and is programmed through the interface SCCB to implement image data processing. An LP3972, which is a multifunctional, programmable power management IC, is used to supply all the powers the PXA310 needed. The connection circuits between PXA310 and TM1902 are shown in Fig. 2, including an external USB transceiver TUSB1105, a current-limiting switch MAX1693, and the modem TM1902. The TM1902 uses UART1 to communicate with the PXA310 for sleeping and waking-up control. The 6-line USB 1.1 port 3 of the PXA310 is connected to the 4-line USB 1.1 port of TM1902 to transfer video data and control signals. The TM1902, which operates in the RF band of 2010-2025 MHz, implements the communication between the video data acquisition unit and a 3G wireless network referred to as TD\_SCDMA.

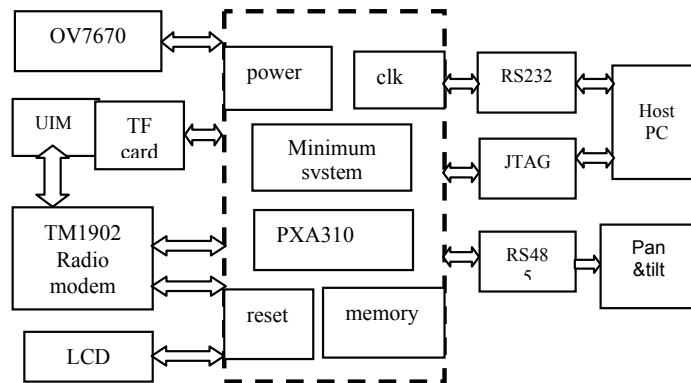


Fig. 1. The hardware composition of the video acquisition unit.

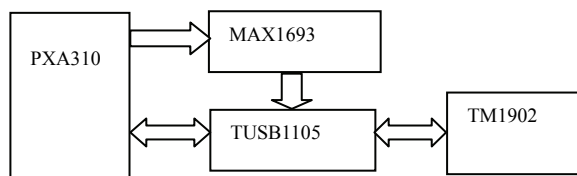


Fig. 2. The connection between the PXA310 processor and the TM1902 wireless modem

In debugging an embedded system, we generally use a Serial interface, a JTAG, a USB or a Network card to download the system image to the target board designed. Advantages of using a Serial Interface are that the serial protocol is simple and the interface is universal. But data rate of the Serial Interface are too slow. In contrast, a JTAG interface

provides a higher data rate. But the disadvantage of this method is that it needs a dedicated JTAG debugger and there is a checksum problem of the image formats. Other methods need a related interface provided by host processor. However, the products designed based on the embedded system generally do not provide such interfaces. This makes it inconvenient to develop and produce the embedded products. On the other hand, with the increasing complexity of applications of the embedded system, a large storage is generally required in design an embedded products. Based on the reasons above, a new method of using a TransFLash card [9] is suggested here. The TransFLash card can be used both for updating mirror files in the process of developing and debugging the embedded systems and as a large storage in the final product.

### 3. Software Design

#### 3.1. General Software Solution

Software development requires first transplant Android operating system [6-8] to the embedded hardware platform. And then implement the software design for the video data acquisition, encoding, extracting video frame data, and transferring the encoded video data into the 3G wireless network. The transplantation of the Android system includes the modification of the boot loader, the Linux kernel and the root file system.

There are two implementation schemes for video data acquisition and processing. The first one is to directly encode video data from the inner CAMERA class of Android. Disadvantages of this software encoding approach are that it takes a lot of processor resources and its output frame rate is generally lower. The second one is the use of the MEDIARECORDER class of Android for video data acquisition and encoding. Since the outputs of the MEDIARECORDER class are the documents in 3GP or MP4 format, they must be transformed into the video data stream for streaming media transmission. This is a hardware encoding approach that does not require the transplantation of code library. Therefore it is easy for implementing and can output a higher frame rate. To output a suitable frame rate, the second method is adopted in the paper. Camera resolution and encode format are configured in the MEDIARECORDER class. The encoded data are packed in file stream of 3GP format. The data for each frame are picked up from the file stream according to the 3GP protocol. Then the frame data picked up is sent to the server via the wireless modem TM1902.

For sending video data through the TM1902 modem, operations needed include dialing wireless TD-SCDMA network, establishing PPP protocol connection and sending video data by an application program calling the Socket interface [10]. Android 2.3 and later versions include a software module supporting TD-SCDMA modems and what needed in achieving above operations is to add TM1902 to the module and configure it accordingly.

The OV7670 camera used has a photosensitive array of  $640 \times 480$ . Maximum frame rate can be 30 f/s when outputting VGA video data with CIF image format and H.264 coding standard. UDP datagram fashion is used for video data transmission and TCP for signaling. Since the maximum transmission unit (MTU) in link layer is 1500 bytes, and considering the total length of IP and UDP datagram heads is 28 bytes, the maximum UDP length in a local area network is 1472 bytes and 576 bytes in Internet. The maximum transmission unit for UDP transferring is 548 bytes.

### 3.2. Transplanting Android Operating System

#### 3.2.1. General Description

There are many kinds of bootloaders in use. Considering the PXA310 Board Development Kit has contained a BLOB, the transplantation of the bootloader in the article is based on the BLOB given.

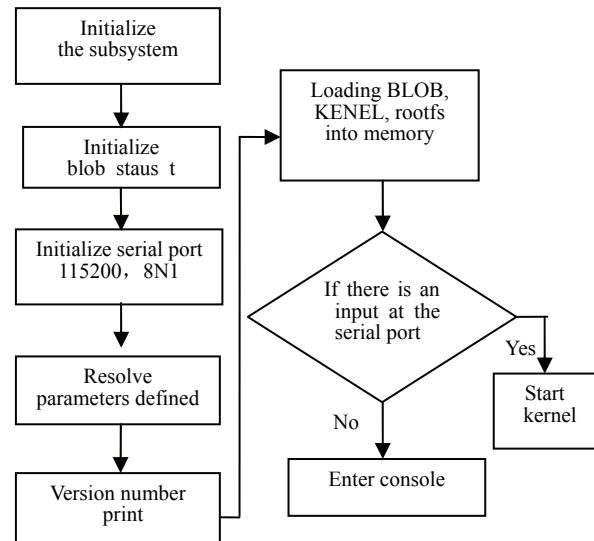


Fig. 3. Flow chart of main function.

The src/blob/start.S is the first file for the BLOB to run. In running the file start.S, the board contained configuration data is read by calling a function process and then orderly initializes GPIOs, clock system, power supply circuitry and the NAND FLASH. The file start.S also calls the TESTRAM module of the TESTMEM.s to check the address of the 1 Mb space for starting-up the system, which is a process of reading-in  $0xaa, 0 \times 55$ , then reading and checking. When the above checking finished, it copies the second stage codes of the BLOB into RAM, jumps to the starting address BLOB\_START in the RAM and runs stage 2. In running stage 2, it first clears away the BSS section, which houses uninitialized variables, and then jumps into the "main" function. The flow chart for running the main function is given in Fig. 3.

#### 3.2.2. Modifying Parameters for Starting up BLOB

PXA310 provides 3 serial I/O ports. In this paper, port 1 of the PXA310 processor is used as the serial interface of the console. The serial port is set to open in the configuration file and its baud rate is set to 115200. In this situation, the data for running the system will be transferred to host from BLOB. Detailed configuration commands are as follows.

```

/* Use STUART */
#define USE_SERIAL11
#define TERMINAL_SPEED
    baud_115200

```

In booting the kernel to start up, it must be insured that all the modules on the hardware platform have been enabled and clocked properly. Since the enable pins of modules connect the processor's GPIOs, in the BLOB the GPIOs should be set to the response level or MFP pins. These settings include camera enable pin, the write-protect pin of the NAND FLASH, the power supply pin of the power manager, and the pins for enabling and clocking TM1902.

It requires BLOB read the kernel image files exactly from NAND FLASH, which implies that the kernel address must be obtained accurately, for booting the system kernel to start up normally. Therefore, the BLOB should be partitioned in light of the image file sizes, and their initial addresses should be marked. Generally, the BLOB is partitioned from address 0, and in the order of BLOB, kernel, Android root file system. The partition sizes are in the image file sizes rounding. Detailed setting commands are as follows.

```

/* and where do they live in flash */
#define BLOB_FLASH_BASE
    (0x00000000)
#define BLOB_FLASH_LEN    (1024* 1024)
#define PARAM_FLASH_BASE
    (BLOB_FLASH_BASE +
    BLOB_FLASH_LEN)
#define PARAM_FLASH_LEN    (0) /* no
parameters */
#define KERNEL_FLASH_BASE(PARAM_
FLASH_BASE + PARAM_FLASH_LEN)
#define KERNEL_FLASH_LEN(3*1024*1024)
#define LOAD_RAMDISK 0/* load ramdisk into
ram */
#define RAMDISK_FLASH_BASE
    (KERNEL_FLASH_BASE+
    KERNEL_FLASH_LEN)
#define RAMDISK_FLASH_LEN(96*1024*
1024)
#define USERDATA_FLASH_BASE
    (RAMDISK_FLASH_BASE +
    RAMDISK_FLASH_LEN)
#define USERDATA_FLASH_LEN    (32 * 1024
* 1024)

```

### 3.3. Transplanting the System Kernel

Transplanting the kernel is modifying and recompiling the kernel to run corresponding hardware platform, which requires add driver programs and other kernel modules to support corresponding new chips and hardware modules on the platform. The main contents of the kernel

transplantation include modifying the kernel booting parameters and adding new device driver programs.

Equipment driver programs are the interfaces between the operating system kernel and platform hardware devices. The driver programs implement functions of initializing or releasing devices, transferring data from kernel to hardware devices or vice versa, reading the data that an application program sends to a device file or responding the data it asking for, detecting device faults and implementing fault-tolerance.

In the operating system Linux, there are mainly three kinds of device files. They are block devices, character devices and network equipments. Jobs of writing device driver programs mainly include the writing of sub functions and putting them into different "file\_operations" fields.

#### 3.3.1. Transplanting the Driver of NAND FLASH

Since the login of an NAND FLASH proceeds its driver, when the NAND driver logs it will match all the devices logged on the bus by matching their names. If the matching is successful, it will execute the probe function of the NAND driver, namely pxa3xx\_nand\_probe(), which is the beginning of running the NAND driver program. Logical flow chart is given in Fig. 4.

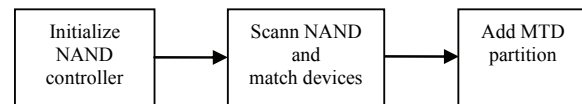


Fig. 4. Structure diagram of NAND Flash driver.

1). Initializing the NAND controller. On starting up, the system will allocate the NAND controller a data structure, in which the configuring data are included such as a controller's clock, a reference address, and the transferring mode. Android system kernel can support various NAND chips. During initializing, the controller can read the ID of the NAND chip by operating a register and match it to the ID in configuration. This operation will continue until the controller finds the chip's configuration data and then completes the controller initialization. Fig. 5 gives the initialization flow chart.

Source codes for the configuration of MT29C2G24MAKJ are as follows.

```

struct type_info[] = {
    .....
    { DFC_FLASH_Toshiba2GbX16,
    &toshiba2GbX16},
    { DFC_FLASH_Micron_2Gb_X_16,
    &micron2GbX16},
    { DFC_FLASH_NULL, NULL},
};

```

```

struct dfc_flash_info micron2GbX16 =
{
.timing = {
.tCH = 10, /* tCH, Enable signal hold time
*/
.tCS = 35, /* tCS, Enable signal setup time */
.tWH = 15, /* tWH, ND_nWE high duration */
.tWP = 25, /* tWP, ND_nWE pulse time */
.tRH = 15, /* tRH, ND_nRE high duration */
.tRP = 25, /* tRP, ND_nRE pulse width */
/* tR = tR+tRR+tWB+1, ND_nWE high to
ND_nRE low for read */
.tR = 25000,
/* tWHR, ND_nWE high to ND_nRE low delay
for status read */
.tWHR = 60,
.tAR = 10, /* tAR, ND_ALE low to ND_nRE
low delay */
},
.enable_arbiter = 1, /* Data flash bus arbiter
enable */
.page_per_block = 64, /* Pages per block */
.row_addr_start = 1, /* Second cycle start, Row
address start position */
.read_id_bytes = 4, /* Returned ID bytes */
.....

```

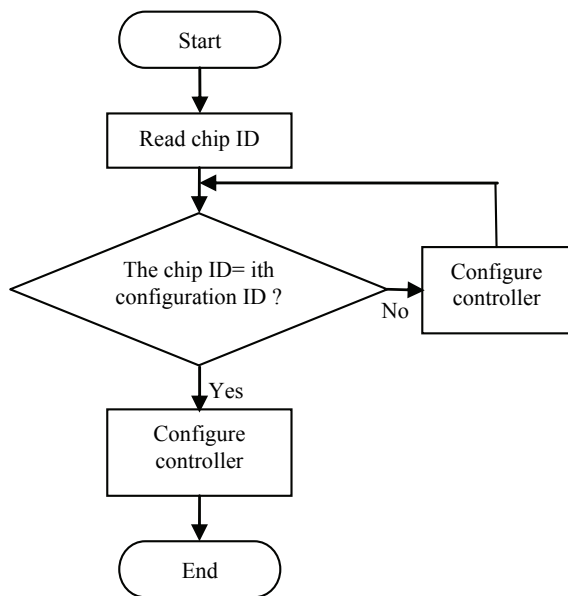


Fig. 5. Flow chart of NAND controller initialization.

2). The function for scanning NAND. This function is used to print device ID in starting up kernel and lookup bad blocks in the NAND and setup a bad block table (BBT), by which the kernel can judge if a data block is normal or not and then complete device scanning.

3). Add MTD subarea information. By using the function “mtd\_part”, an original MTD device can be divided into several parts and logged in “mtd\_table”. In the “mtd\_table” each original MTD partition can be logged as a MTD device. Two functions of

“add\_mtd\_device” and “add\_mtd\_partitions” are used to do this work. Detail codes are as follows.

```

littleton_nand_info.parts =
pxa300_android_128m_partitions;
littleton_nand_info.nr_parts =
ARRAY_SIZE(pxa300_android_128m_partitions
);
add_mtd_partitions(monahans_mtd, pdata->parts,
pdata->nr_parts);

```

### 3.3.2. Compiling Kernel Source Codes

This work contains the following steps.

1) Decompressing kernel. Decompress kernel source codes to the host working environment. In this paper, the kernel version used is Linux-2.6.29 and compressing format is tar.gz. Use “#tar zxvf linux-2.6.29.tar.gz” to decompress the kernel to the working directory.

2) Configuring the kernel to support ARM platform. The kernel source codes include the source codes supporting x86 and ARM system. The source codes supporting ARM platform are in the “arch/arm” directory. In compiling, setup the corresponding infrastructure and cross compile tool chain at the top layer of the “Makefile”, which makes calling the file “arch/arm/Kconfig” as configuring Linux kernel. Commands used are as follows.

```

#ARCH ?=$(SUBARCH)
#CROSS_COMPILE ?=
ARCH=arm
CROSS_COMPILE=arm-eabi-

```

3) Modifying platform clock rate. Modify the line 42 of the file “arch/arm/mach-pxa/pxa3xx.c” in kernel and set the clock rate to 13 MHz, which is the external clock signal frequency of PXA310 processor. Commands are as follows.

```

/* Crystal clock: 13MHz */
#define BASE_CLK 13000000

```

4) Making kernel configuration file. For the kernel used in the paper, when installing a patch package a default configuration file “pxa3xx\_android\_defconfig” will be added in the directory of the configuration file “arch/arm/configs”. The hardware platform in the paper uses this default configuration. Executing command “#make menuconfig”, the PC screen will display a man-machine interface in Fig. 6. On completing kernel configuration and executing command “#cp .config arch/arm/configs/myconfig”, the current configuration files will be stored.

5) Adding hardware platform ID. When BLOB starts system kernel, it first transfers the platform ID stored in the register R1 to the kernel. If the ID has not been added in the kernel, kernel starts up fault. Therefore, the processor ID must be added in the kernel before starting up. The ID of PXA310 is 1388. The codes for adding platform ID are as follows.

Where the command “machine\_is\_xxx” is a function used to judge if the current platform is right, “CONFIG\_xxxx” is a function produced during the kernel configuration, “MACH\_TYPE\_xxx” is the definition of the system platform ID, and “number” is the platform ID value.

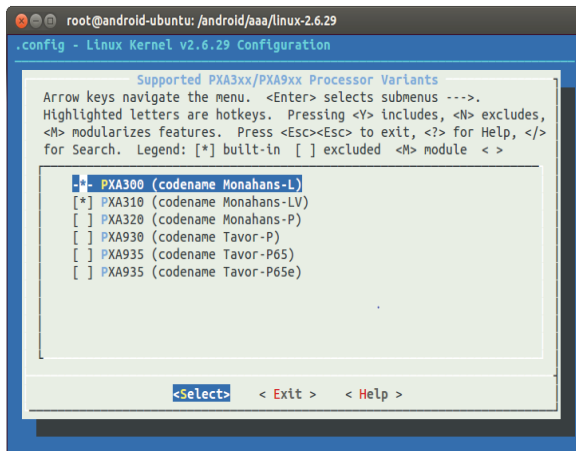


Fig. 6. Printed screen of kernel configuration.

```
#machine_is_xxx
CONFIG_xxxx MACH_TYPE_xxx number
littleton      MACH_LITTLETON
LITTLETON     1388
```

6) Modifying MTD partition. The operation of the kernel is based on the MTD partition. The BLOB and kernel must be partitioned in full accord, including partition name, size, starting address. The MTD information of the kernel is as follow.

```
static struct mtd_partition
pxa300_android_128m_partitions[] = {
    [0] = {
        .name = "Bootloader",
        .offset = 0,
        .size = 0x100000,
        .mask_flags = MTD_WRITEABLE, /* force
read-only */
    },
    [1] = {
        .name = "Kernel",
        .offset = 0x100000,
        .size = 0x300000,
        .mask_flags = MTD_WRITEABLE, /* force
read-only */
    },
    [2] = {
        .name = "system",
        .offset = 0x0400000,
        .size = 0x4000000, /* mount 64M fs */
    },
    [3] = {
        .name = "userdata",
        .offset = 0x4400000,
        .size = 0x2000000,
    },
    .....
},
```

When above modifications completed, the kernel can be compiled. To do this, execute command “#make zImage” and the kernel image named “zImage” will be formed under the “arch/arm/boot” directory. Using a TF card to download [9] and in combining with BLOB command, the kernel image can be burned to the hardware platform, i.e. the target board.

#### 4. Software Implementation of the Video Data Acquisition Front End Based on Android

Video and audio data capturing and processing are implemented by using the “Mediarecorder” class of Android platform. The “Mediarecorder” is based on the “OpenCore” library and achieved in JNI by calling “media\_jni” library file [11]. Image resolution, coding standard and output file type can be set directly in the “Mediarecorder” class. Fig. 7 gives the operation flow chart.

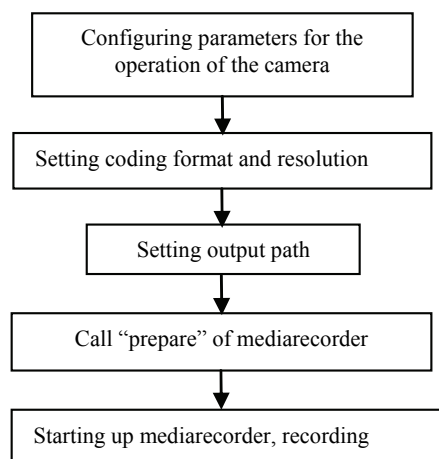


Fig. 7. Mediarecorder configuration flow chart.

The “Mediarecorder” calls “setCamera” to select a camera, “setVideoSource” to capture video data from the camera, and “setOutputFormat” to set output routing path, which must be a file descriptor. The detailed “Mediarecorder” configurations are as follows.

```
mediarecorder.setCamera(c);
mediarecorder.setVideoSource(MediaRecorder.VideoSource.CAMERA);
mediarecorder.setOutputFormat(MediaRecorder.OutputFormat.THREE_GPP);
mediarecorder.setVideoEncoder(MediaRecorder.VideoEncoder.H264);
mediarecorder.setVideoFrameRate(15);
mediarecorder.setVideoSize(640, 480);
```

Because the “Mediarecorder” class can only record local video data, another class called

“LocalSocket” is required for sending the coded video data to network server via socket interface and UDP protocol. The flow chart is shown in Fig. 8.

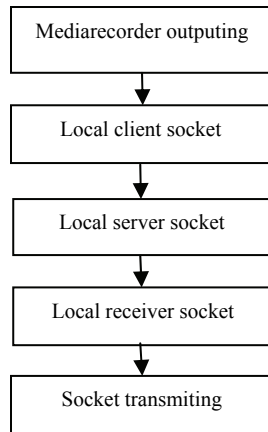


Fig. 8. Logical connection of LocalSocket.

The detailed codes of the “LocalSocket” are as follows.

```

LocalServerSocket mVideoLocalServerSocket =
null;
LocalSocket mVideoLocalClientSocket = null;
LocalSocket mVideoReceiveSocket = null;
mVideoLocalServerSocket = new
LocalServerSocket("Video");
mVideoReceiveSocket.connect(new
LocalSocketAddress("Video"));
mVideoReceiveSocket.setReceiveBufferSize(500
000);
mVideoReceiveSocket.setSendBufferSize(50000
0);
mVideoLocalClientSocket =
mVideoLocalServerSocket.accept();
mVideoLocalClientSocket.setReceiveBufferSize(
500000);
mVideoLocalClientSocket.setSendBufferSize(50
0000);
  
```

The output data of the “Mediarecorder” are file streams in 3GP format. Since no writing back, the file stream can’t be played in stream media; neither the stream server can recognize the files and transfer them. The recorded video data must be further processed to pick up their frame data in H.264 format.

The recorded H.264 data are stored in a media package from which the frame data can be picked up according to the H.264 protocol. The H.264 data are stored in the sequence of NAL cells. Namely a NAL cell stores a frame. Generally there are two fashions for packaging the H.264 data. One is that the first four bytes of each frame is its head 0x00000001 [3]. The other one is that the first four bytes of each frame is its length instead of head. The latter is used in Android “Mediarecorder” outputs. Therefore, in

processing the recorded file stream in 3GP format, first check the “mov” (movie package) in the 3GP file stream and pick up decoding parameters SPS and PPS, add H.264 frame head to the two parameters respectively to form data frames, and send these two data frames to the stream media server. Then, find the media data package “mdat”, read the first four bytes of the “NAL”, calculate their length, read the NAL according to the length calculated. Afterwards, repeat the above operations in circulation till the processing is finished. Flow chart for above processing is shown in Fig. 9.

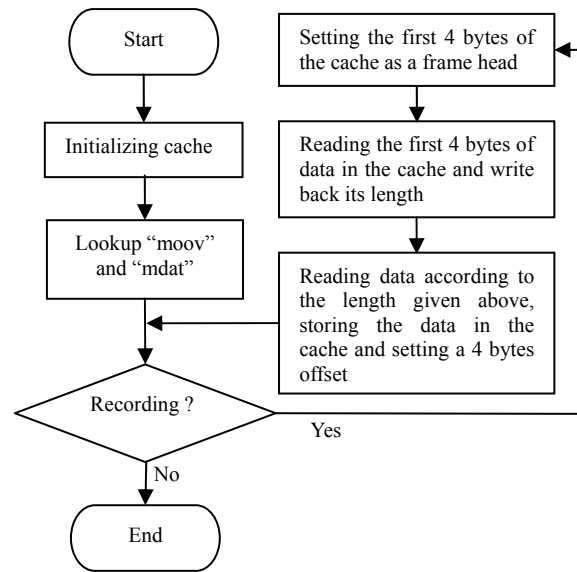


Fig. 9. Flow chart of extracting frames.

The TM1902 is used as a modem transceiver to connect the 3G network TD-SCDMA. The modem is controlled by PXA310 via programmed AT commands. Since data interface of TM1902 is a USB, the USB driver must be transplanted to operate the modem. On the other hand, since the current kernel supports PPP dialing, the Android system can use RIL (Radio Interface Layer) to control the modem. The modem driver is the function “usbserial.ko” for changing the USB interface into a serial port. After loaded the “usbserial.ko”, a node called “ttyUSB\*”, which is used as a channel for transmitting AT commands, will be produced.

1). In the file “reference\_ril.c” of the RIL, there are several operations for using AT commands. These operations must be modified corresponding to different hardware platform, which can be done via the “onRequest” interface. Modify the function “at\_open” in “ril/reference-ril/atchannel.c” to open the channel “ttyUSB0” for modem TM 1902. Detailed source codes are as follows.

```

int fd2 = -1;
while(fd2 < 0) {
fd2 = open ("/dev/ttyUSB0", O_RDWR);
if (fd2 < 0) {
  
```

```

perror ("opening URC interface. retrying...");
sleep(10);
}

```

The modifications in "ril/reference-ril/reference-ril.c" are that delete command

```

"#define PPP_TTY_PATH "/ dev/omap_csmi_tty1"

```

and add command

```

"#define PPP_TTY_PATH "/dev/ppp0".

```

2). Add an access point in the file "apn-conf-sdk.xml". For mobile network TD-SCDMA, the access point is 46007. Source codes for doing this are as follows.

```

<apn carrier="CHINA MOBILE"
mcc="460"
mnc="07"
apn="cmnet"
user="*"
server="*"
password="*"
mmsc="null"
/>

```

3). Modify the file "init.rc" and add "pppd\_gprs" as system server.

Source codes for doing this are as follows.

```

service ril-daemon /system/bin/rild -l
libreference-ril.so -- -d /dev/ttyUSB0
socket rild stream 660 root radio
socket rild-debug stream 660 radio system
user root
group radio cache inet misc
service pppd_gprs /etc/ppp/init.gprs-pppd
/dev/ttyUSB0
user root
group radio cache inet misc
disabled

```

On above modifications finished, Android system can control TM1902 to dial TD-CDMA network and make PPP connection. The Socket requests from application layer will be translated by RIL layer into corresponding AT commands and sent to the hardware at bottom layer. The flow chart for video data acquisition, processing and sending into TD-SCDMA network is shown in Fig. 10.

## 5. Test Results

### 5.1. The Transplantation of Android Platform

In debugging an embedded system, a serial interface is generally used to connect the target board and a host PC. The host uses serial tools such as HyperTerminal to display debugging information. JTAG port is used to download BLOB to the target board. If command lines are displayed on host screen,

it means that the BLOB starts successfully. Since parameters for starting BLOB have been modified and the TF card driver has been transplanted, further adding a download command "tfdownload" is needed. The commands for reading the TF card, downloading and burning the system image are as follows.

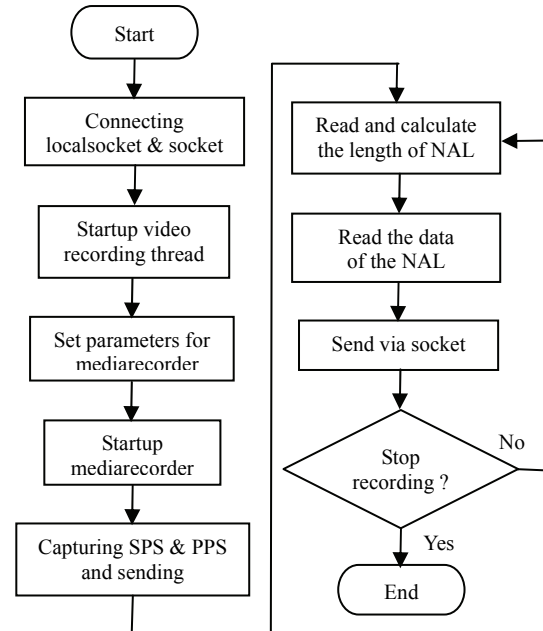


Fig. 10. Flow chart of video data acquisition and processing unit.

```

blob>tfdownload init //initializing TF card [9]
blob>nanderase -z 0x100000 0x300000
//brushing NAND
blob> tfdownload zImage //downloading system
image
blob>nandwrite -z 0x80800000 0x100000
<zImage-actual-length> //burning image
blob>nanderase -y 0x400000 0x4000000
blob> tfdownload system
blob>nandwrite -y 0x80800000 0x400000
<system.img actual length>
blob>nanderase -y 0x4400000 0x2000000
blob>tfdownload userdata
blob>nandwrite -y 0x80800000 0x4400000
<userdata.img actual length>

```

The debugging output information printed on host screen is shown in Fig. 11, which implies that the BLOB starts up successfully and the initialization of the TF card has been completed.

After the BLOB started up, the software has been in a suitable situation for system operation. At this time the operating system will jump to the kernel entry address 0x80800000, and start the kernel.

Fig. 12 gives the starting information and the command line parameters of Linux-2.6.29 system.

Upon starting up, the kernel will check peripheral equipments such as NAND FLASH. If it



```

D/CameraService( 42): stopRecording (pid 42)
D/CameraHardware( 42): ID=0, mProcessTime=4862ms, mThreadTime=2526ms, mRecordFrameCnt=714
D/CameraHardware( 42): Overlay has been closed
D/CameraService( 42): stopRecording(), hardware stopped OK
D/CameraService( 42): stopPreview (pid 42)
D/CameraHardware( 42): stopPreview: 715

AC
# logcat -s VIDEOINF
I/VIDEOINF( 160): oncreat
I/VIDEOINF( 160): filecreat
I/VIDEOINF( 160): recorder.start
I/VIDEOINF( 160): surfacecreat
I/VIDEOINF( 160): surfacechange

```

Fig. 15. Log of the VIDEOINF.

Fig. 16 gives the played video image on a customer terminal.

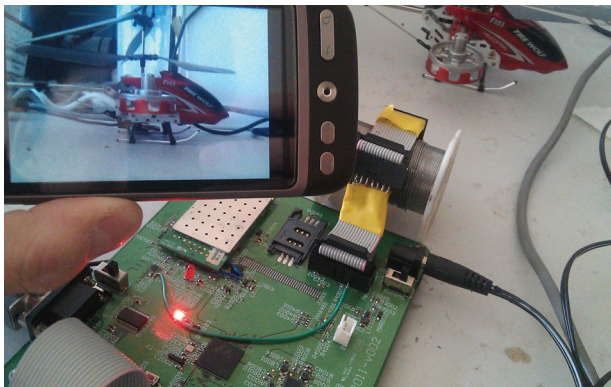


Fig. 16. Whole system rendering

## 6. Summary

The design of a video data acquisition unit has been introduced including unit scheme, hardware platform design, operating system transplantation, application software design and system debugging. The unit uses Marvell PXA310 as the primary processor. Software design is based on an open source operating system Android. The unit designed has been tested in a video surveillance and monitoring system based on a 3G cellular system TD-SCDMA. Test results show that the design is reasonable.

## References

- [1]. D. Gavalas, and D., Economou, Development Platforms for Mobile Applications: Status and Trends, *IEEE Software*, Vol. 28, No. 1, February 2011, pp. 77-86.
- [2]. C. Wei, and F. Zhang, Design of a Surveillance Camera System Based on Android, *Computer Engineering*, Vol. 38, No. 14, July, 2012, pp. 214-216.
- [3]. Zigural Mednieks, Laird Dornin, Programming Android, *O'REILLY*, 2011.
- [4]. Marvell PXA3XX Processor Family, Vol. II: Memory Controller Configuration Developers Manual, *Marvell Corporation*, 2008.
- [5]. Linux Preview Kit Kernel 2.6.21 Board Support Package, *Marvell Corporation*, 2009.
- [6]. Kevin Purdy, The Complete Android Guide, *3Ones*, 2010.
- [7]. Information Technology-coding of audio-visual objects part12: ISO base media file format, *ISO/IEC 14496-12*, 2005.
- [8]. Shane Conder, Lauren Darcey, Android Wireless Application Development, 2<sup>nd</sup> ed., *Addison- Wesley*, 2011.
- [9]. C. Wei, W. Wei, and S. Huang, Applications of a TransFlash in an Embedded System Debugging, *International Journal of Advancements in Computing Technology*, Vol. 5, No. 3, February 2013, pp. 299-307.
- [10]. A. M. Shiddiqi, H. Pratama, and H. T. Ciptaningtyas, A Video Streaming Application Using Mobile Media Application Programming Interface, *Telkomnika*, Vol. 8, No. 3, December 2010, pp. 293-300.
- [11]. <http://download.csdn.net/detail/yusiguyuan/4775440>.
- [12]. J. P. Wagner, and P. Frossard, Distributed Congestion Control of Scalable Video Streams, *Journal of Communications*, Vol. 7, No 3, March 2012, pp. 180-191.
- [13]. M. Halloush, and H. Radha, A Framework for Video Network Coding with Multi-generation Mixing, *Journal of Communications*, Vol. 7, No. 3, March 2012, pp. 192-201.
- [14]. J. Noh, and B. Girod, Time-Shifted Streaming in a Tree-Based Peer-to-Peer System, *Journal of Communications*, Vol. 7, No. 3, March 2012, pp. 202-212.
- [15]. N. Thomos, and P. Frossard, Network Coding and Media Streaming, *Journal of Communications*, Vol. 4, No. 9, October 2009, pp. 628-639.

## Application of Serial Min-max Decoding Algorithm Based on Variable Weighting for Nonbinary LDPC Codes in Optical Communication

<sup>1</sup>Zhongxun Wang, <sup>2</sup>Xinglong Gao

<sup>1</sup>Yantai University, Institute of Science and Technology for Opto-Electronics Information of Yantai University, 264005, China

<sup>2</sup>Key Laboratory of Applied Electronics of Yantai University, graduate student house 305, 264005, China

<sup>1</sup>Tel.: 13723941218

E-mail: ytwzx3@tom.com

*Received: 5 June 2013 /Accepted: 25 August 2013 /Published: 30 September 2013*

---

**Abstract:** In this paper, we perform an analysis on the min-max decoding algorithm for nonbinary LDPC (low-density parity-check) codes and propose serial min-max decoding algorithm. After that, combining with the weighted processing of the variable node message, we propose serial min-max decoding algorithm based on variable weighting for nonbinary LDPC codes. In the end, we perform a detailed analysis on the features of optical communication and show the simulation model in optical communication system. The simulation indicates that when the bit error rate is  $10^{-3}$  and used in optical communication, compared with serial min-max decoding algorithm, traditional min-max decoding algorithm and traditional min-sum algorithm, serial min-max decoding algorithm based on variable weighting can offer additional coding gain 0.2 dB, 0.3 dB and 0.4 dB respectively in (AWGN) additional white Gaussian noise channel and under (OOK) on-off keying modulation. Copyright © 2013 IFSA.

**Keywords:** Nonbinary LDPC code, Min-max decoding algorithm, Variable weighting, Serial decoding, Optical communication system.

---

### 1. Introduction

The next generation of long haul optical fiber transmission system is given signal which travels at the speed of 100 Gbit/s and the reliability must be guaranteed in such long distance. Such standard makes ARQ (Automatic Repeat Request) be not suited in optical fiber communication system. So in order to guarantee low bit error rate, we should add some redundant code words to correct mistake caused by the channel noise, so the role of forward error correction is becoming more and more

important [1-2]. During all the forward error correction codes, TURBO codes [3] and LDPC codes [4] have aroused much attention from many famous research institutes because of their good performance. LDPC code is better than TURBO code in decoding complexity and performance, so LDPC code is suited in optical communication. The paper [5] indicates that nonbinary LDPC code is better than binary LDPC code with the same code length no matter on performance or system latency. We mainly explore on nonbinary LDPC code applying in optical communication.

In the decoding field, nonbinary LDPC code traditionally adopt sum product algorithm based on Galois field. But it owns the computational complexity of  $O(q^2)$  as a result of vast sum and product operations, which influences the application of LDPC codes. So Davey and Barnault proposed a sum product algorithm based on fast Fourier transform which shows the computational complexity of  $O(q \log_2 q)$ . However, it still involves vast product operations. So Wymeersch proposed a sum product algorithm based on log-domain [6], which has the computational complexity of  $O(q^2)$ . To further reduce the complexity, the extended min-sum algorithm was proposed by Declercq [7-8]. It was in [9], the author introduced a min-max decoding algorithm which does not need any sum operations in check node processing and greatly reduces the computational complexity. In the paper, we propose serial min-max decoding algorithm by changing the information scheduling order, which effectively improves the convergence speed of the message and the bit error performance. Combining with paper [10], weighting variable node processing, we propose serial min-max decoding algorithm based on variable weighting for nonbinary LDPC codes, which effectively reduces the correlation between variable nodes and further improves the performance.

The rest of the paper is like this. In the first part, we introduce serial min-max decoding algorithm for nonbinary LDPC codes. Then, serial min-max decoding algorithm based on variable weighting is introduced in the second part. The third part shows the simulation model in optical channel. The concrete performance analysis was made in the fourth part and we finally come to a conclusion in the fifth part.

## 1. Serial Min-max Decoding Algorithm for Nonbinary LDPC Codes

Nonbinary LDPC code is a linear block code defined by its parity-check matrix which has a low density of nonzero elements from Galois field. The structure of the matrix shows a very low complexity in encoding and decoding field. Sum product algorithm based on Galois field is used to decode nonbinary LDPC codes in the conventional sense, which shows high complexity. In paper [9], the author proposed a min-max decoding algorithm, which greatly reduces the computational complexity with a small performance loss. Based on paper [9], we propose serial min-max decoding algorithm by changing the message scheduling order, which effectively improves the convergence speed of the decoder. To further improve the performance, combining with paper [10], we propose serial min-max decoding algorithm based on variable weighting for nonbinary LDPC codes by weighting the variable node processing. The simulation indicates that the convergence speed of the decoder and the

performance can be effectively improved in optical communication when using the algorithm.

We denote the following notations for the purpose of concrete depiction of serial min-max decoding algorithm.

$M(n)=\{m: h_{mn} \neq 0\}$ , the neighboring check nodes about the variable node  $n$ . In other words, the nonzero elements of the  $n$ th column in the matrix.

$M(n)\setminus m$ , the neighboring check nodes about the variable node  $n$  except the check node  $m$ .

$N(m)=\{n: h_{mn} \neq 0\}$ , the neighboring variable nodes about the check node  $m$ . In other words, the nonzero elements of the  $m$ -th row in the matrix.

$N(m)\setminus n$ , the neighboring variable nodes about the check node  $m$  except the variable node  $n$ .

$f_n^a$ , the log-domain message when the variable node  $n$  is  $a$ .

$Q_{mn}^a$ , the log-domain information from the variable node to the check node when the variable node  $n$  is  $a$ .

$R_{mn}^a$ , the log-domain information from the check node to the variable node when the variable node  $n$  is  $a$ .

The whole process of serial min-max decoding algorithm for nonbinary LDPC codes is as follows.

Initialization.

Do as the formula

$$f_n^a = \log(pr(x_n = s_n | channel) / pr(x_n = a | channel)), \quad (1)$$

where  $s_n$  is the most possible value about the variable node  $n$ .

Set  $k=1$  and  $Q_{mn}^a = f_n^a$ .

- ① Decide whether  $k$  reaches the biggest iteration maxiter. If the answer is yes, then exit all the process; otherwise set  $n=1$  and goto ②.
- ② During the  $k$ -th iteration, update variable node information in a  $n=1, 2, \dots, N$  order. Decide whether the comparison expression  $n>N$  is satisfied. If the answer is yes, goto ③; otherwise goto ③.
- ③ The information transformation. In this step, we should do an information exchange of variable nodes according to the parity-check matrix  $H$ . For example, if we know  $Q_{mn}^a$ , then the information to the check node  $m$  across  $h_{mn}$  is  $Q_{mn}^{ah_{mn}}$ , the multiplication and division operations in the formula are performed in Galois field. The check node updating. Perform the following formula.

$$R_{mn}^a = \min\left(\max_{\substack{n' \in N(m) \setminus n \\ b' \in V: x_{n'} = a}}(Q_{mn'}^{b'})\right), \quad (2)$$

V means vector sets which satisfy the m-th parity-check constraints.

⑤ The information transformation. It is the opposite process of ③. Do as the following formula.

$$R_{mn}^{i'a} = R_{mn}^{ah_{mn}^{-1}} \quad (3)$$

⑥ Variable nodes processing. Perform the formula (4).

$$\nabla_{mn}^a = f_n^a + \sum_{m' \in M(n) \setminus m} R_{m'n}^{i'a} \quad (4)$$

Get the minimum value of  $\nabla_{mn}^a$  by the formula (5).

$$\Delta_{mn} = \min_{a \in GF(q)} (\nabla_{mn}^a) \quad (5)$$

Get the information from the variable node to the check node by the following formula.

$$Q_{mn}^a = \nabla_{mn}^a - \Delta_{mn} \quad (6)$$

⑦ Set  $n=n+1$ , goto ④.

⑧ Collect all the information about variable nodes according to the formula (7).

$$Q_n^a = f_n^a + \sum_{m' \in M(n)} R_{m'n}^{i'a} \quad (7)$$

Try to decide all the codeword in terms of the formula (8).

$$\hat{x}_n = \arg \min_{a \in GF(q)} (Q_n^a) \quad (8)$$

Decide whether the operation  $H * x^T$  is equal to zero, if the answer is yes, then exit the whole process; otherwise goto ⑤.

⑨ Set  $k=k+1$ , goto ①.

We find that the updated variable node information can be used faster in serial min-max decoding algorithm, so the convergence speed of the decoder for nonbinary LDPC codes can be effectively improved.

## 2. Serial Min-max Decoding Algorithm Based on Variable Weighting for Nonbinary LDPC Codes

Nonbinary LDPC code is an extension of binary LDPC code in Galois field. In other words, nonbinary LDPC code is defined by its parity-check matrix which owns a low density of nonzero elements from

Galois field. If we get a binary matrix and try to replace the nonzero elements of the matrix with nonzero elements from Galois field, then the nonbinary matrix comes into being. But it is inevitable for binary matrix which is made up of random methods to show short cycles, which results in the oscillation of LLR and degrades the bit error performance. In order to reduce the impact, it was in paper [10], the author proposed a kind of information weighting algorithm based on variable nodes which is used to combine with serial min-max decoding algorithm of nonbinary LDPC codes in the paper. The process is as follows.

The formula (6) can be replaced by the following formula.

$$Q_{mn}^{new} = \lambda_1 (\nabla_{mn}^a - \Delta_{mn}) + \lambda_2 Q_{mn}^{old} \quad (9)$$

As we all know,  $Q_{mn}^{old}$  and  $Q_{mn}^{new}$  almost have the same value when the message tend to be convergent. So we can set  $\lambda_1 = 1 - \lambda_2 = \lambda$ , then the formula (9) can be replaced by the following formula.

$$Q_{mn}^{new} = \lambda (\nabla_{mn}^a - \Delta_{mn}) + (1 - \lambda) Q_{mn}^{old} \quad (10)$$

$\lambda$  can be called weighting factor. So the decoding algorithm can be called serial min-max decoding algorithm based on variable weighting for nonbinary LDPC codes. The simulation indicates that the algorithm shows better performance in medium signal noise ratio region when  $\lambda$  is 0.9.

## 3. The Simulation Model in Optical Channel

In order to meet the need of our paper, we establish the following simulation model in optical channel in Fig. 1 below.

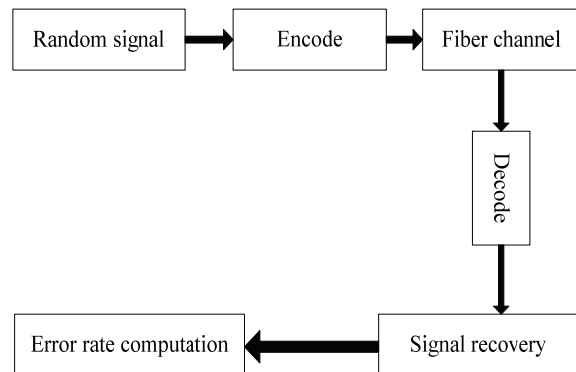


Fig. 1. The simulation model of optical communication system.

With the purpose of convenient analysis, we choose the ideal additive white Gaussian noise channel in our paper [11]. The input signal of the channel is binary signal such as 0 and 1. Because of the existence of additive white Gaussian noise, we can get conditional probability density function about the output signal  $y$  as follows when the input signal is transmitted.

$$f(y|0) = \frac{1}{\sqrt{2\pi}\sigma} \exp\left(-\frac{(y-\mu_0)^2}{2\sigma^2}\right) \quad (11)$$

$$f(y|1) = \frac{1}{\sqrt{2\pi}\sigma} \exp\left(-\frac{(y-\mu_1)^2}{2\sigma^2}\right) \quad (12)$$

$\mu_0$  and  $\mu_1$  are the mean value of the received signal  $y$  when the input signal of the channel is 0

and 1 respectively.  $\sigma^2$  means the variance of the Gaussian noise.

#### 4. The Performance Simulation Analysis

In the paper, we choose 0.5-rate regular nonbinary LDPC code whose code length is 200 to analyze the performance in additive white Gaussian noise channel and under on-off keying modulation. With the purpose of studying the performance of the proposed algorithm, we make a comparison between traditional min-sum algorithm, traditional min-max decoding algorithm and serial min-max decoding algorithm. The result is as follows.

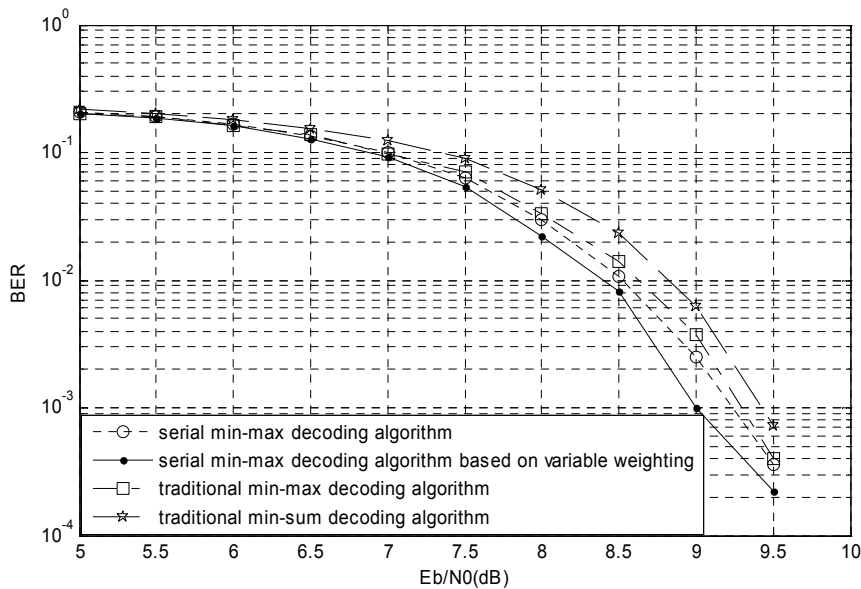


Fig. 2. The relational graph between bit error rate (BER) and signal to noise ratio (Eb/N0).

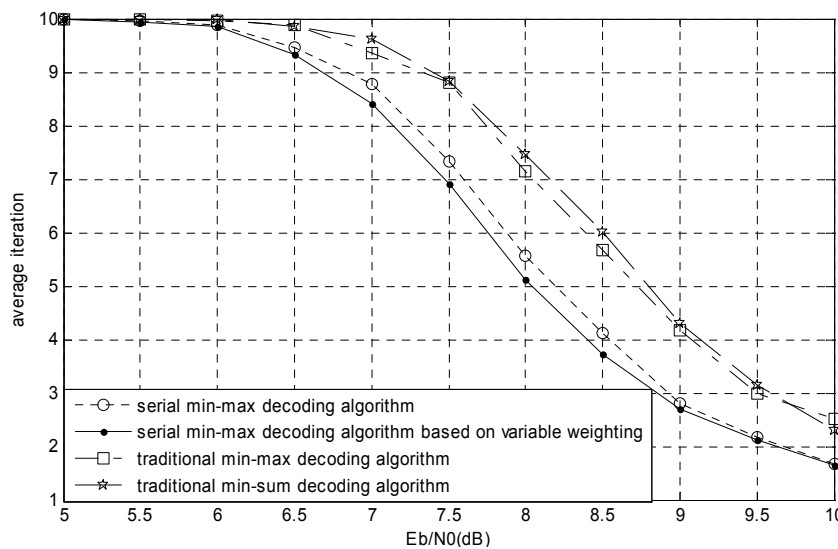


Fig. 3. The relational graph between average iteration and signal to noise ratio (Eb/N0).

What we can find from Fig. 2 is that at the same signal-to-noise ratio, the performance of serial min-max decoding algorithm based on variable weighting outperforms serial min-max decoding algorithm whose performance is better than traditional minmax decoding algorithm and traditional min-sum decoding algorithm. when the bit error rate is  $10^{-3}$ , compared with serial min-max decoding algorithm, traditional min-max decoding algorithm and traditional min-sum algorithm, serial min-max decoding algorithm based variable weighting can offer additional coding gain 0.2 dB, 0.3 dB and 0.4 dB respectively. Fig. 3 shows that the average iteration of serial min-max decoding algorithm based on variable weighting is less than that of serial min-max decoding algorithm whose average iteration is less than traditional min-max decoding algorithm and traditional min-sum decoding algorithm. In a word, serial min-max decoding algorithm based on variable weighting is optimal not only in performance but also in average iteration.

## 5. Conclusions

We make an analysis on traditional min-max decoding algorithm. Then we propose serial min-max decoding algorithm based on variable weighting for nonbinary LDPC codes. The simulation indicates that the proposed algorithm is optimal no matter in performance or in average iteration. So it shows bright future in optical communication and can be treated as one of solutions to decode nonbinary LDPC codes by concrete hardware.

## Acknowledgements

This paper is supported by two Scientific and technological projects of Shandong province (2012J0030009) and (WL10K28).

## References

- [1]. F. Chang, K. Onohara, T. Mizuochi, Forward error correction for 100 G transport networks, *IEEE Communications Magazine*, Vol. 48, Issue 3, 2010, pp. 48-55.

- [2]. F. Yu, C. Xie, L. Zeng *et al.*, Application aspects of enhanced FEC for 40/100G systems, in *Proceedings of the 36<sup>th</sup> European Conference and Exhibition on Optical Communication*, Torino, Italy, 19-23 September 2010.
- [3]. T. Mizuochi *et al.*, Forward error correction based on block turbo code with 3-bit soft decision for 10 Gb/s optical communication systems, *IEEE Journal of Selected Topics in Quantum Electronics*, Vol. 10, Issue 2, 2004, pp. 376-386.
- [4]. I. B. Djordjevic *et al.*, Low-density parity-check codes for 40Gb/s optical transmission systems, *IEEE Journal of Selected Topics in Quantum Electronics*, Vol. 12, Issue 4, 2006, pp. 555-562.
- [5]. M. Arabaci, I. B. Djordjevic, R. Saunders and R. M. Marcoccia, High-rate non-binary regular quasi-cyclic LDPC codes for optical communications, *IEEE/OSA Journal of Lightwave Technology (JLT)*, Vol. 27, Issue 23, 2009, pp. 5261-5267.
- [6]. H. Wymeersch, H. Steendam and M. Moeneclaey, Log-domain Decoding of LDPC codes over GF(q), in *Proceedings of the IEEE International Conference on Communications*, Paris, France, 20-24 June 2004, pp. 772-776.
- [7]. D. Declercq and M. Fossorier, Extended min-sum algorithm for decoding LDPC codes over GF(q), in *Proceedings of the ISIT International Symposium on Information Theory 2005*, Adelaide, Australia, 4-9 September 2005, pp. 464-468.
- [8]. D. Declercq and M. Fossorier, Decoding algorithms for nonbinary LDPC codes over GF(q), *IEEE Transactions on Communications*, Vol. 55, Issue 4, 2007, pp. 633-643.
- [9]. Leilei Yang, Fei Liu and Haitao Li, Min-Max Decoding for Non-Binary LDPC Codes, in *Proceedings of the International Conference on Information Technology and Software Engineering*, Beijing, China, 8-10 December 2012, pp. 125-134.
- [10]. Guojun Han, Xingcheng Liu, Iterative decoding algorithm with channel adaption for LDPC codes, *Journal of Circuits and Systems*, Vol. 15, Issue 1, 2010, pp. 103-105.
- [11]. Kegui Wang, A research of a kind of LDPC codes and their application in optical communication system, *School of Information Science and Technology in South-West Jiaotong University*, Sichuan, 2010.

## The AUV Location and Location Error Analysis Based on Binocular Stereo Vision

\*Jun-Chai GAO, Ming-Yong LIU, Fei XU

School of Marine Engineering, Northwestern Polytechnical University, Xi'an 710072, China

Tel.: 15929319672

E-mail: gaomuyou@126.com

Received: 5 June 2013 /Accepted: 25 August 2013 /Published: 30 September 2013

**Abstract:** In the AUV binocular vision navigation, in order to improve the AUV positioning accuracy, optimizing the stereo vision imaging system structure and weighted least-square method is proposed. The principle of AUV location is analyzed, and that the AUV location accuracy depends on the measurement precision of the three dimensional space point is proposed. Based on the analysis of stereo vision measurement principle, it is put forward that the baseline, the focal length, and the object distance directly affect the stereoscopic vision measurement precision, and mathematical relation model was established for the measurement error. The simulation results show that the model can optimize stereo vision system structure and imaging parameters, and the positioning accuracy of AUV can be effectively controlled. Because measurement error of space point is different with the imaging position, the weighted least squares method is proposed. Measurement data is selectively used according to the measurement error, the positioning. An accuracy of AUV is improved. *Copyright © 2013 IFSA.*

**Keywords:** AUV autonomous location, Binocular stereo vision, Three dimensional measurement error, Error mathematical model, Weighted least squares method.

### 1. Introduction

In the AUV autonomous navigation, AUV positioning accuracy is affected by the accuracy of the landmark measurement and location estimation method. In the stereo vision measurement system, the system parameter of the camera: optical axis angle of cameras, focal length, object distance, and baseline distance directly affects the measurement error. So before measurements start, it is necessary to optimize system structure.

For the stereo vision system structure, Yan Shuhua *et al.* [1] derived parameters relationship between distance resolution, detection range, detection distance, and the baseline distance in the parallel stereoscopic parallax method, which can be

used to optimize the structure parameters; Zhu Xiaoming *et al.* [2] establish mathematical model of the double CCD stereo vision system according to geometrical imaging principle, and comprehensive analysis three parameters relationship between the baseline distance, the object distance and the viewing distance, which can guide for stereo vision system. Yan Long *et al.* [3] research photogrammetry theory and binocular stereo vision measuring system, analyze measurement accuracy of axis convergent structure, which can estimation measurement error according to the camera parameters, baseline length, distance with the measurement precision in the project.

The analysis [4, 5] of the stereo vision system parameters are interrelated, to some extent, which

gives the optimization analysis, but did not give the analysis of the specific conditions. Based on the analysis of parallel stereo vision measurement principle, with one of the factors as the variables, optimization procedure of concrete and feasible is proposed, it is easy to determine the optimal structural parameters. With which the measurement accuracy of the space point is better, and the AUV accuracy can be ensured.

## 2. AUV Locating Principle Based on Stereo Vision

The motion trajectory of AUV is determined by the spatial rotation matrix and translation matrix, including six parameters, so to solve the motion trajectory of AUV, six independent equations, which needed are established. Two equations are determined with one corresponding space point, so at least three corresponding space points are required. Space point coordinates can be located with observed disparity on the same target from binocular stereo vision, based on triangulation principle.

### 2.1. This is a Subtitle Example

AUV navigates with a certain depth from the sea level, two parallel view axis of the camera look down seabed. Based on the principle of stereo vision, the camera of AUV observes the same goal from two viewpoints, then gets two three-dimensional coordinates  $m$ ,  $m'$  of space point  $P$ , then the AUV is located with position relation of two view points through coordinate transformation.

$m$  is the coordinates of three-dimensional point  $P$  in Euclidean space,  $m'$  is the coordinates of three-dimensional point  $P$  after the AUV movement,  $R$  is the rotation matrix of AUV,  $t$  is the translation vector, taking into account the noise data  $\eta_i$  [6, 7]:

$$m'_i = Rm_i + t + \eta_i \quad (1)$$

There are 3 freedom degrees of  $R$ , there are 3 freedom degrees of  $t$ , the movement can be decided at least with three pair noncollinear matching points. Due to noise or measurement error  $\eta_i$ , which is described by a scalar  $w_i$ , motion  $(R, t)$  is estimated by the function minimization:

$$f(R, t) = \sum_{i=1}^n w_i \|m'_i - (Rm_i + t)\|^2 \quad (2)$$

If constraints are ignored between factors of rotation matrix  $R$ ,  $x$  is a vector of 12 dimensional

and  $A_i$  is a matrix of  $3 \times 12$  dimensional,  $0^T = (0,0,0)$  is a zero vector of 3 dimensional.

$$x = (r_{11}, r_{12}, \dots, r_{33}, t_1, t_2, t_3)^T$$

$$A_i = \begin{bmatrix} m_i^T & 0^T & 0^T & 1 & 0 & 0 \\ 0^T & m_i^T & 0^T & 0 & 1 & 0 \\ 0^T & 0^T & m_i^T & 0 & 0 & 1 \end{bmatrix}$$

Then the equation (2) changes into:

$$m'_i = A_i x \quad (3)$$

Motion matrix is obtained with the least squares method when the first order of  $F(R, t)$  derivative to zero

$$x = \left( \sum_i A_i^T A_i \right)^{-1} \left( \sum_i A_i^T m'_i \right) \quad (4)$$

Equation (4) is the motion relationship between AUV two viewpoints, in order to make  $\left( \sum_i A_i^T A_i \right)$

reversible, at least four pairs of spatial coordinates of the two viewpoints is needed.

From the principle of the AUV positioning, it is known that positioning errors of AUV motion is mainly caused by the measurement noise. If the measurement noise is zero mean, and variance is random vector of  $R$ , the least squares estimator is unbiased estimation. The array of the mean square error:

$$E[\tilde{x}\tilde{x}^T] = (A^T A)^{-1} A^T R A (A^T A)^{-1}, \quad (5)$$

where  $\tilde{x} = x - \hat{x}$ .

The mean square error reflects the deviation degree between the estimation value of AUV positioning and the true value, which value is related with variance  $R$  of the spatial point measurement noise. If the measurement noise error is bigger, and the AUV positioning error is bigger too, so the measurement error need to control, and the measurement error can be controlled from the imaging structure.

### 2.2. Three-Dimensional Measurement Principle of Stereo Vision

Space three-dimensional point is measurable when it is respectively observed in the two viewpoints by camera, namely the stereo vision. When two cameras is laid with relative fixed position and orientation, observe the same scene from two

viewpoints with different angles, and acquire the image at different view angle. The 3D information of target is calculated based on triangulation principle with the disparity.

For the parallel binocular vision, the focal length of two cameras are the same, the internal parameters are the same, and the two camera optical axis parallel to each other [8].  $X$  axes is of coincidence,  $Y$  axes parallel to each other. Therefore, the first camera shifts along the  $X$  axis for a distance and coincide with the second camera. As shown in Fig. 1.

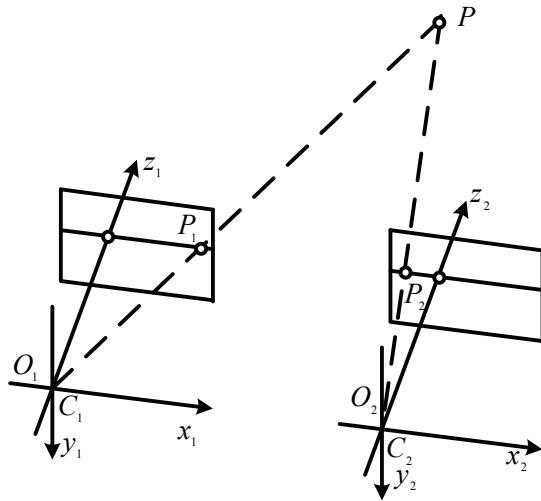


Fig. 1. Parallel binocular imaging model.

$O_1x_1y_1z_1$  and  $O_2x_2y_2z_2$  are coordinate system of two cameras respectively, and there is only a translational in axis direction for the two camera coordinate system [9]. The translation distance is recorded as  $b$ , also known as the baseline length, i.e. the distance between the left and right camera optical center, which can be obtained with camera calibration. The internal parameters of two cameras are the same,  $(u_0, v_0)$  are the center pixel coordinates of the image,  $f$  is the focal length (unit: mm). Because the focal length of pixel expressed is need in the following processing, two parameters  $\alpha_x, \alpha_y$  is defined.  $\alpha_x = -fk_x$ ,  $\alpha_y = -fk_y$ , which are the focal length respectively in the horizontal and vertical pixels unit,  $k_x$  and  $k_y$  are valid pixels number per mm along the  $u$  axis and the  $v$  axis.

For any point  $P$  in the space, its coordinates respectively are  $(x_1, y_1, z_1)$  and  $(x_1 - b, y_1, z_1)$  in the coordinates system  $C_1$  and  $C_2$ ,  $P_1, P_2$  are the image points in left and right camera image plane [10-12].

Coordination  $m$  of  $P$  point is available with the

projection proportion relationship:

$$\begin{cases} x_1 = \frac{b(u_1 - u_0)}{u_1 - u_2} \\ y_1 = \frac{b\alpha_x(v_1 - v_0)}{\alpha_y(u_1 - u_2)} \\ z_1 = \frac{b\alpha_x}{u_1 - u_2} \end{cases} \quad (6)$$

Among them,  $u_0, v_0, \alpha_x, \alpha_y$  are the intrinsic parameters of the camera, which can be obtained with the camera calibration.  $(u_0, v_0)$  is the center coordinates of the left image.  $(u_1, v_1)$  is the pixel coordination of  $P$  point in the left image plane.  $(u_1, v_1)$  is the pixel coordination of  $P$  point in the left image plane.

### 3. Analysis AUV Locating Accuracy of Stereo Vision

#### 3.1. Analysis Measurement Accuracy of Stereo Vision

The space point coordinates are related with parallax, which also can be said that the depth information is related with parallax, and  $x, y$  coordinates are related with depth. following measurement precision of 3D coordination  $(x, y, z)$  of the space target point are calculated.

Depth information is associated with parallax, if the disparity  $|u_1 - u_2|$  is not accurate, such as the corresponding point is error matching, or feature points location is of deviation, which will cause measurement error in the distance  $z_1$ , at the same time, in the  $x_1, y_1$ . Assuming that the measurement error of  $u_1$  is  $\delta u_1$ , the measurement error of  $u_2$  is  $\delta u_2$ , the measurement error of  $v_1$  is  $\delta v_1$ , then

$$\frac{\partial x_1}{\partial u_1} = \frac{b(1 - u_1) + bu_0}{(u_1 - u_2)^2}$$

$$\frac{\partial x_1}{\partial u_1} = \frac{b(u_1 - 1) - bu_0}{(u_1 - u_2)^2}$$

$$\frac{\partial y_1}{\partial u_1} = \frac{-b\alpha_x(v_1 - v_0)}{\alpha_y(u_1 - u_2)^2}$$

$$\frac{\partial y_1}{\partial u_2} = \frac{b\alpha_x(v_1 - v_0)}{\alpha_y(u_1 - u_2)^2}$$

$$\frac{\partial y_1}{\partial v_1} = \frac{b\alpha_x}{\alpha_y(u_1 - u_2)} \quad \Delta x_1 = \frac{\sqrt{2}z^2}{b\alpha_x^2} \sqrt{(1-u_1)^2 + u_0^2} \quad (13)$$

$$\frac{\partial z_1}{\partial u_1} = \frac{-b\alpha_x}{(u_1 - u_2)^2} \quad \Delta y_1 = \frac{z^2}{b\alpha_x\alpha_y} \sqrt{2(v_1 - v_0)^2 + \left(\frac{z_1}{b\alpha_x}\right)^2} \quad (14)$$

$$\frac{\partial z_1}{\partial u_2} = \frac{b\alpha_x}{(u_1 - u_2)^2} \quad \Delta z_1 = \frac{\sqrt{2}z^2}{b\alpha_x} \quad (15)$$

Synthesis the influential factors, then the measurement accuracy in the  $x$  direction is  $\Delta x_1$ :

$$\begin{aligned} \Delta x_1 &= \sqrt{\left(\frac{\partial x}{\partial u_1} \delta u_1\right)^2 + \left(\frac{\partial x}{\partial u_2} \delta u_2\right)^2} = \\ &= \frac{b}{(u_1 - u_2)^2} \sqrt{[(1-u_1) + u_0]^2 (\delta u_1)^2 + [(u_1 - 1) - u_0]^2 (\delta u_2)^2} \end{aligned} \quad (7)$$

The measurement accuracy in the  $y$  direction is  $\Delta y_1$ :

$$\begin{aligned} \Delta y_1 &= \sqrt{\left(\frac{\partial y}{\partial u_1} \delta u_1\right)^2 + \left(\frac{\partial y}{\partial u_2} \delta u_2\right)^2 + \left(\frac{\partial y}{\partial v_1} \delta v_1\right)^2} = \\ &= \frac{b\alpha_x}{\alpha_y(u_1 - u_2)^2} \sqrt{(v_1 - v_0)^2 [(\delta u_1)^2 + (\delta u_2)^2] + (u_1 - u_2)^2 (\delta v_1)^2} \end{aligned} \quad (8)$$

The measurement accuracy in the  $z$  direction is  $\Delta z_1$ :

$$\begin{aligned} \Delta z_1 &= \sqrt{\left(\frac{\partial z}{\partial u_1} \delta u_1\right)^2 + \left(\frac{\partial z}{\partial u_2} \delta u_2\right)^2} = \\ &= \frac{b\alpha_x}{(u_1 - u_2)^2} \sqrt{(\delta u_1)^2 + (\delta u_2)^2} \end{aligned} \quad (9)$$

Taking into account the relationship between ranging accuracy and baseline length, object distance, and the focal length, the  $z$  in the expression (6), (7), (8) is substituted with expression (5):

$$\Delta x_1 = \frac{z^2}{b\alpha_x^2} \sqrt{[(1-u_1) + u_0]^2 (\delta u_1)^2 + [(u_1 - 1) - u_0]^2 (\delta u_2)^2} \quad (10)$$

$$\Delta y_1 = \frac{z^2}{b\alpha_x\alpha_y} \sqrt{(v_1 - v_0)^2 [(\delta u_1)^2 + (\delta u_2)^2] + \left(\frac{z_1}{b\alpha_x}\right)^2 (\delta v_1)^2} \quad (11)$$

$$\Delta z_1 = \frac{z^2}{b\alpha_x} \sqrt{(\delta u_1)^2 + (\delta u_2)^2} \quad (12)$$

The pixel size is 0.01mm,  $\delta u_1 = \delta u_2 = 1$  pixel, then expression (9), (10), (11) change into:

When the camera pixel number is 1024\*1024, object length is 5 m, the baseline distance is 50 cm, the focal length range was 1-30 mm, then the  $x$  measurement error changes with focus and imaging position as shown in Fig. 2 (a), the  $y$  measurement error changes with focus and imaging position as shown in Fig. 2 (b), the  $z$  measurement error changes with the focal length as shown in Fig. 2 (c) shows. It can be seen from Fig. 2, when the focal length is less than 5 mm, the error grows very quickly, in order to reduce the error, a telephoto lens is needed, but lens is longer, field of view is smaller. In order to take into account the view field, the 10 mm lens is selected.

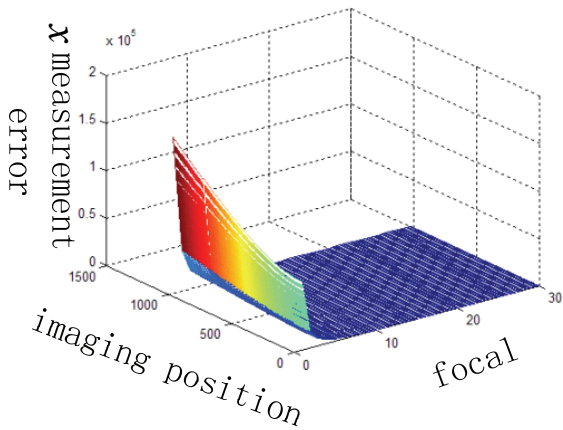
When the focal length is 10 mm, the baseline distance is 50 cm, the object distance ranges from 1 m to 5 m, then the  $x$  measurement error changes with the object distance and image position as shown in Fig. 3 (a), the  $y$  measurement error changes with the object distance and image position as shown in Fig. 3 (b), the  $z$  ranging error changes with the object distance as shown in Fig. 3 (c). It can be seen from Fig. 3, when the distance is more than 3.5 m, the error grows very quickly, in order to reduce the error, near distance is measured, but when the AUV speed is fast, larger field of view or far distance is needed in order to have enough overlap region. In order to take into account the speed of AUV, detection distance of 3 m is select.

When the focal length is 10 mm, the object distance is 3 m, the baseline distance variation range of 10 mm – 160 mm. Then the  $x$  measurement error changes with baseline distance and imaging position as shown in Fig. 4 (a), the  $y$  measurement error changes with baseline distance and the imaging position as shown in Fig. 4 (b),  $z$  ranging error changes with the baseline distance as shown in Fig. 4 (c). It can be seen from Fig. 4, when the focal length is less than 50 mm, the error growth very quickly, in order to reduce the error, longer baseline distance is needed. When the baseline distance is longer, the structure is more complex. In order to take into account the smart structure, baseline length of 50 mm is selected.

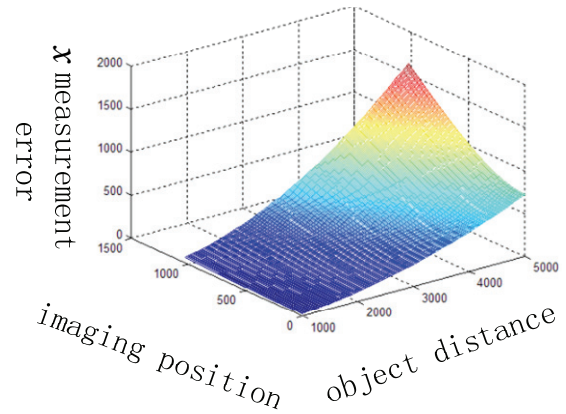
According to the optimization imaging structure of selected, the focal length is 10 mm, length is 3000 mm, the baseline length is 50 mm, the  $x$  measurement error changes with the imaging position

as shown in Fig. 5 (a), the  $y$  measurement error changes with the imaging position as shown in Fig. 5 (b). From formula (14) it is shown, that the  $z$

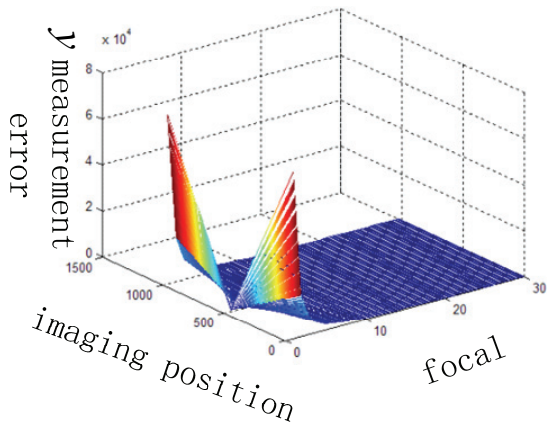
ranging error unchanged with the imaging position. So it can be seen in Fig. 5, the measurement noise variance is different with the imaging position.



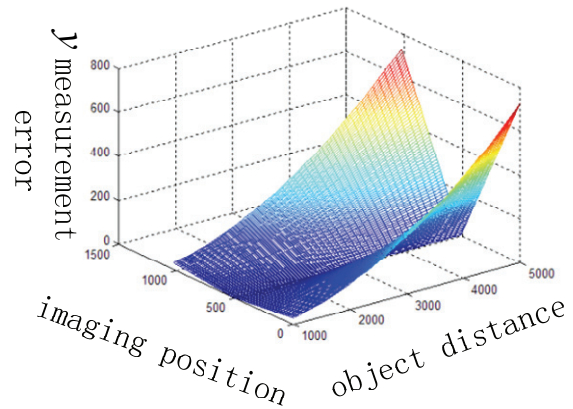
(a)  $X$  measurement error changes with focal length and image position.



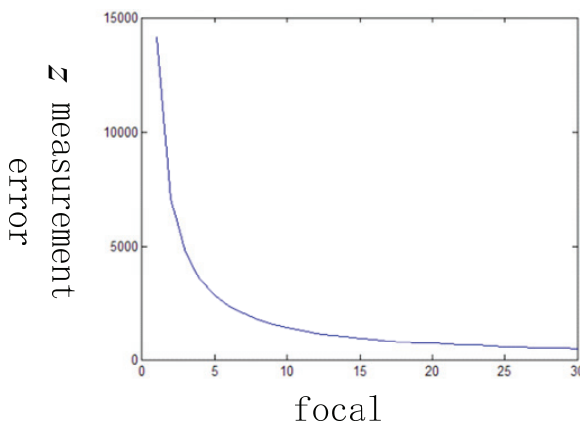
(a)  $X$  measurement error changes with the object distance and image position.



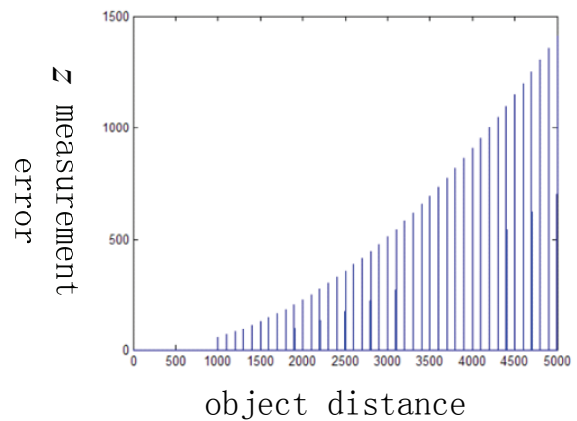
(b)  $y$  measurement error changes with focal length and image position.



(b)  $y$  measurement error changes with the object distance and image position.



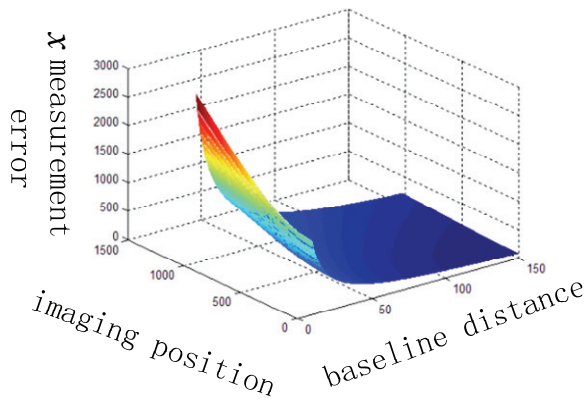
(c)  $Z$  ranging errors changes with the focal length.



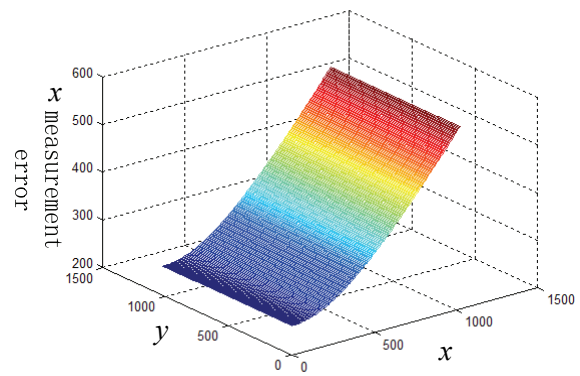
(c)  $Z$  ranging error changes with the object distance

**Fig. 2.** Measurement errors change with focal length and image position.

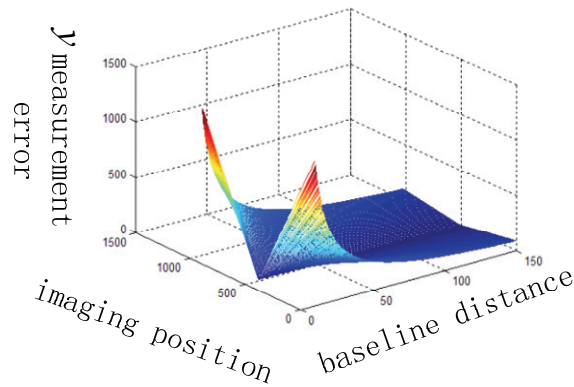
**Fig. 3.** Measurement error change with the object distance and image position.



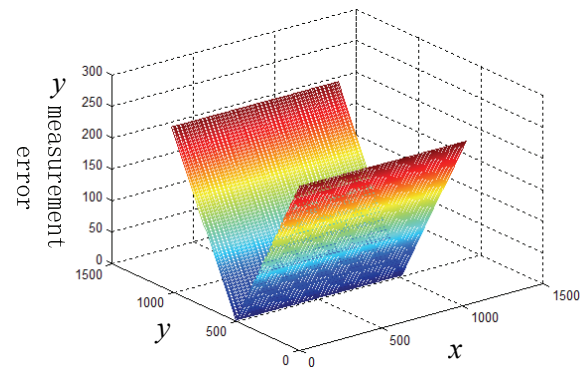
(a) X measurement error changes with baseline distance and imaging position.



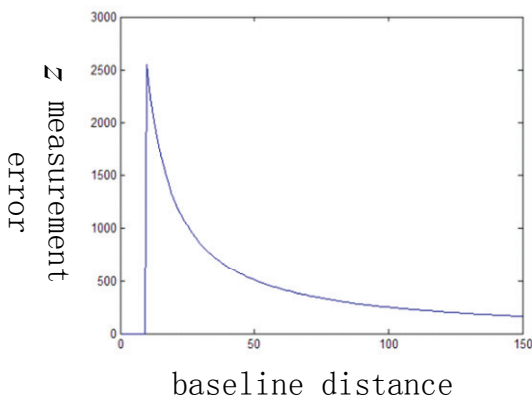
(a) X measurement error changes with the imaging position.



(b) y measurement error changes with baseline distance and imaging position.



(b) y measurement error changes with the imaging position.



(c) Z ranging error changes with the baseline distance.

Fig. 5. Measurement error changes with the imaging position.

Fig. 4. Measurement error change with baseline distance and imaging position.

### 3.2. Analysis of AUV 3D Motion Locating Accuracy

The optimized imaging structure can control the measurement error of space point to a certain extent, and the positioning accuracy of the AUV is controlled. But as shown in Fig. 5, measurement noise variance is different with imaging position, and least squares estimator in the formula (3) uses the

measured value with the same weight, doesn't consider the different, which results in that the AUV location estimation accuracy is not high. If the measured value is treated with the weighted method, the weight of precision high has larger weights, poor precision gets smaller, the weighted estimation of (3) equation is:

$$J(\hat{x}) = (m'_i - A_i \hat{x})^T W (m'_i - A_i \hat{x}) = \min, \quad (16)$$

where  $W$  is the type of positive definite weighting matrix with appropriate value. Here  $W = R^{-1}$ , the weighted least squares estimation is Markov estimation:

$$\hat{x} = \left( \sum_i A_i^T R^{-1} A_i \right)^{-1} \left( \sum_i A_i^T R^{-1} m'_i \right) \quad (17)$$

The mean square error:

$$E[\tilde{x}\tilde{x}^T] = (A^T R^{-1} A)^{-1} \quad (18)$$

The mean square error estimated as such is the minimum, and which is smaller than any other weighted least squares estimation, is the best estimation of the weighted least squares. For different space points measured value, it is used according to the different of precision, the estimation accuracy will be higher than the estimation precision with only high precision measuring value, which can effectively improve the AUV positioning accuracy finally.

#### 4. Conclusion

In the AUV navigating and positioning based on the binocular vision, the measurement error of binocular vision is directly related to the AUV positioning accuracy. Based on the analysis of the measuring principle of binocular vision, the mathematical model is established to optimize the measurement accuracy, and is visualized analyzed with simulation graphics. The system structure and the imaging parameters of stereo vision system are optimized, which further verify the effectiveness of the mathematical model.

#### References

- [1]. Yan Shuhua, Lv Haibao, Wang Yueke, An analysis of the resolution of the range in the stereo parallax method in theory, *Opto-Electronic Engineering*, Vol. 25, Issue 2, 1998, pp. 20-23.
- [2]. Zhu Xiaoming, Gao Zhiyun, Theoretic research on double-CCD stereoscopic system, *Optic Technique*, Vol. 29, Issue 3, 2003, pp. 298-300.
- [3]. Yan Long, Zhao Zhengxu, Zhou Yiqi, Accuracy analysis and configuration design of stereo photogrammetry system based on CCD, *Chinese Journal of Scientific Instrument*, Vol. 29, Issue 2, 2008, pp. 410-412.
- [4]. Zhang Yan, Wang Guochang, Wang Zhi et al., Analysis on rectification precision of IKONOS-2 stereo imagery pairs, *Railway Survey*, 3, 2009, pp. 69-73.
- [5]. Min Xinli, Wan Dean, Zhang Jian, Theoretical study of CCD binocular vision system structure parameters, *Machine Design & Manufacture*, 3, 2001, pp. 54-56.
- [6]. A. Agarwal, C. V. Jawahar and P. J. Narayanan, A survey of planar homography estimation techniques, *IIT Technical Report*, 2005.
- [7]. R. I. Hartley and A. Zisserman, Multiple view geometry in computer vision, 2<sup>nd</sup> Edition, *Cambridge University Press*, 2004.
- [8]. Yan Li, Duan Fajie, Optimum design and accuracy analysis of monocular stereoscopic vision sensor system, *Chineses Journal of Sensors and Actuators*, Vol. 19, Issue 2, 2006, pp. 349-352.
- [9]. Chen Zezhi, We Chengke, Shen Peiyi, Error model analysis of computer vision photogrammetry system, *Journal of Computer-Aided Design and Computer Graphics*, Vol. 14, Issue 5, 2002, pp. 389-393.
- [10]. Zhang Guangjun, Machine vision, 1st ed., *Science Press*, Beijing, 2006.
- [11]. Rodriguez J. J., Affarwal J. K., Stochastic analysis of stereo quantization error, *Pattern Analysis and Machine Intelligence*, Vol. 12, Issue 5, 1990, pp. 467-470.
- [12]. Chang C, Chatterjee S., Quantization error analysis in stereo vision, in *Proceedings of the 26<sup>th</sup> Asilomar Conference*, Pacific Grove, California, 26-28 October 1992, pp. 1037-1041.

## Semi-Supervised Based Hyperspectral Imagery Classification

Zhijun Zheng, Yanbin Peng

School of Information and Electronic Engineering, Zhejiang University of Science and Technology,  
318 Liuhe Road, Xihu District, Hangzhou City, Zhejiang Province, 310023, P. R. China

E-mail: zjzheng9999@163.com

Received: 5 June 2013 /Accepted: 25 August 2013 /Published: 30 September 2013

---

**Abstract:** Hyperspectral imagery classification is a challenging problem. Wherein, the high number of spectral channels and the high cost of true sample labeling greatly reduce the classification precision. In this paper, we proposed a semi-supervised method, which combine linear discriminant analysis and manifold learning, to improve the precision of hyperspectral imagery classification. Experimental results showed that new method had provided considerable insight on the band extraction problem and the new features were good for land-cover classification. *Copyright © 2013 IFSA.*

**Keywords:** Hyperspectral imagery, Classification, Semi-supervised, Linear discriminant analysis, Manifold learning.

---

### 1. Introduction

Hyperspectral sensors collect imagery simultaneously in hundreds of narrow and continuous spectral bands [1]. The information contained in hyperspectral imagery improved the accuracy and robustness of the land-cover classification [2-7]. However, several critical problems should be considered in the classification of hyperspectral imagery, among which, the high number of spectral channels and low number of labeled training samples give rise to the problem of curse of dimensionality. Two kinds of methods can be considered to reduce dimensions, namely, feature extraction [8, 9] and feature selection [10, 11]. Feature extraction transforms the whole initial band set into a new and reduced feature set. Feature selection chooses a subset of bands from the original band set.

Recently, Lots of feature selection methods have been proposed, which can be grouped into supervised method and unsupervised method. Supervised method selects feature subset depends on the class

labels of training samples such that the projected samples of different classes are well separated. Unsupervised method defines a criterion to select suitable feature set. Compared to feature selection method, feature extraction method generally achieves high accuracy of classification in supervised learning. However, due to the high cost of true sample labeling, unlabeled training samples are readily available but labeled ones are fairly expensive to obtain. This circumstance greatly reduces the precision of prediction. Therefore, based on former research work [12-14], this paper imports semi-supervised learning to provide an elegant framework to learn from labeled and unlabeled data. The new proposed method combines linear discriminant analysis (LDA) and manifold learning to improve the precision of hyperspectral imagery classification. Experimental results showed that new method had provided considerable insight on the band extraction problem and the new features were good for land-cover classification.

The remainder of this paper is organized as follows. Section 2 presents a brief overview of LDA algorithm. In Section 3, we provide a brief overview of manifold learning algorithm. We introduce LDA and manifold learning based algorithm for hyperspectral data dimensionality reduction in Section 4. The pixel classifications on real hyperspectral data sets are used to evaluate the performance of the new proposed method in Section 5. Finally, we conclude the paper in Section 6.

## 2. Linear Discriminant Analysis

Linear discriminant analysis [15] is an important method used in statistics, pattern recognition and machine learning to find a linear combination of features which characterizes or separates two or more classes of objects or events. The resulting combination may be used as a linear classifier, or more commonly, for dimensionality reduction before later classification.

LDA seeks directions on which the samples of different classes are far from each other while the samples of the same class are close to each other. Given a  $n$ -dimensional data set  $X = \{x_1, x_2, \dots, x_n\} \subset R^n$  and the corresponding class label set  $A = \{a_1, a_2, \dots, a_n\} \subset R$ . LDA is used to learn a matrix  $w \subset R^{n \times k}$  which transforms  $n$ -dimensional vector  $x_i$  into  $k$ -dimensional vector  $y_i$ . The transformation formula is as follows:

$$y_i = w^T x_i \quad (1)$$

If two data points have the same label, they should be as close as possible after they are transformed by  $w$ . Otherwise, they should be as far as possible. LDA convert this problem into an optimization problem, the objective function of LDA is as follows:

$$w_{optimal} = \arg \min_w \frac{w^T K_{wi} w}{w^T K_b w}, \quad (2)$$

where  $K_{wi}$  is the within class scatter matrix and  $K_b$  is the between class scatter matrix. Suppose we have  $H$  classes sample points. The definition of the within class scatter matrix is:

$$K_{wi} = \sum_{h=1}^H \left( \sum_{i=1}^{n_h} (x_i - \mu_h)(x_i - \mu_h)^T \right), \quad (3)$$

where  $n_h$  is the number of samples in class  $h$  and  $\mu_h$  is the average vector of class  $h$  the definition of the between class scatter matrix is:

$$K_b = \sum_{h=1}^H n_h (\mu_h - \mu)(\mu_h - \mu)^T, \quad (4)$$

where  $\mu$  is the total sample mean vector.

## 3. Manifold Learning

High-dimensional data, meaning data that requires more than two or three dimensions to represent, can be difficult to interpret [16]. One approach to simplification is to assume that the data of interest lie on an embedded non-linear manifold within the higher-dimensional space. If the manifold is of low enough dimension then the data can be visualized in the low dimensional space.

In general, manifold learning algorithm [17] seeks for the optimal projection matrix by solving the following minimization problem:

$$\arg \min_w \sum_{i,j} \| (w^T x_i - w^T x_j) \|^2 M_{ij} \quad (5)$$

where  $M_{ij}$  is similarity weight of sample points  $x_i$  and  $x_j$ , which reflects the local structure of the sample space. By simple mathematical transformation, the objective function can be simplified as follows:

$$\begin{aligned} & \sum_{i,j} \| w^T x_i - w^T x_j \|^2 M_{ij} \\ &= 2w^T X(D-M)X^T w \\ &= 2w^T XLX^T w \\ &= 2Y^T LY, \end{aligned} \quad (6)$$

$$X = [x_1, x_2, \dots, x_n]^T, \quad (7)$$

$$Y = [y_1, y_2, \dots, y_n]^T, \quad (8)$$

$$L = D - M, \quad (9)$$

where  $L$  is Gaussian Laplacian matrix and  $D$  is a diagonal matrix, whose entry is:

$$D_{ii} = \sum_{j=1}^n M_{ij} \quad (10)$$

## 4. Hyperspectral Data Dimensionality Reduction

As shown in Fig. 1, hyperspectral imagery is a three-dimensional data array, whose width and length corresponding to plane dimensions and the third dimension corresponding to spectral bands. We use  $I$ ,  $J$  and  $L$  to represent the three dimensions. Each pixel

is represented as an  $L$  dimensional vector, constitute a sample point.

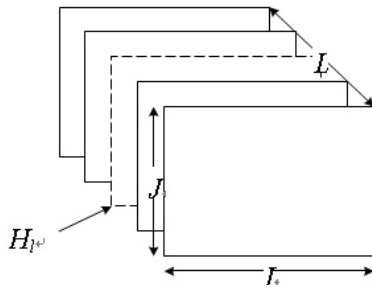


Fig. 1. Image cube of hyperspectral data.

Suppose we are given  $m$  labeled examples  $\{(x_i, t_i)\}_{i=1}^m$  and  $n$  unlabeled examples  $\{(x_j)\}_{j=m+1}^{m+n}$ .  $t_i$  stands for class label. Inspired by linear discriminant analysis and manifold learning algorithm [18, 19], proposed method combines both discriminative information and knowledge of data distribution, by minimizing the following objective function:

$$\arg \min_w \{ML(w) + LDA(w)\} \quad (11)$$

Manifold regularization term is  $ML(w)$ , which makes  $t_i$  varies smoothly by incurring a heavy penalty if two neighboring points in the input space lie far away in the output space. We can build a  $q$ -nearest neighbor graph  $G$  over  $(m+n)$  samples to model the relationship between nearby samples. For each samples  $x_i$ , we find its  $q$  nearest neighbors set  $Q(x_i)$  and put an edge between  $x_i$  and its neighbors. Therefore, the corresponding weight matrix is as follows:

$$M_{M,ij} = \begin{cases} s_{ij} & \text{if } x_i \in Q(x_j) \text{ or } x_j \in Q(x_i) \\ 0 & \text{otherwise} \end{cases} \quad (12)$$

To apply  $q$ -nearest algorithm, we must construct a similarity matrix used to measure how well sample  $x_i$  is similar to sample  $x_j$ . Several measures can be used to build the distances between sample data, such as Euclidean distance, divergence-based distance and mutual information distance. In this paper, we use KL divergence based method. Firstly, we assume that  $p_i(r)$  and  $p_j(r)$  represent the probability distributions of sample  $x_i$  and  $x_j$  respectively. We use grey level histogram to simplify probability distribution, where  $r$  is grey level. KL divergence of  $p_i(r)$  and  $p_j(r)$  is defined as follows:

$$KL(i, j) = \sum_{r=1}^R (p_i(r) \log \frac{p_i(r)}{p_j(r)}) \quad (13)$$

The KL divergence is Asymmetric. However, the similarity matrix is symmetric. Therefore, the similarity between  $p_i(r)$  and  $p_j(r)$  is defined as follows:

$$s_{ij} = (1 - \frac{1}{2} (\sum_{r=1}^R (p_i(r) \log \frac{p_i(r)}{p_j(r)} + \sum_{r=1}^R (p_j(r) \log \frac{p_j(r)}{p_i(r)}))) \quad (14)$$

The corresponding manifold regularization item is as follows:

$$ML(w) = \frac{1}{2} \sum_{i=1}^{m+n} \sum_{j=1}^{m+n} \|w^T x_i - w^T x_j\|^2 M_{M,ij} \quad (15)$$

$$= Y^T (D_M - M_M) Y = Y^T L_M Y,$$

where  $D_M$  is the diagonal matrix, whose entry is:

$$D_{M,ii} = \sum_{j=1}^{m+n} M_{M,ij} \quad (16)$$

A useful classification function should be smooth in class, but produce great contrast between different classes. Therefore, this paper uses  $LDA(w)$  to incorporate discriminative information into our objective. For each sample  $x_i$ ,  $Z_{w_i}(x_i)$  contains samples sharing the same label with  $x_i$ ,  $Z_b(x_i)$  contains the samples having different labels. Specifically,

$$Z_{w_i}(x_i) = \{x_j | l(x_j) = l(x_i)\} \quad (17)$$

$$Z_b(x_i) = \{x_j | l(x_j) \neq l(x_i)\} \quad (18)$$

Within class graph is defined as follows:

$$M_{w_i,ij} = \begin{cases} 1 & \text{if } x_i \in Z_{w_i}(x_j) \\ & \text{or } x_j \in Z_{w_i}(x_i) \\ 0 & \text{otherwise} \end{cases} \quad (19)$$

Between class graph is defined as follows:

$$M_{b,ij} = \begin{cases} 1 & \text{if } x_i \in Z_b(x_j) \\ & \text{or } x_j \in Z_b(x_i) \\ 0 & \text{otherwise} \end{cases} \quad (20)$$

In order to keep the compactness in class, the following objective function should be minimized:

$$T_{w_i} = \frac{1}{2} \sum_{i=1}^{m+n} \sum_{j=1}^{m+n} \|w^T x_i - w^T x_j\|^2 M_{w_i,ij} = \quad (21)$$

$$= Y^T (D_{w_i} - M_{w_i}) Y = Y^T L_{w_i} Y,$$

where  $D_{w_i}$  is the diagonal matrix, whose entry is:

$$D_{wi,ii} = \sum_{j=1}^{a+d} M_{wi,ij} \quad (22)$$

In order to keep the separability between classes, the following objective function should be maximized:

$$T_b = \frac{1}{2} \sum_{i=1}^{m+n} \sum_{j=1}^{m+n} \|w^T x_i - w^T x_j\|^2 M_{b,ij} = Y^T (D_b - M_b) Y = Y^T L_b Y, \quad (23)$$

where  $D_b$  is the diagonal matrix, whose entry is:

$$D_{b,ii} = \sum_{j=1}^{a+d} M_{b,ij} \quad (24)$$

Therefore, the LDA regularization item of is defined as follows:

$$LDA(w) = \beta T_{wi} - (1 - \beta) T_b = Y^T (\beta L_{wi} + (1 - \beta) L_b) Y, \quad (25)$$

where  $\beta \in [0, 1]$ . Because the information that two data are similar is more important, we commend that parameter  $\beta$  should be larger than 0.6. The original objective function is simplified as:

$$\min Y^T L_{LDA-ML} Y \quad (26)$$

$$L_{LDA-ML} = (1 - \alpha) L_M + \alpha (\beta L_{wi} - (1 - \beta) L_b), \quad (27)$$

where  $L_{LDA-ML}$  is the new Laplacian matrix, which combines the discriminative ability of three matrix, namely  $M_{M,ij}$ ,  $M_{wi,ij}$  and  $M_{b,ij}$ .  $M_{M,ij}$  ensures that close data in the input space are prone to be close in the output space.  $M_{wi,ij}$  penalizes those samples originally in the same class and are predicted in the different class.  $M_{b,ij}$  penalizes those samples originally in the different class and are predicted in the same class. The coefficient  $\alpha$  is chosen in the interval  $[0, 1]$ , which is used to control balance between LDA and manifold learning.

## 5. Experiments

The experiments consist of comparing the LDA-ML algorithm with two relevant algorithms ID [20] and MVPCA [21] on real hyperspectral data sets shown as Fig. 2.

Indian pines AVIRIS data set is a section of the scene taken over northwest Indiana's Indian Pines by the Airborne Visible/Infrared Imaging Spectrometer

sensor in 1992. It has  $145 \times 145$  pixels and 220 bands. Fig. 2 shows the 30<sup>th</sup> band image of the data. In the experiment, 200 out of the 220 bands are used. The bands of lower signal to noise ratio are discarded.

In order to evaluate the performance of our proposed method, support vector machine (SVM) and k-Nearest Neighbor algorithm (KNN) is used to classify the pixel in hyperspectral imagery.



Fig. 2. Image of 30<sup>th</sup> band in India pines data set.

### 5.1. SVM

In the environment of non-linear separable and small training sample sets, SVM has shown a great potential against other classifier in solving classification and regression problem. Our experiment chooses RBF kernel function. Since SVM is used to handle two class problems, this paper uses one-against-all method to handle multi-class classification problem. Fig. 3 shows the classification results by ID, MVPCA and LDA-ML respectively.

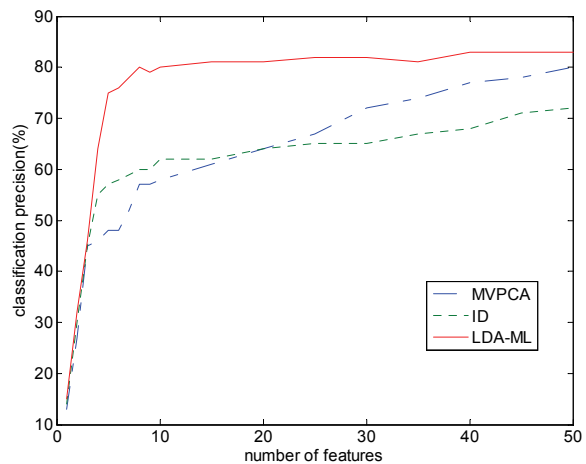


Fig. 3. Classification results of SVM.

As Fig. 3 shows, the classification accuracies of algorithm ID, MVPCA and LDA-ML improve along with the increase of the number of features. Among them, LDA-ML algorithm has the highest prediction precision.

## 5.2. KNN

The KNN algorithm is a method for classifying samples based on closest training samples in the sample space. It is the simplest machine learning algorithm. In KNN algorithm, a sample is classified by a majority vote of its neighbors, where the sample is assigned to the class which is the most common class in its k nearest neighbors. Fig. 4 shows the classification results of KNN by ID, MVPCA and LDA-ML respectively. Likewise, the accuracies obtained by LDA-ML are better than that of the other two methods.

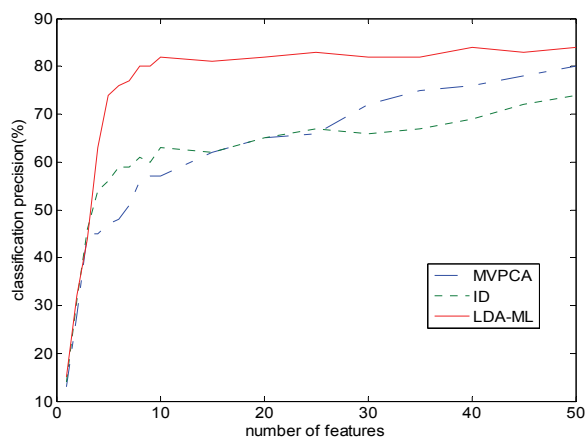


Fig. 4. Classification results of KNN.

## 6. Conclusions

In this paper, we propose a new semi-supervised method to classify pixels in hyperspectral imagery. The proposed method makes efficient use of labeled and unlabeled samples, and integrates LDA and manifold algorithm to improve the precision of land-cover prediction. The labeled samples are used to maximize the discriminating power, while the unlabeled samples are used to preserve the structure of data. Experimental results demonstrate the effectiveness of our method.

## Acknowledgements

This work was supported by grants from National Natural Science Foundation of China (No. 61175058), Zhejiang Provincial Natural Science Foundation of China (No. Z12F020019, LY12F02018&LQ13F020015), Research program supported by the department of education in Zhe Jiang Province (No. Y201016929 & Y201222997).

## References

- [1]. Camps-Valls G., Bandos Marsheva T., Zhou D., Semi-supervised graph-based hyperspectral image classification, *IEEE Transactions on Geoscience and Remote Sensing*, Vol. 45, Issue 10, 2007, pp. 3044-3054.
- [2]. Alajlan N., Bazi Y., Melgani F., et al., Fusion of supervised and unsupervised learning for improved classification of hyperspectral images, *Information Sciences*, Vol. 217, Issue 7, 2012, pp. 39-55.
- [3]. Du B., Zhang L., Zhang L., et al., A discriminative manifold learning based dimension reduction method for hyperspectral classification, *International Journal of Fuzzy Systems*, Vol. 14, Issue 2, 2012, pp. 272-277.
- [4]. Sun L., Wu Z., Wei Z., et al., Supervised hyperspectral image classification combining sparse unmixing and spatial constraint, in *Proceedings of the International Conference on Computer Vision in Remote Sensing (CVRS)*, 2012, pp. 110-115.
- [5]. Sun Z., Wang C., Li P., et al., Hyperspectral image classification with SVM-based domain adaption classifiers, in *Proceedings of the International Conference on Computer Vision in Remote Sensing (CVRS)*, 2012, pp. 268-272.
- [6]. Wen Y., Gao Y., Liu S., et al., Hyperspectral image classification with hypergraph modelling, in *Proceedings of the 4<sup>th</sup> International Conference on Internet Multimedia Computing and Service*, 2012, pp. 34-37.
- [7]. Xu Y., Yu P., Guo B., et al., On hyperspectral remotely sensed image classification based on MNF and AdaBoosting, in *Proceedings of the 2012 International Conference on Audio, Language and Image Processing (ICALIP)*, 2012, pp. 605-609.
- [8]. Jimenez-Rodriguez L. O., Arzuaga-Cruz E., V. Lez-Reyes M., Unsupervised linear feature-extraction methods and their effects in the classification of high-dimensional data, *IEEE Transactions on Geoscience and Remote Sensing*, Vol. 45, Issue 2, 2007, pp. 469-483.
- [9]. Kumar S., Ghosh J., Crawford M. M., Best-bases feature extraction algorithms for classification of hyperspectral data, *IEEE Transactions on Geoscience and Remote Sensing*, Vol. 39, Issue 7, 2001, pp. 1368-1379.
- [10]. Guyon I., Elisseeff A., An introduction to variable and feature selection, *Journal of Machine Learning Research*, Vol. 3, Issue 1, 2003, pp. 1157-1182.
- [11]. Qian Y., Yao F., Jia S., Band selection for hyperspectral imagery using affinity propagation, *Computer Vision, IET*, Vol. 3, Issue 4, 2009, pp. 213-222.
- [12]. Li J., Jia S., Peng Y., Hyperspectral Data Classification with Spectral and Texture Features by Co-training Algorithm, *Opto-Electronic Engineering*, Vol. 39, Issue 11, 2012, pp. 88-94.
- [13]. Peng Y., Ai J., Hyperspectral Imagery Classification Based on Spectral Clustering Band Selection, *Opto-Electronic Engineering*, Vol. 39, Issue 2, 2012, pp. 63-67.
- [14]. Li J., Qian Y., Clustering-based hyperspectral band selection using sparse nonnegative matrix factorization, *SCIENCE C, Journal of Zhejiang University*, Vol. 12, Issue 7, 2011, pp. 542-549.

- [15]. [http://en.wikipedia.org/wiki/Linear\\_discriminant\\_analysis](http://en.wikipedia.org/wiki/Linear_discriminant_analysis)
- [16]. [http://en.wikipedia.org/wiki/Manifold\\_learning#Manifold\\_learning\\_algorithms](http://en.wikipedia.org/wiki/Manifold_learning#Manifold_learning_algorithms)
- [17]. Belkin M., Niyogi P., Sindhvani V., Manifold regularization: A geometric framework for learning from labeled and unlabeled examples, *Journal of Machine Learning Research*, Vol. 7, Issue 1, 2006, pp. 2399-2434.
- [18]. Cai D., He X., Han J., Semi-supervised discriminant analysis, in *Proceedings of the IEEE 11<sup>th</sup> International Conference on Computer Vision (ICCV' 07)*, 2007, pp. 1-7.
- [19]. Cai D., He X., Zhou K., *et al.*, Locality sensitive discriminant analysis, in *Proceedings of the 20<sup>th</sup> International Joint Conference on Artificial Intelligence*, 2007, pp. 708-713.
- [20]. Chang C.-I., Wang S., Constrained band selection for hyperspectral imagery, *IEEE Transactions on Geoscience and Remote Sensing*, Vol. 44, Issue 6, 2006, pp. 1575-1585.
- [21]. Chang C.-I., Du Q., Sun T.-L., *et al.*, A joint band prioritization and band-decorrelation approach to band selection for hyperspectral image classification, *IEEE Transactions on Geoscience and Remote Sensing*, Vol. 37, Issue 6, 1999, pp. 2631-2641.

---

2013 Copyright ©, International Frequency Sensor Association (IFSA). All rights reserved.  
(<http://www.sensorsportal.com>)



**International Frequency Sensor Association**

is a professional association and Network of Excellence,  
created with the aim to encourage the researches and developments  
in the area of quasi-digital and digital smart sensors and transducers.



For more information about IFSA membership, visit  
<http://www.sensorsportal.com>

## Humidity Sensing Properties and Temperature Conductivity Studies of Sol-Gel Derived Novel Nanomaterials of Lanthanum Strontium Chromites

<sup>1</sup> B. Avila Josephine, <sup>2</sup> V. Jeseentharani, <sup>1</sup> V. Mary Teresita,  
<sup>1</sup> Mary George, <sup>3\*</sup> S. Arul Antony

<sup>1</sup> Department of Chemistry, Stella Maris College, Chennai-600 086

<sup>2</sup> Department of Chemistry, Loyola Institute of Frontier Energy (LIFE), Loyola College,  
Chennai-600034

<sup>3</sup> PG & Research Department of chemistry, Presidency College, Chennai-600 005

<sup>1</sup> Tel.: 9840224515, fax: 044-28111129,

E-mail: avi\_joe@yahoo.com, teres\_cvd@yahoo.co.in

Received: 12 June 2013 /Accepted: 25 August 2013 /Published: 30 September 2013

**Abstract:** Lanthanum strontium chromite mixed metal oxides were prepared by sol-gel method by varying the mole ratios of strontium and chromium in the compound. The compounds were sintered at 700 °C for 6 hrs and were subjected to DC resistance measurements at RH 5-98 % and temperature dependent studies. The change in surface conductivity as a function of applied field was measured using picoammeter (Keithely-6485). Among the various mole ratios of compounds LCS-4 shows the highest sensitivity factor of  $3.34 \times 10^4$  and LCS-1 shows the lowest sensitivity factor  $6.66 \times 10^{-1}$ . Response and recovery times were measured. The compounds were characterized by X-ray diffraction, FT-IR, scanning electron microscopy (SEM) and nitrogen adsorption/desorption studies were employed to study the structural phases, vibrational frequencies, surface morphology of the highest humidity sensing compounds. Copyright © 2013 IFSA.

**Keywords:** Chemosensors, Chromites, Mixed metal oxide, Relative humidity.

### 1. Introduction

Humidity sensors have been used in an increasing number of applications in industrial processing and environmental control. Growing demands for controlling water vapour have led to considerable interest in the development of sensing materials [1-5]. Measurement and control of humidity in an environment is important in both human comfort and many of industrial processes [6]. There are some major requirements for a good

humidity sensor: high-sensitivity, reversibility, fast response time, long life time, high-humidity selectivity and stability [7]. In recent years many efforts have been in investigations of well performance humidity sensors. Many kinds of materials have been studied as sensing elements/compounds in humidity sensors. The principle sensor groups of interest include ceramics [8, 9], conductive polymers [10, 11] and electrolyte [6].

Relationship between nanostructures and their

implications on the electrical, optical and thermal properties of materials is an extremely interesting area of material science. Metal oxides form attractive domain therein due to their wide range of properties like ferroelectricity, superconductivity and piezoelectricity. Perovskite type oxides (general formula  $ABO_3$ ) is closely related to the materials that show interesting electrical properties and sensing behavior of these oxides may be modified by an appropriate substitutions of cations at the A and B sites [12]. These in the form of bulk thick or thin films are being used as multifunctional sensor i.e. sensing temperature, gas and humidity [13, 14]. These perovskite type oxides can be synthesized in three different ways they are thermal decomposition, co-precipitation and sol-gel method. Among them the materials prepared by sol-gel method has shown increase in the surface area of the material which is an essential factor for a sensing material [15].

In the present investigation a novel nano structured  $LaSr_xCr_{1-x}O_{3-\delta}$  ( $x=0$  to 1) which was prepared by sol-gel method reveals both excellent humidity and thermal sensitivity properties. The novelty of this material is achieved by preparing the mixed metal oxide has a single phase compound which is done by sintering the samples for 8 hours at 800 °C in tubular furnace. This supported by the XRD reports. The material is characterized by SEM, XRD, and IR. The humidity dependent electrical properties of Perovskite oxide  $LaSr_xCr_{1-x}O_{3-\delta}$  have been studied by preparing different mole ratios of  $LaSr_xCr_{1-x}O_{3-\delta}$  by altering the addition of  $Cr^{3+}$  with  $Sr^{2+}$ . It has been found in the humidity sensing studies that the material shows high sensitive factor by the substitution of  $Cr^{3+}$  with  $Sr^{2+}$  due to the change in the surface morphology of the material. Electrical conductance can occur through internal surface layers of adsorbed water [16], the tiny pores can fill with water as determined by the Kelvin equation [17] leading to electrolytic conduction through the moisture or the conductance of the semiconductor itself can change due to an interaction of its surface energy states with hydroxyl radicals, especially at the grain boundaries [18, 19].

## 2. Experimental Procedure

### 2.1. Sample Preparation

Sol-gel method: A known amount of citric acid and ethylene glycol (AR) were mixed well by keeping it over a magnetic stirrer for 10 minutes around 150 °C and to this the dissolved nitrate solutions of  $La(NO_3)_3 \cdot 6H_2O$ ,  $Cr(NO_3)_3 \cdot 9H_2O$  and  $Sr(NO_3)_2$  of appropriate mole ratios were added and stirred for 30 minutes and the mixture was heated to 150 °C till powder form is obtained. The resulting LCS compounds were compacted to pellet at a pressure of 4 ton/sq.inch. The diameter of the pellet is 13 mm and the thickness is 2 mm. These solid

pellet were sintered at 800 °C for 8 hrs in ambient air atmosphere. The samples were cooled down to room temperature at the natural cooling rate of the furnace. As the concentration of strontium increased at particular level was shown to enhance the sensitivity of humidity sensors. Since our interest is to prepare a nanomaterial the compounds were synthesized specifically by sol-gel method.

### 2.2. Characterization and Humidity Sensing Studies

The DC electrical resistance at different relative humidity levels of the samples in the form of pellets was determined by a two-probe method as. The electrical contacts were made on the surface of the pellet by means of two thin copper wires affixed with silver paint. Given the high resistivity of the materials under investigation, the potential inaccuracy due to contact resistance is assumed negligible. The pellet was inserted in the middle of the pyrex tube of 5 cm diameter on which kanthal wire was uniformly wounded externally. The kanthal wire ends were connected to avarian to vary the temperature and a copper-constantan thermocouple kept at the pellet was used to measure the temperature of the sample. The electrodes were connected to DC power supply and the Keithley 6485 picoammeter in series. The temperature dependent conductance experiments in the temperature range of 120 – 300 °C under ambient conditions were carried out to determine the activation energies for electrical conduction of the samples using linearized form of the expression

$$I = I_0 \exp^{-E_a/kT},$$

where  $I$  is the current,  $E_a$  is the activation energy,  $k$  is the Boltzmann constant and  $T$  is the temperature.

Controlled humidity environments of relative humidity 5, 31, 51, 79 and 98 % were achieved by using anhydrous  $P_2O_5$ , saturated aqueous solution of  $CaCl_2 \cdot 6H_2O$ ,  $Ca(NO_3)_2 \cdot 4H_2O$ ,  $NH_4Cl$  and  $CuSO_4 \cdot 5H_2O$  in a closed desiccators at an ambient temperature of 298 K. Prior to the saturation of the pellets in the above buffers, the pellets were heated at 393 K for 12 hrs to remove the adsorbed water. A degassed chamber of about 200 cm<sup>3</sup> was used for evaluating the response and recovery characteristics. This chamber has a provision for two-way inlet, one for transpiring the dry air and the other for moist air from a wet candle. Air drying was accomplished by transpiring the air stream through drying columns packed with anhydrous  $CaCl_2$  and dry  $P_2O_5$  connected in series. The resistance measurements in the dry air as well as in moist air alternatively helped to establish the response and recovery time of the compounds.

The structural studies were carried out using a Philips X'pert diffractometer for  $2\theta$  values ranging from 10 to 80 ° using  $CuK\alpha$  radiation at  $\lambda = 1.54 \text{ \AA}$ .

The Fourier transform infrared (FT-IR) spectra were recorded with Perkin – Elmer spectrometer using KBr pellets whose thickness was about 1.3 mm. Each spectrum was collected at room temperature under the atmospheric pressure. The samples were dispersed in spectroscopic grade KBr pellets and were scanned in the range of 4000-400  $\text{cm}^{-1}$ .

The surface morphology of the samples was observed on a Ultra 55 FESEM with EDS analyzer using gold coated samples.

The surface area and pore size distribution were derived from the nitrogen adsorption–desorption isotherms using liquid nitrogen at 77 K. The nitrogen adsorption–desorption isotherms of the composites were measured using an automatic adsorption instrument (Quantachrome Corp. Nova1000 gas sorption analyzer).

### 3. Results and Discussion

#### 3.1. X-Ray Diffraction Studies

The powder XRD patterns of LCS-1 to 6 compounds (Fig. 1) showed the characteristic peaks corresponding to  $\text{LaSr}_x\text{Cr}_{1-x}\text{O}_{3-\delta}$  confirming the absence of impurities and presence of mixed oxide intermediate peaks of new phases in LCS-2 to LCS-5. The XRD pattern of LCS-1 (JCPDS-75-0441) data corresponds to pure lanthanum chromite which is simple cubic system with ‘a’ value 3.880 whereas the XRD pattern of LCS-6 (pure lanthanum strontium oxide) which is a known compound it does not match with the existing patterns. The XRD pattern of compounds LCS-2 to LCS-5 were studied by comparing LCS-1 and LCS-6. The uniqueness of these XRD patterns is a proof that the compounds LCS-2 to LCS-6 is of novel.

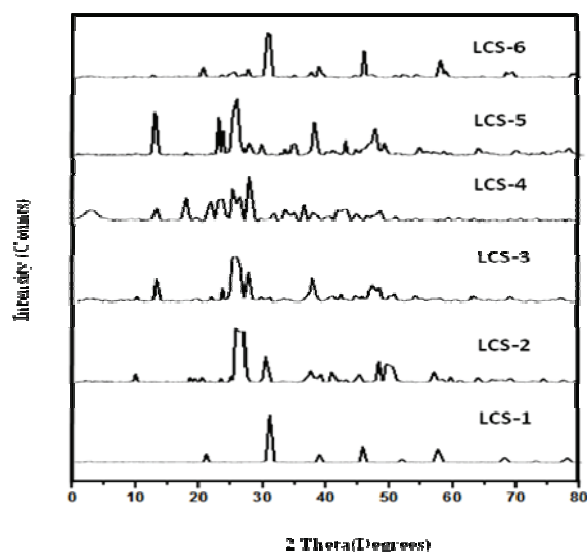


Fig. 1. XRD patterns of LCS-1 to LCS-6 compounds.

#### 3.2. FT-IR Spectroscopy

The FT-IR spectra of LCS-1 to 6 compounds (see Fig. 2) exhibit a common broad band near 3400  $\text{cm}^{-1}$  due to the OH-stretching vibrations of free and hydrogen-bonded hydroxyl groups, and a second typical absorption region at 1630  $\text{cm}^{-1}$  is assigned to the deformative vibration of water molecules which is most probably due to water adsorption during the compaction of the powder specimens with KBr [20, 21]. The metal–oxygen stretching frequencies in the range 400–1000  $\text{cm}^{-1}$  are associated with the vibrations of La-O, Cr-O and Sr-O bonds which is existing has mixed metal oxides. FT-IR spectra of the compounds showed sharp band around 625 and 512  $\text{cm}^{-1}$  which are characteristic of metal chromite spinels [22]. From the FT-IR spectra of the LCS-1 to 6 compounds it is evident that the band near 3400  $\text{cm}^{-1}$  and 1600  $\text{cm}^{-1}$  are broader for LCS-4 compound. This indicates that the surface adsorption of water on the ceramic surface is more in LCS-4 compound than in other compounds.

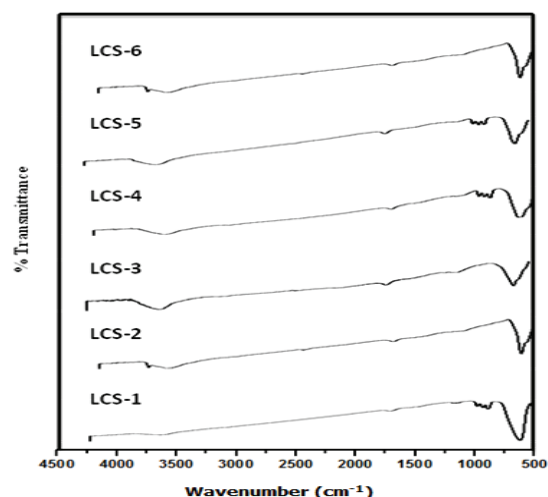


Fig. 2. FT-IR spectra of LCS-1 to LCS-6 compounds.

#### 3.3. Scanning Electron Microscopy (SEM)

The SEM micrographs of LCF-1 and LCF-6 (Fig. 3. a&c) is of the pure lanthanum chromite with the particle size 150 – 200 nm and pure lanthanum strontium oxide with the particle size 1  $\mu\text{m}$ , which doesn't show much of porosity. The LCS-4 (Fig. 3 (b) is of the mixed metal oxides of lanthanum chromium and strontium oxide in the mole ratio of 1: 0.4:0.6 which is formed as a compound by the sol-gel method. The particle size of LCS-4 is 85 - 100 nm. On comparing the SEM micrographs, LCS-4 shows a larger grain size and decrease in the particle size than LCS-1 & LCS-6. The surface morphology is well defined in the LCS-4 compound than in LCS-1 & LCS-6. The well developed porosity in LCS-4 is very important in humidity sensing studies.

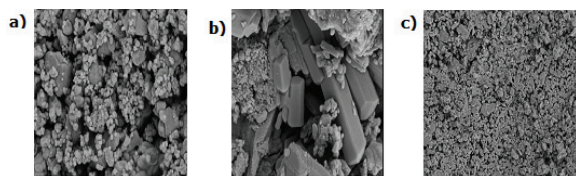


Fig. 3. SEM micrographs of (a) LCS-1, (b) LCS-4 and (c) LCS-6.

### 3.4. Nitrogen Adsorption/Desorption Studies

Nitrogen adsorption/desorption isotherms (at 77 K) of LCS-1, LCS-4 and LCS-6 were studied (Fig. 4(a) to Fig. 4(c)). Among them LCS-4 compound which possessed maximum sensitivity. The BET surface area of chromites and for composites has already been reported by Manoharan *et al.* [20] and Saha *et al.* [23]. The isotherms of LCS-1, LCS-4 and LCS-6 compounds showed a hysteresis effect with the slope of the plateau increasing with a significant increase in the nitrogen uptake through the entire pressure range. The increase in uptake of nitrogen in the samples is a result of the major increase in porosity which is observed for LCS-4 compound more compared to LCS-1 & 6 compounds. This is due to the presence of 0.6 mole of  $\text{Sr}^{2+}$  and 0.4 mole of  $\text{Cr}^{3+}$  in LCS-4 compound. LCS-1 is pure lanthanum chromite and LCS-6 is pure lanthanum stontium oxide both does not have mixture ratio like LCS-4. The LCS-4 compound exhibited the most prominent hysteresis effect, which can be characterized by the formation of intergranular pores as a result of 0.6 mole of  $\text{Sr}^{2+}$  and 0.4 mole of  $\text{Cr}^{3+}$  in the  $\text{LaSr}_x\text{Cr}_{1-x}\text{O}_{3-\delta}$  matrix. The amount of nitrogen adsorbed increased corresponding to the BET surface area of  $26.27 \text{ cm}^3/\text{g}$  for LCS-4 compound while it was only  $11.47 \text{ cm}^3/\text{g}$  for LCS-6 and  $8.95 \text{ cm}^3/\text{g}$  for LCS-1 compounds. The addition of 0.6 mole of  $\text{Sr}^{2+}$  and 0.4 mole of  $\text{Cr}^{3+}$  retards the growth of the bulk phase, leading to an increase in the surface area, an enhancement in the formation of a considerable amount of micro and mesopores.

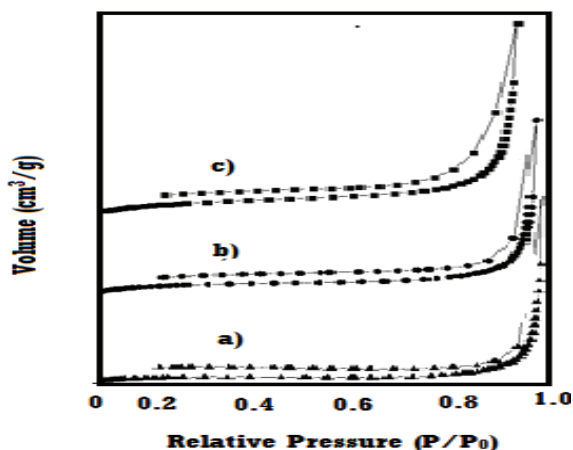


Fig. 4. Nitrogen adsorption and desorption isotherm curves of (a) LCS-1 (b) LCS-6 and (c) LCS-4.

### 3.5. Humidity Measurements

The LCS compounds were subjected to the relative humidity studies at various RH % environment. The humidity sensing measurements showed a decrease in resistance with an increase in % RH. The LCS-4 compound showed a highest humidity sensitivity of 33,400 with a resistance of  $1.67 \times 10^{11} \Omega$  at RH 5 % and  $5.00 \times 10^6 \Omega$  at RH 98 % whose BET surface area is  $26.27 \text{ cm}^3/\text{g}$ . At low humidity levels, chemisorption takes place, leading to formation of free surface hydroxyls with the charge transport occurring by the hopping mechanism [24]. While at high humidity levels, water is physisorbed on the top of the chemisorbed layer. As a result, the condensation of water in the capillary like pores leads to a liquid like layer leading to electrolytic conduction. The optimum concentration of  $x=0.6$  mole ratio shows good sensor towards humidity. The increase in porosity as evidenced from SEM images confirms the presence of more sites for water adsorption in LCS-4 compound. The sensitivity of the compounds with various molar ratios of LCS-1 to LCS-6 is shown in Table 1.

The SEM micrographs also reveal that the LSF-4 compound produces fine grains with maximum porosity compared with the other, indicating that the smaller the grain size, the higher the surface energy and the adsorption capacity. The sintered porous semiconductor has a large internal surface area for the adsorption of water vapor. Further the coordination of water molecule to  $\text{Cr}^{3+}$  ions in LCS-1 to LCS-6 compounds increase the acidity thereby releases  $\text{H}^+$ . Good linearity in the log R versus RH % plot is an important criterion for good humidity sensitivity material (see Fig. 5).

Table 1. Resistance at RH 5 % and RH 98 %, Sensitivity factor, Energy of activation of LCS compounds.

Sample Codes	R( $\Omega$ ), at RH 5 %	R( $\Omega$ ), at RH 98 %	S <sub>r</sub> (R <sub>RH 5 %</sub> / R <sub>RH 98 %</sub> )	E <sub>a</sub>
LCS-1	$3.33 \times 10^6$	$5.00 \times 10^6$	0.66	0.271
LCS-2	$1.00 \times 10^{10}$	$1.11 \times 10^7$	901	0.102
LCS-3	$5.00 \times 10^{10}$	$5.00 \times 10^6$	10,000	0.098
LCS-4	$1.67 \times 10^{11}$	$5.00 \times 10^6$	33,400	0.042
LCS-5	$1.25 \times 10^{11}$	$1.67 \times 10^7$	7,490	0.082
LCS-6	$3.33 \times 10^{11}$	$1.67 \times 10^7$	19,900	0.063

The results suggest that the more linear the plot, the better the response, recovery and sensitivity of the material. The LCS-6 compound which is the next highest humidity sensing material with the sensitivity factor of 19,900 has a resistance of  $3.33 \times 10^{11} \Omega$  at RH 5 % and  $1.67 \times 10^7 \Omega$  at RH 98 %. The LCS-1 is the lowest humidity sensing material among all the compounds with the humidity sensitivity factor of 0.66 has a resistance of  $3.33 \times 10^6 \Omega$  at RH 5 % and  $5.00 \times 10^6 \Omega$  at RH 98 % due to fewer sites for water

adsorption on the ceramic surface compared to that of LSF-4 compound.

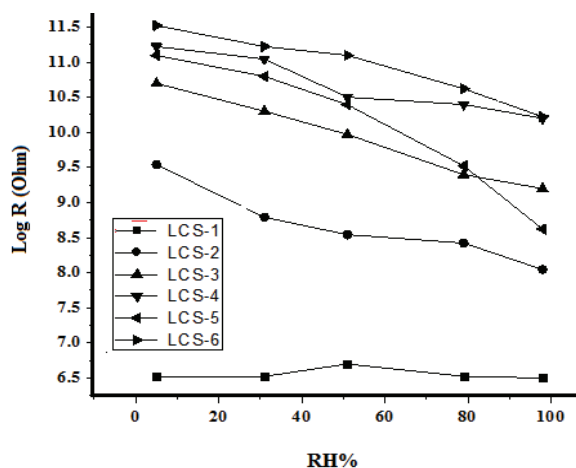


Fig. 5. Plot of log R vs. RH % of LCS-1 to 6 compounds.

### 3.6. Temperature Dependant Studies

The temperature dependence of the electrical conductance was carried out in the temperature range 120 °C to 350 °C suggested that the current (I) increased with an increase in temperature (T). The electrical conductance measurements of LCS-1 to LCS-6 compounds at room temperature prior to relative humidity measurements signified that the current increased linearly with the applied voltage, indicating the ohmic contact of the electrodes. The activation energies calculated from the temperature dependence of conductance data are also shown in Table 1. The activation energy for electrical conduction in polycrystalline materials generally involves the combination of the energy required to raise the carriers from the dominant levels to their corresponding transport bands and the energy required to create the carriers in the dominant levels [25]. The low activation energy of LCS-4 compound predicts that the small polaron conduction dominates in the studied temperature range.

### 3.7. Response and Recovery Characteristics

The response and recovery time obtained from the plot of Log R vs. Time (Fig. 6.)

For LCS-4 were found to be 200 s and 90 s, respectively. The longer time taken for the restoration of the resistance to that in dry air could be understood by the fact that these experiments are conducted at 25 °C at which temperature the desorption kinetics is expected to be slow thus evidencing a surface controlled phenomena. For LCS-4 the invariant resistance in dry air is in the order of  $10^{11} \Omega$ . The resistance drops (see Fig. 6) by four orders of magnitude to reach the constant value of approximately  $10^6 \Omega$  within 270 s on purging the

moist air. The time taken for the restoration of the original signal is approximately 90 s.

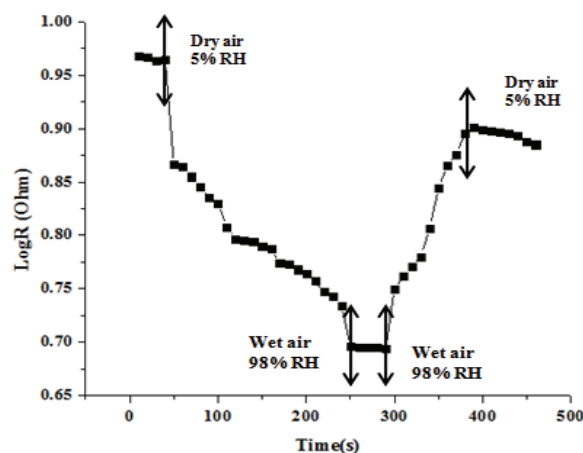


Fig. 6. Plot of log R vs. time of LCS-4 compound.

## 4. Conclusions

The LCS ( $\text{LaSr}_x\text{Cr}_{1-x}\text{O}_{3-\delta}$ ) compounds with different mole ratios  $x = 0, 0.2, 0.4, 0.6, 0.8$  &  $1.0$  were prepared by sol-gel method. Humidity sensitivity measurements, Temperature dependence, FT-IR, BET, SEM, XRD studies were done. Their purity was confirmed by XRD analysis. The intensity of XRD peaks shows a variation from LCS-2 to LCS-5 due to the presence of  $\text{La}^{3+}$ ,  $\text{Cr}^{3+}$  and  $\text{Sr}^{2+}$ . The novelty of the compound has been proved by the XRD patterns which is different from the existing phases. The surface morphology of the compounds were studied by the SEM micrographs. FT-IR study showed the characteristic metal oxide vibrational frequencies. BET study gave the surface area of the highest humidity sensitive compound. The LCS-4 ( $\text{LaSr}_{0.6}\text{Cr}_{0.4}\text{O}_{3-\delta}$ ) compound showed the highest humidity sensitivity factor of  $3.34 \times 10^4$ . Temperature dependent studies showed the low activation energy of all the compound confirming the involvement of small polaron hopping mechanism in the conduction. The good response and recovery time of LCS-4 compound and its highest sensitivity factor might be a promising humidity sensing material for practical application.

## Acknowledgements

The authors also thank University Grants Commission of Delhi for granting UGC-DAE project for supporting our research work.

The authors would like to thank the Head of Loyola college, the Director of Loyola Institute of Frontier Energy (LIFE) and the Head of Stella Maris College for giving permission to use the instruments and other facilities.

## References

- [1]. Y. F. Qiu, S. H. Yang, ZnO nanotetrapods: controlled vapor-phase synthesis and applications for humidity sensing, *Adv. Funct. Mater.*, 17, 2007, pp. 1345-1352.
- [2]. C. L. Dai, M. C. Liu, F. S. Chen, C. C. Wu, M. W. Chang, A nanofiber WO<sub>3</sub> humidity sensor integrated with micro-heater and inverting amplifier circuit on chip manufactured using CMOS-MEMS technique, *Sens. Actuators B: Chem.*, 123, 2007, pp. 896-901.
- [3]. J. Yang, K. Hidajat, S. Kawi, Synthesis of nano-SnO<sub>2</sub>/SBA-15 composite as a highly sensitive semiconductor oxide gas sensor, *Mater. Lett.*, 62, 2008, pp. 1441-1443.
- [4]. C. T. Wang, C. L. Wu, Electrical sensing properties of silica aerogel thin films to humidity, *Thin Solid Films*, 496, 2006, pp. 658-664.
- [5]. P. Kapa, L. Pan, Bandhanadham, J. Fang, K. Varahramyan, W. Davis, H. F. Ji, Moisture measurement using porous aluminum oxide coated microcantilevers, *Sens. Actuators B: Chem.*, 134, 2008, pp. 390-395.
- [6]. E. Traversa, Ceramic sensors for humidity detections: the state-of-the-art and future developments, *Sens. Actuators B*, 23, 1995, pp. 135-156.
- [7]. Y. C. Yeh, T. Y. Tseng, D. A. Chang, Electrical properties of porous titania ceramic humidity sensors, *J. Am. Ceram. Soc.*, 72, 1989, pp. 1472-1475.
- [8]. G. Larsen, R. V. Ortiz, K. Minchow, A. Barrero, I. G. Loscertales, A method for making inorganic and hybrid (organic/inorganic) fibers and vesicles with diameters in the submicrometer and micrometer range via sol-gel chemistry and electrically forced liquid jets, *J. Am. Chem. Soc.*, 125, 2003, pp. 1154-1155.
- [9]. E. Moral, D. P. Fagg, E. Chinarro, J. C. C. Abrantes, J. R. Jurado, G. C. Mather, Impedance analysis of Sr-substituted CePO<sub>4</sub> with mixed protonic and p-type electronic conduction, *Ceram. Int.*, 35, 2009, pp. 1481-1486.
- [10]. M. V. Fuke, A. Vijayan, M. Kulkarni, R. Hawaldar, R. C. Aiyer, Evaluation of copolyaniline nanocomposites thin films as humidity sensor, *Talanta*, 76, 2008, pp. 1035-1040.
- [11]. B. M. Kulwick, Humidity Sensors, *J. Am. Ceram. Soc.*, 74, 1991, pp. 697-708.
- [12]. B. Li, P. T. Lai, S. H. Zeng, M. Q. Huang, *Smart Materials and Structures*, 9, 2000, p. 498.
- [13]. Z. Zhigang, Z. Gang, *Ferroelectric*, 101, 1990, p. 43.
- [14]. W. Qu, R. Green, M. Austin, *Measurement Science & Technology*, 11, 2000, p. 1111.
- [15]. G. Adachi, N. Imanika, Z. C. Kang, Binary rare earth oxides, *Kluwer Academic Publishers*, 2009, p. 141.
- [16]. J. H. Anderson, G. A. Parks, The electrical conductivity of silica gel in the presence of adsorbed water, *J. Phys. Chem.*, 72, 1968, pp. 3662-3668.
- [17]. T. Seiyama, N. Yamazoe, H. Arai, Ceramic humidity sensors, *Sens. Actuators B*, 4, 1983, pp. 85-96.
- [18]. S. L. Yang, J. M. Wu, ZrO<sub>2</sub>-Ti-O<sub>2</sub> ceramic humidity sensors, *J. Mater. Sci.*, 26, 1991, pp. 631-636.
- [19]. J. L. Zhang, Electrical conduction of Ba<sub>0.5</sub>Sr<sub>0.5</sub>TiO<sub>3</sub> ceramics under d.c. voltage, *J. Mater. Sci. Lett.*, 11, 1992, pp. 294-295.
- [20]. S. S. Manoharan, C. Patil Kashinath, Combustion synthesis of metal Chromite powders, *J. Am. Ceram. Soc.*, 75, 4, 1992, pp. 1012-1015.
- [21]. D. Dvoranova, V. Nrezova, M. Mazur, M. A. Malati, Investigations of metal doped titanium dioxide photo catalysts, *Appl. Catal. B: Environ.*, 37, 2002, pp. 91-105.
- [22]. J. Preudhomme, P. Tarte, Infrared study of spinels-III, *Spectrochim. Acta*, 27A, 1971, pp. 1817-1835.
- [23]. D. Saha, R. Giri, K. K. Mistry, K. Sengupta, Magnesium chromate-TiO<sub>2</sub> spinel tape cast thick film as humidity sensor, *Sens. Actuators B*, 107, 2005, pp. 323-331.
- [24]. S. Pokhrel, K. S. Nagaraja, Electrical and humidity sensing properties of molybdenum (VI) oxide and tungsten (VI) oxide composites, *Phys. Stat. Sol., A*, 198, 2, 2003, pp. 343-349.
- [25]. Z. A. Ansari, T. G. Ko, J. H. Oh, Humidity sensing behavior of thick films of strontium-doped lead-zirconium-titanate, *Surf. Coat. Technol.*, 179, 2004, pp. 182-187.

## Synthesis, Characteristics and Enhanced Sulfur Dioxide Sensing Properties of Cu-doped SnO<sub>2</sub> Microspheres

\* Shudi Peng, Gaolin Wu, Wei Song

Chongqing Electric Power Research Institute, Chongqing, 401123, China

\* Tel.: +86-23-63230512, fax: +86-23-63230512

E-mail: pengshudi@163.com, 13983842134@139.com, 48012641@qq.com

Received: 5 August 2013 / Accepted: 25 August 2013 / Published: 30 September 2013

**Abstract:** Sulfur dioxide (SO<sub>2</sub>) is a typical sulfur hexafluoride (SF<sub>6</sub>) decomposition by product in gas insulated switchgear (GIS). Online monitoring and analyzing SO<sub>2</sub> gas concentration can timely and effectively evaluate the insulation performance of SF<sub>6</sub>-gas-insulated apparatus. In this study, pure and 3 at % Cu-doped SnO<sub>2</sub> microspheres were synthesized via a simple and facile hydrothermal method, and were characterized by X-ray powder diffraction, field emission scanning electron microscopy, transmission electron microscopy, energy dispersive X-ray spectroscopy and X-ray photoelectron spectroscopy, respectively. Chemical gas sensors were fabricated with the conventional indirect heating technology and their gas sensing properties versus SO<sub>2</sub> were investigated in detail. The gas sensor fabricated with 3 at % Cu-doped SnO<sub>2</sub> microspheres exhibits lower optimum operating temperature and higher gas response than that of pure SnO<sub>2</sub> microspheres. Meanwhile, it demonstrates good stability and fast response-recovery. Most importantly, this sensor holds excellent discrimination with other SF<sub>6</sub> decompositions, including SOF<sub>4</sub>, SOF<sub>2</sub>, SO<sub>2</sub>F<sub>2</sub> and HF. All results provide a good candidate in fabricating high-performance SO<sub>2</sub> sensor in practice. Copyright © 2013 IFSA.

**Keywords:** Sulfur dioxide, Gas sensing properties, Cu-doped SnO<sub>2</sub>, Chemical gas sensor.

### 1. Introduction

Gas insulated switchgear (GIS) filled with pressurized SF<sub>6</sub> gas for electrical insulation and arc extinction, has been widely used in electrical power systems in the past decades [1-3]. When compared with the conventional open high-voltage switchgear installations, GIS has the advantages of small floor space, high stability and reliability, high-strength insulation, lower maintenance cost, and so on [4-5]. Despite these excellent advantages, there still exist some unavoidable insulation defects in GIS design, preparation, installation and running process. Partial discharge (PD) may occur at these insulation defects and cause SF<sub>6</sub> gas decomposition [6-7].

Till now, researches both at home and abroad have reported that SOF<sub>4</sub>, SOF<sub>2</sub>, SO<sub>2</sub>F<sub>2</sub>, SO<sub>2</sub> and HF

are the mainly characteristic decompositions of SF<sub>6</sub> gas in GIS apparatus [8-10]. So it is available and effective to evaluate the insulation performance of SF<sub>6</sub> in GIS through detecting and analyzing these decomposed chemical products [11-12].

In recent years, interest in SF<sub>6</sub> decompositions detection has been greatly stimulated, and numerous methods have been reported, such as semiconductor gas sensors [1, 8, 10], spectroscopy [9] and carbon nanotubes [11, 12]. Peng *et al.* [1] successfully synthesized flower-like ZnO nanorods and investigated their gas sensing properties to SOF<sub>2</sub>, SO<sub>2</sub>F<sub>2</sub>, and SO<sub>2</sub>. Zhang *et al.* [11] reported the adsorption properties of SF<sub>6</sub> decomposition products adsorbed on single-walled carbon nanotubes (SWNT) from the first principles calculation. However, some limitations still need to be further improved

[1, 8, 10, 11], such as high operating temperature, low gas response and especially poor selectivity with potential interference gases.

Hence, in this study, we reported a simple and facile hydrothermal method to prepare pure and Cu-doped SnO<sub>2</sub> microspheres. Gas sensors were fabricated with traditional indirect heating technology and gas sensing properties of the fabricated sensors to SO<sub>2</sub> gas were measured in detail, including optimum operating temperature, gas response, response and recovery time, stability and reproducibility. Moreover, cross sensitivity and selectivity between SO<sub>2</sub> gas and other SF<sub>6</sub> decompositions were also investigated. Finally, a possible sensitivity mechanism was proposed.

## 2. Experimental

### 2.1. Synthesis of Materials

All chemicals were analytical-grade reagents purchased from Chongqing Chuandong Chemical Reagent Co. Ltd. and were used as received without any further purification. In this study pure and 3 at % Cu-doped SnO<sub>2</sub> microspheres were synthesized with a simple and facile hydrothermal method. The detailed synthesis processes were as follows:

In a typical synthesis process of 3 at % Cu-doped SnO<sub>2</sub> microspheres [13-15]: 2.104 g (6.0 mmol) of SnCl<sub>4</sub>·5H<sub>2</sub>O, 0.031 g (0.18 mmol) of CuCl<sub>2</sub>, and 1.080 g of NaOH were dissolved completely into 30 ml distilled water and 30 ml absolute ethanol in a beaker of 100 ml capacity. Then 0.588 g (2.0 mmol) of C<sub>6</sub>H<sub>5</sub>Na<sub>3</sub>O<sub>7</sub>·2H<sub>2</sub>O (≥99.5 %) and 2.5 ml EG were added to the beaker. The mixture was magnetically stirred for 30 min to generate a transparent solution and then transferred into a 100 ml Teflon-lined stainless steel autoclave, sealed and maintained at 160 °C for 18 h in an electric furnace. After the heating treatment, the autoclave was cooled to room temperature naturally. Finally the products were harvested by centrifugation, washed three times with distilled water and absolute ethanol, respectively, and dried at 100 °C overnight to remove the solvent.

Pure SnO<sub>2</sub> microspheres were obtained in a similar process as 3 at % Cu-doped SnO<sub>2</sub> microspheres, but no addition of copper salt CuCl<sub>2</sub> was added to the precursor mixture.

### 2.2. Structure Characterization

The crystalline structures of the as-prepared pure and 3 at % Cu-doped SnO<sub>2</sub> microspheres were investigated by X-ray powder diffraction (XRD, Rigaku D/Max-1200X) with Cu K $\alpha$  radiation, 40 kV, 200 mA,  $\lambda=1.5418$  Å, and  $2\theta$  ranging from 20° to 80°. The surface morphologies of the samples were characterized with a Nova 400 Nano field emission scanning electron microscope (FESEM,

Hillsboro equipped with energy dispersive X-ray (EDX) spectroscopy) and transmission electron micrographs (TEM, Hitachi S-570). Analysis of the X-ray photoelectron spectra (XPS) was performed on an ESCLAB MKII using Al as the exciting source.

### 2.3. Fabrication of Gas Sensor

Chemical gas sensors were fabricated with the conventional indirect heating technology [14]. Each obtained sample was ground into fine powder and mixed with absolute ethanol and deionized water in a weight ratio of 8:1:1 to form a homogenous paste. Then the paste was coated on an alumina ceramic tube to form a sensing film with a thickness of about 350  $\mu$ m, where a pair of Au electrodes was previously printed. Pt lead wires were attached to the as-printed Au electrodes to collect the electrical signals.

After the ceramic tube was calcined at 300 °C in an electric furnace for 2 h, a Ni-Cr heating wire was inserted into the alumina tube as a heater controlling the operating temperature of sensing material as shown in Fig. 1. The tube was welded on the sensor pedestal. The distance between the two Au electrodes is estimated to be 6 mm and the diameter of the alumina tube is 1.2 mm. Finally, the sensor was further aged in an aging chamber at 120 °C for 36 h to improve the stability and repeatability. Fig. 2 is the photography of as-fabricated chemical gas sensor.

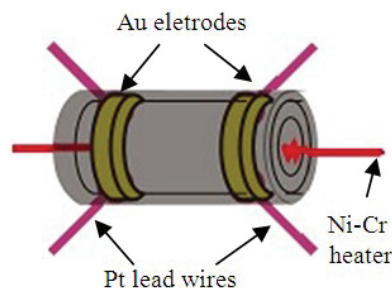


Fig. 1. Structure representation of the ceramic tube.

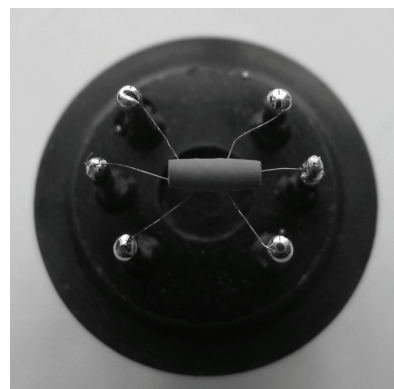


Fig. 2. A photography of the fabricated indirect heating gas sensor.

## 2.4. Gas Sensing Property Measurement

Gas sensing properties of the as-fabricated sensors were measured by a CGS-8 [14] (Chemical gas sensor-8) intelligent gas sensing analysis system purchased from Beijing Elite Tech Co., Ltd, China, as shown in Fig. 3. The sensors were pre-heated at different operating temperatures for about 30 min. When the resistances of all the sensors were stable, saturated target gas was injected into the test chamber (20 l in volume) by a microinjector through a rubber plug. The saturated target gas was mixed with air by two fans in the analysis system.

After the sensor resistances reached a new constant value, the test chamber was opened to recover the sensors in air. The sensor resistance, gas response, ambient temperature and humidity values were recorded timely and automatically by the intelligent gas sensing analysis system.

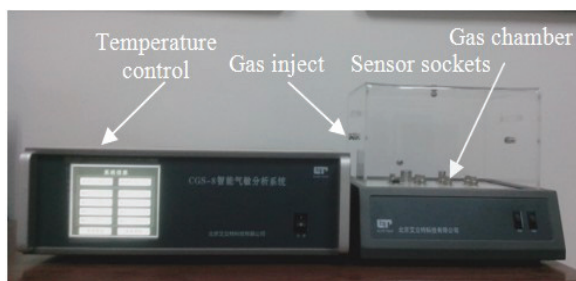


Fig. 3. Schematic image of the CGS-8 intelligent gas sensing measuring equipment.

The gas response value  $S$  was defined as  $S=R_a/R_g$ , where  $R_a$  was the sensor resistance value in air and  $R_g$  was that in a mixture of target gas and air [15]. The time taken by the sensor to reach 90 % of the total resistance change was defined as the response time in the case of gas adsorption or the recovery time in the case of gas desorption [13]. All measurements were repeated several times to ensure the repeatability and stability of the sensor.

## 3. Results and Discussion

### 3.1. Structural Characterization

XRD measurement was first performed to characterize the crystalline structure and chemical composition of the as-synthesized products. As shown in Fig. 4 all the diffraction peaks of pure and Cu-doped  $\text{SnO}_2$  microspheres were well indexed to the standard data file of rutile  $\text{SnO}_2$  (JCPDS file no. 41-1445, space group  $P4_2/mnm$ ). No diffraction peaks from any impurities were detected, which means a high purity of our prepared samples. And there are no characteristic peaks from dopants, which may be attributed to the high dispersion or the poor crystallinity of copper related nanostructures.

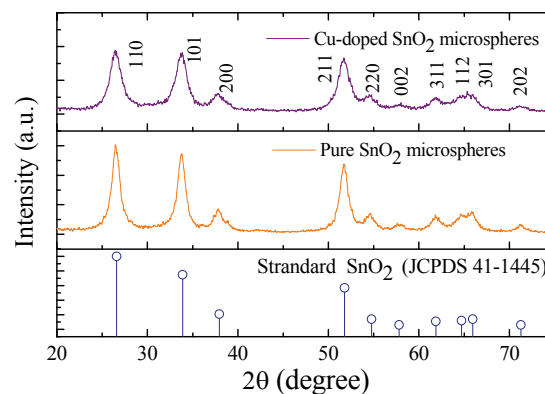


Fig. 4. XRD patterns of the prepared  $\text{SnO}_2$  microspheres.

To check whether dopants have been successfully doped into the synthesized nanostructures, EDS analysis was conducted. As shown in Fig. 5 characteristic energy spectrum of Cu element appeared at 0.98, 8.09 and 8.87 keV, which confirms the availability of dopants Cu on the  $\text{SnO}_2$  matrix. The composition of the Cu dopant is calculated to be about 2.92 at %, which matches well with its nominal concentration.

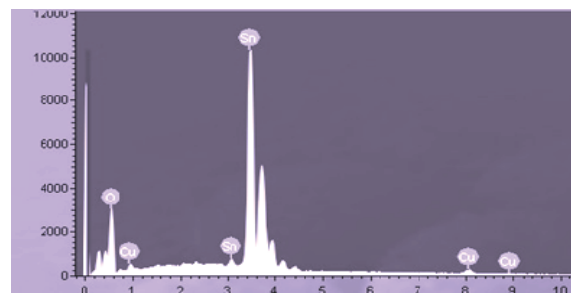
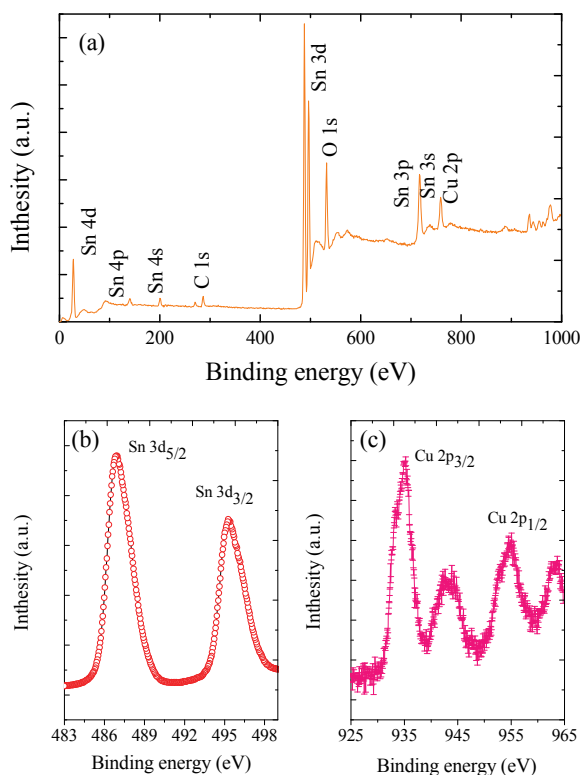


Fig. 5. EDS spectra of 3 at % Cu-doped  $\text{SnO}_2$  microspheres.

XPS data of the 3 at % Cu-doped  $\text{SnO}_2$  microspheres is collected and presented in Fig. 6 to further confirm the existence of Cu element and their valences. Fig. 6 (a) shows its wide spectrum, which is mainly consisted of Sn, O and Cu elements. The binding energies in Fig. 6 (b) at 486.5 and 493.8 eV correspond to  $\text{Sn}^{4+}$  of rutile  $\text{SnO}_2$ . From the narrow spectrum of Cu element as shown in Fig. 6 (c), the peak at 934.23 eV is identified as Cu  $2p_{3/2}$ , which possibly can be attributed to  $\text{Cu}^{2+}$  ions (933.90 eV). And it ruled out the presence of metallic Cu and  $\text{CuO}_2$  in our sample, whose binding energy is 932.60 eV and 932.90 eV in standard XPS data, respectively.

Thus, based on the XRD, EDS and XPS results, the  $\text{Cu}^{2+}$  ions are believed to be successfully incorporated into the  $\text{SnO}_2$  nanocrystals.

FESEM were further used to investigate the surface morphologies and microstructures of the synthesized samples. Fig. 7 (a) and Fig. 7 (b) illustrate the FESEM images of pure and 3 at % Cu-doped  $\text{SnO}_2$  nanostructures, respectively.



**Fig. 6.** XPS spectra of 3 at % Cu-doped SnO<sub>2</sub> microspheres (a) wide spectrum (b) Sn 3d and (c) Co 2p.

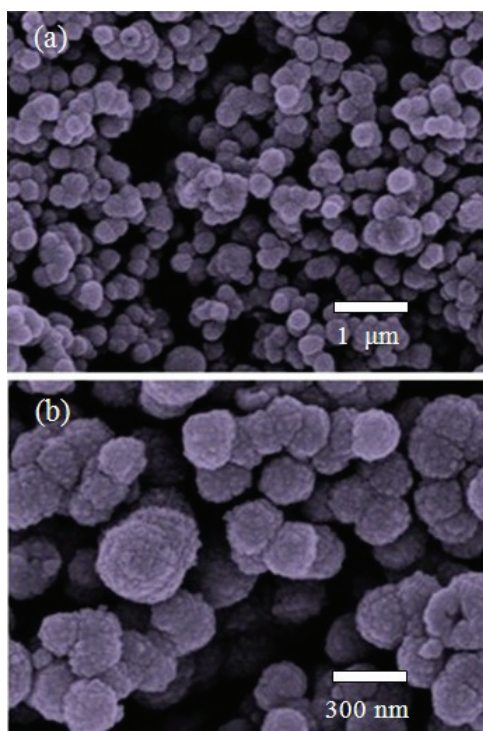


**Fig. 7.** FESEM images of (a) pure and (b) 3 at % Cu-doped SnO<sub>2</sub> microspheres.

One can clearly see in Fig. 7 that both samples are made up of a large scale of SnO<sub>2</sub> microspheres. These spheres are uniform in size and shape with good dispersion in the whole FESEM images. Cu

doping in our experiments has nearly no influence on the morphology of SnO<sub>2</sub> nanostructures. The diameters of both samples are in the scope of 200 to 250 nm.

Fig. 8 shows typical TEM and HRTEM images of 3 at % Cu-doped SnO<sub>2</sub> nanostructures. As shown in Fig. 8 (a) that the single microsphere is composed of many SnO<sub>2</sub> particles with average diameter of 2-3 nm. Fig. 8 (b) shows a HRTEM image of 3 at % Cu-doped SnO<sub>2</sub> sample, and the fringe space is measured to be about 0.335 nm, which is consistent well with the (110) plane of rutile SnO<sub>2</sub>.

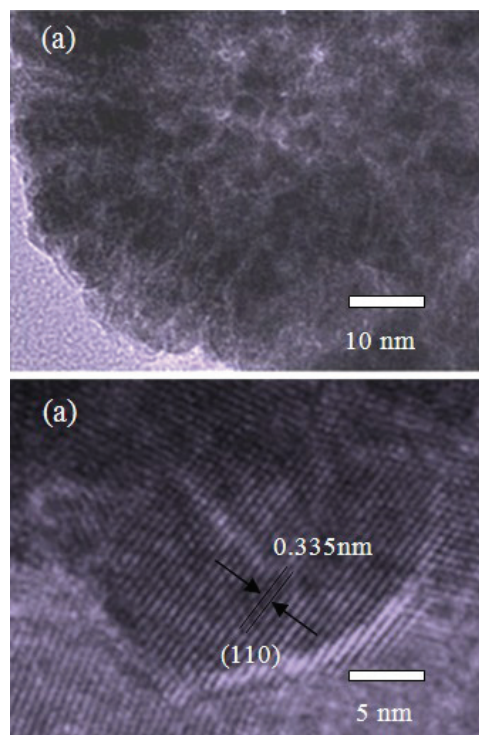


**Fig. 8.** TEM and HRTEM images of 3 at % Cu-doped SnO<sub>2</sub> microspheres.

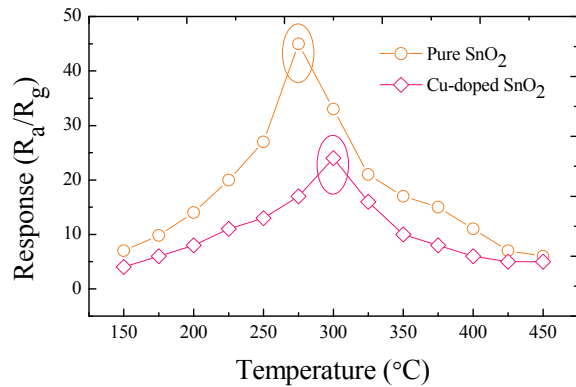
### 3.2. Gas Sensing Properties

Gas sensing properties of the as-fabricated sensors are investigated in detail as follows.

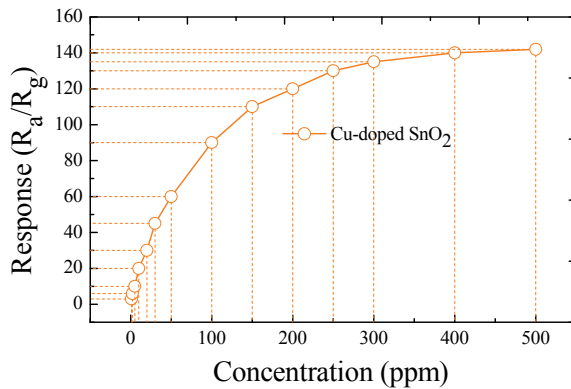
The gas responses of the pure and Cu-doped SnO<sub>2</sub> based sensors to 30 ppm of SO<sub>2</sub> with working temperature from 150 to 450 °C were firstly measured and shown in Fig. 9. One can see that the 3 at % Cu-doped sensor exhibits exclusive lower operating temperature than that of pure sensor. It is measured to be about 300 °C and 275 °C for pure and 3 at % Cu-doped sensors. And the highest gas response of the pure and 3 at % Cu-doped sensors versus 30 ppm of SO<sub>2</sub> is estimated to be about 43.15 and 23.37 respectively.

Fig. 10 shows the gas responses of the 3 at % Cu-doped sensor towards SO<sub>2</sub> at 275 °C with gas concentration from 1 to 500 ppm. One can clearly see in Fig. 10 that the gas response of the sensor increases rapidly with increasing SO<sub>2</sub> concentration

below 50 ppm. And then the sensor shows a slower increase with further increasing the gas concentration from 50 to 300 ppm, and finally reaches saturation at nearly about 500 ppm.



**Fig. 9.** Gas Response of the sensors to different operating temperature under 30 ppm of  $\text{SO}_2$ .



**Fig. 10.** Gas Response of the sensor versus  $\text{SO}_2$  concentration from 1 to 500 ppm.

If the response of gas sensor matches linear or quasi-linear relationship with the concentration of target gas, the sensor can be applied to engineering application in practice. The linear fitting curve of the 3 at % Cu-doped sensor towards  $\text{SO}_2$  at 275 °C with gas concentration from 1 to 50 ppm is shown in Fig. 11. As seen in Fig. 11 the linear correlation coefficient  $R^2$  is estimated to be about 0.9869. Such a higher linear dependence implies the product a promising  $\text{SO}_2$  sensing material.

Response-recovery property and stability are other two key parameters to evaluate the sensing performances of semiconductor gas sensors. As shown in Fig. 12 the response and recovery time of the 3 at % Cu-doped sensor to  $\text{SO}_2$  gas is measured to be about 5-8 s and 12-20 s, respectively. During the four testing cycles, the electric resistance of the sensor invariably returns to its initial value, which means good reproducibility and excellent stability of the as-prepared sensor for  $\text{SO}_2$  detection.

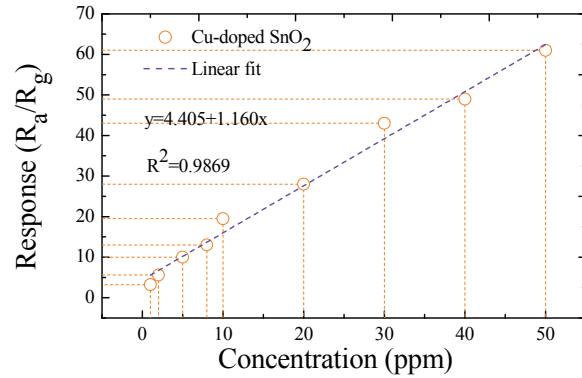


**Fig. 11.** Gas Response of the sensor versus  $\text{SO}_2$  concentration from 1 to 50 ppm.

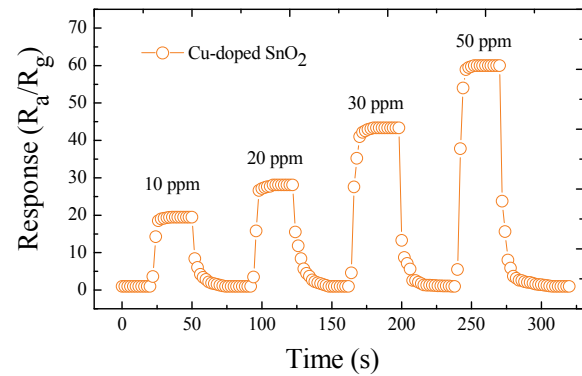


**Fig. 12.** Response and recovery characteristics of the sensor to 10, 20, 30 and 50 ppm of  $\text{SO}_2$ .

Selectivity is another very important indicator for semiconductor sensors, especially with potential interference gases. Fig. 13 depicts the gas response histogram of the 3 at % Cu-doped sensor exposed to 10 and 30 ppm of  $\text{SO}_2$  and other  $\text{SF}_6$  decomposition byproducts, including  $\text{SOF}_4$ ,  $\text{SOF}_2$ ,  $\text{SO}_2\text{F}_2$ , and HF. The results imply that the sensor is sensitive to  $\text{SO}_2$ , but nearly insensitive to  $\text{SOF}_4$ ,  $\text{SOF}_2$ ,  $\text{SO}_2\text{F}_2$  and HF. Thus, the 3 at % Cu-doped sensor exhibits high selectivity to  $\text{SO}_2$  with other  $\text{SF}_6$  decompositions.

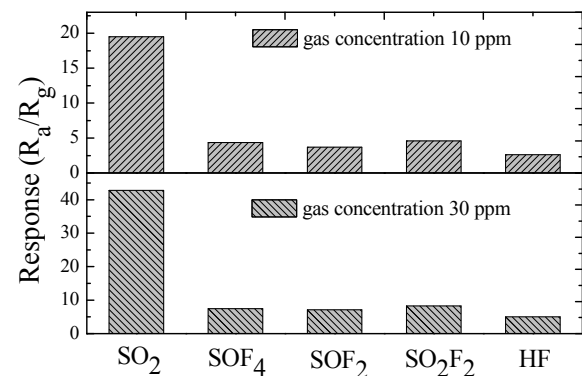


**Fig. 13.** Selectivity of the sensor to 10 and 30 ppm of  $\text{SO}_2$ ,  $\text{SOF}_4$ ,  $\text{SOF}_2$ ,  $\text{SO}_2\text{F}_2$  and HF.

The sensing process of SO<sub>2</sub> adsorbed on SnO<sub>2</sub> based sensors has discussed in our former paper [1]. A possible sensing mechanism for the enhanced SO<sub>2</sub> sensing properties was discussed as follows. The enhanced SO<sub>2</sub> sensing performances of the present Cu-doped SnO<sub>2</sub> microspheres may be attributed to two main aspects. The first one is relating to the possible chemical effect of the catalytic activity of CuO nanoparticles. CuO is a far better oxygen dissociation catalyst than SnO<sub>2</sub> [16], adsorbed oxygen can diffuse faster to surface vacancies and capture electrons from the conduction band of SnO<sub>2</sub> to generate various kinds of chemical adsorbed oxygen species, namely O<sub>2</sub><sup>-</sup>, O<sup>2-</sup> and O<sup>-</sup> [1, 17]. The second aspect can be attributed to the synergic interaction between CuO nanoparticles and SnO<sub>2</sub> microspheres. An additional barrier and depletion layer at the interface of CuO-SnO<sub>2</sub> may be formed, accelerating the charge transfer between valence band and conduction band in the sensing process [18]. Thus, an excellent SO<sub>2</sub> sensing property are observed in our measurements.

#### 4. Conclusions

In conclusion, pure and 3 at % Cu-doped SnO<sub>2</sub> microspheres were successfully synthesized via a simple and facile hydrothermal method and characterized by XRD, EDS, XPS, SEM and TEM. Chemical gas sensors were fabricated with the conventional indirect heating technology and sensors properties were investigated in detail. The optimum operating temperature of the pure and Cu-doped sensor versus SO<sub>2</sub> is measured to be above 275 °C and 300 °C. The Cu-doped one exhibits high-linear gas response with  $R^2=0.9869$  to 1-50 ppm SO<sub>2</sub> and its response and recovery time is measured to be about are 5-8 s and 12-20 s. Moreover, the 3 at % Cu-doped SnO<sub>2</sub> sensor shows a remarkable discrimination between SO<sub>2</sub> and other SF<sub>6</sub> decomposition byproducts. Therefore, the 3 at % Cu-doped SnO<sub>2</sub> microspheres may be potentially exploited into an effective SO<sub>2</sub> sensing material for chemical sensors.

#### References

- [1]. S. D. Peng, G. L. Wu, W. Song, Q. Wang, Application of flower-like ZnO nanorods gas sensor for detecting SF<sub>6</sub> decompositions, *Journal of Nanomaterials*, Vol. 2013, Issue 1, 2013, pp.1-9.
- [2]. J. Tang, F. Liu, X. X. Zhang, Q. H. Meng, J. B. Zhou, Partial discharge recognition through an analysis of SF<sub>6</sub> decomposition products part 1: decomposition characteristics of SF<sub>6</sub> under four different partial discharges, *IEEE Transactions on Dielectrics and Electrical Insulation*, Vol. 19, Issue 1, 2012, pp. 29-36.
- [3]. J. Tang, F. Liu, X. X. Zhang, Q. H. Meng, J. G. Tao, Partial discharge recognition through an analysis of SF<sub>6</sub> decomposition products part 2: feature extraction and decision tree-based pattern recognition, *IEEE Transactions on Dielectrics and Electrical Insulation*, Vol. 19, Issue 1, 2012, pp. 37-44.
- [4]. I. Sauers, H. W. Ellis, L. G. Christophoro, Neutral decomposition products in spark breakdown of SF<sub>6</sub>, *IEEE Transactions on Electrical Insulation*, Vol. 21, Issue 2, 1986, pp. 111-120.
- [5]. R. J. Van Brunt, J. T. Herron, Fundamental processes of SF<sub>6</sub> decomposition and oxidation in glow and corona discharges, *IEEE Transactions on Electrical Insulation*, Vol. 25, Issue 1, 1990, pp. 75-94.
- [6]. M. L. Shih, W. J. Lee, C. H. Tsai, P. J. Tsai, C. Y. Chen, Decomposition of SF<sub>6</sub> in an RF plasma environment, *Journal of the Air & Waste Management Association*, Vol. 52, Issue 11, 2002, pp. 1274-1280.
- [7]. W. T. Tsai, The decomposition products of sulfur hexafluoride (SF<sub>6</sub>): reviews of environmental and health risk analysis, *Journal of Fluorine Chemistry*, Vol. 128, Issue 11, 2007, pp. 1345-1352.
- [8]. J. Singh, A. Mukherjee, S. K. Sengupta, J. Im, G. W. Peterson, Sulfur dioxide and nitrogen dioxide adsorption on zinc oxide and zirconium hydroxide nanoparticles and the effect on photoluminescence, *Applied Surface Science*, Vol. 258, Issue 15, 2012, pp. 5778-5785.
- [9]. R. Kurte, C. Beyer, H. M. Heise, D. Klockow, Application of infrared spectroscopy to monitoring gas insulated high-voltage equipment: electrode material-dependent SF<sub>6</sub> decomposition, *Analytical and Bioanalytical Chemistry*, Vol. 373, Issue 7, 2002, pp. 639-646.
- [10]. X. X. Zhang, J. B. Zhang, Y. C. Jia, P. Xiao, J. Tang, TiO<sub>2</sub> nanotube array sensor for detecting the SF<sub>6</sub> decomposition product SO<sub>2</sub>, *Sensors*, Vol. 12, Issue 3, 2012, pp. 3302-3313.
- [11]. X. X. Zhang, J. B. Zhang, J. Tang, B. Yang, Gas-sensing simulation of single-walled carbon nanotubes applied to detect gas decomposition products of SF<sub>6</sub>, *Journal of Computational and Theoretical Nanoscience*, Vol. 9, Issue 8, 2012, pp. 1096-1100.
- [12]. W. D. Ding, R. Hayashi, K. Ochi, J. Suehiro, K. Imasaka, Analysis of PD-generated SF<sub>6</sub> decomposition gases adsorbed on carbon nanotubes, *IEEE Transactions on Dielectrics and Electrical Insulation*, Vol. 13, Issue 6, 2006, pp. 1200-1207.
- [13]. W. G. Chen, Q. Zhou, X. P. Su, L. N. Xu, S. D. Peng, Morphology control of tin oxide nanostructures and sensing performances for acetylene detection, *Sensors & Transducers*, Vol. 154, Issue 7, July 2013, pp. 195-200.
- [14]. Q. Zhou, W. G. Chen, L. N. Xu, S. D. Peng, Study on sensing properties and mechanism of Pd-doped SnO<sub>2</sub> sensor for hydrogen and carbon monoxide, *Sensors & Transducers*, Vol. 151, Issue 4, 2013, pp. 84-89.
- [15]. L. L. Wang, Z. Lou, T. Zhang, H. T. Fan, X. J. Xu, Facile synthesis of hierarchical SnO<sub>2</sub> semiconductor microspheres for gas sensor application, *Sensors and Actuators B-Chemical*, Vol. 155, Issue 1, 2011, pp. 285-289.
- [16]. H. X. Gao, Y. Luo, H. X. Hao, Y. Gao, H. Wang, S. W. Li, CuO-SnO<sub>2</sub> nanocomposite powders: synthesis and characterization, *Chinese Journal of Inorganic Chemistry*, Vol. 21, Issue 8, 2005, pp. 1218-1222.
- [17]. W. Wei, Y. Dai, B. B. Huang, Role of Cu doping in SnO<sub>2</sub> sensing properties toward H<sub>2</sub>S, *Journal of*

Physical Chemistry C, Vol. 115, Issue 38, 2011, pp. 18597-18602.

[18]. L. Liu, T. Zhang, L. Y. Wang, S.C. Li, Improved ethanol sensing properties of Cu-doped SnO<sub>2</sub>

nanofibers, Materials Letters, Vol. 63, Issue 23, 2009, pp. 2041-2043.

2013 Copyright ©, International Frequency Sensor Association (IFSA). All rights reserved.  
(<http://www.sensorsportal.com>)

## BioMEMS 2010

Yole's BioMEMS report 2010-2015



**IFSA offers  
a SPECIAL PRICE**

### Microsystems Devices Driving Healthcare Applications

**The BioMEMS 2010 report** is a robust analysis of the Micro Devices with the most advances to develop solutions for vital bio-medical applications. The devices considered are:

<p>Pressure sensors Silicon microphones Accelerometers Gyroscopes Optical MeMs and image sensors</p>	<p>Microfluidic chips Microdispensers for drug delivery Flow meters Infrared temperature sensors Emerging MeMs (rfiD, strain sensors, energy harvesting)</p>
--	--

Also addressed are the regulation aspects for medical device development.

<http://www.sensorsportal.com/HTML/BioMEMS.htm>



## Promoted by IFSA

# Gyroscopes and IMUs for Defense, Aerospace & Industrial Report up to 2017

This report highlights market share analysis by application field and technology, as well as global company shipments and technology breakdown

**Order online:**  
[http://www.sensorsportal.com/HTML/Gyroscopes\\_and\\_IMUs\\_markets.htm](http://www.sensorsportal.com/HTML/Gyroscopes_and_IMUs_markets.htm)



## Preparation and Test of Fe/Cr/Al -Ni/Cr Composite Film Micro-heater

\* Qiaohua Feng, Yunbo Shi, Mengmeng Wang, Fang Du, Lining Sun

The Higher Educational Key Laboratory for Measuring & Control Technology and Instrumentation of Heilongjiang Province, Harbin University of Science and Technology,

No. 52, Xuefu Road, Harbin, 150080, China

Tel: +86 0451-86390840, fax: +86 0451-86390840

\* E-mail: fengqiaohua80@126.com

Received: 18 June 2013 / Accepted: 25 August 2013 / Published: 30 September 2013

**Abstract:** MEMS gas sensor is one of the development directions of the sensor, and it must work at a certain temperature, so micro heater is an important part of MEMS gas sensor. In this paper, aiming at the high cost and complex process of Pt film heater, we developed the research of Fe/Cr/Al and Ni/Cr cheap metals replacing Pt metal. With Fe/Cr/Al and Ni/Cr metal as the targets respectively, Fe/Cr/Al and Fe/Cr/Al-Ni/Cr composite thin film was prepared by DC sputtering on the wafer substrate and was made into micro-heater by wet etching after heat treatment. Finally, the film was characterized by scanning electron microscope (SEM), and the performance of micro heater was test. The characterization indicated that the thickness of film was between 500 nm and 800 nm, the grain size of Fe/Cr/Al was about 40 nm. The test results showed that the change of resistance was small in the range of 0-200 °C, so the film suited to be made into micro heater. The relationship between power of micro heater and temperature of chip was linear. The ambient temperature had certain influence on the temperature of chip. In certain DC voltage conditions, when the temperature of chip was 200 °C, power consumption of 75 Ω Fe/Cr/Al-Ni/Cr composite film was less than 700 mW, and the heating rate was more than 0.5 °C/s. It can satisfy the requirement of MEMS micro gas sensor, which has research value for the substitution of Pt thin film micro heater. *Copyright © 2013 IFSA.*

**Keywords:** Composite film, Magnetron sputtering, Micro heater, MEMS sensor, Fe/Cr/Al.

### 1. Introduction

Resistive semiconductor gas sensor is highly regarded in the various types of gas sensors, after decades of change its structure develops from ceramics sintered type, thick film type to film type, array, silicon-based micro-structure type, main development trend is direction of miniaturization, integration, multi-function and low-cost.

As is well known, resistive semiconductor gas sensor needs heat treatment for a longer time before used in order to improve the stability of the sensor

and to be periodically heated at work to shorten the recovery time of the sensor, a gas usually reacts with the catalyst at a specific temperature, and a large area of the uniform temperature district is needed to ensure its selectivity and sensitivity. Metal oxide gas-sensitive element normally operates in high temperature (200 to 450 °C). The most commonly used sintered tin oxide (SnO<sub>2</sub>) gas-sensitive element works generally at 200 to 300 °C. Zinc oxide (ZnO) thin film gas sensor works at a higher temperature of 400-500 °C. The usually working temperature of the organic polymer semiconductor gas sensor is

100-200 °C. Therefore, the micro-heater is an important part of the MEMS gas sensor.

At present different material micro-heaters are extensively researched at home and abroad. A heater of Al-doped polysilicon was developed by Rong Hao and suitable for performance requirements of thermo-mechanical micro-nanofabrication of polymer materials [1]. Ni/Cr micro-heater array was manufactured on the Si substrate by Chen Sihai and the resistance was about 10  $\Omega$ , when the voltage was 10 V, the temperature could reach thousands of degrees, which could be used in MEMS chip level hermetically sealed package [2]. Cr and Ni-Cr metal film micro-heater was developed and able to meet the requirements of PCR biochip and silicon thermal distributed micro flow sensor by Professor Yan Weiping [3]. Permalloy micro heater was designed based on the principle of induction heating by Liu Bedong and had advantages of easy processing and convenient for seal [4]. RuO<sub>2</sub> heater was integrated on the aluminum oxide ceramic substrate by Bo Zikui through titration covering film formation method with a pulsed YAG laser micro-machining, the average consumption was less than 500 mW, the thermal response time was less than 20 s, and the temperature gradient was less than 5 °C/mm, which could fully collect the gas sensitive information of gas-sensitive materials [5]. SiC micro heater was used in NO gas sensors by Jae-Cheol Shim, power consumption was 13.5 mW when the chip temperature was 300 °C, and had an advantage in the high-voltage and high temperature [6]. Ni-Cr-Pt three layer metals were used to make hot-film velocity sensor by Que Ruiyi [7]. But the most widely used micro-heater was polycrystalline silicon thin-film micro-heater [8-10] and Pt film micro-heater [11-17].

Platinum is expensive, has poor adhesion of the platinum film and the silicon or silica, and needs titanium or other film as an intermediate layer, which makes the platinum resistance temperature characteristic complex [18]. Platinum is a difficult corrosive metal, the lift-off process instead of the normal wet etching process is used in the preparation of the Pt resistance, and the preparation process is complicated [19].

Fe/Cr/Al and Ni/Cr films have the advantages of easy manufacture, the relatively mature process, the small temperature coefficient of resistance, cheap and good adhesion with the silicon or silicon dioxide, can be prepared through a normal wet etching process, which has great significance to the research of micro-heater. While compared with the nickel-chromium alloy, Fe/Cr/Al alloy has the advantages of a long life, high surface load, good oxidation-resistance, small specific gravity, less influence of cold working and heat treatment on resistivity and cheap, so research of Fe/Cr/Al thin film heater is more practical.

Because the resistivity of Fe/Cr/Al was higher than Ni/Cr, in order to reduce the resistance of the film of the same film thickness and improve the heating efficiency, in this paper the Fe/Cr/Al thin

film was sputtered on the surface of nickel-chromium thin film to form Fe/Cr/Al-Ni/Cr composite film and made into micro-heater, and heating performance of micro-heater was test.

## 2. Experimental Details

### 2.1. Structure Design of the Micro-Heater

In this paper, the metal thin film heater developed was mainly used for MEMS organic semiconductor gas sensor, design of the micro-heater should make the temperature distribution as uniform as possible and the working temperature of the gas-sensitive film as 100 to 200 °C.

The structure of indirectly heated semiconductor gas sensor was shown in Fig. 1.

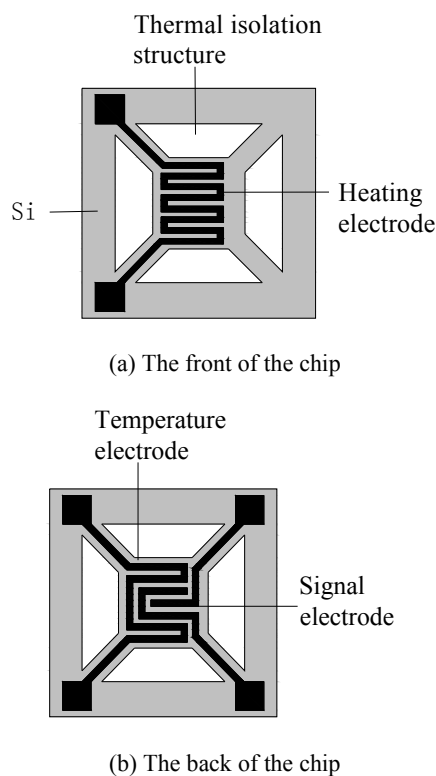


Fig. 1. The configuration diagram of micro-heater.

The configuration diagram of micro-heater herein was shown in Fig. 1 (a), the metal thin film was designed into serpentine in order that the thermal field distribution was uniform [20]. The substrate was monocrystalline with the crystal orientation (100), a thickness of 200  $\mu\text{m}$  and the size of 3 mm  $\times$  3 mm, and the surface of the wafer was deposited silicon dioxide with a thickness of 300 nm. The heating electrode was Fe/Cr/Al and Fe/Cr/Al-Ni/Cr composite film respectively, each of the strip width was 50  $\mu\text{m}$ , the spacing was 50  $\mu\text{m}$ , the size of the line was 1 mm  $\times$  50  $\mu\text{m}$ . The thermal isolation structure was isosceles trapezoid, the upper

base was 0.5 mm, and the lower bottom was 1.4 mm, and the height was 0.5 mm. The thermal isolation structure was cut by micro-laser processing and could reduce the heat exchange between the micro-heater and the substrate, energy loss and power consumption. In order to test the working temperature of the chip, temperature sensor was produced in the back of the chip and made of Pt, as shown in Fig. 1 (b). The type of temperature sensor was Pt1000. Signal electrode was used to test the resistance of sensitive material.

## 2.2. Heater Preparation Process

In the experiment iron-chromium-aluminum alloy (82 % iron, 14 % chromium, 4 % aluminum) and nickel-chromium (80 % nickel, 20 % chromium) alloy as targets were made into thin film with JGP560C ultra-high vacuum sputtering mechanism by magnetron sputtering method, magnetron sputtering could ensure alloy material component unchanged during deposition, to obtain a dense film structure and metal film was firmly bonded with the substrate.

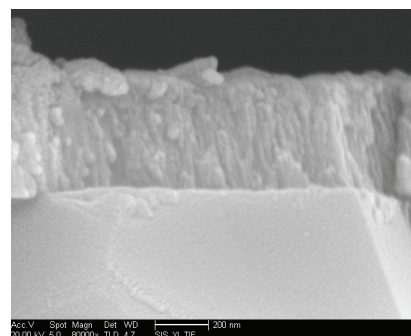
The steps of thin film resistor production process were as follows: at first, the wafer was pretreated with acetone, ethanol, deionized water for 10 min respectively through ultrasonic cleaning and dried in oven to remove the contaminants on the substrate, which enhanced the adhesion between substrate and film; then thin film of 500 nm to 800 nm was plated on a silicon wafer with a DC magnetron sputtering method, the main production process conditions of thin film were that the body vacuum was  $2 \times 10^{-5}$  Pa, striking pressure was 1.6 Pa, the working pressure was 0.5 Pa, sputtering power was 50 W and sputtering time was about 1-2 h; Fe/Cr/Al and Ni-Cr thin film needed to be heat-treated at 400 °C for 3 hours, components of the alloy were diffused each other and lattice defects could also be eliminated, which improved the thermal stability of thin-film, eliminated internal stress, and enhanced the adhesion of the film and the substrate, eliminated the adsorption of the gas molecules in the film and protected the film from contamination and corrosion; after that the resistance pattern was made through the wet etching process with the homemade etching liquid and thermal isolation structure on the chip was cut by micro-laser processing; finally leads were welded and heating performances were test.

## 3. Results and Analysis

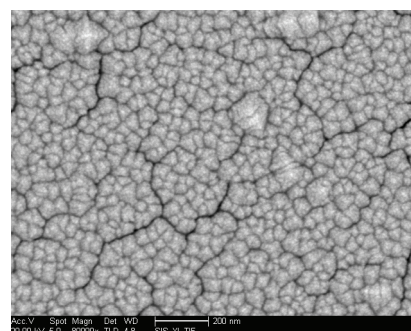
### 3.1. Analysis of Film Performance

The scanning electron micrographs were obtained by Quanta 200 scanning electron microscope. Fig. 2 was a scanning electron micrograph of the Fe/Cr/Al film (sputtering power of 50 W, the sputtering time of 2 h). Film thickness was about 600 nm and particles

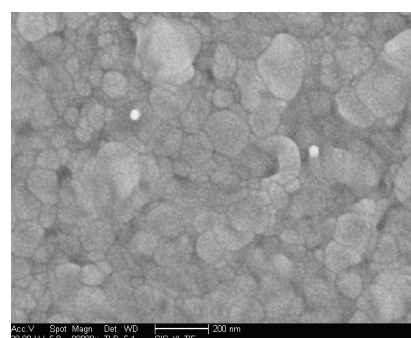
arranged neatly as shown in Fig. 2 (a). Film surface was made of particles arranged compactly and uniformly, the particle was about 40 nm (the sizes of Fe, Cr and Al particles were different), there were no voids, high flatness and cracking stripes on the film surface as shown in Fig. 2 (b); the size of grain in the film grew after the heat treatment, cracking of film surface was improved, and the flatness of the film was also improved, as shown in (c), at the same time, after the annealing treatment, the resistance of the metal thin film was the stable which was conducive to the performance test of the heater.



(a) Fracture



(b) Surface



(c) After heat treatment

Fig. 2. The SEM pictures of Fe/Cr/Al film.

### 3.2. Analysis of Heater Performance

In order to understand whether the Fe/Cr/Al and Fe/Cr/Al-Ni/Cr composite metal thin-film heater prepared in this paper could meet the requirements

above, the heaters with different resistances were put into TEMI880 high and low temperature alternating experimental box to test the heating effect. In the experiment the different resistances of heaters were obtained by changing the thickness of Fe/Cr/Al film or Ni/Cr film.

### 3.2.1. Temperature Stability of Film Resistivity

Temperature stability of the film resistivity was discussed from the two aspects of the characteristics of resistance with the change of temperature and the relationship between the heating voltage and heating current, respectively.

Metal film heaters required the resistivity varied as little as possible with the temperature and had high stability [3]. Fig. 3 was a characteristic curve of the heater resistance with the change of temperature, A, B, C were Fe/Cr/Al thin-film resistors, and D, E were the Fe/Cr/Al-Ni/Cr composite thin film resistors. Within 0-150 °C the resistance value of the all heaters changed little and was relatively stable. The highest test temperature of high and low temperature alternating experimental box used in this experiment was 150 °C, therefore the resistance change within 150 °C was only test.

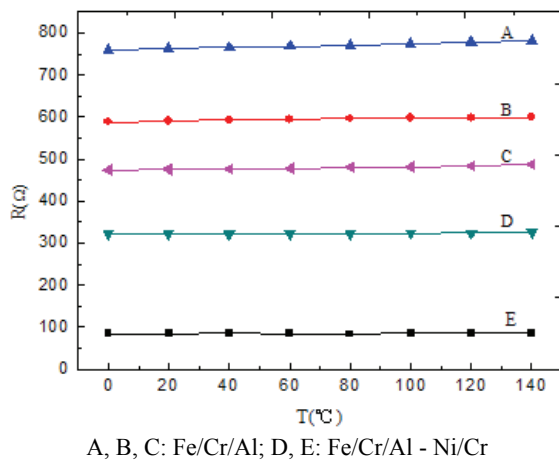


Fig. 3. The curve of resistance changing with temperature.

Fig. 4 was the relationship curve between the heating voltage and heating current of the four different resistance heaters working properly at constant ambient temperature of 25 °C. As can be seen from Fig. 4, the relationship between the heating voltage and heating current was approximately linear, i.e. when the heater was loaded the input voltage, the resistance change was little and relatively stable; and under the same voltage, smaller the resistance of the heater, the greater the heater power consumption increased, and the faster the temperature rose.

From above, the resistivity of Fe/Cr/Al thin film and Fe/Cr/Al-Ni/Cr composite thin film was stable,

and varied little with the change of temperature of environment and the heating voltage loaded, therefore, they were suitable for heater.

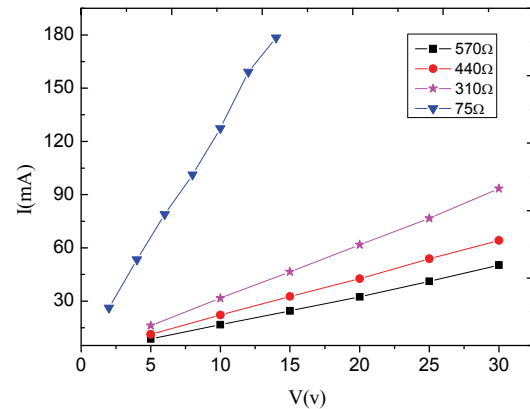


Fig. 4. The relation of voltage and current.

### 3.2.2. Thermal Power Characteristics of the Thin Film Heater

When the thermal power of the heaters was different, the highest temperature of the chip was test in order to control the temperature of chip through the heater power. Thermal power characteristics of the thin film heater was discussed from the three aspects of the relationships between the heating voltage and the chip temperature, power consumption and chip temperature, the influence of ambient temperature on the chip temperature, respectively.

Fig. 5 was a relationship curve of the heating voltage and chip temperature at constant ambient temperature of 25 °C, the resistor of 75 Ω was Fe/Cr/Al-Ni/Cr composite film resistor, and the rest were Fe/Cr/Al thin film resistors. As shown in Fig. 5, all the heaters could reach 200 °C under a certain voltage, while at the same voltage, the smaller the resistance, the higher the temperature of the heater would be. Therefore, in order to meet the requirements of the MEMS gas sensor working at a low voltage, the resistance value of the heater was reduced. Because the resistivity of the Fe/Cr/Al thin film was relatively large, on the basis of without increasing the thickness of the film, the Fe/Cr/Al-Ni/Cr composite film was used to achieve a low resistance value. The rate of chip warming up was greater than 0.5 °C/s.

Fig. 6 was the relationship curve of the heater power of different resistance and chip temperature at constant ambient temperature of 25 °C, the temperature of the chip increased gradually with the increase of power consumption of the heater, the relationship between the heater power and the chip temperature was approximately linear; under the same power consumption the lower the resistor value, the higher the temperature was; when the chip

temperature needed to achieve 200 °C, power consumption of 75  $\Omega$  Fe/Cr/Al-Ni/Cr thin film was less than 700 mW, while the power consumption of 310  $\Omega$  Fe/Cr/Al film was nearly 800 mW, moreover, in order to achieve the same working temperature, the power of both heater was greater than the Pt thin-film heater [6], which because the Fe/Cr/Al film resistor value was larger.

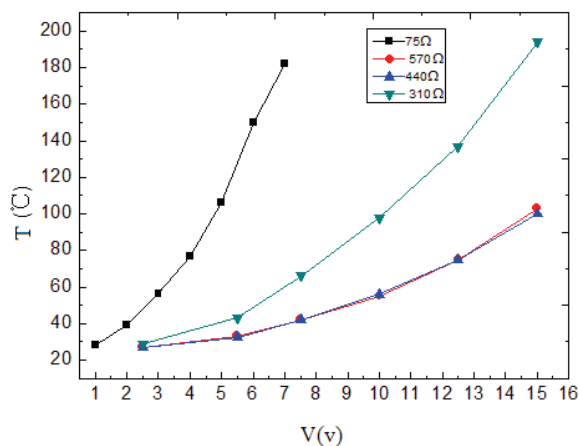


Fig. 5. The relation of voltage and temperature.

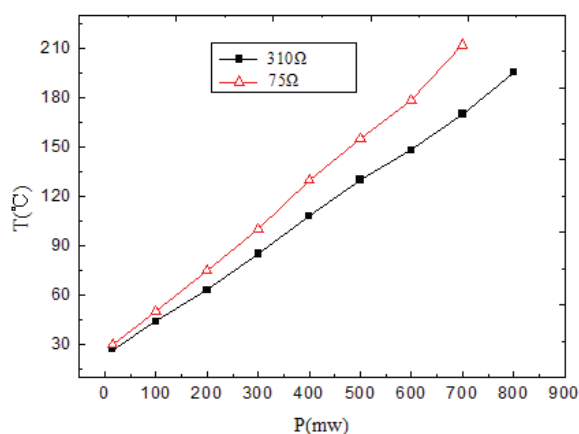


Fig. 6. The relation of power and temperature.

Fig. 7 was the relationship curve of the 570  $\Omega$  Fe/Cr/Al thin film heater power and chip temperature at ambient temperature of -20 °C and 25 °C respectively. As shown in Fig. 7, the influence of ambient temperature on the heater was great, under the same power consumption, chip temperature at 25 °C of ambient temperature was higher than the chip 45 °C at -20 °C of ambient temperature, which was just the temperature difference of the two environments; at the different ambient temperatures, the relation of the heater power and the chip temperature was still linear, and with the increase of power consumption, two heater temperatures increased at the same rate. Therefore, when the micro-sensor worked in different environments, we must take into account the impact of ambient temperature on the heater, that is to say we must take

into account the temperature difference between the environment and at room temperature in order to adjust the power consumption of the micro heater to achieve the desired operating temperature.

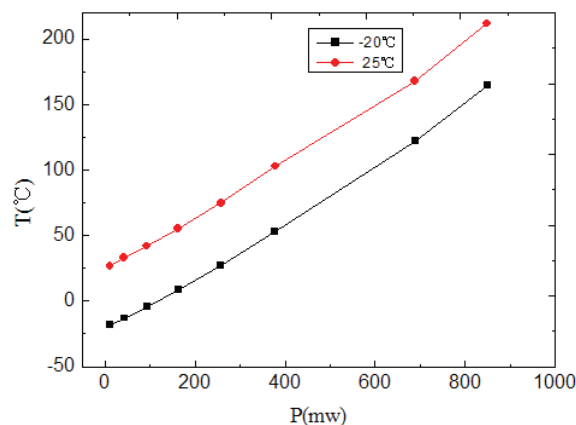


Fig. 7. The relation of power and temperature under different ambient temperature.

#### 4. Discussion

As shown from temperature stability of the composite film resistivity discussed above, for the thin film process, micro heater film was doped low-resistance metal to form composite film, temperature stability of the composite film resistivity varies little, which can reduce resistivity of micro heater film, and reduce the thickness of micro heater film, which has practical significance for reducing costs of micro heater and simplifying preparation process of micro heater.

As shown from the thermal power characteristics of the thin film heater discussed above, the temperature of chip was related to the environment temperature, the resistance of the chip and the heating voltage. According to the energy conservation, in order to maintain a system a certain temperature the power consumption of heater is determined by heat dissipation. Therefore, the environment temperature is different, the heat dissipation system is different, and therefore power required is different in order to maintain the same temperature. While the voltage and the environment temperature are constant, the smaller the resistance, the greater heating power and the higher the equilibrium temperature reached.

It was tested in the experiments that the resistance of the heater did not vary with temperature and the heating voltage, so as long as the heating voltage was constant, power consumption of heater was constant, and the relationship of the thermal power and chip temperature was established by experiments, thus the relationship curve between the heating voltage and the chip temperature can be established, so we can easily know the temperature of the chip through the heating voltage level.

## 5. Conclusions

In this paper, aiming at the high cost and complex process of precious metal Pt thin film heater, we selected the Fe/Cr/Al and Ni-Cr cheap metal to prepare micro-heater. The Fe/Cr/Al thin film resistivity varied little with temperature and the heater could reach 200 °C in a certain DC voltage conditions, but because of the large resistance value, high voltage was needed to reach the desired temperature. Therefore, in order to reduce the film resistance, on the basis of without increasing the thickness of the film, the Ni-Cr film was coated on the surface of Fe/Cr/Al film to form the Fe/Cr/Al-Ni/Cr composite film, whose resistivity varied little with temperature either and was suitable for micro-heater. The experimental results were as follows: 75 Ω Fe/Cr/Al-Ni/Cr composite thin-film heater in 700 mW power consumption could reach 200 °C, and the heating rate was greater than 0.5 °C/s; the influence of ambient temperature on the micro-heater temperature was great, so the temperature difference between the environment and room temperature should be considered to adjust the power consumption of the micro-heater to achieve the desired operating temperature at the non-room temperature. In general, the Fe/Cr/Al and Ni-Cr cheap metal thin-film heater could meet the requirements of the MEMS micro gas sensor and had certain significance for replacing precious metals Pt thin-film heater.

## Acknowledgements

Thanks the support of Key Projects from Natural Science Foundation of Heilongjiang Province (No. ZD201217), Technological Innovation Talent Research Special Funds of Harbin (No. 2010RFXXG009), and Youth Scientific Research Fund of Harbin University of Science and Technology (No. 2011YF028).

## References

- [1]. Rong Hao, Zhao Gang, Chu Jiaru, Al doped poly-Si micro-heater for thermomechanical fabrication of micro/nano structure, *Optics and Precision Engineering*, Vol. 19, Issue 1, 2011, pp. 124-131.
- [2]. Chen Sihai, Chen Mingxiang, Yi Xinjian, et al., Design and fabrication of microheater array for MEMS wafer-level scale hermetic package, *Micronanooelectronic Technology*, Issue 7/8, 2003, pp. 249-250.
- [3]. Yan Weiping, Zhu Jianbo, Ma Lingzhi, et al., Research of Metal Membrane Heater, *Chinese Journal of Sensors and Actuators*, Issue 4, 2004, pp. 615-618.
- [4]. Liu Bendong, Jiao Bingfeng, Li Desheng, Design of Micro Heater Based on Induction Heating, *Chinese Journal of Scientific Instrument*, Vol. 31, Issue 8, 2010, pp. 48-51.

- [5]. Bai Zikui, Wang Aihua, Xie Changsheng, Experimental Study of the Integrated Nano Gas Sensor Arrays Fabricated by Laser Micro-Machining and Their Corresponding Characteristics, *Chinese Journal of Sensors and Actuators*, Issue 4, 2004, pp. 655-659.
- [6]. Jae-Cheol Shim, Gwi-Sang Chung, Fabrication and Characteristics of Pt/ZnO NO Sensor Integrated SiC Micro Heater, in *Proceedings of the Conference on 9th IEEE Sensors Conference (SENSORS 2010)*, Waikoloa, HI, United States, November 1-4, 2010, pp. 350-353.
- [7]. Que Ruiyi, Zhu Rong, Liu Peng, et al., Combined hot-film anemometers for measuring flow speed vectors, *Optics and Precision Engineering*, Vol. 19, Issue 1, 2011, pp. 103-109.
- [8]. P Kahroba, I Mirzaee, P Sharifi, et al., The microcavity-based micro-heater: an optimum design for micro-heaters, *Microsyst. Technol.*, Issue 14, 2008, pp. 705-710.
- [9]. Wen-Chie Huang, Chung-Nan Chen, Shang-Hung Shen, et al., Study of the Annealing Effect of Low-Temperature Oxide on the Etch Rate in TMAH Solutions for Micro-Heater Applications, in *Proceedings of the IEEE Conference on 3rd International Conference on Nano/Molecular Medicine and Engineering (NANOMED 2009)*, Tainan, Taiwan, October 18-21, 2009, pp.175-179.
- [10]. Ching-Liang Dai, Mao-Chen Liu, Nanoparticle SnO<sub>2</sub> Gas Sensor with Circuit and Micro Heater on Chip Fabricated Using CMOS-MEMS Technique, in *Proceedings of the IEEE Conference on the 2nd International Conference on Nano/Micro Engineered and Molecular Systems*, 2007, pp. 959-963.
- [11]. Wang Junqing, Wu Cinan, Zhang Pu, et al., Study on Characterization of Micro Heater Used for Micro PCR Chip, *Semiconductor Technology*, Vol. 37, Issue 6, 2012, pp. 442-447.
- [12]. Bobby Reddy, Oguz H. Elibol, Pradeep R. Nair, et al., Silicon Field Effect Transistors as Dual-Use Sensor-Heater Hybrids, *Anal. Chem.*, Issue 83, 2011, pp. 888-895.
- [13]. S. E. Moon, J.-W. Lee, N.-J. Choi, et al., High-response and Low-power-consumption CO Micro Gas Sensor Based on Nano-powders and a Micro-heater, *Journal of the Korean Physical Society*, Vol. 60, Issue 2, 2012, pp. 235-239.
- [14]. Hyung-Kun Lee, Seung Eon Moon, Nak-Jin Choi, et al., Fabrication of a HCHO Gas Sensor Based on a MEMS Heater and Inkjet Printing, *Journal of the Korean Physical Society*, Vol. 60, Issue 2, 2012, pp. 225-229.
- [15]. Prasad Mahanth, Yadav R. P., Sahula V., et al., Design and simulation of double-spiral shape micro-heater for gas sensing applications, *Sensors & Transducers*, Vol. 129, Issue 6, June 2011, pp. 135-141.
- [16]. Liu Zewen, Tian Hao, Liu Chong, Experiment and thermal calculation of micro heater, *Optics and Precision Engineering*, Vol. 19, Issue 3, 2011, pp. 612-619.
- [17]. Xue Yanbing, Tang Zhenan, Gas sensor array based on ceramic micro-hotplate for flammable gas detection, *Optics and Precision Engineering*, Vol. 20, Issue 10, 2012, pp. 2200-2206.
- [18]. Ting Xu, Hui Li, Zhihong Wang, et al., A Novel Method of Growing Aligned Carbon Nanotubes at Low Temperature by Using Integrated Micro-Heater,

in *Proceedings of the 58<sup>th</sup> Conference on Electronic Components and Technology Conference (ECTC)*, Lake Buena Vista, FL, United States, May 27-30, 2008, pp. 1395-1399.

- [19]. Zhao Wenjie, Zhou Zhen, Shi Yunbo, *et al.*, Study on Si-based Plate Microstructure Gas Sensor Integrated with Temperature Sensor, in *Proceedings of the 4<sup>th</sup> Conference on International Symposium on Computational Intelligence and Industrial*

*Applications (ISCIA 2010)*, Harbin, China, August 2-8, 2010, pp. 279-282.

- [20]. Sidek, M. Z. Ishak, M. A. Khalid, *et al.*, Effect of Heater Geometry on the High Temperature Distribution on a MEMS Micro-hotplate, in *Proceedings of the 3<sup>rd</sup> Asia Symposium on Quality Electronic Design (ASQED 2011)*, Kuala Lumpur, Malaysia, July 19-20, 2011, pp. 100-104.

2013 Copyright ©, International Frequency Sensor Association (IFSA). All rights reserved.  
(<http://www.sensorsportal.com>)

## MEMS Energy Harvesting Devices, Technologies and Markets, 2009

**Market drivers analysis for challenges that go beyond energy density!**

*This report focuses on MEMS energy harvesting devices from both technology and market points of view.*

*Executive summary*

1. Introduction to micropower & energy harvesting technologies
2. Technology review – energy harvesting technologies
3. Technology review – energy storage technologies
4. Applications Energy harvesting devices

**IFSA offers  
a SPECIAL PRICE**

[http://www.sensorsportal.com/HTML/MEMS\\_Energy\\_Harvesting\\_Devices.htm](http://www.sensorsportal.com/HTML/MEMS_Energy_Harvesting_Devices.htm)



Promoted by IFSA

## Status of the MEMS Industry Report up to 2017

Report includes MEMS device markets, key players strategies, key industry changes and MEMS financial analysis. It also includes major MEMS manufacturing evolutions as well as an update on the “emerging” MEMS device markets.

Order online:

[http://www.sensorsportal.com/HTML/Status\\_of\\_MEMS\\_Industry.htm](http://www.sensorsportal.com/HTML/Status_of_MEMS_Industry.htm)

## Digital Double-loop PID Controller for Inverted Pendulum

Ming Li

College of Mathematics & Computer Science, Wuhan Textile University, Wuhan, 430070, China

Tel.: 0086-27-59367297

E-mail: lettermail.lm@gmail.com

Received: 5 June 2013 /Accepted: 25 August 2013 /Published: 30 September 2013

---

**Abstract:** Inverted pendulum system is a complicated, unstable and multivariable nonlinear system. In order to control the angle and displacement of inverted pendulum system effectively, a novel double-loop digital PID control strategy is presented in this paper. Based on impulse transfer function, the model of the single linear inverted pendulum system is divided into two parts according to the controlled parameters. The inner control loop that is formed by the digital PID feedback control can control the angle of the pendulum, while in order to control the cart displacement, the digital PID series control is adopted to form the outer control loop. The simulation results show the digital control strategy is very effective to single inverted pendulum and when the sampling period is selected as 50 ms, the performance of the digital control system is similar to that of the analog control system. Copyright © 2013 IFSA.

**Keywords:** Inverted pendulum, Double-loop PID control, Digital control, Sampling period.

---

### 1. Introduction

In the development of control theory, the correctness and feasibility of the theory must be validated by a typical object. The inverted pendulum system, which can reflect some problems in control systems such as nonlinearity, robustness, stabilization, and following control, etc., is an ideal platform to carry out these experiments. The rocket's flight control can be simplified as an inverted pendulum system, so as the step robot control and the satellite attitude control. Therefore it has remarkably theoretical and practical significances to research how to control inverted pendulum systems.

Inverted pendulum is a kind of complicated, unstable and multivariable nonlinear system. There are many types of inverted pendulum systems. According to the shapes of the inverted pendulum, there have linear type and ring type etc.; according to

stage numbers, there have single, double and multi-stage inverted pendulum systems; but according to the types of control electric motor, there have single motor, multi motors etc. [1-3]. From 1960 s, there are increasingly interests to research inverted pendulum systems. L. F. Sun *et al.* [3] introduced some control methods for inverted pendulum and holded that intelligent control method is better than linear control method. Some researchers [4-8] have developed some control strategies for the cart-pole inverted pendulum system using fuzzy logic controller. Siuka *et al.* [9] deals with the application of energy based control methods for the inverted pendulum on a cart model and presented a swing up controller. There have been some studies [10-12] on PID methods for the purpose of balance control of inverted pendulum system. Also, some other people [13, 14] have researched the adaptive control problems of inverted pendulum systems. Aguilar-Ibanez *et al.* [15] present

an output feedback stabilization method for the Inverted Pendulum Cart system around its unstable equilibrium point, and adapt an observer based controller devoted to render the closed-loop system to the origin. Mladenov [16] had used two Neural Network controllers to swing a pendulum attached to a cart from an initial downwards position to an upright position. But this works are based on state-space representation, were focused on the analog PID controller which can't be implemented by the computer program easily.

In this paper, under considering there exits the cart's friction, in order to control the displacement of the cart of the inverted pendulum system meanwhile guaranteeing the pendulum verticality, the model of the single inverted pendulum system is divided into two parts based on impulse transfer function. A novel double-loop digital PID control strategy and how to choose its sampling period are researched in this paper. Finally Use matlab/simulink to verify the performance of the presented control strategy.

## 2. Model of Linear Inverted Pendulum System

The single inverted pendulum system consists of a cart and a pendulum, as Fig. 1 (a) shows.

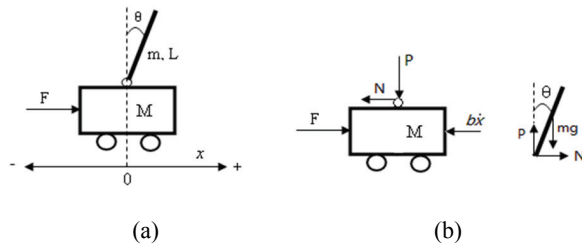


Fig. 1. Single inverted pendulum system.

By ignoring the air friction and some minor fictions, the force diagrams of the cart and the pendulum are shown as Fig. 1 (b), where  $M$  is the cart mass,  $x$  is the cart position,  $F$  is the force impacted on the cart,  $b$  is the cart friction coefficient,  $m$  is the pendulum mass,  $2L$  is the pendulum length,  $\theta$  is the included angle between the pendulum and the vertical direction, and  $I$  is the pendulum rotary inertia.

The dynamic models of the single inverted pendulum system are nonlinear differential equations. If selecting the working points  $\theta_0 = 0$ ,  $x_0 = 0$  and linearizing the system, we have the simplified mathematical models of the inverted pendulum system. They are:

$$\begin{cases} (I + ml^2)\ddot{\theta} + ml\ddot{x} = ml g \theta \\ (M + m)\ddot{x} + b\dot{x} + ml\ddot{\theta} = F \end{cases} \quad (1)$$

The transfer function of the linear inverted pendulum is:

$$\begin{aligned} G(s) &= \frac{X(s)}{F(s)} = \\ &= \frac{ml g - (I + ml^2)s^2}{-(MI + Mml^2 + ml)s^4 - b(I + ml^2)s^3 + (M + m)mlgs^2 + bmlgs} \end{aligned} \quad (2)$$

The control goal of the linear inverted pendulum is to make the horizontal displacement of the cart controllable while guaranteeing the pendulum verticality. This problem is a type of classic control systems with one input (external force  $F$ ) and two outputs (angle of pendulum  $\theta$  and car displacement  $x$ ). In order to control two output parameters effectively, we must establish the mathematical model of the linear inverted pendulum. According to formula (2), we can get two transfer functions for two controllable parameters.

$$\begin{aligned} G_1(s) &= \frac{\theta(s)}{F(s)} = \\ &= \frac{mls}{-(MI + Mml^2 + ml)s^3 - b(I + ml^2)s^2 + (M + m)mlgs + bmlg} \end{aligned} \quad (3)$$

$$G_2(s) = \frac{X(s)}{\theta(s)} = \frac{ml g - (I + ml^2)s^2}{mls^2} \quad (4)$$

## 3. PID Controller

The PID controller consists of three components that are proportion, integral and differential. The mathematical expressions are

$$u(t) = K_p \left\{ e(t) + \frac{1}{T_I} \int e(t) dt + T_D \frac{de(t)}{dt} \right\}, \quad (5)$$

$$D(s) = \frac{U(s)}{E(s)} = K_p \left( 1 + \frac{1}{T_I s} + T_D s \right) = K_p + \frac{K_I}{s} + K_D s$$

where

$$K_I = \frac{K_p}{T_I}, K_D = K_p T_D \quad (6)$$

If  $T$  denotes the sampling period, we can conclude the positional PID controller as

$$u(k) = K_p' e(k) + K_I' \sum_{j=0}^k e(j) + K_D' [e(k) - e(k-1)], \quad (7)$$

where

$$K_p' = K_p, K_I' = K_p \frac{T}{T_I} = TK_I, K_D' = K_p \frac{T_D}{T} = \frac{K_D}{T} \quad (8)$$

According to Z transformation, we can get the impulse transfer function of the digital PID controller

$$D(z) = \frac{U(z)}{E(z)} = \frac{(K'_p + K'_i + K'_D)z^2 + (-K'_p - 2K'_D)z + K'_D}{z^2 - z} \quad (9)$$

The block diagram of single-loop analog PID control system is shown in Fig. 2 that can only control the displacement  $x$  of the car.

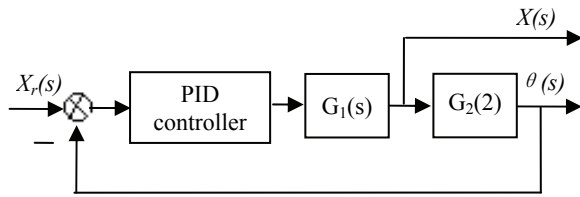


Fig. 2. Single-loop PID control system for single inverted pendulum.

and two outputs, we can divide the mathematical model into two parts, as shown in equations (3) and (4). When we use the double-loop PID controller, the inner loop controls the pendulum angle and the outer loop controls the cart horizontal position.

Fig. 3 shows the block diagram of the analog double-loop PID control system. In order to simplify the computation, two PID controllers are all designed as PD controllers. An amplifier  $G$  is placed in the inner loop in order to suppress interference and unit negative feedback is used in the outer loop in order to obtain better following performance.

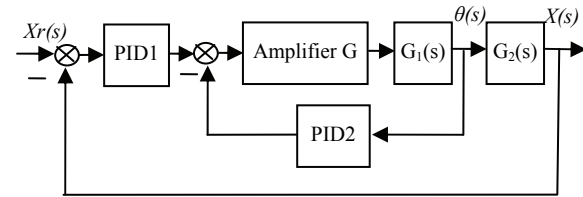


Fig. 3. Analog double-loop PID control system for inverted pendulum.

#### 4. Double-loop Digital PID Controller

As to single-loop PID control system, three components, the proportion, integral, differential, are located in the forward channel of control system. But as to double-loop PID control system, a PID controller and the object can form an inner loop that can make the unstable object stable; in the forward channel of the control system, another PID controller and the object form an outer loop that can make the control system have the expected performance [17]. Because the single inverted pendulum has one input

Although the analog double-loop PID controllers can make the performance of the inverted pendulum system good, they can't be implemented by computer easily and their development cost is very expensive. Therefore we must design a digital controller that can make the performance of the inverted pendulum control system meet the control requirements. Based on the analog double-loop PID control system, we can get the control strategy of the digital double-loop controller using sampling control theory that is illustrated in Fig. 4.

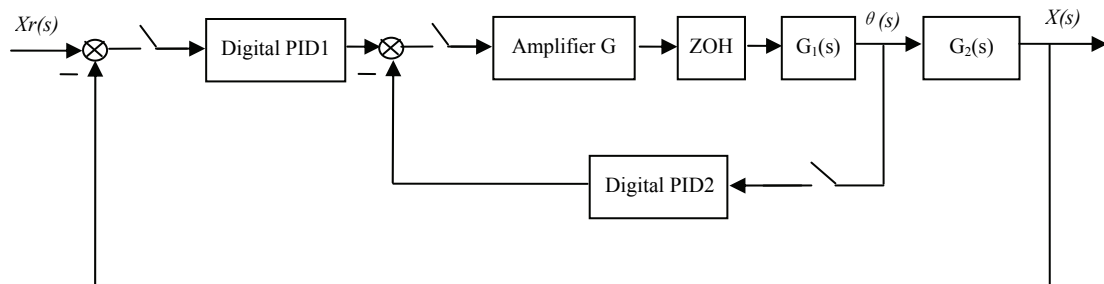


Fig. 4. Structure of digital double-loop PID control system for inverted pendulum.

The sampling period  $T$  is a very important parameter in digital control system. We must choose the sampling period according to the performance requirements and the development cost of the digital control systems. When the sampling period is larger, the demands for the operation speed of computers are lower, so it is helpful to cut down the cost of digital controllers, but too large sampling period will degrade the performance of control systems. While the sampling period is smaller, the performance of

digital control systems will be improved, but the demands for the operation speed of computers are higher, which lead to increase the development cost of digital control systems. Furthermore, excessive sampling period has little help to improve the control performance. Therefore the sampling period  $T$  must be chosen correctly. In this paper, we suppose the inner loop and the outer loop in the digital double-loop control system have the same sampling period.

## 5. Simulation Analysis

In order to compare and analyze the control results of these control strategies for linear inverted pendulum, Matlab/Simulink [18] is used to simulate. Suppose the parameters of the linear inverted pendulum are:  $M=1$  kg,  $m=1$  kg,  $2L=0.6$  m,  $b=0.1$  N/m.s,  $I=0.03$  kg.m<sup>2</sup>. From equations (2), (3) and (4), we can get:

$$G(s) = \frac{X(s)}{F(s)} = \frac{-0.12s^2 + 3}{-0.15s^4 - 0.012s^3 + 6s^2 + 0.3s}$$

$$G_1(s) = \frac{\theta(s)}{F(s)} = \frac{0.3s}{-0.15s^3 - 0.012s^2 + 6s + 0.3}$$

$$G_2(s) = \frac{X(s)}{\theta(s)} = \frac{-0.12s^2 + 3}{0.3s^2}$$

The analog single-loop PID control system, illustrated in Fig. 2, can be simulated by Simulink. The simulation results show that no matter how to modify the parameters  $K_P$ ,  $K_I$  and  $K_D$  of the controller, the control system is always unstable, which proves the single-loop PID controller isn't fit for the control of this type of inverted pendulum system.

When simulation of analog double-loop PID control system for the linear inverted pendulum, we set the parameters of the control system as  $K_{p1}=0.12$ ,  $K_{D1}=0.12$ ,  $K_{p2}=1.625$ ,  $K_{D2}=0.175$  and  $G=-32$ . Then the step response of the control system can be get in Fig. 5, from which we can conclude that for the pendulum angle, the overshoot is 12.33 % and the setting time is 3.12 s ( $\pm 2\%$ ); as to the cart position, the overshoot is 15.55 % and the setting time is 6.15 s ( $\pm 2\%$ ). The results show the analog double-loop PID controller is effective to control the linear inverted pendulum system.

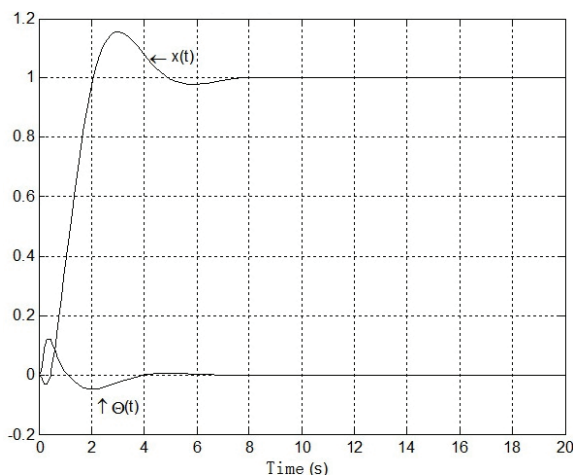


Fig. 5. Step response of analog double-loop PID control system.

In order to obtain the control results of digital double-loop PID control system, set the sampling period  $T$  as 100 ms, 90 ms, 80 ms, 50 ms, 10 ms and 5 ms respectively. According to equation (8), the parameters of the digital PID controller will be obtained directly from the analog PID controller. The results are shown in Table 1.

Table 1. Parameters of the digital PID controller.

Sampling period $T$	Digital PID1		Digital PID2	
	$K_{P1}'$	$K_{D1}'$	$K_{P2}'$	$K_{D2}'$
100 ms	0.12	1.2	1.625	1.75
90 ms	0.12	1.33	1.625	1.94
80 ms	0.12	1.5	1.625	2.19
50 ms	0.12	2.4	1.625	3.5
10 ms	0.12	12	1.625	17.5
5 ms	0.12	24	1.625	35

When  $T$  is set as 100 ms, the simulation result is shown in Fig. 6 (a). While  $T$  is set as 90 ms and 80 ms, the results can be seen in Fig. 6 (b). The Fig. 6 (c) is the simulation results when  $T$  is set as 50 ms, 10 ms and 5 ms.

From the simulation results, we can get the performance indexes of the digital double-loop PID control system as Table 2 shows.

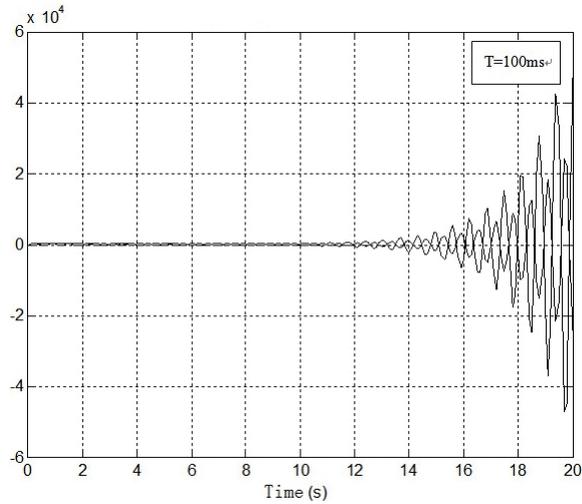
Table 2. Performance indexes of the digital double-loop control system.

Sampling period	Cart position $x$		Pendulum angle $\theta$	
	Over-shoot	Setting time	Over-shoot	Setting time
100 ms	Unstable	Unstable	Unstable	Unstable
90 ms	85.5 %	33.03 s	104.7 %	40.23 s
80 ms	50.6 %	5.92 s	103.02 %	4.64 s
50 ms	38.2 %	6.05 s	82.3 %	2.4 s
10 ms	38.5 %	6.13 s	60.7 %	2.46 s
5 ms	38.5 %	6.14 s	59 %	2.46 s

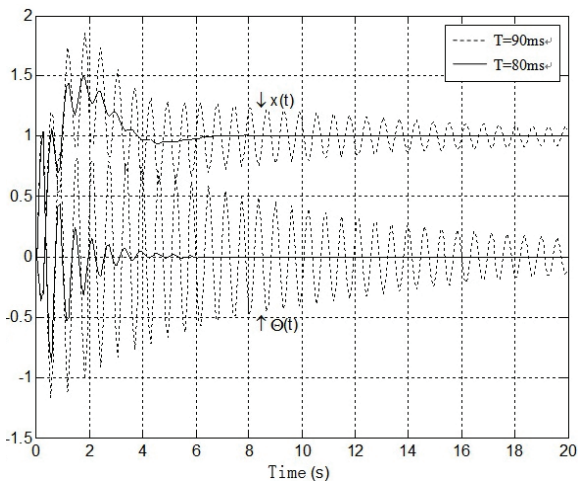
From Table 2, we can conclude that when  $T=100$  ms the digital control system is unstable; When  $T=90$  ms the control system become stable, but the performances are very bad which means the control system has little practical value; when  $T=80$  ms, the system performances is improved greatly. When  $T$  is between 5 ms and 50 ms, we can see that the performances of the digital control system have little change and are very similar to those of the analog double-loop control system.

The simulation results further prove that when the analog control system is transformed into the digital control system, the system performances will degrade. So we must select the sampling time  $T$  correctly when we use digital control system. As to the single inverted pendulum, the controlled

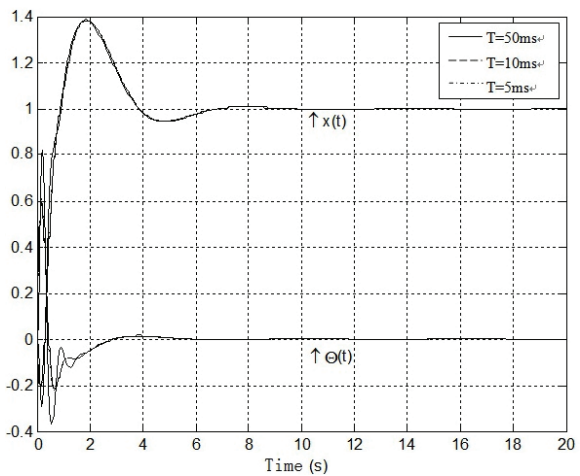
parameter  $\theta$  changes very quickly, so it is better that the sampling time  $T$  is set as 50 ms. Finally we can conclude that the digital double-loop PID controller is a good solution to control the single inverted pendulum system.



(a)



(b)



(c)

Fig. 6. Step responses of digital PID controller.

## 6. Conclusions

The inverted pendulum system is a complicated, unstable and multivariable nonlinear system that can reflect many typical problems in control systems, so researching inverted pendulum control system has remarkably theoretical and practical significance. Because the digital controller can be easily implemented by the computer program, it is a cheap controller and has very high practical value. The research results in this paper show: the single-loop PID controller is not suitable to control the single inverted pendulum that is unstable and has one input and multiple outputs. As to this type of problems, the controlled objects can be divided into different parts according to the numbers of the controlled parameters and also different mathematical models should be established. The digital double-loop PID controller is a good solution for the single inverted pendulum with one input and two outputs. For the controlled parameter  $\theta$  changes very quickly, it is a good way that the sampling time  $T$  is set as 50 ms in order that the digital control system has good performance and cheaper cost.

## References

- [1]. H. M. Liu, C.-F. Zhang, Stability Control and realization of single link rotary inverted pendulum on LQR controller, *Journal of Central South University (Science and Technology)*, Vol. 43, Issue 9, 2012, pp. 3496-3501.
- [2]. H. Ashrafiuon, A. M. Whitman, Closed-loop dynamic analysis of a rotary inverted pendulum for control design, *Journal of Dynamic Systems, Measurement and Control, Transactions of the ASME*, Vol. 134, Issue 2, 2012.
- [3]. L. F. Sun, H. Kong, C. G. Liu, Overview of the control of the inverted pendulum system, *Machine Tool & Hydraulics*, Vol. 36, 2008, pp. 306-310, 313.
- [4]. S. Kizir, Z. Bingul, C. Oysu, Fuzzy control of a real time inverted pendulum system, *Journal of Intelligent & Fuzzy Systems*, Vol. 21, 2010, pp. 121-133.
- [5]. M. K. B. M., Nor, S. Okubo, Fuzzy servo control of an inverted pendulum system, *Artificial Life and Robotics*, Vol. 17, Issue 2, 2012, pp. 245-250.
- [6]. C. H. Huang, W. J. Wang, C. H. Chiu, Design and implementation of fuzzy control on a two-wheel inverted pendulum, *IEEE Transactions on Industrial Electronics*, Vol. 58, Issue 7, 2011, pp. 2988-3001.
- [7]. D. Wang, S. Wu, L. Zhang, et al., Study of inverted pendulum robot using fuzzy servo control method, *International Journal of Advanced Robotic Systems*, 2012.
- [8]. H. L. Bui, D. T. Tran, N. L. Vu, Optimal fuzzy control of an inverted pendulum, *Journal of Vibration and Control*, Vol. 18, Issue 14, 2012, pp. 2097-2110.
- [9]. A. Siuka, M. Schöberl, Applications of energy based control methods for the inverted pendulum on a cart, *Robotics and Autonomous Systems*, Vol. 57, 2009, pp. 1012-1017.
- [10]. A. Ghosh, T. R. Krishnan, B. Subudhi, Robust proportional-integral-derivative compensation of an

- inverted cart-pendulum system: An experimental study, *IET Control Theory and Applications*, Vol. 6, Issue 8, 2012, pp. 1145-1152.
- [11]. S. Y. Yang, L. P. Xu, P. J. Wang, Study on PID control of a single inverted pendulum system, *Control Engineering of China*, Vol. 14, 2007, pp. 23-24,53.
- [12]. T. C. Kuo, Y. J. Huang, B. W. Hong, Adaptive PID with sliding mode control for the rotary inverted pendulum system, in *Proceedings of the IEEE/ASME International Conference on Advanced Intelligent Mechatronics*, Singapore, Singapore, 14-17 July 2009, pp. 1793-1798.
- [13]. S. Rudra, R. K. Barai, Robust adaptive backstepping control of inverted pendulum on cart system, *International Journal of Control and Automation*, Vol. 5, Issue 1, 2012, pp. 13-26.
- [14]. M. Fallahi, S. Azadi, Adaptive control of an inverted pendulum using adaptive PID neural network, in *Proceedings of International Conference on Signal Processing Systems*, Singapore, Singapore, 15-17 May 2009, pp. 589-593.
- [15]. C. Aguilar-Ibanez, M. S. Suarez-Castanon, N. Cruz-Cortes, Output feedback stabilization of the inverted pendulum system: a Lyapunov approach, *Nonlinear Dynamics*, Vol. 70, Issue 1, 2012, pp. 767-777.
- [16]. V. Mladenov, Application of neural networks for control of inverted pendulum, *WSEAS Transactions on Circuits and Systems*, Vol. 10, Issue 2, 2011, pp. 49-58.
- [17]. S. J. Song, J. L. Liu, Z. H. Zhang, A simple method for improving the performance of PID controller, *Drive and Control*, Issue 5, 2007, pp. 32-35.
- [18]. J. J. Wang, Simulation studies of inverted pendulum based on PID controllers, *Simulation Modelling Practice and Theory*, Vol. 19, Issue 1, 2011, pp. 440-449.

---

2013 Copyright ©, International Frequency Sensor Association (IFSA). All rights reserved.  
(<http://www.sensorsportal.com>)

Promoted by IFSA

## Status of the MEMS Industry Report up to 2017

Report includes MEMS device markets, key players strategies, key industry changes and MEMS financial analysis. It also includes major MEMS manufacturing evolutions as well as an update on the “emerging” MEMS device markets.

Order online:

[http://www.sensorsportal.com/HTML/Status\\_of\\_MEMS\\_Industry.htm](http://www.sensorsportal.com/HTML/Status_of_MEMS_Industry.htm)

## Computational Method of Aging Index for Catalytic Converter Based on Wavelet Transform

<sup>1</sup>Guosheng Feng, <sup>2</sup>Bo Feng, <sup>1</sup>Sumei Jia, <sup>1</sup>Xiaoyan Niu

<sup>1</sup> Shijiazhuang Tiedao University, Shijiazhuang, 050043, China

<sup>2</sup> Hebei Construction Investment Group Railway Co. Ltd, 050080, China

Tel.: 13102828580

E-mail: fgs2005@126.com

*Received: 6 June 2013 /Accepted: 25 August 2013 /Published: 30 September 2013*

---

**Abstract:** In order to control vehicle exhaust emission effectively, the conversion efficiency of catalytic converter is one of the key monitoring and evaluated indexes. The signal monitoring system of oxygen sensor is built by the TI2812 microcontroller. The method is to obtain the eigenvector and correlation coefficient of signal energy distribution, and to determine the two signal correlativity by using the Daubechies wavelet functions to analyze voltage signals of front and back oxygen sensors. The noise and vibration source are identified with the correlation coefficient. The aging level of catalytic converter is estimated according to the value of correlation coefficient. Experiments show that the method is more simple and effective than the traditional one.

*Copyright © 2013 IFSA.*

**Keywords:** Automobile, Catalytic converter, Wavelet transform, Correlation coefficient.

---

### 1. Introduction

Motor vehicle catalytic converter is the most efficient outside purification technique to meet the discharge standard. But catalytic converter is easy to generate the chemical poisoning, heat aging and mechanical damage, coking carbon deposit and pollution etc during the motor vehicle running. It causes transformation efficiency decrease and catalyst converter fail, and makes engine emission worsen sharply. Therefore, it is necessary to monitor the catalyst efficiency of conversion. Automobile emissions standards have the strict request for engine and vehicle emission pollution in cold starting, and compels vehicle to install on-board diagnosis system (OBD). The key monitoring objects have three indicators, one is whether the conversion efficiency of catalytic converter has decreased or not. One is whether the engine catch fire or not, and another one is the oxygen sensor is degradation or not. Therefore,

we require the catalytic converter performance strictly, which both must have high conversion efficiency and good durability.

Transformation efficiency is the main performance indicators of catalytic converter, and which is obtained by monitoring and calculating the concentration of pollutants from the front and back catalyst converter. The method was adopted barely with which measure the concentration of pollutant from engine emission for diagnosis. The relationship between the other sensor (such as oxygen sensor, the temperature sensor) and catalyst conversion efficiency was established and estimated indirectly. At present the catalyst conversion efficiency was monitored with three kinds of methods such as oxygen capacity estimation [1-3], exhaust component analysis and reaction heat analysis [4]. Among them, the methods of catalyst diagnosis based on the ability of storing oxygen were widely used.

The TI2812 digital signal processor was chosen and the signal monitoring system from oxygen sensor was established in this paper. The voltage signal from the front and back oxygen sensor was obtained. The correlation between the output signal of front and back oxygen sensor was analyzed by wavelet transform method. According to the correlation coefficient of catalytic converter, we can judge the degree of ageing and then evaluate the conversion efficiency.

## 2. The Monitoring System of Oxygen Sensor

The methods of OBD-II system monitoring catalytic converter efficiency is commonly using the front and back dual oxygen sensor method which is installing an oxygen sensor respectively in the upstream and downstream of catalytic converter, by monitoring upstream and downstream of oxygen sensor signal to estimate the oxygen storage capacity. To get the oxygen sensor signal and the development of electronic control unit, TI2812 digital signal processor is selected as the core to design the data acquisition system of output signal from oxygen sensor which is shown in Fig. 1, mainly including A/D converter, interrupt handling, the SCI serial port, the LabVIEW serial read and data storage, the data acquisition process is shown in Fig. 2.

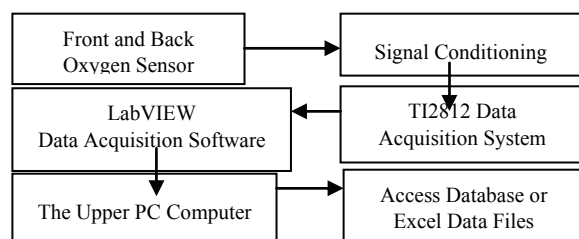


Fig. 1. Acquisition and Monitoring System of Oxygen Sensor Signal

### 2.1. Program of Receiving Data

TI2812 as lower computer after completing the acquisition of sensor data, the data from host PC were monitored by the RS-232 and the VISA interface of LabVIEW. LabVIEW is used for completing the work of serial read and data storage, the program flow chart is shown in Fig. 3.

The writing of driving program in LabVIEW changes with the difference of drive mode, which makes the versatility and compatibility of the application become poor. In order to solve this problem, NI has developed a convenient and high-level application programming interface what is called VISA for all kinds of instruments bus to communicate. VISA function includes a simple control function set to complete the configuration of

the serial port and read the work. In the design, the serial port is configured by the configuration of serial node of VISA and the VISA resource name is COM1, the baud rate is 9600.

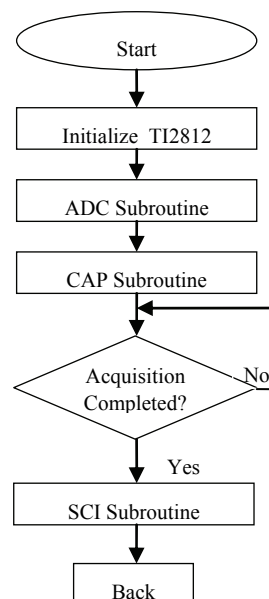


Fig. 2. Data Acquisition Flowchart.

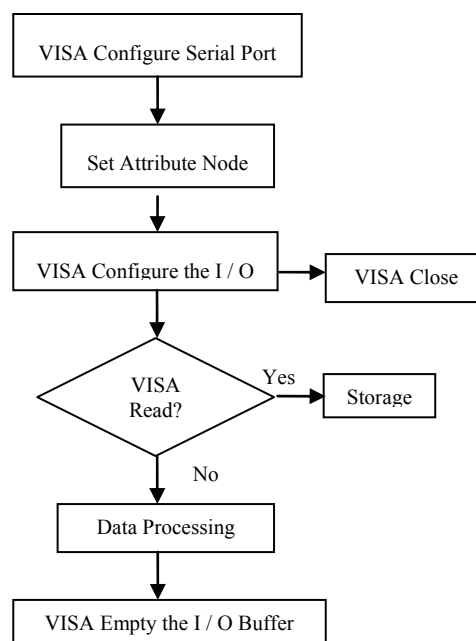


Fig. 3. VISA Read the Serial Flow Chart.

### 2.2. Data Storage

Factors of affecting the relationship between upstream and downstream oxygen sensor signal include sensor performance, measurement error and interference etc. The sensitivity, stability, noise, and dynamic characteristics of oxygen sensor were

compared and analyzed. Multiple measurement method, which can effectively limit or reduce the random error and the larger value of the error should be discarded when the test results are stored. The output voltage of oxygen sensor was up to 1.0 V, low voltage (0.3 V or lower), and RC filter and voltage follower were used in the signal conditioning circuit for reducing interference.

In order to analyze data conveniently, the read data in serial was saved by the LabVIEW program. The data from multi channel into an array using local variables, then the array was converted into strings by the function of string conversion, and the gotten date/time string were connected. Finally the information was written into the text file in order to achieve saving data.

### 2.3. The Aging Index of Catalytic Converter

A three-way catalytic converter in gasoline engine has many performance indicators. The main performance indicators are pollutant conversion efficiency and exhaust flow resistance. After the exhaust from the motor vehicle engine there is a catalytic reaction in the catalytic converter, and its harmful pollutant concentration obtained reduction in varying degrees. The conversion efficiency of the catalytic converter is defined as:

$$\eta_i = \frac{c(i)_{in} - c(i)_{out}}{c(i)_{in}} \times 100\%, \quad (1)$$

where  $c(i)_{in}$  is the concentration of entrance in catalytic converter for exhaust pollutants  $i$ ,  $c(i)_{out}$  is the concentration of outlet in catalytic converter for exhaust pollutant  $i$ . The conversion efficiency of a contaminant in the catalytic converter depends on the composition of the contaminants, the activity of a catalyst, the operating temperature, space velocity and other factors. The air-fuel ratio characteristics, the ignition characteristics and airspeed characterization of the catalytic converter are used for the representation of these factors, and the flow resistance of exhaust gas in catalytic converter is used for the representation of flow characterization.

It was supposed that the output signal of upstream oxygen sensor is  $x(t)$ , the output signal of downstream oxygen sensor is  $y(t)$ , the current catalytic converter aging index (ID) is defined as [5]

$$\begin{aligned} ID &= \text{Max} \{ \phi_{xy} / \phi_{xx} \} \\ \phi_{xx} &= \int x^2(t) dx \\ \phi_{xy} &= \int x(t)y(x - \tau) d\tau \end{aligned} \quad (2)$$

If the catalytic converters are aging, the maximum value of ID is about 1.0. It indicates that the voltage signal waveforms of two oxygen sensor are similar.

### 3. The Basic Principle of Wavelet Transforms

Establish the signal  $x(t)$  is a square integrable function,  $\psi(t)$  is called the function of a basic wavelet or mother wavelet, the wavelet transform of the signal  $x(t)$  can be defined as ( $a > 0$ ) (3)

$$\begin{aligned} WT_x(a, b) &= \frac{1}{\sqrt{a}} \int_{-\infty}^{\infty} x(t) \psi^* \left( \frac{t-b}{a} \right) dt, \quad (3) \\ &= \langle x(t), \psi_{a,b}(t) \rangle \quad a > 0 \end{aligned}$$

where  $a$ ,  $b$  are called scale parameter and displacement parameters,  $*$  is complex conjugate,  $\langle x, y \rangle$  stands for inner product which means

$$\langle x(t), y(t) \rangle = \int x(t)y(t) dt \quad (4)$$

$$\psi_{a,b}(t) = \frac{1}{\sqrt{a}} \psi \left( \frac{t-b}{a} \right) \quad (5)$$

The above equation is the expansion of displacement and scale in the basic wavelet, whose equivalent frequency domain expression is

$$WT_x(a, b) = \frac{1}{2\pi} \int X(\omega) \Psi^*(a\omega) e^{j\omega b} d\omega \quad (6)$$

where  $X(\omega)$ ,  $\Psi(\omega)$  are the Fourier transformations of  $x(t)$  and  $\psi(t)$ .

So, if the complex frequency characteristics of  $\Psi(\omega)$  is more concentrated band-pass function, wavelet transform has the ability to characterize the local property of signals  $X(\omega)$  to be analyzed in the frequency domain. When using different values of 'a', the center frequency and bandwidth of  $\Psi(a\omega)$  are not the same, but the quality factor [(center frequency)/(bandwidth)] remains the same. So different scales for the wavelet transform is roughly equivalent to a set of band-pass filter processing the signal in the frequency domain.

Mallat has proposed the concept of multi-resolution in the signal processing using filter bank equivalently computing discrete wavelet, so that the calculation method is greatly simplified. Mallat tower algorithm can be described as follows.

For the discrete sequence signal  $x(t)$ , as follows

$$\begin{aligned}
 x_k^{(0)} &= x(k) \quad k = 0, 1, 2, \dots, N-1 \\
 x_k^{(j)} &= \sum h_{n-2k}^* x_n^{(j-1)} \\
 d_k^{(j)} &= \sum g_{n-2k}^* x_n^{(j-1)}
 \end{aligned} \quad (7)$$

where  $N$  is the sampling signal points,  $x_k^{(j)}$  is the smooth approximation when resolution is  $2^{-j}$  (the  $j$  layer wavelet decomposition),  $d_k^{(j)}$  is the detail signal when resolution is  $2^{-j}$ ,  $h_k$  and  $g_k$  are the impulse responses of conjugate mirror filter, Mallat has made a detailed study on its value.

Mallat algorithm is using a set of band-pass filter to filter the signal, in order to decompose the signal into different frequency channels. Suppose the analysis frequency of original signal is  $f$ . Firstly the signal is decomposed into the high frequency signal details ( $[2^{-1}f, f]$ ) and low frequency ( $[0, 2^{-1}f]$ ) discrete approach signal. Then every time conduct the decomposition, the last decomposition of low-frequency discrete approximation signal is decomposed into sub-high-frequency and low frequency. After each decomposed layer, half the number of data points, double the sampling interval, so the decomposition carry on  $N$  times, the wavelet decomposition results of the  $N$  layer is obtained.

As the results of the wavelet decomposition of each frequency channel is equivalent to the original signal by filtering and reducing the sampling point in the time domain signal, the signal can be analyzed according to the results in the time domain. But after the minus point sampling of wavelet analysis the temporal resolution is decreased. If improve the calculation accuracy, the results in this frequency channel can be reconstructed to restore the temporal resolution of the original signal.

The reconstruction algorithm can be finished by the following formula, namely

$$x_k^{(j-1)} = \sum_n h_{2k-n}^* x_n^{(j)} + \sum_n g_{2k-n} d_n^{(j)} \quad (8)$$

The construction and selection of wavelet functions use different principles depends on the purposes of application [6]. In recent years, the selection of wavelet function  $\psi(t)$ , the wavelet decomposition of function  $x(t)$  and the reconstruction algorithm have been made great progress, and a number of general calculation procedures are appear. According to the purpose of calculating aging index, the selection of wavelet function was carried out. The real time voltage signals from front and back oxygen sensor were decomposed and reconstructed by selecting different wavelet function  $\psi(t)$  in MATLAB. By comparison and analysis, the Daubechies wavelet function was adopted.

#### 4. Eigenvectors and Correlation Coefficient of the Signal

It is supposed that  $x(t)$  is the output signal of oxygen sensor, decompose  $x(t)$  in four layers of wavelet, the decomposition is

$$x = a_1 + d_1 + a_2 + d_2 + a_3 + d_3 + a_4 + d_4$$

where  $a_i, d_i$  are  $i$  layer reconstructed signal of four-layer wavelet decomposition.

Suppose

$$\begin{aligned}
 E_{ai} &= \int_{-\infty}^{+\infty} a_i^2(t) dt \\
 E_{di} &= \int_{-\infty}^{+\infty} d_i^2(t) dt \\
 E_{ai} &= \left( \sum_1^4 E_{ai}^2 + \sum_1^4 E_{di}^2 \right)^{1/2}
 \end{aligned}$$

Define the characteristics vector of the signal  $x(t)$  as [7, 8]

$$T = \{E_{a1}, E_{d1}, E_{a2}, E_{d2}, E_{a3}, E_{d3}, E_{a4}, E_{d4}\} / E \quad (9)$$

It is supposed that  $x(t), y(t)$  are output signals of upstream and downstream oxygen sensor,  $T_x, T_y$  are the feature vector of the response. Define the correlation coefficient of  $x(t)$  and  $y(t)$  as

$$R_{xy} = T_x T_y \quad (10)$$

Correlation coefficient  $R_{xy}$  reflects the degree of correlation, which can be used to decide the degree of correlation of the output signals from upstream and downstream oxygen sensor.

#### 5. The Correlation Analysis of Catalytic Converter

The fuel injection is controlled by the output signal from oxygen sensors, to ensure that the air fuel ratio is in theory air-fuel ratio nearly is the main technique in control gasoline vehicles emission [9]. The voltage signal from the upstream and downstream oxygen sensor which is collected before and after the purification of automobile exhaust is different. The signal from upstream oxygen sensor changes is smaller, while signal from downstream oxygen sensor changes is larger with the use (aging) time of catalytic converter, which is shown in Fig. 4, Fig. 5 and Fig. 6. It can be seen from Fig. 4 to Fig. 6 that before the aging the catalyst oxygen storage capacity is

relatively strong which can release oxygen in the poor oxygen and storing oxygen in the rich oxygen, so that the harmful exhaust gases undergo chemical changes to achieve the goal of purifying the exhaust gas. The corresponding fluctuation-resistant ability is very strong and the downstream oxygen sensor has a relatively long lag time. With the increasing aging time, the catalyst oxygen storage capacity decreased, resistance to fluctuations in the capacity dropped, the lag time of the downstream oxygen sensor shortened, the amplitude of the dynamic response of the downstream oxygen sensor and the output cycle will gradually close to the upstream oxygen sensor[10]. Thus, by comparing the output waveform of front and back oxygen sensor of catalytic converter, it can determine the catalytic converter's oxygen storage capacity and the degree of the aging of the catalytic converter is obtained which is through the analysis of correlation of the output waveform of front and back oxygen sensor to determine the performance of the catalytic converter.

The output waveform of front and back oxygen sensors is stored as discrete data which is acquainted in the monitoring system. The information of each

band can be gotten using the wavelet transform, using the feature vectors of the energy element constructors formula (9), after obtaining the feature vectors directly calculate the correlation coefficient of front and back oxygen sensor in accordance with the formula (10), then the correlation analysis of front and back oxygen sensor is completed. The data from front and back oxygen sensor in a fresh state was selected for analyzing. The results of wavelet analysis are shown in Fig. 7, Fig. 8, the calculated correlation coefficient is shown in Table 1.

The method of dual oxygen sensor was used to judge the performance of catalytic converter. As a matter of fact, that is the detection of oxygen storage capacity of catalytic converter. The one which has a strong oxygen storage capacity has higher conversion efficiency. The method of wavelet transform described earlier can be used to obtain the correlation the front and back oxygen sensor under different aging state, which is shown in Table 1. The greater correlation, the waveform of front and back oxygen sensor is the closer and the degree of aging of the catalytic converter is the higher [11].

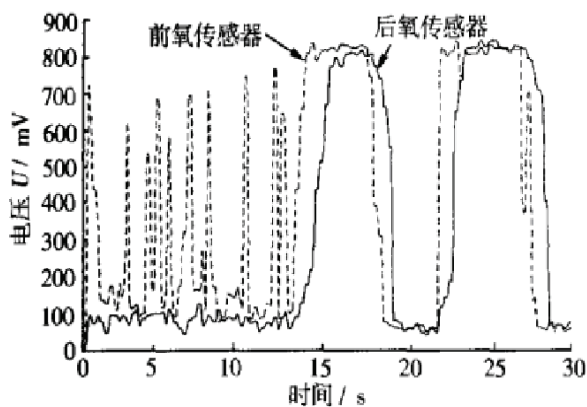


Fig. 4. Output Signal in Fresh state.

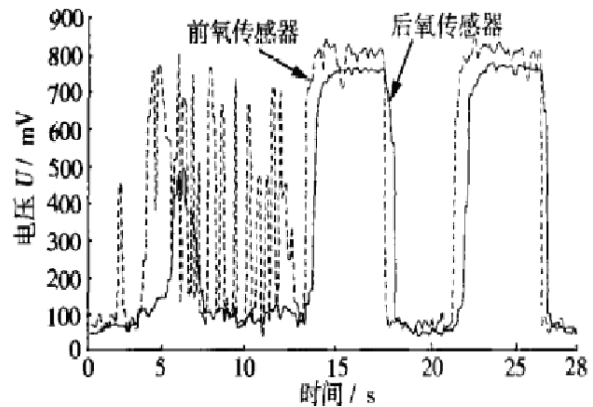


Fig. 5. Output Signal after Aging an Hour.

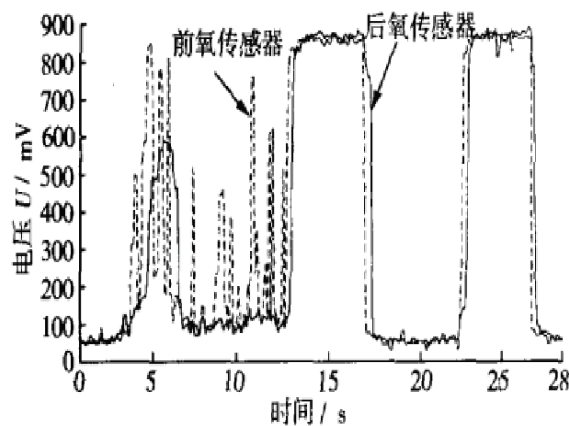


Fig. 6. Output Signal after Aging b Hour.

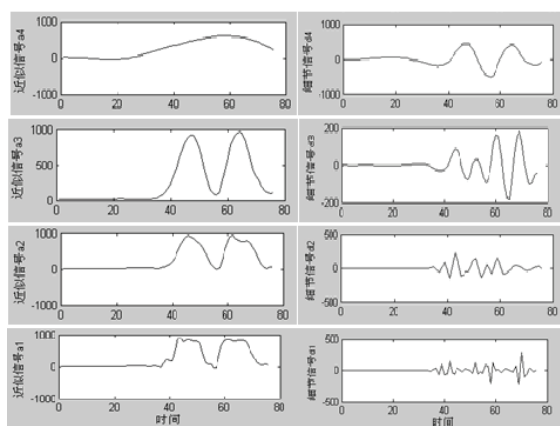


Fig. 7. Reconstructed Signal of the front Oxygen Sensor.

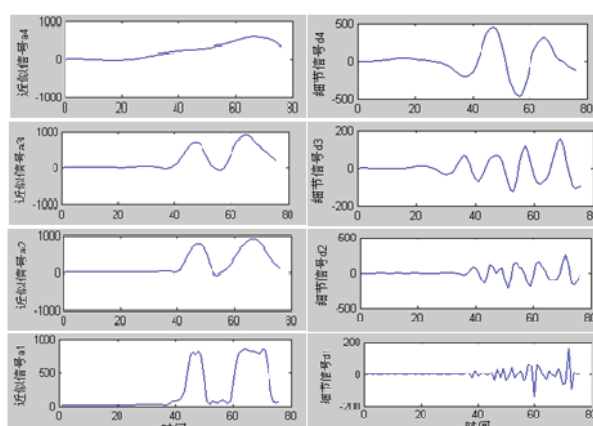


Fig. 8. Reconstructed Signal of the back Oxygen Sensor.

Table 1. The Feature Vector and Correlation Coefficient in Different Aging Degree.

The Degree of Aging	Feature Vector	Correlation Coefficient
Fresh	$T_1=[0.283,0.486,0.322,0.219,0.022,0.009,0.029,0.023]$	0.876
	$T_2=[0.423,0.510,0.505,0.375,0.012,0.078,0.026,0.066]$	
After a hour	$T_1=[0.330,0.186,0.116,0.070,0.016,0.100,0.041,0.004]$	0.968
	$T_2=[0.514,0.210,0.129,0.083,0.011,0.114,0.048,0.004]$	
After b hour	$T_1=[0.383,0.243,0.156,0.081,0.015,0.025,0.033,0.011]$	0.994
	$T_2=[0.399,0.304,0.187,0.112,0.022,0.019,0.036,0.012]$	

## 6. Conclusion

1) The signal monitoring system of oxygen sensor is built based on TI2812 microcontroller. The voltage signal of front and back oxygen sensor can be collected real time and effectively. The analysis data were supplied in order to evaluate the efficiency of catalytic converter.

2) The theoretical analysis and experimental verification shows that using the four wavelet decomposition gets feature vectors of the energy distribution from front and back oxygen sensor signal. The correlation between the front and back oxygen sensor signal is studied based on the correlation coefficient of the signal energy distribution. The calculating method of aging index of catalytic converter which can be evaluated by the correlation coefficient is given. It is more simple and effective using the method in the evaluation of catalytic converter aging than the traditional analysis method.

## Acknowledgement

This project was supported by the National Nature Science Fund of China (Grant No.11272220) and Scientific Research Fund of Hebei Province, China (10212118D).

## References

- [1]. Soumelidis M. I., Stobart R. K., Jackson R. A., A nonlinear dynamics model for three-way catalyst control and diagnosis, *SAE Technical Paper*, 2004-01-1831, 2004.
- [2]. Peyton-Jones C., Muske K. R., A novel approach to catalyst OBD, *SAE Paper*, 2005-01-0024.
- [3]. Muske K. R., Jones J. C. P., Howse J. W., A model-based approach to automotive three-way catalyst on-board monitoring, *Journal of Process Control*, 18, 2008, pp. 163-172.
- [4]. Qiu Zhaowen, Study on Monitoring Three-Way Catalyst Converter Efficiency Based on Exotherm, *Chang an University*, Xi an, 2008.
- [5]. Ye Hongling, Wang Jixian, Li Jun., OBD system of modern low-emission vehicles, *Mechanical Engineers*, 9, 2007, pp. 13-15.
- [6]. Ge Zhexue, Wavelet analysis theory with MATLAB R2007, *Publishing House of Electronics Industry*, Peking, 2007.
- [7]. Feng Guosheng, Li Jinsong, Liu Peng, Passenger car noise and vibration source identification based on wavelet transform, *Vibration, Testing and Diagnosis*, 26, 3, 2006, pp. 196-199.
- [8]. Jing L., Ming J., Zuo Ken R Fyfe, Mechanical fault detection based on the wavelet de-noising technique, *Journal of Vibration and Acoustic*, 126, 1, 2004, pp. 9-16.

- [9]. Ye Hongling, Wang Jixian, Li Jun., Study of Automotive calibration failure of the catalytic converter emission deterioration index consistency, *Vehicle Engines*, 2008, 4, pp. 7-70.
- [10]. Theophil S. Auckenthaler, Christopher H. Onde, Hans P. Geering., Online Estimation of the Oxygen Storage Level of a Three Way Catalyst, *SAE Paper*, 2004-01-0525.
- [11]. Niu Xiaoyan, Develop of board diagnostic OBD performance testing evaluation system, *Shi Jiazhuang Tiedao University*, Shi Jiazhuang, 2012.

---

2013 Copyright ©, International Frequency Sensor Association (IFSA). All rights reserved.  
(<http://www.sensorsportal.com>)

Promoted by IFSA

## **MEMS for Cell Phones & Tablets Report up to 2017**

Market dynamics, technical trends, key players, market forecasts for accelerometers, gyroscopes, magnetometers, combos, pressure sensors, microphones, BAW filters, duplexers, switches and variable capacitors, oscillators / resonators and micromirrors.

Order online:

[http://www.sensorsportal.com/HTML/MEMS\\_for\\_Cell\\_Phones\\_and\\_Tablets.htm](http://www.sensorsportal.com/HTML/MEMS_for_Cell_Phones_and_Tablets.htm)

## The Short-term Predicting Method of Algal Blooms Based on Libsvm and Elman Neural Network Modeling

<sup>1</sup>Mengxun Li, Zaiwen Liu Wei, <sup>2</sup>Hua, Xue Zhang, <sup>3</sup>Chengrui Wu

<sup>1</sup>School of Computer and Information Engineering, Beijing Technology and Business University, Beijing 10048, China

<sup>2</sup>Suzhou City Water Company Limited, Suzhou, China

<sup>3</sup>Anheng Company Limited, Beijing, China

E-mail: Limx\_310@hotmail.com, liuzw@th.btbu.edu.cn

*Received: 5 June 2013 / Accepted: 25 August 2013 / Published: 30 September 2013*

---

**Abstract:** After the major reasons of water bloom were analyzed, using the rough set theory and principal component analysis respectively to identify the main factors affecting the forecast algal blooms. On this basis, to take advantage of the Libsvm water bloom prediction model and Elman water bloom prediction model for the short-term prediction of algal blooms phenomenon respectively. Obtained through the fitting networks in the long-term forecasting of algal blooms, the Libsvm prediction accuracy is much higher than the prediction accuracy of artificial neural network. And the Elman neural network can predict the variation of chlorophyll in short-term well, which laid the foundation for in-depth study of the short-term water blooms prediction methods, since the Elman neural network ability of generalization is stronger, of network prediction is more accurate, of fitting performance is better.  
*Copyright © 2013 IFSA.*

**Keywords:** Water bloom, Libsvm, Elman, Prediction, Modeling.

---

### 1. Introduction

The water bloom is a phenomenon that refers to freshwater ponds, rivers, lakes, reservoirs and other water bodies are contaminated, resulting in a substantial increase in nitrogen, phosphorus and other nutrients, and the water reach the eutrophication or severe eutrophication state. Some algae is explosive breeding, water clarity and dissolved oxygen changes under the certain conditions such as the temperature and light, that resulting in the deterioration of water quality, and present the phenomenon of the surface of the water or thin or thick green or other colors algae floats. This problem has become one of the major water pollution problems faced by today's river lake body. The governance and the prevention of water bloom prediction has always been a difficulty, which is

complicated because the mechanism of water bloom is intricate, come down to a lot of influence factors, and establish directly the blooms mechanism ecological models are more difficult.

Ref. [1, 2] With the development of the artificial intelligence methods, the BP network of artificial neural network in the prediction of water bloom could be better to solve the difficult problems in application of the traditional mechanism of water bloom prediction. The artificial neural network theory in dealing with non-linear pattern recognition show good characteristics, so it has unique information processing and computing power, applied to the mechanism which is unclear, high-dimensional nonlinear systems, and in the ecosystem modeling, ecological data processing as well as remote sensing, ecological parameters extraction has been widely used.

This article is mainly to make the short-term forecasts water bloom model based on Libsvm and Elman neural network model to predict and compare. These two methods, both in the generalization capability, network complexity, or on the sample size requirements relative to the BP network has been significantly improved. Therefore, the selection of these two networks of lakes and reservoirs water bloom prediction, designed to improve the prediction accuracy.

## 2. The Study of Libsvm Support Vector Machine-based on the Short-term Prediction of Water Bloom

### 2.1. Water Bloom Prediction Model Based on the Libsvm Model

Support Vector Machine (for short SVM) is a new machine learning technique which is developed based on statistical learning theory. SVM is based on the structural risk minimization principle export, with minimize empirical risk to use the upper bound of minimize the error to improve the generalization ability. Ref.[3,4] The introduction of kernel function idea which can be successfully applied in the field of time series prediction is to solve practical problems of the small sample, nonlinearity, high dimension and local minima points. The basic idea of Support vector machine (SVM) is based on Mercer kernel expansion theorem. Through nonlinear mapping  $\phi$ , the sample space is mapped to a high-dimensional and even infinite dimensional feature space (the Hilbert space); the search for the algorithm of optimal linear regression hyper plane is summed up in solving a convex constraint of a convex programming problem. Ref.[5]. And we can obtain the global optimal solution, which can be applied linear machine learning methods to solve highly nonlinear regression of the sample space in the feature space. Support vector machine principle shown in Fig. 1.

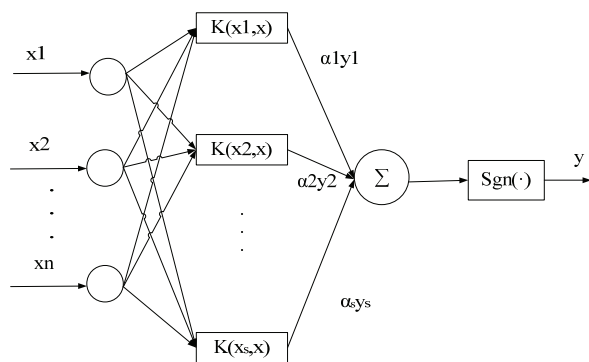


Fig. 1. Support Vector Machine Schematics.

Wherein: the first layer of the N inputs and a second layer of the support vector is based on the nonlinear operation of the N number of support vectors, i.e. core computing.

For nonlinear problems, set the sample as n dimensional vector, N samples of some region and its value is expressed as:

$$(x_1, y_1), (x_2, y_2), \dots, (x_N, y_N) \in R^n \times R \quad (1)$$

First of all, using a nonlinear mapping  $\Psi(\cdot)$ , take a sample from the original space mapped into feature space:

$$\Psi(x) = (\Phi(x_1), \Phi(x_2), \dots, \Phi(x_N)) \quad (2)$$

Again, use the high dimensional feature space structure the optimal decision function:

$$y(x) = \omega \phi(x) + b \quad (3)$$

which is suitable for weight vector  $\omega$ ,  $b$  for threshold. Thus the nonlinear prediction functions into high dimensional feature space linear prediction.

Support vector machine (SVM) as the forefront technology of classification learning and data mining involved in knowledge of the related data is and its complex. For ordinary users is more difficult which through programming method to achieve its corresponding algorithm. So some scholars at home and abroad will put the corresponding research results published on the Internet, for the use of relevant personnel and research.

Libsvm package is developed and designed by Zhiren Lin of Taiwan University associate professor and others. It is based on a simple, fast, and effective SVM pattern recognition and regression software program. This designer not only provide compiled corresponding implementation file in the Windows series and Linux series, but also provide the corresponding source code for reference and modify. Ref. [6]. In Libsvm algorithm, it provides many system default parameters; most of these default parameters can solve a lot of problems, and also provide the cross-validation (Cross Validation) function.

Ref. [7]. The core algorithm of Libsvm is decomposition algorithm (Decomposition) and sequences the minimum optimal method (SMO). The nature of the algorithm is to solve a quadratic programming problem:

$$\min \frac{1}{2} \alpha^T Q \alpha - e^T \alpha; \quad (4)$$

$$0 \leq \alpha_i \leq C \quad i = 1, \dots, l \quad (5)$$

$$y^T \alpha = 0 \quad (6)$$

Ref. [8]. In the above formula, is the unit vector, and  $C$  as a parameter on the boundary,  $Q$  is positive definite or semi-definite matrix. By the decomposition

algorithm to solve this problem, Specific steps such as shown below:

1) For the number of given elements  $|B| = q \leq 1$ , and it accuracy requirement, we set starting point is  $1 = \begin{pmatrix} \partial_B \\ \partial_n \end{pmatrix}$ , and set  $K = 1$ .

2) If  $K$  is the optimal solution of the problem, then stop solving. Otherwise, again to find the working set  $B \in \{1, -1\}$ ,  $|B| = q$ , then define the  $N = \frac{\{1, -1\}}{B}$ , and define the  $\frac{K}{B}$  and  $\frac{K}{N}$  to be the vector quantity  $K$  as the sub vector. They were corresponding  $B$  and  $N$ .

3) For solving the quadratic equation for  $B$ :

$$\min \frac{1}{2} \alpha_B^T Q_{BB} \alpha_B - (e^B - Q_{BN} \alpha_N^K)^T \alpha_B \quad (7)$$

$$0 \leq (\alpha_B)_i \leq C, i = 1, \dots, q \quad (8)$$

$$y_B^T \alpha_B = -y_N^T \alpha_N^K \quad (9)$$

$$Q = \begin{bmatrix} Q_{BB} & Q_{BN} \\ Q_{NB} & Q_{NN} \end{bmatrix} \quad (10)$$

4) Presume  $\frac{K+1}{B}$  is the optimal solution of formula

$$(7), \text{ and } \frac{K+1}{N} = \frac{K}{N}. \text{ Then } K+1 \rightarrow K,$$

afterwards repeat Step 2.

Above described is Libsvm decomposition algorithm, its minimum sequence of a method for optimizing is similar to the decomposition algorithm similar. Just makes  $|B| = 2$ , i.e., select only two elements, we can obtain the solution about formula (4) and (7). Overall, Libsvm algorithm is also decomposition algorithm. Select working set  $B$ , using minimum sequence optimization method to solve quadratic about the  $B$ .

## 2.2. The Analysis of the Predictive Ability Based on the Libsvm Model

In the analysis of the predictive ability in Libsvm model, mainly use of the Suzhou water sources data to realize the prediction and analyses the predictive ability by different time intervals. And obtained the Libsvm model based on the RBF kernel function which required the less samples, had strong generalization ability and high prediction accuracy, so that the Libsvm can predict the short-term variation of chlorophyll well, provide an effective method for the short-term prediction of water bloom.

### 2.2.1. Select the Model Parameters by Using the Rough Set

Rough set theory is a kind of describing incompleteness, uncertainty mathematical tool. It can take advantage of the data on the upper and lower approximation approximate classification of data; only rely on the information provided by the data itself. Ref. [9]. It can also retain key information, data simplification, and attribute to achieve a minimum reduction, seek knowledge minimum expression. The main factors affecting water bloom is divided into three main categories: biological factors, chemical factors and physical factors. The algae is the subject of the water blooms, the concentration of the chlorophyll is the most direct indicator for characterizing the existing amount of algae in water, and is also the main biological factors that affect water bloom. Nitrogen and phosphorus are aquatic plant growth and reproduction of the source of essential nutrients; they are the most important chemical factors that limit the growth of algae. Ref. [10]. The occurrence of algal blooms is also subject to a number of physical factors, such as: water temperature, lighting, electrical conductivity, pH value, transparency, dissolved oxygen concentration and water flow rate.

Ref.[11] In this paper, mainly analyses the one year data from June to August provided by Suzhou water source by making use of the rough set method; and the same time make the data partitioning universe and calculate its roughness, attributes minimum reduction. The water predictor rough set analysis results as shown in Table 1.

**Table 1.** The analysis results of the water bloom influencing factors rough set.

I	Chl_a TP Temperature
	90 % 95 % 85 %
II	TN Light DO
	75 % 70 % 65 %
III	Transparency EC pH Value
	45 % 30 % 55 %

The Table 1 shows that the biggest contribution rate of the factors is the Chl\_a, TP and Temperature, followed by the TN, Light and DO from the Suzhou water source. Therefore, we determine to use the TN, TP, Temperature, Chl\_a, Light and DO as the input variables of the predictive model. Chlorophyll A (Chl\_a) is one of the most important indicators of characterization of water blooms, so we use this index as the forecast model output variable.

### 2.2.2. Data Preprocessing and Modeling

According to the historical data of Suzhou water source, we select a total of 736 sets of data as a model sample library during the period from 2010.7 to 2012.6.

This sample library is divided into training data and forecast data.

1) Data preprocessing.

The first thing is to normalize the 736 sets of daily data, which can accelerate the speed of the model operation. So the data mapping formula used is as follows:

$$T = 2(X - X_{\min}) / (X_{\max} - X_{\min}) - 1 \quad (11)$$

In the formula:  $X$  is stand for the original data;  $T$  is the transformed data; and the  $X_{\max}$ ,  $X_{\min}$  is representative the maximum and minimum of the original data respectively.

2) Kernel functions and model parameters.

The support vector machine used the common kernel function like the polynomial kernel function, radial basis function (RBF) kernel function and the multi-layer Sigmoid kernel functions. Ref. [12]. And compare the performance of the various kernel functions, the RBF kernel function is the best performance of all the common kernel functions. So in this paper, decide to use the RBF kernel function:

$$k(x_k, x) = -\frac{\|x_k - x\|^2}{2\sigma^2} \quad (12)$$

$$\|x_k - x\|^2 = \sqrt{\sum_{i=1}^n (x_i^k - x_i)^2} \quad (13)$$

$\sigma$  is the kernel function width.

Ref. [13] Based on the RBF kernel function of Libsvm forecast model contains two important parameters:  $c$  and  $g$ . Usually, we selected the parameters using a grid search method for support vector machine regression prediction problem.

Ref. [14]  $C$  parameter is set to C-SVC, e-SVR and v-SVR parameters, namely the loss function; and the  $g$  parameter is set for the kernel function gamma function. The optimal parameters results shown in Table 2.

**Table 2.** The optimal parameters values.

parameter	2 days later	7 days later
c	0.5	1
g	1	1

3) Predictive modeling.

Based Libsvm forecast model structure is as follows:

- 6 input variables: Temperature, DO, Light, TP, TN, Chl\_a (A day before);
- An output variable: Chl\_a;
- Parameter optimization function: SVMcgForRegress;
- Training function: svmtrain;
- Forecasting function: svmpredict.

**2.2.3. The Analysis of the Predict the Results**

Use the 736 sets of the normalized data into the Libsvm water bloom prediction model of Suzhou water source. The former 368 sets of data are used of the model training, and the later 368 sets of data are used of the model prediction. Forecast the level of the Chl\_a in 2 days and the prediction result is shown in Fig. 2. (The ordinate is Chl\_a (units of mg/L), the abscissa is the number of the sample group).

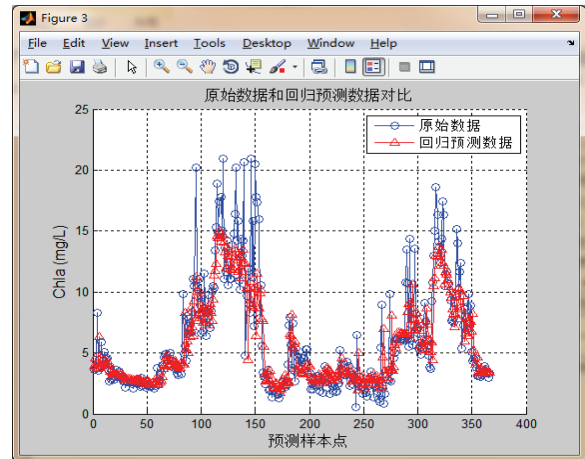


**Fig. 2.** The Libsvm model forecast the Chl\_a in 2 days.

To establish the Suzhou water source in order to predict the change of chlorophyll content in one week, the prediction result is shown in Fig. 3. The data used in support vector machine is daily sampled values.

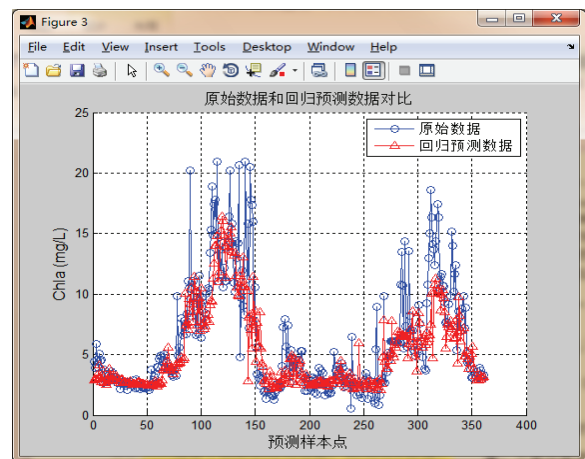


**Fig. 3.** The Libsvm model forecast the Chl\_a in 7 days.

Different time period of the Libsvm water bloom prediction accuracy results shown in Table 3.

As showed from Table 3: based on Libsvm model predictive simulation results, the model has a strong function generalization performance. Use the same data into the Libsvm model to predict the Chl\_a content in 2 days and 7 days later from the comparison of prediction

accuracy results, the two days prediction accuracy is higher than the seven days'. Therefore, based on the Libsvm prediction model is suitable of the short-term trend forecast in the water bloom.

**Table 3.** The different Libsvm interval prediction accuracy compared.

Time	2 days later	7 days later
Accuracy	0.0143267	0.0210643

### 3. The Study of Elman Based on the Short-term Prediction of Water Bloom

#### 3.1. Elman Functions and Network Design

Elman artificial neural network is put forward by Elman in 1990 and the model is a recurrent neural network, which generally can be divided into four layers: input layer, hidden layer, undertakes layer and output layer. The input layer, hidden layer and output layer of Elman artificial neural network is similar to a feed forward neural network, and the neurons of the input layer play the role of signal transmission, the neurons transfer function of the hidden layer can be linear or non-linear, the neurons of the output layer play the role of linear weighting. Middle undertake layer distinguishes Elman artificial neural network from feed forward neural network, which memorizes the previous output value of implicit layer, this can be described as one step delay operator, and makes Elman network have memory function. The model of Elman artificial neural network is shown in Fig. 4.

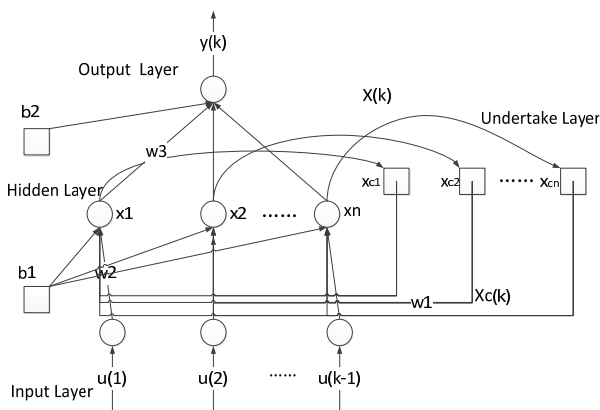


**Fig. 4.** Elman neural network model structure.

Besides memory function, Elman neural network structures can approximate nonlinear function with arbitrary precision, so if you have sample dates of input and output, you can network modeling without considering the impact of external noise on the network system.

Ref. 15]. The mathematical model expression of Elman network is:

$$y(k) = g[w^3 x(k) + b_2] \tag{14}$$

$$x(k) = f\{w^1 x_c(k) + w^2 [u(k-1)] + b_1\} \tag{15}$$

$$x_c(k) = x(k-1), \tag{16}$$

where,  $k$  represents the moment;  $y$  represents the 1-dimensional vector of output node,  $x$  represents the  $m$  dimension unit vector of hidden layer nodes,  $u$  is the  $n$  dimensional vector of input vector,  $x_c$  represents the feedback state of the  $m$ -dimensional vector. And  $w_1, w_2, w_3$  respectively represent connection weights of undertake layer to the hidden layer, the input layer to the hidden layer, hidden layer to the output layer.  $f(\cdot)$  Function is the transfer function of hidden layer, which uses non-linear transfer function, and  $g(\cdot)$  function is output transfer function, which using the linear *purelin*.  $b_1$  and  $b_2$  are the threshold value of the input layer and output layer.

The purpose of the network learning is getting the difference between the desired output values of network and the output value of sample data to adjust weighting value and threshold value to make the squared sum of error of the network output layer become the minimum, in order to achieve the accuracy and requirements of the network training. Assuming at the  $k$  moment, the desired output vector is  $y_d(k)$  and in the time period of  $(0, T)$ , the error function of network is defined as:

$$E = \frac{1}{2} \sum_{k=1}^T [y_d(k) - y(k)]^2 \tag{17}$$

$$E = \frac{1}{2} \max_{1 \leq k \leq T} \{|y_d(k) - y(k)|\} \tag{18}$$

#### 3.2. Fitting Capability Analysis of Elman Network

##### 3.2.1. The Choice of the Number of Hidden Layer Neurons

For multilayer neural network model, the number of hidden layer neurons is very important and selection results will directly affect the network performance. The role of the hidden layer nodes is to extract its internal laws from the sample bank and stores the internal laws. Each hidden layer node has several weights, and each weight is the parameter of enhancing network mapping capabilities. If the number of hidden nodes is too small, the network ability of obtaining information from a sample library is too weak, and cannot summarize and embody the law in the training set of sample; if the number of hidden layer nodes is too many, the network

may remember the irregular laws to form so-called "over-match" problem, which reduces the generalization capability of the network. Besides, the excessive hidden nodes also increase the training time.

Ref. [16] However, there is still not an ideal expression to determine the number of hidden layer neurons. Theoretical proof shows that for feed forward neural networks, three-forward network can well approximate any continuous function. Ref. [17]. So, in the modeling process, the first step is to determine a three-tier network based on the Kolmogorov theorem. If the input layer of the network has  $m$  neurons, the hidden layer will have  $2m+1$  neurons. After initially determining the theoretical value of the hidden layer neurons, hidden nodes is determined according to the related references and the trial and error method proposed rules. Ref. [18]. In other words,  $n \leq 4\sqrt{m(k+3)+1}$ ,  $n$  is the hidden nodes,  $m$  is the input layer nodes and is the output layer nodes. According to simulation comparison in  $(l-\delta, l+\delta)$ ,  $\delta \in n$  interval,  $l$  means the theory value of hidden nodes, we can get the best hidden layer nodes of neural network model.

So in the Elman neural network model structure, the network hidden layer nodes are determinate by the Kolmogorov theorem first to calculate the theoretical value is 21. And then according to the interval  $(l-\delta, l+\delta)$ ,  $\delta \in n$  to make the numerical comparison, determine the range of values of the hidden layer nodes ( $l$  is the theoretical value of the hidden nodes). At last, arrive at the best neural network model hidden nodes. Method mentioned in the reference [17] shows that  $n \leq 24$ , get  $\delta = 3$ , so the hidden layer nodes desirable values are: 18,19,20,21,22,23,24. The neural network node hidden layer nodes selected comparative results are shown in Table 4.

**Table 4.** The comparison of the selected results in the number of hidden nodes.

Hidden layer neurons	Training results	Training times	Error objective	Target training times
18	0.0852	95	0.0001	300
19	0.0924	93	0.0001	300
20	1.3232	26	0.0001	300
21	0.0861	96	0.0001	300
22	0.4989	91	0.0001	300
23	1.5034	24	0.0001	300
24	0.0740	104	0.0001	300

According to the results in Table 4, the effect on function approximation is the best of the Elman network when the hidden node is 24, followed by the hidden nodes theoretical value is 21. At the same time, the phenomenon could be seen from the table is that the better performance of the network by setting the number of training, the more times the training in the actual network learning process.

### 3.2.2. Establish the Elman Network Model

Use the data of 2010.7 to 2012.6 which is provided from Suzhou water-source region as well. In order to make the full use of the historical data, increase the precision of the predict model. We will do the following data processing: Separating the data from odd number (1, 3, 5) to even number (2, 4, 6) as the training data and the testing data of 368 group, respectively. So it can be insurance the time continuity of data. Base on the indicator system of water bloom which is provided from the water-source region of Suzhou, built a four-Layer testing Elman modeling what is multiple input and single output, the following is the network parameter:

- Six input layer nerve cells: Temperature, DO, Light, TP, TN, Chl\_a (A day before);
- One output layer nerve cells: Chl\_a;
- The excitation function of hidden layer: Tan-sig function;
- The excitation functions of output layer: Purline function;
- The network learning algorithm: Gradient descent algorithm;
- The theoretical node of hidden layer: 21;
- The precision of network training: 0.0001.

The definition parameter as follows:

```
net.trainparam.epochs = 300;
% Training times
net.trainparam.show = 20;
% Step of training between the two displays
net.trainParam.goal=0.0001;
% Training target
net.trainParam.lr_inc=1.05;
% The learning rate growth scale factor
net.trainParam.lr_dec=0.7;
% The learning rate descend scale factor
net.trainParam.max_fail=5;
% the confirmed maximum number of failure
```

When the network achieves the maximum training time, achieves the network error performance target value, the training time gets the maximum value, the gradient reduce makes the minimal value of performance function, or the consecutive authentication failures exceed the maximum number of times, the network will stop training.

### 3.3. Prediction Results Analysis

Based on the odd-even number principle, people can predict the chlorophyll value two days later and one week later. When hidden layer nodes equal to 21 or 24, the accuracy for the model is presented on Table 5.

**Table 5.** Forecast comparison results of the two hidden nodes in different time intervals.

Time Interval	2 days later	7 days later
21 hidden layer nodes	0.3303	0.8272
24 hidden layer nodes	0.1328	0.6196

Comparing the prediction, the closest result occurs when there are 24 hidden layer nodes in the time interval.

Following Figs. 5, 6 present the Elman neutral network matching prediction under 24 hidden layer nodes.

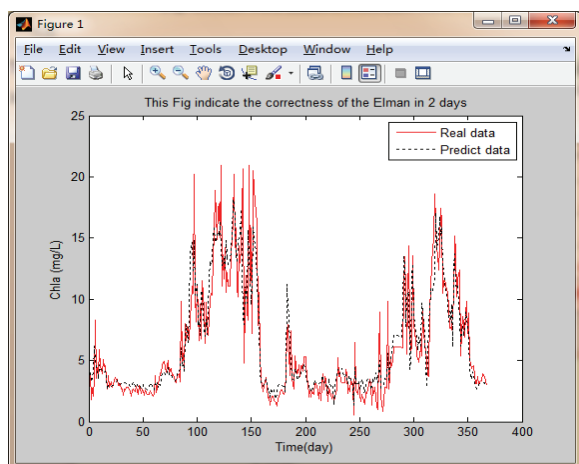


Fig. 5. Elman network matching prediction result of water resource in SuZhou (Two days later).

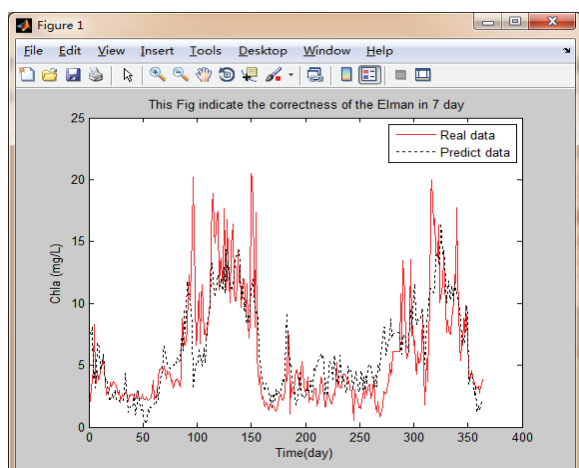


Fig. 6. Elman network matching prediction result of water resource in SuZhou (One week after).

Based on the graphs, Elman neutral network model can predict chlorophyll value in water accurately. Therefore, Elman neutral network can be used to detect and monitor alga bloom in water resources. The accuracy of model is decreasing when interval increases. Even though the chlorophyll keeps the same trend when time increases, the prediction accuracy in two days is better than the prediction after one week.

### 3.4. The Comparison between Neutral Network Model with Supported Vector Model

The examination testifies the accuracy comparison between neutral network models with vector supported model presenting the result on Table 6.

Table 6. The comparison between different models.

Prediction interval	2 days later	7 days later
Libsvm	0.0143	0.0211
Elman	0.1328	0.6196

Based on the accuracy comparison between Libsvm model and Elman model, vector supported Libsvm model has better accuracy and advantage on short-term simulation prediction.

## 4. Conclusions

The improvement of Support Vector Machine (SVM) arithmetic—Libsvm and Elman neutral network for predicting algal bloom is made after algal bloom generating factors and evaluation index analysis. The compare and contrast between Libsvm and Elman neutral network is done before the SVM improvement.

The Rough Set Theory is been used on analysis algal bloom generating factors in Libsvm arithmetic research. Combining algal bloom generating factors, six elements (Total Nitrogen, Total Phosphorus, Temperature, Chlorophyll a, Illumination & Dissolved Oxygen) have been selected for predicting inputs. Chlorophyll a is predicted output. The prediction concludes that Libsvm needs less samples; has short prediction cycle, good generalization ability and high accuracy. It is an effective method for predicting chlorophyll variance in a medium or long term.

Research on Elman model is made by selecting different hidden nodes. When Elman model has 24 hidden nodes, the best simulation result occurs. Moreover, Elman model also works for short-term forecasting simulation. The result is more accurate when choosing shorter intervals. Based on the research for two models, this conclusion is that Libsvm is a more effective and efficient Water Bloom Prediction method.

## Acknowledgment

Supported by Jiangsu Water Conservancy Science and Technology Project (2011014), Beijing Natural Science Foundation (8101003), and the Beijing Municipal Commission of Education (PHR201007123) and the Beijing Municipal Commission of Education Science and Technology Foundation Project.

## References

- [1]. Ren Li, Dong Zeng-Chuan, Li Shao-Hua, Application of artificial neural network model to assessment of Taihu Lake eutrophication, *Journal of Hehai University (Natural Sciences)*, 32, 2, 2004, pp. 147 – 150.
- [2]. Pei Hong-Ping, Luo Ni-Na, Jiang Yong, Applications of back propagation neural network for predicting the concentration of chlorophyll-a in West Lake, *Acta Ecologica Sinica*, 2004, 24, 2, pp. 246 - 251.

- [3]. Zhang Xuegong, Introduction To Statistical Learning Theory And Support Vector Machines, *Journal of Automation*, 2000, 26, 1, pp. 32-42.
  - [4]. Dominique M, Alistair B., Nonlinear Blind Source Separation Using Kernels, *IEEE Trans. on Neural Networks*, 14, 1, 2003, pp. 228 -235.
  - [5]. Stolarski T A. System for wear prediction in lubricated sliding contacts, *Lubrication Science*, 8, 4, 1996, pp. 315 -351.
  - [6]. Zhao Hongbo, Feng Xiating, Application of support vector machines function fitting in slope stability evolution, *Chinese Journal of Rock Mechanics and Engineering*, 2003, 22, 2, pp. 241- 245.
  - [7]. Vapnik V., Golowich S., Smola A., Support vector method for function approximation, regression estimation, and signal processing, in Proceedings of the 10<sup>th</sup> Conference on Neural Information Processing Systems, Denver, Colorado, 1996, pp. 281-287.
  - [8]. Luo Cheng-Shi, Research on grain moisture detection data fusion based on Libsvm, *Science Technology and Engineering*, 1, 2, 2012, pp. 292-295.
  - [9]. Liu Qing, Rough Set and Rough Reasoning, *Science Press*, Beijing, 2001.
  - [10]. Zhou Yunlong, Yu Ming, The occurrence of hazards and prevention of algal blooms, *Bulletin of Biology*, 39, 6, 2004, pp. 11 - 16.
  - [11]. Wu Yi-Feng, Lu Xi-Wu, Rough Analysis on Driving Factors of Eutrophic Water, *Safety and Environmental Engineering*, 12, 4, 2005, pp. 12-14.
  - [12]. Van Gestel T., Suykens J., Viacne S., etc. Benchmarking Least Squares Support Vector Machine Classifiers, *Machine Learning*, 54, 1, 2004, pp. 5-32.
  - [13]. Reioh Y., Barai S. V., Evaluating Machine Learning Models for Engineering Problems, *Artificial Intelligence in Engineering*, 13, 1999, pp. 257-272.
  - [14]. Wu Cheng-Wei, Hu Peng-Hao, Miao En-Ming, Foundation of thermal error model for nc machine tool based on libsvm, *Manufacturing Automation*, 4, 33, 2011, pp. 97-100.
  - [15]. Lv Siying, Liu Zaiwen, Wang Xiaoyi *et al.*, Short-term predicting model for water bloom based on Elman neural network, *Technical Committee on Control Theory, Chinese Association of Automation*, 7, 2008, pp. 218-221.
  - [16]. Jin Fan, Investigation on Some Key Technical Problems of FNCIS, in *Proceedings of the China Neural Network and Signal Processing Conference*, 1999.
  - [17]. Wang Junke, Wang kecheng. Neural network modeling, forecasting and control, *Harbin Engineering University Press*, Heilongjiang, 1996.
  - [18]. Zhang Zhiguo, Research on Bridge Damage Identification Method Based on Modal Analysis Theory and Neural Networks, Master's Degree Thesis, *Wuhan University*, 2005.
-

## A NLOS Localization Algorithm Based on BPNN

<sup>1</sup> Bi Zeng, <sup>1</sup> Xiao Hu Chen, <sup>2\*</sup> Jian Qi Liu, <sup>2</sup> Xiao Hua Han

<sup>1</sup> School of Computer, Guangdong University of Technology, Guangzhou, Guangdong, 510006, China

<sup>2</sup> School of Information Engineering, Guangdong Jidian Polytechnic

Guangzhou, Guangdong, 510515, China

E-mail: 409980812@qq.cn, z9215@163.com, liujianqi@ieee.org

Received: 1 July 2013 / Accepted: 25 August 2013 / Published: 30 September 2013

---

**Abstract:** Artificial neural network (ANN) is a humanly constructed network which is based on the human brain neural network. BP neural network (BPNN), as a typical forward ANN, can approximate any nonlinear continuous rational function. In this paper we use the BPNN to modify the Non-Line-of-Sight (NLOS) Time Difference of Arrival (TDOA) measurement value to make it closer to the Line-of-Sight (LOS) measurement value. Then we use the Chan algorithm to estimate the Mobile Station (MS) position in order to obtain higher localization accuracy. The experimental results show that the positioning accuracy has a more positive improvement in the adjusted BPNN algorithm. *Copyright* © 2013 IFSA.

**Keywords:** ANN, BPNN, TDOA, NLOS, Chan algorithm.

---

### 1. Introduction

ANN is a humanly constructed network which is based on the human brain neural network [1-4]. It is a mathematical model of the neural network system and is an information processing system based on imitating the human brain neural network structure and function. ANN has many favorable features and capabilities, such as massively parallel processing ability, distributed information storage, strong fault tolerance and robustness, well adaptive ability and strong self-learning, which has brought hope to our human technology revolution. Compared with the traditional random adaptive system, ANN not only has strong learning function, but also has the ability of memory, association, choice, abstraction and recognition. BPNN, as a typical forward ANN, has been widely used in various fields in recent years. Especially in nonlinear modeling and controller design of the smart system, pattern classification and pattern recognition, it has caused great concern. By training the BPNN, we are likely to find a new and effective method to solve the problem of NLOS error in wireless localization [5].

NLOS is the main error sources in distance, Angle positioning system [6]. In the case of NLOS error statistical properties is unknown, the traditional parameter estimation method can't give the location information of the MS accurately. Therefore how to reduce the NLOS influence on localization accuracy between the Base Station (BS) and MS becomes a problem that must be solved. In this paper we use the BPNN to modify the NLOS TDOA measurement value to make it more closer to the LOS measurement value [7-9]. Then we use the Chan algorithm to estimate the MS position in order to obtain higher localization accuracy. The experimental results show that the positioning accuracy has a more positive improvement in the adjusted BPNN algorithm.

### 2. The Chan Algorithm of TDOA

Set the coordinate of MS is  $(x, y)$ , the coordinate of  $BS_i$  are  $(x_i, y_i)$ , among them  $BS_1$  is the serving BS,  $r_{i,1}$  is the distance difference between

MS to  $BS_i$  and MS to  $BS_1$ ,  $c$  is the wave propagation speed. According to the wave propagation time (TOA), we can establish the following distance equation

$$\begin{aligned} r_i^2 &= (c\tau_i)^2 = (x_i - x)^2 + (y_i - y)^2 \\ &= K_i - 2x_i x - 2y_i y + x^2 + y^2 \end{aligned} \quad (1)$$

Since  $r_{i,1} = r_i - r_1$ , formula (1) can be rewritten as the following type:

$$r_{i,1}^2 + 2r_{i,1}r_1 = -2x_{i,1}x - 2y_{i,1}y + K_i - K_1, \quad (2)$$

where  $K_i = x_i^2 + y_i^2$ ,  $x_{i,1} = x_i - x_1$ ,  $y_{i,1} = y_i - y_1$

Set  $z_a = [x, y, r_1]^T$  to be the unknown vector, then we can establish the linear equation:

$$h = G_a z_a \quad (3)$$

When the system measuring error  $n_{i,1}$  of TDOA is existing, we can get the error vector as flowing:

$$\psi = h - G_a z_a^0 \approx \begin{bmatrix} cr_{2,1}^0 n_{2,1} \\ cr_{3,1}^0 n_{3,1} \\ \vdots \\ cr_{M,1}^0 n_{M,1} \end{bmatrix} = cBn, \quad (4)$$

where  $z_a^0$  is the corresponding  $z_a$  value of the true location of MS.

$$h = \begin{bmatrix} (r_{2,1}^2 - K_2 + K_1)/2 \\ (r_{3,1}^2 - K_3 + K_1)/2 \\ \vdots \\ (r_{M,1}^2 - K_M + K_1)/2 \end{bmatrix}, \quad G = \begin{bmatrix} -x_{2,1} & -y_{2,1} & -r_{2,1} \\ -x_{3,1} & -y_{3,1} & -r_{2,1} \\ \vdots & \vdots & \vdots \\ -x_{M,1} & -y_{M,1} & -r_{M,1} \end{bmatrix}$$

The covariance matrix of  $N$  is  $Q = \text{diag}\{\sigma_{2,1}^2, \sigma_{3,1}^2, \dots, \sigma_{M,1}^2\}$ , when TDOA error is small, the error vector can be represented as  $\psi = BQB$ . Where  $B = \text{diag}\{r_2^0, r_3^0, \dots, r_M^0\}$ . By weighted least squares (WLS), we can get the first solution

$$z_a = (G_a^T \psi^{-1} G_a)^{-1} G_a^T \psi^{-1} h \quad (5)$$

We can get the new matrix  $B$  by using the value  $z_a$ . Also we can get the improved estimates

position by using the above process to make a WLS calculation again. You must know that we have assumed the elements among  $z_a$  are independent, infact the position of  $r_1$  is related to the position of MS. therefore we can get more accurate position by using this relationship. Firstly we calculate the covariance matrix of the position  $z_a$ , it can be represented as flowing:

$$\begin{aligned} \Delta z_a &= c(G_a^{0T} \psi^{-1} G_a^0)^{-1} G_a^{0T} \psi^{-1} B_n \text{cov}(z_a) \\ &= E(\Delta z_a \Delta z_a^T) = (G_a^{0T} \psi^{-1} G_a^0)^{-1} \end{aligned} \quad (6)$$

where  $G_a^0$  can be got by the result of the formula (5). We can construct the new error vector  $\psi'$ , according to the relationship  $r_1^2 = (x - x_1)^2 + (y - y_1)^2$ :

$$\psi' = h' - G_a' z_a^0, \quad (7)$$

$$\text{where } h' = \begin{bmatrix} (z_{a,1} - x_1)^2 \\ (z_{a,2} - y_1)^2 \\ z_{a,3}^2 \end{bmatrix}, G_a' = \begin{bmatrix} 1 & 0 \\ 0 & 1 \\ 1 & 1 \end{bmatrix}, z_a^0 = \begin{bmatrix} (x - x_1)^2 \\ (y - y_1)^2 \end{bmatrix}.$$

The covariance matrix is:

$$\begin{aligned} \psi' &= E[\psi' \psi'^T] = 4B' \text{cov}(z_a) B' \\ B' &= \text{diag}\{x^0 - x_1, y^0 - y_1, r_1^0\} \end{aligned} \quad (8)$$

$(x^0, y^0)$  can be replaced by the second WLS calculation results similarly.

$$z_a' = (G_a'^T \psi'^{-1} G_a')^{-1} G_a'^T \psi'^{-1} h' \quad (9)$$

The final MS positioning can be represented as flowing:

$$z_p = \sqrt{z_a'} + \begin{bmatrix} x_1 \\ y_1 \end{bmatrix} \quad (10)$$

### 3. The Modification of TDOA Measurements by BPNN

Set  $\tau_i$  is the TOA measurement between MS and  $BS_i$ , because of the measurement error and the time delay error caused by the NLOS,  $\tau_i$  can be represented as flowing:

$$\tau_i = \tau_i^0 + n_i + \tau_{ei}, i = 1, 2, \dots, M, \quad (11)$$

where  $\tau_i^0$  is the TOA value under the LOS,  $n_i$  is the system measurement error, which obeys the Gaussian distribution, whose mean is zero and variance is  $\sigma_n^2$ ;  $\tau_{ei}$  is the additional time delay error caused by NLOS, which is a positive mean random variables, whose mean is  $\mu_{ei}$  and variance is  $\sigma_{ei}^2$ . Each  $\tau_{ei}$  is independent. Then we can get:

$$\begin{aligned} \tau_{i,1} &= \tau_i - \tau_1 = (\tau_i^0 - \tau_1^0) + (n_i - n_1) - (\tau_{ei} - \tau_{e1}) \\ &= \tau_{i,1}^0 + n_{i,1} + \tau_{ei,1}, i = 1, 2, \dots, M \end{aligned} \quad (12)$$

where  $\tau_{i,1}^0$  is the TDOA measurement under the LOS,  $n_{i,1}$  is the system measurement error, which obeys the Gaussian distribution, whose mean is zero and variance is  $\sigma_{ni,1}^2$ ;  $\tau_{ei,1}$  is the additional time delay error caused by NLOS, which is a positive mean random variables, whose mean is  $\mu_{ei,1}$  and variance is  $\sigma_{ei,1}^2$ . Each  $\tau_{ei,1}$  is independent. According to the formula(11) we can get:

$$\mu_{ei,1} = E(\tau_{ei} - \tau_{e1}) = \mu_{ei} - \mu_{e1} \quad (13)$$

$$\sigma_{ei,1}^2 = D(\tau_{ei} - \tau_{e1}) = \sigma_{ei}^2 - \sigma_{e1}^2 \quad (14)$$

Therefore  $\tau_{i,1}$  can be rewritten as:

$$\tau_{i,1} = \tau_{i,1}^0 + \mu_{ei,1} + n_{i,1}, \quad (15)$$

where  $n_{i,1}$  is a random variable, whose mean is 0 and variance is  $\sigma^2$

$$\sigma^2 = \sigma_{ni,1}^2 + \sigma_{ei,1}^2 \quad (16)$$

The BPNN learning algorithm can be represented as follows: Suppose that there are P neurons in the input layer, whose input is  $P_i$ ; the number of hidden layer neurons is H, whose activation function is  $f_1$  and the output is  $H_j$ ; the number of output layer neurons is R, whose activation function is  $f_2$  and the output is  $R_k$ .  $w_{ij}$  is the connection weight between the input layer and the hidden layer,  $w_{jk}$  is the connection weight between the hidden layer and output layer.

The output of j neurons in the hidden layer is:

$$H_j = f_1\left(\sum_{i=1}^H w_{ij} p_i + \theta_j\right), j = 1, 2, \dots, H \quad (19)$$

The output of K neurons in the output layer is:

$$R_k = f_2\left(\sum_{i=1}^R w_{jk} H_j + \theta_k\right), k = 1, 2, \dots, R \quad (20)$$

The error function is:

$$E(W, \theta) = \frac{1}{2} \sum_{k=1}^R (t_k - R_k)^2 \quad (21)$$

We can get the weight change and the error back propagation by using the gradient descent method. Since there is a positive relationship between the weight change of the output layer and the negative gradient of output layer weights for the error function, we can get the weight changes by the flowing formula:

$$\begin{aligned} \Delta w_{jk}(t) &= -\eta \frac{\partial E}{\partial w_{jk}} = -\eta \frac{\partial E}{\partial R_k} \cdot \frac{\partial R_k}{\partial w_{jk}} \\ &= \eta (t_k - R_k) \cdot f_2' H_j \end{aligned} \quad (22)$$

The weight of output layer can be changed by the formula (22):

$$w_{jk}(t+1) = w_{jk}(t) + \Delta w_{jk}(t) \quad (23)$$

The change of the hidden layer weight is proportional to the negative gradient of output layer weights for the error function:

$$\begin{aligned} \Delta w_{ij}(t) &= -\eta \frac{\partial E}{\partial w_{ij}} = -\eta \frac{\partial E}{\partial R_k} \cdot \frac{\partial R_k}{\partial H_j} \cdot \frac{\partial H_j}{\partial w_{ij}} \\ &= \eta \sum_{k=1}^R (t_k - R_k) \cdot f_2' \cdot w_{jk} \cdot f_1' \cdot P_i \end{aligned} \quad (24)$$

The weight of hidden layer can be changed by the formula (24):

$$w_{ij}(t+1) = w_{ij}(t) + \Delta w_{ij}(t) \quad (25)$$

Fig. 1 has shown the modification BPNN model of the TDOA measurements under the NLOS: BPNN is composed of input layer, hidden layer and output layer, in which the input layer is consisted of six TDOA measurement provided by seven related BS.

The input vector is:

$$P = [P1, P2, P3, P4, P5, P6] \quad (26)$$

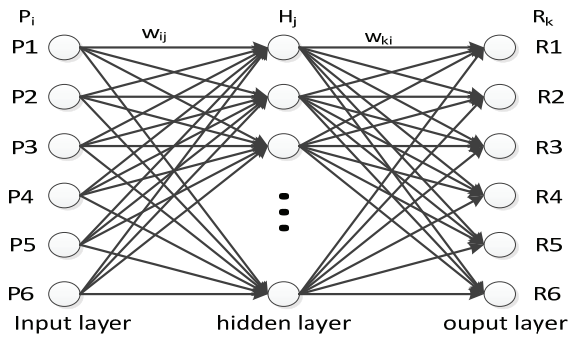


Fig. 1. The BPNN modification model of TDOA measurements under the NLOS.

Then number of hidden layer neurons can be obtained by empirical formula, that is  $H \geq \log_2 D$ , where  $H$  is the number of the hidden layer,  $D$  is the dimension of the training samples. The increase of hidden layer neurons number may improve the localization accuracy, but it will bring a greater amount of calculation. Since we focus on the localization accuracy, we set 18 as the hidden layer neurons number since we just consider the accuracy. Selecting the Sigmoid function  $f_1(x) = \tanh(x)$  as the transfer function, whose input value is arbitrary and output value is between -1 and +1. Output layer is consisted of six neurons, whose transfer function is Purlin, that is  $f_2(x) = kx$ . Its output values are the modification TDOA values. The output vector is :

$$R = [R_1, R_2, R_3, R_4, R_5, R_6] \quad (27)$$

#### 4. The TDOA Location Algorithm Based on BP Neural Network

Chan algorithm has excellent localization accuracy when the TDOA error is small and the random variable obeys the zero mean Gaussian distribution. However, when it has a bigger TDOA error under the NLOS, its localization accuracy will be affected largely. We are trying to reduce the TDOA measurements error under the NLOS by using the BPNN model. Then we can get a higher accuracy by using the Chan localization algorithm. The specific localization steps of the algorithm are shown in Fig. 2.

#### 5. The Simulation and Analysis

In this paper we have analyzed the accuracy of the BPNN modification model in different channel environments. At the same time we have also taken a comparison between the Chan algorithm and the BPNN modification in the same condition. Each BS position is shown in Fig. 3 and their coordinates are:

$$BS_3 \left( \frac{3}{2}R, \frac{\sqrt{3}}{2}R \right), \quad BS_4 \left( \frac{3}{2}R, -\frac{\sqrt{3}}{2}R \right),$$

$$BS_5(0, -\sqrt{3}R), \quad BS_6 \left( -\frac{3}{2}R, -\frac{\sqrt{3}}{2}R \right),$$

$$BS_7 \left( -\frac{3}{2}R, \frac{\sqrt{3}}{2}R \right).$$

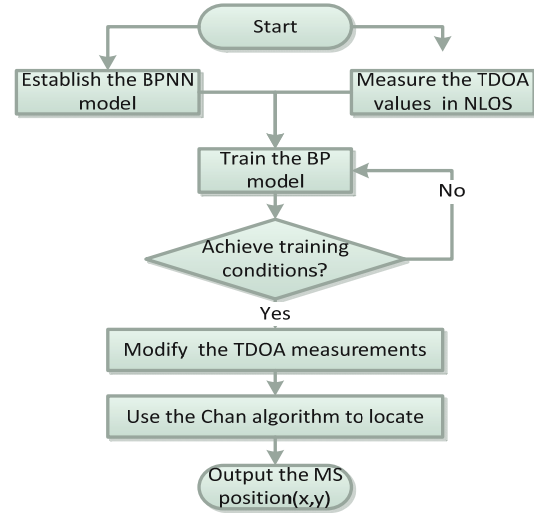


Fig. 2. The steps of BPNN modification model.

#### 5.1. The Effect of the Radius on the Localization Accuracy

The position of the MS: In the simulation, we suppose that the MS distributes in the area of the shaded part uniformly, which is shown in Fig. 3. We have selected 1000 positions to simulate and analyze. Except analysis the impact of the radius on the localization accuracy, we all take one kilometer as the radius. Assuming that the TDOA measurement system error is an independent Gaussian random variables distribution whose mean is zero and the standard deviation is  $0.1 \mu s$  (about 30 m). The environments between MS and BS are all NLOS .

From the Fig. 4, we can see that the mean square error of the two algorithms are both growing while the localization error probability are both reducing with the increasing of the radius. The reason is that the error caused by the NLOS will become bigger as the distance increasing. Because of the increasing of the radius, the distance between the MS and BS becomes bigger. As a result, the NLOS error grows and the localization accuracy declines. Between the two algorithms, the Chan algorithm has a bigger error, for its only considering the impact of the system measurement error, while the NLOS error effect is greater than the system measurement error. The BPNN presented in this paper is superior to the Chan algorithm obviously. This is because the BPNN has modified the TDOA values, which can eliminate the influence of the NLOS error to some extent, as a result it has improved the localization accuracy.

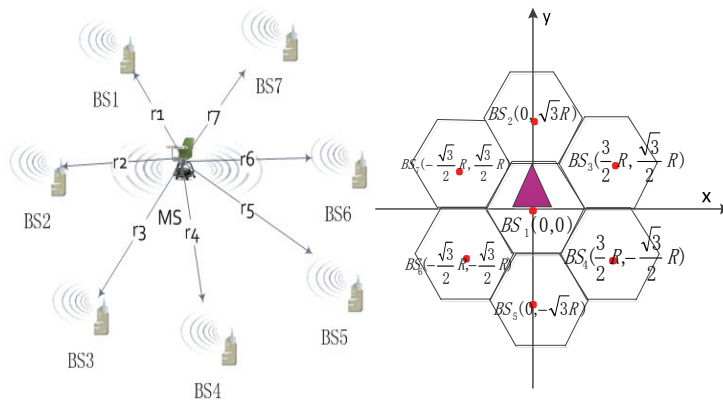


Fig. 3. The distribution of the BS and MS.

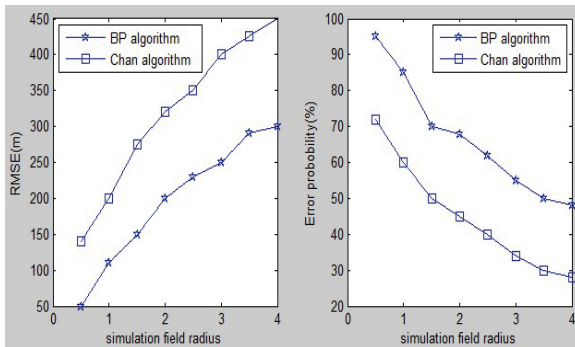


Fig. 4. The effect of the radius on the localization accuracy.

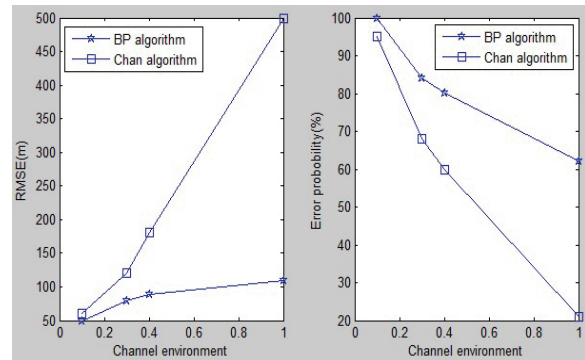


Fig. 5. The effect of the channel on the localization accuracy.

### 5.2. The Effect of the Channel on the Localization Accuracy

From the Fig. 5 we can see that the localization accuracy of the both two algorithms has a certain decline with the worsening of the channel environment. This is because the NLOS error will become bigger with the worsening of the channel environment. Obviously, the BPNN presented in this paper is superior to the Chan algorithm in different channel environment. In different channel environment, this paper positioning performance of the algorithm is better than Chan algorithm. In addition, as the worsening of the channel environment, the error growth speed of the BPNN presented in this paper is lower than the Chan algorithm. That is to say the BPNN suppresses the growth of the localization error effectively. Therefore it has a better stability. When it is in the outer suburbs which the channel environment is better, both of the two algorithms are similar, this is because the NLOS error is small at this time.

### 5.3. The Effect of the Number of the BS on the Localization Accuracy

From the Fig. 6 we can see that the localization accuracy of the both two algorithms has a certain

improve with the increasing of the number of the BS. This is because it will increase more redundant information with the increasing of the number of the BS which makes the localization accuracy improve. Obviously, the BPNN presented in this paper is superior to the Chan algorithm from the localization effect under the condition of various number of BS. In addition, as the decreasing of the number of the BS, the error growth speed of the BPNN presented in this paper is lower than the Chan algorithm. That is to say the BPNN has a better self-adaption to the number of the BS.

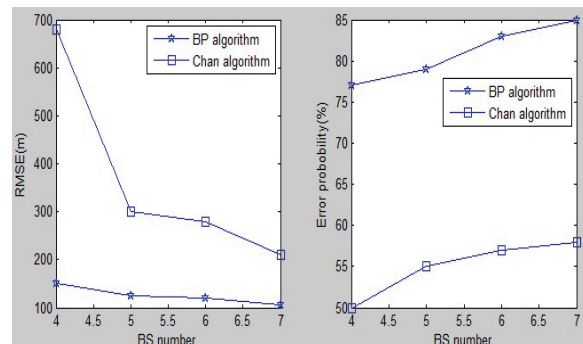


Fig. 6. The effect of the number of the BS on the localization accuracy.

## 6. Conclusions

In this paper, we have put forward a BPNN model to modify the NLOS TDOA measurement values to make it closer to the LOS measurement values by using the neural network's faster learning characteristics and the ability to approximate any nonlinear mapping. The simulation results show that the algorithm has the advantages of a strong inhibition to the NLOS error, a more effective inhibitory to the growth of the localization error, a better self-adaption to the number of the BS and a better stability. By using the BPNN model to modify the NLOS error, the localization accuracy and reliability have increased obviously, which provides a new feasible method for the elimination of the NLOS error in the wireless localization.

## Acknowledgements

The authors would like to thank the Natural Science Foundation of Guangdong, China (No. 9151009001000021, S201101000115 5), the Ministry of Education of Guangdong Province Special Fund-Funded Projects through the Cooperative of China (No. 2009B090300 341), the National Natural Science Foundation of China (No. 61262013), and the High-level Talent Project for Universities, Guangdong, China (No. 431, Yue Cai Jiao 2011) for their support in this research.

## References

- [1]. J. P. Kim and S. K. Park, The geometrical learning of binary neural networks, *IEEE Transactions on Neural Networks*, Vol. 6, Issue 1, 1995, pp. 237 - 247.
- [2]. S. Beresford and R. Basic, Concepts of artificial neural network (ANN) modeling and its application in pharmaceutical research, *Pharmaceutical and Biomedical Analysis*, Vol. 25, No. 5, 2000, pp. 717-727.
- [3]. N. Antiknock and R. Kookier, Neural network approach to prediction of bending strength and hardening behavior of particulate reinforced (Al-Si-Mg) aluminum matrix composites, *Materials and Design*, Vol. 25, No. 7, 2004, pp. 595-602.
- [4]. G. E. Hinton and R. J. Williams, et al., Representation by back propagation errors, *Nature*, Vol. 3, No. 6, 1986, pp. 899-905.
- [5]. D. Sengupta and R. Iltis, A Neural Solution to the Multitarget Tracking Data association Problem, *IEEE Trans. on Aerospace and Electronic System*, 1989, pp. 96-108.
- [6]. WiMAX's technology for Los and NLOS environments, White Paper, *WiMAX Forum*, <http://www.Wimaxforum.com>, 2004, pp. 1-6.
- [7]. Ma Changlin, R. Klukas, and G. Lachapelle, An enchanted two-step least squared approach for TDOA/AOA wireless localization, in *Proceedings of the ICC' 2003*, Anchorage, Alaska, USA, Vol. 2, 2003, pp. 987-991.
- [8]. R. Ertel, P. Cardieri, and K. W. Sowerby, et al., Overview of spatial channel models for antenna array communication systems, *IEEE Personal Communications*, 1998, pp. 10-20.
- [9]. J. H. Han and D. K. Jeon, Comparisons of error characteristics between TOA and TDOA positioning, *IEEE Trans. Aerospace and Electronic System*, Vol. 38, No. 1, 2002, pp. 307-311.

## A Frequent Pattern Mining Algorithm Based on Concept Lattice

<sup>1, 2, 3</sup> Changsheng Zhang, <sup>4</sup> Jing Ruan, <sup>3,\*</sup> Haijiang Xia,  
<sup>3</sup> Hailong Huang, <sup>1</sup> Bingru Yang

<sup>1</sup> School of Computer and Communication Engineering, University of Science and Technology  
Beijing, Beijing, BJ10, China

<sup>2</sup> Beijing Key Laboratory of Knowledge Engineering for Materials Science, Beijing, BJ10, China

<sup>3</sup> College of Physics & Electronic Information Engineering,  
Wenzhou University, Zhejiang, ZJ577, China

<sup>4</sup> Wenzhou Vocational & Technical College, Zhejiang, ZJ577, China

<sup>1</sup> Tel.: 0086-0577-86590275, fax: 0086-0577-86689010

E-mail: [jsj\\_zcs@126.com](mailto:jsj_zcs@126.com), [ruanjing1979@126.com](mailto:ruanjing1979@126.com),  
[156732998@qq.com](mailto:156732998@qq.com), [hhl@wzu.edu.cn](mailto:hhl@wzu.edu.cn), [bryang\\_kd@yahoo.com.cn](mailto:bryang_kd@yahoo.com.cn)

Received: 5 June 2013 / Accepted: 25 August 2013 / Published: 30 September 2013

---

**Abstract:** The concept lattice is an effective tool for data analysis and rule extraction, it is often well to mine frequent patterns by making use of concept lattice. In this paper, a frequent itemset mining algorithm FPCL based on concept lattice which builds lattice in batches, the algorithm builds lattice down layer by layer through the layer concept nodes and temporary nodes based on hierarchical concept lattice; and seeks up the parent-child relationship upward concept nodes layer by layer, which can be generated the Hasse diagram with the inter-layer connection. In addition, in the process of the generation of each lattice node, we do the dynamic pruning for the concept lattice based on the minimum support degree and relevant properties, and delete a large number of non-frequent, repeat and containing nodes, such that redundant lattice nodes do not generate, thus the space and time complexities of the algorithm are greatly enhanced. The experimental results show that the algorithm has a good performance. *Copyright © 2013 IFSA.*

**Keywords:** Data mining, Frequent itemset, Concept lattice, Dynamic pruning.

---

### 1. Introduction

Formal concept analysis, proposed by Professor Wille in 1980s can be seen philosophical understanding of the concepts [1]; formal concepts of core data structure can accurately and succinctly describe the layers relationship between concepts, so it now becomes a kind of important method for knowledge representation, along with the development of research, more and more researchers have focused on formal concept analysis, it applied to data mining field increasingly, and becomes an

effective tool for processing and organizing large-scale data. The main reason is because formal concept analysis can organize judiciously to data by the concept lattice, the node of concept lattice embodies the unification of intension and extension of concepts, so it is very suitable to mining rule knowledge, the form of knowledge expression is clear and easy.

The concept lattice is a concept hierarchical structure according to binary relation, which is an effective tool for data analysis and rule extraction. The essence of generating concept lattice from the

data set is a conceptual clustering process, the concept lattice induced by binary relation is a very useful formal tool, it embodies the unification of concept connotation and denotation, reflecting the relation of objects and attributes and the relationship of generalization instantiation between concepts, thus it is very suitable to mine potential concepts and knowledge from data sets.

In the process of the application of the concept lattice, it is firstly to solve the construction problem of lattice. Therefore, it is important to the construction algorithm of concept lattice. The construction method of concept lattice can be divided into two categories: batch processing algorithms and incremental construction algorithm. There are many literatures have proposed the construction algorithm of concept lattice, such as [2-4].

In view of the characteristics of the concept lattice, it is suitable for mining association rules and characteristics rules from data, the Eclat algorithm proposed by Zaki *et al.* [5] used the representation of longitudinal data, and mined frequent itemsets through lattice and item clustering technique. Hu [6] proposed the integrated mining methods based on the classification of concept lattice and association rules, this approach has considered all nodes and produced a large number of redundant rules. Wang and Hu [7] provided association rule mining based on quantitative concept lattice, and improved the algorithm in the literature [5], generated frequent concept lattice, and extracted rules on frequent concept lattice. Godin [8] proposed the extraction algorithm to determine the association rules; Missaoui [9] provided the extraction algorithm of approximate association rules. Pasquier *et al.* [10] proposed a base of the extraction of deterministic association rules, as well as the proper base and structure base of approximate association rules, subsequently extracted association rules on concept lattice [11]. Hu [12] also proposed quick algorithm on association rules based on the reduct concept lattice, other scholars have studied mining algorithms of association rules based on concept lattice [13-22].

But in the practical applications, the spatial and temporal complexities of frequent pattern mining algorithms based on concept lattice need to be improved, in this paper, a new frequent pattern mining algorithms FPCL (Frequent Pattern Mining Based on Concept Lattice) is provided based on the theory of concept lattice, which only needs to scan the database once to generate all frequent patterns. This algorithm employs a core data structure concept lattice Hasse diagram in formal concept analysis theory to store frequent concepts, and designs quick building lattice algorithm in batches. It builds lattice layer by layer based on hierarchical concept lattice, and generates cross-layer connections Hasse diagram. The algorithm do the dynamic pruning for the concept lattice based on the minimum support degree and relevant properties, and delete a large number of non-frequent concepts, just reserve frequent concepts, such that the space and time complexities of the

algorithm are greatly enhanced. The experimental results show that the efficiency of the algorithm is superior to previous algorithms.

## 2. Basic Concepts

### 2.1. Concept Lattice

In the formal concept analysis, it can be understood as follows, the extension of a concept  $C$  is a set of all objects that belong to the  $C$ , the common feature or attribute set of all these objects is called the connotation of the concept  $C$ , and each concept in concept lattice is a set of objects of the greatest common properties. All concepts together with the relationships of generalization / instantiation form the concept lattice. The concept lattice is the core data structure of formal concept analysis theory, the corresponding Hasse diagram realize data visualization. And for a formal context, the construction of concept lattice structure is unique, that is to say, it does not influenced by the ranking of data or attributes, which is a very significant advantage of the concept lattice.

**Definition 1:** Let  $I=\{i_1, i_2, \dots, i_m\}$  is a set of items, the transaction database  $D=\langle T_1, T_2, \dots, T_n \rangle$ , each transaction  $T$  is a set of items,  $T \subseteq I$ , if  $X \subseteq T$ , then  $X$  is called an itemset, if  $X$  has  $k$  elements, then  $X$  is called  $k$ -itemset. If the support degree is greater than or equal to a given threshold  $\text{minsup}$  of an itemset  $X$ , then  $X$  is a frequent itemset or frequent pattern.

**Definition 2.** A formal context is a triple  $K=(G, M, I)$ , where  $G$  is a set of objects,  $M$  is a set of attributes,  $I$  is a binary relation between the  $G$  and  $M$ , i.e.  $I \subseteq G \times M$ ,  $g/m$  denotes it exists a relationship  $I$ .

**Definition 3.** In the formal context  $K$ , a binary groups  $(A, B)$  from  $G \times M$  exists the following two properties:

1)  $B=f(A)$ , where  $f(A) = \{m: (m \in M) \wedge (\forall g \in A \subseteq G, g/m)\}$ ;

2)  $A=g(B)$ , where  $g(B) = \{g: (g \in G) \wedge (\forall m \in B \subseteq M, g/m)\}$ ;

In the formal context  $K$ ,  $(A, B)$  is called as a concept, where  $B$  is referred to as intent of the concept, and  $A$  is called the extension of the concept. Each concept is a node of concept lattice, the maximum element of lattice is  $(G, f(G))$ , the minimum element of lattice is  $(g(M), M)$ .

**Definition 4.** A partial order relation between the concept nodes is established. Given  $C_1=(A_1, B_1)$  and  $C_2=(A_2, B_2)$ , then  $C_1 > C_2 \Leftrightarrow B_1 \subset B_2 \Leftrightarrow A_1 \supset A_2$ , the leading order means  $C_1$  is the parent node of  $C_2$  or the generalization. If concepts  $C_1=(A_1, B_1)$  and  $C_2=(A_2, B_2)$  satisfy  $A_2 \subset A_1$ , and there does not exist the concepts  $(A, B)$  such that  $A_2 \subset A \subset A_1$ ; then  $C_1$  is called the direct super-concept of  $C_2$ ,  $C_2$  is a direct sub concept of  $C_1$ , referred to as  $(A_1, B_1) > (A_2, B_2)$ . The linear diagram of concept lattice is generated

based on the partial order relation, which is Hasse diagram.

**Definition 5.** In the form context  $K=(G, M, I)$ , the relationship between the object  $g \in G$  and the property  $m \in M$  is  $(g, m) \in I$  or  $(g, m) \notin I$ . A limited form background can be represented by a matrix, if  $(g, m) \in I$ , we use digit 1 to represent in the matrix; if  $(g, m) \notin I$ , we use digit 0 to represent in the matrix, this matrix is said to be a transaction matrix  $T$  in formal context  $K$ .

**Definition 6.** For the concept  $C(X, Y)$ ,  $C'(|X|, Y)$  is quantized by the concept  $C$ , and  $C$  is the real concept of  $C'$ .  $|X|$  is the cardinality of the epitaxial  $X$ , the posed lattice is quantified by quantitative concept, which is quantitative concept lattice.

**Definition 7.** Given concept  $C(A, B)$ ,  $B \in M$ ; given a threshold  $\text{minsup} \in [0, 1]$ , the support degree of attribute set  $B$  in forms background  $K$  is  $\text{sup}(B) = |g(B)| / |G|$  (where  $g(B) = \{g \in G \mid \forall m \in B: (g, m) \in I\}$ ), if  $\text{sup}(B) \geq \text{minsup}$ , then  $B$  is called the frequent attribute set, and  $C$  is a frequent concept. That if the connotation of concept is frequent, then the connotation is called as the concept of frequent connotation, which is also called as frequent concept,  $\text{sup}(C) = |g(B)| / |G| = |A| / |G| \geq \text{minsup}$ , where  $|A|$  is the epitaxial base of concept  $C$ ,  $|G|$  is the total number of transactions in the database  $D$ .

**Definition 8.** Let  $K=(G, M, I)$  be a form context, for an attribute  $y \in M$ , in the matrix of  $K$ , if  $y$  corresponding to the columns has numbers of  $n$  equal to 1, we call the rank of the attribute is  $n$ , denoted as  $r(y) = n$ . Denoted by  $m = \max\{r(y) \mid y \in M\}$ ,  $m$  is the rank of form context.

**Definition 9.** In the concept lattice, if  $B$  in the concept  $(A, B)$  contains the number of attributes is  $K$ , called  $(A, B)$  is the lattice nodes of the  $K$ -th layer, the layer is referred to as the  $L_k$ .

The following properties can be obtained from the above definitions.

**Property 1.** Any one lattice nodes in the  $N$ -th layer, which at least is covered by one of the lattice nodes in the  $N-1$ -th layer.

**Property 2.** The concept nodes in  $L_k$  layer and other concept nodes or temporary nodes intersect in pair, and generate  $L_{k+1}$  layer nodes, where the non-concept nodes are called temporary nodes.

**Property 3.** For  $C_1=(a, b)$  and  $C_2=(a', b')$ , if it satisfies  $a' \subseteq a$ ,  $b' \subseteq b$ , then directly discard  $C_2$ .

**Property 4.** For  $C_1=(a, b)$  and  $C_2=(a', b')$ , if it satisfies  $a'=a$ ,  $b' \neq b$ ,  $C_1=(a, b \cup b')$ , then directly discard  $C_2$ .

**Property 5.** For  $C_1=(a, b)$  and  $C_2=(a', b')$ , if it satisfies  $a' \neq a$ ,  $b'=b$ ,  $C_1=(a \cup a', b)$ , then directly discard  $C_2$ .

## 2.2. The Relation Between Concept Lattice and Frequent Itemsets

The relationship between the set of attributes values (itemset) has been reflected in the concept

lattices. If take  $G$  as a set of transaction set TIDS in association rules,  $M$  as a set of items,  $I$  as the relationship between them, that is to say, which transaction has the same items set, then each concept lattice node is actually a maximum itemset. The lattice node can be expressed as  $C=(A, B)$ , where  $|A|$  is the cardinality of the set of all cases belongs to  $C$ ,  $B$  is their common properties. Obviously, for each node  $(A, B)$ , if  $|A|/|D|$  is greater than the minimum support degree  $\text{minsup}$ , then  $B$  is a frequent itemset, and  $|A|$  is the support degree count of frequent itemset.

## 3. FPCL Algorithm

### 3.1. The Descriptions of Algorithm

From the structure of the concept lattice, it can easily be seen that concept lattice is composed of two parts: the node of concepts and the connections between nodes. Therefore, the essence of constructing concept lattice in the batch algorithm is to generate the concept nodes and the connection relationship between them. The two tasks are included in constructing concept lattice:

- 1) Generate all lattice nodes;
- 2) Establish the direct predecessor and direct successor relations between all the lattice nodes.

In the batch processing algorithms, the Bordat algorithm is simple, intuitive, and representative [2]. The lack of this algorithm is to generate a lot of duplicate lattice nodes. Each node has many parent nodes, so it is generated a number of times. In this paper, the designed algorithm FPCL draws the characteristics of Bordat algorithm, it is simple, intuitive and easy-to-parallel computing, and the core designed idea of this algorithm is as follows. For the concept node  $C=(g(m), m)$  in  $L_k$  layer and other concept nodes  $C'=(g(n), n)$  or the temporary nodes  $C^*=(g(n), n)$ , do such operations: construct the intersection operation of the extension and the combination operation of the connotation  $g(m) \cap g(n)$ ,  $m \cup n$  for every two nodes, and the results are taken as the extension and the connotation of the newly generated node for  $L_{k+1}$  layer; generate a new node each time is then to call `PruningConceptLattice()`, do the pruning operation and delete the duplicate, contained and non-frequent nodes; after pruning, if nodes should be reserved, then call on the function `IsConceptLattice()` to determine whether the concept node, the non-concept nodes are marked with \* as provisional nodes, such as  $C^*$ ; and for each newly generated node, we call the function `GenerateLine()` to connect the new generated nodes to the upper concept parent nodes to generate the parent-child relationship, the key of this step is to judge the parent node is a temporary node in  $k$  layer, if it is, we must look for the parent concept of concept nodes from  $k = k-1$  layer continually and do the connections; after generating all the nodes in

$L_{k+1}$  layer, we need to delete all temporary node in  $L_k$  layer to free the space up, until finish generating  $L_{k+1}$  layer and establish a father and son connection between nodes. Repeat the above steps it will be to build a complete concept lattice, at the same time, the methods of seeking the parent-child relationship of concept nodes up to layer by layer, such that this algorithm can generate the Hasse diagram of inter-layer connection.

### 3.2. Pseudo Codes

#### Algorithm: FPCL

**Input:** A formal context (K), a minimum support (minsup)

**Output:** Concept lattice L corresponding Hasse diagram

// Initialization

D=0; // numbers of all transaction records

$C_{max}$ =Null; // maximum element

$L_k$ =Null; //save the concept lattice nodes

Flag=false;

Begin;

$K \rightarrow T'$ ; //formal context K is changed into transaction matrix  $T'$

$T' \xrightarrow{\text{sort by } r(m) \text{ in a descending order}} T$ ; // generate sorted matrix T

$D=|G|$ ; // G is a set of all records

$C=C_{max}=(G, \phi)$ ,  $m \in M$ ,  $C^*=(g(m), m) \rightarrow L_{k=0}$ ;

$k=0$ ;

While  $L_k \rightarrow L_{k+1}$

For each  $C_m \in L_k$  //  $C_m$  is a concept node

For each  $C_n \in L_k - C_m$  //  $C_n$  is a concept node or a temporary node

$C_m \bowtie C_n \xrightarrow{g(m) \cap g(n), m \cup n} C \in L_{k+1}$ ;

PruningConceptLattice(C); // Pruning

IsConceptLattice(C); // determine whether is the concept node

IF Flag==false and C.Extent== $C_{max}$ . Extent

THEN

$C_{max}=C$ ; // find the maximum element to replace  $C_{max}$

Flag=true;

ELSE IF Flag==false and

C.Extent  $\neq$   $C_{max}$ .Extent THEN

Add edge  $C \rightarrow C_{max}$ ;

ELSE IF

GenerateLine(C, k); //connect to generate a parent-child relationship

END IF

End For

End For

// Delete all temporary nodes in  $L_k$  layer

For each  $C^* \in L_k$

Delete  $C^*$  From  $L_k$ ;

End For

$k++$ ; // continue to generate the nodes in next layer

End While

END

Function: PruningConceptLattice(C)

BEGIN

//sup(C) represents a epitaxial base of C

IF sup(C)/D < minsup

Delete C From  $L_k$ ;

End IF

For each  $C'=(a', b') \in L_k - C=(a, b)$

IF  $a' \subseteq a$  And  $b' \subseteq b$

Delete  $C'$  From  $L_k$ ;

Else IF  $a'=a$  And  $b'=b$

Delete  $C'$  From  $L_k$ ;

Else IF  $a'=a$  And  $b' \neq b$

$C=(a, b \cup b')$ ;

Delete  $C'$  From  $L_k$ ;

Else IF  $a' \neq a$  And  $b'=b$

$C=(a \cup a', b)$ ;

Delete  $C'$  From  $L_k$ ;

End If

End For

End

Function: IsConceptLattice(C)

BEGIN

// if the base of connotation property of C is larger than the layer ID k, then C is not a concept in this layer, marked as a temporary concept node

If ( $|C.Intent| > k$ )

{  $C \rightarrow C^*$ ; }

Else

{  $g(m), T \rightarrow T', t_m$ ; //  $T'$  is a matrix composed of g(m) rows in T;  $t_m$  is a column vector with all 1's after the merger of m columns in  $T'$ ;

For each  $t \in T'_{M-m}$

If( $(t_m[0]*t[0])*(t_m[1]*t[1])* \dots *(t_m[|M|-1]*t[|M|-1])=1$ )

{  $C \rightarrow C^*$ ;

Break; }

End For

}

End

Function: GenerateLine(C, k)

BEGIN

For each  $C_p \in L_k$

IF  $C_p$  is C's parent node And No edge  $C \rightarrow C_p$

IF  $C_p$  is a concept node

reAdd edge  $C \rightarrow C_p$ ;

Else IF  $C_p$  is a temporary node

GenerateLine(C, k-1); //after finding the parent concept nodes of nearest layer C then plus edge

End IF

End IF

End For

End

### 3.3. Example

The formal context K is determined by the front eight things in the transaction database D as shown in Table 1, the fixed number of attributes is 7, the minimum support degree minsup=20 %.

Table 1. Formal context.

No.	a	b	c	d	e	f	g
1	1	0	1	1	0	1	0
2	1	1	1	1	0	1	0
3	1	0	1	0	0	0	1
4	1	1	0	0	0	0	1
5	1	1	0	0	0	0	1
6	1	1	1	0	0	0	1
7	1	1	0	1	0	1	0
8	1	0	1	1	1	0	0

Input: the formal context K is shown in Table 1, the minimum support degree minsup =20%.

Output: the corresponding Hasse diagram of concept lattice L.

// Initialization

D=0;// numbers of all transaction records

C<sub>max</sub>=Null; // maximum element

L<sub>k</sub>=Null; // save the concept lattice nodes

Flag=false;// whether to find maximum element

Step 1: Let formal context K is changed into transaction matrix, sort in a descending order according to r(m)=n, and generate matrix T;

D=8; C<sub>max</sub>=(12345678, φ);

	a	b	c	d	g	f	e
1	1	0	1	1	0	1	0
2	1	1	1	1	0	1	0
3	1	0	1	0	1	0	0
4	1	1	0	0	1	0	0
5	1	1	0	0	1	0	0
6	1	1	1	0	1	0	0
7	1	1	0	1	0	1	0
8	1	0	1	1	0	0	1

Fig. 1. The transaction matrix T after ordering.

For each  $m \in M$ , generate  $C^*=(g(m), m) = \{C_{01}^*=(12345678, a)^*, C_{02}^*=(24567, b)^*, C_{03}^*=(12368, c)^*, C_{04}^*=(1278, d)^*, C_{05}^*=(3456, g)^*, C_{06}^*=(127, f)^*, C_{07}^*=(8, e)^*\}; C=C_{max}$  and  $C^*$  are composed of the set of the temporary layer nodes  $L_{k=0}$ .

The generated process from  $L_{k=0}$  to  $L_{k=0}$  is as follows: for the concept nodes  $C=(g(m), m)$  and other temporary nodes  $C^*=(g(n), n)$  in the current layer  $L_{k=0}$ , construct the intersection operation of the extension and the combination operation of the connotation  $g(m) \cap g(n), m \cup n$ , and generate new nodes in  $L_{k=1}$  layer, and for each newly generated

node, we call for the function PruningConceptLattice() to do the pruning. At each time it generates a new node and then calls the function PruningConceptLattice() to do the pruning for nodes, and remove duplicate, contained and non-frequent nodes, where only the node support degree  $sup(C_{17})=1/8 < 20\%$  of node  $C_{17}=(8, e)$ , so this step is only to remove the  $C_{17}$  node; after pruning for each node, we call function IsConceptLattice() to determine whether the node is a concept node, if not, the non-concept nodes marked with \* as temporary nodes, when  $C_{11}=(12345678, a)$  is determined by the concept, because  $Flag=false$  and  $C_1.Extent=C_{max}.Extent$ , so  $C_{max}=C_{11}$  is a maximum element, and make  $Flag = true$ , to find the maximum element; other nodes from  $C_{12}^*$  to  $C_{16}^*$  are temporary nodes; for each newly generated node, we call for GenerateLine() function to generate a new node and connect with the concept parent node of the recent upper layer, due to the nodes in  $L_{k=1}$  layer have no upper parent node, it does not need to increase the edges; after generating the parent-child relationship, then to delete the temporary nodes in  $L_{k=0}$  layer, the set of nodes in  $L_{k=1}$  layer is:  $\{C_{11}=(12345678, a), C_{12}^*=(24567, b)^*, C_{13}^*=(12368, c)^*, C_{14}^*=(1278, d)^*, C_{15}^*=(3456, g)^*, C_{16}^*=(127, f)^*\}$ .

The nodes of current layer  $L_{k=1}$  can compute the new nodes for layer  $L_{k=2}$ , owing to layer  $L_{k=1}$  only includes concept node  $C_{11}$ ,  $C_{11}$  and the other temporary node is computed, at last, the set of nodes in layer  $L_{k=2}$  is  $\{C_{21}=(24567, ab), C_{22}=(12368, ac), C_{23}=(1278, ad), C_{24}=(3456, ag), C_{25}^*=(127, af)^*\}$ ; according to function PruningConceptLattice() to prune the nodes in current layer, and there are not deleted nodes; according to function IsConceptLattice(), these nodes have yet to is concept nodes,  $C_{25}^*=(127, af)^*$  is only temporary node, according to function GenerateLine(), the link is connected between the node  $C_{11}$  and the other nodes, then delete all temporary nodes in layer  $L_{k=1}$ , the process as shown in Fig. 2.

The nodes of current layer  $L_{k=2}$  can compute the new nodes for layer  $L_{k=3}$ , the set of nodes in layer  $L_{k=3}$  is  $\{C_{31}=(26, abc), C_{32}^*=(27, abdf)^*, C_{33}=(456, abg), C_{34}^*=(27, abf)^*, C_{35}=(128, acd), C_{36}=(36, acg), C_{37}^*=(12, acf)^*, C_{38}=(127, adf)\}$ ; according to function Pruning ConceptLattice(), the nodes  $C_{32}^*$  and  $C_{34}^*$  is combined to the new node  $C_{32}^*=(27, abdf)^*$ ; and according to function IsConceptLattice(), although the node  $C_{32}^*=(27, abdf)^*$  is concept node, it is not node in current layer, so this node is labeled to temporary nodes. At last, the set of nodes in layer  $L_{k=3}$  is  $\{C_{31}=(26, abc), C_{32}^*=(27, abdf)^*, C_{33}=(456, abg), C_{35}=(128, acd), C_{36}=(36, acg), C_{37}^*=(12, acf)^*, C_{38}=(127, adf)\}$ ; According to function GenerateLine(), the relationship between father and son nodes are connected, the process as shown in Fig. 3.

The nodes of current layer  $L_{k=3}$  can compute the new nodes for layer  $L_{k=4}$ , the set of nodes in layer  $L_{k=4}$  is  $\{C_{41}^*=(2, abcdf)^*, C_{42}=(6, abcg),$

$C_{43}^*=(2, abcd)^*$ ,  $C_{44}^*=(2, abcf)^*$ ,  $C_{45}=(12, cdf)$ ,  $C_{46}=(27, abdf)$ ; According to function PruningConceptLattice(), Delete less support nodes  $C_{41}^*=(2, abcdf)^*$ ,  $C_{42}=(6, abcg)$ ,  $C_{43}^*=(2, abcd)^*$ ,  $C_{44}^*=(2, abcf)^*$  for  $\text{sup}(C_{kn})=1/8 < 20\%$ ; According to function IsConceptLattice(), determine whether the concept nodes, at last, the set of nodes in layer  $L_{k=4}$  is  $\{C_{45}=(12, acdf)$ ,  $C_{46}=(27, abdf)\}$ ; According to function GenerateLine(), the relationship between father and son nodes are connected, then the all temporary nodes in layer  $L_{k=4}$  is deleted, the father

link between node  $C_{46}$  and  $C_{38}=(127, adf)$ , the cross-layer father link between node  $C_{46}$  and  $C_{21}=(24567, ab)$  are built, the process as shown in Fig. 4.

The nodes of current layer  $L_{k=4}$  can compute the new nodes for layer  $L_{k=5}$ , the set of nodes in layer  $L_{k=5}$  is  $\{C_{51}=(2, abcdf)\}$ , owing to the less  $\text{sup}(C_{51})=1/8 < 20\%$  for  $C_{51}$ ; according to function PruningConceptLattice(), the node is deleted, the process as shown in Fig. 5.

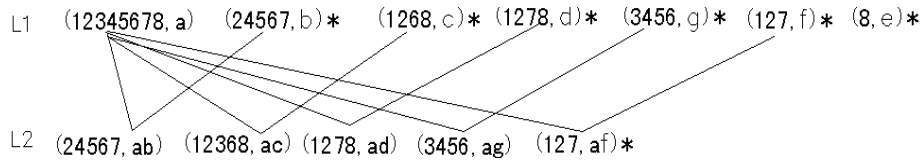


Fig. 2. Layer  $L_{k=2}$  be generated by layer  $L_{k=1}$ .

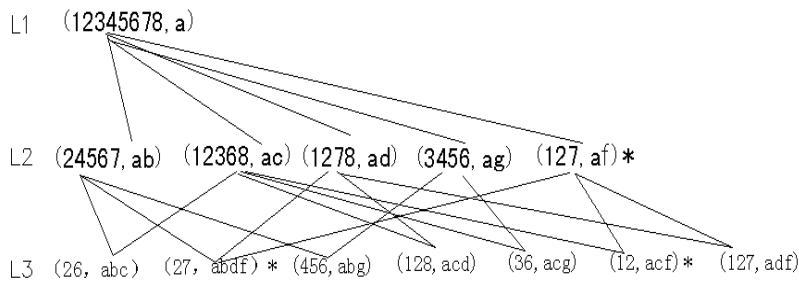


Fig. 3. Layer  $L_{k=3}$  be generated by layer  $L_{k=2}$ .

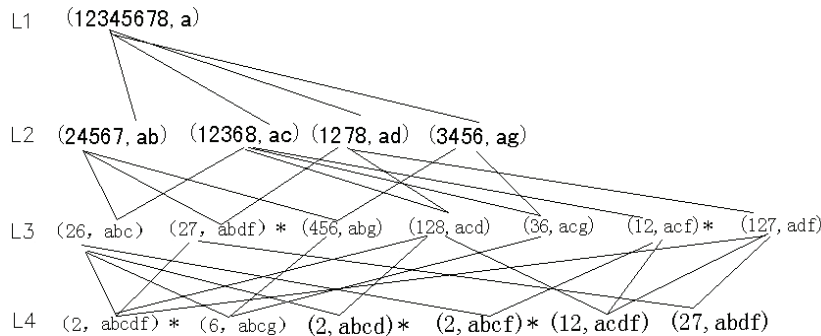


Fig. 4. Layer  $L_{k=4}$  be generated by layer  $L_{k=3}$ .

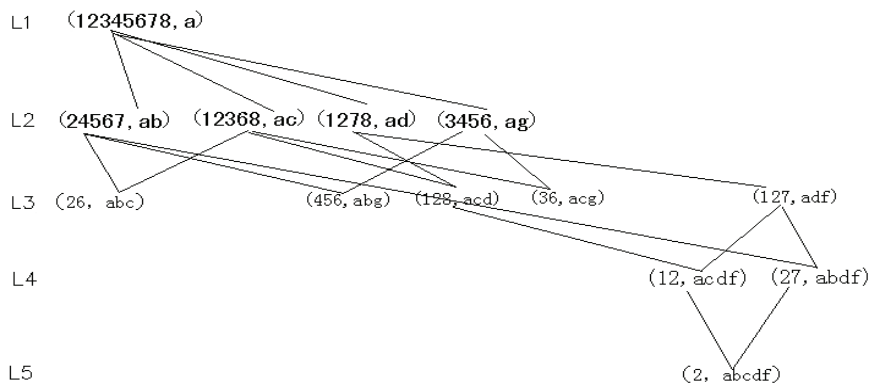


Fig. 5. Layer  $L_{k=5}$  be generated by layer  $L_{k=4}$ .

So there are not the nodes of next layer, at last, the link between the least element ( $\emptyset$ , abcdefg) and the above node is constructed, the entire process for building concept is finished.

Aiming at the core steps, we give an example, where calling IsConceptLattice() function to judge to determine the node whether is a concept node or not: in the generated process from  $L_{k=1}$  to  $L_{k=2}$ , example as follows: by the operator  $C_{11}$  and  $C_{14}^*$  to generate  $C_{23}=(1278, ad)$ , the judgement method is firstly to take  $T'$  and  $t_{ad}$  from the formal context matrix as shown in Fig. 6; multiply each element of  $ad$  column vector and the elements correspond to the remaining column vector in  $T'$ , the multiplied value is also the product, and its values can only be 0 or 1, if there exists the multiplied value of one column is 1, then it explain that there exists the identical column vectors between the rest columns in  $T'$  and  $t_{ab}$ , and therefore it does not satisfy the definition 3, so the node is not a concept. The determination results are as follows:

$$\begin{aligned} ad*b &= (1*0)(1*1)(1*1)(1*0)=0, \\ ad*c &= (1*1)(1*1)(1*0)(1*1)=0, \\ ad*g &= (1*0)(1*0)(1*0)(1*0)=0, \\ ad*f &= (1*1)(1*1)(1*1)(1*0)=0, \end{aligned}$$

Since the multiplication results of the  $ad$  and  $b, c, g, f$  are 0, thus the  $ad$  is a concept.

	ad	b	c	g	f
1	1	0	1	0	1
2	1	1	1	0	1
7	1	1	0	0	1
8	1	0	1	0	0

Fig. 6. Temporary matrix  $T'$ .

While the generated process from the  $L_{k=2}$  layer node to the  $L_{k=3}$  layer node,  $C_{21}=(24567, ab)$  and  $C_{23}=(1278, ad)$  generate  $C_{32}^*=(27, abd)^*$ ,  $C_{21}=(24567, ab)$  and  $C_{25}^*=(127, af)$  generate  $C_{34}^*=(27, abf)^*$ , by pruning function PruningConceptLattice(), it synthesize  $C_{32}=(27, abdf)$ , then calling function IsConceptLattice(), though  $C_{32}$  is a concept, due to  $|C_{32}.Intent|>3$ , thus  $C_{32}$  is not the layer concept, which is marked as a temporary node  $C_{32}^*=(27, abdf)^*$ .

In the generated process of  $L_{k=4}$  layer node, through the concept node  $C_{38}=(127, adf)$  and temporary node  $C_{32}^*=(27, abdf)^*$  to generate the concept node  $C_{46}=(27, abdf)$ , node  $C_{46}=(27, abdf)$  is connected to line with the two parent nodes, it finds that the parent node  $C_{32}^*=(27, abdf)^*$  is a temporary node, then continue to be found to the parent node from upper layer  $C_{21}=(24567, ab)$  to establish the parent-child connection.

The Hasse diagram corresponding to the obtained concept lattice is shown in Fig. 8.

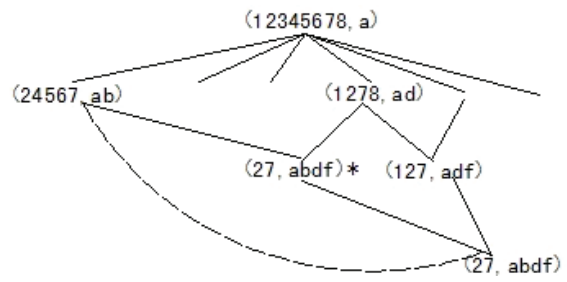


Fig. 7. To find the upper parent concept node.

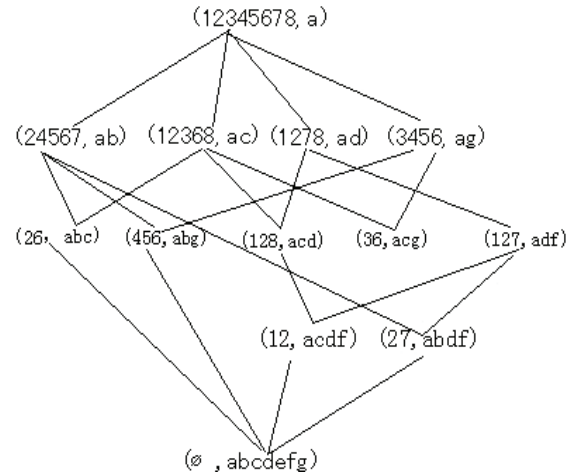


Fig. 8. The Hasse diagram corresponding to the concept lattice  $L$ .

#### 4. Experimental Analysis

Because the FP-Growth algorithm [23] has good time efficiency, we choose FP-Growth and the FPCL to make a comparative analysis to analyze the performance of the algorithm. The experimental environment is a Pc machine of a Windows Server 2003 operating system, I7 2.0G 64-bit quad-core eight lines with the processor, 8G memory, and the program runs in the environment of JAVA SDK1.4.2. The data set Mushroom is selected from machine learning databases UCI provided by the University of California (<http://archive.ics.uci.edu/ml/>), the data set contains a total of 8124 objects, 23 attributes, under different minimum support degrees (1%, 5%, 10%, 15%, 20%), the two algorithms are do the test for the generated process of frequent itemsets, and the experimental results show that the number of two algorithms generate the same number of all frequent itemsets, and the performance results are shown in Fig. 9.

The comparison results show that when the minimum support is 1%, the efficiency of the two algorithms for generating frequent item sets is similar, because the number of the generated frequent items is more at low support degree, the time overhead is great for constructing trees of the FP-Growth algorithm or the constructing lattice of

the FPCL algorithm. However, with increasing support degree, the advantages of the FPCL algorithm is obvious, due to much pruning for non-frequent items, it reduces the time of the constructing lattice, such that the efficiency is significantly improved.

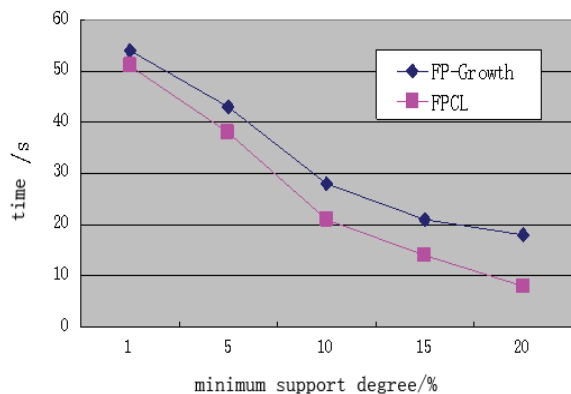


Fig. 9. The comparisons of running time by two algorithms.

In addition, our designed algorithm FPCL dose the layer for concept lattice nodes, by a breadth-first approach it is to construct lattices down layer by layer, and sort the rank size of each attribute vector in the formal context matrix, then it determines the temporary node as soon as possible when judging whether are the concept nodes; the nodes in lower layer are generated by the upper concept nodes and other concept nodes or temporary nodes for pairwise operations; screening the newly generated nodes by the minimum support degree, and delete the duplication and contained nodes, in the following to determine each node whether belongs to concept node or temporary nodes, if it is a temporary node, then mark with \*; thus the generated node has no redundancy and duplication, such that there exists no redundancy and duplication nodes in the next layer, so as to speed up the construction of lattices. To determine new node whether belongs to the concept, it uses the transaction matrix to extract parts of rows that attributes intersect are equal to 1 to compose the validation matrix so as to judge quickly. Therefore, it speeds up the speed of the judgment nodes. At the same time, the approaches of concept nodes seeking the parent-child relationship up layer by layer, such that this algorithm can generate the Hasse diagram of the inter-layer connection.

## 5. Conclusions

In this paper, a frequent itemset mining algorithm FPCL based on concept lattice constructing lattice in batches approach. With the introduction of the stratified nodes of concept lattice, and discuss the property of the hierarchical concept lattice, by the

breadth-first approach of constructing the lattice layer by layer, such that each layer node does not generate duplicate node. Therefore, the generation of the nodes in the next layer does not occur as the case that duplicate nodes generate the nodes, such that the generation speed of the nodes is improved, so as to improve the solving efficiency of the frequent itemsets, and some examples are given to illustrate the specific steps and correctness of the algorithm. The experiments also proved the superiority of the space and time complexities of the algorithm. Our direction and future research work are to expand the applications of the algorithm and make use of the mining results to generate non-redundant association rules quickly.

## Acknowledgements

This work was supported in part by the National Natural Science Foundation of China (No. 60875029, No. 61175048); The Project of Beijing Key Laboratory of Knowledge Engineering for Materials Science (No. Z121101002812005), The Project supported by Zhejiang provincial Natural Science Foundation of China (No. LY13F020024).

## References

- [1]. Wille R., Restructuring lattice theory: an approach based on hierarchies of concepts, in Rivall. (Eds.), *Ordered Sets*, Reidel, Dordrecht, 1982.
- [2]. Bordat J. P., Calcul pratique du treillis de Galois d'une correspondance, *Match Sci Hum*, Vol. 96, 1986, pp. 31-47.
- [3]. Zhi Hui Lai, Zhi Dong-Jie, Liu Zong-Tian, Theory and Algorithm of Concept Lattice Union, *Acta Electronica Sinica*, Vol. 38, No. 2, 2010, pp. 455-459.
- [4]. Qu Wen-Jian, Tan Guang-Xing, Qiu Tao-Rong, New Algorithm of Generating Concept Lattice Using Universal Matrix, *Journal of Chinese Computer Systems*, Vol. 33, No. 3, 2012, pp. 558-564.
- [5]. M. J. Zaki, S. Parthasarathy, M. Ogihara and W. Li, New algorithms for fast discovery of association rules, in *Proceedings of the Conference on Knowledge Discovery and Data Mining (KDD' 1997)*, Newport Beach, California, August 1997, pp. 283-286.
- [6]. Hu Ke Yun, Lu Yu Chang, Shi Chun Y, An Integrated Mining Approach for Classification and Association Rule Based on Concept Lattice, *Journal of Software*, Vol. 11, No. 11, 2000, pp. 478-483.
- [7]. Wang De Xing, Hu Xue Gang, Wang Hao, Algorithm of mining association rules based on Quantitative Concept Lattice, *Journal of Hefei University of Technology (Natural Science)*, Vol. 25, No. 5, 2002, pp. 678-682.
- [8]. R. Godin, R. Missaoui, Incremental concept formation for learning from Databases, *Theoretical Computer Science*, Vol. 133, 1994, pp. 87-419.
- [9]. R. Missaoui, R. Godin, A. Boujenoui, Extracting exact and approximate rules from databases, in *Proceedings of the Sofieks Workshop on*

- Incompleteness and Uncertainty in Information System*, London, Springer-Verlag, New York, 1993.
- [10]. N. Pasquier, Y. Bastide, R. Taouil, et al., Closed set based discovery of small covers for association rules, in *Proceedings of the 15emes Journees Basees Donnees Avancees (BDA 1999)*, 1999, pp. 361-381.
- [11]. Y. Bastide, N. Pasquier, R. Taouil, et al., Mining minimal non-redundant association rule using frequent closed itemsets, in *Proceedings of the Conference on Computational Logic (CL 2000)*, London, UK, 24-28 July 2000, pp. 972-986.
- [12]. Hu X. G., Wang Y. Y., Representation and resolution of reduction based on the concept lattice, *Computer Engineering and Application*, No. 22, 2005, pp. 180-183.
- [13]. Wang Hui, Wang Jing, Non-redundant association rules extraction of frequent concept lattice based on FP-tree, *Computer Engineering and Applications*, Vol. 48, No. 15, 2012, pp. 12-14.
- [14]. Chen Xiang, Wu Yue, Association Rule Mining Algorithm Based on Base Set and Concept Lattice, *Computer Engineering*, Vol. 36, No. 19, 2010, pp. 34-36.
- [15]. Xue-Gang Hu, Hui Chen, Feng Ma, The Mining of Classification Rules Based on Multiple Extended Concept Lattices, in *Proceeding of the Conference on Machine Learning and Cybernetics (ICMLC' 2005)*, Guangzhou, China, 2005, pp. 2063-2066.
- [16]. Zhao Xu-Jun, Zhang Ji-Fu, Ma Yang and Cai Jiang-Hui, Novel Classification Rule Acquisition Algorithm, *Journal of Chinese Computer Systems*, Vol. 33. No. 5, 2012, pp.1126-1130.
- [17]. Lv Yuejin, Liu Hongmei, Improved algorithm for attribute reduction on concept lattice, *Computer Engineering and Applications*, Vol. 47, No. 8, 2011, pp. 146-148.
- [18]. Taoying Li, Yan Chen, Jinsong Zhang, Logistics Service Provider Segmentation Based on Improved FCM Clustering for Mixed Data, *Journal of Computers*, Vol. 7, No. 11, 2012, pp.2629-2633.
- [19]. Wang Yuanyuan, Hu Xuegang, A Fast Algorithm for Mining Association Rules Based on Concept Lattice, in *Proceeding of the Conference on Machine Learning and Cybernetics (ICMLC' 2004)*, Shanghai, China, August 2004, pp. 1687-1691.
- [20]. Mohammed J. Zaki, Ching-Jui Hsiao, Efficient Algorithms for Mining Closed Itemsets and Their Lattice Structure, *IEEE Transaction on Knowledge and Data Engineering*, Vol. 17, No. 4, 2005, pp. 462-478.
- [21]. Sg J., Chen C., MMFI: an effective algorithm for mining maximal frequent itemsets, in *Proceeding of the Conference on International Symposium on Information Processing (ISIP' 2008)*, Moscow, Russia, 23-25 May 2008, pp. 144-148.
- [22]. Zhengjiang Wu, Jingmin Zhang, Yan Gao, An Attribute Reduction Algorithm Based on Genetic Algorithm and Discernibility Matrix, *Journal of Software*, Vol. 7, No. 11, 2012, pp. 2640-2648.
- [23]. J. Han, J. Pei and Y. Yin, Mining Frequent Patterns without Candidate Generation, in *Proceedings of the Conference on ACM SIGMOD International Conference on Management of Data (SIGMOD '00)*, Dallas, TX, May 2000, pp. 54-87.

## The Algorithms of Image Wavelet Optimize Splicing and Fusion based on Improved Region Energy

\* Xiangqian Chen, Dong Dai

Department of Computer Science and Technology, Henan Mechanical and Electrical Engineering College, Henan Xinxiang, 453003, China

\* Tel.: 15837324242

\* E-mail: chenxiangqianedu@163.com

*Received: 23 June 2013 / Accepted: 25 August 2013 / Published: 30 September 2013*

---

**Abstract:** When the wavelet image mosaics, first of all have to wavelet decomposition, the mosaic image is decomposed into multiple scales. In this paper, based on the improved area energy fusion method matching the appearance of negative, through the introduction of absolute value, eliminate the negative phenomenon. The paper presents the algorithms of image wavelet optimize splicing and fusion based on improved region energy. The algorithm to achieve the mosaic effect chart maintained from the source image information is the largest while eliminating the seams, and verify the validity and rationality. The simulation results verify the correctness and the validity of the algorithm, but also to enhance the clarity of the image fusion provides an effective way. Copyright © 2013 IFSA.

**Keywords:** Wavelet optimize, Region energy, Image mosaic, Image fusion.

---

### 1. Introduction

Fusion refers to the imaging of the multi-sensor of the same target, or the same scene or a single imaging sensor in accordance with certain rules, certain processing, generating a comparison with the original image information is more comprehensive and accurate and stable and having a the new image of redundant and complementary information [1]. Image fusion in the military field and non-military fields such as remote sensing images, medical images, machine vision has been widely used.

The image is reflected to the objective things or process space, time, the array of information of the amount of interrelated features. The digital image with various observing systems in different forms and means of observation of the objective world can be direct or indirect role in the human eye and thus produce visual perception entity. The meaning of the image quality mainly includes two aspects: image fidelity and image intelligibility. The fidelity of the

image refers to the degree of similarity between an image and reference image, image processing or usually distorted after transmission or experiencing interference, it is compared with the original image, will be able to reflect the processing or in the image quality of the transmission system aspects of the performance of the pros and cons. The intelligibility image Relevance refers to the image with some purpose people, for example, the beautiful, clear, rich layers of clear goals highlight characteristics reflects the value of the other aspects of the case.

Image fusion is generally divided into three categories: the pixel level, feature-level and decision-level fusion. The pixel-level fusion as basic fusion, feature fusion and decision level fusion. Pixel-level image fusion process can generally be divided into four steps: pre-processing, transformation and inverse transform (reconstructed image). The pretreatment includes a filtering and the registration processing on the original image to be fused. Alignment to the original image is to be fused to make the necessary

conversion, are aligned so that each of the pixels of the fused image.

Seamless image stitching technology today photogrammetry, and it is very active in the field of computer vision, digital image processing and computer graphics, remote sensing image processing, medical image processing, such as disciplinary research focus. Everyday life, ordinary camera to get wide-field must adjust the camera focal length, shot through the zoom lens to complete the scene, but the acquired panoramic photo resolution is relatively low, because the camera's resolution is certain, so shoot scene larger scene image of lower resolution, in order to obtain high-resolution scene photographs had by zooming the camera lens to reduce the field of vision of shooting, but it is not a complete scene photos and therefore require in the size of the scene and compromise between high and low resolution, so produce multiple images together to form one big scene.

Seamless image stitching technology widely used in the field of remote sensing processing, virtual reality, has aroused extensive attention of domestic and foreign researchers and research. Only from the impact of the visual evaluation patchwork eliminate aspects of seamless process multiple images in a two-dimensional plane of the research object to explore the following questions: based the existing stitching fusion algorithm, consider the image to be processed there is a big gray scale differences, the image distorted and partial mismatching may make the processed image in the mosaic, mosaic border at double boundary and a rough transition issues, put forward a more perfect stitching fusion algorithm.

Image fusion based on regional energy proposed a fusion method based on image fusion algorithm based on wavelet transform. Wavelet transform-based image fusion algorithm is mainly the fact that the use of the human eye is more sensitive to the changes in the local contrast according to certain fusion rule, selected the most significant feature in the original image, multiple, for example edge segment, and these characteristics are retained in the final synthesized image. Wavelet transform of an image, the absolute value of the wavelet coefficients corresponding to the edge of the more significant characteristics, largely based on wavelet transform image fusion algorithm to study how to select the wavelet coefficients in the composite image, that is, three the direction of the high-frequency coefficients, so as to achieve the purpose of preserving image edges. The paper presents the algorithms of image wavelet optimize splicing and fusion based on improved region energy.

## 2. Image Fusion Method Based on the Regional Energy

Region-based fusion rules and it is based on regional energy, regional variance, and regional gradient. Which, based on the integration of the

regional energy rules consider the correlation between each pixel in the region and it is the local characteristics of the image can be further manifestation, therefore, this rule has been widely adopted in image fusion [2]. Larger regional energy center pixel represents a distinctive feature of the image, the image edge segment corresponds to the absolute value of the wavelet coefficients, so will measure the size of the area of energy as fusion rules.

Two image (or multiple images) through the decomposition of the two-dimensional wavelet transform, respectively, to obtain a low frequency component and high frequency components of the corresponding image. High-frequency component includes a horizontal high-frequency component, a vertical high-frequency component and a diagonal high-frequency component. The low frequency component corresponding to the low frequency coefficients and it is the high frequency component corresponding to the frequency coefficient (wavelet coefficient).

For the low-frequency coefficients, select a simple weighted average fusion algorithm as the fusion rule; while for the high-frequency coefficient (wavelet coefficient), since the larger the center pixel of the region energy represents the obvious features in the image corresponding to the edges of the image, the line segment characteristics such absolute the large value of wavelet coefficients, determines the size of the area of energy, directly after the decomposition of the corresponding image is selected larger regional energy of the wavelet coefficients as a fusion image wavelet coefficient.

Image Fusion is a new concept in the late 1970 s, it is a modern high-tech combination of sensors, image processing, signal processing, computer and artificial intelligence technology. (Wide spatial and temporal coverage, high goals and measuring dimension reconstruction ability, redundancy, complementarily, time superiority and relatively low cost, etc.), highlight the superiority of the probe image fusion system has advanced technology in the international countries are highly valued, and has made considerable progress, as is shown by equation (1).

$$\begin{aligned} S_x &= E[(Y - EY)(Y - EY)^T] \\ &= E[AX - E(AX)][AX - E(AX)]^T \quad (1) \\ &= E[(A - EA)X][(A - EA)X]^T \end{aligned}$$

Original image fusion algorithm based on regional energy introduced the concept of "matching" of matching the degree of closeness represents the energy of two images corresponding to the local area, or away from the degree [3]. Artificially defined threshold (typically 0.9). If the match is greater than this threshold, it shows that the area of the two images corresponding local energy is relatively similar, take a weighted fusion algorithm, the comprehensive two regional energy wavelet

coefficients corresponding final draw wavelet coefficients of the fusion image.

Improved image fusion method based on the area of energy, a detailed analysis of the reasons for this phenomenon, as the introduced matching degree plus the absolute value of the corresponding fusion algorithms. If we add the absolute value of the match less than a defined threshold, the wavelet coefficients taken directly select the corresponding local area energy; plus the absolute value of the matching degree greater than a defined threshold.

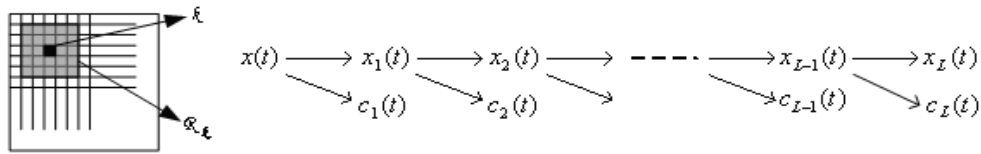


Fig. 1. Improved image fusion method based on the area of energy figure.

Finally, the fusion of the wavelet coefficients inverse wavelet transform fusion image fusion algorithm based on wavelet transform is the first image is decomposed wavelet coefficients of different frequency bands, and then using the fusion rules of wavelet coefficients for each frequency band fusion image [4]. Wavelet coefficients fusion rules can be divided into two major categories of pixel-based and region-based. For pixel-based fusion rules, by the size of the wavelet coefficients directly compare the image transformed to select the wavelet coefficients of the fusion image.

Fully consider regional energy-based image fusion of the local features of the image often can not be expressed by one pixel, it is characterized by a plurality of pixels in a local area and embodied within a local area of the normal image tend to have a strong correlation between each pixel, so to overcome the one-sidedness of the pixel-based fusion rules, and get a further manifestation of the local features of an image. Now the use of regional energy integration as image fusion rules article after another has become a hot research, as is shown by equation (2).

$$x = \sum_{i=1}^n x_i + \prod_{j=1}^m x_j' \quad (2)$$

This method is relatively pixel-based fusion rules tend to have a strong correlation this characteristic, due to the consideration of the respective pixels within the local region between fusion results obtained better visual characteristics, details richer and prominent effects, information amount to get a raise. However, relative to the original two local regional energy similar case directly to select area larger energy wavelet coefficients based on regional energy image fusion and improved image fusion based on regional energy likely to cause relative loss of information.

The wavelet transform has a "mathematical microscope" focus function, and thus the pace of reunification of the time domain and frequency domain, but also be able to orthogonal frequency domain decomposition, wavelet transform image fusion growing. Dyadic wavelet transform is more commonly used the three enters or more into the wavelet algorithm, however, expected to achieve better results in this regard, as is shown by Fig. 1.

Original image fusion algorithm based on regional energy, as opposed to the simple fusion algorithm based on the regional energy, with some improvement, considering the energy of two images corresponding to the local area in the case of similar regional energy wavelet coefficients means a combination of the information included in the two images among the fused image. However, because the images are often incomplete with prospective situations exist, often makes the application of traditional rules based on the integration of the regional energy regional energy obtained matching degree negative lead the energy proximity between the areas is difficult to determination will result in some loss of information, affect the clarity of the fusion image.

In this paper, based on wavelet transform, a detailed analysis of the image fusion method based on the area of energy, for the original suggestions for improvement based on the existing problems in the regional energy image fusion method, namely improved image fusion method based on the regional energy; in pixel-based and region-based fusion method two categories, the selection of wavelet basis function.

Wavelet analysis is a signal and information processing tools, at the time - described in the scale plane non-stationary signals overcome a Fourier analysis of the function of a single variable (time or frequency) signal disadvantage. As a new multi-resolution analysis method has been widely used in the field of engineering studies.

Application of wavelet transform in another important advantage is that: the computational complexity. Fast Fourier transform has complexity, however fast wavelet transform only. Now consider a continuous signal which is in the space (all square integral function), and produced the following approximate sequence [5]. If the size of the image as the basis for the principle of halving the pixels of the

image decomposition, the largest for the decomposition times, but in practical applications, it is not possible to take so much, otherwise the sub-picture pixel too few points will cause severe distortion. Conversely, the decomposition level too little not reflect the multi-scale thinking, generally take 3 to 4 layers appropriate (scholars believe that 2 to 3 layers appropriate), as is shown by equation (3).

$$p' = W(p, D, \theta) = s \begin{pmatrix} \cos \theta & \sin \theta \\ -\sin \theta & \cos \theta \end{pmatrix} p + \begin{pmatrix} d_1 \\ d_2 \end{pmatrix} \quad (3)$$

As long as it meets the above requirements, so in the following discussion content can be applied to any kind of wavelet function. In the absence of special conditions, for simplicity and effectiveness, we will be Haar wavelet as the example. Chart depicted in one of two binary tree recursive relations. Assuming that there is a time sequence, the sequence in the two forks tree at the same sampling interval is projected onto the scales.

The wavelet transform as a new mathematical tool, the time between function domain (spatial domain) representation and a frequency domain representation. It in the time domain and frequency domain at the same time has a good localized nature, to gradually fine time domain (spatial domain) The sampling step can be "in focus" to any of the details of the object on the high-frequency component and thus known as the "mathematical microscope". A signal it can be decomposed into a separate part of the signal on the space and time, without loss of the information contained in the original signal and can be found in the orthogonal basis, to achieve non-redundant signal decomposition.

Fusion the basic idea of the image data is the first multi-source image, the two-dimensional wavelet decomposition; then to compare the details of the image information, at different angles to achieve fusion, to extract important wavelet coefficients in the wavelet transform domain through; finally, an inverse wavelet transform image can be obtained after the data fusion. The basic steps are as follows:

1) Calculated according to equation (3) the image of the two-dimensional wavelet transform and decomposition level is it;

2) The wavelet transform domain in the two images, respectively, of the horizontal, vertical and diagonal components fusion [6]. The high frequency coefficients of the two images of each scale will be compared to the position corresponding to the larger absolute value coefficient as significant wavelet coefficients retained;

3) After the two images by the wavelet transform approximation coefficients for processing, since the image is fuzzy representation of the details (or high-frequency information) lost more contrast, the overall information (or the low frequency information) to maintain good two image the difference between the approximation coefficients after wavelet decomposition to be much smaller than the difference

between the wavelet coefficients, and therefore the fusion after the approximation coefficients by equation (4).

$$STD = \sqrt{\frac{\sum_{i=0}^{M-1} \sum_{j=0}^{N-1} (F(i, j) - MEAN)^2}{M \times N}} \quad (4)$$

At present, the fusion performance evaluation mainly includes subjective and objective evaluation method. The objective evaluation method is often divided into three categories:

1) According to a single image source image and fused image statistical characteristics);

2) According to the fused image and the reference image;

3) According to the fused image and the source image relationship. Let  $M \times N$  image area  $F(x, y)$  of the total gray series  $L$ ,  $P_i$  said the gray value of pixels and the pixels total ratio.

Entropy reflects the size of the image carrying information number; average image is the pixel gray mean value, to the human eye as reflected in the average luminance; standard deviation reflected the image relative to the average gray value of the discrete case, to some extent, can also be used to evaluate the image contrast and visibility of size; evaluation of image clarity is the key index. Entropy, mean, standard deviation and visibility of 4 parameter value is increasingly big, shows that the effect of image fusion.

Image fusion demising effect principle of evaluating information, whether to improve noise is suppressed, homogeneous region noise suppression is strengthened, the edge information is retained, enhance image mean does [7].

Wavelet transform first choose a wavelet function on the image first layer wavelet decomposition, a low frequency image and a three high frequency image, and then for the low-frequency images of second layer wavelet decomposition, and so on, the number of decomposition, wavelet decomposition, fusion frequency range and more abundant, the fusion result details the more abundant, but this is not to say that the number of wavelet decomposition, image fusion quality is higher, but the fusion effect will decrease, of course the decomposition layer cannot exceed image size range [8].

### 3. Wavelet Optimization Method

Wavelet transform image processing, the selection of wavelet base in image processing effect has a great influence on. General wavelet basis the main basis of the choice (1) (2) orthogonal linear phase (symmetry) (3) compact support (4) continuous four features, only with these characteristics, image decomposition of spatial image to each other, have better local and smooth degree, which can completely reconstruct the original image information.

However, this can also have a few wavelet function almost does not exist, in order to adapt to the different requirements of image processing technology, the characteristics of the different trade-offs, produced with different characteristics of wavelet algorithm [9]. Orthogonal wavelet decomposition algorithm can guarantee the subspace

image processing independently of each other, realize splicing can be on low frequency sub image multi-scale decomposition, and according to the different frequency selecting different stitching width, will be spliced image according to its content features targeted splicing, has realized the seamless, smooth transition, as is shown by Fig. 2.

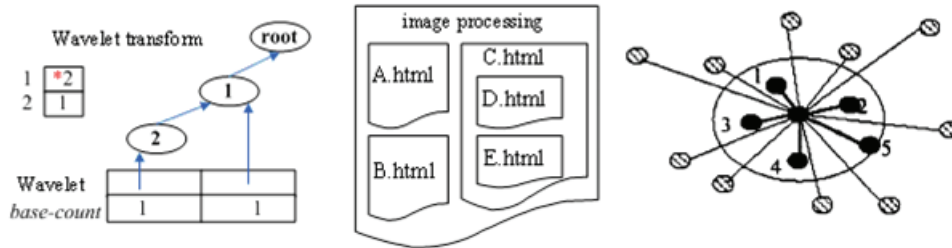


Fig. 2. Wavelet transform image processing figure.

Orthogonal wavelets derived low-pass and high-pass filter, and the four functions are decomposed image frequency information, high level, high frequency vertical detail information of high frequency details and diagonal detail information, and the subspace decomposition of the sub picture information is orthogonal to each other, and there is no redundant information, thus effectively to improve the efficiency of information transmission and reduce the storage capacity [10]. At the same time, the image of each frequency band characteristic details of expression very image, lifelike, ensure the sub-band image reconstruction when the integrity.

Orthogonal wavelet in image stitching application, can make the image is decomposed into different frequency bands on a sub-graph without correlation, it can maintain the energy decomposition without loss. And Fourier transform, Gabor transform, wavelet transform can in time and frequency domain local analysis, it can be telescopic, translation operation will signal or function multi-scale gradually thinning, ultimately achieve high frequency time breakdown at low frequency, frequency segmentation, automatic adaptive time-frequency signal analysis requirements, which can focus signal any details.

For seamless image stitching technology research, this paper mainly discusses the effective elimination is flat-fell seam [11]. As we know, the influence of different factors may lead to different joints, and joints have generally can be divided into: the rules of seam and random process. This chapter first discusses when there is rules seam processing method when the seams and the most common correction method are in the stitching region using the weighted average method.

In recent years, multi-resolution techniques have been proposed in efficient image mosaic algorithm, such as Laplace of Pyramid, according to the different frequency band overlapping width selection structure function of weighted, and the overlapping

width is and the band into a certain proportion; multi-resolution spline technique also has very good effect of stitching. The multi-resolution signals decomposition and reconstruction technology in the unique advantages, it is widely used in the field of image processing. But based on the Laplace gold tower algorithm, Gauss pyramid algorithm, in different scales of the sub image without wavelet transform that has a direction (the better able to explain the subgraph features), so this paper uses wavelet transform to complete a seamless image mosaic, as is shown by equation (5) [12]:

$$\begin{cases} \{x_1, \dots, x_d\} = \arg \max J(x) \\ x_i^T x_j = 0, i \neq j, i, j = 1, \dots, d \end{cases} \quad (5)$$

The first step after stitching image stitching is seam as an example to illustrate the rules of one-dimensional weighting function selection method. General splicing processing effect in the vicinity of the pixel values of the required seam size must be continuous gradient that is smooth transition, in order to make the seam to eliminate, and ideal gradient should meet three conditions: 1 is a gradual process resulting in the intermediate state should keep the monotone smooth change; 2 is the intermediate state boundary surface should be kept smooth; the initial object and the target object is shared by a number of features in a gradual process should be retained.

To solve this problem, through continuous regulation of sine function and obtain better results, or looking for a better weighting function, but if use the example of mosaic source may still see the splice region, so need to be designed with the weighted value [13]. Such rules can be used for splicing the arctangent gradient weighted function, but they must satisfy the above gradient conditions, if specific to the splicing of weighting function selecting principle.

Because the MEM algorithm successfully breaks through the Rayleigh limit, thus further to attract the

majority of scholars on this issue in-depth and extensive research, such as the double linear prediction algorithm. These LP algorithm research for feature subspace algorithm for the rise of foundation, but also promote the LP algorithm research. LP type algorithms have a common drawback is the spectrum peak search will appear when the artifact peaks, but through some method to suppress.

Objective assessment of image quality and visual effect of the results are often inconsistent, sometimes better image makes the vision to accept. But the subjective image quality evaluation by the observer, preferences, mood and mind, the severe refashion of the element, it is difficult to make an objective judgment. So the image quality evaluation of the trend is able to balance the two, from both subjective and objective to obtain precise evaluation system. Because the final identification image quality is the human vision, so the reasonable evaluation of the image quality of the method should fully conform to the characteristics of human vision (HVS), as is shown by equation (6):

$$\begin{cases} \langle \phi, \phi \rangle = I & \langle \psi, \psi \rangle = I \\ \langle \phi, \psi \rangle = 0 \end{cases} \quad (6)$$

Generally speaking, different weighting functions corresponding to different splicing effect, and different effect of stitching and corresponding to different evaluation index. Single factor evaluation indicators can be from one side of the image after stitching evaluation to measure the effectiveness of the algorithm, so the single factor index often has very strong specific aim, can objectively reflect the image content distribution, frequency of activity, carry information on local details characteristics, contribute to the processing algorithm improvement or correction.

In order to make the image after stitching and to be spliced image deformation and the degree of twist is as small as possible; the pixel value variation amount should be as small as possible, and so as to maintain to be spliced images in the mosaic effect diagram characteristic integrity. More and more small, then spliced to be spliced image from image is extracted from the information quantity is more, its deformation and distortion is smaller, ideally = 0; but if = 0, then spliced image and image mosaic no gray value difference, then the image of the joint will not be modified.

The image is essentially a source; it can be used to describe the information entropy. Image entropy is expressed by image carrying information volume, i.e., the image information more rich, gray change wind speed, the contrast is better, the details of the more prominent, the clearer the image, its entropy is also bigger [14]. In addition, the image entropy transform, entropy size only with local gray distribution relation, and with a single pixel gray value size, by a single noise impact is small, thereby

improving the image of real content description precision, as is shown by Fig. 3.

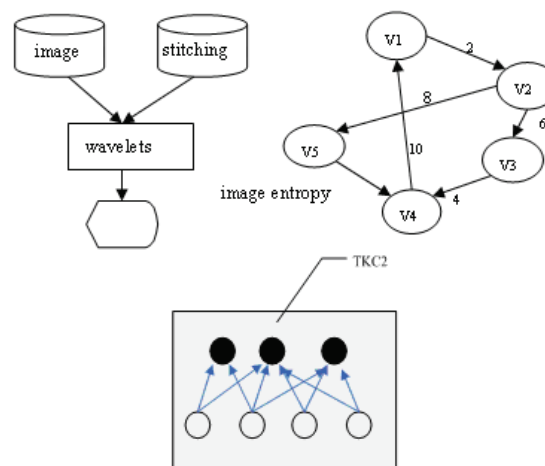


Fig. 3. Image entropy and stitching image figure.

Mutual information in information theory is an important concept, it is the two variable correlations metric, or as a variable to contain another variable information quantity measuring, so you can use this concept to measure image mosaic with the source image mutual information, thus the evaluation of splicing effect.

Based on the mechanism analysis of visual “attention” and it is if in the mosaic processing results of seam will cause great attention to visual perception, thereby undermining the overall effect. Assuming the image mosaic processing, only the presence of a mosaic area, so the mosaic image effect diagram may only exist in the following two situations: one is the embedded boundary exists together, another is mosaic area compared to other regional brightness is not harmonious sex.

Image mosaic, mosaic final processing results are judged by human performance, and from the visual psychology point of view, the vision is a kind of positive feelings, and physiological factors related to not only, still of considerable extent depends on the psychological factors. People in the observation and understanding image are often unconsciously on some regional interest.

#### 4. The Algorithms of Image Wavelet Optimize Splicing and Fusion Based on Improved Region Energy

First introduced the two dimensional wavelet image decomposition method, and then introduces the general image fusion method based on wavelet transform, finally introduces the fusion results evaluation index. Wavelet transform in time domain and frequency domain at the same time has good localization, the high frequency components using a

progressively finer time domain (spatial) sampling step length, can be "focused" any object to details, thus known as the "mathematical microscope", so the image fusion has been used widely.

Static image mosaic manner generally using batch processing image sequences in the image at the same time are converted into the same coordinate system for registration, and then select different filter methods for image seamless fusion, thereby obtaining optimal stitching effect. The coordinate system is often based on regular users select their own, but the splicing process this coordinate system is fixed. What tell here refers to the splicing process coordinates do not transform, does not refer to the scene motionless.

When the mosaic image registration, splicing is the main task to eliminate the seam, to achieve gray fusion splicing, even after the image in the joint smooth and natural. Vertical or horizontal seam elimination rule is based on the thought of effective fusion rules. In this rule, overlap with intensity of average and weighted fusion is the simpler of the two kinds of fusion algorithms. The use of average light intensity is very narrow, it is only in the direct combination based on a little progress, and the weighted fusion method is simple, fast method is more commonly used. Weighted fusion mainly focused on how to select the weighting function, in order to obtain more appropriate fusion weights, as is shown by equation 7.

$$p(s(\kappa)) = \frac{1}{(2\pi\sigma_{s(\kappa)}^2)^{1/2}} \exp\left[-\frac{(s(\kappa) - S_0(\kappa))^2}{2\sigma_{s(\kappa)}^2}\right] \quad (7)$$

In order to verify the validity of the improved algorithm, using traditional algorithm and the improved algorithm for image fusion results of comparative study, observation is improved, at the same time compared with using traditional algorithm and the improved algorithm the fusion image information entropy size. Fusion images of the entropy value is greater, the better the performance of fusion method.

A considerable part of image region corresponding to the energy matching degree is less than zero, as can be seen, the improved based on area energy fusion image obtained than the original area energy fusion rules based on the fusion image sharpness is high, and the image edge features more obvious. We can see from the improved fusion method to obtain the fusion image entropy than by the traditional fusion methods the fusion image entropy increase, the amount of information is increasing, as is shown by Fig. 4.

The paper presents the algorithms of image wavelet optimize splicing and fusion based on improved region energy. Stitching image algorithm from the mosaic image pixel distortion degree and the image after processing in joint space near the continuous degrees two aspects, through the fuzzy integral evaluation values in different frequency

bands for wavelet realize splicing optimum weighting function. Pixel distortion describes the images before and after processing of information loss degree, spatial continuity describes to eliminate the seam degree, but they are conflicting. Through the fuzzy integral comprehensive evaluation value of the feedback to optimize the seamless image stitching algorithm, realized the mosaic effect graph is maintained from the source image information is the largest while eliminating the seams, and verify its effectiveness and rationality.

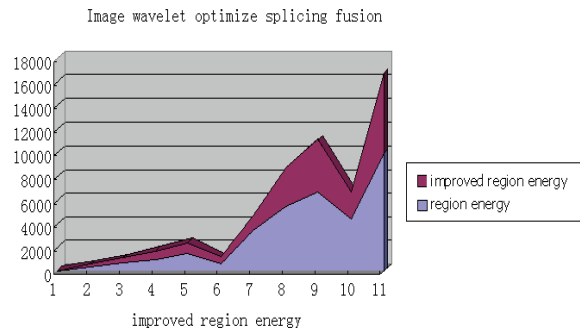


Fig. 4. Compare of algorithms of image wavelet optimize splicing and fusion based on improved region energy.

## 5. Conclusions

Region based image fusion rule is currently one of the hot topics. In this paper, it is based on the regional energy fusion method. "Match" the appearance of negative, through the introduction of absolute value, eliminating the matching negative phenomenon, and based on this idea the corresponding fusion rules. The simulation results verify the correctness and the validity of the algorithm, but also to enhance the clarity of the image fusion provides an effective way. The paper presents the algorithms of image wavelet optimize splicing and fusion based on improved region energy. Image mosaic technology (Mosaic) is defined for a given image sequence, the image registration and positioning, and then fusion splicing, produce a seamless, high resolution and large scene image.

## References

- [1]. Xu Han, Jiang Tong-Bin, Multi-Source Remote Sensing Image Fusion Algorithm Based on Combined Wavelet Transform and HIS Transform, *JCIT*, Vol. 7, No. 18, 2012, pp. 392-400.
- [2]. Guojiang Xin, Beiji Zou, Haoyu Zhou, Jianfeng Li, Meiling Cai, Image Fusion Based on the Curvelet Transform, *JCIT*, Vol. 7, No. 14, 2012, pp. 140-148.
- [3]. Nannan Yu, Tianshuang Qiu, Image fusion in Compressive Sensing based on Piella index, *JCIT*, Vol. 7, No. 8, 2012, pp. 354-362.
- [4]. Xuewen Ding, Guangquan Xu, Zengmin Wang, JiapengWu, Aiping Yang, Zhaojun Xue, Application

- of Image Fusion in Intelligent Transport System, *JDCTA*, Vol. 6, No. 1, 2012, pp. 413-420.
- [5]. A. I. Adamu, T. Mantoro, M. A. Shafii, Dynamic Interactive 3D Mobile Navigation Aid, *Journal of Theoretical and Applied Information Technology*, Vol. 37, No. 2, 2012, pp. 159-170.
- [6]. Xiaoli Zhang, Xiongfei Li, Yuncong Feng, Multi-scale Feature-Level Model for Evaluating Performance of Image Fusion, *JDCTA*, Vol. 6, No. 14, 2012, pp. 398-406.
- [7]. Guojiang Xin, Beiji Zou, Haoyu Zhou, Meiling Cai, Jianfeng Li, Image Fusion Based on the Discrete Wavelet Transform, *JDCTA*, Vol. 6, No. 6, 2012, pp. 8-15.
- [8]. Zhang Yong, Jin Wei-Qi, Study to the Influence of Registration Error to Fusion Image Quality, *AISS*, Vol. 3, No. 10, 2011, pp. 233-239.
- [9]. Li Fan, Yudong Zhang, Zhenyu Zhou, David P. Semanek, Shuihua Wang, Lenan Wu, An Improved Image Fusion Algorithm Based on Wavelet Decomposition, *JCIT*, Vol. 5, No. 10, 2010, pp. 15-21.
- [10]. Li Jin-Jiang, An Zhi-Yong, Fan Hui, Li Ye-Wei, Multifocus Image Fusion Algorithms Using Dyadic Non-subsampled Contourlet Transform, *JDCTA*, Vol. 4, No. 6, 2010, pp. 36-47.
- [11]. Michael Zimba, Sun Xingming, Digital Image Splicing Detection Based on Local Complexity of Local Maximum Partial Gradient of DWT Coefficients, *JDCTA*, Vol. 6, No. 5, 2012, pp. 1-9.
- [12]. Bo Wang, Xiangwei Kong, Lanying Wu, Different-quality Re-demosaicing in Digital Image Forensics, *JCIT*, Vol. 7, No. 17, 2012, pp. 492-505.
- [13]. Li Hua, Dawei Meng, Research on the Image Quality Evaluation Method Based on the Improved Human Visual Characteristics, *JCIT*, Vol. 7, No. 16, 2012, pp. 459-467.
- [14]. Zhang Yong, Jin Wei-Qi, Study to the Influence of Registration Error to Fusion Image Quality, *AISS*, Vol. 3, No. 10, 2011, pp. 233-239.
-

## Aptamer Biosensor for Antibiotic Residues Detection in Food Analysis

<sup>1,2</sup> Yemin Guo, <sup>\*2</sup> Xiangyou Wang, <sup>\*2</sup> Xia Sun

<sup>1</sup> School of Engineering, Northeast Agricultural University,  
No. 59 Mucai Street Xiangfang District Harbin, P. R. China

<sup>2</sup> School of Agriculture and Food Engineering, Shandong University of Technology,  
No. 12, Zhangzhou Road, Zibo 255049, Shandong Province, P. R. China

\*Tel.: +86-533-2786558, fax: +86-533-2786558

E-mail: wxy@sdut.edu.cn

*Received: 23 August 2013 / Accepted: 25 September 2013 / Published: 30 September 2013*

---

**Abstract:** Antibiotics are widely used to kill or inhibit microorganisms, but their abuse results in various types of side effects in humans and the appearance of super bacteria with tolerance to antibiotics. Excess residual antibiotics in food products have become a serious problem, and so a more reliable, accurate, and easier detection system has been required. Aptamers have strong potential as sensitive bioprobes for the development of biosensors for antibiotics detection, a specially designed aptamer for an antibiotic may be suitable for this purpose. Aptamers are synthetic RNA or DNA single-stranded oligonucleotide sequences which can be generated by an *in vitro* selection process called SELEX (Systematic Evolution of Ligands by Exponential enrichment) technique. Antibiotics are small molecule targets, therefore, they cannot act as an antigen independently and high specificity and affinity antibiotics antibody are difficult to prepare. Aptamers have advantages over antibodies, such as easy chemical synthesis, easy modification, and less immunogenic response, thus, which can be considered as a valid alternative to antibodies receptors to bind to the target molecules with high affinity. In this review, we concentrated on recent advances made in detection and quantification of antibiotics residues with aptamers biosensor. In this paper, the preparation of aptamers biosensor, the selection of analysis methods and the detection of real samples are introduced in detail. Future prospects toward the development of selective, sensitive aptamers biosensor systems are also discussed. *Copyright © 2013 IFSA.*

**Keywords:** Antibiotics residues, Detection, Aptamers, Biosensor.

---

### 1. Introduction

Antibiotics are widely used to kill or inhibit microorganisms, but their abuse results in various types of side effects in humans and the appearance of super bacteria with tolerance to antibiotics [1]. Therefore, it is critical to develop sufficiently sensitive methods to detect antibiotics residues for food safety and clinical diagnosis. Recently, many analytical methods, such as

capillary electrophoresis [2], surface plasmon resonance [3], square-wave cathodic adsorptive stripping voltammetry [4], immunoassay [5], HPLC [6], the microbiological multi-residue system [7] and Enzyme-linked immunosorbent assay (ELISA) [8] have been reported for the detection of antibiotics. However, most of those above-mentioned methods are time-consuming, expensive and cannot be adapted to high-throughput screening and on-site detection. Thus, a low

cost, less reagent consumption, sensitive and selective technique for kanamycin detection is very desirable.

In recent years, the generation of antibodies against antibiotics has seen significant progress leading to the introduction of immunosensors for sensitive small molecules antibiotics in food samples [9-11]. Consequently, immunosensors have already gained a place in the analytical benchtop as alternative or complementary methods for antibiotics rapid detection [12-15]. They are fast, economic, and at least as sensitive as usual chromatographic techniques. However, immunosensors have not been used for analytical applications as much as expected, principally due to the instability of antibodies. Antibodies are commonly selected as the molecular recognition element but they present some limitations such as limited shelf life, thermal and chemical instability leading to denaturation of proteins and loss of binding ability. As alternatives to antibodies, aptamers (APTs) have recently attracted increasing attention due to their capability to bind a wide range of targets: nucleic acids, proteins, metal ions and other molecules with high affinity and sensitivity [16, 17]. Aptamers are peptides or oligonucleotides, which are synthesized by *in vitro* process with no need for animal or cell cultures [18, 19]. Aptamers exhibit many advantages as recognition elements in biosensing when compared to traditional antibodies. They are small in size, chemically stable and cost effective. More importantly, because of their simple structure, sensor layers based on aptamers can be regenerated more easily than antibody-based layers, are more resistant to denaturation and have a much

longer shelf life [20, 21]. Especially for antibiotics small molecule targets, the aptamers show superior specificity to antibodies since small molecules cannot act as an antigen independently and high specificity and affinity antibody are difficult to prepare. Therefore, the search for specific aptamers for antibiotics small molecules has drawn substantial interest [22-24].

In this review, we summarize recent advances in the development of aptamer-based biosensors for antibiotics detection. We will review the key steps to construct the electrochemical aptamer biosensor including the immobilization protocols used for formation of a bio-recognition interface and the electrode modification. We also will discuss the trends and challenges associated with designing a reliable aptamer biosensor for practical applications in detail.

## 2. Selection of Aptamers

Since the SELEX (systematic evolution of ligands by exponential enrichment) technique was developed by both Gold's group and Szostak's group in 1990 [25], especially nanomaterials and magnetic beads are introduced to aptamer biosensor, many researchers have successfully prepared aptamer biosensors for antibiotics residues detection. To date, only a part of aptamers against antibiotics have been selected for antibiotics detection applications. As shown in Table 1, the aptamer sequence of antibiotics has been selected. Therefore, for commercial applications, many aptamer sequences of antibiotics still need be selected.

**Table 1.** Selection aptamer sequence of antibiotics reported in literature.

Antibiotics	Aptamer sequence 5'-3'	Conference
Sulfadimethoxine	GAGGGCAACGAGTGTATAGA	[26]
Kanamycin	TGGGGTGTGAGGCTAAGCCGA	[26]
Chloramphenicol	AGCAGCACAGAGTTCAGATGACTTCAGTGAGTTG TCCCACGGTCGGCAGTCGGTGGTAGCCTATGCGT GCTACCGTGAA	[27]
Tobramycin	GGCACGAGGUUUAGCUACACUCGUGCC	[28]
Ampicillin	GCGGGCGGTTGTATAGCGG	[22]
Oxytetracycline	GGAATTCGCTAGCACGTTGACGCTGGTGCCCGTT GTGGTGCAGAGTGTGTGTGGATCCGAGCTCCACGT G	[29]
Tetracycline	CGTACGGAATTCGCTAGCCCCCGGCAGGCCACG GCTTGGGTTGGTCCCCTGCGCGTGGATCCGAGCT CCACGTG	[30]
Daunomycin	GGGAATTCGAGCTCGGTACCATCTGTGTAAGGGGT AAGGGGTGGGGTGGGTACGTCTAGCTGCAGGCA TGCAAGCTTGG	[21]
Nenomycin B	GGCCUGGGCGAGAAGUUUAGGCC	[31]
Streptomycin	GGGGTCTGGTGTCTGCTTGTCTGTGCGGGTTCGT	[32]

## 3. The Preparation of Electrochemical Aptamer Biosensor

The label-free aptamer biosensor supplies a simpler and faster preparation and detection process compared with label-dependent aptamer biosensor.

As a consequence, a great number of research papers have appeared over the last years describing the development of novel aptamer biosensors for detecting amounts of antibiotics residues in food samples. While an important disadvantage of this kind of electrochemical aptamer biosensor is that the

signal changes due to biomolecular recognition are generally very small. Especially, antibiotics such small molecule sensing using electrochemical biosensor is more challenging. It requires us to offer highly sensitive small molecule aptamer biosensor technologies through careful consideration of sensor interface design and signal enhancement.

The oligonucleotide aptamers can easily be modified with signal moieties and can be produced at low cost. Up to now, a variety of assays have been successfully developed for aptamer based analysis of biomolecules. Nanomaterials usually can enhance the speed of electron-transfer, which lead to high background and low signal-to-noise ratio. The application of nanomaterials provides a novel approach to develop really label-free, high-sensitivity biosensors. For example, Zhou *et al.*, have reported a simple electrochemical tetracycline (TET) aptamer biosensor with multi-walled carbon nanotubes (MWCNTs) modification [30]. The anti-TET aptamer was immobilized on the glassy carbon electrode (GCE) modified with MWCNTs. The format provides a “label-free” method to electrochemically monitor the aptamer-target interaction. Herein, MWCNTs played a role in the increase of the electroactive surface area and provided the conducting bridges for the electron-transfer of  $\text{Fe}(\text{CN})_6^{3-}/\text{Fe}(\text{CN})_6^{4-}$ . Therefore, the proposed aptamer biosensor improved its sensitivity with a detection limit of  $5 \times 10^{-9}$  M in spiked milk samples. The fabrication of aptasensor was shown in Fig. 1.

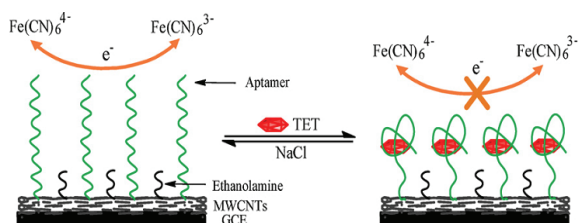


Fig. 1. The fabrication of aptasensor modified with MWCNTs.

Chandra *et al.*, have used Au nanoparticles deposited conducting polymer to immobilized aptamer onto glassy carbon electrode [16]. At the same time, Au nanoparticles deposited conducting polymer can also enhance the speed of electron-transfer between solution and electrode.

Zhu *et al.*, have reported a label-free aptamer biosensor for kanamycin detection. The sensor probe is fabricated by covalently immobilizing an *in vitro* selected DNA aptamer for kanamycin onto gold nanoparticle comprised conducting polymer. The self-assembled poly-DPB (AuNP) nanocomposite exhibited significantly improved sensitivity.

González-Fernández *et al.*, used amino groups to covalently immobilize tobramycin onto the surface of carboxylated magnetic microparticles [28]. They

used a monovalent system for introducing the enzyme conjugate on a tagged-aptamer for specifically recognizing tobramycin. Compared with multivalent systems such as biotin-streptavidin, the sensitivity is greatly improved. The proposed tobramycin inhibition assay with monovalent labeling system is shown in Fig. 2.

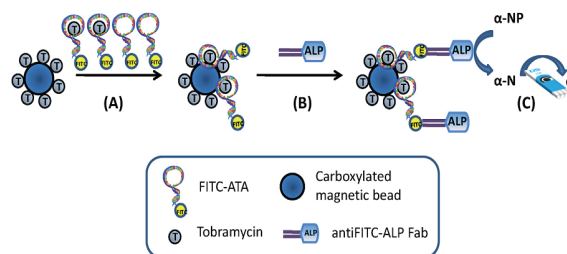


Fig. 2. The proposed tobramycin inhibition assay with monovalent labeling system.

Therefore, nanomaterials can make biomolecules such as aptamer immobilize easily onto the electrode surface, and keep its bioactivity. At the same time nanomaterials can enhance the speed of electron-transfer, thus, increase the response of current of aptamer biosensor.

Microfluidic chip can develop the efficiency of antibiotics detection and realize on-site detection. Daprà *et al.*, have reported an aptamer biosensor for kanamycin and ampicillin detection based on microfluidic chip [22]. As shown in Fig. 3 is the structure of microfluidic chip. At the same time, the polymer film is one of the immobilization methods of biomolecules on electrode surface. This entrapment process, theoretically, should occur without chemical reaction between the electrically conducting polymer (CP) films and the biomolecules, thus, this immobilization method can preserve biomolecules biological activity.

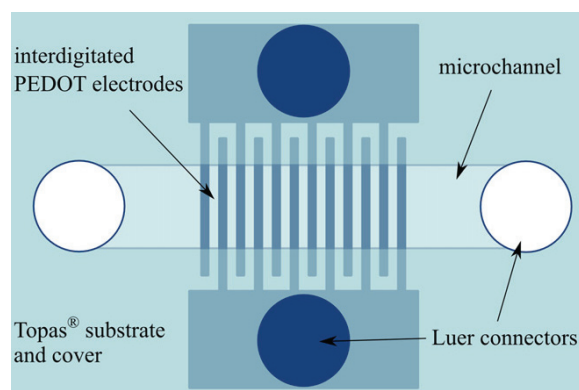


Fig. 3. The structure of Daprà *et al.*, assembled microfluidic chip.

The ampicillin or kanamycin A aptamer was immobilized onto microfluidic chip with conductive

bilayer tosylate doped poly (3, 4 - ethylenedioxythiophene) (PEDOT : TsO) and the hydroxymethyl derivative PEDOT-OH : TsO, respectively. After the immobilization of aptamer, the detection based on microfluidic chip. The ampicillin or kanamycin A aptamer was immobilized onto microfluidic chip with conductive bilayer tosylate doped poly (3, 4 - ethylenedioxythiophene) (PEDOT : TsO) and the hydroxymethyl derivative PEDOT-OH : TsO, respectively. After the immobilization of aptamer, the impedance had a significant increase.

The use of an array of microelectrodes can overcome the disadvantage, because one of the main benefits of using a microelectrode in a sensor application is the greater sensitivity that arises from the enhanced mass-transport at these small electrodes.

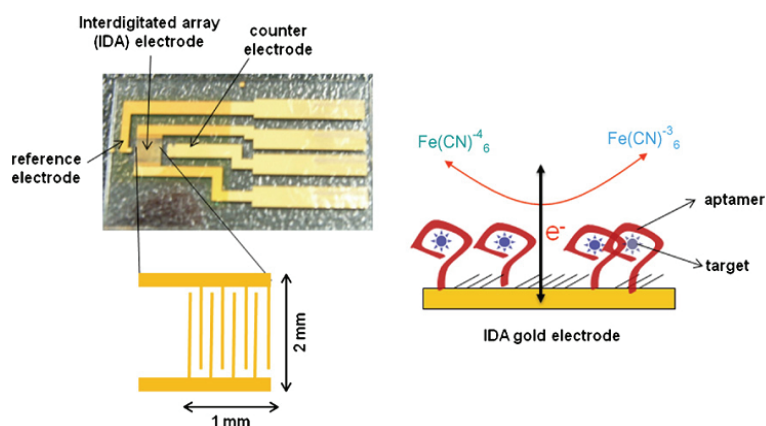


Fig. 4. The oxytetracycline detection progress with gold interdigitated array electrode chip.

#### 4. Trends and Challenges of Aptamers Biosensor for Antibiotics Detection

The use of aptamers for the detection of small molecules still represents a challenge because of the lower affinity interaction when compared with large molecules. For small molecules, this induced fit can be very small leading to minute changes in the analytical signal. However, it has been shown that the stability of such molecules can be improved by chemical modification of the ribose ring at the 3'-position or 5'-position [33-35].

Matrix complexity is one of the greatest challenges for aptamer-based biosensor to detect antibiotics in food samples. Several components regularly present in food samples can produce interference or cross-reaction in immunology-based and aptamer-based detection systems [36, 37]. However, several aptamer biosensor platforms for detecting antibiotics have been developed. Aptamer biosensors for antibiotics detection are a promising and challenging application, with potential advantages over existing immunological biosensors [38, 39].

Hemispherical diffusion layers are formed at such electrodes and a much faster diffusion of electroactive substances occurs due to the multi-dimensional nature of this process, resulting in sigmoidal (or steady-state) cyclic voltammograms (CVs). The advantages are in the improved response time (faster response), greater sensitivity and increased response per unit electrode surface area (greater current density, increasing the signal-to-noise ratio).

Kim *et al.*, have reported electrochemical sensing system for oxytetracycline (OTC) detection. The ssDNA aptamer was immobilized on gold interdigitated array (IDA) electrode chip by covalent chemistry [29]. As shown in Fig. 4, the aptamer is immobilized onto gold interdigitated array (IDA) electrode chip.

#### Acknowledgements

This work was supported by the National Natural Science Foundation of China (No. 30972055, 31101286), Agricultural Science and Technology Achievements Transformation Fund Projects of the Ministry of Science and Technology of China (No. 2011GB2C60020) and Shandong Provincial Natural Science Foundation, China (No. Q2008D03).

#### References

- [1]. R. Oertel, V. Neumeister, W. Kirch, Hydrophilic interaction chromatography combined with tandem-mass spectrometry to determine six aminoglycosides in serum, *Journal of Chromatography A*, Vol. 1058, Issue 1-2, 2004, pp. 197-201.
- [2]. P. Kowalski, Capillary electrophoretic method for the simultaneous determination of tetracycline residues in fish samples, *Journal of Pharmaceutical and Biomedical Analysis*, Vol. 47, Issue 3, 2008, pp. 487-493.
- [3]. F. Fernández, F. Sánchez-Baeza, M. P. Marco, Nanogold probe enhanced Surface Plasmon Resonance immunosensor for improved detection of

- antibiotic residues, *Biosensors and Bioelectronics*, Vol. 34, Issue 1, 2012, pp. 151-158.
- [4]. A. M. Beltagi, Determination of the antibiotic drug pefloxacin in bulk form, tablets and human serum using square wave cathodic adsorptive stripping voltammetry, *Journal of Pharmaceutical and Biomedical Analysis*, Vol. 31, Issue 6, 2003, pp. 1079-1088.
  - [5]. C. Cháfer-Pericás, Á. Maquieira, R. Puchades, J. Miralles, A. Moreno, Multiresidue determination of antibiotics in feed and fish samples for food safety evaluation. Comparison of immunoassay vs. LC-MS-MS, *Food Control*, Vol. 22, Issue 6, 2011, pp. 993-999.
  - [6]. L. Monser, F. Darghouth, Rapid liquid chromatographic method for simultaneous determination of tetracyclines antibiotics and 6-epidoxycycline in pharmaceutical products using porous graphitic carbon column, *Journal of Pharmaceutical and Biomedical Analysis*, Vol. 23, Issue 2-3, 2000, pp. 353-362.
  - [7]. O. Nagel, M. P. Molina, R. Althaus, Microbiological system in microtitre plates for detection and classification of antibiotic residues in milk, *International Dairy Journal*, Vol. 32, Issue 2, 2013, pp. 150-155.
  - [8]. L.O. White, The development of microbiological and immunological assays for antibiotics, *TrAC Trends in Analytical Chemistry*, Vol. 5, Issue 2, 1986, pp. 29-31.
  - [9]. E. Valera, A. Muriano, I. Pividori, F. Sánchez-Baeza, M. P. Marco, Development of a Coulombimetric immunosensor based on specific antibodies labeled with CdS nanoparticles for sulfonamide antibiotic residues analysis and its application to honey samples, *Biosensors and Bioelectronics*, Vol. 43, 2013, pp. 211-217.
  - [10]. X. Wu, H. Kuang, C. Hao, C. Xing, L. Wang, C. Xu, Paper supported immunosensor for detection of antibiotics, *Biosensors and Bioelectronics*, Vol. 33, Issue 1, 2012, pp. 309-312.
  - [11]. F. Conzuelo, M. Gamella, S. Campuzano, D. G. Pinacho, A. J. Reviejo, M. P. Marco, J. M. Pingarrón, Disposable and integrated amperometric immunosensor for direct determination of sulfonamide antibiotics in milk, *Biosensors and Bioelectronics*, Vol. 36, Issue 1, 2012, pp. 81-88.
  - [12]. Q. Wei, Y. Zhao, B. Du, D. Wu, H. Li, M. Yang, Ultrasensitive detection of kanamycin in animal derived foods by label-free electrochemical immunosensor, *Food Chemistry*, Vol. 134, Issue 3, 2012, pp. 1601-1606.
  - [13]. F. Conzuelo, M. Gamella, S. Campuzano, A. J. Reviejo, J. M. Pingarrón, Disposable amperometric magneto - immunosensor for direct detection of tetracyclines antibiotics residues in milk, *Analytica Chimica Acta*, Vol. 737, 2012, pp. 29-36.
  - [14]. C. C. Wu, C. H. Lin, W. S. Wang, Development of an enrofloxacin immunosensor based on label-free electrochemical impedance spectroscopy, *Talanta*, Vol. 79, Issue 1, 2009, pp.62-67.
  - [15]. F. Fernández, K. Hegnerová, M. Piliarik, F. Sanchez-Baeza, J. Homola, M. P. Marco, A label-free and portable multichannel surface plasmon resonance immunosensor for on site analysis of antibiotics in milk samples, *Biosensors and Bioelectronics*, Vol. 26, Issue 4, 2010, pp. 1231-1238.
  - [16]. P. Chandra, H. B. Noh, M. S. Won, Y. B. Shim, Detection of daunomycin using phosphatidylserine and aptamer co-immobilized on Au nanoparticles deposited conducting polymer, *Biosensors and Bioelectronics*, Vol. 26, Issue 11, 2011, pp. 4442-4449.
  - [17]. S. Song, L. Wang, J. Li, C. Fan, J. Zhao, Aptamer-based biosensors, *TrAC Trends in Analytical Chemistry*, Vol. 27, Issue 2, 2008, pp. 108-117.
  - [18]. W. Winkler, A. Nahvi, R. R. Breaker, Thiamine derivatives bind messenger RNAs directly to regulate bacterial gene expression, *Nature*, Vol. 419, 2002, pp. 952-956.
  - [19]. E. González-Fernández, N. de-los-Santos-Álvarez, M. J. Lobo-Castañón, A. J. Miranda-Ordieres, P. Tuñón-Blanco, Impedimetric aptasensor for tobramycin detection in human serum, *Biosensors and Bioelectronics*, Vol. 26, Issue 5, 2011, pp. 2354-2360.
  - [20]. Y. Peng, D. Zhang, Y. Li, H. Qi, Q. Gao, C. Zhang, Label-free and sensitive faradic impedance aptasensor for the determination of lysozyme based on target-induced aptamer displacement, *Biosensors and Bioelectronics*, Vol. 25, Issue 1, 2009, pp. 94-99.
  - [21]. A. Wochner, M. Menger, D. Orgel, B. Cech, M. Rimmel, V. A. Erdmann, J. Glökler, A DNA aptamer with high affinity and specificity for therapeutic anthracyclines, *Analytical Biochemistry*, Vol. 373, Issue 1, 2008, pp. 34-42.
  - [22]. J. Daprà, L. H. Lauridsen, Alex Toftgaard Nielsen, Noemi Rozlosnik, Comparative study on aptamers as recognition elements for antibiotics in a label-free all-polymer biosensor, *Biosensors and Bioelectronics*, Vol. 43, 2013, pp. 315-320.
  - [23]. K. H. Leung, H. Z. He, D. S. H. Chan, W. C. Fu, C. H. Leung, D. L. Ma, An oligonucleotide-based switch-on luminescent probe for the detection of kanamycin in aqueous solution, *Sensors and Actuators B: Chemical*, Vol. 177, 2013, pp. 487-492.
  - [24]. K. M. Song, M. Cho, H. Jo, K. Min, S. H. Jeon, T. Kim, M. S. Han, J. K. Ku, C. Ban, Gold nanoparticle-based colorimetric detection of kanamycin using a DNA aptamer, *Analytical Biochemistry*, Vol. 415, Issue 2, 2011, pp. 175-181.
  - [25]. C. Tuerk, L. Gold, Systematic evolution of ligands by exponential enrichment: RNA ligands to bacteriophage T4 DNA polymerase, *Science*, Vol. 249, 1990, pp. 505-510.
  - [26]. A. Chen, X. Jiang, W. Zhang, G. Chen, Y. Zhao, T. M. Tunio, J. Liu, Z. Lv, C. Li, S. Yang, High sensitive rapid visual detection of sulfadimethoxine by label-free aptasensor, *Biosensors and Bioelectronics*, Vol. 42, 2013, pp. 419-425.
  - [27]. J. Mehta, B. V. Dorst, E. Rouah-Martin, W. Herrebout, M. L. Scippo, R. Blust, J. Robbens, In vitro selection and characterization of DNA aptamers recognizing chloramphenicol, *Journal of Biotechnology*, Vol. 155, Issue 4, 2011, pp. 361-369.
  - [28]. E. González-Fernández, N. de-los-Santos-Álvarez, A. J. Miranda-Ordieres, M. J. Lobo-Castañón, Monovalent labeling system improves the sensitivity of aptamer-based inhibition assays for small molecule detection, *Sensors and Actuators B: Chemical*, Vol. 182, 2013, pp. 668-674.
  - [29]. Y. S. Kim, J. H. Niazi, M. B. Gu, Specific detection of oxytetracycline using DNA aptamer-immobilized interdigitated array electrode chip, *Analytica Chimica Acta*, Vol. 634, Issue 2, 2009, pp. 250-254.
  - [30]. L. Zhou, D. J. Li, L. Gai, J. P. Wang, Y. B. Li, Electrochemical aptasensor for the detection of tetracycline with multi-walled carbon nanotubes

- amplification, *Sensors and Actuators B: Chemical*, Vol. 162, Issue 1, 2012, pp. 201-208.
- [31]. L. Yan, C. Luo, W. Cheng, W. Mao, D. Zhang, S. Ding, A simple and sensitive electrochemical aptasensor for determination of Chloramphenicol in honey based on target-induced strand release, *Journal of Electroanalytical Chemistry*, Vol. 687, 2012, pp. 89-94.
- [32]. N. Zhou, J. Wang, J. Zhang, C. Li, Y. Tian, J. Wang, Selection and identification of streptomycin-specific single-stranded DNA aptamers and the application in the detection of streptomycin in honey, *Talanta*, Vol. 108, 2013, pp.109-116.
- [33]. S. Tombelli, M. Minunni, M. Mascini, Analytical applications of aptamers, *Biosensors and Bioelectronics*, Vol. 20, Issue 12, 2005, pp. 2424-2434.
- [34]. K. M. Song, E. Jeong, W. Jeon, H. Jo, C. Ban, A coordination polymer nanobelt (CPNB)-based aptasensor for sulfadimethoxine, *Biosensors and Bioelectronics*, Vol. 33, Issue 1, 2012, pp. 113-119.
- [35]. S. Tombelli, M. Minunni, M. Mascini, Aptamers-based assays for diagnostics, environmental and food analysis, *Biomolecular Engineering*, Vol. 24, Issue 2, 2007, pp. 191-200.
- [36]. P. D. Skottrup, Small biomolecular scaffolds for improved biosensor performance, *Analytical Biochemistry*, Vol. 406, Issue 1, 2010, pp. 1-7.
- [37]. V. Velusamy, K. Arshak, O. Korostynska, K. Oliwa, C. Adley, An overview of foodborne pathogen detection: In the perspective of biosensors, *Biotechnology Advances*, Vol. 28, Issue 2, 2010, pp. 232-254.
- [38]. B. V. Dorst, J. Mehta, K. Bekaert, E. Rouah-Martin, W. D. Coen, P. Dubruel, R. Blust, J. Robbins, Recent advances in recognition elements of food and environmental biosensors: A review, *Biosensors and Bioelectronics*, Vol. 26, Issue 4, 2010, pp. 1178-1194.
- [39]. P. Burgstaller, A. Girod, M. Blind, Aptamers as tools for target prioritization and lead identification, *Drug Discovery Today*, Vol. 24, Issue 7, 2002, pp. 1221-1228.
-

## Electrochemical Immunosensor for Pesticide Residues Detection in Food Analysis

Yemin Guo, Zhili Gong, Yaoyao Cao, \* Xiangyou Wang, Xia Sun

School of Agriculture and Food Engineering, Shandong University of Technology, No. 12,  
Zhangzhou Road, Zibo 255049, Shandong Province, P. R. China

\* Tel.: +86-533-2786558, fax: +86-533-2786558

\* E-mail: wxy@sdut.edu.cn

*Received: 2 September 2013 / Accepted: 29 September 2013 / Published: 30 September 2013*

---

**Abstract:** Electrochemical immunosensors have emerged as a highly sensitive and rapid technique for chemical contaminants detection in environmental monitoring, food safety and quality control. This review concentrates on recent advances made in detection and quantification of chemical contaminants such as pesticides and antibiotics residues with electrochemical immunosensors. In this paper, the preparation of immunosensors, the selection of analysis methods and real samples detection are introduced in detail. Future prospects toward the development of selective, sensitive immunosensors systems are also discussed. *Copyright © 2013 IFSA.*

**Keywords:** Electrochemical immunosensors, Chemical contaminants, Pesticides residue, Detection.

---

### 1. Introduction

Pesticides are widely used in agriculture produce, and antibiotics are also being used on a large scale in livestock production. These lead to the excessive chemical residues in foods and cause severe impairment of human health. The analysis of foods to assess the presence of chemical contaminants is a practice of crucial importance for ensuring food safety and quality. Currently, the majority of chemical contaminants are commonly analyzed by various analytical techniques such as gas chromatography (GC), high-pressure liquid chromatography (HPLC), capillary electrophoresis (CE) and mass spectrometry (MS) [1-4]. These conventional methods are very sensitive and reliable, but have disadvantages such as complexity, extensive time consumption, and the need for costly, bulky instrumentation. For these reasons, the development of rapid and efficient monitoring methods becomes more and more important.

In recent years the generation of antibodies against pesticides residues has seen significant progress leading to the introduction of several immunoassays for environmentally sensitive small toxic molecules [5-9]. As consequence, immunochemical methods, such as enzyme-linked immunosorbent assays (ELISAs), have already gained a place in the analytical benchtop as alternative or complementary methods for routine pesticide and veterinary drugs analysis. They are fast, economic, and at least as sensitive as usual chromatographic techniques. However, the analyte detection in ELISAs is always indirect because one of the immunoreagent is labeled. Moreover, that need extensive sample handling such as rather large number of washing steps. On the contrary, in immunosensors the detection is direct: one of the immunoreagents is immobilized on the surface of the transducer, and a direct physical signal is produced when the immunochemical interaction occurs. This label-free direct detection represents an essential

advantage of immunosensors as compared to label-dependent immunoassays [10-13]. As consequence, a great number of research papers have appeared over the last years describing the development of novel immunosensors for detecting trace amounts of chemical residues in environmental and food samples.

Among the immunosensors, the electrochemical immunosensors for pesticide residue detection have attracted extensive interest in recent years [14-16]. Fig. 1 is the schematic diagram of electrochemical immunosensor for analyte [17].

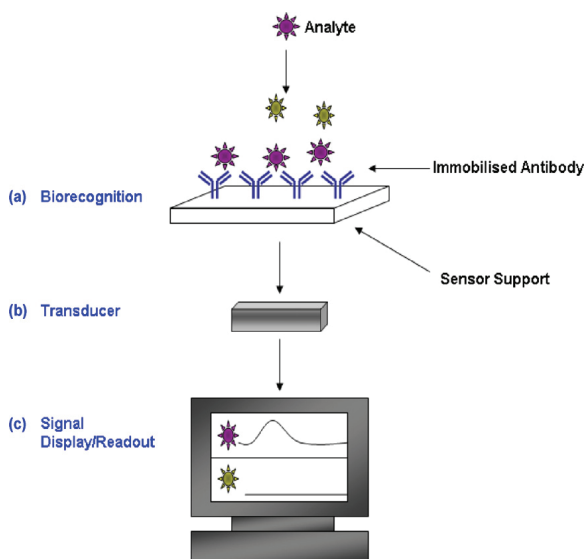


**Fig. 1.** The schematic diagram of electrochemical immunosensor for analyte.

Electric impedance spectroscopy (EIS) is a sensitive technique, which detects the electrical response of the system studied after application of a periodic small amplitude AC signal. Impedance immunosensors detect the pesticide residue concentrations by the measurement the changes of electrical conductivity of the solution and capacity due to the Ab-Ag interaction on the electrode surface, which also can be reflected in impedimetric response. Enrique Valera's group [18-23] has reported series methods about impedance immunosensor for atrazine detection based on the interdigitated microelectrode array. The complete assay process and the mechanism of the immunosensing reaction are shown in Fig. 2 and Fig. 3, respectively. However, the detection of pesticide residue such small molecule compound is usually performed under competitive conditions involving the competition between the free antigen (analyte) and a fixed amount of coated antigen for a limited amount (low concentration) of antibody (Ab). At the end of the reaction the amount of Ab captured on the electrode surface and hence the free antigen (analyte) is determined, as schematically shown in Fig. 3.

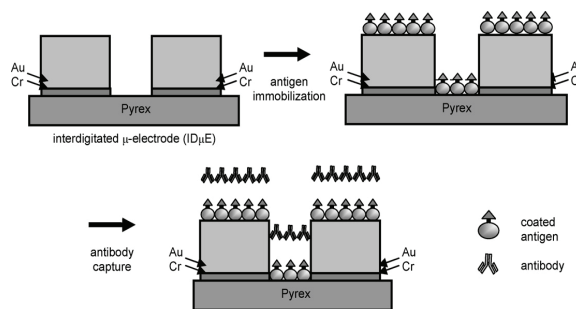


**Fig. 2.** Schematic diagram of the complete assay system performed on the IDμE's.

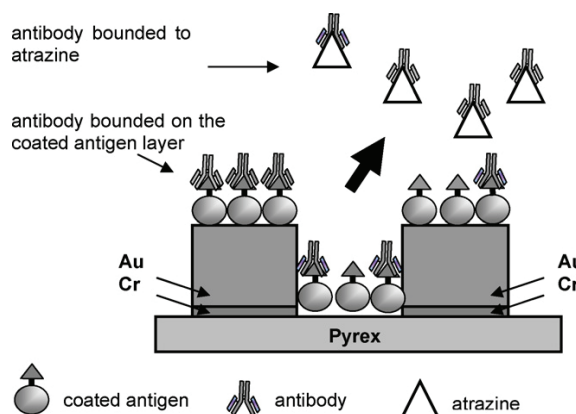


**Fig. 3.** Immunosensor reaction. An amount of the specific antibody is bounded on the coated antigen layer. Other amount is evacuated of the IDμE's, this amount is related to the atrazine concentration.

Except for few transducing principles already well established (i. e., SPR, surface plasmon resonance) [24-26], most of the immunosensors reported until now, rely on the use of labels to reach the necessary detection limits required by the legislation. As it is well known, the competitive assay is complex. In order to obtain simpler and faster immunosensing methodology, direct detection of pesticide residues in food products without the use of labels (fluorescent compounds, enzymes, etc.) are increasingly meeting these challenges. Different sensor approaches have been published to avoid the use of labels when the target analyte is a biomacromolecule, a bacteria or a virus, but only a few immunosensors are used to detect haptens which are difficult to immobilize and have little effect on electron transfer of the electrochemical mediator in solution, since haptens usually are small molecular compounds. For the detection of electroactive hapten, it also has been reported that the antibody was immobilized on the electrode to capture the hapten, then the hapten adsorbed on the electrode showed well-shaped redox responses [10] (Hu *et al.*, 2003). It can suffer from steric hindrance between the small antigen and large antibodies. However, it is difficult to detect non-electroactive small molecules. Therefore, it requires offer highly sensitive small

molecule immunosensor technologies through careful consideration of sensor interface design and signal enhancement [24].

However, there is a time gap between current status in the field and the most recent reviews. Thus, in this review, we specifically provide an overview of the research carried out during the last 5 years relative to electrochemical immunosensor for food and environment safety. We will review the key steps to construct an immunosensor including the immobilization protocols of antibody, the formation of a bio-recognition interface, and the electrode modification. We also will discuss the trends and challenges associated with designing a reliable immunosensor for practical applications in detail.

## 2. The Antibody Immobilization Methods

Using nanomaterials as electrode modification materials, the antibody is immobilized the modified electrode surface. This method is the most of reported antibody immobilization methods. Sun *et al.*, fabricated amperometric immunosensor for carbofuran detection using deposited gold nanocrystals/4,4'-thiobisbenzenethiol multilayers membranes to modify Au electrode [14]. Suri *et al.*, immobilized diuron antibody onto electrode modified with Prussian blue-gold nanoparticle film to prepare immunosensor for diuron detection [27].

Another immobilization strategy is based on the antibody bonding through Fc fragment to Protein A or G. The bond strength from strong to weak between Protein A (or G) and an antibody are greatly affected by the antibody classes and subclasses. The binding involves the formation of multiple non-covalent bonds between the Protein A and amino acids of the binding Fc site [28].

Antibodies or antigens are also immobilized at the surface of magnetic beads and all immunological steps are performed in micro-tubes using a rotation sample mixer. After each incubation or washing step, the magnetic beads are concentrated on the side wall of the micro-tubes by placing the tubes in a specially designed magnetic particle separator allowing the supernatant to be discarded. Finally, the magnetic beads are concentrated onto the magnetized working electrode surface and the electrochemical measurements are carried out. Using this approach, which combines the selectivity of the antibodies with the sensitivity of the electrochemical detection and the possibility of concentrating magnetic particles on the electrode surface, it is possible to achieve remarkable enhancement in the performance of classical immunoassays [29].

## 3. The Selection of Electrode Materials

At the present, the most of reported immunosensors use normal three electrode system, such as glass carbon electrode, gold electrode and so

on. Usually, before immobilizing antibody onto electrode surface, the electrode is first modified with nanomaterials to enhance electron transfer between electrode and testing solution.

To overcome this problem, in recent years the application of single use screen-printed electrodes (SPEs), characterized by low-cost fabrication and mass production, has attracted an increasing interest for the development of immunosensors (especially enzyme immunosensors). Tothill *et al.*, have developed an immunosensor for herbicide detection with membrane-based screen printed electrode [30]. Using screen printed electrode, the detection process is simplified, shortened, which can realize portable and miniaturization. However, the signal of immunosensor with screen printed electrode is instability, and low sensitivity.

Another kind of electrode is microelectrodes. The use of an array of microelectrodes can overcome the disadvantage, because one of the main benefits of using a microelectrode in a sensor application is the greater sensitivity that arises from the enhanced mass-transport at these small electrodes. Hemispherical diffusion layers are formed at such electrodes and a much faster diffusion of electroactive substances occurs due to the multi-dimensional nature of this process, resulting in sigmoidal (or steady-state) cyclic voltammograms (CVs). The advantages are in the improved response time (faster response), greater sensitivity and increased response per unit electrode surface area (greater current density, increasing the signal-to-noise ratio) [31].

## 4. Trends and Challenges of Immunosensor for Pesticide Residues Detection

In any case, the general strategy for immunosensor construction is to place the biological material in close contact with the transducer in order to obtain high sensitivity and to minimize the time of measurement. Several immunosensors for the detection of biological and chemical contaminants are reported in the literature, but only a few have actually been applied to food analysis.

Electrochemical biosensors have revolutionized modern chemical analysis because of their technical simplicity and fast response due to the direct transduction of the biomolecular recognition event into electronic signals [19]. Mass fabrication, low cost, and decentralized in-field analysis are other important features of these electrochemical sensors.

A disposable amperometric immunosensor for 2,4-D was described by Kaláb and Skládál [32, 33], who could measure concentrations in the range of 0.1  $\mu\text{g/l}$  but required an assay time of 60 min per test due to a long preincubation step. Compared to optical detection systems, amperometric sensors have several advantages. They are very sensitive and usually exhibit a wide linear range. The transducers

are easily prepared and quite inexpensive; portable devices are also available.

Ciumasu *et al.* reported a versatile, portable miniaturized flow-injection immunosensor instrument for TNT, diuron and atrazine detection (Fig. 4) [34].

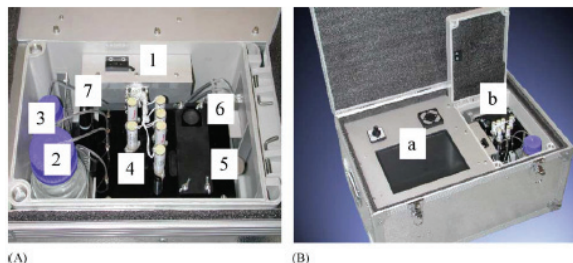


**Fig. 4.** The portable miniaturized flow-injection immunosensor instrument.

The applicability and advantages of immunosensors have been particularly demonstrated in the field of pesticide analysis. Nonetheless, biosensors cannot compete with HPLC or GC (with selective detection), when it comes to detailed sample composition analysis. In most environmental applications, multi-analyte determination is needed, and because biosensors can only normally detect single analytes, chromatographic methods are preferred. These techniques generally feature the immobilization of antibodies or other receptor molecules in discrete locations of a sensor surface. A planar array immunosensor equipped with a chargecoupled device (CCD) as detector have been developed and applied to the determination of different bacteria, viruses, and toxins (some of them of particular concern because of their potential use as biological warfare agents) [35].

## Acknowledgements

This work was supported by the National Natural Science Foundation of China (No. 30972055, 31101286), Agricultural Science and Technology Achievements Transformation Fund Projects of the Ministry of Science and Technology of China (No. 2011GB2C60020) and Shandong Provincial Natural Science Foundation, China (No.Q2008D03).

## References

- [1]. E. P. Syrago-Styliani, G. Evagelos, T. Anthony, A. S. Panayotis, Gas chromatographic-tandem mass spectrometric method for the quantitation of carbofuran, carbaryl and their main metabolites in applicators' urine, *Journal of Chromatography A*, Vol. 1108, Issue 1, 2006, pp. 99-110.
- [2]. O. Eva, S. Manuel, Monitoring some phenoxy-type N-methylcarbamate pesticide residues in fruit juices using high-performance liquid chromatography with peroxyoxalate-chemiluminescence detection, *Journal of Chromatography A*, Vol. 1007, Issues 1-2, 2003, pp. 197-201.
- [3]. N. L. Pacioni, A. V. Veglia, Determination of carbaryl and carbofuran in fruits and tap water by cyclodextrin enhanced fluorimetric method, *Analytica Chimica Acta*, Vol. 488, Issue 2, 2003, pp. 193-202.
- [4]. A. P. Ghanem, F. Bados, R. Perreau, C. Benabdallah, L. Plagellat, Alencastro, J. Einhorn, Multiresidue analysis of atrazine, diuron and their degradation products in sewage sludge by liquid chromatography tandem mass spectrometry, *Anal Bioanal Chem*, Vol. 391, Issue 1, 2008, pp. 345-352.
- [5]. J. N. Zhu, M. J. Jin, W. J. Gui, Y. R. Guo, R. Y. Jin, C. M. Wang, Development of a direct competitive enzyme-linked immunoassay for carbofuran in vegetables, *Food Chemistry*, Vol. 107, Issue 4, 2008, pp. 1737-1742.
- [6]. X. S. Jiang, D. Y. Li, X. Xu, Y. B. Ying, Y. B. Li, Z. Z. Ye, J. P. Wang, Immunosensors for detection of pesticide residues, *Biosensors and Bioelectronics*, Vol. 23, Issue 11, 2008, pp. 1577-1587.
- [7]. E. Mallat, C. Barzen, R. Abuknesha, G. Gauglitz, D. Barcelo, Part per trillion level determination of isoproturon in certified and estuarine water samples with a direct optical immunosensor, *Analytica Chimica Acta*, Vol. 426, Issue 12, 2001, pp. 209-216.
- [8]. T. C. Tang, A. Deng, H. J. Huang, Immunoassay with a microtiter plate incorporated multichannel electrochemical detection system, *Analytical Chemistry*, Vol. 74, Issue 11, 2002, pp. 2617-2621.
- [9]. P. Sharma, K. Sablok, V. C. Bhalla, A novel disposable electrochemical immunosensor for phenyl urea herbicide diuron, *Biosensors and Bioelectronics*, Vol. 26, Issue 4, 2011, pp. 4209-4212.
- [10]. S. Q. Hu, J. W. Xie, Q. H. Xu, K. T. Rong, G. L. Shen, R. Q. Yu, A label-free electrochemical immunosensor based on gold nanoparticles for detection of paraoxon, *Talanta*, Vol. 61, Issue 6, 2003, pp. 769-777.
- [11]. M. Wang, H. Kang, D. Xu, C. Wang, S. Liu, X. Hu, Label-free impedimetric immunosensor for sensitive detection of fenvalerate in tea, *Food Chemistry*, Vol. 141, Issue 1, 2013, pp. 84-90.
- [12]. L. Zhang, M. Wang, C. Wang, X. Hu, G. Wang, Label-free impedimetric immunosensor for sensitive detection of 2, 4-dichlorophenoxybutyric acid (2,4-DB) in soybean, *Talanta*, Vol. 101, 2012, pp. 226-232.
- [13]. W. Jin, G. Yang, L. Wu, Q. Wang, H. Shao, A. Qin, B. Yu, D. Li, B. Cai, Detecting 5-morpholino-3-amino-2-oxazolidone residue in food with label-free electrochemical impedimetric immunosensor, *Food Control*, Vol. 22, Issue 10, 2011, pp. 1609-1616.
- [14]. X. Sun, Y. Zhu, X. Y. Wang, Amperometric immunosensor based on deposited gold nanocrystals / 4, 4'-thiobisbenzenethiol for determination of carbofuran, *Food Control*, Vol. 28, Issue 1, 2012, pp. 184-191.
- [15]. X. Sun, X. Y. Wang, S. Y. Du, W. P. Zhao, Q. Q. Li, X. B. Han, Label-free amperometric immunosensor for the detection of carbofuran pesticide, *Sensor Letters*, Vol. 9, Issue 3, 2011, pp. 958-963.
- [16]. W. Wei, X. Zong, X. Wang, L. Yin, Y. Pu, S. Liu, A disposable amperometric immunosensor for chlorpyrifos-methyl based on immunogen/platinum doped silica sol-gel film modified screen-printed

- carbon electrode, *Food Chemistry*, Vol. 135, Issue 3, 2012, pp. 888-892.
- [17]. P. J. Conroy, S. Hearty, P. Leonard, R. J. O'Kennedy, Antibody production, design and use for biosensor-based applications, *Seminars in Cell & Developmental Biology*, Vol. 20, Issue 1, 2009, pp. 10-26.
- [18]. J. Ramón-Azcón, E. Valera, A. Rodríguez, A. Barranco, B. Alfaro, F. Sanchez-Baeza, M. P. Marco, An impedimetric immunosensor based on interdigitated microelectrodes (ID $\mu$ E) for the determination of atrazine residues in food samples, *Biosensors and Bioelectronics*, Vol. 23, Issue 9, 2008, pp. 1367-1373.
- [19]. E. Valera, J. Ramón-Azcón, A. Rodríguez, L. M. Castañer, F. J. Sánchez, M. P. Marco, Impedimetric immunosensor for atrazine detection using interdigitated  $\mu$ -electrodes (ID $\mu$ E's), *Sensors and Actuators B: Chemical*, Vol. 125, Issue 2, 2007, pp. 526-537.
- [20]. A. Rodríguez, E. Valera, J. Ramón-Azcón, F. J. Sanchez, M. P. Marco, L. M. Castañer, Single frequency impedimetric immunosensor for atrazine detection, *Sensors and Actuators B: Chemical*, Vol. 129, Issue 2, 2008, pp. 921-928.
- [21]. E. Valera, D. Muñoz, A. Rodríguez, Fabrication of flexible interdigitated  $\mu$ -electrodes (FID $\mu$ Es) for the development of a conductimetric immunosensor for atrazine detection based on antibodies labelled with gold nanoparticles, *Microelectronic Engineering*, Vol. 87, Issue 2, 2010, pp. 167-173.
- [22]. E. Valera, J. Ramón-Azcón, F. J. Sanchez, M. P. Marco, A. Rodríguez, Conductimetric immunosensor for atrazine detection based on antibodies labelled with gold nanoparticles, *Sensors and Actuators B: Chemical*, Vol. 134, Issue 1, 2008, pp. 95-103.
- [23]. E. Valera, J. Ramón-Azcón, A. Barranco, B. Alfaro, F. Sánchez-Baeza, M. P. Marco, A. Rodríguez, Determination of atrazine residues in red wine samples. A conductimetric solution, *Food Chemistry*, Vol. 122, Issue 3, 2010, pp. 888-894.
- [24]. J. Mitchell, Small molecule immunosensing using surface plasmon resonance, *Sensors*, Vol. 10, Issue 8, 2010, pp. 7323-7346.
- [25]. W. Lee, D. Lee, B. Oh, W. H. Lee, J. Choi, Nanoscale fabrication of protein A on self-assembled monolayer and its application to surface plasmon resonance immunosensor, *Enzyme and Microbial Technology*, Vol. 35, Issues 6-7, 2004, pp. 678-682.
- [26]. T. Kawaguchi, D. R. Shankaran, S. J. Kim, K. Matsumoto, K. Toko, N. Miura, Surface plasmon resonance immunosensor using Au nanoparticle for detection of TNT, *Sensors and Actuators B: Chemical*, Vol. 133, Issue 2, 2008, pp. 467-472.
- [27]. P. Sharma, K. Sablok, V. Bhalla, C. R. Suri, A novel disposable electrochemical immunosensor for phenyl urea herbicide diuron, *Biosensors and Bioelectronics*, Vol. 26, Issue 10, 2011, pp. 4209-4212.
- [28]. E. Zacco, R. Galve, M. P. Marco, S. Alegret, M. I. Pividori, Electrochemical biosensing of pesticide residues based on affinity biocomposite platforms, *Biosensors and Bioelectronics*, Vol. 22, Issue 8, 2007, pp. 1707-1715.
- [29]. F. Ricci, G. Volpe, L. Micheli, G. Palleschi, A review on novel developments and applications of immunosensors in food analysis, *Analytica Chimica Acta*, Vol. 605, Issue 2, 2007, pp. 111-129.
- [30]. D. E. H. Baskeyfield, F. Davis, N. Magan, I. E. Tothill, A membrane-based immunosensor for the analysis of the herbicide isoproturon, *Analytica Chimica Acta*, Vol. 699, Issue 2, 2011, pp. 223-231.
- [31]. C. O. Parker, I. E. Tothill, Development of an electrochemical immunosensor for aflatoxin M1 in milk with focus on matrix interference, *Biosensors and Bioelectronics*, Vol. 4, Issue 8, 2009, pp. 2452-245
- [32]. T. Kaláb, P. Skládal, A disposable amperometric immunosensor for 2, 4-dichlorophenoxyacetic acid, *Analytica Chimica Acta*, Vol. 304, Issue 3, 1995, pp. 361-368.
- [33]. P. Skládal, T. Kaláb, A multichannel immunochemical sensor for determination of 2,4-dichlorophenoxyacetic acid, *Analytica Chimica Acta*, Vol. 316, Issue 1, 1995, pp. 73-78.
- [34]. I. M. Ciomasu, P. M. Krämer, C. M. Weber, G. Kolb, D. Tiemann, S. Windisch, I. Frese, A. A. Kettrup, A new, versatile field immunosensor for environmental pollutants: Development and proof of principle with TNT, diuron, and atrazine, *Biosensors and Bioelectronics*, Vol. 21, Issue 2, 2005, pp. 354-364.
- [35]. C. O. Parker, Y. H. Lanyon, M. Manning, D. W. M. Arrigan, I. E. Tothill, Electrochemical immunochip sensor for aflatoxin M1 detection, *Analytical Chemistry*, Vol. 81, Issue 13, 2009, pp. 5291-5298.

## Forecast Surface Quality of Abrasive Water Jet Cutting Based on Neural Network and Verified by Experiments

Gui-Lin Yang

Department of Electromechanical Engineering, Heze University, Heze, 274015, Shandong, China

Tel.: 15965819701

E-mail: [ygl88803@126.com](mailto:ygl88803@126.com)

*Received: 7 September 2013 /Accepted: 21 September 2013 /Published: 30 September 2013*

**Abstract:** In this study, firstly, the YL12 aluminum alloy is used as experimental materials, then in the following experiments it is cut in JJ-I-type water jet machines, and 1,000 group data are gotten by measurement. In each group data, pressure, material thickness, surface roughness, abrasive flow and traversing speed are included. Next, BP artificial neural network is established. In this network, there are four inputs and one output. The inputs are pressure, material thickness, surface roughness and abrasive flow rate; the output is traverse speed. And then the BP artificial neural network is programmed by one toolbox of Matlab. Using the former 1,000 group data, the BP artificial neural network is trained, and its forecast function is obtained. Finally, the BP neural network is tested to verify through using different thickness of aluminum alloy verifies its forecast function. According to given pressure, material thickness, roughness and abrasive flow, traverse speed is predicted. The YL12 aluminum alloy is cut by the predicted traversing speed. The maximum error between the prediction values of surface roughness and the actual values of the surface roughness is 6.5 %.

*Copyright © 2013 IFSA.*

**Keywords:** Abrasive water jet cutting, BP neural network, Surface quality, Forecast, Verification.

### 1. Introduction

Abrasive water jet (AWJ) is the solid liquid two phases jet beam. Through the jet beam, the material can be grinded, scraped, erode and extruded. Compared with the laser beam, plasma cutting and abrasive water jet, AWJ is new type of cutting tool and has the unique superiority—during the process, without lateral force and recoil, the workpiece will never be out of shape by mechanical force and deformation damage or mechanical vibration. Therefore, AWJ has the reputation of the most durable cutting tool [1, 2]. On the other hand, the speed of AWJ cutting is fast, the cutting gap is narrow and the quality is high. Using AWJ cutting, both of labors and material can be saved. It is easy to

cooperate the NC system to process the material arbitrarily and realize the automation [3, 4].

AWJ is one of soft cutting tool, so the processing performance has its obvious disadvantage, which is called Jet Lag. As the nozzle moves as a certain speed and the workpiece has a thickness, the time of entering the workpiece and the exit of workpiece is different. The latter is comparatively slower, so this is so-called Jet Lag [5]. This lag causes arc lines on the surface, showed in Fig. 1. On the other hand, when the high energy water beam leaves the sprayer, the beam will scatter somewhat. The energy will weaken with the increase of distance, so there will be obvious taper when AWJ cutting workpiece [6]. At the same time, the lag will cause the distinct surface quality differences, that is to say, the surface on the

top is smooth and the bottom is rough [7, 8]. But through the speed adjusting, in fact, energy compensation, the problem of Jet Lag will be solved.

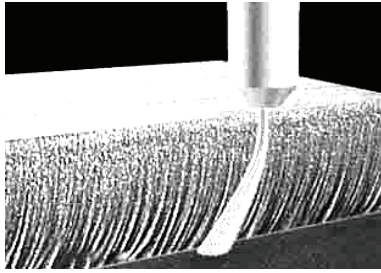


Fig. 1. Water jet section cutting diagram.

During the process of AWJ cutting, not only the factor of AWJ itself, but also the elements of the machine tool characteristic, material and technology, the relationship between AWJ parameters and the machining accuracy is highly nonlinear. As a result, it is difficult to control the processing precision and surface quality [9]. The process is often operated by experience. Based on fuzzy neural network, this study establishes the machining model of AWJ. Through the specific water jet machine tool, the sample data are obtained. Using these data, the BP neural network is trained and has prediction function. The model will realize the processing of the higher requirements of precision and intelligent control.

## 2. Building Model of Water Jet Cutting

### 2.1. Parameter Determination

The surface quality of Water Jet cutting is related to jet system, material and thickness of workpiece and the parameters of the machine tool working [10, 11]. To make it simple, selecting specific materials (YL12 duralumin) processing, so the influence of material property will not be taken into consideration.

On the side of AWJ system, considering the specific diameter of water nozzle and nozzle as well as the most commonly used abrasive particle size of abrasive research, the pressure of water jet and the flow rate of abrasive will be studied as the main parameter [12]. On the side of machine tool, due to the specific study of water jet machine tool, therefore the influence caused by machine tool's property on surface cutting quality will be neglected. In this study, only the transverse speed of nozzle will be used as machine tool parameter, the thickness of material as the processed workpiece parameter. The rate of surface roughness  $R_a$  (here, the rate of surface roughness takes the place of the surface cutting quality of workpiece.) will be as studied here, the other two elements the taper and surface morphology will be excluded [13].

### 2.2. Establishment of BP Neural Network

AWJ cutting technology of fuzzy artificial neural network structure is shown in Fig. 2. Fuzzy system has four inputs:  $E_1$ ,  $E_2$ ,  $E_3$  and  $E_4$ . They represent the water jet pressure  $P$ , abrasive flow rate of  $M_a$ , material thickness of  $H$ , and the cutting surface roughness  $R_a$ . Fuzzy artificial neural network the system output is the speed of cutting nozzle  $V$ . If the single hidden layer neural network only be selected in the study, it is difficult to adjust the weight coefficient in neural network training, what's more, it is more complicated, and hardly to meet the requirements [14]. As a result, the double hidden layer should be chosen in FNN. But it is lack of the unity and complete theory of how to choose the hidden layer nodes [15]. The number of nodes and input / output unit are directly related to how much they have and also with the other factors [16]. This paper uses Matlab for test selection, gain better nodes.

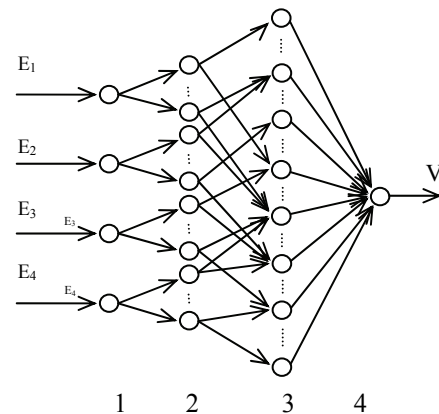


Fig. 2. FNN neural network.

Considering experimental conditions of the study,  $E_1$ ,  $E_2$ ,  $E_3$  and  $E_4$  numerical interval of each are identified as (150, 300) MPa, (0, 0.18) kg/min, (10, 30) mm, (2.5, 25)  $\mu\text{m}$ . On  $E_1$ ,  $E_3$  and  $E_4$  parameter, each defines 3 Fuzzy sets, note separately:

$$B_1^1 = \{ \text{Low pressure} \}$$

$$B_1^2 = \{ \text{Intermediate pressure} \}$$

$$B_3^1 = \{ \text{The thinner} \}$$

$$B_3^2 = \{ \text{Moderate thickness} \}$$

$$B_3^3 = \{ \text{Thickness} \}$$

$$B_4^1 = \{ \text{Fine Processing} \}$$

$$B_4^2 = \{ \text{Semi fine processing} \}$$

$$B_4^3 = \{ \text{Rough machining} \}$$

$E_2$  is defined by 2 Fuzzy Sets, Note separately:

$$B_2^1 = \{ \text{Moderate} \}, B_2^2 = \{ \text{Overdose} \}$$

Chooses Gauss function as membership function, and the cutting surface roughness of the membership

function is  $\mu_A(x) = e^{-\frac{x^2}{6}}$ ,  $\mu_A(x) = e^{-\frac{(x-6.4)^2}{6}}$  and  $\mu_A(x) = e^{-\frac{(x-12.5)^2}{6}}$ , as shown in Fig. 2.

There are 54 fuzzy rules in fuzzy system. The general form of fuzzy rules: If  $E1=B_1^1$  and  $E2=B_2^1$  and  $E3=B_3^1$   $E4=B_4^1$  then  $y=\theta_1$  ( $l=1, 2, 3, \dots, M$ ,  $M$  represents the number of rules) and  $\alpha_1$  is the first rule activation degree, then the fuzzy system output is:

$$V = \sum_{i=1}^M \theta_i \alpha_i \quad (1)$$

### 2.3. Sample Data Acquisition

Water jet machine of type JJ-I is used as the experimental device. The maximum pressure of Ultra high pressure generator is up to 380 MPa, the maximum displacement is 2.7 L/min, water spray nozzle diameter is 0.28 mm, sand nozzle diameter is 0.76 mm, cutting angle is  $90^\circ$ , abrasive is 40 # garnet and target distance is 5.0 mm. In the experiment, the thickness of 20 mm, 35 mm and 50 mm YL12 duralumin will be chosen as the test piece. The TR200 roughness is used to measure the specimen surface roughness Ra.

## 3. Neural Network Programmed by Matlab

### 3.1. BP Neural Network Establishes Function

The Nnbox toolbox of Matlab software can provide specialized function newff() for establishing neural network. The method of the function's application [17]:

```
net=newff(A, 1, c, Trainfun)
```

Network properties and parameters can be stored in this net, in which the network parameters respectively stands for each input vector of the maximum or minimum value; L is a row vector and each element represents the number of neurons per layer; C is character vector and elements are each layer of neuronal transmission's function; Trainfun is a string variable, which is the network training function name.

### 3.2. BP Neural Network Trains Function

When the neural network is established, the network should be trained. The essence of this training is, through the repetition of comparison between input parameter and output parameter, to adjust the different layer of neurons' weights and biases, and finally to get the network which can be

suited to all samples. Obviously, the prediction of network and the number of training group have direct relationship. In Matlab, network can be trained through Train function, used as following style:

```
net = train (net, u, y)
u: sample matrix of input
y: sample matrix of output
```

### 3.3. BP Neural Network Simulates Function

For the trained network, it can be used to deal with the practical problems. Matlab provides a function sim(), to realize the neural network's simulation function. This function is simple and convenient to be used. The using method is the actual network output matrix:

```
a = sim (net, p)
```

Type in P: processing parameter matrix.

BP neural network training scheme is shown in Fig. 3.

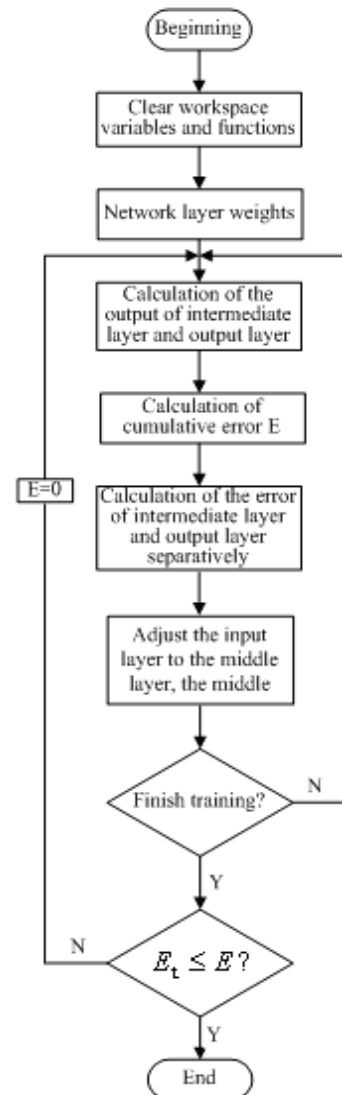


Fig. 3. Training ANN by MATLAB.

In this paper, (Fig. 2) the procedures of the BP neural network model are as follows:

```

lc
clear
load matlab;
t=output;
p=input;
[pn,minp,maxp,tn,mint,maxt] prenmnx(p,t);
% Initialize neural network
net=newff(minmax(pn),[30],
{'tansig','purelin'},'trainlm');
net.trainParam.mu=0.001;
net.trainParam.show=1;
net.trainParam.mu_dec=0.2;
net.trainParam.mu_inc=10;
net.trainParam.epochs=1000;
net.trainParam.goal=0.00001

```

#### 4. Experimental Verification

Using the trained neural network predicts the speed of different curves and then using the predicted speed programs and cuts the car model which thickness is 5mm and 8mm and material is YL12 duralumin. The recorded data are the shown in the Table 1.

$$\text{Cutting surface quality error} = \frac{\text{A given surface roughness}}{\text{Average value of Surface roughnes}} - \frac{\text{A given surface roughness}}{\text{A given surface roughness}}$$

In experimental verification, the biggest cutting quality's maximum error is 6.5 %.

#### 5. Conclusions

According to the actual needs of sophisticated processing pieces, this study utilizes the BP neural network to establish YL12 duralumin's model cut by AWJ. Under the condition of given water beam pressure, the rate flow of abrasive quality, the thickness of AL and required processed the roughness of transverse section, the model can rapidly and reliably predict the desired nozzle's cutting speed. Using the gained experimental data to train the neural network, when the variance of transverse speed reaches to the fastest convergence, the hidden layer node number is 55, as a result, in BP neural network, 55 is chosen to be he hidden layer node number; using the trained neural network the speed of different curve's part is forecast. This speed is to be programmed and cut, at last, the biggest error of the rate of surface roughness is 6.5 %. The quality of transverse section is in the allowed range. The prediction model can be applied to practical production.

**Table 1.** Comparison of experimental data and prediction data.

No.	Jet Presuree (MPa)	Brasive flow (kg/min)	Thickness workpiece (mm)	Demand Roughness ( $\mu\text{m}$ )
1	150	0.1155	5.0	27.5
2	200	0.1480	5.5	7.8
3	150	0.1155	6.0	12.6
4	250	0.1385	6.0	60.03
5	240	0.1306	8.0	3.26
6	280	0.1540	9.0	4.15
7	260	0.1498	9.0	4.15
8	240	0.1306	8.0	4.5
9	220	0.1436	6.0	50.32
10	220	0.1480	5.5	12.5
11	180	0.1260	5.0	11.6

**Table 1.** (Continued).

No.	Prediction Speed (mm/min)	Target distance (mm)	Measured surface Roughness ( $\mu\text{m}$ )
1	29.25	5	28.11
2	57.32	5	8.31
3	82.51	6	13.02
4	175.85	7	63.03
5	28.64	8	3.34
6	37.40	6	4.32
7	32.8	5	3.98
8	38.6	6	4.32
9	158	4	48.5
10	70.36	5	11.8
11	42.6	6	11.0

#### Acknowledgements

This work is supported by the Scientific Research Foundation of Heze University of Shandong Province of China under Grant No. XY09JX01 and the University Technological Plan Project of Shandong Province of China under Grant No. J09LD55.

#### References

- [1]. Meyer L., Uberruck T., Koch A., Gastinger I., Resection of the spleen using the water jet dissection technique, *Laparoendosc Adv Surg Tech A*, Vol. 5, Issue 6, 2011, pp. 321–324.
- [2]. Siores, E., Chen, Letal, Improving surface finish generated by the abrasive water jet process,

- International Symposium on Advances in Abrasive Technology*, Vol. 138, Issue 6, 2010, pp. 187-192.
- [3]. Kovacevic R., Mohan R. and Zhang Y. M., Cutting force dynamics as a tool for surface profile monitoring in AWJ, *ASME Journal of Engineering for Industry*, Vol. 15, Issue 3, 2005, pp. 340-346.
- [4]. Hashish M., Characteristics of surface machined with abrasive waterjets, *ASME Journal of Manufacturing Science and Engineering*, Vol. 8, Issue 6, 2000, pp. 358-363.
- [5]. Jiansheng Wang, Jiajun Sun, Mar, Accelerating mechanism of abrasive particle in the collimated water jet, *High-pressure Water Jet*, Vol. 9, Issue 5, 1993, pp. 23-29.
- [6]. U. Caydas, A. Hascalik, A study on surface roughness in abrasive water jet machining process using artificial neural networks and regression analysis method, *Materials Processing Technology*, Vol. 202, Issue 6, 2008, pp. 574-582.
- [7]. Savanick G. A., An abrasive jet device for cutting deep kerfs in hard rock, in *Proceedings of the 3<sup>rd</sup> U.S. Water Jet Conference*, December 15-17, 1999, pp. 98-121.
- [8]. Li Xiaohong, Liu Ailin, Zheng Jinlong, Lu Yiyu, The study of self-excited oscillation pulsed abrasive jet, *China Safety Science Journal*, Vol. 5, Issue 6, 2003, pp. 161-165, in Chinese.
- [9]. P. Palanisamy, I. Rajendaran, S. Shanmugasundaram, Optimization of machining parameters using genetic algorithm and experimental validation for end milling operations, *Advanced Manufacturing Technology*, Vol. 32, Issue 10, 2007, pp. 644-655.
- [10]. Li Xiaohong, Experimental investigation of hard rock cutting with collimated abrasive water jets, *International Journal of Rock Mechanics & Mining Sciences*, Vol. 37, Issue 7, 2000, pp. 1143-1148.
- [11]. Hu Shougen, Ding Sheng, The principle and status of high pressure pulsed water jet, *J. East China University of Technology*, Vol. 19, Issue 3, 1997, pp. 1-9, in Chinese.
- [12]. S. Band Yopad Hyay, S. K. Pal, C. A. Murthy, Simulated annealing based pattern classification, *Information Science*, Vol. 109, Issue 5, 1998, pp. 165-184.
- [13]. Tang Chuanlin, Li Xiaohong, Liao Zhenfang, The study of oscillation jet nozzle with flowcontrol oscillator, in *Proceedings of the 12<sup>th</sup> Int. Symp. on Jet Cutting Technology*, Vol. 10, Issue 2, 1996, pp. 62-68, in Chinese.
- [14]. G. A. Savanick and W. G. Krawaz, An abrasive jet rock drill, in *Proceedings of the 4<sup>th</sup> U.S. Water Jet Conference, Univ. of California, Berkeley*, Vol. 26, Issue 2, 1987, pp. 129-132.
- [15]. Wang J., Kuriyagawa T. and Huang C. Z., An experimental study to enhance the cutting performance in abrasive waterjet machining, *MachSci Technol*, Vol. 7, Issue 6, 2003, pp. 191-207.
- [16]. Hashish M., Model for abrasive-waterjet (AWJ) machining, *EngMater Technol Trans ASME*, Vol. 111, Issue 9, 2009, pp. 154-162.
- [17]. Wang J., Guo D. M., A predictive depth of penetration model for abrasive waterjet cutting of polymer matrix composites, *Mater ProcTechnol*, Vol. 121, Issue 5, 2002, pp. 390-394.

## Computational Simulation and Analysis of Energy-saving Glazing Units in Residential Buildings

Zhuolun Chen

Architectural Design & Research Institute, South China University of Technology,  
Guangzhou, Guangdong, P. R. China, 510640  
State Key Laboratory of Subtropical Building Science, South China University of Technology,  
Guangzhou, Guangdong, P. R. China, 510640

*Received: 24 August 2013 / Accepted: 25 September 2013 / Published: 30 September 2013*

---

**Abstract:** Building materials have played a more and more important role in saving building energy since the central government of China set higher standards and requirements for new-constructed and retrofit buildings after 2005. Glazing units, especially energy-saving units including LOW-E coated glazing units and PVB laminated glass, are utilized nation-wide. This paper employs energy simulation to analyze the energy-saving effects of different glazing units in residential buildings in the city of Guangzhou, as an example of hot-humid climate in China. It appears that the PVB laminated glass can refuse 44 % solar radiation to enter rooms and reduce 40 % of the shading coefficient comparing to clear glass. Meanwhile, in the aspects of operation and design of the HVAC system, 28 % of cooling load, 21 % of installed capacity and 8.6 % of full-load operation time can be saved. *Copyright © 2013 IFSA.*

**Keywords:** Energy-saving glazing units, Residential buildings, Thermal properties, Energy conservation, Computational simulation.

---

### 1. Introduction

Glazing units, as common building materials, are widely utilized in China. Large windows are considered to be attractions of residential buildings, especially in hot-humid climate areas like Guangzhou etc. It is estimated that China produced and consumed approximately 2/3 of the total glazing units in the world.

However, design standards of building energy conservation for both commercial and residential buildings required higher thermal properties in energy saving of glazing units. It is reported that the heat transferred through windows in summer consumes 20 %-40 % of total energy of air conditioning. As a result, various types of glazing units, including LOW-E coated glazing units and PVB laminated glass, were employed to meet the mandatory requirements of energy saving ratio in recent years.

This paper take residential buildings in Guangzhou as an example to study the energy-saving effects of five widely-used glazing units in local building markets, including 12 mm and 8 mm clear glass, 6 mm LOWE coated glass, 7 mm and 11 mm PVB laminated glass. The simulation tool DeST-h (Designer's Simulation Toolkit) was employed to simulate hourly room base temperature and cooling load. Based on the simulation results, thermal properties in energy saving of different glazing units are evaluated.

### 2. Solar-optical Properties of the Tested Glazing Units

The main request to thermal properties of glazing units in hot-summer-warm-winter areas in China can be concluded as following: natural lights should

transmit as much as possible so as to satisfy the indoor lighting demand while the solar radiation is reflected to outside. That is, in the precondition of keeping visible light transmittance stable, the cooling load of solar radiation through glazing units is decreased and the air-conditioning consumption in summer is reduced. The major parameters of glazing units can be summarized as following two aspects:

## 2.1. Solar Radiation Control

### 2.1.1. Total Solar Energy Transmittance $g$

Constituted by solar direct transmittance and secondary heat transfer factor  $q_i$ , it indicates the ratio of the total solar radiation on glass to the ones which gets into the room. According to the ISO and GB standards, solar direct transmittance can be calculated by using the following formula:

$$\tau_e = \frac{\int_{300}^{2500} S_\lambda \cdot \tau(\lambda) \cdot d_\lambda}{\int_{300}^{2500} S_\lambda \cdot d_\lambda} \approx \frac{\sum_{350}^{1800} S_\lambda \cdot \tau(\lambda) \cdot \Delta\lambda}{\sum_{350}^{1800} S_\lambda \cdot \Delta\lambda}, \quad (1)$$

where  $\tau(\lambda)$  is the solar spectral transmittance of the glazing,  $S_\lambda$  is the spectral distribution of the solar radiation,  $\Delta\lambda$  is the spectral bandwidth. The values of  $S_\lambda \cdot \Delta\lambda$  can be found in the ISO and GB standards.

### 2.1.2. Shading Coefficient $S_e$

It is defined as the ratio of the total solar energy transmittance  $g$  of glass or glazing units with coatings and other hi-tech improvements to the one of 3 mm normal plat glazing. Namely,

$$S_e = \frac{g}{g_n}, \quad (2)$$

where  $g$  indicates the total solar energy transmittance of improved glass or glazing units,  $g_n$  indicates the total solar energy transmittance of 3 mm normal plat glazing. It shows the change of solar energy after transmitting these constructions. The total solar energy transmittance of 3 mm flat glass is prescribed as 88.9 %.

### 2.1.3. Solar Heat Gain Coefficient SHGC

It refers to the proportion between the total inner heat gain through glass, including refraction and absorption, and the outer heat quantity. It shows the ability of accepting solar radiation. When sun light is irradiated to the surface of an object with certain

angle of incidence  $i$ , the Solar Heat Gain Coefficient SHGC of this object can be expressed as:

$$SHGC(i, \lambda) = \tau(i, \lambda) + N(i, \lambda), \quad (3)$$

where  $N = \frac{h_i}{h_e + h_i}$ , in which,  $h_i$  is the heat

convection resistance inside the window,  $h_e$  is the heat convection resistance outside the window.

### 2.1.4. Thermal Conductance $K$

It is composed of the heat transfer coefficients towards the inside and outside respectively and the heat transfer coefficient in the construction itself.

$$K = \frac{1}{R_0} = \frac{1}{\sum R_i + R_n + R_w}, \quad (4)$$

where  $R_0$  is the total heat resistance, including the heat resistance of each layer  $R_i$ , the heat transfer resistance of inner  $R_n$  and outer  $R_w$  surface. In the case that the position of glazing is vertical,  $\varepsilon_i=0.83$  and the wind velocity of outside surface is approximately 4 m/s, the value of  $h_e$  and  $h_i$  is 23 W/(m<sup>2</sup> K) and 8 W/(m<sup>2</sup> K) [6] respectively.

## 2.2. Optical Properties

### 2.2.1. Visible Light Transmittance $\tau_v$

It indicates the transmittance capability of glass, coating and other kinds of transparent constructions in the spectrum 380 nm-780 nm (visible light). According to [7, 8],  $\tau_v$  can be calculated using the following formula:

$$\tau_v = \frac{\int_{380}^{780} D_\lambda \cdot \tau(\lambda) \cdot V(\lambda) \cdot d_\lambda}{\int_{380}^{780} D_\lambda \cdot V(\lambda) \cdot d_\lambda} \approx \frac{\sum_{380}^{780} D_\lambda \cdot \tau(\lambda) \cdot V(\lambda) \cdot \Delta\lambda}{\sum_{380}^{780} D_\lambda \cdot V(\lambda) \cdot \Delta\lambda}, \quad (5)$$

where  $\tau(\lambda)$  is the spectral visible light transmittance,  $D_\lambda$  is the relative spectral power distribution of illuminant  $D_{65}$ ,  $V(\lambda)$  is the photonic luminous efficiency function defining the standard observer for photometry,  $\Delta\lambda$  is the spectral bandwidth.

The higher this value is, the more light can transmit through the glass, and the more natural light should be taken into use. Thus, the less electrical lighting would be used.

### 2.2.2. Visible Light Reflectance $\rho(\lambda)$

It shows the reflectance capability of glazing units in the spectrum 380 nm-780 nm (visible light). It can

be calculated using the same formula to (2), but the value of  $\tau(\lambda)$  needs to change to  $\rho(\lambda)$ :

$$\tau_v = \frac{\int_{380}^{780} D_\lambda \cdot \rho(\lambda) \cdot V(\lambda) \cdot d_\lambda}{\int_{380}^{780} D_\lambda \cdot V(\lambda) \cdot d_\lambda} \approx \frac{\sum_{380}^{780} D_\lambda \cdot \rho(\lambda) \cdot V(\lambda) \cdot \Delta\lambda}{\sum_{380}^{780} D_\lambda \cdot V(\lambda) \cdot \Delta\lambda} \quad (6)$$

Flat clear glass, LOW-E coated glass and PVB laminated glass with different thickness are taken as samples. All the optical data, such as spectral transmittance and reflectance of the samples, in this paper are tested by spectrophotometer. The total solar energy transmittance and shading coefficient are calculated in response to standards, as is shown in Table 1.

**Table 1.** Solar-optical properties of the tested glass.

Items	12 mm Clear Glass	8 mm Clear Glass	6 mm LOWE Glass	7 mm PVB laminated Glass	11 mm PVB laminated Glass
Hemispherical Emissivity	0.89	0.89	0.43	0.84	0.84
Visible Light Transmittance $\tau_v$ , %	85.97	88.65	81.18	64.12	57.89
Visible Light Reflectance $\rho_v$ , %	8.35	8.87	8.26	8.08	7.12
Solar Direct Transmittance $\tau_{es}$ , %	72.93	80.22	53.80	41.87	30.34
Solar Direct Reflectance $\rho_{es}$ , %	7.38	8.06	6.85	6.56	5.95
Solar Direct Absorptance $\alpha_{es}$ , %	19.69	11.72	39.35	51.57	63.71
Total Solar energy Transmittance $g$ , %	78.01	83.24	61.92	52.52	43.50
Shading Coefficient $Sc$	0.88	0.94	0.70	0.59	0.49
Solar Heat Gain Coefficient $SHGC$	0.77	0.82	0.61	0.51	0.43

### 3. Simulation Analysis

The simulation tool DeST-h (Designer’s Simulation Toolkit) was employed to simulate hourly room base temperature and cooling load with different envelope types and glazing units. The current energy-saving standards in hot-summer-warm-winter zone and Guangdong set baseline according to the U-value and thermal inertia of walls, which are divided into heavy-weight walls and light-weight walls. The definitions of walls and roof in the standards are listed in Table 2.

**Table 2.** Definitions of envelopes in national and regional energy-saving standards of residential buildings.

Heavyweight walls	Lightweight walls
$K=2.0, D=3.0$	$K=1.0, D=1.5$
<b>Note:</b> D is the index of thermal inertia, K is the U value.	

#### 3.1. Calculation Principles

Heat balance equation of building envelope inner surface: heat conduction + indoor heat convection + radiation heat between each surface + direct radiation heat = 0.

$$q_i(n) + \alpha_i^c [t_r(n) - t_r(n)] + \sum_{k=1}^{N_i} C_b \varepsilon_{ik} \varphi_{ik} \left[ \left( \frac{T_k(n)}{100} \right)^4 - \left( \frac{T_i(n)}{100} \right)^4 \right] + q_i^n(n) = 0 \quad (7)$$

Indoor heat balance equation: heat convection of each surface + various convection heat + air infiltration heat + the influence of the air-conditioning system = heat increment in unit time.

$$\sum_{k=1}^{N_i} F_k a_k^c [t_k(n) - t_r(n)] + [q_1^c(n) - q_2^c(n)] + L_a(n)(c\rho)_a [t_a(n) - t_r(n)] / 3.6 - HE_S(n) = V(c\rho)_r \frac{t_r(n) - t_r(n-1)}{3.6 \times V_r} \quad (8)$$

The room base temperature within a building can be obtained ignoring the influence of the air-conditioning system.

The thermal resistance of a single glass can be calculated according to the thermal conductivity and its thickness. The size of the total thermal resistance of the window has decisive importance on the heat convection inside and outside the window. To reduce this part of heat convection, the thermal resistance should be as large as possible. The window is composed of frame material and glass system. Assume that the heat transfer of the glass and the frame obeys a strict parallel relationship, the total thermal resistance of the window is:

$$R = \left[ \frac{1}{F_g + F_f} \left( \frac{F_g}{R_{go}} + \frac{F_f}{R_{fo}} \right) \right]^{-1}, \quad (9)$$

where  $R_{go}$  and  $R_{fo}$  is the thermal resistance of the glass system and frame material respectively;

$F_g$  and  $F_f$  is the area of the glass system and frame material respectively.

$$\eta_f = \frac{F_f}{F_g + F_f} \quad (10)$$

The term  $U$  is adopted to denote the corresponding heat transfer coefficient, and we obtain the following relationship:

$$U = U_g + \eta_f(U_r - U_g) \quad (11)$$

The thermal performance is measured using factors such as heat resistance, thermal conductance, and thermal inertia index. These factors are expressed in formulae (9)-(11).

The total heat resistance of the exterior walls and roof:

$$R_0^1 = \sum R_i + R_n + R_w = \sum \frac{\delta_i}{\lambda_i} + R_n + R_w \quad (12)$$

The total heat resistance of the inner walls and floor slabs:

$$R_0^2 = \sum R_i + 2R_n = \sum \frac{\delta_i}{\lambda_i} + 2R_n \quad (13)$$

Thermal conductance  $K$ :

$$K = \frac{1}{R_0} \quad (14)$$

Thermal inertia index:

$$D = \sum D_i = \sum R_i S_i, \quad (15)$$

where  $\lambda_i$  is the heat conductivity of each layer;  $\delta_i$  is the thickness of each layer;  $S_i$  is the heat storage coefficient of each layer.

### 3.2. Simulation Models and Settings

According to the national and regional energy-saving design standards of residential buildings, the trade-off method requires that the annual cooling and heating energy consumption of proposed design building should not exceed the reference building, which is considered as benchmarking building of saving 50 % energy. In this paper, this reference building, which is referred in the appendix of the national standard, is utilized as baseline. The other parameters and settings of baseline and simulation cases are listed in Table 3.

In this paper, the baseline energy models with both heavy-weight and light-weight walls, as defined in the national and regional standards, are utilized to evaluate the energy saving effects of different glazing

units. Meanwhile, these models with various window-to-wall ratios are simulated respectively to study the relationship between shading coefficient value and energy consumption of cooling. Thus the differences in energy saving of glazing units can be concluded.

**Table 3.** Settings of baseline and simulation cases.

	Baseline	Simulation Cases
Floors and height (m)	6, 18 m	6, 18 m
U value of exterior wall	2.1-2.9 (W/m <sup>2</sup> K)	2.3 (W/m <sup>2</sup> K)
U value of roof	0.64 (W/m <sup>2</sup> K)	0.63 (W/m <sup>2</sup> K)
Window-wall ratio	0.44	0.42
Window parameters	5.6 (W/m <sup>2</sup> K)	5.3 (W/m <sup>2</sup> K)
Interior environment	22.3 °C	22.3 °C
Indoor heat gain	10%-38%	28%
HVAC equipments	60%	58%

#### 3.2.1. Room Base Temperature

The distributions of max and average room base temperature in each month are shown in Figs. 1-2 respectively. According to the simulation results, the maximums of average and max room base temperature of 8 mm clear glass are at least 2.4°C and 5.6°C higher than those of 11 mm PVB laminated glazing units respectively. It indicates that the ability to control the change of inner temperature of 8 mm clear glass is weaker than 11 mm PVB laminated glazing units. In other words, it is more suitable to utilize 11 mm PVB laminated glazing units other than clear glass in the place where cooling load is the major building energy consumption.

#### 3.2.2. Cooling Load

In order to make a clear guide for choosing proper energy-saving glass and calculate the time period for recovery of investment in future practice, after obtaining the room base temperature of different glazing products in the worst condition, the annual cooling load and the max of annual cooling load with different window-to-wall ratio are simulated. The simulation results are shown in Fig. 3-6.

As shown in the figures above, as the window-to-wall ratio or shading coefficient become larger, the cooling load correspondingly increases. The largest amplitude can reach 31.8 % and 27.9 % respectively. The less the window-to-wall ratio is, the less change in cooling load because of using different kinds of glazing products. The amplitude would be around 16 %-28 %. In the condition of same window-to-wall ratio, the utilization of energy-efficient glazing units can not only save 20 % power consumption in air conditioning, but also decrease 15 % installed capacity and 5 % full-loaded operation time.

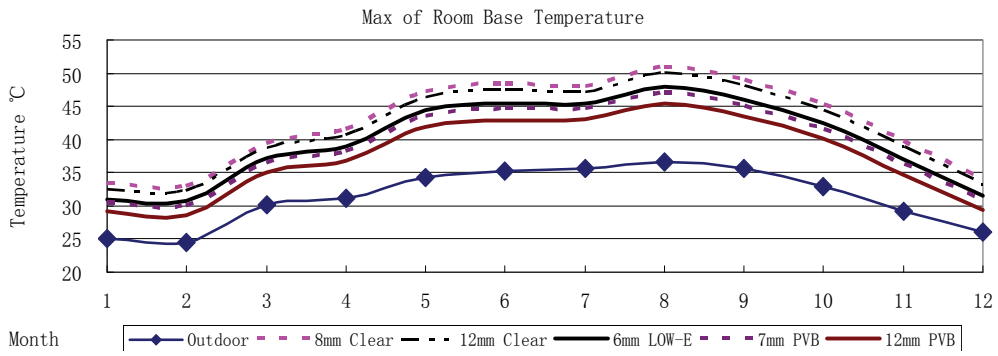


Fig. 1. Max of room base temperature.

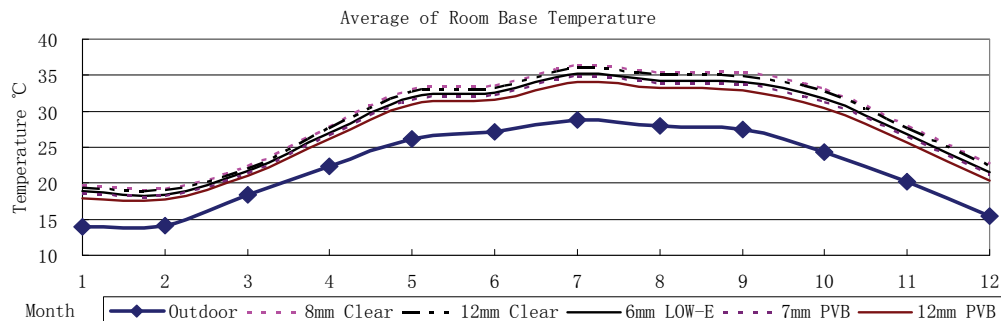


Fig. 2. Average of room base temperature.

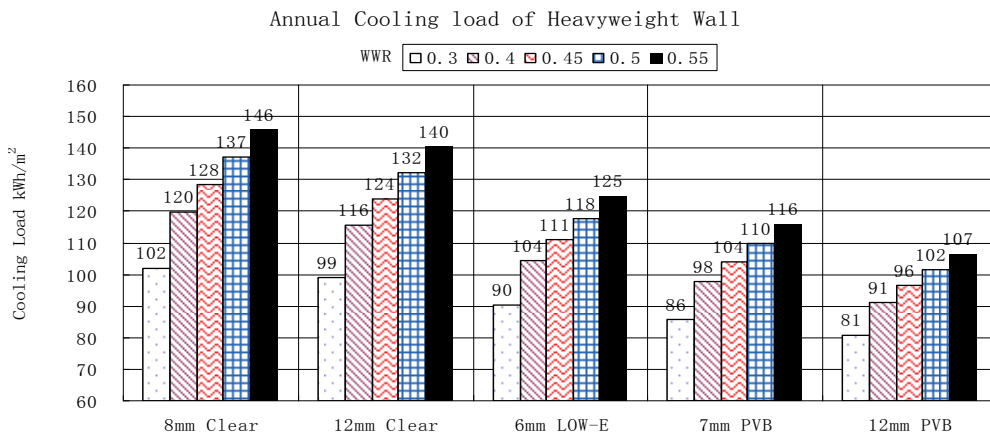


Fig. 3. Annual cooling load of heavyweight wall.

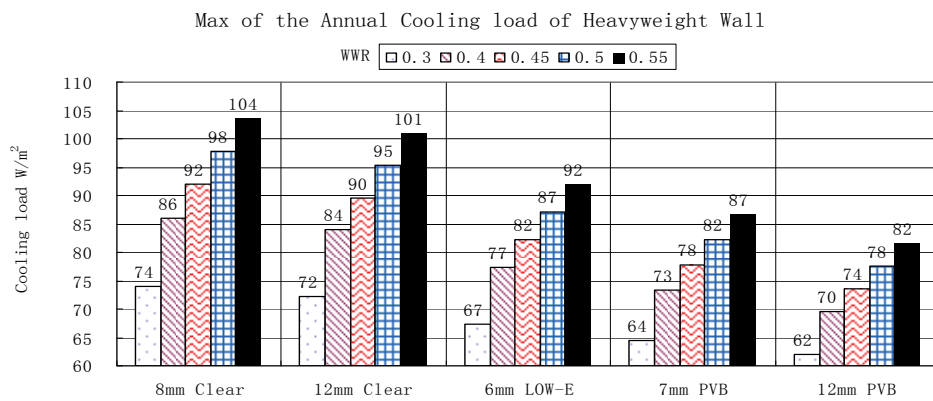


Fig. 4. Max of annual cooling load of heavyweight wall.

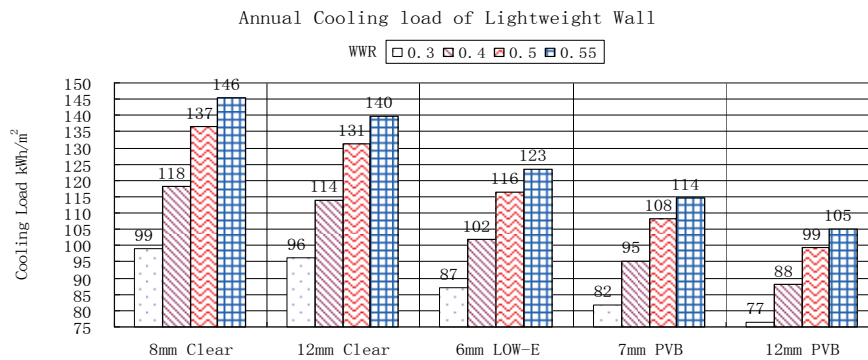


Fig. 5. Annual cooling load of lightweight wall.

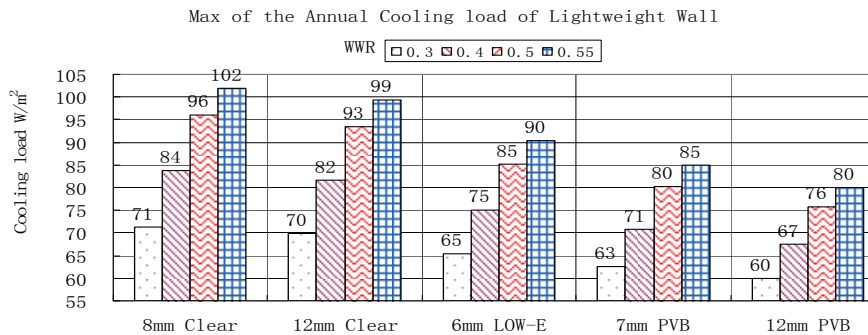


Fig. 6. Max of annual cooling load of lightweight wall.

Therefore, although increasing investment in the envelope, employing energy-efficient glass in hot-summer-warm-winter zones, such as Guangzhou city, can obviously reduce the investment in air-condition machines and operation fee.

#### 4. Conclusions

Based on the simulation results of clear glass, LOW-E coated glass and PVB laminated glass, their effects on the room base temperature and cooling load in hot-summer-warm-winter zone are analyzed.

Compared with clear glass, PVB laminated glass can prevent 44 % of solar radiation entering indoor, reduce 40 % in shading coefficient. Meanwhile, in the field of choice and operation of air-conditioning machines, it can decrease 28 % of cooling load, 21 % of installed capacity and 8.6 % of full-loaded operation time.

#### Acknowledgement

This study is sponsored by the Youth Science Fund of National Natural Science Foundation of China (No. 51108185) and the funding of State Key Laboratory of Subtropical Building Science (No. 2013KB24).

#### References

- [1]. Zhang Q., The design and construction manual of building glass curtain walls and glass sky light roof, *China Building Industry Publishing Company*, Beijing, China, 2002.
- [2]. JGJ 75-2003, Design standard for energy efficiency of residential buildings in hot summer and warm winter zone, *China Standard Press House*, Beijing, China, 2003.
- [3]. DBJ 15-50-2006, Guangdong Detailed Standard of Design standard for energy efficiency of residential buildings in hot summer and warm winter zone, *Guangdong Standard Press House*, Guangzhou, China, 2006.
- [4]. GB 50189-2005, Design standard for energy efficiency of public buildings, *China Standard Press House*, Beijing, China, 2005.
- [5]. Zhang L., Energy-saving design of windows in hot-summer-warm-winter zone, *Shanghai Construction Technology*, 1, 2009, pp. 56-57.
- [6]. Dong Z. Z., Thermal properties of LOW-E glass. Technology of Energy-Efficient Windows, *China Building Industry Publishing Company*, Beijing, China, 2003.
- [7]. GR/T2680-94, Determination of light transmittance, solar direct transmittance, total solar energy transmittance for glass in building and related glazing factors, *China Standard Press House*, Beijing, China, 1994.
- [8]. International Standard Organization, ISO9050 Glass in building-Determination of light transmittance, solar direct transmittance and ultraviolet transmittance, and related glazing factors, 1990.



Organizing Committee:

**General Chair:**

Juan Carlos Miguez, Region 9

**Technical Program Chair:**

Daniel Slomovitz, UTE Laboratory

**Technical Program Co-Chairs:**

Bernardo Tellini, University of Pisa

Wendy Van Moer, VUB Brussels

**Publications Chair:**

Pablo Thomasset, IMS Chapter Chair

**Tutorials Chair:**

Alfredo Arnaud, Universidad Catolica Uruguay

**Special Sessions Chair:**

Conrado Rossi, Universidad de la Republica Uruguay

Important Deadlines:

**October 15, 2013**

Submission of Extended Abstracts

**January 15, 2014**

Notification of paper acceptance

**March 15, 2014**

Deadline for Camera-ready papers

Sponsored By:



Web Page:

[imtc.ieee-ims.org](http://imtc.ieee-ims.org)

## 2014 IEEE International Instrumentation and Measurement Technology Conference

**Montevideo, Uruguay May 12-15**

I<sup>2</sup>MTC 2014 spans research, development and applications in the field of instrumentation and measurement science and technology. This includes Industrial Tracks, where research merges with practical applications in industrial technology used every day. The Conference fosters the exchange of know-how between industry and academia. Paper contests will include a Conference Best Paper Award and Student Best Poster Awards. In addition to papers, the conference will also have Tutorials and Exhibits covering the entire range of Instrumentation and Measurement Technology.

The Conference focuses on all aspects of instrumentation and measurement science and technology—research, development and applications. The program topics include:

- Advances in Instrumentation and Measurement Developments and Techniques
- Biomedical Systems
- Data Acquisition Systems and Techniques
- Energy and Power Systems
- Industrial Process Control
- Measurement and Instrumentation for Industrial Applications
- Measurement Applications
- Measurement of Electric and Magnetic Quantities
- Measurement of Materials and Mechanical Quantities
- Measurement, Instrumentation and Methodologies Related to Healthcare Systems
- Measurement Systems and Theory
- Non-invasive Measurement Techniques and Instrumentation
- Real-Time Measurement
- Robotics and Controls
- Sensors and Sensor Fusion
- Signal & Image Processing Techniques
- Software Development for Measurement and Instrumentation Support
- Techniques related to Instrumentation
- Transducers
- Virtual Measurement Systems
- Wireless Sensors and Systems

Given that the 2014 conference's theme is "**Instrumentation and Measurement for Sustainable Development**", we strongly encourage submissions in the areas of energy, communication instrumentation, measurement, system development and recent advances.

Potential authors are invited to submit extended abstracts via the I<sup>2</sup>MTC website.

Each extended abstract (3 or 4 pages in English) should report results of the original research of theoretical or applied nature. The extended abstract should, moreover, explain the significance of the contribution and contain a list of key references. It must be prepared according to the abstract preparation guidelines provided on the I<sup>2</sup>MTC website. A Student Poster Contest will be held for both graduate and undergraduate student papers, with cash awards for the best papers and travel subsidies ranging from USD 300 to USD 1000, depending on student location. Extended abstracts should be submitted by the students according to the rules posted on the website and should be identified as student papers. Check the website for detailed instructions and deadlines.

Authors of accepted papers must register for the Conference and attend to present their papers. The authors of papers presented during I<sup>2</sup>MTC 2014 will be allowed to submit expanded and extended versions of their papers to the Special Issue of IEEE Transactions on Instrumentation & Measurement on I<sup>2</sup>MTC 2014 to be published in 2015.

## Aims and Scope

*Sensors & Transducers* is a peer reviewed international, interdisciplinary journal that provides an advanced forum for the science and technology of physical, chemical sensors and biosensors. It publishes original research articles, timely state-of-the-art reviews and application specific articles with the following devices areas:

- Physical, chemical and biosensors;
- Digital, frequency, period, duty-cycle, time interval, PWM, pulse number output sensors and transducers;
- Theory, principles, effects, design, standardization and modeling;
- Smart sensors and systems;
- Sensor instrumentation;
- Virtual instruments;
- Sensors interfaces, buses and networks;
- Signal processing and interfacing;
- Frequency (period, duty-cycle)-to-code converters, ADC;
- Technologies and materials;
- Nanosensors;
- Microsystems;
- Applications.

Further information on this journal is available from the Publisher's web site:  
<http://www.sensorsportal.com/HTML/DIGEST/Submission.htm>

## Subscriptions

An annual subscription includes 12 regular issues and some special issues. Annual subscription rates for 2013 are the following:

Electronic version (in printable pdf format): 400.00 EUR

Printed with b/w illustrations: 640.00 EUR

Printed full color version: 760.00 EUR

40 % discount is available for IFSA Members.

Prices include shipping costs by mail. Further information about subscription is available through IFSA Publishing's web site: [http://www.sensorsportal.com/HTML/DIGEST/Journal\\_Subscription.htm](http://www.sensorsportal.com/HTML/DIGEST/Journal_Subscription.htm)

## Advertising Information

If you are interested in advertising or other commercial opportunities please e-mail [sales@sensorsportal.com](mailto:sales@sensorsportal.com) and your enquiry will be passed to the correct person who will respond to you within 24 hours. Please download also our Media Planner 2013: [http://www.sensorsportal.com/DOWNLOADS/Media\\_Planner\\_2013.pdf](http://www.sensorsportal.com/DOWNLOADS/Media_Planner_2013.pdf)

## Books for Review

Publications should be sent to the IFSA Publishing Office: Ronda de Ramon Otero Pedrayo, 42C, 1-5, 08860, Castelldefels, Barcelona, Spain.

## Abstracting Services

This journal is cited, indexed and abstracted by Chemical Abstracts, EBSCO Publishing, IndexCopernicus Journals Master List, ProQuest Science Journals, CAS Source Index (CASSI), Ulrich's Periodicals Directory, Scirus, Google Scholar, etc. Since 2011 *Sensors & Transducers* journal is covered and indexed by EI Compendex index (including a Scopus, Embase, Engineering Village and Reaxys) in *Elsevier* products.

## Instructions for Authors

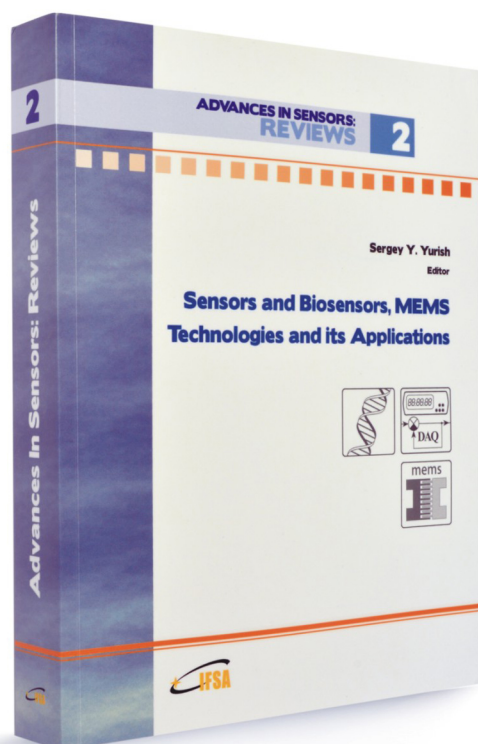
Please visit the journal web page <http://www.sensorsportal.com/HTML/DIGEST/Submission.htm> Authors must follow the instructions very carefully when submitting their manuscripts. Manuscript must be send electronically in both: MS Word 2003 for Windows (doc) and Acrobat (pdf) formats by e-mail: [editor@sensorsportal.com](mailto:editor@sensorsportal.com)

# ADVANCES IN SENSORS: REVIEWS

# 2

**Sergey Y. Yurish**  
Editor

## Sensors and Biosensors, MEMS Technologies and its Applications



The second volume titled '*Sensors and Biosensors, MEMS Technologies and its Applications*' from the '*Advances in Sensors: Review*' Book Series contains eighteen chapters with sensor related state-of-the-art reviews and descriptions of the latest achievements written by experts from academia and industry from 12 countries: China, India, Iran, Malaysia, Poland, Singapore, Spain, Taiwan, Thailand, UK, Ukraine and USA.

This book ensures that our readers will stay at the cutting edge of the field and get the right and effective start point and road map for the further researches and developments. By this way, they will be able to save more time for productive research activity and eliminate routine work.

Built upon the series *Advances in Sensors: Reviews* - a premier sensor review source, it presents an overview of highlights in the field and becomes. This volume is divided into three main parts: physical sensors, biosensors, nanoparticles, MEMS technologies and applications. With this unique combination of information in each volume, the *Advances in Sensors: Reviews* Book Series will be of value for scientists and engineers in industry and at universities, to sensors developers, distributors, and users.

Like the first volume of this Book Series, the second volume also has been organized by topics of high interest. In order to offer a fast and easy reading of the state of the art of each topic, every chapter in this book is independent and self-contained. The eighteen chapters have the similar structure: first an introduction to specific topic under study; second particular field description including sensing applications.

Order online:

[http://sensorsportal.com/HTML/BOOKSTORE/Advance\\_in\\_Sensors\\_Vol\\_2.htm](http://sensorsportal.com/HTML/BOOKSTORE/Advance_in_Sensors_Vol_2.htm)



www.sensorsportal.com

ISSN 1726- 5479



9 771726 547001